NATURAL CONVECTION HEAT TRANSFER IN AN INCLINED CIRCULAR CYLINDER

Dr. Akeel A. Mohammed **Dr. Mahmoud A. Mashkour** **Raad Shehab Ahmed**

Mech . Eng. Dep, University of Technology, Iraq- Baghdad

ABSTRACT

Experiments were carried out to investigate natural convection heat transfer in an inclined uniformly heated circular cylinder . The effects of surface heat flux and angle of inclination on the temperature and local Nusselt number variations along the cylinder surface are discussed . The investigation covers heat flux range from 92 W/m² to 487 W/m², and angles of inclination 0° (horizontal) , 30° , 60° and 90° (vertical) . Results show an increase in the natural convection as heat flux increases and as angle of inclination moves from vertical to horizontal position. An empirical equation of average Nusselt number as a function of Rayliegh number was deduced for each angle of inclination .

الخلاصة

أجريت تجارب لدراسة عملية انتقال الحرارة بالحمل الحر في أسطوانة دائرية مائلة مسخنة تسخين منتظم. تم مناقشة تأثيرات الفيض الحراري للسطح وزاوية الميل على تغيرات درجة الحرارة و رقم نسلت الموقعي خلال سطح الأسطوانة. غطت الدراسة مدى الفيض الحراري من (92 الى 487) واط/متر مربع و زوايا ميل 0°(افقي)، 30°،60° و 90° (عمودي) . بينت النتائج بأن الحمل الحر يزداد كلما زاد الفيض الحراري و كلما تغيرت زاوية الميل من الوضع العمودي إلى الوضع الأفقي. تم استنباط معادلة تجريبية لمعدل رقم نسلت كدالة لرقم رايلي لكل زاوية ميل.

KEY WORDS: Heat Transfer, Natural Convection, Cylinder.

INTRODUCTION

The problem of natural convection heat transfer across a channel of various cross-section(rectangular , circular , concentric annulus and parallel plates) has received considerable attention in view of its fundamental importance germane to numerous engineering application such as electronic systems , chemical process equipments , combustion chambers , environmental control systems and so on .Bae and Hun (2003) carried out a study on air cooling in an unsteady laminar natural convection in a vertical rectangular channel with three flush mounted heat sources on one vertical wall .The results show the effects of the thermal conditions of the lowest source on the downstream sources . The study emphasizes that the transient temperatures may exceed average values in time . This is important for designing electronic equipment projects . Madhavan and Sastri (2003) developed a parametric study of natural convection in a set of boards inside an enclosure . Each board has heat sources . This layout has direct application on electronic equipment cooling . Its noted that the Rayliegh and the Prandtl numbers as well as the boundary conditions strongly affect the fluid flow and heat transfer features . Vande Sande and Hamer (1979) have obtained empirical correlations for natural convection heat transfer in concentric and eccentric annuli of constant heat flux inner cylinder while the outer cylinder was subjected to the ambient temperature . An empirical equation of average Nusselt number as a function of Rayliegh number was deduced . There are no available literatures concerning the heat transfer by natural convection in an inclined insulated circular cylinder . The present study covers this lack and gives a clear view to actual physical behavior in the heat transfer process by natural convection

EXPERIMENTAL APPARATUS

The apparatus consists essentially of settling chamber (D), cylinder as a test section mounted on an iron frame, which can be rotated around a horizontal spindle (to adjust the inclination angle of cylinder as required) as shown in Fig.(1). A well designed teflon bell mouth (H) was fitted at the beginning of aluminum cylinder (I) and bolted in the other side inside the settling chamber (D). Another Teflon piece (M) represents the cylinder exit and has the same dimensions as the inlet piece. The teflon was chosen due to its low thermal conductivity to reduce the heat loss from the aluminum cylinder ends. The inlet air temperature was measured by one thermocouple located in the settling chamber (J) while the outlet bulk air temperature was measured by two thermocouples located in the test section exit (Z). The local bulk air temperature was calculated by using a straight line interpolation between the measured inlet and outlet bulk air temperatures. The test section consists of 3.5 mm wall thickness, 59.3 mm outside diameter and 1.2 m long aluminum cylinder. The cylinder was heated electrically using an electrical heater which consisted of a 1 mm in diameter and 60 m in length nickel-chrome wire electrically isolated by ceramic beads, wounds uniformly as a coil with 10 mm pitch. The outside of the test section was then thermally insulated, covered with 60 mm and 5.7 mm as thickness for asbestos rope layer and fiber glass, respectively. To enable the calculation of heat loss through the lagging (P) to be carried out, six thermocouples are inserted in the lagging as two thermocouples at three points along the heated section 390 mm apart. Using the average measured temperature drop and thermal conductivity of lagging the heat losses through lagging can be calculated.

The cylinder surface temperature were measured by eighteen asbestos sheath thermocouples (type K), arranged along the cylinder. The thermocouples were fixed by drilling 18 holes of 2mm diameter and approximately 3 mm deep in and along the cylinder wall while the ends of the holes chamfered by drill then the measuring junction were secured permanently in the holes by a high temperature application epoxy steel adhesive. The excess adhesive was removed and the cylinder surface was cleaned carefully by fine grinding paper. All the thermocouple wires and heater terminals were taken out the test section. All thermocouples were used with leads and calibrated using the melting point of ice made from distilled water as reference point and the boiling points of several pure chemical substances. To determine the heat loss from the test section ends, two thermocouples were fixed in each teflon piece. Knowing the distance between these thermocouples and the thermal conductivity of the teflon, the heat ends loss thus can be calculated.

Experimental Procedure

To carry out the experiments the following procedure was followed:

1. The inclination angle of the cylinder was adjusted as required.
2. The electrical heater was switched on and the heater input power then adjusted to give the required heat flux.
3. The apparatus was left at least two hours to establish steady state condition. The thermocouples readings were measured every half an hour by means of the digital electronic thermometer until the reading became constant, a final reading was recorded. The input power to the heater could be increased to cover another run in a shorter period of time and to obtain steady state conditions for next heat flux. Subsequent runs for other ranges of cylinder inclination angles were performed in the same previous procedure.
4. During each test run , the following readings were recorded:

a. The angle of inclination of the cylinder in degree.

b. The readings of the thermocouples in ˚C.

d. The heater current in amperes.

e. The heater voltage in volts.

Data Analysis

Simplified steps were used to analyze the heat transfer process for the air flow in a cylinder when its surface was subjected to a uniform heat flux.

The total input power supplied to the cylinder can be calculated:

$$Q_t = V'' \times I \qquad \textbf{...(1)}$$

The convection and radiation heat transferred from the cylinder is :

$$Q_{cr} = Q_t - Q_{cond} \qquad \textbf{...(2)}$$

where Q_{cond} is the conduction heat loss which was found from the following equation:

$$Q_{cond.} = \frac{\Delta T_{oi}}{\dfrac{\ln \frac{r_o}{r_i}}{2\pi k_a L}} \qquad \textbf{...(3)}$$

where:

$\Delta T_{oi} = T_o - T_i$

The convection and radiation heat flux can be represented by:

$$q_{cr} = Q_{cr}/A_o \qquad \textbf{...(4)}$$

The local radiation heat flux can be calculated from the expression [Holman 1984]:

$$q_r = F_{1-2}\,\varepsilon\,\sigma\left[\left((T_s)_z + 273\right)^4 - \left((T_s)_z + 273\right)^4\right] \qquad \textbf{...(5)}$$

but, $F_{1-2} \approx 1$

hence the convection heat flux at any position is:

$$q = q_{cr} - q_r \qquad \textbf{...(6)}$$

The radiation heat flux is very small and can be neglected.

hence:

$q_{cr} \approx q$ = convection heat flux

The local heat transfer coefficient can be obtained as:

$$h_z = \frac{q}{(T_s)_z - (T_b)_z} \qquad \textbf{...(7)}$$

All the air properties are evaluated at the mean film air temperature

$$(T_f)_z = \frac{(T_s)_z + (T_b)_z}{2} \qquad \textbf{...(8)}$$

The local Nusselt number (Nu_z) then can be determined as:

$$Nu_z = \frac{h_z D_h}{k} \qquad \text{…(9)}$$

The average values of Nusselt number Nu_m can be calculated as follows:

$$Nu_m = \frac{1}{L}\int_0^L Nu_z dz \qquad \text{…(10)}$$

The average values of the other parameters can be calculated based on calculation of average cylinder surface temperature and average bulk air temperature as follows:

$$\overline{T}_s = \frac{1}{L}\int_{z=0}^{z=L} (T_s)_z \; dz \qquad \text{...(11)}$$

$$\overline{T}_b = \frac{1}{L}\int_{z=0}^{z=L} (T_b)_z \; dz \qquad \text{...(12)}$$

$$\overline{T}_f = \frac{\overline{T}_s + \overline{T}_b}{2} \qquad \text{…(13)}$$

$$Gr_m = \frac{g \;\beta\; D_h^3 \left(\overline{T}_s - \overline{T}_b\right)}{\nu^2} \qquad \text{...(14)}$$

$$Pr_m = \frac{\mu \;\; C_p}{k} \qquad \text{…(15)}$$

$$Ra_m = Gr_m Pr_m \qquad \text{...(16)}$$

where;

$$\beta = 1 \big/ \left(273 + \overline{T}_f\right)$$

All the air physical properties ρ, μ, ν, and k were evaluated at the average mean film temperature ($\overline{T}_f$) [Grimson 1971].

Error Analysis

The accuracy of obtaining experimental results depends upon two factors: the accuracy of measurements and the nature of rig design. There is no doubt that, the maximum portion of errors in calculations referred essentially to the errors in the measured quantities. Hence, to calculate the error in the obtained results, Kline and McClintock method [Holman 1984] is used in this field.

Let the result R be a function of n independent variables: $v_1, v_2 \ldots.. v_n$

$$R = R(v_1, v_2 \ldots\ldots\ldots v_n) \qquad \text{…(17)}$$

For small variations in the variables, this relation can be expressed in linear form as [Holman 1984]:

$$\delta R = \frac{\partial R}{\partial v_1}\delta v_1 + \frac{\partial R}{\partial v_2}\delta v_2 + \ldots\ldots + \frac{\partial R}{\partial v_n}\delta v_n \qquad \text{...(18)}$$

Hence, the uncertainty interval (w) in the result can be given as:

$$w_R = \left[\left(\frac{\partial R}{\partial v_1} w_1\right)^2 + \left(\frac{\partial R}{\partial v_2} w_2\right)^2 + \ldots\ldots\ldots + \left(\frac{\partial R}{\partial v_n} w_n\right)^2\right]^{1/2} \qquad \text{...(19)}$$

Eq.(19) is greatly simplified upon dividing by R to nondimensionalize:

$$\left(\frac{w_R}{R}\right)^2 = \left(\frac{\partial R}{\partial v_1}\frac{w_1}{R}\right)^2 + \left(\frac{\partial R}{\partial v_2}\frac{w_2}{R}\right)^2 + \ldots\ldots\ldots + \left(\frac{\partial R}{\partial v_n}\frac{w_n}{R}\right)^2 \qquad (20)$$

Hence, the experimental errors that may happen in the used variables are given in Table(1) which is taken from measuring devices as follows:

Independent variables (v)	uncertainty interval (w)
Surface to bulk air temperature	**± 0.16 ^oC**
Voltage of the heater	**± 0.04 volt**
Current of the heater	**± 0.0003 Amp**
Hydraulic diameter	**± 0.0002 m**
Average outer and inner lagging surface temperature	**± 0.11 °C**

The local Nusselt number equation can be written as follows:

$$Nu_z = \frac{\left(Q_t - Q_{cond.}\right)D_h}{\Delta T_s A_s k}$$

$$Nu_z = \frac{\left(V.I - \dfrac{\Delta T_{oi}}{\dfrac{\ln\frac{r_o}{r_i}}{2\pi k_a L}}\right)D_h}{\Delta T_s A_s k} = \frac{\left(V.I - \dfrac{\Delta T_{oi}}{C}\right)D_h}{\Delta T_s A_s k} \qquad \text{…(21)}$$

Where C is constant $= \dfrac{\ln \frac{r_o}{r_i}}{2\pi k_a L}$

The experimental errors in the local Nusselt number calculation can be expressed in the following manner:

$$\frac{\partial Nu_z}{\partial V}=\frac{I.D_h}{\Delta T_s A_s k}$$

$$\frac{\partial Nu_z}{\partial I}=\frac{V.D_h}{\Delta T_s A_s k}$$

$$\frac{\partial Nu_z}{\partial D_h}=\frac{\left(V.I-\frac{\Delta T_{io}}{C}\right)}{\Delta T_s A_s k}$$

$$\frac{\partial Nu_z}{\partial \Delta T_s}=-\frac{\left(VI-\frac{\Delta T_{oi}}{C}\right)D_h}{(\Delta T_s)^2 A_s k}$$

$$\frac{\partial Nu_z}{\partial \Delta T_{oi}}=-\frac{D_h}{C\Delta T_s A_s k}$$

$$\frac{\partial Nu_z}{\partial A_s}=-\frac{\left(V.I-\frac{\Delta T_{oi}}{C}\right)D_h}{(A_s)^2 \Delta T_s k}$$

$$w_{Nuz}=\left[\left(\frac{\partial Nu_z}{\partial V}w_v\right)^2+\left(\frac{\partial Nu_z}{\partial I}w_I\right)^2+\left(\frac{\partial Nu_z}{\partial D_h}w_{D_h}\right)^2+\left(\frac{\partial Nu_z}{\partial \Delta T_s}w_{\Delta t_s}\right)^2+\left(\frac{\partial Nu_z}{\partial A_s}w_{A_s}\right)^2+\left(\frac{\partial Nu_z}{\partial \Delta T_{oi}}w_{\Delta T_{oi}}\right)^2\right]^{1/2} \qquad (22)$$

or,

$$\left(\frac{w_{Nu_z}}{Nu_z}\right)^2=\left[\left(\frac{w_V}{V}\right)^2+\left(\frac{w_I}{I}\right)^2+\left(\frac{w_{D_h}}{D_h}\right)^2+\left(\frac{w_{\Delta T_s}}{\Delta T_s}\right)^2+\left(\frac{w_{A_s}}{A_s}\right)^2+\left(\frac{W_{\Delta T_{oi}}}{\Delta T_{oi}}\right)^2\right]$$

RESULTS AND DISCUSSION

TEMPERATURE VARIATION

The variation of cylinder surface temperature for different heat flux and for angle of inclination $\alpha = 0°$ (horizontal) , 30°, 60°,and 90°(vertical) are shown in Figs.(2- 5) ; respectively . It is obvious from these figures that the surface temperature increases as heat flux increases because of faster increasing of the thermal boundary layer as heat flux increases (i.e. , increasing of buoyancy effect) . Fig.6 & 7 show the effect of angle of inclination on the temperature distribution along the cylinder surface for low heat flux q= 103 w/m² and high heat flux q=420 w/m² ; respectively .It is clear that the surface temperature increases as angle of inclination moves from horizontal to vertical position . This behavior can be attributed to the fact that says as the air is heated and dilates , the difference between air density near the wall and the cylinder center causes a circulation which displaces the wall air in a direction parallel to the gravity vector . When the heat transfers through the wall of a horizontal cylinder , the warmer air moves upward along the side walls , and by continuity the heavier air near the center of the cylinder flows downward . As a result , a two symmetrical spiral, like motion is formed along the cylinder . The circulation is driven by radial temperature variation , and at the same time it reduces this temperature variation . These two spiral vortex weak as the angle of inclination moves from horizontal to vertical position to be single vortex only . Therefore ; it is expected that the heat transfer process in horizontal position is better than that in other positions .

LOCAL NUSSELT NUMBER

The local Nusselt number variation along the cylinder surface for different heat flux and for angle of inclination α =0° (horizontal) , 30° ,60° ,and 90° (vertical);are shown in Figs.(8-11) ; respectively. Generally , It is obvious from these figures that the local Nusselt number values increase as the heat flux increases because of increasing natural convection currents which improves the heat transfer process . The effects of angle inclination on the local Nusselt number variation are shown in Fig. (12 & 13) for low heat flux q = 103 w/m² , and high heat flux q =420 w/m² ; respectively . As be expected ,it is clear from these two figures that , the local Nusselt number increases relatively as angle of inclination moves from vertical to horizontal position for the same heat flux . This fact appears more pronounced in low heat flux than high heat flux.

AVERAGE NUSSELT NUMBER

Figs. (14–17) show the logarithmic of mean Nusselt number versus logarithmic Rayliegh number for α = 0° (horizontal) , 30° , 60° , and 90° (vertical) ; respectively . An empirical equations have been deduced from these figures as follows :-

$Nu_m = 5.7099\ Ra^{-1.1553}$ $\alpha = 0°$ (horizontal)
$Nu_m = 6.1366\ Ra^{-1.2168}$ $\alpha = 30°$
$Nu_m = 3.1263\ Ra^{-1.6637}$ $\alpha = 60°$
$Nu_m = 2.5031\ Ra^{-1.3296}$ $\alpha = 90°$ (vertical)

CONCLUSIONS

1. The extent of the local mixing increases as the heat flux increases .
2. The heat transfer process improves as heat flux increases and as angle of inclination moves from vertical to horizontal .
3. The effect of buoyancy is small at the cylinder entrance and increases downstream.

REFERENCES

Akeel Abdullah Mohammed " Natural convection heat transfer in a vertical concentric annulus " J. of Engineering , a scientific Refereed Journal Published by college of Engineering University of Baghdad , No. 2 Vol. 13 pp June 2007.

Bae ,J. H. and Hun ,J.M. "Time-dependent Buoyant convection in an Enclosure with Discrete Heat sources " ,Int. J. Thermal sciences , In press (2003)

Grimson, J. " Advance fluid dynamic and heat transfer", McGraw-Hill, England, (1971).

Holman, J. P. " Experimental Method For Engineers", McGraw-Hill, Tokyo, Japan, 4th Edition (1984)

Madhavan , P.N. and sastri , V.M.K. "Conjugate Natural convection cooling of Protruding Heat Sources Mounted on a substrate placed Inside an Enclosure : a parametric study " , Comput Methods Appl. Mech . Eng. , 188,187-202 (2003)

Vande Sarde , E. and Hamer , B. J . G ." Steady and transient natural convection in enclosures between horizontal circular cylinders (constant heat flux). Int. J . Heat Mass Transfer , 1979 , 22 , 361 – 370.

NOMENCLATURE

A_o =outer surface area of cylinder $=2\pi\ r_o\ L$
A_s = cylinder surface area = $\pi\ D_i\ L$
c, specific heat of fluid at constant pressure ;
g , gravitational body force per unit mass ;
Gr , modified Grashof number , $q''g\beta L^4/k\nu^2$;
L=length of cylinder
k_a=thermal conductivity of asbestos=0.161 $W/m^3.°C$
k=thermal conductivity of air = 0.6099 $W/m^2°C$
Nu_z; local Nusselt number
Pr, Prandtl number , $\mu c/k$;
q, heat flux;
r_o=the distance from center of cylinder to the outer lagging surface
r_i=the distance from center of cylinder to the beginning lagging (radius of outer cylinder surface)
T_o=average outer lagging surface temperature
T_i=average inner lagging surface temperature

$(T_s)_z$ = local temperature of cylinder.
$\overline{(T_s)}_z$ = average temperature of cylinder.
$(T_b)_z$ = Local bulk air temperature.
T_f = Local mean film air temperature.
$\Delta T_s = T_s - T_b$

Greek symbols

β , volumetric coefficient of thermal expansion ;
ρ , fluid density ,
μ , dynamic viscosity of fluid ;
ν , kinematic viscosity of fluid ;
σ = Stefan beltzman constant = 5.66×10^{-8} $W/m^2\ °K^4$
ε = emissivity of the polished aluminum surface=0.09

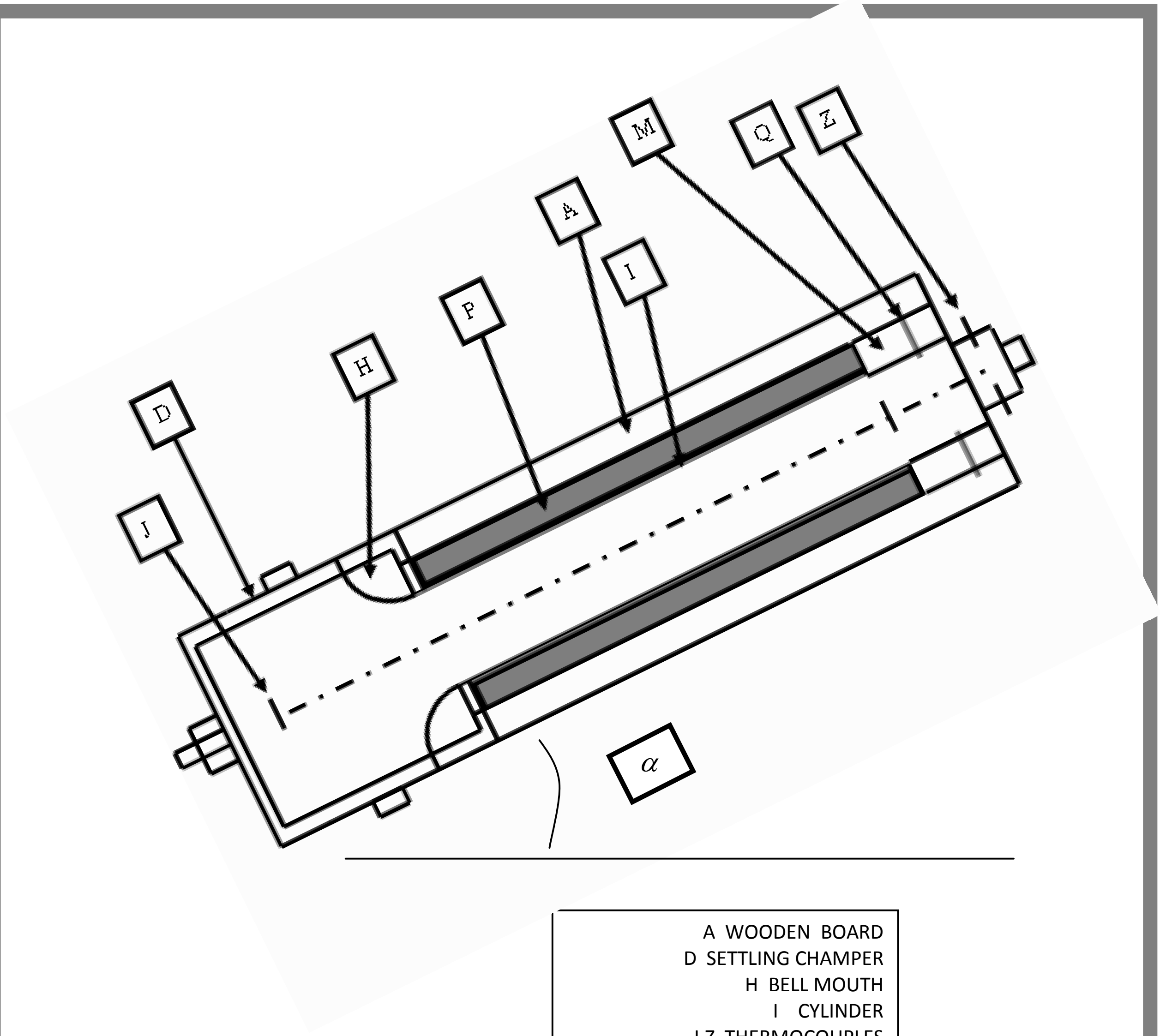

A WOODEN BOARD
D SETTLING CHAMPER
H BELL MOUTH
I CYLINDER
J,Z THERMOCOUPLES
M TEFLON PIECE
P LAGGING
Q SCREW
ANGLE of INCLINATION α

Fig.(1): Diagram of Experimental Apparatus.

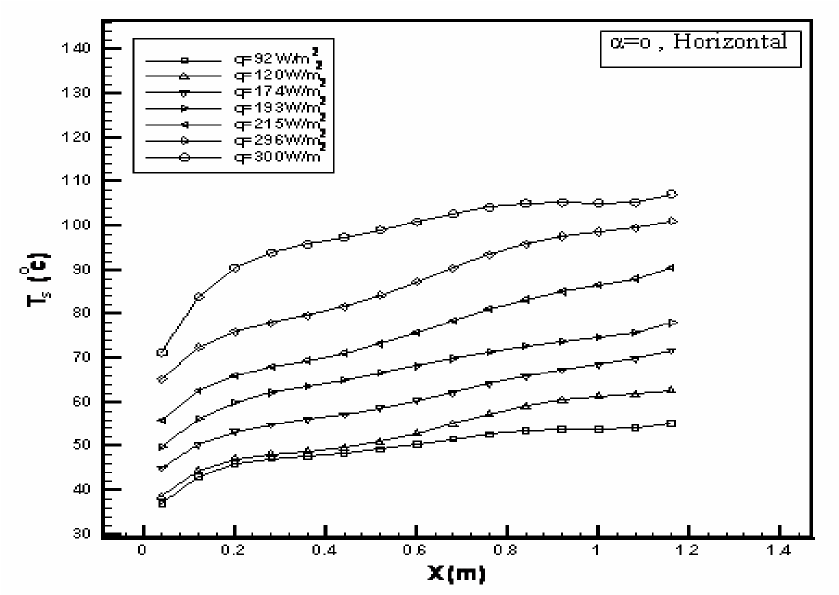

Fig. (2): Experimental Variation of the Surface Temperature with the Axial Distance, $\alpha = 0^{\circ}$ (Horizontal).

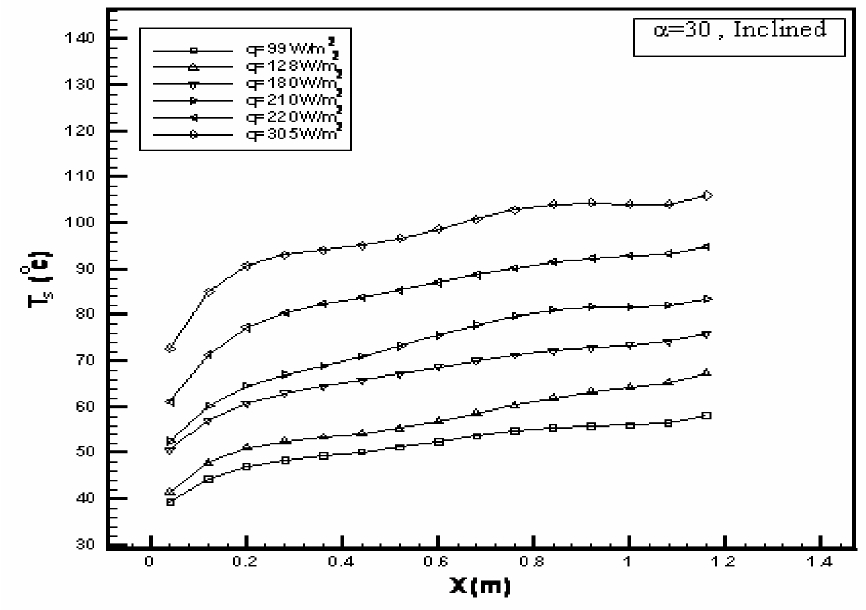

Fig. (3): Experimental Variation of the Surface Temperature with the Axial Distance, $\alpha = 30^{\circ}$ (Inclined).

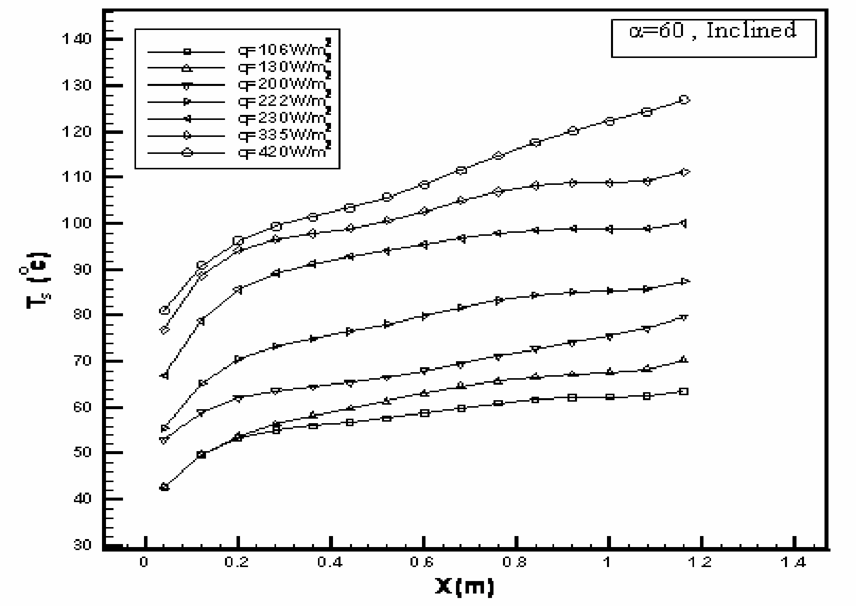

Fig. (4): Experimental Variation of the Surface Temperature with the Axial Distance, $\alpha = 60^{\circ}$ (Inclined).

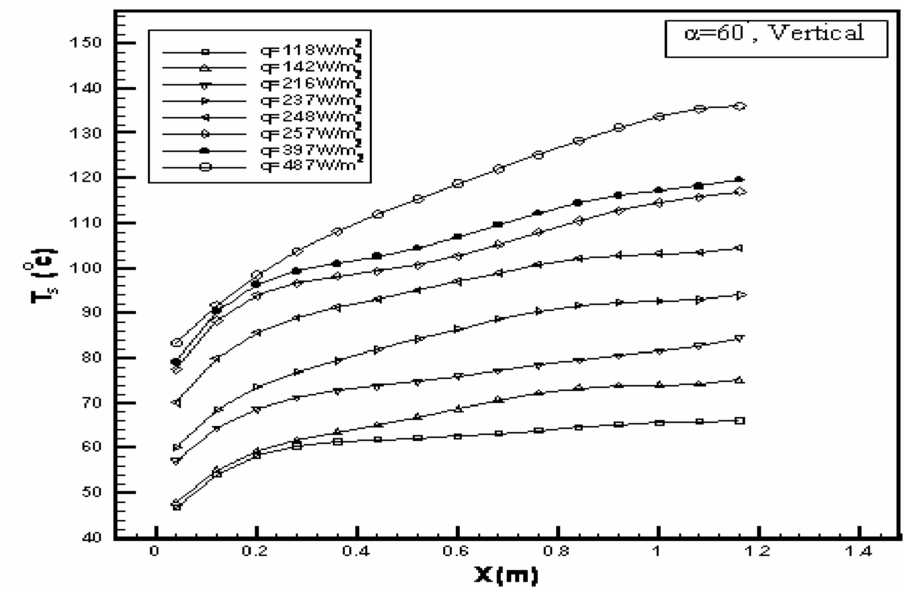

Fig. (5): Experimental Variation of the Surface Temperature with the Axial Distance, $\alpha = 90^{\circ}$ (Vertical).

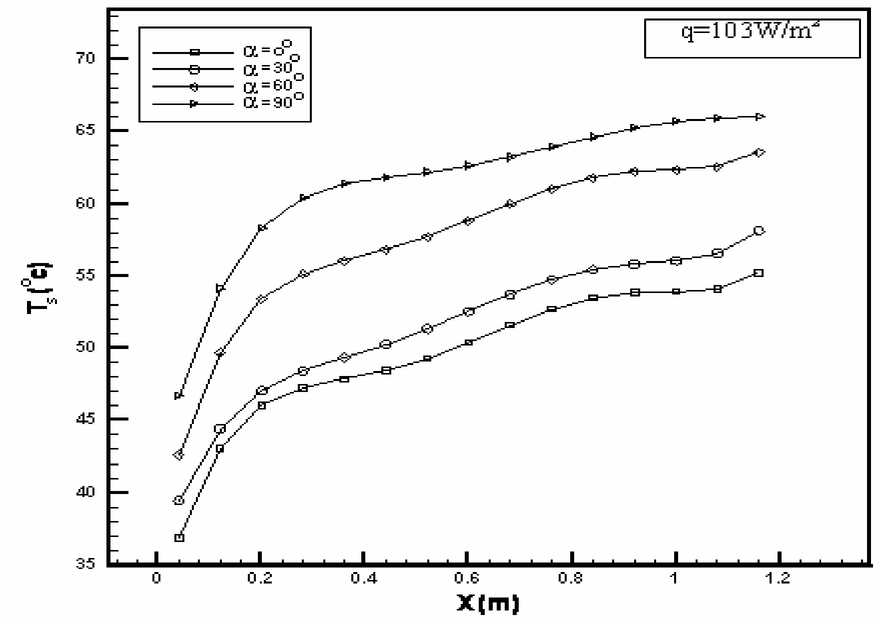

Fig.(6): Experimental Variation of the Surface Temperature with the Axial Distance for Various Angles, q=103W/m^2.

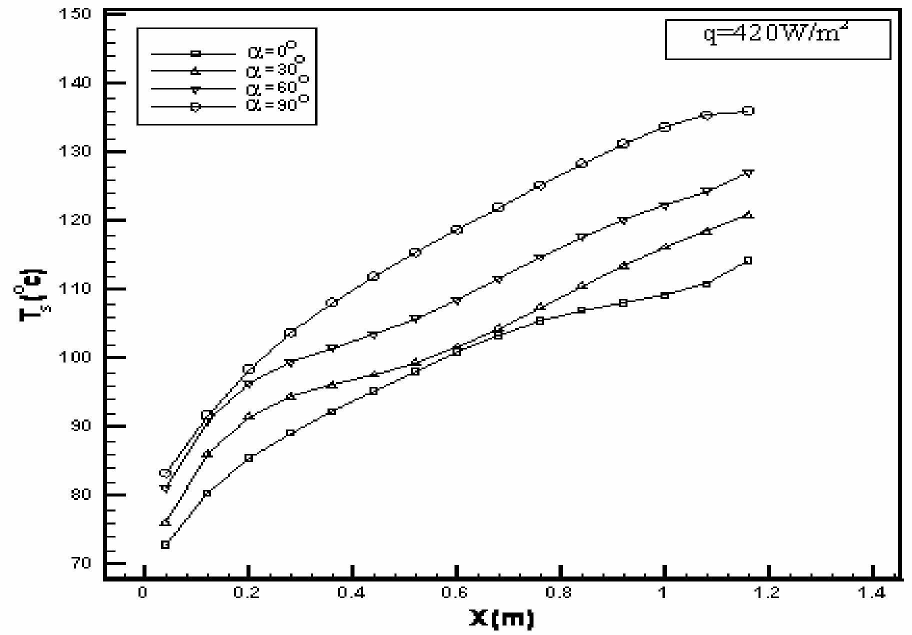

Fig.(7): Experimental Variation of the Surface Temperature with the Axial Distance for Various Angles, q=420W/m^2.

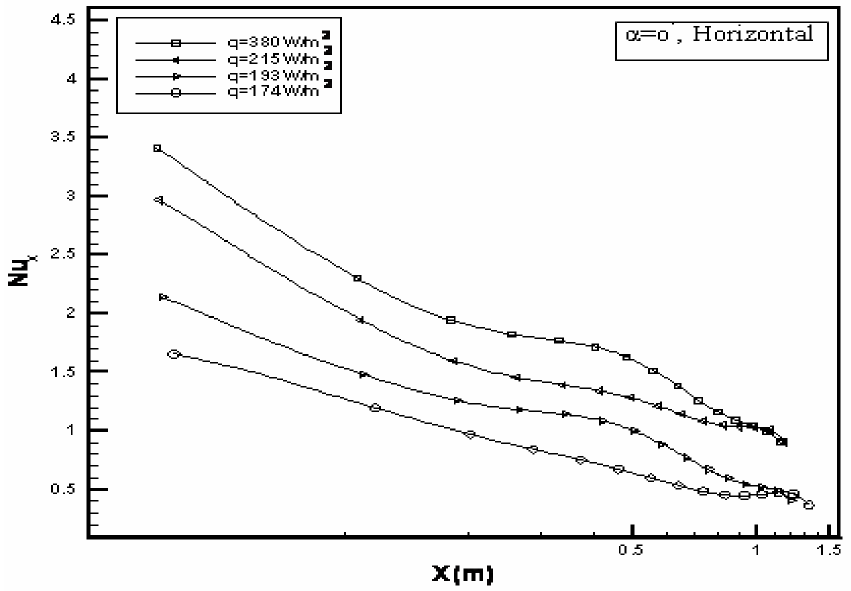

Fig.(8): Experimental, Variation of the local Nusselt number with the Axial Distance, $\alpha = 0^{o}$ (Horizontal).

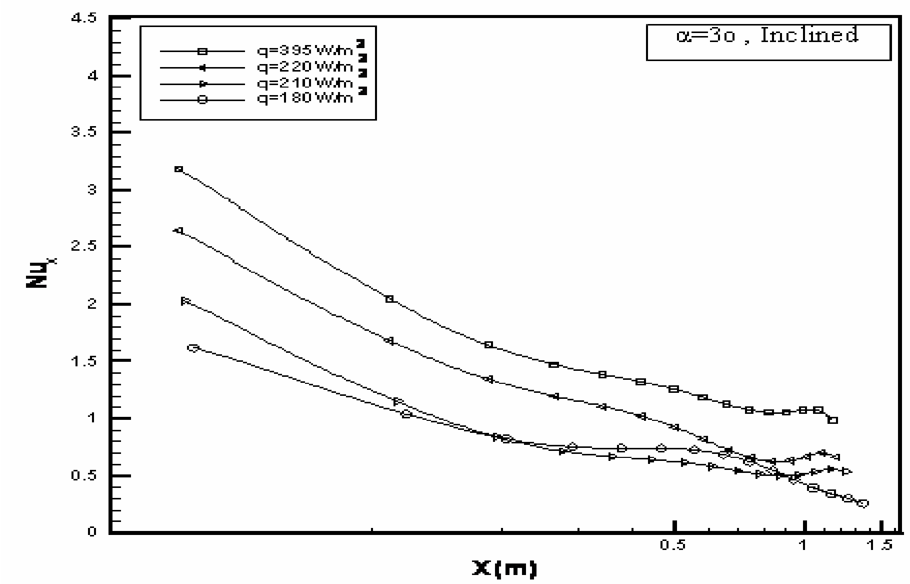

Fig.(9): Experimental, Variation of the local Nusselt number with the Axial Distance, $\alpha = 30^{o}$ (Inclined).

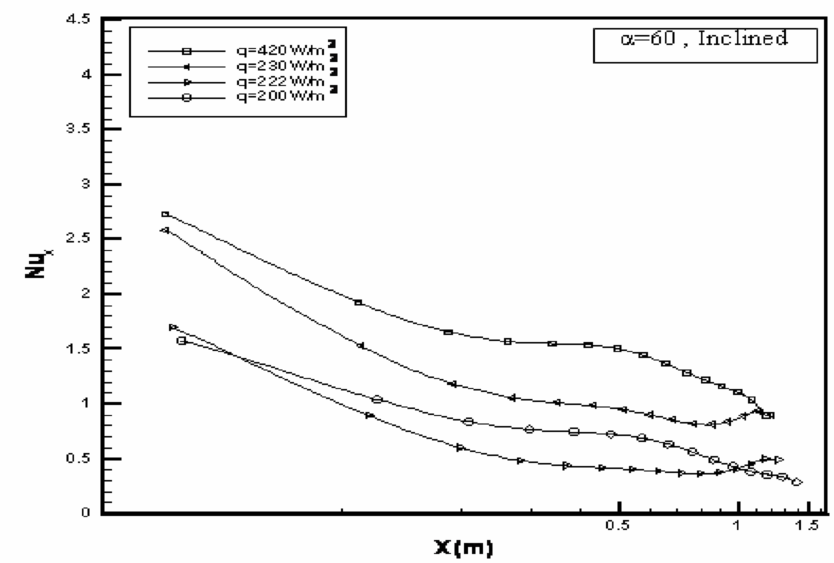

Fig.(10): Experimental, Variation of the local Nusselt number with the Axial Distance, α =60° (Inclined).

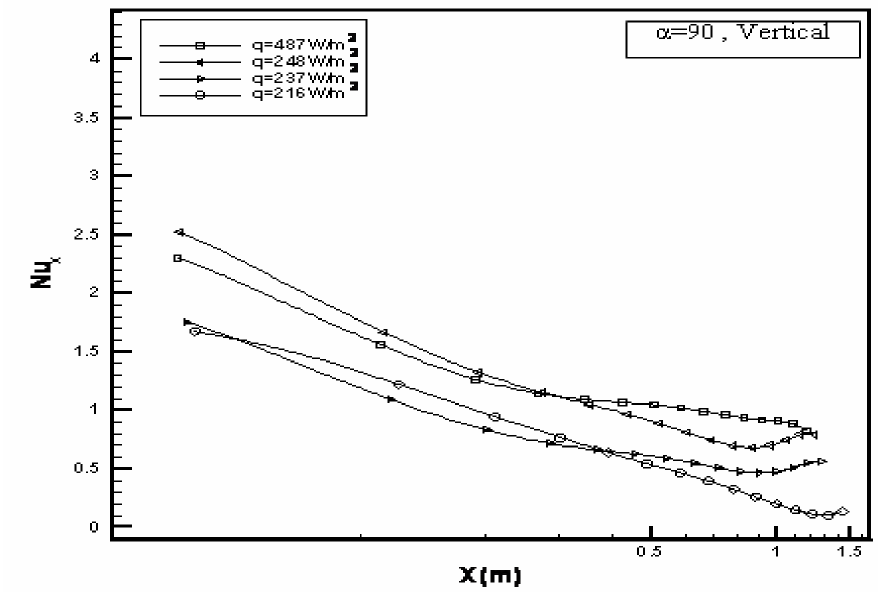

Fig.(11): Experimental, Variation of the local Nusselt number with the Axial Distance, α =90^o (Vertical).

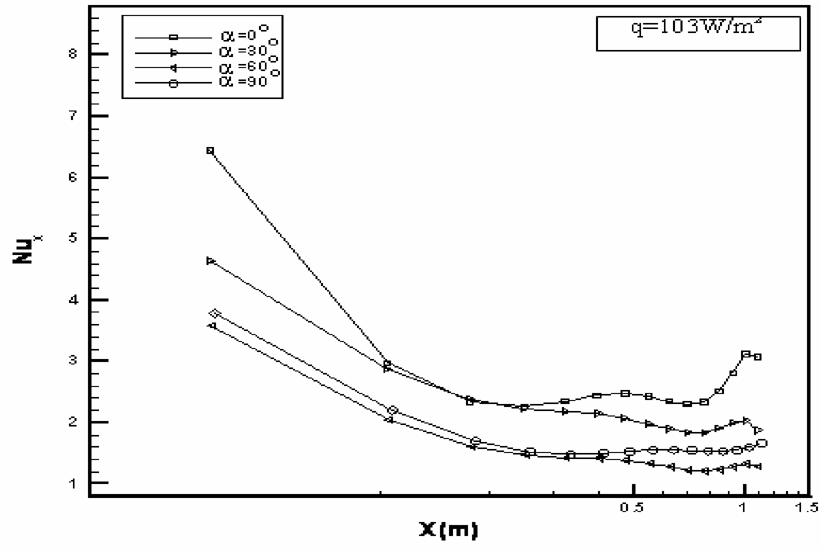

Fig.(12): Experimental Variation of the Local Nussel number with the Axial Distance for Various Angles, q=103W/m^2.

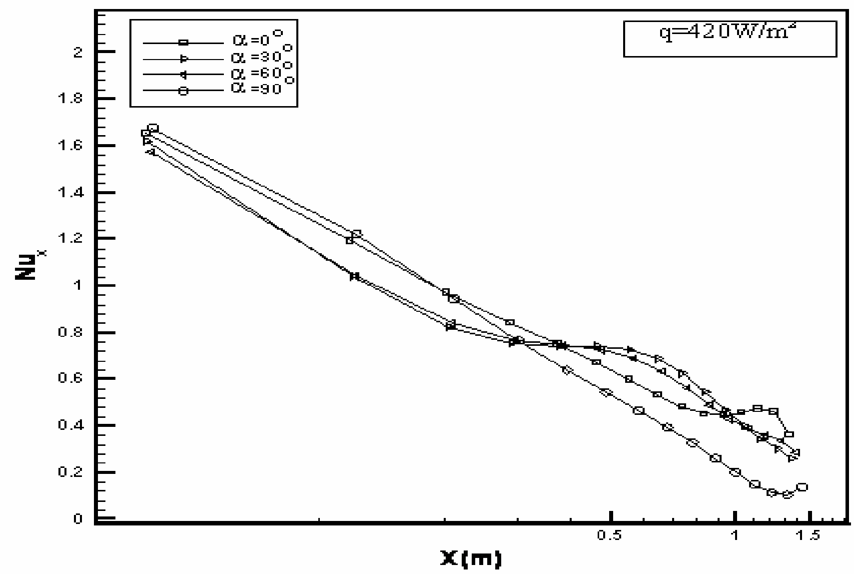

Fig.(13): Experimental Variation of the Local Nussel number with the Axial Distance for Various Angles, q=420W/m^2.

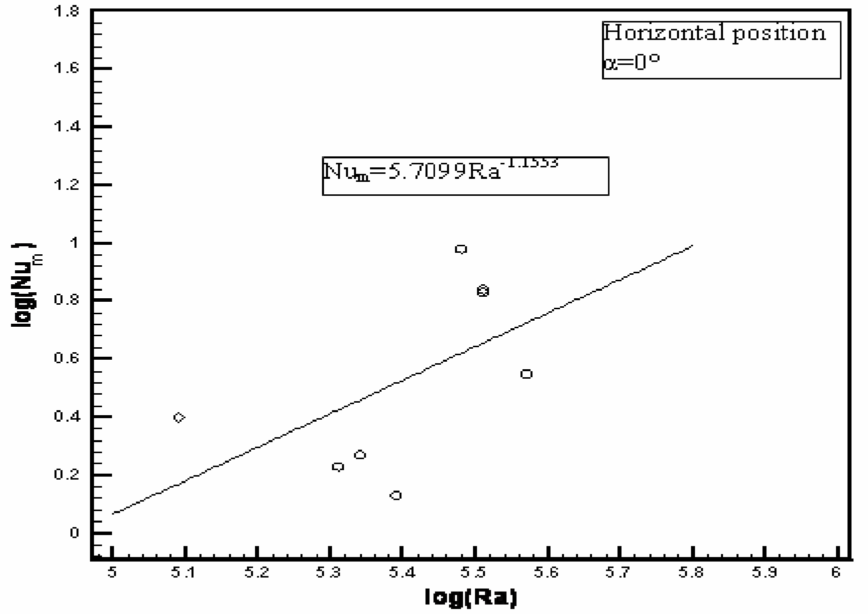

Fig.(14): Experimental Average Nusselt number Versus Ra, $\alpha = 0^{\circ}$.

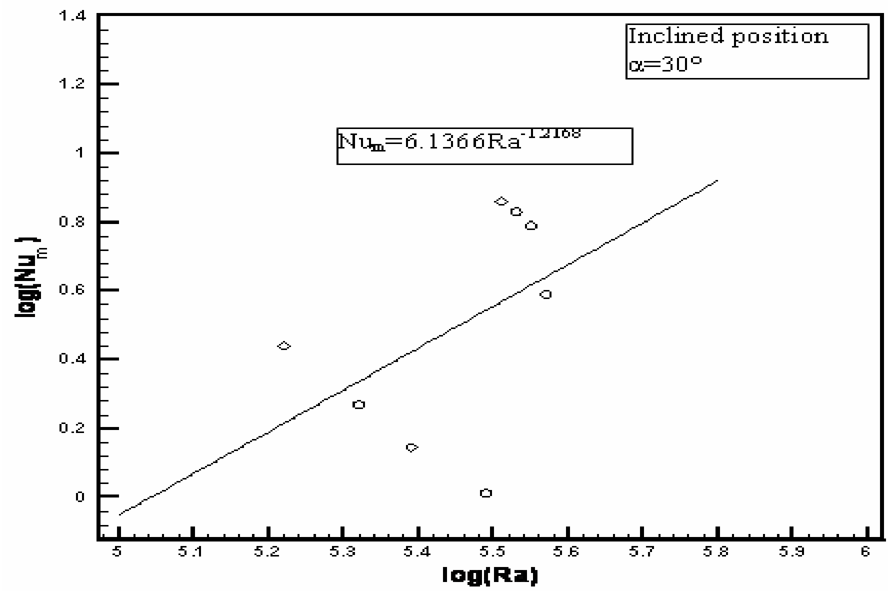

Fig.(15): Experimental Average Nusselt number Versus Ra, $\alpha = 30^{\circ}$.

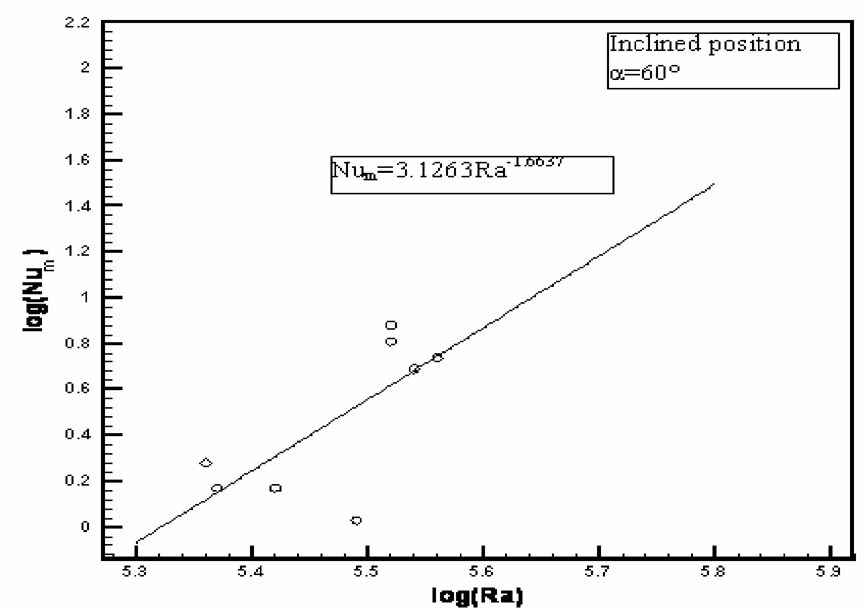

Fig.(16): Experimental Average Nusselt number Versus Ra, α =60°.

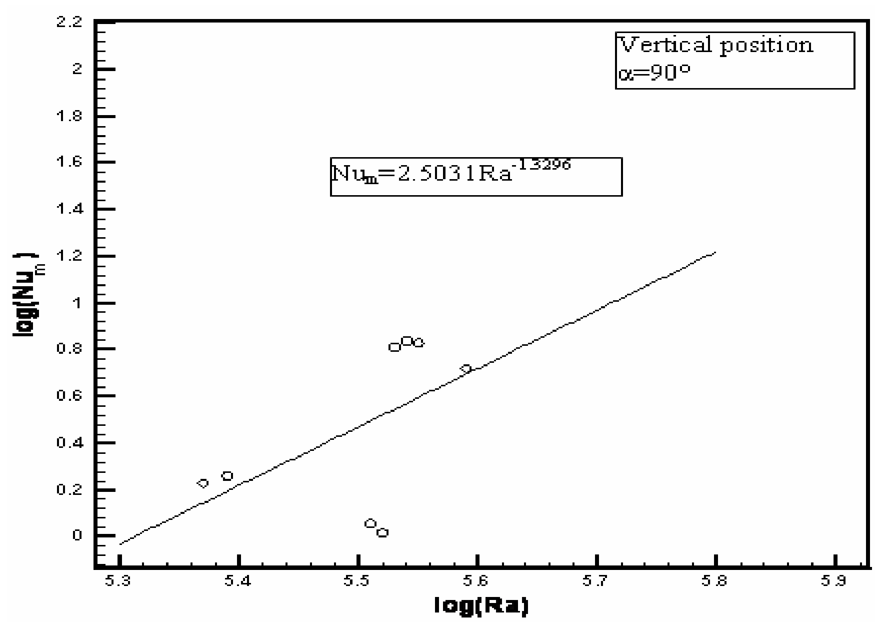

Fig.(17): Eperimental Average Nusselt number Versus Ra, α =90°.

INVESTIGATION OF TWISTED TAPE TURBULATOR FOR FIRE TUBE BOILER
Part I. Heat Transfer

Ass. Prof. Dr. Karima E. Amori **Rashid K. Insayif***
***MSc. student (Univ. of Baghdad, College Of Engineering, Mech. Eng. Dept.)**

ABSTRACT:

The present work presents a new experimental study of the enhancement of turbulent convection heat transfer inside tubes for combined thermal and hydrodynamic entry length of one popular "turbulator" (twisted tape with width slightly less than internal tube diameter) inserted for fire tube boilers. Cylindrical combustion chamber was used to burn (1.6 to 7kg/h) fuel oil #2 to deliver hot gases with ranges of Reynolds number (10500 to 21700), and (11400 to 24150) for both empty and inserted tube respectively.A uniform wall temperature technique was used by keeping approximately constant water temperature difference (25ºC) between inlet and exit cooling water in parallel flow shell and tube heat exchanger. The test tube consisted of smooth carbon steel tube of (2400mm) long and (52mm) internal diameter. This test tube instrumented to derive local heat transfer coefficient and local flue gasses static pressure.The experimental results show that for the same fuel consumption, twisted tape insert with (H/D = 11.15) enhanced the mean Nusselt number in (75.2%), (68.8%), (49.8%), (40.3%), and (16.7%) for fuel consumption (7kg/h), (6.16kg/h), (4.5kg/h), (3.24kg/h), and (1.6kg/h) respectively.A set of empirical correlations that permit the evaluation of the mean Nusselt number (for developing and fully developed region), and average Nusselt number (for developed region) for empty and inserted tube are generated for engineering applications.

Keywords: **fire tube boiler; twisted tape; heat transfer enhancement**

الخلاصة:

هذا البحث يقدم دراسة عملية جديدة لتحديد التحسين الحاصل في معامل انتقال الحرارة لغازات الاحتراق المارة داخل انابيب مراجل انابيب النار عند ادخال شريط معدني ملتوي بعرض يقل قليلا عن قطر الانبوب.تم تجهيز غازات الاحتراق من غرفة احتراق اسطوانية الشكل يتم فيها حرق كمية من الوقود السائل الخفيف رقم 2 تتراوح من (1.6 – 7 كغم/ساعة) بحيث يعطي رقم رينولدز من (10500-21700) للانبوب الفارغ و(11400-24150) للانبوب المدخل فيه الشريط الملتوي.تمت المحافظة على درجة حرارة جدار الأنبوب منتظمة وذلك بالسيطرة على فرق 25 درجة مئوية بين درجة حرارة الماء الداخل والخارج في مبادل حراري نوع (الغلاف والانبوب) بجريان متوازي بطول انبوب 2400 ملم وقطر داخلي 52ملم . ربطت على هذا الانبوب مجموعة من اجهزة القياس التي ساعدت على حساب معامل انتقال الحرارة والضغط الاستاتيكي الموقعي على طول الانبوب .بينت نتائج الحسابات ان الشريط الملتوي يُحسن القيمة المتوسطة لرقم نسلت بمقدار (75.2%) ، (68.8%) ، (49.8%) ، (40.3%) ، (16.7%) لنفس الكمية من صرف الوقود (7. 6.16 4.5 3.2 1.6 كغم /ساعة) على التوالي .تم استنتاج مجموعة من المعادلات لحساب القيمة المتوسطة لرقم نسلت على طول الانبوب فضلا عن احتساب قيمة متوسطة لرقم لنسلت في منطقة الجريان التام التطور للانبوب الفارغ والمدخل فيه الشريط الملتوي .

INTRODUCTION

Fire-Tube Boilers (FTB) are the most common heating devices that transfer heat from the combustion gases (flue gases) to water in order to have hot-water up to 3000 kW or saturated steam ranging up to 25 ton/h at 25 bar. In fire tube boiler, the furnace is filled with flame and hot gases, while tubes are filled with hot gases. These tubes and furnace are submerged in same water, giving the boiler name - fire tube boiler.

The efficiency of the first design of FTB until 1985 is very low, up to 70% due to utilizing too many tubes, too much refractory, and in many cases too small furnace. All of this as a direct consequence of poor knowledge of heat transfer inside FTB. After 1985 new FTB design starts, energy saving and reducing fuel consumption has been studied extensively, taken into consideration air pollution. Modes of Heat Transfer in Fire Tube Boilers are divided into: (1-) radiation which is the main mode of heat transfer in furnace, (2-) convection which represent up to 95% of heat exchange in hot gases tubes (the influence of radiation will be lower due to lower temperature and smaller diameter) (Advanced Boiler Technology Group, 2002).

Normally enhanced HTC techniques in FTB is used with the reversed flame furnace, because: (1) temperature of exit flue gases from the reversed furnace ranged between (600-700ºC) which assist to use turbulator material actually cheaper than if the flue gases exit temperature from furnace was (900-1100ºC) in the other type design. (2) Low overall pressure drop in two pass reversed furnace boiler than the other types of boilers.

Turbulators used inside tubes of FTB to improve the turbulent convective heat transfer coefficient in the gas side, since the heat transfer coefficient on the outside is very high with boiling water. The overall objective in this application is to improve the boiler efficiency, although other factors such as (pressure drop), (air-fuel ratio), (changes in the water side heat transfer coefficient), (fouling), and (manufacturing cost) are also important.

Turbulators were appeared in different shapes, like: twisted tape (helical), coiled-wire (spiral), bent-strip, bent-tab, louvered strip, conical ring, and truncated half-cylindrical surface…etc.

An inappropriate assessment of a turbulators' impact on pressure drop can cause the choking of the burner because its fan would be unable to overcome the increased pressure drop in the boiler due to an inaccurate assessment of the turbulators' combined effect on heat exchanger and pressure drop. Today twisted tape and coiled wire turbulators are the most widely used in FTB.

The kind of turbulator that used in the present work is twisted tape insert. Twisted tape inserts can be used in all tubes sizes of FTB (from 38mm OD to 89mm OD).

LITERATURE REVIEW

Junkhan *et al.* (1985) studied experimentally three commercial turbulator inserts to determine the thermal – hydraulic performance in fire-tube boiler. Two types of bent-strip inserts, and one twisted tape with width slightly less than tube diameter. The twisted tape has width (66mm), thickness (1.4mm), length (1.892m), and pitch (H=0.712m) for one full twist (360º), (twisted ratio y= (H/D) = 10.48). Test tube of (76mm) OD, (67.9mm) ID, and 1.823m long is made of carbon steel. The water calorimeter for cooling the gas is made of (6.35mm) ID copper tubing wound around the tube and soldered at the outside. An electrically heated flow facility was developed to deliver fully developed velocity profile hot air at a temperature about (170ºC) before entering the cooled steel tube instrumented to derive sectional average heat transfer coefficients for four regions of tubes. The calorimeter tubing was connecting as four separate segments in series, with water temperature measured at inlet and outlet of each segment. The measurable temperature rise of (8ºC) a cross each segment (455mm), (42ºC between inlet and exit water), and nearly isothermal tube wall. The heat transfer enhancements for these three inserts were measured to be (135%, 157%, and 65%) over a plain empty tube at Reynolds number of (10,000), while the corresponding increase in pressure drop were (1100%, 1000%, and 160%) at the same Reynolds number. For twisted tape (y = 10.48) this correlation was predicted:

$$(Nu_{avg}) = 0.122\ Re^{0.649}\ (T_b/\ T_s)^{0.45} \quad (1)$$

In order to identify the effect of the inserts on the flow characteristics in a fire-tube boiler application , Nirmalan *et al.* (1986a) described the initial thermal-hydraulic and flow visualization studies of seven different geometrical variation of one type of bent-strip insert to enhance turbulent heat transfer in tubes, with particular application to fire-tube boilers. The same test rig that adopted by Junkhan *et al.* (1985) was used. Heat transfer coefficient increases from (175% to 285%) at Reynolds numbers of (10,000) with corresponding pressure drop increase of (400% to 1800%). A preliminary correlation of these data was given. Increasing the number of contacting points would appear to increase the heat transfer coefficient, however with larger increase in pressure drop due to:

a- In the visual observations indicate that the flow disturbance is most sever where the bent strip comes in contact with the tube wall while the flow remains relatively intact in the region where the bent-strip does not touch the wall.
b- Conduction heat transfer from turbulator to tube wall in contact points because turbulator temperature can be consider equal to flue gases temperature.

In a subsequent study, Nirmalan *et al.* (1986b) tested experimentally three new geometrical variations of one type of bent strip, also with the same test rig used by Junkhan *et al.* (1985). He studied the insert entrance region and find that an insert length of 1.5 times pitch is necessary to obtain fully developed enhanced heat transfer conditions. Correlations to predict the average heat transfer and pressure drop are given. To differentiate the wall and core regions, one insert was cut apart to provide core and wall inserts that were tested separately. This investigation also indicates that the core region of the insert is responsible for the major part of the heat transfer augmentation.

Junkhan *et al.* (1988) studied two configurations of inserts, bent – tab inserts, and bent –strip insert, used the same test of (Junkhan, *et al.* 1985). The maximum heat-transfer enhancement for bent strip inserts of about (300%) was achieved, but this was accompanied by a pressure–drop increase of about (1800%). Junkhan suggest a new insert, termed a “bent tab” insert, was design based on results of the core and wall regions test from the partial–insert studies by Nirmalan *et al.* (1986b). The favorable enhancement is available in Reynolds number range of (3000 to 30,000) under a constant pumping power constraint. However, under a constant pressure drop constraint, favorable enhancement is available only in the lower Reynolds number range of about (3000 to 5000).

Ayhan and Demirtas (2001) studied experimentally five different types of turbulator inserts for FTB contain 200 tubes. Four new types of turbulator consisted of truncated conical ring are tested, it was found that turbulators increase the boiler efficiency from (8% to 12%). A fifth new turbulator, consisting of a truncated half-cylindrical surface and placed in tandem with flow direction, provided a (4%) increase in the boiler efficiency. It was also shown that there was no need to use an excess fan for the flue gas in the chimney because of the very low pressure drop in the new types of turbulator.

Neshumayev *et al.* (2004) investigated the heat transfer of the twisted tape, straight tape and combined turbulator in the gas heated tubes of fire-tube boilers by measuring the temperature of the flue gas at the input and output of the tubes array, and also the temperature of cooling water at the input and output from boiler as well as the volume flow rate of the cooling water are recorded. Comparison of the experimental data for the twisted tape with correlation by Manglik and Bergles shows the agreement within (18%). The mean heat transfer of the combined turbulator is higher than the mean heat transfer for the twisted tape and the helical-wire-coil insert cases.

EXPERIMENTAL APPARATUS AND PROCEDURES

A novel model of Fire-Tube boiler design is built up to operate a single hot gases tube in order to study the actual process system that existed in each part of Fire Tube-Boiler separately, for fuel consumption between (1.6 kg/h to 7 kg/h) that produce range of flue gases tube specific gas flow rate from (5 to 15kg/m².s) which was represent the popular range from (5 to 25kg/m².s) that was specified in BS standard 2790 (1989) for tube of FTB.

This model is named as (single tube FTB) as shown in Fig. (2). In this work only the tube part for both empty and inserted plain tube will be studied.

The test rig consists of a burner, combustion chamber, test tube, smoke chamber and chimney, and cooling water devise, each will be described separately.

Description of Test Rig Parts

Referring to Insayif, 2008 the test rig can be classified as follow:

The Burner

Burner is a device, which produces multiple flames' dimensions in the combustion chamber according to the way of burning injected fuel in the furnace. The test rig burner consists of a centrifugal air blower delivered maximum volume flow rate (3.5 m³/min), (13000 rpm), (650W), and 50mm outlet nozzle diameter. The volume flow rate can be adjusted by varying motor speed. The burner case also contains a circular shadow sight glass of (40mm) diameter in order to inspect the flame inside the chamber. An oil pump was operated by a motor of 2750 rpm, 220V, and 150W named (OLBRENNER MOTOR) SUNTEG oil pump France made contains adjustable screw to control the fuel oil pressure in the discharge line and hence the fuel mass flow rate.

Combustion Chamber

The combustion chamber was designed as a reversed flame chamber type. Depending on the flame dimensions furnace dimensions (780mm) length, and (360mm) inside diameter were specified from (RIELLO S.P.A. 2001), and (8mm) wall thickness from (ASME, 1989). The cylindrical shell of furnace was surrounded with a jacket filled with water flow to cool the furnace shell as a tube and shell heat exchanger. The cooled door was designed from two ellipsoidal different size head welded on the ring forming a space filled with water enter and exit from specified opening and nozzle in the upper and lower part from cold head. Exit hole (D = 110mm) was made on each of these two heads to exhaust the reversed gases from the combustion chamber through two concentric 90º elbows to the hot gases tube. Concentric elbows conserve the internal elbow (contact with hot gases) from thermal damage, the cold water coming from cold door is allowed to flow through the annuals space of the elbow.

Test Tube Assembly

The basic part in the present work is the test tube, which was divided to the hot gases tube, and shell. The hot gases coming from the combustion chamber flow inside hot gases tube which is inserted inside a shell tube. (15mm) annulus space was filled with water to simulate the control volume around one tube of tube bundle distribution in FTB (staggered arrangement).

A seamless carbon steel tube (A192) according to ASME standard was used as a hot gases tube (same material and dimension as actual FTB). Dimensions of hot gases tube were (52mm ID, 60mm OD, 2470mm L) and that of shell were (90mm ID, 94mm OD, 2440mm L).

The test tube was connected to the chamber and smoke chamber by a flanges gave the ability to separate the test tube from cold door and smoke chamber while in the actual the hot gases tube ends welded directly with front and rear tube sheet. The tube was welded from front face of flange such that to simulate the actual case in FTB where the tube was welded to the front face of tube sheet.

Temperature and pressure measurements were taken at 13 selected positions along the test tube by inserting the instruments through right and left bushes at these positions. The bushes were made from carbon steel of dimensions (12mm ID, 16mm OD, and 16mm L).

As shown in Fig. (2) bushes that used for thermocouples fixed at angle 180 degree along the tube, while static pressure bushes fixed at angle (0°) along the tube. At the centre point of static pressure bushes 1mm diameter drilled and flashing from the inner and outer of the tube wall.

A carbon steel shell tube (2mm) wall thickness, (90mm) ID, and (2440mm) length was made from two semicircular parts welded together to permit welding bushes upper end on the shell tube in which the temperature and pressure measuring instrument were inserted.

On each of the thirteen axial positions, at angle 90º fixed thirteen thermocouples to measure the water temperature at each of these thirteen points in direct contact with water.

Inlet and outlet water flow nozzles (ID = 17mm) were welded to the beginning and ending of the shell respectively. Finally, the test tube shell was brushed, painted and insulated with 2-inch glass wool.

Smoke Chamber and Chimney

A carbon steel A283 smoke chamber (460mm length, 160mm OD, and 6mm thickness.) was manufactured to provide approximately the same space to the exit gases per tube in the actual rear smoke chamber for range of fuel consumption (1.6kg/h to 7kg/h) per tube at FTB. A tube 52mm ID, and 150mm length was welded to this smoke chamber at one end and to the flange at the other end. The chimney consists of two parts, pipe of (OD =114mm, 1500mm height) as a base connected on it through reducer a tube (50mm ID, 2500mm height) to gave Reynolds number ranges accepted with the actual chimney in the fuel consumption from (1.6kg/h to 7kg/h) per tube.

Cooling System Device

Water is used as a cooling fluid. Cooling system in this work was designed as that for hot water FTB. The calculations showed that it is more economic to preserve constant temperature difference between inlet and exit water flow by blow down part of hot water from furnace shell exit and compensate of it with fresh water at 25 ºC in the storage tank to maintain a constant inlet temperature during steady state operation.

25m³/h, 32m head water pump was used to circulate the water between the storage tank and combustion chamber and test tube. Pressure gage fixed on the furnace water shell. There was four branches out from the water pump discharge line and one suction line connected with lower part from the storage tank. Every branch from the discharge line is connected with inlet nozzle that fixed in different positions depended on the cooled part from the test rig.

Twisted Tape

Carbon steel tape of (50.5 mm) width, (2470mm) long, and (3mm thickness) is twisted by machine to twisted ratio (y = H/D = 11.15), where H is the pitch of full twist (360º) and D is the tube diameter as shown in Fig. (1).

Measurement Instruments

Mass Flow Rate Measurements

Air Mass Flow Rate Measurements

A square edge orifice plate with flange tapping is used in the test rig to measure the pressure drop across the orifice plate to calculate air mass flow rate. The specification of this orifice plate are: Stainless steel square edge flange taping orifice from CRANE company, flange type, DN50 PN16 with ß equal to 0.735 where ß = d/D and (d) is the throat diameter and (D) is the inside upstream pipe diameter.

On each pressure tap, needle valve was used to control the pressure tap and hence the manometer reading. ISO 5167, 2003, parts 1, and 2 are used to specify the orifice recommendations. (1050mm) upstream length, (960mm) down stream length from the orifice device and 90 º elbows was fixed between (790mm) blower tube and upstream line as shown Fig. (2).

Based on ISO 5167, 2003, parts (1, and 2) a bundle of 19 tube straighter is fixed inside the upstream line to reduce the recommended upstream tube length required to reach developed flow. The straighter was manufactured from 19 copper tube (each of 8mm ID), and 134 mm length soldered together as a bundle.

Fuel Mass Flow Rate

The fuel mass flow is an important parameter, since it affects the air mass flow rate required in combustion, then the flue gases Reynolds number in the test tube. A float meter type (HEINRICHS MESSGERATE) was used to measure fuel volume flow rate in the range (1 L/h to 10 L/h water at 20 ºC).

This float meter was fixed between fuel pump and fuel tank. Also it was calibrated using different cylinders (from 10mL to 500mL), and a stop watch of accuracy (0.01s).

Water Mass Flow Rate

Float type flow meter (BLUE – WHITE F- 400), (2 to 20 LPM, Sp.Gr.1) installed on the outlet nozzle at the end of test tube assembly in vertical position is used to measure water volume flow rate and hence water mass flow rate is obtained through multiply the volume flow rate by water density at exit temperature. Calibration for float meter scale was done by using cylinder of volume (1.5 L) and stop watch of accuracy (0.01 sec) at different fuel consumption (1.6 to 7kg/h) depending on exit water temperature.

Temperature Measurements

Thirty-nine type K thermocouples were used in the test rig. Thirteen thermocouples were used to measure water temperature along the shell, and another thirteen thermocouples were used to measure the outside wall temperature along the hot gases tube. Two thermocouples were used to measure hot flue gases temperature, one at inlet and the other on outlet test tube.

Temperature of two Teflon ring faces were measured by two thermocouples fixed on each face for both front and rear Teflon ring. Inlet and exit water temperatures from test tube were measured by installed thermocouple in the inlet and exit nozzle. Water outlet temperature from furnace shell, rear wall, cold door, ambient temperature, and upstream orifice line were measured also.

All these type K thermocouples have the same length (1.5) m and were connected to the selector switch box. The selector switch box have 20 switches, every one have three manual stack position, upper, lower, and middle positions. Nineteen thermocouples were connected to the upper position and other 20 thermocouple connected to lower positions. In the middle position, all the 38 switches were connected in parallel with wire type K which is going to reference junction point at (0 ºC) with copper wire. Positive and negative copper wires are going to the digital voltmeter reading from 0.1 DC mV to 200 DC mV (Zemansky and Richard, 1982).

Depending on using 0ºC (ice and water kept in cold store) and 100ºC (water boiling) the (39) thermocouples were calibrated to temperature range (0 – 100ºC). For temperature large than 100 ºC a Tempilasik made in USA was used to calibrate the thermocouples for temperature range reach (800ºC).

Manometer

Two kinds of manometers were used, inclined and vertical manometer. Inclined manometer used to measure the pressure differential across the orifice, and vertical manometer used to measure the static pressure in the upstream line.

MATHEMATICAL MODEL

This part describes the calculation procedure that is used in order to reach locally thermal – hydraulic calculations, and its average values for developed region and the mean value for developing and fully developed region and for more details go to Insayif, 2008.

The energy balance and the subsequent analysis are performed with the following assumptions:

1- The heat exchanger is insulated from its surrounding, in which case the only heat exchange is between the hot and cold fluids.

2- Axial conduction along the tube is negligible.

3- All fluids temperatures used in the calculations are bulk temperatures.

4- Potential and kinetic energy changes are negligible.

5- Neglecting fouling effect.

Combustion Products

Referring to (Warga, 1999) the chemical composition of light oil #2 is (C= 87.62%, S = 0.12%, H2 = 11.95%, O2 = 0.26%, N2 = 0.05%). The complete combustion process produces a mixture of gases, (Carbon dioxide, Water vapor, Nitrogen, Sulfur dioxide). The weight percentage of these components depends on the weight percentage of the fuel chemical composition (Chattopadhyay, 1998).

$C + O_2 = CO_2$ + heat (408.8 kJ/mol) (2)
1mole 1 mole 1 mole

$S + O_2 = SO_2$ + heat (292.2 kJ/mol) (3)
1mole 1 mole 1 mole

$H_2 + 0.5O_2 = H_2O$ + heat (242 kJ/mol) (4)
1mole 0.5 mole 1 mole

Thermo-Physical Properties of Combustion Products:

Calculation of the combustion gases physical properties, (density, dynamic viscosity, thermal conductivity, specific heat) is the first step in calculating the amount of heat released from the combustion gases flow inside heat exchanger tubes. Least squares method (polynomial regression) was used in (Graphing Advantage Plus-Curve Fitting Program) in order to convert the gases physical properties tables data to equations that will be need in the program that build in Microsoft Excel 2003 to perform all the calculation and graphs where the mixture gases physical properties were calculated from TEMA, 1988.

$$\rho_{\text{mixture}} = \sum_{i=1}^{n} \rho_i X_i \tag{5}$$

$$\mu_{mixture} = \frac{\sum_{i=1}^{n} \mu_i Y_i (M_{wi})^{1/2}}{\sum_{i=1}^{n} Y_i (M_i)^{1/2}} \tag{6}$$

$$Cp_{\text{mixture}} = \sum_{i=1}^{n} Y_i Cp_i \tag{7}$$

$$K_{mixture} = \frac{\sum_{i=1}^{n} K_i Y_i (M_{wi})^{1/3}}{\sum_{i=1}^{n} Y_i (M_i)^{1/3}} \tag{8}$$

where the mean combustion gases physical properties can be calculated by integration the local physical properties along tube length.

Water Temperature Gradient

Along the shell side of heat exchanger, thirteen local water temperatures were measured beside the inlet and outlet temperatures of water.

Local thermal calculation is needed to predicate the bulk water temperature in any point along the test tube. The only suitable curve fitting convenient to water temperature along heat exchanger length is the logarithmic curve and to keep the bulk temperature along this curve, only the inlet and exit water temperatures are used to find equation constants (a and b).

$$T = a \, Ln\,(X/D) + b \tag{9}$$

Tube Wall Temperature Gradient

The outer surface of flue gases tube wall temperature is measured by thirteen thermocouples located along the tube length.

Since the difference between the water inlet and outlet temperatures are approximately (25^{O}C) along cooling tube length, thus uniform wall surface temperature will be considered (Junkhan, *et al.* 1985). Referring to (Kays and London, 1964) the cooling of very high temperature gases by a liquid can usually be approximated by a constant wall temperature due to the relative thermal resistance and relative capacity rates. Also local thermal calculation program is needed to predicate the tube wall temperature at any point along the test tube. Linear curve-fitting fit tube wall temperature as:

$$T_w = a + b(X/D) \quad (10)$$

Air and Combustion Gases Mass Flow Rate

According to (ISO 5167, 2003, part 1,2) air mass flow rate is calculated from:

$$m=[\acute{C}/(1-\beta^4)^{0.5}]*E*(\pi/4)*d^2*(2\Delta p*\rho_1) \quad (11)$$

Square edge orifice flange taping is used in this work. The combustion gases mass flow rate is equal to the summation of fuel and air mass flow rate that supplied to combustion chamber.

Local Thermal Calculation Procedure

In order to calculate the thermal local values (Nusselt number, heat transfer coefficient, heat flux), the test tube length is divided theoretically into segments of (1mm) length each is considered as a heat exchanger connected in serious (McAdams, 1954). Thus when applying the energy balance between the hot and cold side for every 1mm segment, the obtained data in the outlet segment used as the inlet condition to the second segment and so on. Thus segmental heat balance can be written as:

$$Q_w = Q_g$$
$$m_w*Cp_w(T_{wout}-T_{win})= m_g*Cp_g(T_{g\,in}-T_{g\,out}) \quad (12)$$

This calculation is repeated for each segment of the tube to determine local combustion gases bulk temperature.

The gas temperature variation obtained from the above procedure shows a logarithmic temperature distribution along the tube length.

$$T_g = a \,\mathrm{Ln}\,(X/D) + b \quad (13)$$

Combustion Gases Heat Flux

The local heat flux can be calculated such as:
From eq.12 [$Q_w = m_w * Cp_w\ (T_{w\,out} - T_{w\,in})$] where Cp_w is calculated at segment average temperature.

According to (Kays, and Perkins, 1973) the constant heat flux Nusselt number is always greater than the constant surface temperature Nusselt number. The difference becomes quite negligible for (Pr > 1) and since the length of segment is very small (1mm) and combustion gases Prandtl number have a range from (0.73 to 0.78), thus will assume constant heat flux distribution along the (1mm) length segment, and thus when dividing the segment heat flux that calculated from the upper procedure by the segment heat transfer area (π* D*L) will be obtained local heat flux. By using Microsoft Excel program this procedure will repeated for all the (2351) segment and will specified the local heat flux distribution along the tube length.

Heat Transfer Coefficient

Since the local heat flux is constant across the test tube section, thus using Newton's equation:

$$Q = U_i * A_i * (T_g - T_{SO}) \quad (14)$$

$$h_{xi} = q_x / [(T_g - T_{SO}) - (q_x * R)] \quad (15)$$
where $R = [(r_i / k) * \mathrm{Ln}(r_O / r_i)]$.
The derivation of eq. 15 was clarified in Insayif, 2008.

Local Nusselt number can be calculated from:
$$Nu_x = h_x * D / k_x \quad (16)$$
where k_x local thermal conductivity.

Reynolds Number

Combustion gases local Reynolds number (Re_X) can be calculated as:
$(Rex = 4\, m_g/ \pi\mu_x D\,)$

Where m_g is equal to the summation of fuel consumption rate plus air mass flow rate that calculated in eq. 11 and μ_x is calculated in eq. 6, while the mean value is calculated as:

$$Re_{mean.} = (1/L) * \int_0^L Re_x . d_x \qquad (17)$$

Mean and Average Combustion Gases Heat Transfer Coefficient

Since the mean heat transfer coefficient in heat exchanger application is more benefit than the local heat transfer coefficient, thus the mean heat transfer coefficient along the tube length and average heat transfer coefficient along the fully developed region is calculated by integrating the local heat transfer coefficient curve as below:

$$h_{mean}=(1/L)* \int_0^L h_x \, d_X \qquad (18)$$

$$h_{avg.} = (1/L) * \int_{10D}^{L} h_x . d_X \qquad (19)$$

Experimental Uncertainty

The tests on the test rig were run under the same conditions for every fuel consumptions rates. The average difference between test tube thermal outputs calculated from repeated tests under the same conditions was less than ±0.8 %.

The relative uncertainties in Nusselt number, Prandtl number, and Reynolds number, were estimated from a typical run at fuel consumption rate (7kg/h), according to Moffat (1985), and Kline (1985).The following uncertainties are typical of the uncertainties that can be expected in other test runs: Nu_{mean}= ± 6%, Re_{mean} = ± 3.5%, Pr_{mean} = ± 3.5.

RESULTS AND DISCUSSIONS

From the experimental measurements of (water, wall tube, inlet and exit combustion gases temperatures, water and combustion gases mass flow rate, combustion gases static pressure), the combustion gases local: physical properties, combustion gases temperature, heat flux, and convection HTC, have been predicted.

Since the abrupt contraction (sharp–edged contraction) used as the entrance in the test tube as in the actual FTB without using calming length, combined thermal and hydrodynamic boundary layer will grow starting from zero thickness at ((X/d)=1.173).

From (Kays and Crawford, 1980) the abrupt contraction entrance cause flow contraction and then re expansion during the first diameter of tube length, and from (Kays and Perkins, 1973) when abrupt contraction used, boundary layer separation (stall) and very high convection HTC will gained after the boundary layer reattaches. So that the cooling starting point taken at ((X/D)= 1.173) in this work test tube.

Fig. (3) shows the variation of combustion gases HTC along empty and inserted test tube for different fuel consumptions rates. Referring to this figure, maximum convection HTC will be at the ((X/D) = 1.173), (cooling start point) and decreasing rapidly in exponential curve until arrive ((X/D) =10) from which the decreasing in convection HTC in the flow direction become very smooth. So that ((X/D) =10) point is the end of the thermally developing region and the beginning of the thermally fully developed region. In this work analysis, the convection HTC did not take a constant value in the fully developed region because of the change in combustion gases physical properties along the tube as the combustion gases temperature decreasing in the flow direction.

Referring to (Holman, 1992) the assumption of constant convection HTC throughout the heat exchanger is serious because of entrance effects, fluid viscosity, and thermal conductivity changes, etc. Due to inserted twisted tape (with twisted ratio H/D = 11.15) inside the test tube, the HTC curve for inserted tube is above that for empty test tube for same fuel consumption rate

Since the dimensionless Nusselt number value equal to the convection HTC multiply by inside tube diameter over combustion gases thermal conductivity, thus local Nusselt number will take the same behavior of convection HTC as shown in Fig. (4), because of linear proportionality between Nusselt number and convection HTC and the smaller change in combustion gases thermal conductivity value along the cooling tube length.

Fig. (4) shows the variation of combustion gases Nusselt number along empty and inserted test tube for different fuel consumptions rates. As shown in this figure, local Nusselt number with twisted tape is greater than the empty tube for the same fuel consumptions, because of:

1- The increase of flow path length.
2- Producing rotational and secondary flow, which reduces the thermal resistance.

Fig. (5) shows mean Nusselt number variation with mean Reynolds number for combustion gases flow inside empty and inserted test tube. It is clear in this figure the enhancement in mean Nusselt number increase as Reynolds number increase, where there is linear proportionality between fuel consumption and mean Reynolds number.

The percentage increase for mean Nusselt number of combustion gases due to inserted twisted tape inside the test tube for same fuel consumption rate are (75.2%), (68.8%), (49.8%), (40.3%), and (16.7%) for fuel consumption (7kg/h), (6.16kg/h), (4.5kg/h), (3.24kg/h), and (1.6 kg/h) respectively.

Extracted Thermal Correlations

In order to estimate a correlations for the mean and average Nusselt number, an integral to the curves in Fig. (4), were done to find the mean values (from (X/D) > 1.173 to the end of the tube), and average values (from (X/D) > 10 to the end of the tube) of Nusselt , and Reynolds number, where its values were plotted in Fig.s 5, 6, and 7. Convection HTC (h) is functionally connected with the following quantities (Klaczak, 1973):

$h = f(\bar{u}, \rho, D, \mu, Cp, k, T'_g, T'_s)$

The dimensional analysis of the foregoing function gives the dependence of four dimensionless criterion numbers:

$$(hD/k) = a\,(\bar{u}\rho D/\mu)^b \cdot (\mu\, Cp/k)^c \cdot (T'_g/T'_s)^d$$

$$Nu = a\, Re^{b}\, Pr^{c}\, (T'_g/T'_s)^d \qquad (20)$$

The linear equations with four unknowns were obtained after taking logarithms of this equation .

$$\text{Log}(a)+b\text{Log}(Re) + c\,\text{Log}(Pr) + d\,\text{Log}(T'_g/T'_s) = \text{Log}(Nu) \qquad (21)$$

Equation (21) is used to calculate the general correlation equations. Here, method of least squares was used, giving:

$$(Nu_{mean}) = 0.011 Re^{0.9114}\, Pr^{0.9467}\, (T'_g/T'_s)^{-0.1302} \qquad (22)$$

for twisted tape inserted,((H/D)=11.15), (X/D> 1.173)

$$(Nu_{avg.}) = 0.0103\, Re^{0.8887}\, Pr^{1.2721}\, (T'_g/T'_s)^{-0.1716} \qquad (23)$$

for twisted tape inserted,((H/D)=11.15) , (X/D > 10)

$$(Nu_{mean}) = 1.3864 Re^{0.217}\, Pr^{-3.4816}\, (T'_g/T'_s)^{0.5377} \qquad (24)$$

for empty tube,(X/D > 1.173)

$$(Nu_{avg.}) = 2.411 Re^{0.1063}\, Pr^{-3.7672}\, (T'_g/T'_s)^{0.5627} \qquad (25)$$

for empty tube , (X/D> 10)

Comparison With the Other Works

In order to make comparison with other works for developed flow in empty test tube, equations listed below were plotted together with correlation eq. 25 in Fig.6.

Comparison equations are:

Colburn equation, which was modified from Dittus-Boelter equation for fully developed turbulent flow (thermal and hydraulic) in smooth tube that given by Kays, and Perkins (1973):

$$(Nu_{avg}) = 0.023\, Re^{0.8}\, Pr^{1/3} \qquad (26)$$

another modification equation for constant surface temperature was given by Kays, and Perkins (1973):

$$(Nu_{avg}) = 0.021\, Re^{0.8}\, Pr^{0.6} \qquad (27)$$

and a new equation for heat transfer in turbulent pipe and channel flow was given by Gnielinski, (1976) :

$$(Nu_{avg}) = \frac{(f/8)\,(Re - 1000)\,Pr}{\quad}\,[1 + (d/L)^{2/3}]\,[(T_b/T_s)^{0.45}] \qquad (28)$$

$1+ 12.7 (f/8)^{0.5} (Pr^{2/3} - 1)$

where drag (Darcy) coefficient was calculated from Filonenko equation for isothermal flow

$$f = (1.82 (\log Re) - 1.64)^{-2} \quad (29)$$

or from Blasius equation

$$f = 0.3164 / (Re)^{1/} \quad (30)$$

In addition, comparison with other work for developed flow inside tube inserted with twisted tape is done by plotting correlation (23) and Junkhan equation (1) in Fig. (7) for (pitch / diameter = 10.48).

In Fig.s (6), and (7), correlation (25), and (23) give lower values than other correlations, the reason is related to the use of the following in the present work:

1- Actual combustion gases fluid flow which cause:

a – Higher inlet temperature with range (400-800°C) to test tube, while the others used air with temperature range 270ºC or liquid and modified its equation to gases.

b – Soot covers the inner tube surface, which added thermal resistance decreases the heat transfer, and hence convection HTC.

2- Local values along tube length of temperature, physical properties, and hence heat flux, Reynolds number, convection HTC, Nusselt number, as explained in 13.

3- Parallel flow shell and tube heat exchanger.

4- Friction factor that used in Genleski equation was derived for isothermal flow.

CONCLUSIONS

The following conclusions can be extracted from this work:

The maximum convection heat transfer coefficient is located at first cooling point and decreasing rapidly in exponential trend until arrive ((X/D)=10) from which the decrease in heat transfer coefficient in the flow direction become very smooth. So that (X/D)=10) is the end of thermally developing region and the beginning of the fully developed region. Also the percentage enhancement in mean Nusselt No. due o the inserted twisted tape was (75.2, 68.8, 49.8, 40.3 and 16.7) for fuel consumption (7 kg/hr, 6.16 kg/hr, 4.5 kg/hr, 3.24 kg/hr and 1.6 kg/hr respectively).

REFERENCES

Advanced Boiler Technology Group, 2002. ”Advanced fire-tube boiler project”.

Ayhan, B. and Demirtas. 2001. “Investigation of turbulators for fire-tube boilers using exergy analysis”. Turk J. Engin. Environ Sci. pp.249-258.

British Standard, European Standard ISO 5167-1. 2003. “Measurement of fluid flow by means of pressure differential devices inserted in circular cross-section conduits running full”- Part 1 : General principles and requirements .

British Standard, European Standard ISO 5167-2.2003. “Measurement of fluid flow by means of pressure differential devices inserted in circular cross-section conduits running full” - Part 2.

British Standard, 2790. 1989. ”British standard specification for design and manufacture of shell boiler of welded construction”.

Chattopadhyay, P. 1998. “Boiler Operation Engineering”. Tata Mc Graw – Hill, New Delhi.

Gnielinski, V. 1976. “New equations for heat and mass transfer in turbulent pipe and channel flow”. International Chemical Engineering. Vol. 16, No. 2, pp. 359-368.

Insayif, R. K. 2008. “An investigation of thermal behavior of fire tube boiler utilizing unconventional tubes”. M.Sc. thesis, College of Engineering, Baghdad University.

Junkhan, G.H. ; Bergles, A.E. ; Nirmalan, V.; and Ravigururajan, T. 1985.“Investigation of turbulators for fire-tube boilers”.Journal of Heat Transfer, Vol. 107, pp. 354-360.

Junkhan, G.H. ; Bergles, A.E. ; Nirmalan, V.; and Hanno, W. (1988).“Performance evaluation of the effects of a group of turbulater in inserts on heat transfer from gases in tubes”. ASHRAE Transactions. pp. 1195-1212.

Kays, W.M. and Crawford, M.E. 1980. “Convective heat and mass transfer ”. McGraw- Hill, New York.

Kays, W.M. and London, A.L. 1964. “Compact heat exchangers”, McGraw- Hill, New York.

Kays, W.M. and Perkins, H. C. 1973. “Forced convection ,internal flow in ducts”. In “ Handbook of heat transfer”, Rohsenow,W. M. and Hartnett,J. P. (eds.). McGraw- Hill, New York.

Klaczak, A. 1973. “Heat transfer in tube with spiral and helical turbulators”. Journal of Heat Transfer, pp. 557-559.

Kline, S. J. 1985. “The purposes of uncertainty analysis”. Journal of Fluids Engineering. Vol. 107, pp. 153-160.

McAdams, W.H. 1954. “Heat transmission”. McGraw- Hill, New York.

Moffat, R. J. 1985. “Using uncertainty analysis in the planning of an experiment”. Journal of Fluids Engineering. Vol. 107, pp. 173-178.

Neshumayev, D.; Ots, A. ; Laid, J.; and Tiikma, T. 2004. “Experimental investigation of various turbulator inserts in gas-heated channels”. Experimental Thermal and Fluid Science, vol. 28, pp. 877-886.

Nirmalan, V.; Junkhan, G.H. ; and Bergles, A.E. (1986a). “Investigation of the effect of turbulence –producing insrts on heat transfer in tubes with application to fire- tube boilers”. ASHRAE Transaction, Vol. 92, part 1B, pp. 791-809.

Nirmalan,V. ; Junkhan, G.H. ; and Bergles, A.E. (1986b). “Mechanisms of enhancement with turbulators for fire-tube boilers”. ASHRAE Transactions ,Vol. 92, part 2B, pp. 496-505.

Riello S.p.A. 2001. “Forced Draught Burner handbook”. Legnago – Italy.

Standards of the tubular exchanger manufacturers association (TEMA). 1988. Seventh edition. New York.

The American Society of Mechanical Engineers. 1989. (ASME) boiler and pressure vessel code. Section I, Power boilers. New York.

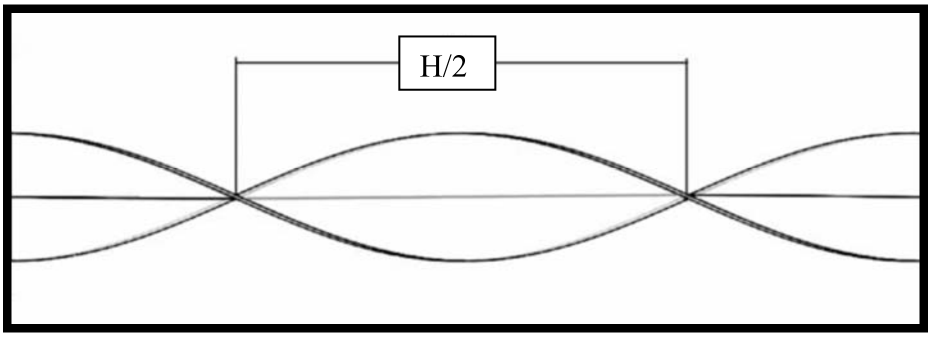

Fig. 1 Schematic Diagram of the Twisted Tape

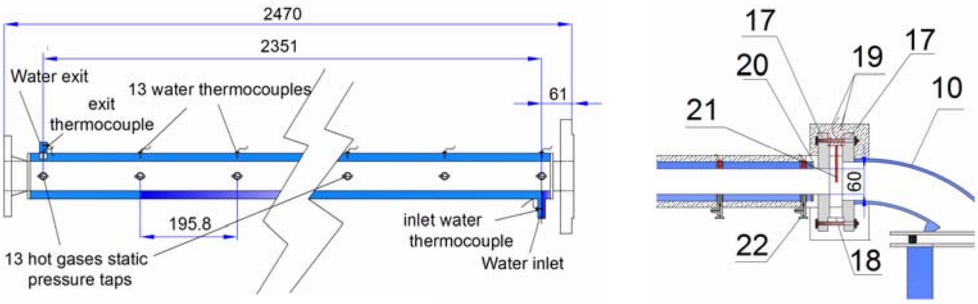

Test tube

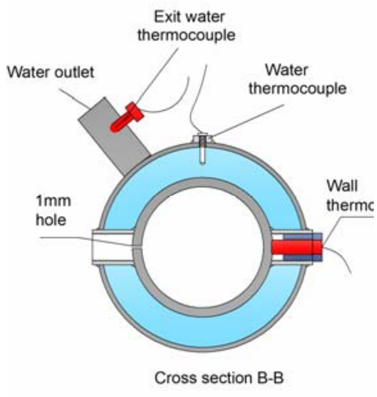

Test tube left
connection

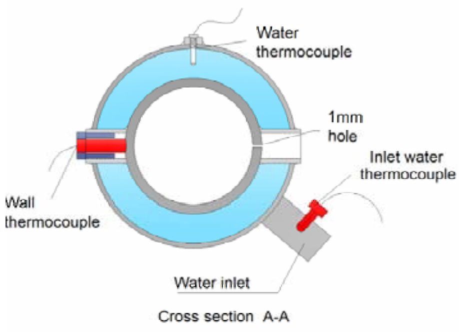

Test tube right
connection

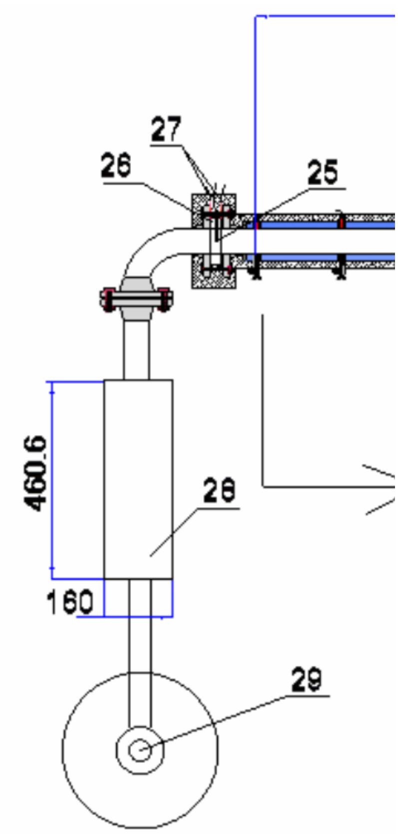

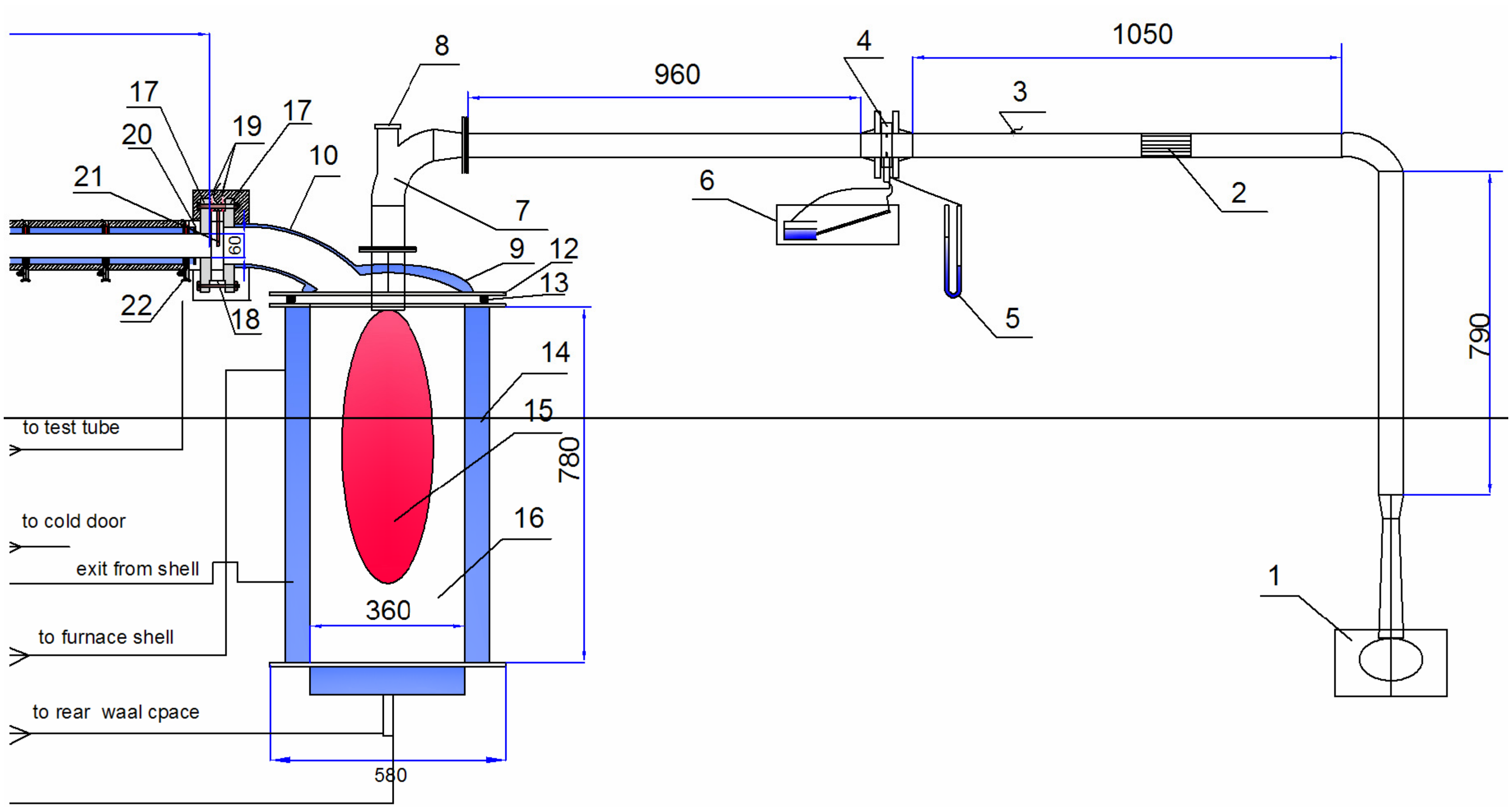

Note/ All Dimensions are in mm.

Fig. (2)Layout of the Test Rig

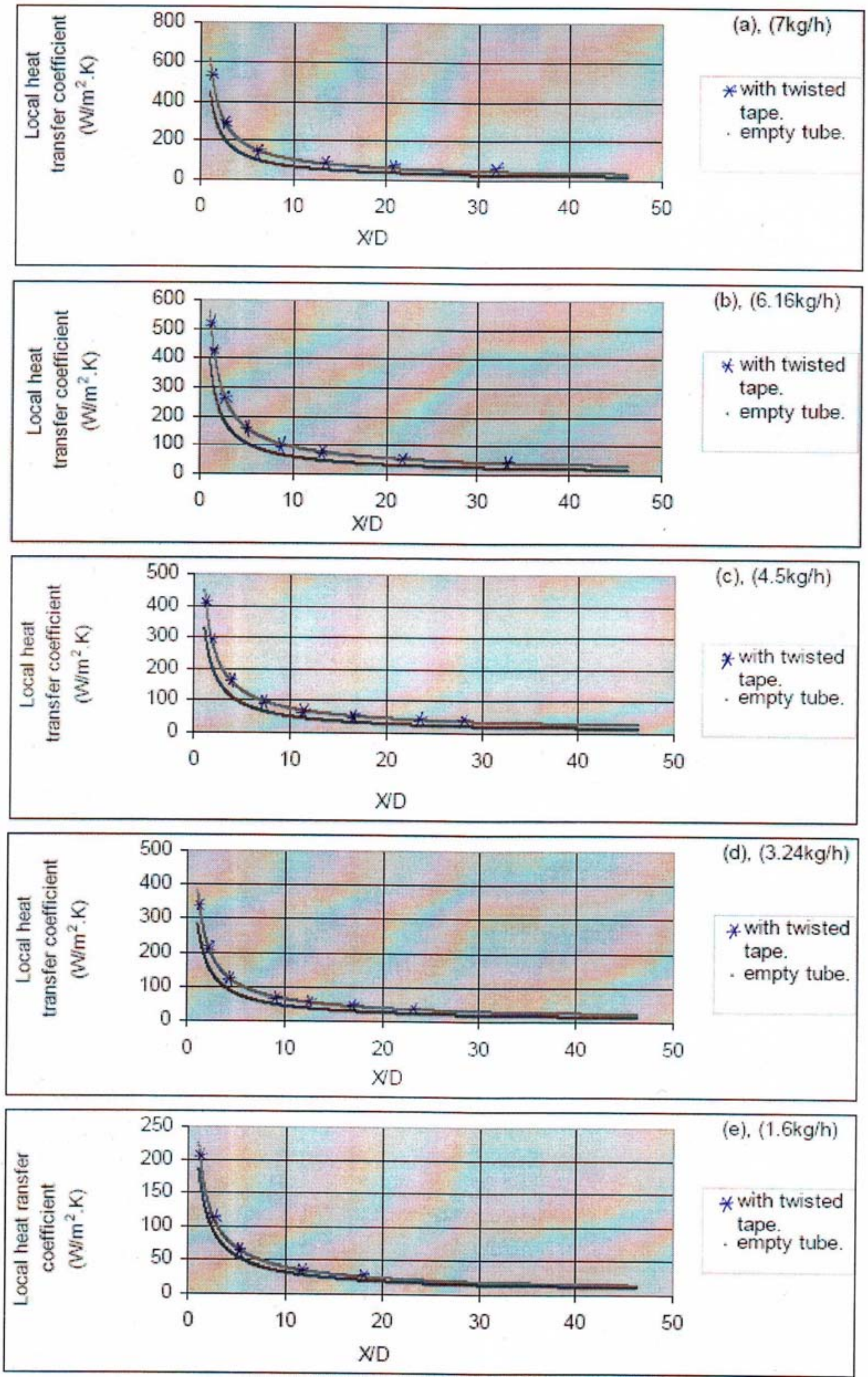

Fig. 3 Variation of Combustion Gases HTC along Empty and Inserted Test Tube for Different Fuel Consumptions Rates.

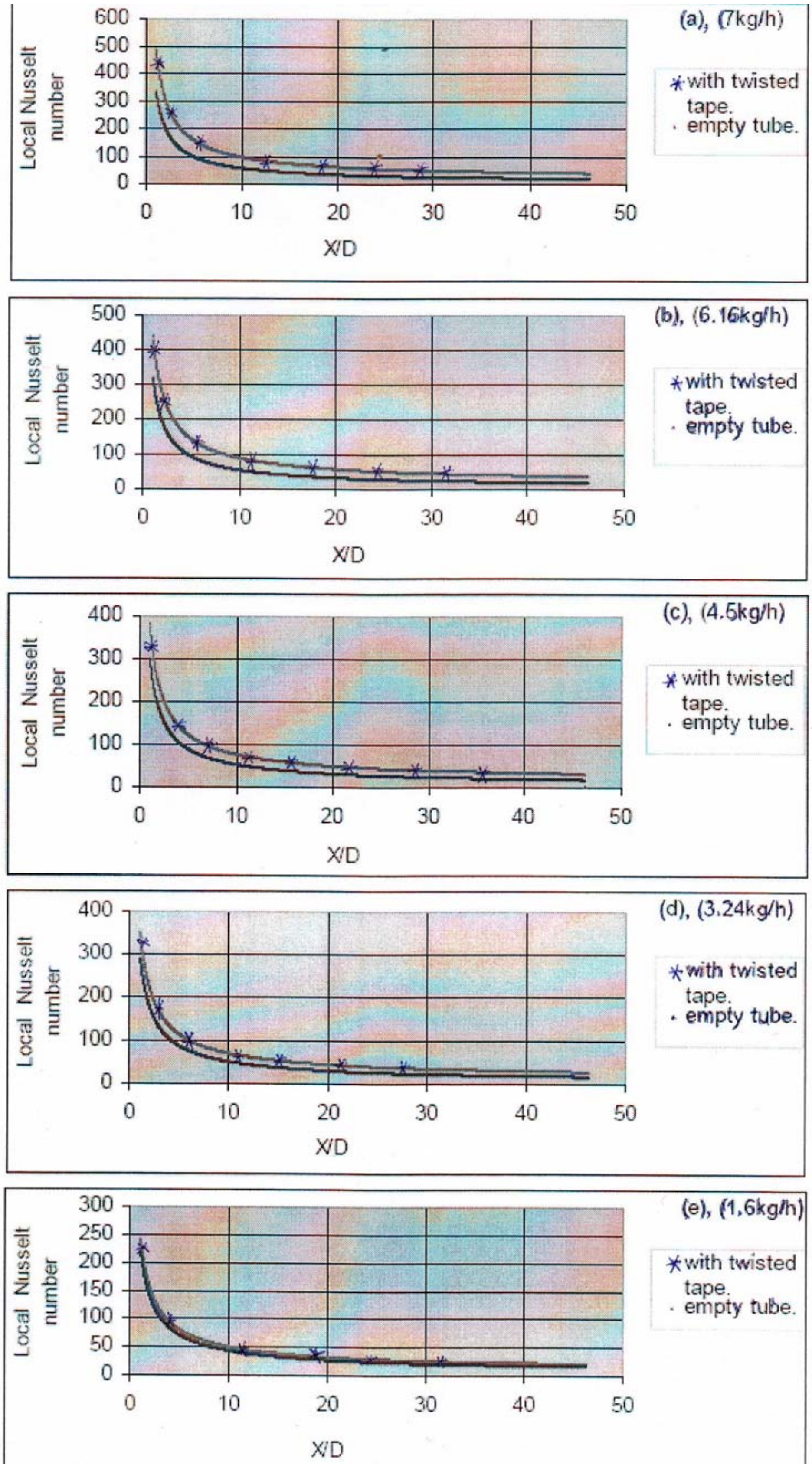

Fig. 4 Variation of Combustion Gases Nusselt Number along Empty and Inserted Test Tube for Different Fuel Consumptions Rates.

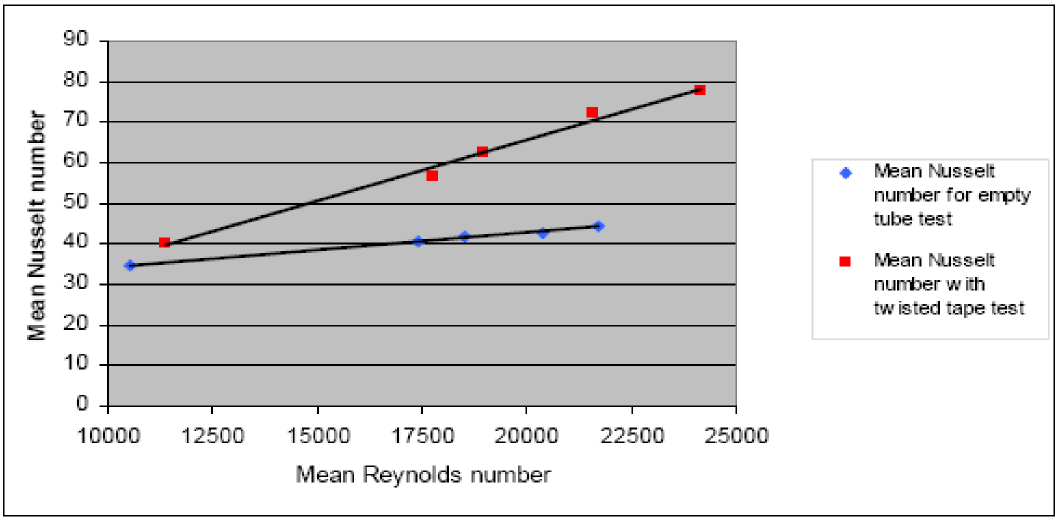

Fig. 5 Mean Nusselt Number Variation with Mean Reynolds Number inside Empty and Inserted Test Tube.

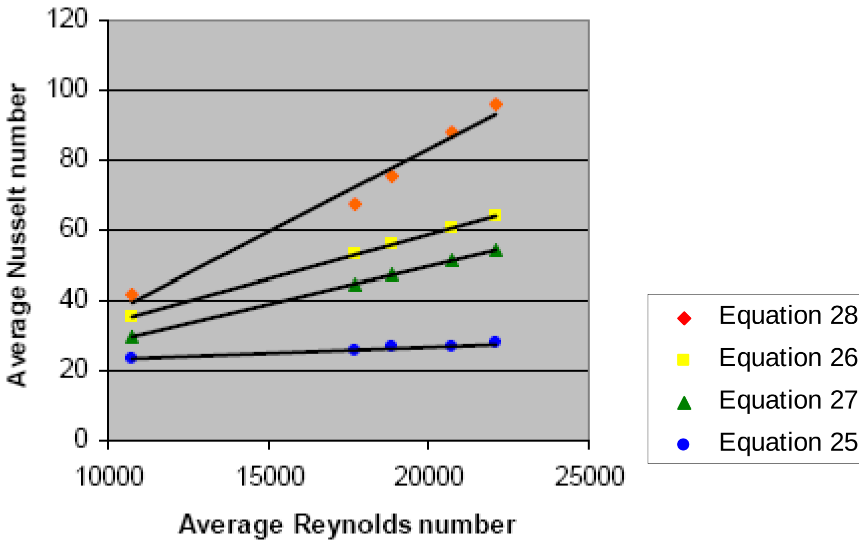

Fig. 6 Variation of Average Nusselt Number with Average Reynolds Number for the Present Empty Test Tube and Others Similar Works.

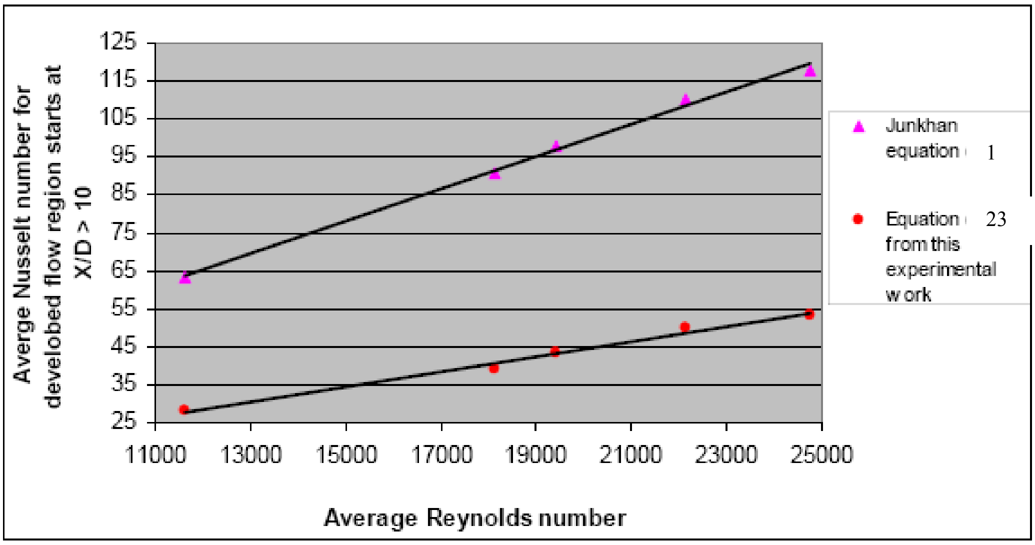

Fig. 7 Variation of Average Nusselt Number with Average Reynolds Number the Present Inserted Test Tube and Other Similar Work.

NOMENCLATURE

$\acute{C}$	Orifice discharge coefficient	Nu	Nusselt number
Cp	Specific heat J/mol.K	Pr	Prandtl number
d	Orifice diameter m	q	Local heat flux W/m²
D	Inside tube diameter m	Q	Heat flow W
E	Expansibility (expansion) factor	r	Tube radius m
f	Darcy Friction factor	R	Thermal resistance K. m^2/W
g	Gravitational acceleration m/s²	Re	Reynolds number
G	Tube specific gas flow rate kg/m².s	R_O	Universal gas constant = 8.314 J/mol.K
h	Heat transfer coefficient W/m².K	T	Temperature ºC
H	Pitch of full twist (360º) m	U	Overall heat transfer coefficient W/m².K
k	Thermal conductivity W/m.K	$\bar{u}$	Average cross section velocity m/s
$\acute{K}$	Specific heat ratio	V	gas volume m^3
L	Length m	W	Mass of one gas kg
m	Mass flow rate kg/s	X_i	Mass fraction ($X_i = W_i / W_{mixture}$)
mV	Volt/1000 mV	y	Twisted ratio (H/D)
Mw	Molecular weight kg	Y_i	mole fraction ($Y_i = N_i / N_t$)
n	Number of gases content in the flue gases	X	Longitudinal distance m
N	moles number of the gas		

Greek Symbols

ρ	Density kg/m³	β	d/D
μ	Dynamic viscosity N.s/m^2	π	22/7

Superscripts & Subscripts

$(\,)_1$	Upstream line	$(\,)_{out}$	outlet
$(\,)_2$	Down stream line	$(\,)_s$	Internal tube surface
$(\,)'$	Absolute value	$(\,)_{SO}$	Outer surface
$(\,)_b$	At bulk temperature	$(\,)_t$	Total gases
$(\,)_D$	For tube	$(\,)_w$	Water
$(\,)_g$	Gases	$(\,)_{w\,in}$	At water inlet
$(\,)_i$	Inside	$(\,)_{w\,out}$	At water outlet
$(\,)_{in}$	Inlet	$(\,)_x$	Local
$(\,)_m$	kind of the gas	$(\,)_{xi}$	Local inside
$(\,)_O$	outside		

Abbreviations

AF	(Air/Fuel) ratio	OD	Outside Diameter
FTB	Fire Tube Boiler	HTE	Heat Transfer Enhancement
ID	Inside Diameter	HTC	Heat Transfer Coefficient

Nomenclatures of Figure (2)

Part No.	Part name	Part No.	Part name
1	Air blower	16	Furnace
2	Straighter	17	4” flange
3	Up stream thermocouple	18	Teflon Ring
4	Orifice plate	19	Thermocouple
5	U-tube manometer	20	Ring
6	Inclined manometer	21	Hot gases thermocouple
7	Burner	22	Static pressure valve
8	Shadow sight glass	23	Insulation
9	Cold door ellipsoidal head	24	Tube wall thermocouple
10	Cold concentric elbow	25	Hot gases thermocouple
11	Flange	26	Teflon ring
12	Cold Door ring	27	Thermocouple
13	Asbestos belt	28	Smoke chamber
14	Water	29	Chimney
15	Flame		

Note/ All Dimensions are in mm.

NUMERICAL INVESTIGATION OF LAMINAR MIXED CONVECTION IN TROMBE WALL CHANNEL

Asst. Prof. Dr. Saad M. Saleh
Mech. Engr. Dept .
College of Engineering
University of Baghdad

Yasser A. Abd
Mechanical Engineer

ABSTRACT

The two dimensional steady, combined forced and natural convection in vertical channel is investigated for laminar regime. To simulate the Trombe wall channel geometry properly, horizontal inlet and exit segments have been added to the vertical channel. The vertical walls of the channel are maintained at constant but different temperature while horizontal walls are insulated. A finite difference method using up-wind differencing for the nonlinear convective terms, and central differencing for the second order derivatives, is employed to solve the governing differential equations for the mass, momentum, and energy balances. The solution is obtained for stream function, vorticity and temperature as dependent variables by iterative technique known as successive substitution with overrelaxation. The flow and temperature patterns in the channel are obtained for Reynolds numbers and Grashof number ranging from 25 to 100 and (100 to 1,000,00,) respectively.

A computer program (**Fortran 90**) is built to calculate the fraction factor and the total average Nusselt number (*Nu*) also the average heat transfer *Q* in steady state and for Aspect ratio Ar (10) and Grashof number GR ($10^2 - 10^5$), the fluid Prandtl number is fixed at (Pr=0.733) and Reynolds number *Re* (25-100).

The results show reasonable representation to the relation between Nusselt number and friction factor with other parameters (Ar, GR and *Re*). *Nu* is increased with increasing Re and GR but it decreases with Ar increase and (*Q*) is increased with increasing Re ,GR and Ar. At the same time, the product friction factor(*fRe*) increased with (GR) and (Ar)increased and (*Re*)decrease.

Comparison of the result with the previous work shows a good agreement.

الخلاصة

دراسة الحمل الحراري ثنائي الأبعاد المنتظم والمختلط القسري والطبيعي في قناة عمودية بالنسبة للنظام الطباقي. ومن اجل دراسة هندسة قناة تروب الجدارية بصورة صحيحة، تمت اضافة قطع إدخال وإخراج أفقية الى القناة العمودية. وتم حفظ الجدران العمودية بدرجات حرارية ثابتة ولكن مختلفة بينما تم عزل الجدران الأفقية. وقد استخدم طريقة الفروق المحددة بأستخدام طريقة الفرق (up-wind) للحدود الحمل الحرارية اللاخطية وطريقة الفرق المركزي للمشتقات من الدرجة الثانية من اجل حل المعادلات التفاضلية الحاكمة والموزونة هي الكتلة والزخم والطاقة. والحصول على حل لدالة الأنسياب والدوامية ودرجة الحرارة كمتغيرات معتمدة بواسطة التقنية التكرارية كبديل تتابعي ذي ارتخاء زائد. وقد تم الحصول على نماذج جريان ودرجة الحرارة في القناة لأرقام رينولدز وكراشوف التي تتراوح مابين 25 الى 100 و 100 الى 1000000 على التوالي.

تم بناء برنامج حاسوبي من نوع(فورتران 90) لحساب معامل الاحتكاك ***fRe*** و رقم نسلت***Nu*** , ومعدل انتقال الحرارة ***Q*** في الحالة المستقرة وكذلك للنسبة الباعية (10) ورقم كراشوف (100-100000) ورقم براندتل تم تثبيته على (733,.) ورقم رينولدز (25-100).
وأظهرت النتائج تميثيلا" للعلاقة مابين معدل رقم نسلت ومعدل الحرارة ومعامل الاحتكاك مع بقية المعاملات بواسطة رسم مخططات تمثل تأثير كل من (***Re***, **GR** ,**Ar**) على قيمة ***Q*** , ***Nu*** و ***fRe*** . وبصورة عامة، فأن رقم نسلت سوف يزداد مع زيادة كلا" من ***Re*** و **GR** ولكنه يقل بزيادة **Ar** أما معدل الحرارة يزداد بزيادة ***Re*** , **GR** و **Ar** وفي نفس الوقت، فأن معامل الاحتكاك سوف يزداد مع زيادة (**GR, Ar**) وانخفاض ***Re***.

KEY WORDS: Flow and Heat Transfer, Laminar, Mixed Convection, Trombe Wall Channel.

INTRODUCTION

The class of internal natural and mixed convection problems has significant potential for application to thermosyphon technology, heat transfer in air gaps in building walls, and nuclear reactors. Rapidly growing acceptance of solar energy as the means of heating and cooling has further stimulated research in the area of thermo-gravitational flows in open - ended cavities and parallel wall channel configuration that simulate passive solar systems such as the Trombe wall.

In a typical Trombe wall configuration, the solar energy is absorbed in the black - painted, south - facing storage wall. The resultant high temperature of the wall face drives the flow through the narrow gap. This chimney effect causes the cooler air from a room to be drawn in the from the bottom vent in the wall. This is usually referred to as the natural convection mode. Two addition modes, namely, forced and combined forced and natural modes, are possible when a mechanical device such as a blower is used to circulate the air for achieving better control of heat transport. The incident energy is also transferred to the conditioned space by conduction through the storage wall. The fluid mechanical and thermal analyses of a Trombe wall system are complicated due to several factors. It has been reported by **(Robert, 1978)** that the flow in the channel, in either free or forced modes, can be laminar or turbulent depending on the applied temperature difference (Grashof number dependent effect in the natural convection mode), velocity (Reynolds number dependent effect in the forced mode), and the geometrical parameters characterizing the Trombe wall channel geometry. The sharp convex corners and the attend adverse local pressure gradients can also cause the flow to separate and for large recirculating eddies in the channel. In view of the complexities of the problem, a prudent approach would rule out the consideration of the problem in its entirety. Such an attempt would also obscure

the effects of individual factors on the internal natural convection phenomenon. in the present work, only the fluid mechanical and heat transfer characteristics of combined forced and natural convective modes in laminar regime are investigated. And the present work investigates numerically the flow and heat transfer characteristics of a Trombe wall-like channel operating in the mixed convection mode with constant wall temperature condition by solving full elliptic Navier-stokes and energy equations. Also expose the ability reach the best theoretical design for Trombe wall channel for more powerful thermal energy stored through day and use it in heating of the buildings.

GOVERNING EQUATIONS

Steady state, two dimensional , incompressible, fully developing laminar flow

Accordingly the governing, continuity, momentum and energy conservation as follows **(Nogotov, 1978)**:-

Continuity equation:

$$\frac{\partial u}{\partial x}+\frac{\partial v}{\partial y}=0 \quad (1)$$

Momentum Equation:

$$\frac{\partial u}{\partial t}+u\frac{\partial u}{\partial x}+v\frac{\partial u}{\partial y}=-\frac{1}{\rho}\frac{\partial p}{\partial x}+\nu\left[\frac{\partial^2 u}{\partial x^2}+\frac{\partial^2 u}{\partial y^2}\right] \quad (2)$$

$$\frac{\partial v}{\partial t}+u\frac{\partial v}{\partial x}+v\frac{\partial v}{\partial y}=-\frac{1}{\rho}\frac{\partial p}{\partial y}+\nu\left[\frac{\partial^2 v}{\partial x^2}+\frac{\partial^2 v}{\partial y^2}\right]+g\beta\Delta T \quad (3)$$

Energy Equation:

$$\frac{\partial T}{\partial t}+u\frac{\partial T}{\partial x}+v\frac{\partial T}{\partial y}=\alpha\left[\frac{\partial^2 T}{\partial^2 x}+\frac{\partial^2 T}{\partial y^2}\right] \quad (4)$$

The dimensionless form:

$(X= x/b)$ (6)

$(Y= y/b)$ (5)

$(U = u/v_{\infty})$ (6)

$(V = v/v_{\infty})$ (7)

$P = p/\rho v_{\infty}^{2}$ (8)

$$\theta=\frac{T-T_{\infty}}{T_w-T_{\infty}} \quad (9)$$

$$Gr=\frac{g\beta\Delta T\, b^3}{\nu^2} \quad (10)$$

$\tau = t\, v_{\infty} / b$ (11)

$Pr = \alpha/ \nu$ (12)

$Re = v_{\infty}\, b/\nu$ (13)

By using these dimensionless forms, can be written the equations of continuity, momentum and energy as follows.

$$\frac{\partial U}{\partial X}+\frac{\partial V}{\partial Y}=0 \quad (14)$$

$$\frac{\partial U}{\partial \tau}+U\frac{\partial U}{\partial X}+V\frac{\partial U}{\partial Y}=-\frac{\partial P}{\partial X}+\frac{1}{\mathrm{Re}}\left[\frac{\partial^2 U}{\partial X^2}+\frac{\partial^2 U}{\partial Y^2}\right] \quad (15)$$

$$\frac{\partial V}{\partial \tau}+U\frac{\partial V}{\partial X}+V\frac{\partial V}{\partial Y}=-\frac{\partial P}{\partial Y}+\frac{1}{\mathrm{Re}}\left[\frac{\partial^2 V}{\partial X^2}+\frac{\partial^2 V}{\partial Y^2}\right]+\frac{Gr}{\mathrm{Re}^2}\theta$$

(16)

$$\frac{\partial\theta}{\partial\tau}+U\frac{\partial\theta}{\partial X}+V\frac{\partial\theta}{\partial Y}=\frac{1}{\Pr\mathrm{Re}}\left[\frac{\partial^2\theta}{\partial X^2}+\frac{\partial^2\theta}{\partial Y^2}\right] \qquad (17)$$

The equations (14, 15, 16 and 17) are depend on the variable (U,V,P,θ) which are called the dependent variable. Combining the definition of vorticity and the velocity components in the terms of vorticity, and cross-differentiating the equations to reduce the number of equations and eliminate the pressure terms, a new vorticity transport equation is obtained **(Samarsky, 1971):**

$$\frac{\partial\omega}{\partial\tau}+\frac{\partial(U\omega)}{\partial X}+\frac{\partial(V\omega)}{\partial Y}=\frac{Gr_b}{\mathrm{Re}^2}\frac{\partial\theta}{\partial X}+\frac{1}{\mathrm{Re}}\left[\frac{\partial^2\omega}{\partial X^2}+\frac{\partial^2\omega}{\partial Y^2}\right] \qquad (18)$$

For this flow field, the only non-zero component of the vorticity is:

$$\omega=\frac{\partial V}{\partial X}-\frac{\partial U}{\partial Y} \qquad (19)$$

From the definition of stream function which verify the continuity equation, vertical and horizontal velocity components can be written as:-

$$V=-\frac{\partial\psi}{\partial X} \qquad (20)$$

$$U=\frac{\partial\psi}{\partial Y} \qquad (21)$$

By substituting equation (20) and equation (21) in to the equation (19) to obtain the following stream equation:

$$-\omega=\frac{\partial^2\psi}{\partial X^2}+\frac{\partial^2\psi}{\partial Y^2}=\Delta^2\psi \qquad (22)$$

Energy equation become:

$$\frac{\partial\theta}{\partial\tau}+\frac{\partial(U\theta)}{\partial X}+\frac{\partial(V\theta)}{\partial Y}=\frac{1}{\Pr\mathrm{Re}}\left[\frac{\partial^2\theta}{\partial X^2}+\frac{\partial^2\theta}{\partial Y^2}\right] \qquad (23)$$

Initial Conditions;

Initial conditions may be chosen as zero:

$\Psi=\omega=\theta=U=V=0$ (No slip condition)

Boundary Conditions;

The imposed boundary conditions, rewritten in terms of stream function and vorticity, with reference to figure (1.1), are:

at GH $\quad \frac{\partial\psi}{\partial Y}=0 \quad \frac{\partial\psi}{\partial X}=0 \quad \frac{\partial\theta}{\partial Y}=0 \quad \Psi=-1$

at BC → $\quad \frac{\partial\psi}{\partial X}=0 \quad \frac{\partial\psi}{\partial Y}=0 \quad \theta=0 \quad \Psi=0$

at FG → $\quad \frac{\partial\psi}{\partial Y}=0 \quad \frac{\partial\psi}{\partial X}=0 \quad \theta=1 \quad \Psi=-1$

at AB → $\quad \frac{\partial\psi}{\partial Y}=0$ → $\frac{\partial\theta}{\partial Y}=0$ → $\frac{\partial\psi}{\partial X}=0 \quad \Psi=0$

at CD $\quad \frac{\partial\psi}{\partial Y}=0 \quad \frac{\partial\psi}{\partial X}=0 \quad \frac{\partial\theta}{\partial Y}=0 \quad \Psi=0$

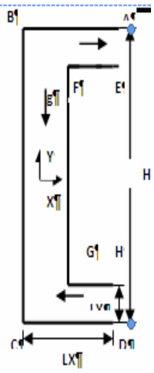

Fig. (1.1)

NUMERICAL SOLUTION

By developed method for the numerical solution results by **(Samarsky, 1971)**:

$$\theta_{i,j} = \frac{a_\theta \theta_{i+1,j} + b_\theta \theta_{i-1,j} + c_\theta \theta_{i,j+1} + d_\theta \theta_{i,j-1}}{A_\theta} \qquad (24)$$

Where

$$a_\theta = [(1+0.5|U_{i+1/2,j}|\Pr \operatorname{Re} h)\Pr \operatorname{Re} h]^{-1} - 0.5(\ U_{i+1/2,j} - |U_{i+1/2,j}|\ ) \qquad (25)$$

$$b_\theta = [(1+0.5|U_{i-1/2,j}|\Pr \operatorname{Re} h)\Pr \operatorname{Re} h]^{-1} + 0.5(\ U_{i-1/2,j} - |U_{i-1/2,j}|\ ) \qquad (26)$$

$$c_\theta = [(1+0.5|V_{i,j+1/2}|\Pr \operatorname{Re} h)\Pr \operatorname{Re} h]^{-1} - 0.5(\ V_{i,j+1/2} - |V_{i,j+1/2}|\ ) \qquad (27)$$

$$d_\theta = [(1+0.5|V_{i,j-1/2}|\Pr \operatorname{Re} h)\Pr \operatorname{Re} h]^{-1} + 0.5(\ V_{i,j-1/2} - |V_{i,j-1/2}|\ ) \qquad (28)$$

$$A_\theta = a_\theta + b_\theta + c_\theta + d_\theta \qquad (29)$$

$$\omega_{i,j} = \frac{a_\omega \omega_{i+1,j} + b_\omega \omega_{i-1,j} + c_\omega \omega_{i,j+1} + d_\omega \omega_{i,j-1}}{A_\omega} + \frac{(Gr/2\operatorname{Re}^2)(\theta_{i+1,j} - \theta_{i-1,j})}{A_\omega} \qquad (30)$$

$$\psi_{i,j} = \frac{\psi_{i+1,j} + \psi_{i-1,j} + \psi_{i,j+1} + \psi_{i,j-1} + h^2 \omega_{i,j}}{4} \qquad (31)$$

Where

$$a_\omega = [(1+0.5|U_{i+1/2,j}|\operatorname{Re} h)\operatorname{Re} h]^{-1} - 0.5(\ U_{i+1/2,j} - |U_{i+1/2,j}|\ ) \qquad (32)$$

$$b_\omega = [(1+0.5|U_{i-1/2,j}|\operatorname{Re} h)\operatorname{Re} h]^{-1} + 0.5(\ U_{i-1/2,j} - |U_{i-1/2,j}|\ ) \qquad (33)$$

$$c_\omega = [(1+0.5|V_{i,j+1/2}|\operatorname{Re} h)\operatorname{Re} h]^{-1} - 0.5(\ V_{i,j+1/2} - |V_{i,j+1/2}|\ ) \qquad (34)$$

$$d_\omega = [(1+0.5|V_{i,j-1/2}|\operatorname{Re} h)\operatorname{Re} h]^{-1} + 0.5(\ V_{i,j-1/2} - |V_{i,j-1/2}|\ ) \qquad (35)$$

$$A_\omega = a_\omega + b_\omega + c_\omega + d_\omega \qquad (36)$$

The iteration procedure for $\theta_{i,j}, \omega_{i,j}$, and $\psi_{i,j}$ is as follows:

$$\omega_{i,j} = \frac{a_\omega \omega_{i+1,j} + b_\omega \omega_{i-1,j} + c_\omega \omega_{i,j+1} + d_\omega \omega_{i,j-1}}{A_\omega}$$

$$\theta^{s+1}_{i,j} = (1-F_\theta)\theta^s_{i,j} + \frac{F_\theta}{A_\theta}\left[a_\theta \theta^s_{i+1,j} + b_\theta \theta^{s+1}_{i-1,j} + c_\theta \theta^s_{i,j+1} + d_\theta \theta^{s+1}_{i,j-1}\right] \qquad (37)$$

$$+ \frac{(Gr/2\operatorname{Re}^2)(\theta_{i+1,j} - \theta_{i-1,j})}{A_\omega} \qquad (38)$$

$$\psi^{s+1}_{i,j} = (1-F_\psi)\psi^s_{i,j} + \frac{F_\psi}{A_\psi}\begin{bmatrix} a_\psi \psi^s_{i+1,j} + b_\psi \psi^{s+1}_{i-1,j} \\ + c_\psi \psi^s_{i,j+1} \\ + d_\psi \psi^{s+1}_{i,j-1} + h^2 \omega^{s+1}_{i,j-1} \end{bmatrix} \qquad (39)$$

For all cases in the present study, an overrelaxation parameters F_{θ}, F_{ψ}, and F_{ω} equal to 0.7, 0.5, and 0.7, are used experiments **(Gosman,1969)**.

An average vertical velocity can be calculated:

$$\bar{V} = 1/A \int_A v \, dA \qquad (40)$$

The local Nusselt number at the heated wall:

$$Nu_{L(j)} = \frac{\partial \theta}{\partial X} \qquad (41)$$

The average Nusselt number along a single channel wall is defined by **(Shih, 1984)**:

$$Nu = -\frac{1}{Ar} \int_0^{Ar} \left(\frac{\partial \theta}{\partial X} \right)_j dY \qquad (42)$$

The overall heat transfer can be calculated by:

$$Q = Ar \, Nu \qquad (43)$$

The friction factor can be obtained as follow :

$$\tau_s = \mu \, \partial v / \partial y \qquad (44)$$

The shear stress at the wall may be expressed in term of friction factor *f* as follow:

$$f(\rho \bar{V}^2/2) = \mu \partial v / \partial y \qquad (45)$$

By using the dimensionless parameters the equation above becomes:

$$f \, \mathrm{Re}_L = \frac{2}{\bar{V}^2} \frac{\partial V}{\partial Y} \qquad (46)$$

average *fRe* can be calculated from the equations below:

$$f \, \mathrm{Re} = \frac{1}{Ar} \int_0^{Ar} f \, \mathrm{Re}_L dY \qquad (47)$$

DISCUSION RESULTS AND

Fig.1 shows indicate effects of variation of *Re* on the temperature contour maps of air. For Grashof number of 10^5, and aspect ratio equal 10, and the inlet temperature is(ϑ) 0.3. Temperature contour lines are always perpendicular to the horizontal walls since an insulated boundary condition is imposed there. At low Reynolds number, the isotherms near the heated wall are found to be inclined towards the cooler left wall. As *Re* is increased, the inclination shifts towards the heated wall. This illustrates the tendency of inertial force to dominate the buoyancy force as the fluid inlet velocity increases. Also, it is noted that at low Reynolds number, there is some upstream influences indicated by the cooling of fluid in the horizontal channel even before it enters the vertical channel. As *Re* increases, this upstream influence in the lower horizontal portion of the channel decays since convection dominates the thermal diffusion of heat in the upstream direction. The temperature contour maps for low *Re* are qualitatively similar in natural to the contour maps of free convection heat transfer in the closed vertical channel**(Yasser,2008)**.

Fig.2 shows the effect of variation of Reynolds number on the streamline for fixed GR, aspect ratio, and inlet temperature of 10^5, 10 and 0.3, respectively. The channel Reynolds number varied from 25 to 100. For the low Reynolds number, which the effect of free convection prevails over the effect of forced convection, the streamline pattern appears more like the one encountered in pure natural convection in a closed rectangular cavity **(Davis, 1983)**. This is clearly illustrated by the closed eddies circulating in the vertical portion of the channel. The fluid flows up in the vicinity of the hot surface and flows down on the cooler side. It is important to note that, due to stong buoyancy effects at the inner wall, there is no flow separation at the lower inner corner. Forced convection effects increase with increasing Reynolds number, and the recirculating flow patterns in the middle of the channel gradually disappears. As the Reynolds number is further increased, the closed eddies are finally " swept away " by the rapidly moving stream. Furthermore, due to increased inertia effect, the flow in the lower horizontal channel is unable to negotiate the bend, and it separates at the lower inner corner forming a separation bubble on the hot vertical surface. It is also noted that a dividing streamline (*ψ=0*) exists in the vertical channel which divides the recirculating region from the forced flow coming from the inlet.

Fig.3 show the variation of Reynolds number on the temperature distribution of air in the channel for different GR. At constant GR, Ar=10 and *Re* equal 25and 100. for different nondimensional channel elevation of 0.2, 0.4, 0.6 and 0.8 the value of temperature dcreased with increase *Re* at fixed GR because increased the vertical velocity and the rcirculation motion decreased with increasing *Re* that lead to decrease temperature, also the temperature at elevation 0.2 is higher from inlet to mid channel because the effect of buoyancy force is higher at this part**(Yasser,2008)**.

Fig.4 show influence variation of *Re* on the velocity profile distribution of air at nondimensional channel elevations 0.2, 0.4, 0.6 and 0.8 at constant GR. The velocity increased with increasing *Re* because increased vertical velocity and that lead to decrease the positive and negative peak velocity occurs near heated wall that result from the recirculation motion of air decreased with increased *Re* the negative peak velocity disappears dependence on the value of Gr/Re^2.

Fig.5 illustrates the variation of average heat transfer with *Re* through the channel for different GR ($10^2 - 10^5$). It is shown that the total heat transfer collected dependence on the Reynolds number and Grashof number. For fixed Grashof number, as Reynolds number is increased, the heat transfer from the warm wall to the fluid increases somewhat gradually while heat transfer from the circulating fluid to the cooler wall decreases sharply due to change in the flow regime. Thus, increasing the value of *Re* implies that larger net energy is delivered to the conditioned space because of increasing the vertical velocity. Although this effect is relatively small at GR=10^{2} and 10^{3}, it is much more effect with increase value of GR at GR=10^4 and 10^5 because of increasing the effect of buoyancy force and that lead to increase the intensity and the value of velocities, also the total heat transfer increased with increasing Ar because of increasing of heat transfer exchange area, the effect of GR=10^2 will be neglected**(Yasser,2008)**.

While, **Fig.6** illustrates the effect of *Re* on *fRe* value with increasing in GR. It is shown that the *fRe* decreased with increasing *Re* this effect results from increasing of vertical velocity of the flow. That lead to decrease the friction factor between the air and the wall, and the effect of GR lead to increase *fRe* with increasing GR because increased the buoyancy force (natural convection) and lead to increase the intensity and value of the vorticity of air at constant Ar **(Yasser,2008)**.

Fig.7 show the isotherms for constant *Re*, Ar=10 and GR equal 10^{3} to 10^{5}. At 10^5 the isotherm patterns are qualitatively similar to those seen in Figs [(5-5c)-(5-8c)] at constant GR for different *Re* . At moderately high GR, e.g., 10^{5}, the contour lines show nearly uniform temperature in the core region of the vertical channel and a steep temperature gradient near walls. The temperature contour maps for low *Re* and moderately high GR are also qualitatively similar to the contour maps for natural convection in the closed vertical channel. The temperature lines inclination towards hot lines increased with decrease GR until becomes uniform temperature lines**(Yasser,2008)**.

Fig.8 show the effect of variation of GR for fixed *Re*, aspect ratio, inlet temperature of 100, 10, and 0.3, respectively and Ar=10. I note that only , the recirculating flow pattern exits in the vertical part of the at GR=10^{5} channel. The recirculating due to the increased GR the effect natural convection prevails over the effect of forced convection, the stream line more likely the one encountered in pure natural convection in a closed rectangular cavity at GR=10^{5}, the effect is similar to keep GR fixed and reducing Reynolds number**(Yasser,2008)**.

Fig.9 illustrate the effect of inlet temperature variation on the streamline patterns of air (Pr = 0.733) in a channel of aspect ratio (the ratio of vertical channel height, *H*, to its width, *b*). The nondimensional inlet temperature is varied from 0.0 to 1.0 while the Grashof number and Reynolds number for these cases are fixed at 10^{5} and 100, respectively. The scale is exaggerated in the horizontal direction to illustrate more clearly the flow features in the vertical portion of the channel. It is noted that, for most inlet temperature values, a large recirculating motion exists in the vertical channel. However, as inlet temperature decreases, the strength as well as the extent of the recirculating motion decreases, At higher values of the temperature recirculating pattern extends to the lower horizontal part of the channel, the stream lines are qualitatively similar to those seen in **Fig.8**. At GR decrease from (10^5 -10^5) with constant *Re*(**Yasser,2008)**.

Comparison of the Results

The comparison was made for the value of *Q* at the wall of the channel , temperature and velocity profiles at mid section across the vertical channel with the previous results obtained by **(Chaturvedi,1988)**. These comparison are shown in **Fig.10**. From these figures, a difference (approximately 13%) is found between these results.

CONCLUSIONS

1- The flow patterns are strongly influenced by GR, and *Re*. For a fixed GR and Pr, as Reynolds number is increased the flow pattern undergoes a change from the natural convective flow patterns, characterized by strong eddying motion in the vertical channel, to forced convective flow patterns governed by boundary layer type flow on the wall hot face. Increasing the Grashof number, for a given *Re* and Pr, enlarges and intensifies the circulatory motion in the vertical channel. At low Reynolds number (natural convection limit), the flow patterns are similar to the ones found in the natural convective flow rectangular cavities
2- The shape of isotherms are also strongly influenced by the fluid mechanical parameters GR and *Re*. At low Reynolds number, the horizontal contour lines, indicating isothermal region, are clearly indicated in the middle portion of vertical channel. At high Reynolds number, representing the forced convective limit, isotherm contour maps roughly parallel to the vertical wall are developed.
3- The investigation showed a direct dependence of velocity and temperature profile on the channel elevation and fluid mechanical parameters such as *Re* and GR. Peak velocity was found to shift toward the hot wall as the Grashof number was increased.
4- The variation of inlet temperature from 0.0 to 1.0 indicated that, the recirculating flow pattern existed for most inlet temperature for $GR/\mathrm{Re}^2 \geq 0.$
5- The net energy delivered to the conditioned space is strongly governed by *Re* and GR. At high GR, the energy convected to the conditioned space can be increased substantially if the Reynolds number is increased to its forced convective limit, also energy increased with increasing Ar. And the *fRe* increases with increasing GR and Ar but decreased with increasing *Re.*

REFERENCES

Robert, J. L , and Trombe, F., (1978) "Experimental study of passive Air-cooled Flat - Plate Solar Collectors: Characteristics and working Balance in the Obeillo Solar House, " Energy conservation in Heating and cooling and Ventilating Buildings, Hemisphere Publishing Corp., Washington, Vol. 2, pp. 761-782.

Nogotov, E. F., (1978) Application of Numerical Heat Transfer, Hemisphere Publishing Corp., Washington.

Samarsky, A. A. (1971) " Vvedenie *v* teoriyu raznostnkyh skhem"("Introduction to the difference secheme theory") , P. 496, Moskva, Nauka.

Gosman, D., (1969) Heat and Mass Transfer in Recirculating Flows, Academic Press, New York.

Shih T. M, (1984) "Numerical Heat Transfer", McGraw-Hill, Washignton,.

Davis, G., de Vahl, (1983) "Natural Convection of Air in a Square Cavity: A Bench Mark Numerical Solution," International Journal of Numerical Methods in Fluids, Vol.3, pp. 249-264.

Chaturvedi, S. K., and Huang, G. C., (1988)"Mixed Laminar convection in Trombe Wall channels" Solar Energy, Vol. 110, pp. 31-37.

Yasser, A., Al Whabb " Numerical Investigation of Laminar Mixed Convection in Tromb Wall Channel", Department of Mechanical Engineering, University of Baghdad, M.SC., 2008.

NOMENCLATURE

LATIN SYMBOLS

A	Surface Area	m^2
b	Horizontal channel Width	m
H	Height of channel	m
Ar	Aspect ratio (H/b)	-
K	Thermal conductivity	W/m K
L	Length	m
g	Gravity acceleration	m/s^2
Pr	Prandtl number (Pr=ν/α)	–
Re	Reynolds number (Re= v b/ ν)	–
GR	Grashof number (Gr= $\frac{g\beta b^3(T-T_\infty)}{\nu^2}$)	
p	Air pressure	N/m^2
P	Dimensionless air pressure	-
h	Heat transfer coefficient	$W/m^2.K$
u, v	Velocity components in x and y direction respectively	m/s
U, V	Dimensionless velocity components in X and Y direction	
$\bar{V}$	Average vertical velocity	m/s
$\bar{V}$	Dimensionless average verical velocity	–
T	Temperature	K
i,j	X and Y direction directories	-
x,y	Physical coordinates of the channel	m
X, Y	Dimensionless physical coordinates of the channel	–
$\dot{m}$	Mass flow	
t	Time	Sec
Nu_L	Local Nusselt number	–
Nu	Average Nusselt number	–
q	Overall heat transfer	W
Q	Dimensionless overall heat transfer	
f	Friction factor($f = \frac{2}{\bar{V}^2 \mathrm{Re}} \frac{\partial V}{\partial n}$)	–
fRe	Average friction factor	–
$f\,\mathrm{Re}_L$	Local friction factor	–

Creak Symbols

μ	Viscosity	kg/m.s
ν	Kinematic viscosity	m^2/s
β	Coefficient of volume expansion	1/K
α	Thermal diffusivity	m^2/s
ρ	Air density	kg/m^3
τ	Dimensionless time	–
ϑ	Dimensionless temperature	-
τ_S	Shear stress	N/m^2
ψ	Dimensionless stream function	–
ω	Vorticity	–
Δ	Difference between two values	–
Γ	Bounding mesh	-

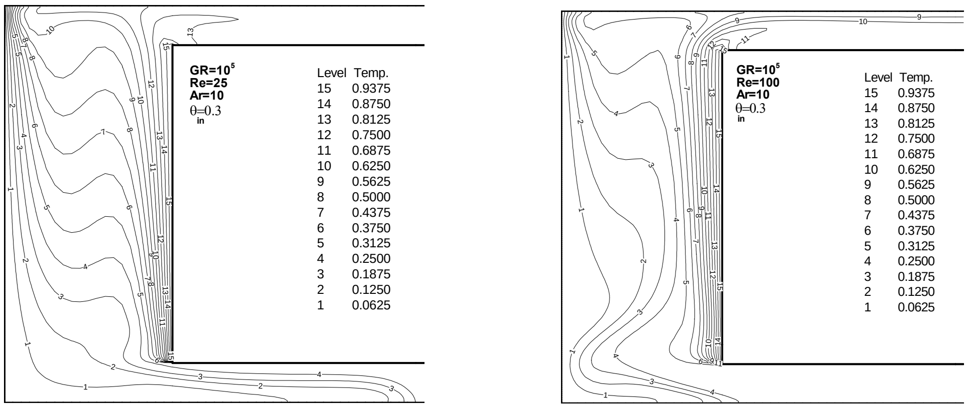

Fig 1: Isotherm contour maps for GR=10^{5} , Ar=10 for different values of Re

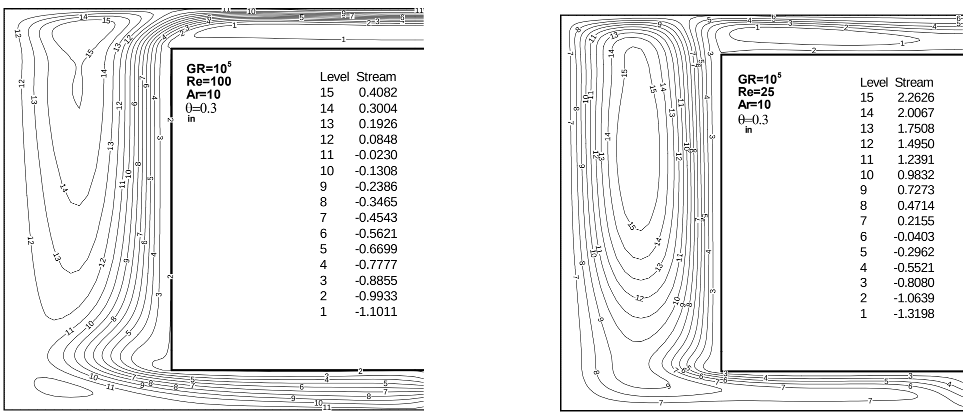

Fig 2: Streamline contour maps for GR=10^{5} , Ar=10 for different values of Re

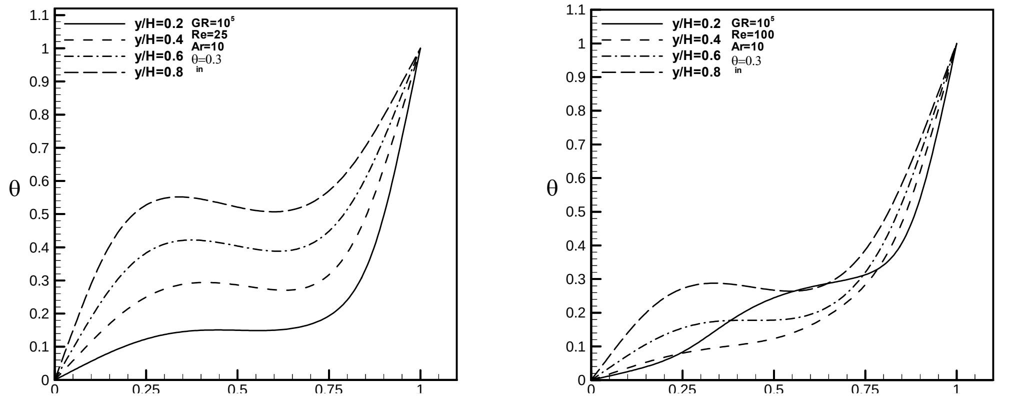

Fig 3: Variation of temperature profile for different Reynolds number at Ar=10, GR=10^5

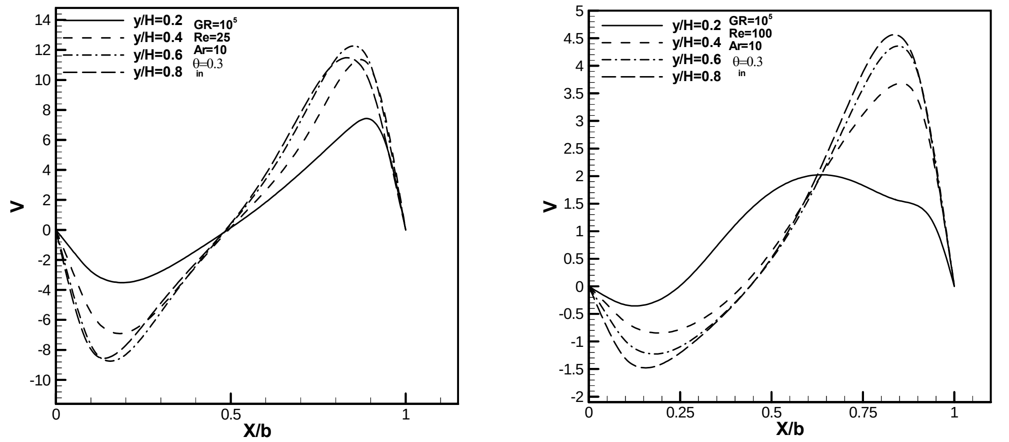

Fig 4: Variation of velocity profile for different Reynolds number at Ar=10,

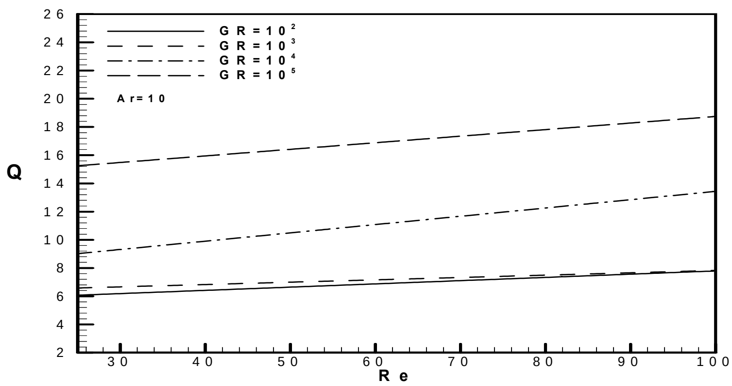

Fig 5: Variation of *Q* with *Re* for different of GR at Ar=10

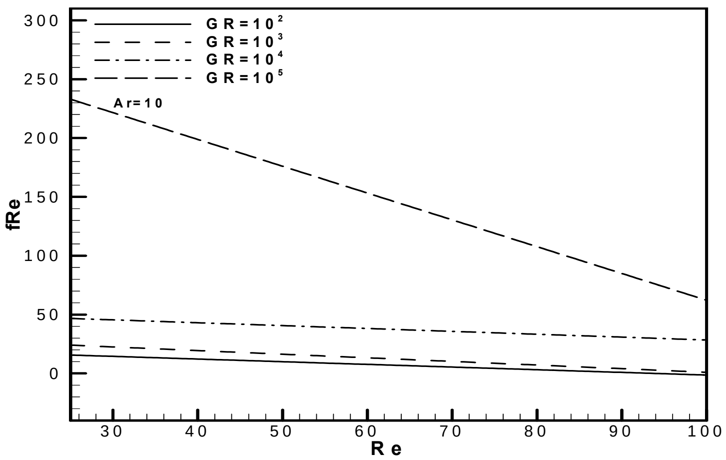

Fig 6: Variation of *fRe* with *Re* for different values of GR

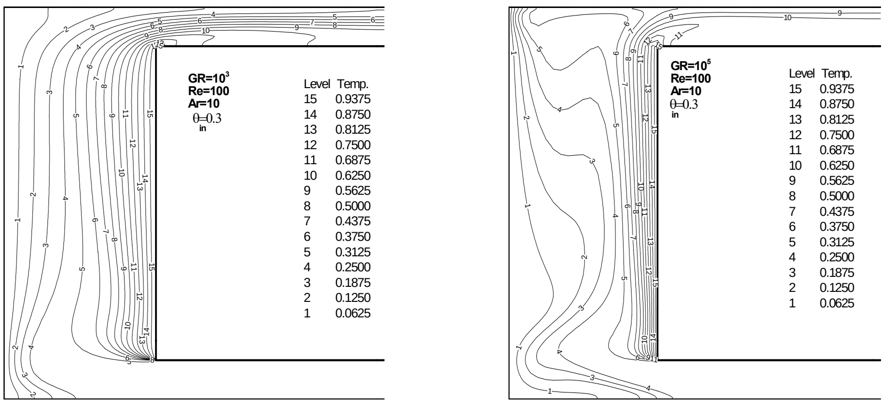

Fig 7: Isotherm contour maps for Re=100, Ar=10 for different values of GR

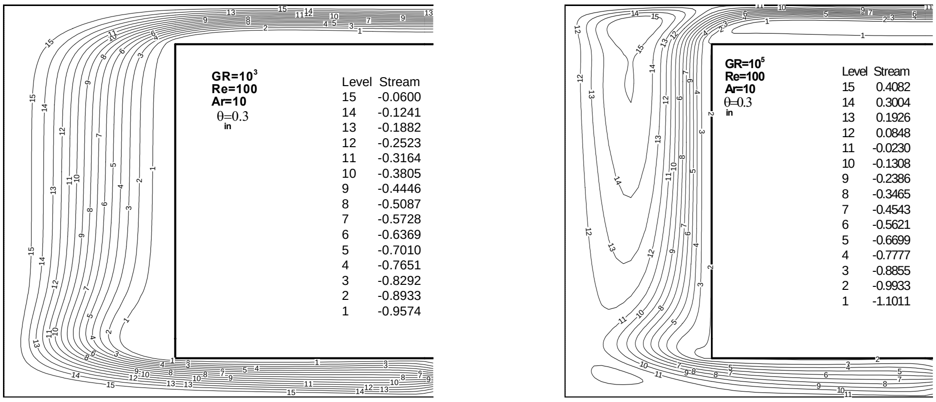

Fig 8: Streamline contour maps for Re =100 ,Ar=10 for different values of GR

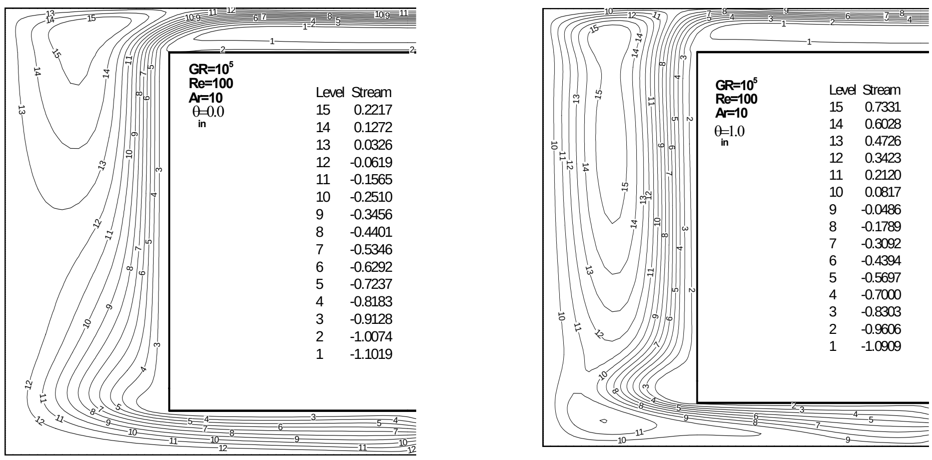

Fig 9: Streamline contour maps for Re=100, Ar=10, *ϑ=0.0* and *1.0*

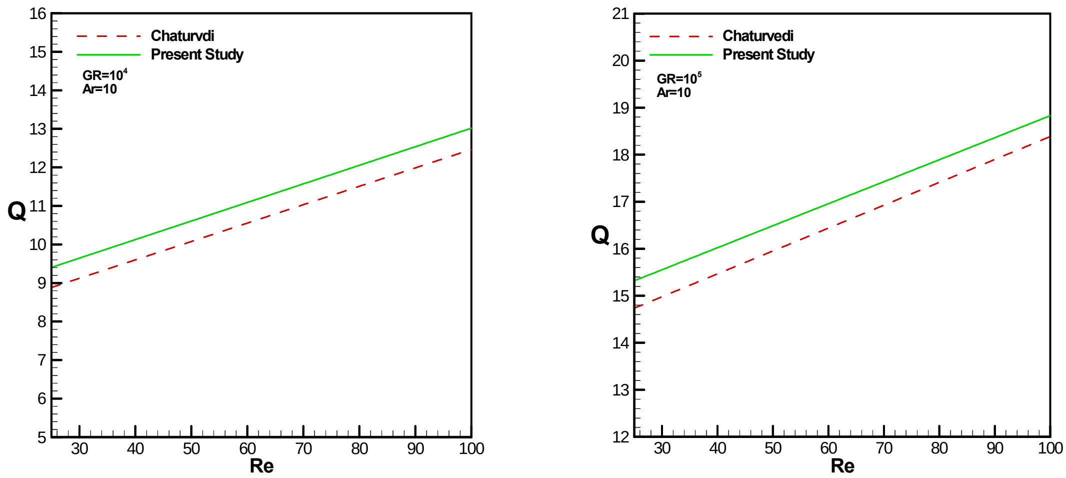

Fig 10: Comparison between present study and (Chaturvedi, 1988) for the relation between Re and *Q* at GR=10^4 and GR=10^5

EFFECT OF THE SAND MOULD ADDITIVES ON SOME MECHANICAL PROPERTIES OF CARBON STEEL CK45 CASTS

Asst. Prof. Dr. Hani Aziz Ameen
Technical College / Al-Musaib
Pumps Eng. Dept.

Khairia Salman Hassan
Institute of Technology - Baghdad
Mechanical Dept.

ABSTRACT

The research targets study of influence of additives on sand mold's properties and, consequently, on that of carbon steel CK45 casts produced by three molds. Three materials were selected for addition to sand mix at weight percentages. These are sodium carbonates, glycerin and oat flour. Sand molds of studied properties were produced to get casts from such molds. The required tests were made to find the best additives with respect to properties of cast. ANSYS software is used to demonstrate the stresses distribution of each produced materials. It is shown that the mechanical properties of casts produced is improved highly with sodium carbonates and is less with oat flour and it is seem a few with glycerin additives. It can be concluded that the sodium carbonates let to get the cast produced with highly mechanical properties.

الخلاصة

يهدف البحث الى دراسة تأثير الاضافات على خواص القالب الرملي وبالتالي على خواص مصبوبات الفولاذ الكربون CK45 المنتج في هذه القوالب. اذ تم انتخاب ثلاثة مواد اضيفت الى المزيج الرملي وبنسب وزنية مختلفة وهي كاربونات الصوديوم والكليسرين والشوفان . تم انتاج قوالب رملية ذات خواص تم دراستها والحصول على مصبوبات من هذه القوالب واجراء الفحوصات اللازمة وايجاد افضل مادة مضافة من حيث الخواص التي تم الحصول عليها . وتم دراسة توزيع الاجهادات على المسبوكات الناتجة ببرنامج ANSYS. وقد لوحظ ان الخواص الميكانيكية للمنتوجات قد تحسنت بشكل كبير في حالة اضافة كاربونات الصوديوم واقل تحسنا في حالة الشوفان وظهر تحسن قليل بالخواص في حالة الكليسرين. ومن هذا نستنتج ان اضافة كاربونات الصوديوم الى القالب يؤدي الى حصول منتوج ذو مواصفات ميكانيكية عالية .

KEYWORDS: casting, additives, mechanical properties, finite element method, ANSYS software , metallurgy .

INTRODUCTION

Casting is an operation for fabrication of the important and essential metals concerned with metal forming in the liquid state, i.e. casting the molten metal in a mold with a cavity whose form coincides with part to be produced.

Sand casting is considered as the most extensively used method of casting due to its low cost, ease of dealing with it and adequacy for repeated use in spite of importance of use of metal molds at casting. Its use is limited due to high cost and difficulty of fabricating the small and large forms. Thus, casting by use of sand molds is the trend . Such molds must possess the required specifications (strength, permeability , thermal properties ..etc)(Abid Al-Razaq I. Khdiar,2000). The sand is mixed with suitable binders and additives to improve its mechanical properties which determine the stability of the cast and type of its surface (St. dobosz. D. Drozyuski and A. chojecki,1997). The determination of the required percentages for mixing should be conducted according to scientific consideration for obtaining the optimum result with least possible costs (Asaad K. Mezher,2004). A group of factors influence the selection of a suitable casting method, the most important of these factors are:

- Design of the product to be fabricated .
- Form and size of the cast.
- Properties of the produced cast .
- The economic feasibility for the operation compared with forming operations
- Cost of tools and devices used .
- The required surface quality of the cast.

Few papers studied the effect of mould on the cast produced . Abbas A. A. Al-Raid ,1978, studied the Iraqi sand properties which is used in casting process. Najia Yousif Khaiou ,2005, studied the effect of additives on properties of sand moulds and then on the properties of cast iron. The effect of additives on sand moulds is studied in this research, in which three types of different additives is used, then their effects on the properties (mechanical and chemical) of the cast is investigated. Also the finite element analysis via ANSYS program is used to show the difference in the stresses distribution in the product's cast.

EXPERIMENTAL PART

It includes the following:

Sand Preparation

Sand *Arthoma* from Al-Anbar governorate was chosen for many reasons. Most important of which are its content of higher percentage of silica SiO_2, the dominating sub- angular grain shape and its high strength and binding force. The chemical composition is shown in **Table 1**

Sieve Analysis

The sieve analysis of sand was conducted to determine the distribution of grain size and fineness number by mechanical vibrating sieve consisting of (11) sieves starting with no. of 2000 microns hole up to the last sieve of (53) microns.

The test was conducted on 100 grams quantity for 15 minutes. After determination of finesses number, sand was used which passes from grid no. 44 of grain size (35-355) microns. Sizes (500-2000) micron were excluded for coarseness .

Preparation of the Binding Material

Iraqi Bentonite was chosen. It is the traditional binding material for moist sand mold casting, type Calcium . **Table 2 ,** shows the chemical composition for the percent bentonite binding material .

The total percentage is 91.5% and the rest is clay.

Additives

The following materials were added.

A- <u>Glycerol</u>

It is a pure chemical. Its trade name is Glycerin. Its pure composition is
$(CH_2OH)- (CHOH) – (CH_2OH)$.

B- <u>Oat Flour</u>

It is a cereal crop, when water is added becomes a slurry of high viscosity. (Douglas Doehlert,2000). **Table3 ,** show its consistent.

Also there are other elements in the oat flour consistent as shown in **Table 4.**

C- Sodium Carbonates (Na_2 CO_3)

Most crude bentonite in the world is of calcium bentonite. It is capable of swelling, viscous, low heat resistance. It can be transformed to sodium bentonite by chemical treatment of adding sodium carbonates. The following equation illustrates it [J.G. Sylvia,1972 ; K.strauss ,1970).

Calcium bentonite + Sodium carbonate Na_2CO_3 → Soduim bentonite + calcium carbonate $CaCO_3$

Preparation of Sand Mixture

Regulation of mixture percentage require a little flexibility (stability) between the high strength to be evidenced by the mold during casting and fragmentation / breakage without which the sand can not be returned to preparation units for reuse a new, therefore, to attain the required properties (moist permeability, moist hardness, strength to moist compression and strength to dry compression), the optimum mixture percentage (sand, water, bentonite and additive) are to be chosen, therefore, the effect of sand (mixture percentage change was tested as follows:

Bentonite Percentages

Bentonite was added by 15% weight , and water was added at 5% .

Additives

The mentioned materials were added by weight percentage as shown in **Table 5**

Preparation of sand Sample

After mixing the materials by a mixer, a quantity was taken for standard samples (5x5 cm) making for testing for compressibility and permeability. **Table 6** , illustrated the properties of the sand mold The sand casting was made. The metal was melted for casting to acquire castings (50 mm diameter x 30 cm long specimen each) .

RESULTS OF CASTINGS INSPECTION

A casting is considered to have achieved its purpose only after the casting is ascertained of being up to the required specifications. This entails the following tests:

1- Chemical Composition

The chemical composition of steel CK45 was tested. **Table 7** , illustrated it.

2- Non- Destructive Tests

(a) Visual inspection

An inspection was conducted for any apparent defect (tears and cracks) .

(b) Penetration Inspection This penetration inspection used to detect surface defects which can not be determined visually.

(c) Radiographic

(a) x-ray (short wave ray) was used for inspection of the casting to detect internal defects. These rays can penetrate metal, passing via the casting to be inspected. It records on a photographic film, indicating the passing ray's density. Defects appear as opaque spots. Thus, their locations are determined. Inspection time was 2.5 min at 200 KV by German Feifer1 Apparatus No. 020386-17 .

(b) Ultrasonic inspection

This inspection was implemented to detect minute defects, inside the metal, which can not be detected by x- ray. USK7-5 apparatus with SEB2H probe and electronic oscillograph was used. The same prepared surface is inspection (3-15-2-2) was used . A gelatinic materials was used. A gelatinic material was used to facilitate movement of the probe along the surface.

Above inspections were conducted at State Company for Heavy Engineering Equipment / Quality Control.

(d) Surface Roughness Inspection

Talysurfu Apparatus of Technology University – Production and Metals Dept. was used to inspection the surface roughness.

(e) Mechanical Properties inspection

(1) Tensile Strength

Tensile specimen castings were obtained according to ASTM-A48-83, whose axsymmetric dimensions are specified in **Fig.1.**

(2) A tensile test by Instron 1195 apparatus was conducted. Fig.(2) shows the stress- strain curves for the steel CK45 in the three cases

(i.e when the Sodium Carbonate, Oat flour and Glycerin are used)

Table 8, illustrates the results of tensile test .

(3) Impact Strength

The specimens which were prepared of the same casting according to ASTM-A48-83 specifications was chosen for impact strength by Charpy method. The dimensions are as shown in the **Fig.3** , the apparatus used was Heckrt type.

Table 9, illustrated the results of impact test .

(4) Hardness Tests

Brinell method for hardness test was used , implementing a quenched steel ball , 5mm diameter and load 750 Kg, by Leybod Harris apparatus .Table-10- illustrated the results of hardness test .

MICROSCOPIC TEST OF SPECIMEN

Casting specimens were microscopically tested as follows:

- The specimen is made fine by smoothing apparatus of different grades (120, 200, 350, 500, 800, 1000).
- It is then polished by a polishing cloth with alumina solution of 0.3 micron. It is then washed and dried .
- Chemical treatment by Nital solution (1.8 nitric acid, 0.98 methyl alcohol)
- It is tested by optical microscope (Nikon73346) at X27 magnification, then photographed by a digital camera attached to the microscope. The photos of microscope are shown in the **Fig.4** .
- **MODEL GENERATION BY ANSYS**
- The ultimate purpose of a finite element analysis is to re-create mathematically the behavior of an actual engineering system. In other words, the analysis must be an accurate mathematical model of a physical prototype. In the broadest sense, the model comprises all the nodes, elements, material properties, real constants, boundary conditions and the other features that used to represent the physical system.
- In ANSYS terminology, the term model generation usually takes on the narrower meaning of generating the nodes and elements that represent the special volume and connectivity of the actual system. Thus, model generation in this study will mean the process of defining the geometric configuration of the model's nodes and elements. The program offers the following approaches to model generation (Saeed Mouveni ,1999).
  - a) Creating a solid model
  - b) Using direct generation
  - c) Importing a model created in a computer-aided design CAD system.
- The method used in this research to generate a model is solid model. In solid modeling some one can be described the boundaries of the model, establish controls over the size and desired shape elements automatically, i.e. drawing the two dimensional specimen model and meshing using meshtool and express the axsymmetrical condition . Solid modeling is usually more powerful and versatile than other modeling, and is commonly the preferred method for generation models. The Two Dimension model of specimen is done by drawing and meshing two dimensional axisymmetry specimen with element plan82. **Fig.5**, shows the specimen model in ANSYS. (ANSYS on-line-help,1996).

Fig.6, shows the stresses distribution and the deformed shape in the specimen when the glycerin additive is used to the mould sand. **Fig.7**, shows the stresses distribution and the deformed shape in the specimen when the sodium carbonate additive is used to the mould sand. **Fig.8** , shows the stresses distribution and the deformed shape in the specimen when the oat flour additive is used to the mould sand. From these figures it can be get that, in the case of glycerin additives the max. stress is (0.359 GPa) and with sodium carbonate additives (0.328 GPa) and for oat flour additives (0.321 GPa), from these results it can be concluded that the sand mold with additives glycerin is produced specimen bearing stresses more than the other additives.

CONCLUSIONS

1- The additives to the sand made improvement in impact, tensile strength and hardness for the carbon steel CK45 casts produced

2- It found that sodium carbonate was led to high improvement in these properties of casts and after that the addition of oat flour which also effect in improvement the mechanical properties of casting compared with the casting without additives.

3-Also it’s found that the stresses distribution in case of sodium carbonate additive is more efficient than the other two cases and the cast produced bearing more stresses than the others.

REFERENCES

Abbas A. A. Al-Raid, “Study the Iraqi Sand Properties by CO_2 Method”, M.Sc. Thesis, Univ. of Technology, 1978.

Abid Al-Razaq I. Khdiar , “Casting Technology” , University of Technology Published, 2000.

Asaad K. Mezher, “Stresses Analysis of the Casting Dies by Finite Element Method”, M.Sc. Thesis, Univ. of Technology, 2004.

Basic Structural Non-linearities, Training Manual, (ANSYS Inc., (ANSYS on-line-help),1996.

Douglas Doehlert, “www.Fargo.ars-usda.gov/cer.Acl.htm”, 2000.

J.G. Sylvia, "Cast Metals Technology", Canada, 1972.

K.Strauss, "Applied Science in the Casting of Metals" , Pergamon Press, NewYork 1970.

Najia Yousif Khaiou, “Effect of Additives on Properties of Sand Moulds”, M.Sc. Thesis, Technical College , Baghdad , 2005.

Saeed Mouveni, “Finite Element Analysis - Theory and Application with ANSYA”, 1999.

St. dobosz. D. Drozyuski and A. chojecki, “Mechanical Damage Mechanism of Moulding Sands”, Engineering University of Mining and Metallurgy, Krakow, Poland, 1997.

www.egsma gov.eg/bentonite, 1998.

www.flauqnart.com, Oat, Oat flour, December, 2000.

Table-1- Chemical composition of the used sand

Loss on Ignition	K_2O % Max.	MgO %	CaO%	Fe_2O_3 % Max	Al_2O_3%	SiO_2% Min
0.6	0.1	0.3	0.8	0.2	0.3	97.7

Table-2- Chemical composition of the bentonite binding material

% Loss on Ignition	CaO % Max.	Fe_2O_3 % Max	Al_2O_3% Min	SiO_2% Max
10.5	5.5	5.5	13	57

Table -3- Oat Flour consistent

Moisture	Fat %	Starch and Glucose %	Protein%
8.5	8	66	10

Table- 4- Elements in Oat Flour consistent

Phosphore	Magnesium	Potassium	Sodium	Calcium
405 mg/100g	17 mg/100g	268 mg/100g	6 mg/100g	54 mg/100g

Table – 5 – The weight percentage of the additives

Sodium Carbonate	Oat flour	Glycerin
0.5	0.25	0.25

Table – 6 - Properties of the sand mold

Strength of dry compression (MPa)	Strength to moist compression (MPa)	Moist hardness No. B. scale	Permeability No.	% of Addition	Additives
1.7	0.035	65	70	---	None
0.425	0.045	73	55	0.5	Na_2CO_3
0.325	0.032	56	80	0.25	Oat flour
0.43	0.04	72	51	0.25	Glyceral

Table – 7 – Chemical composition for Carbon Steel CK45

Element Wt%	C	Si	Mn	P	S	Cr	Mo	Ni
Standard Value	0.4-0.5	0.4	0.5-0.8	0.035	0.035	0.4	0.1	0.04
Actual Value	0.4	-	0.573	-	-	0.051	0.018	0.077

Table – 8 – Tensile test results

Mech. Properties of steel CK45 / cast Type of Sand Additive	Yield strength MPa	Ultimate Strength MPa	Elongation %	Yonug Modulus GPa
Sodium Carbonate	297.27	743.18	9.58	3.100
Oat flour	258.57	790.6	12.03	2.154
Glycerin	331.788	683.09	7.5	4.43

Table – 9 – Impact test results

	Oat flour	Sodium Carbonate	Glycerin
Impact Stress N/mm^2	169.13	209.75	171.1

Table –10 – Hardness test results

	As received	Oat flour	Sodium Carbonate	Glycerin
Hardness Kg/mm^2	162.4	168.8	172	153

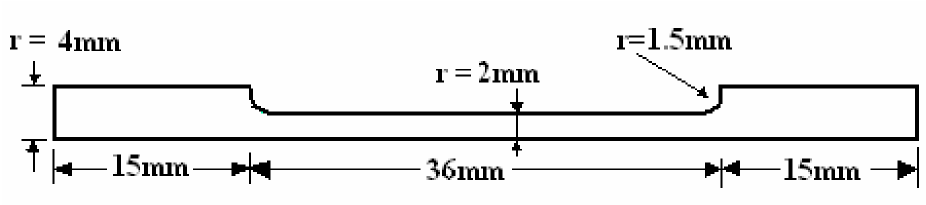

Fig.(1) Dimensions of tensile specimen

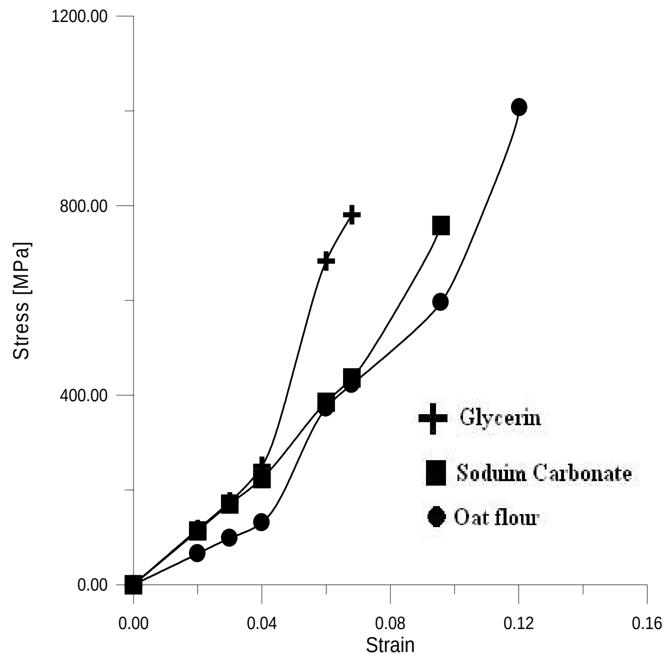

Fig.(2) Stress- Strain curves for the steel CK45 cast in the three cases (Sodium Carbonate, Oat flour and Glycerin)

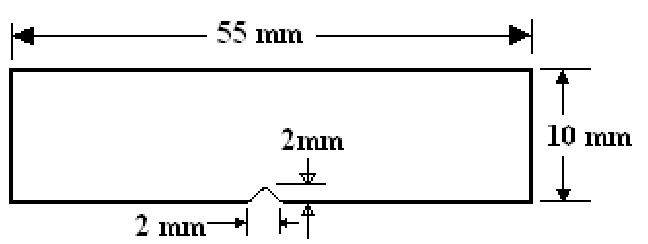

Fig.(3) Impact test specimen

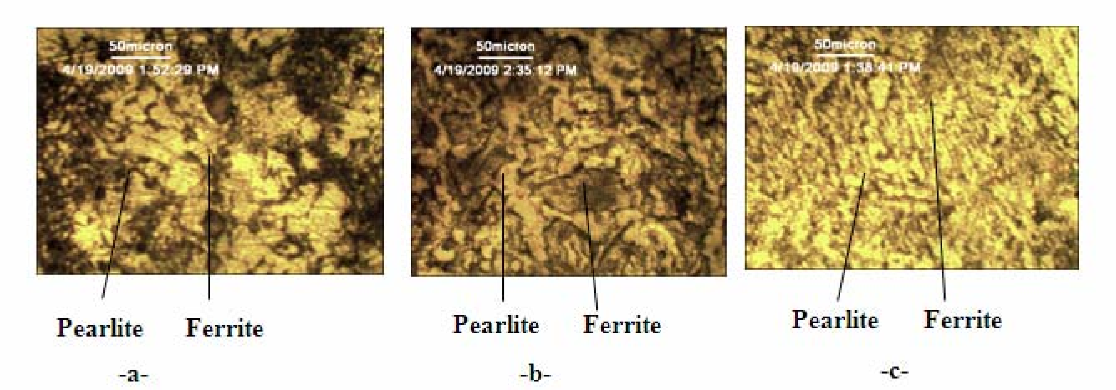

Fig.(4) microscopic structure of the cast produced (a) mould sand with Glycerin (b) mould sand with Sodium Carbonate (c) mould sand with Oat flour

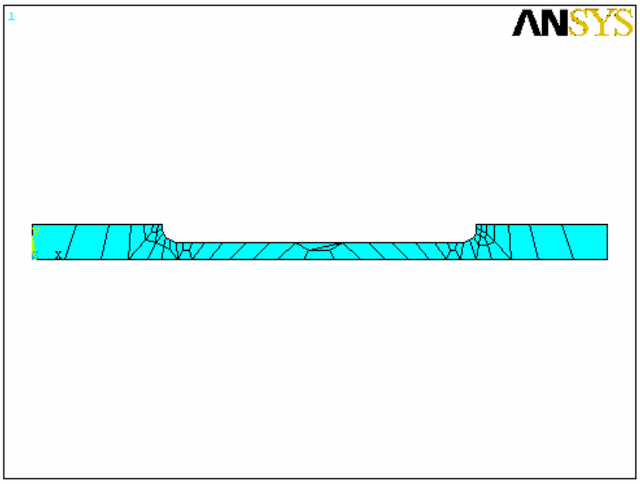

Fig.(5) Model of the specimen in ANSYS

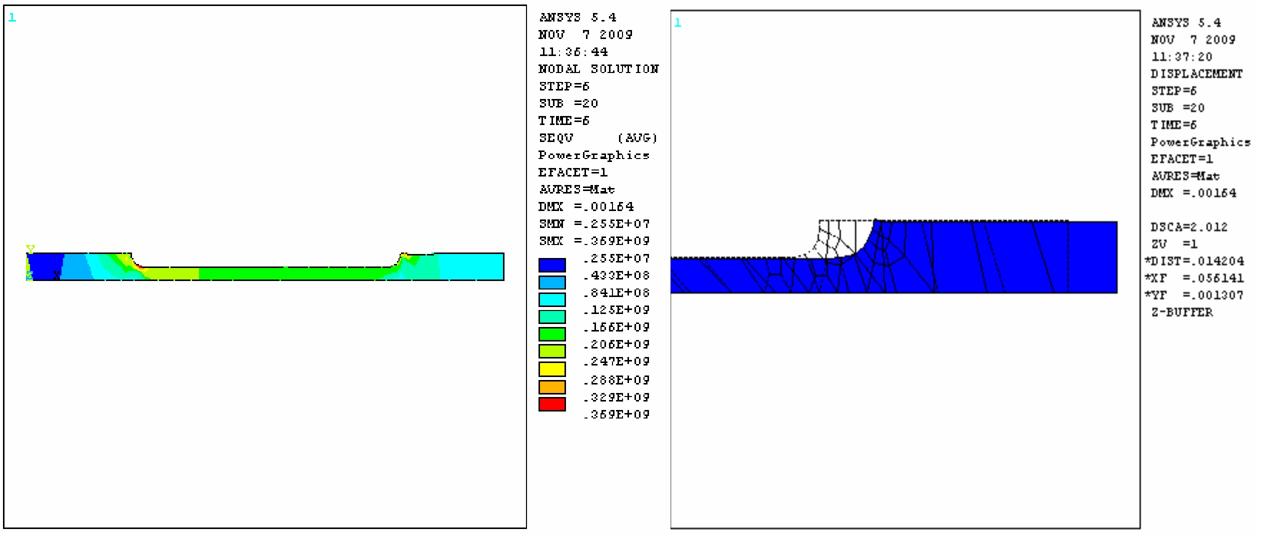

(a) Stresses distribution (b) deformed shaped

Fig.(6) Stresses distribution and the deformed shape in the specimen when the glycerin additive is used to the mould sand

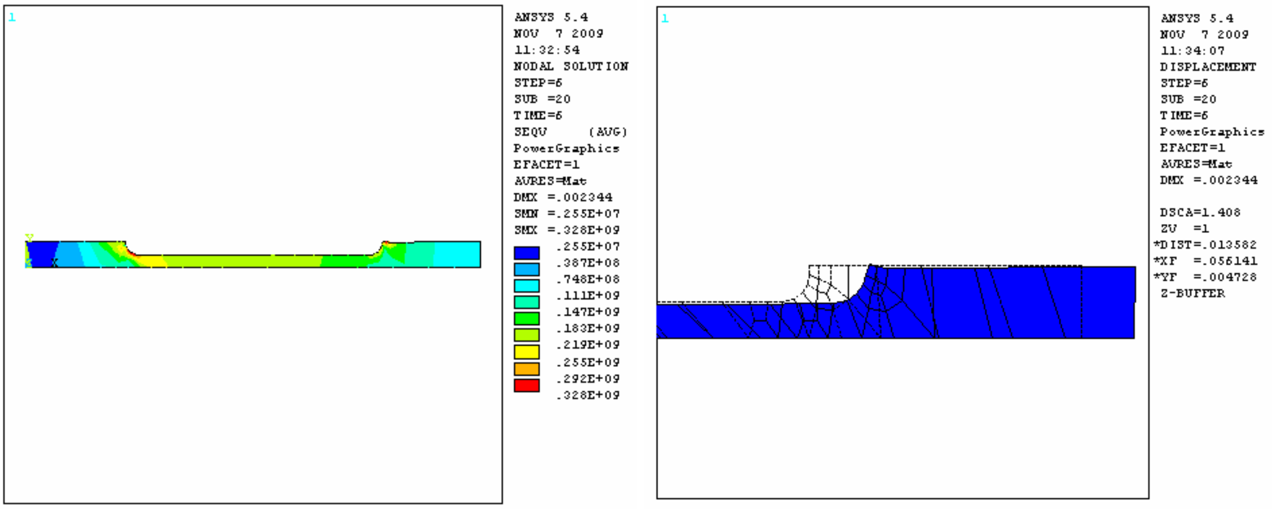

(a) Stresses distribution (b) deformed shaped

Fig.(7) Stresses distribution and the deformed shape in the specimen when the sodium carbonate additive is used to the mould sand

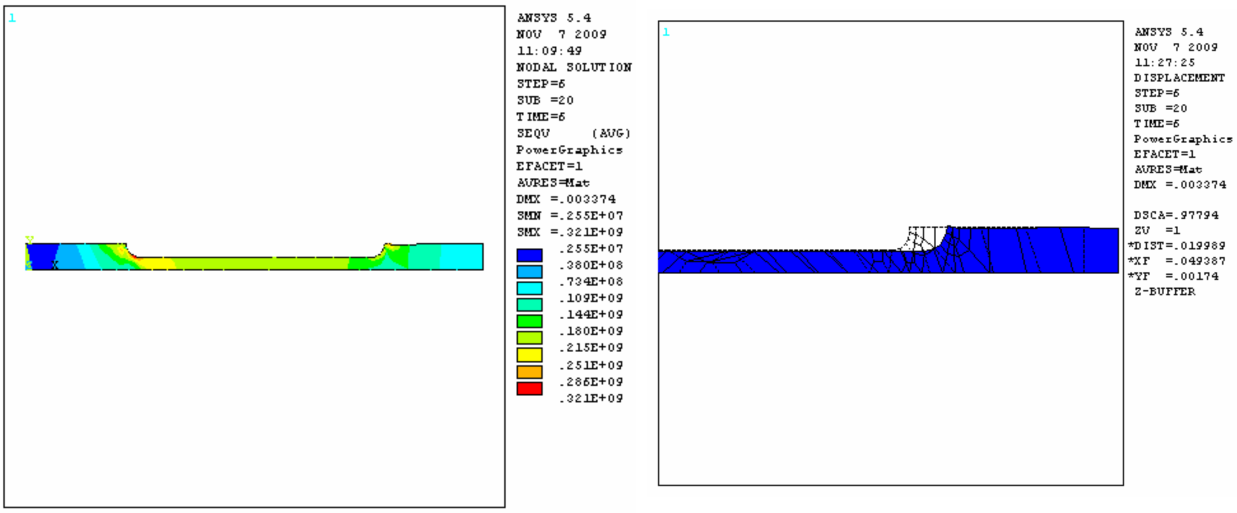

(a) Stresses distribution (b) deformed shaped

Fig.(8) Stresses distribution and the deformed shape in the specimen when the oat flour additive is used to the mould sand.

Preservation of Required Chlorine Concentration in Baghdad Water Supply Networks using On-Site Chlorine Injection

Prof. Dr. Rafa H.Al-Suhaili● **Riadh Fadhil Nsaif Al-Azzawe●●**

Dean of the college of engineering University of Baghdad. M.sc Environmental engineering

Abstract

The chlorine concentration variation in Baghdad water networks was studied. The chlorine data were collected from Mayoralty of Baghdad and Ministry of Environment (MOE) for the networks for both sides of the city Karkh and Rasafa for (2008-2009). The study of these data indicates that there are no systematic testing program .Classified GIS maps showed that the areas far from the treatment plants have almost always low chlorine concentration .This indicates that the problem of the low chlorine concentration in the far areas is due to cracks of pipe along the conveyance path ,as expected. The area's most frequently have low concentration are Al-sadir,Al-Kadhimya, and Al-Amiria . It was found also that the chlorine concentrations were lowest in summer months than those in winter months.The Amiria area district (636) was selected as a case study to test the ability of using the quantitative- qualitative model in the EPANET software, to find the required onsite chlorine injection point number, locations and dose, so as to raise the chlorine concentration to the acceptable limits in the other nodes of the network. The bulk decay coefficient was found to be (-2.212)1/day and the wall coefficients were found to be between (-0.001)to(-0.9)1/day The main conclusion of this study is that the onsite injection can improve the chlorine concentration in Baghdad water supply networks. The EPANET model can be used effectively to obtain the required injection program for this purpose.

الخلاصة

حفظ تركيز الكلور المطلوب في شبكات مياه الشرب في بغداد بأستعمال حقن الكلور في الموقع .

في البحث تم دراسة تلوث المياه في شبكات ماء بغداد من ناحية تركيز الكلور المتبقي فقط. ثم جمع المعلومات والخرائط الخاصة بشبكات المياه ومشاريع التصفية في بغداد من الكرخ والرصافة .كما تم جمع البيانات الخاصة بقياسات تركيز الكلور في تلك الشبكات من الجهات التي لهاعلاقة (وزارة البيئة وأمانة بغداد) وتم توحيدها في نظام المعلومات الجغرافية(GIS). البيانات المتوفرة لسنتين (2008-2009).

من خلال دراسة تلك البيانات تبين عدم وجود نظام قياسات متبع لاجراء القياسات في أوقات محددة أو أماكن محددة ،ولكن هناك مبدأ عام هو أن يكون هناك قياس واحد على الاقل شهريا. أما من ناحية الاماكن التي يتم فيها القياس فأن المبدأ العام المتبع من قبل تلك الجهات هو تغطية جانبي الكرخ والرصافة قدر الامكان شهريا.

بين التحليل لتاك البيانات والخرائط المنتجة بنظام المعلومات الجغرافية بأن أكثر المناطق تلوثا هي المناطق الواقعة في أطراف المدينة مما يوكد بأن سبب المشكلة هي ما يطرأ من مشاكل على المياه أثناء عملية جريان المياه في الانابيب وكلما زادت المسافة كلما زاد أحتمال التلوث وبالتالي نقصان تركيز الكلور. من تلك المناطق مدينة الصدر ،الكاظمية ،العامرية.كما بين التحليل أن تركيز الكلور في فصل الصيف يكون أقل منه في الشتاء.تم أختيار منطقة العامرية (جزء من الشبكة فيها) محلة (636) كحالة دراسية لاختبار أمكانية أستخدام نموذج النوعية – الكمية الموجود في برنامج (EPANET) لايجاد نقاط الحقن الموقعي بالكلور وكمية الجرعة بحيث ترفع نسبة الكلور في نقاط تلك الشبكة الى 0,5 ملغم/لتر أو اعلى بقليل.قبل أمكانية تطبيق البرنامج يتطلب حساب معامل التحلل العام (Bulk decay coefficient) ومعامل التحلل بجدار الانبوب (Wall decay coefficient) .لحساب المعامل الاول جمعت عينات من الماء تم فحصها باوقات مختلفة لايجاد تغاير تركيز الكلور مع الزمن ومن ثم تم أيجاد المعامل على انه انحدار المنحني ($\frac{C_t}{C_0}$) مع الزمن (t) وقد كانت قيمته (2.212-)1\day.أما بخصوص حساب معامل التحلل لجدار الانبوب فقد تم أولا أجراء قياسات حقلية لتركيز الكلور في الشبكة المستخدمة كحالة دراسية في 17 نقطة ولمدة (6) أشهر وتم حساب معامل الجدار باستخدام طريقة المحاولة والخطأ بأستخدام البرنامج (EPANET) حيث يضخ البرنامج في نقطة المصدر بالقيمة المقاسة ويحسب بالنقاط الاخرى بأستخدام قيم مفروضة ويتم تعديلها الى ان تتطابق القيم المقاسة مع القيم المحسوبة بالبرنامج .أعتمد مبدأ مجموع مربعات الفروق بين القيم المقاسة والقيم المحسوبة.قد بينت النتائج أن قيم معامل التحلل للجدارتتراوح بين - 0.9- to (0.001)1/day.

تم تطبيق البرنامج EPANET لايجاد نقاط الضخ الموقعي للكلور على حالة معدل الجريان اليومي وتم استخدام عدة حالات ادرجت منها افضل حالتين .حالة (A)حيث ان نقطة ضخ الكلور الموقعي في نقطة رقم (5) وخلال فترتين في اليوم من الساعة 7-11 صباحا ومن الساعة 4-8 مساءا وبجرعة (1.5) ملغم/لتر .أما الحالة (B) بنفس النقطة ونفس الفترة ولكن بجرعة قدرها (0.8) ملغم/لتر. أظهرت النتائج بأن الحالة (A) هي الافضل لكونها ترفع تركيز في تلك الفترات في النقاط المختلفة للشبكة الى قيمة تقع ضمن الحدود المقبولة لتركيز الكلور وهي (2-0.5) ملغم/لتر.ولكن يجب الاشارة الى انه أن كان هناك تلوث كبير في الشبكة الحالة (A)هي المفضلة أما في حالة التلوث القليل فأن الحالة (B) هي الافضل .

Key word: Water ,Supply ,Network , EPANET , Geographical ,Information ,System , Sectoral, Chlorine, Injection .

Introduction

As it is well known, Baghdad is one of the largest cities in the middle east. During the last three decades the city was subjected to large extension which effects the level of infra-structure services such as water supply networks. Due to wars and sanction these old networks were subjected to deterioration, Such as many cracks in pipes and leakage. These factors had resulted many water pollution detected in the networks. in order to solve this problem large maintenance efforts and pipes changing are required . This solution is rather expensive and needs large efforts and may disturb the life activities and traffic movement specially in old crowded areas near the center of the city .An inexpensive solution is required to improve the water quality in these networks by using onsite injection of chlorine in a selected points and with the required dosage. In order to evaluate such solution a quantitative qualitative water model is required. Using such model the required number of these injection points their locations and the proper chlorine dosage can be found. There are many water quality testing points in the networks of Baghdad available from the Ministry of Environment (MOE) and Mayoralty of Baghdad .These testing points can be used to classify the water quality in Baghdad networks using GIS. The water quantitative qualitative model can be built to evaluate the effectiveness of an onsite injection program using one of the areas as a case study , where a low chlorine concentration is deducted and classified through the GIS model.

Previous Studies:

Islam and Chaudhry (1997), had presented. The Surface Water Treatment Rule under the Safe Drinking Water Act and its amendments require that the water utilities maintain a detectable disinfectant residual throughout the distribution system at all times. A computer model was presented to directly calculate the chlorine concentrations needed at the source(s) to have specified residuals at given locations in a pipe network in unsteady flow conditions by using an inverse method.

Rossman,et .al. (1994), had presented, a mass-transfer-based model developed for predicting chlorine decay in drinking-water distribution networks. The model considers first-order reactions of chlorine to occur both in the bulk flow and at the pipe wall.

Clark, et.al.(1988), had presented . The Safe Drinking Water Act (SDWA) of 1974 requires that the U.S. Environmental Protection Agency (EPA) establish maximum contaminant levels (MCLs) for each contaminant which may have an adverse effect on the health of persons. The approach suggested in this research will provide useful insight into the water quality variations that may impact consumers at the tap and the development of time and spatially sensitive monitoring strategies.

Clark, et.al. (1993). Had presented, that the Safe Drinking Water Act and its Amendments (SDWAA) will pose a massive challenge for the drinking-water industry in the United States. As the SDWAA regulations reach implementation, increasing effort will be devoted to understanding the factors causing deterioration of water quality between treatment and consumption. Models are used to predict the propagation of chlorine residual in one portion of the water supply system. It was found that residuals varied widely both spatially and temporally.

Shang, and et.al. (2002), had presented, it was a novel input-output model of water quality in water distribution systems .presented as a particle (water parcel) backtracking algorithm (PBA). The PBA is a simpler and more efficient version of that described by **Zierolf and et.al. (1998)** and is extended to allow storage tanks and multiple water sources and quality inputs.

Zierolf , (1998), had presented ,that chlorine concentrations within drinking water distribution system (DWDS) must be maintained between an Environmental protection agency enforced minimum and maximum values driven by formation of harmful disinfectant byproducts .The DWDS input-output (I-O) model developed expresses the chlorine concentration at a given pipe junction and time as a weighted average of exponentially decayed values of the concentrations at all adjacent upstream junctions.

Dominic and et. al:(1998), had presented, that a booster disinfection is the addition of disinfectant at location distributed throughout a water distribution system. such a strategy can reduce the mass of disinfectant required to maintain a detectable residual at points of conception in the distribution system.

Rossman, and et.al. (1993), had presented. An explicit dynamic water-quality modeling algorithm developed for tracking dissolved substances in water-distribution networks. The algorithm is based on a mass-balance relation within pipes that considers both advective transport and reaction kinetics.

Boulos and et.al.(1995), had presented , an efficient system simulation methodology that solves the contaminant-transport problem in drinking-water-distribution systems is developed. **Islam and chaudhry (1998)**,had presented ,a new computer model is presented to predict the spatial and temporal distribution of residual constituent in a pipe network under slowly varying unsteady flow conditions.

Geographical Information System Analysis

Baghdad has a large water supply networks. These networks could be an old one, or relatively new one. As these networks ,were constructed in different times ,different pipe types were used ,such as ductile ,asbestos ,p.v.c ,and others. Since many of these networks were subjected to deterioration due to sanction and wars ,it has many defects such as leaks and interference with sewerage water ,which cause water contamination in these networks. Due to the problem of local contamination of the water in the networks because of the defects mentioned above ,and as traditional monitoring system for water quality related authorities were conducting a water testing program. Amanat Baghdad and Ministry of Environment (MOE) are the main water quality monitoring authorities for Baghdad water supply systems. There are no systematic clear testing program for water testing in the city, i.e. no certain time period for the frequency of testing. However it can be approximately considered that the testing program is on monthly measurements basis. In addition, the testing program may be affected by a call from the ministry of health, if water borne disease is recorded in a certain location. Moreover testing points and frequency were increased at the areas, where the network is considered as old.The chlorine data available for the water quality in Baghdad networks are as shown in table (1) below.

The locations of measurements were randomly distributed. Upon discussion with the testing teams of Amanat Baghdad and the Ministry of Environment (MOE), the researcher observed the followings.

1- There is no coordination between the two – teams of both autherties.

2- Even though the testing locations were selected randomly, both teams clarify that, their concept of testing location selection is trying to cover the areas of the city ,in both sides karkh and Rasafs each month.

3- Sometimes the location of testing is selected accoarding to claims of citizens in a certain area of bad water quality water ,or due to a notice from the Ministry of Health (MOH). The GIS analysis was conducted for two years (2008to 2009),where the data is available.Fig(1) shows the chlorine distribution in Baghdad water supply networks.This GIS map includes all the data collected during 2008. This shows that the chlorine concentration is less than 0.5 mg/L, for (4.167) %of the area of Baghdad. Figs (2) and (3) shows the GIS map of chlorine concentration in year 2008 in winter and summer respectively. It is clear from comparison that the case is better in winter than that in summer. The percentages of area of chlorine less than 0.5 mg/L are (1.827)% and (5.676)% respectively.Figs (4), (5) shows the GIS map of chlorine concentration in year 2009 in winter and summer respectively. Same condusions as in year 2008 could be concluded that the case is better in winter than in summer. The percentages area of less than 0.5 mg/L chlorine concentrations are (0.989) % and (1.582) % respectively. Fig (6) shows the chlorine distribution in Baghdad water supply networks, for year 2009.

Experimental Work ,and EPANET Modeling For Onsite Chlorine injection .

From the GIS analysis presented in the previous section , any location had introduced chlorine concentration less than 0.5mg/L during, any periods in years 2008and 2009, can be used as a case study for the onsite chlorine injection presentation. One of these locations were selected as a case study, that is district 636 in the karkh side, Al-Amiria .The water supply network at this district is shown in fig (7)

A site testing program for chlorine concentration was conducted during six month in 2009; Jan; Feb; March (winter), and (June, July, and August), summer. Tables (2) and (3) show the locations, NE coordinates, pipes and nodes details, and the chlorine concentration during the six months. Table (5) shows the average and standard deviation of chlorine concentration in each node.

The measurements were conducted using portable chlorine concentration measuring device (ELAMOTTE,OCTA-SLIDE.CODE1100) .In order to apply the EPANET model for the case study ;the bulk decay coefficient of chlorine should be estimated .The measurement were conducted using 16 samples collected .

The measured chlorine concentration is then calculated in different times as shown in Table(6).

1- Bulk Decay Coefficient:
Referring to table (6) the data of log($c_1/c_\circ$) versus time is plotted as shown in fig(8) the slope of this line (-2.212)/day is the bulk decay coefficient .

2- Wall Decay Coefficient
The wall decay coefficient can be estimated using EPANET by a trial and error approach. This can be accomplished by assuming a wall decay coefficient for all or, each pipe. Then after running the hydraulic and quality analysis using EPANET ,the chlorine concentration in the other nodes could be estimated .IF these values compare well with the measured values ,the assumed wall decay coefficients were considered as the real values .IF these values were significantly different ,adjustment of the assumed values were done until a good match was obtained . Table (7) shows the final wall decay coefficients for each pipe of the case study .They are estimated using average measured concentration values on table (5)of summer months (June,July,August). Fig (9) shows the comparison between measured and estimated values which shows good match.

In order to find the location (s) of the required injection points and the required injection dose and patterns the EPANET water quality model is used. This model is used for the expected hydraulic condition of the network. The hydraulic pattern is either constant daily demand (average), or daily variation demand pattern. In order to apply the EPANET model for the network of the case study the values of the Bulk Decay coefficient and the wall Decay Coefficients of the pipes are fed to the software. After which different onsite injection proposals are tried to find which proposal is useful to raise the chlorine concentrations at the nodes of the network case study to an acceptable one. Since the operation base is daily, the concept is to use injection pattern to raise the chlorine concentrations to these acceptable values during the hours of high use of water. For the case of presentation two cases were selected .Fig, (10) shows the node numbering system of the case study network.

1- aseA:Injection of Chlorine at node 5 with 1.5 mg/lit dose for the 4 hrs from (07-11)am and 4hrs (4-8) pm.The results of the chlorine concentrations at different nodes are shown in figures (11) to (20) below. It is obvious from these figures that the injection raise the chlorine concentrations to an acceptable values for all the nodes. **(Note that the time axis start at 6.00Am in these Figures)**
2- 2-Case B :Injection of Chlorine at node 5 with 0.8 mg/lit dose for the 4 hrs from (07-11)am and 4hrs (4-8) pm.The results of the

chlorine concentrations at different nodes are shown in figures (21) to (30) below. It is obvious from these figures that the injection raise the chlorine concentrations to an acceptable values for all the nodes.

3- Comparing the two cases indicates that the first case is preferable since at most nodes most of the concentration are within (0.5-2)mg/lit. However, for high contaminated water case (A) is the better, while for low contamination case (B) is preferable. Table (8) shows the concentrations at the nodes for the two cases.

Conclusions.

1. There is no obvious chlorine testing program for Baghdad water networks adopted by the responsible Authorities. However concerning temporal variation, one can say the testing is on monthly basis. Random spatial test selection locations is selected by these authorities trying to cover Karkh and Rasafa each month. Moreover there are no any coordination between the two authorities responsible for this testing.
2. Geographical Information System analysis for Baghdad water networks chlorine concentrations had indicated the followings.
   a) The number of locations of low chlorine concentration is increased in summer months than those in winter, due to chlorine depletion.
   b) The most frequent areas of low chlorine concentration are at Al-sader, Al-Zafarinia, Al-Kadhimia, and Al-Amiria .
   c) The areas of low chlorine concentrations usually located distances far from the treatment plants, which indicates that this low concentrations is due to conveyance problems.
3. The Experimental work indicated that the Bulk decay coefficients for the water network of the selected case study (Al-Amiria network) is (-2.212)/ day.
4. The wall decay coefficient found using EPANET for all the pipes of the network case study is within the range (-0.001 to -0.9).

   EPANET model can be used to find the injection strategy for the selected network. Application of the onsite injection for the network of the case study is used using two cases A and B. For case A the injection at node 5 with 1.5 mg/lit dose of chlorine within two periods during the day each for 4 hrs. The first is for (7 to 11) am and the second for (4-8) pm. For case B the injection is at the same node and periods, but with a dose of 0.8 mg/lit. The results indicates that case A is preferable since it raise the chlorine concentration to values within the acceptable limits of (0.5 to 2) mg/lit.

References.

1.M. Rashidul Islam and M. Hanif Chaudhry (October 1997) "Inverse Modeling of Chlorine Concentration in Pipe Networks under Dynamic Condition"J. Envir. Engrg. Volume 123, Issue 10, pp. 1033-1040 (October 1997).

2. L.A. Rossman, R.M Clark, and W.M. Grayman. Modeling chlorine residuals in drinking-water distribution systems. Journal of Environmental Engineering,

ASCE, 120(4):803{820, July-August 1994.

3. M. Clark, Walter M. Grayman, and Richard M. Males (1988)"Contaminant Propagation in Distribution Systems"J. Envir. Engrg. Volume 114, Issue 4, pp. 929-943 (1988).
4. M. Clark, Member, ASCE; Walter M. Grayman, Member, ASCE; Richard M. Males, Member, ASCE; and Alan F. Hess, (1993)"Modeling Contaminant Propagation in Drinking-Water Distribution Systems"J. Envir. Engrg. Volume 119, Issue 2, pp. 349-364 (1993).
5. Feng Shang, James G. Uber, and Marios M. Polycarpou (2002)"Particle Backtracking Algorithm for Water Distribution System Analysis"J. Envir. Engrg. Volume 128, Issue 5, pp. 441-450 (2002).
6. Zierolf, M.L.; Polycarpou, M.M.; Uber, J.G. Jul 1998"Development and auto calibration of an input-output model of chlorine transport in drinking water distribution systems" Control Systems Technology, IEEE Transactions on Volume 6, Issue 4, 1998.
7. Dominic L. Boccelli, et.al (1998)"Optimal Scheduling of Booster Disinfection in Water Distribution Systems"J. Water Resour. Plng. and Mgmt. Volume 124, Issue 2, pp. 99-111 (1998).
8. Lewis A. Rossman1, Paul F. Boulos,2 and Tom Altman3 (1993) "Discrete Volume-Element Method for Network Water-Quality Models"J. Water Resour. Plng. and Mgmt. Volume 119, Issue 5, pp. 505-517 (1993).
9. Paul F. Boulos, et.al (1995)"Discrete Simulation Approach for Network-Water-Quality Models"J. Water Resour. Plng. and Mgmt. Volume 121, Issue 1, pp. 49-60 (1995).
10. M. Rashidul Islam and M. Hanif Chaudhry (1998)"Modeling of Constituent Transport in Unsteady Flows in Pipe Networks"J. Hydr. Engrg. Volume 124, Issue 11, pp. 1115-1124 (1998).

Table(1) chlorine Data used for GIS classification :

Year	Months	Average No.of location
2008	Jan,Fab,Mar,April,May,June,July,October,November.	1250
2009	Jan,Fab,Mar,April,May,June,July,August,September,October,November.	930

Table (2) Field Testing Chlorine Measurement

Nods No.	East North	Chlorine conc. Mg/l Jun	Chlorine conc. Mg/l July	Chlorine conc. Mg/l Augusts	Chlorine conc. Mg/l Jan	Chlorine conc. Mg/l Feb	Chlorine conc. Mg/l March
1-	44.17.17,1 33.18.10	0.6	0.5	0.6	1.5	1.1	1
2-	44.17.06,8 33.18.06,8	0.55	0.45	0.58	1.4	0.9	0.6
3-	44.17.03,6 33.18.09,8	0.5	0.4	0.5	1	0.8	0.7
4-	44.16.54,2 33.18.05,6	0.48	0.36	0.49	0.7	0.5	0.6
5-	44.16.50,4 33.18.04,3	0.45	0.32	0.45	0.5	0.1	0.2
6-	44.16.51,4 33.18.04,4	0.42	0.3	0.42	0.3	0.2	0.2
7-	44.16.55,6 33.18.01,9	0.4	0.27	0.4	0.6	0.4	0.3
8-	44.16.55,6 33.17.58,8	0.37	0.25	0.36	0.5	0.1	0.4
9-	44.16.54,1 33.17.56,0	0.35	0.2	0.32	0.3	0.2	0.1
10-	44.16.51,6 33.17.59,9	0.3	0.18	0.3	0.4	0.3	0.2
11-	44.16.49,3 33.18.02,9	0.38	0.39	0.39	0.48	0.35	0.3
12-	44.16.51,1 33.17.55,6	0.2	0.12	0.25	0.45	0.45	0.2
13-	44.16.46,5 33.18.01,7	0.35	0.29	0.32	0.45	0.45	0.4
14-	44.16.43,4 33.18.00,8	0.32	0.25	0.32	0.4	0.35	0.45
15-	44.16.41,0 33.17.59,3	0.28	0.23	0.29	0.37	0.4	0.45
16-	44.16.46,7 33.17.52,0	0.08	0.05	0.1	0.3	0.49	0.49
17	44.16.50,0 33.17.50,5	0.19	0.11	0.23	0.25	0.4	0.45

Table (3) Pipe Details of the Case Study

Pipe No.	Dia mm	Length m
1-	100mm	300m
2-	100mm	100m
3-	100mm	260m
4-	100mm	50m
5-	75mm	40m
6-	75mm	160m
7-	75mm	60m
8-	75mm	60m
9-	75mm	120m
10-	75mm	100m
11-	100mm	150m
12-	75mm	220m
13-	75mm	280m
14-	100mm	50m
15-	100mm	280m
16-	75mm	50m
17-	100mm	50m
18-	100mm	50m

Table (4) Nodes Details of the Case Study

Node No.	Number of the Served person	Estimated Average Demand Liter/min
2-	29	5.03472
3-	7	1.21528
4-	7	1.21528
5-	6	1.04167
6-	8	1.38889
7-	10	1.73611
8-	4	0.69444
9-	7	1.21528
10-	7	1.21528
11-	12	2.08333
12-	14	2.43056
13-	13	2.25694
14-	14	2.43056
15-	7	1.21528
16-	8	1.38889
17-	13	2.25694

Table (5) Average and Standard Deviation of the Measured Chlorine Concentration in the Nodes of the Network Case Study

Node	Av: Conc:	Standard déviation	Av summer
1-	0.883333	0.386868	0.566667
2-	0.746667	0.35393	0.526667
3-	0.65	0.225832	0.466667
4-	0.521667	0.116003	0.443333
5-	0.336667	0.159583	0.406667
6-	0.306667	0.098522	0.38
7-	0.395	0.115542	0.356667
8-	0.33	0.138275	0.326667
9-	0.245	0.094604	0.29
10-	0.28	0.08	0.26
11-	0.381667	0.059133	0.386667
12-	0.278333	0.139344	0.19
13-	0.376667	0.067429	0.32
14-	0.348333	0.06969	0.296667
15-	0.336667	0.083347	0.266667
16-	0.251667	0.204491	0.076667
17-	0.271667	0.129061	0.176667

Table (6) Chlorine Concentration Tested at Different Times.

Time hr.	Chlorine conc. Mg/L
0	0.7
1.5	0.65
3	0.6
4.5	0.55
6	0.45
7.5	0.4
9	0.35
10.5	0.32
12	0.3
13.5	0.27
15	0.25
16.5	0.22
18	0.2
19.5	0.15
21	0.1
22.5	0.07

Table (7) Pipes Wall Decay Coefficients

Pipe No.	Wall decay coefficient
1	-0.2
2	-0.9
3	-0.1
4	-0.1
5	-0.5
6	-0.02
7	-0.5
8	-0.01
9	-0.01
10	-0.10
11	-0.50
12	-0.50
13	-0.20
14	-0.70
15	-0.001
16	-0.01
17	-0.90
18	-0.10

Table (8) Obtained Chlorine Concentrations at the Nodes for the Two Cases

Node Number	Chlorine Concentration Mg/lit case A	Chlorine Concentration Mg/lit case B
1	0.566	0.566
2	0.526	0.526
3	0.47	0.47
4	0.44	0.44
5	1.5	0.80
6	1.39	0.74
7	1.27	0.68
8	1.15	0.61
9	0.98	0.51
10	1.02	0.49
11	1.5	0.66
12	0.7	0.39
13	1.23	0.78
14	1.11	0.59
15	0.98	0.51
16	0.61	0.35
17	0.61	0.33

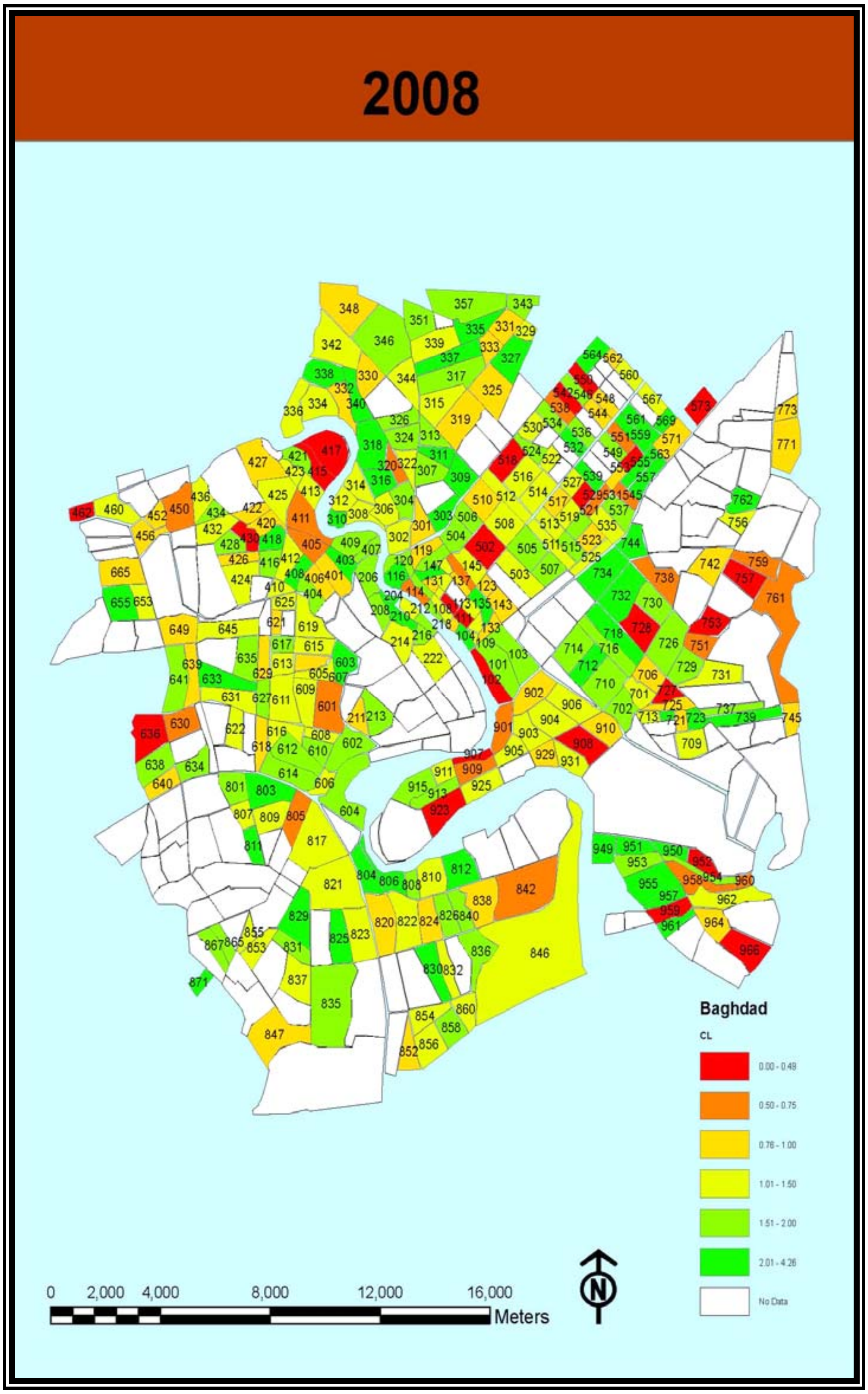

Fig (1) Residual chlorine distribution in Baghdad water supply Networks Year, 2008.

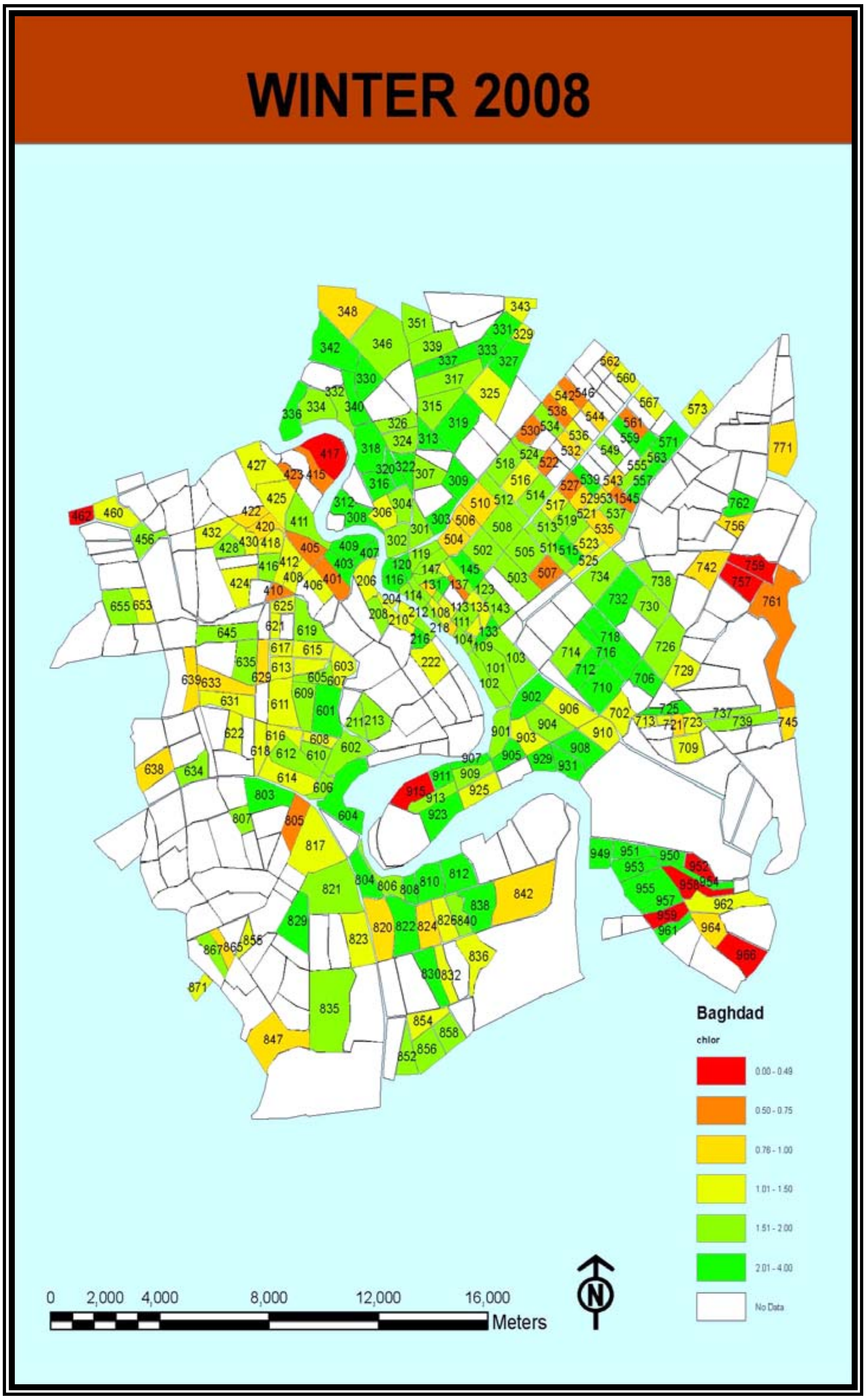

Fig (2) Residual chlorine distribution in Baghdad water supply Networks Win, 2008.

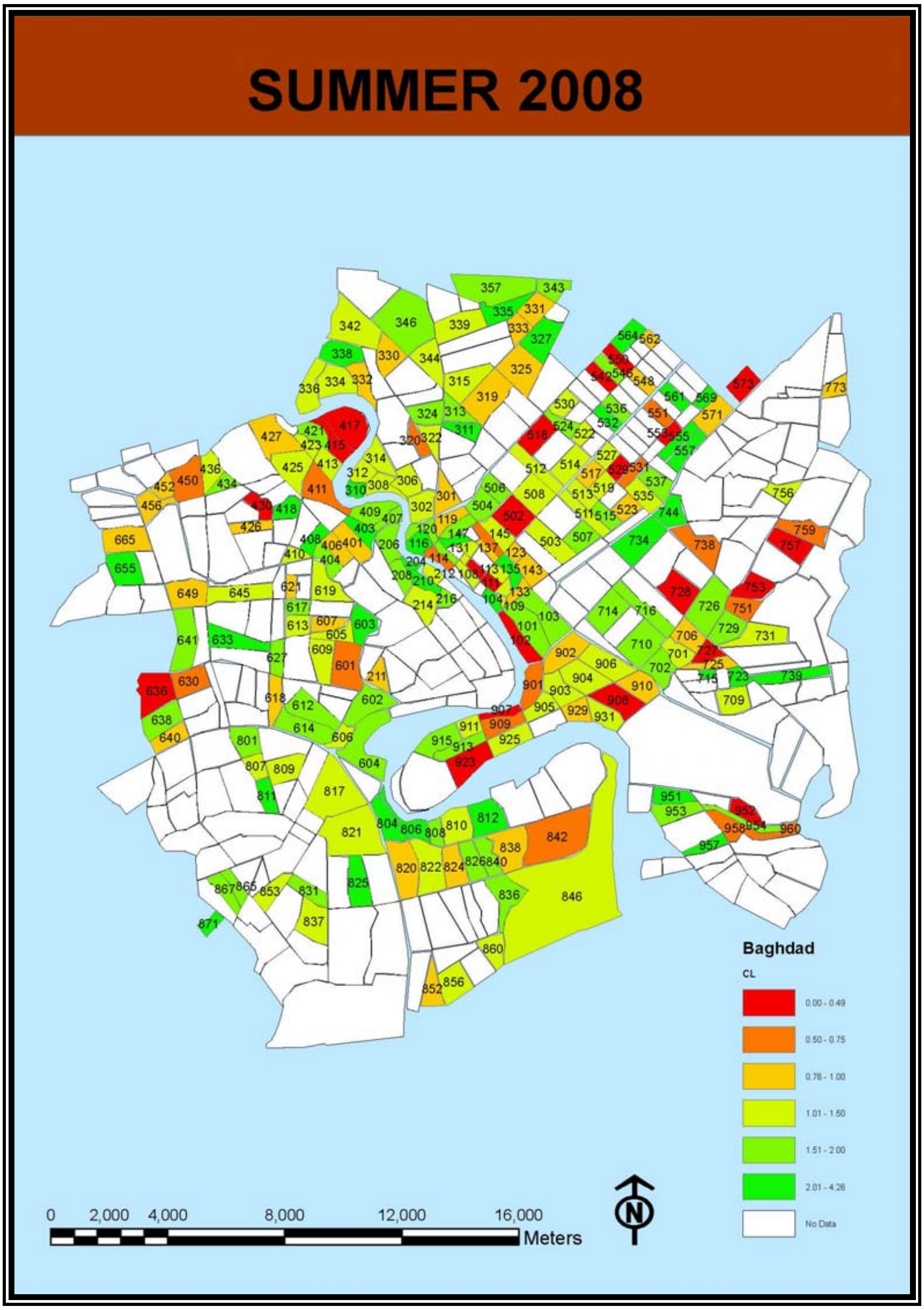

Fig (3) Residual chlorine distribution in Baghdad water supply Networks Sum, 2008.

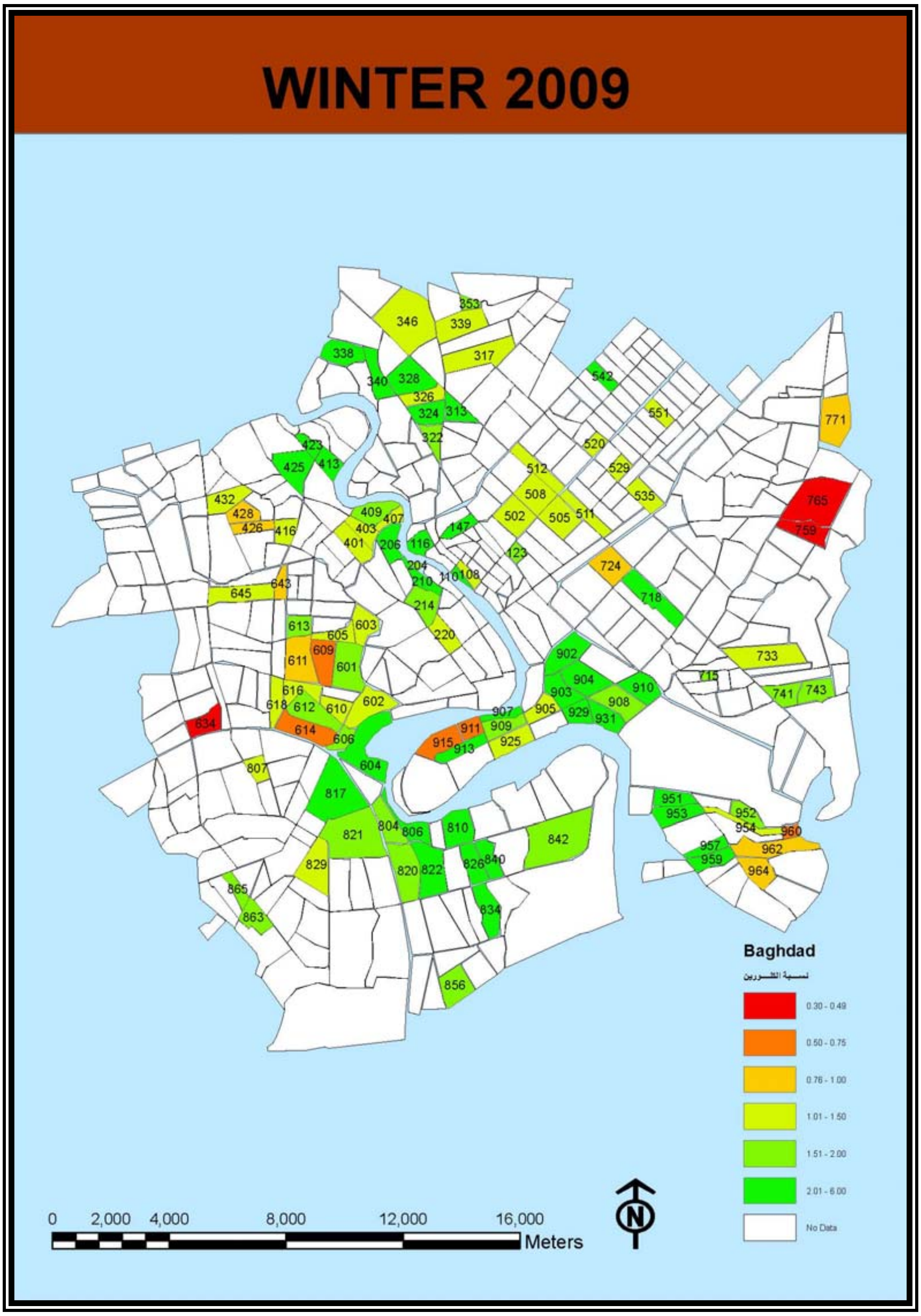

Fig (4) Residual chlorine distribution in Baghdad water supply Networks Win, 2009.

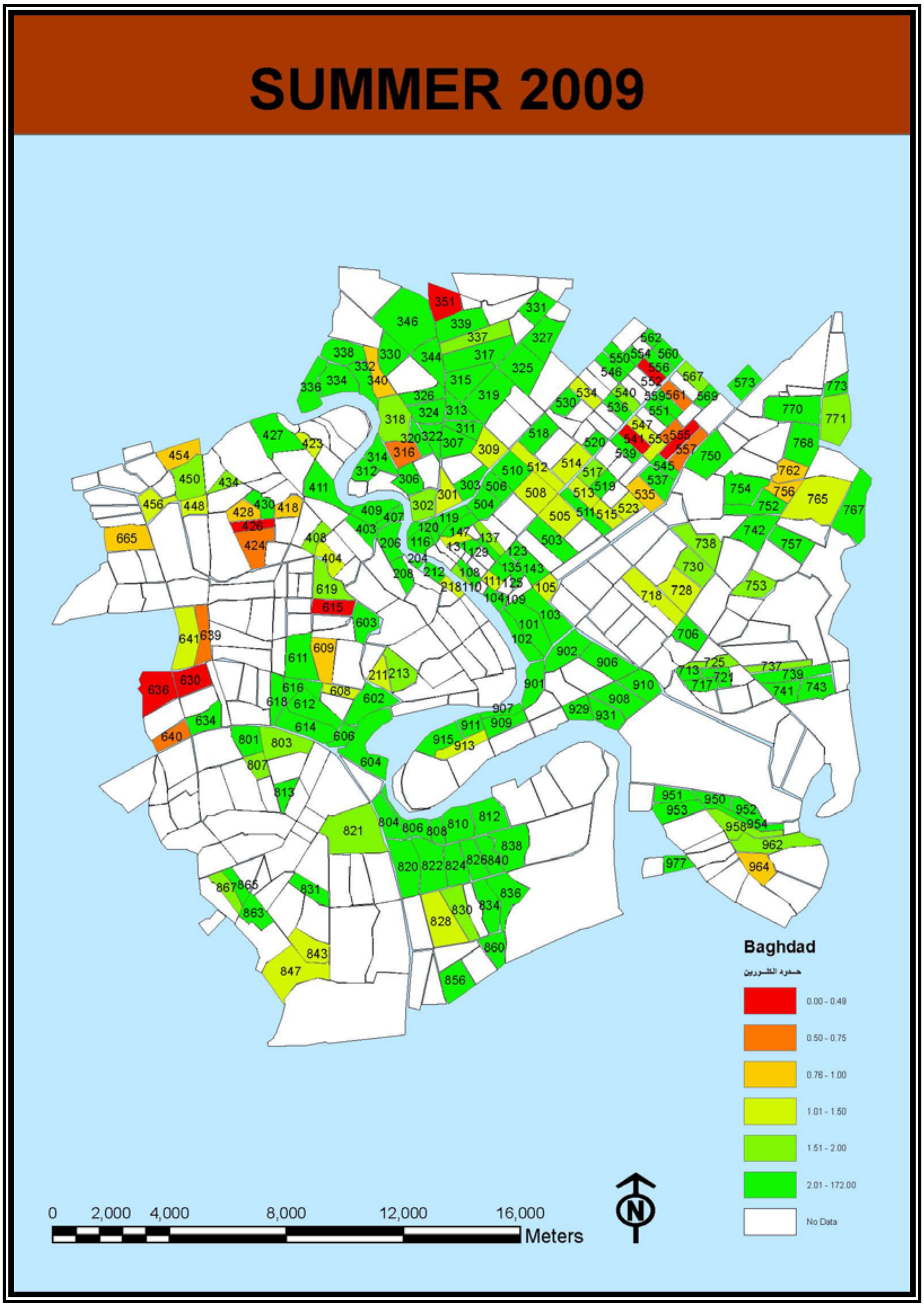

Fig (5) Residual chlorine distribution in Baghdad water supply Networks Sum, 2009 .

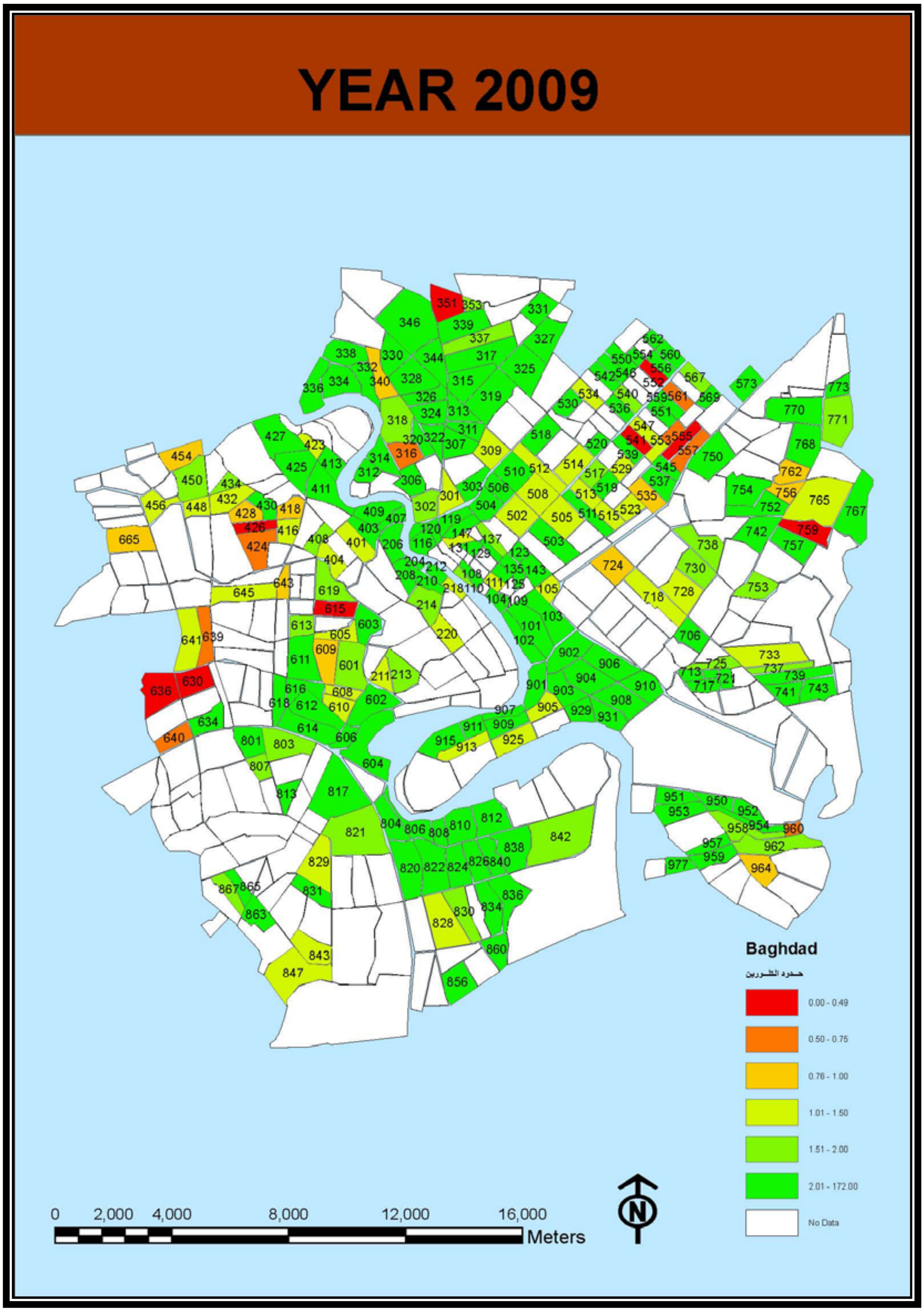

Fig (6) Residual chlorine distribution in Baghdad water supply Networks Year, 2009.

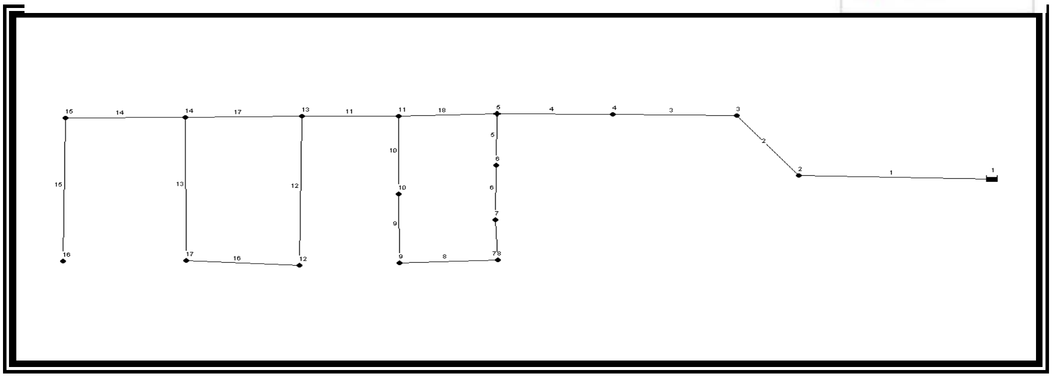

Fig (7)The Water Supply Network in District 636 AL-Amiria , Karkh, Baghdad.

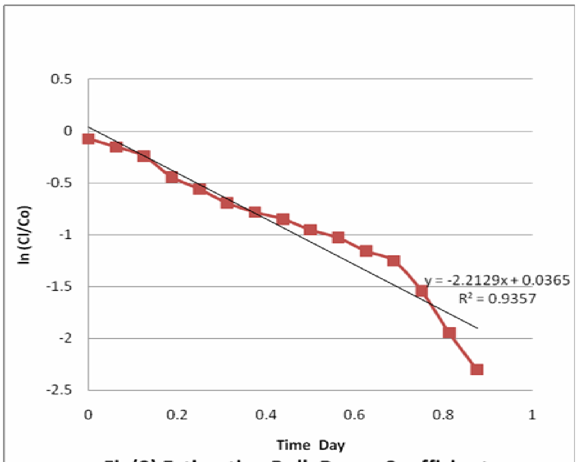

Fig(8) Estimating Bulk Decay Coefficient.

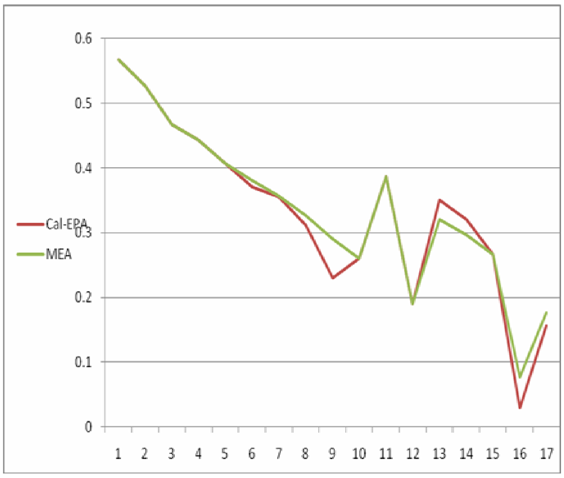

Fig(9) Comparison between measured and estimated values During Summer Months.

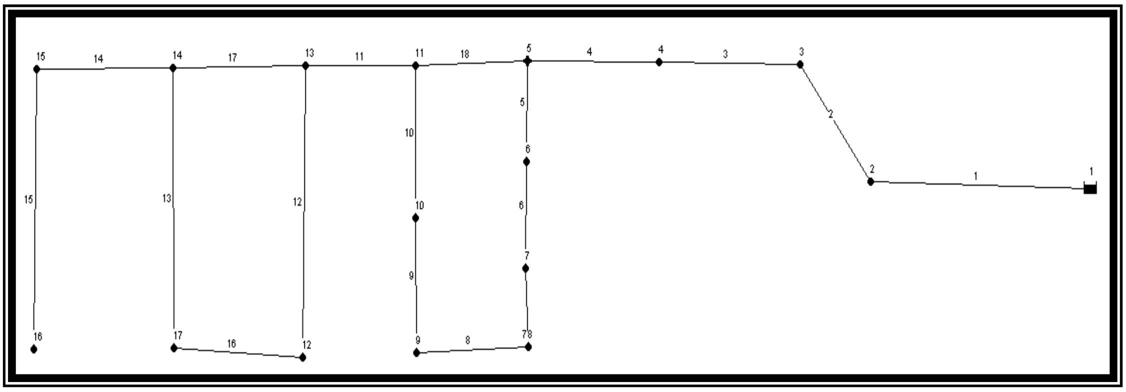

Fig. (10) Nodes Numbering of the case Study Al-Amiria.

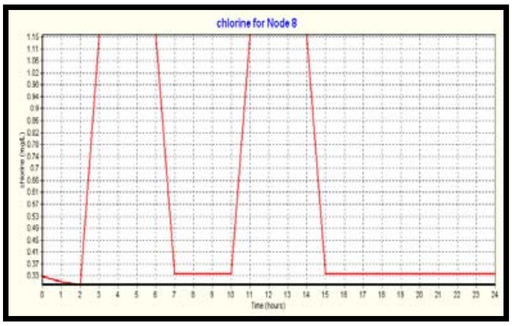

Fig.(11) Chlorine Concentration at node (8).

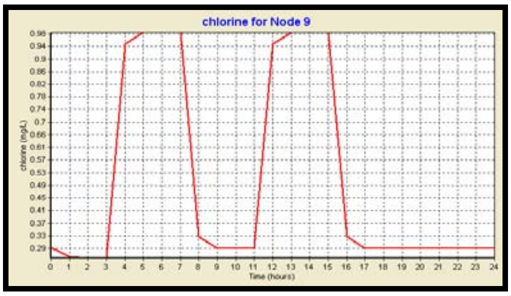

Fig.(12) Chlorine Concentration at node (9).

Fig.(13) Chlorine Concentration at node (10).

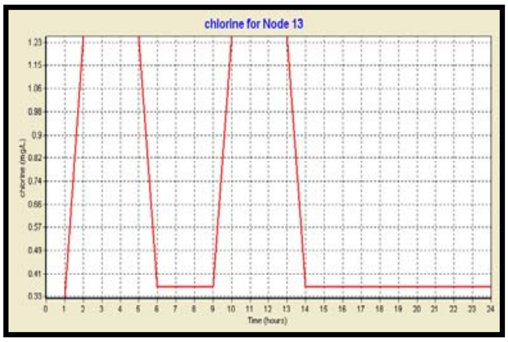

Fig.(14) Chlorine Concentration at node (13).

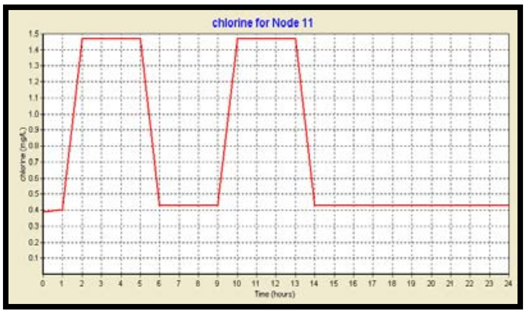

Fig.(15) Chlorine Concentration at node (11).

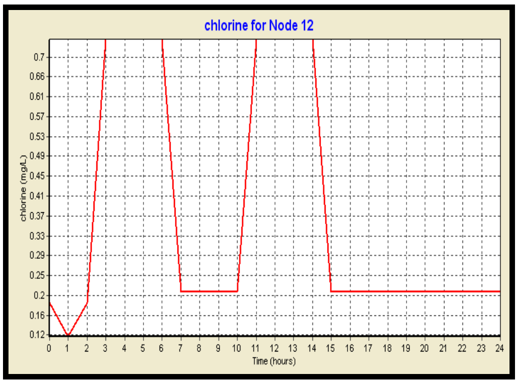

Fig.(16) Chlorine Concentration at node (12).

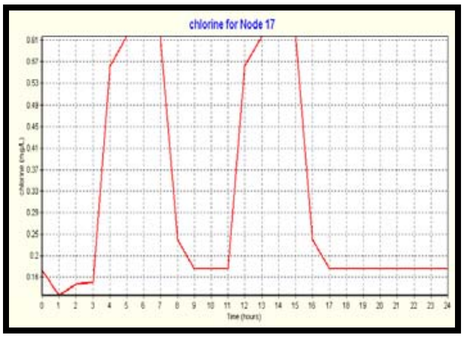

Fig.(17) Chlorine Concentration at node (17).

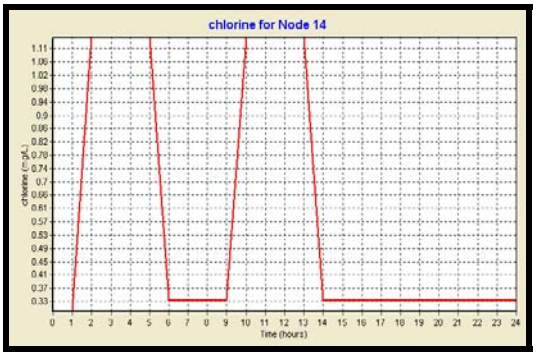

Fig.(18) Chlorine Concentration at

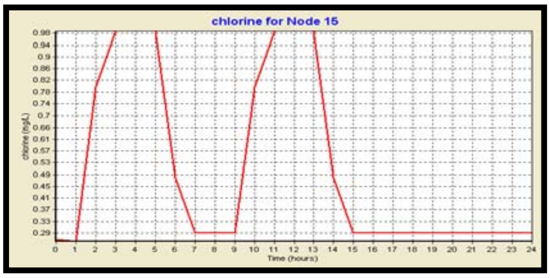

node (14).

Fig.(19) Chlorine Concentration at node (15).

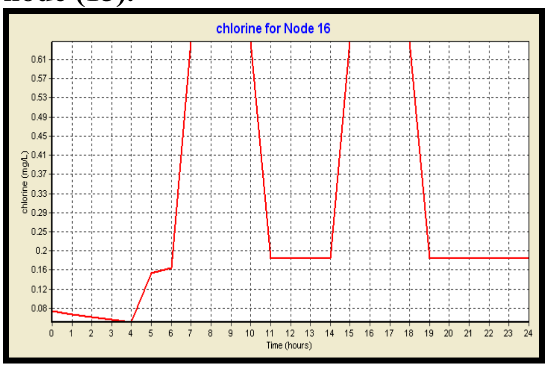

Fig.(20) Chlorine Concentration at node (16).

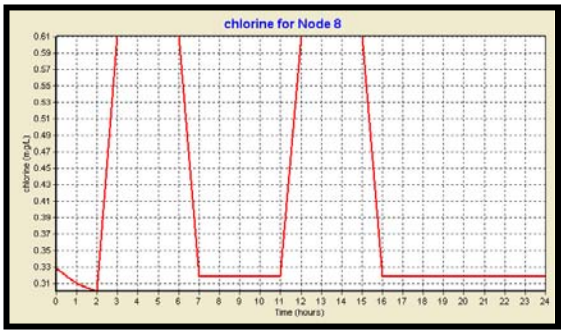

Fig.(21)Chlorine Concentration at node (8).

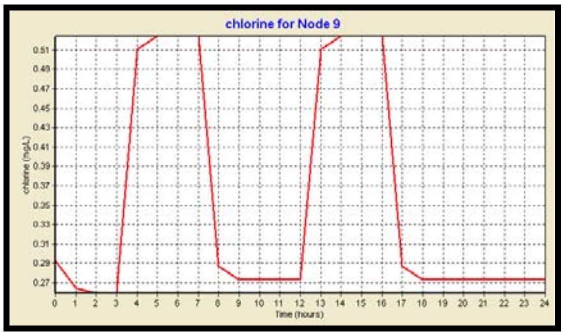

Fig.(22) Chlorine Concentration at node (9).

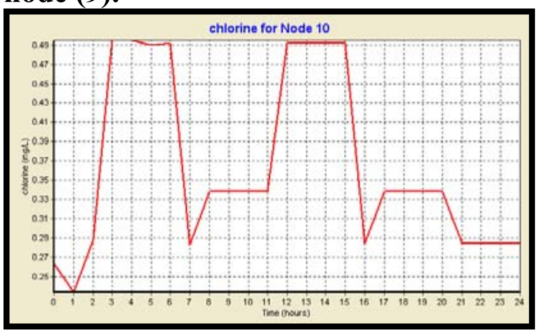

Fig.(23) Chlorine Concentration at node (10).

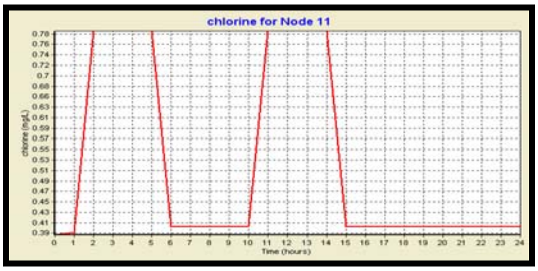

Fig.(24) Chlorine Concentration at node (11).

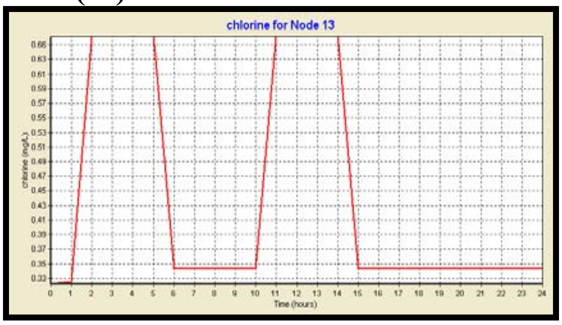

Fig.(25) Chlorine Concentration at node (13).

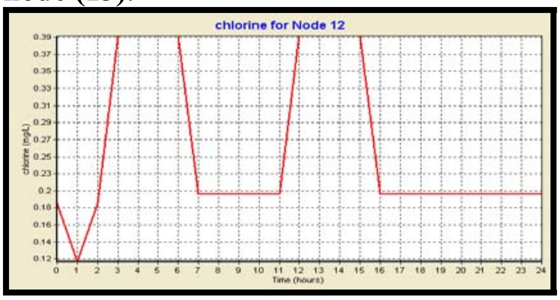

Fig.(26) Chlorine Concentration at node (12).

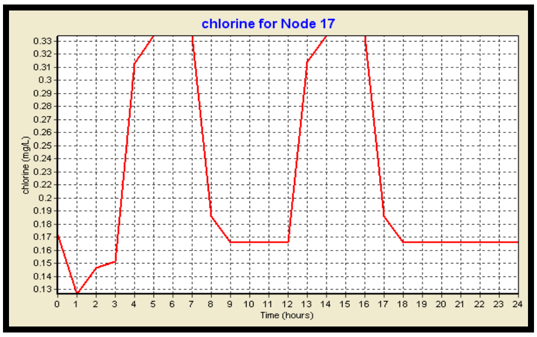

Fig.(27) Chlorine Concentration at node (17).

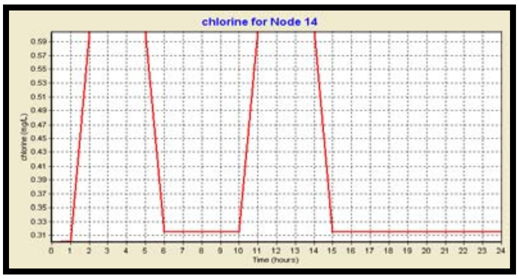

Fig.(28) Chlorine Concentration at node (14).

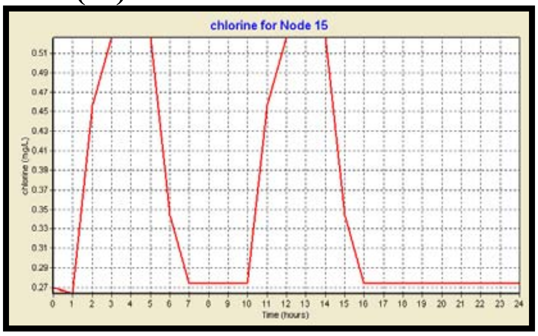

Fig.(29) Chlorine Concentration at node (15).

Fig.(30) Chlorine Concentration at node (16).

NUMERICAL INVESTIGATION OF STATIC AND DYNAMIC STRESSES IN SPUR GEAR MADE OF COMPOSITE MATERIAL

Asst. Prof. MOHAMMAD Q. ABDULLAH & THAR M. BADRI

ABSTRACT

In this current work, ***Purpose***; to clearly the fundamental idea for constructing a design and investigation of spur gear made of composite material its comes from the combination of (high speeds, low noise, oil-les running, light weight, high strength, and more load capability) encountered in modern engineering applications of the gear drives, when the usual metallic gear cannot too overwhelming these combinations.

An analyzing of stresses and deformation under static and dynamic loading for spur gear tooth by finite element method with isoparametric eight-nodded in total of 200 brick element with 340 nods in three degree of freedom per node was selected for this analysis. This is responsible for the catastropic failure studying of spur gear made of composite material. Also obtain the natural frequencies and the mode shape of the composite tooth under (concentrated and or moving on surface profile) load of one half sinusoidal type impulse for two types of composite materials (Glasses/Epoxy & Graphite/Epoxy) and they are compared with the mild steel gear values.

The appearances that improve the successfully of composite gear in the weight, stiffness, load capability, and dynamic behavior respect to the mild steel, which is found that composite materials may also be thought of as a material for power transmission gearing, from a stress point of view.

الخلاصة

في الدراسة الحالية و التي تبحث في الفكرة ا ستغلال المواد المركبة لصناعة التروسس و التي استنبطت من خلال متطلبات تصاميم التروسس الحديثة وهي (السرع العالية، اقل ضوضاء، اقل مستوى لتزييت، وزن اقل، صلابة عالية، مع قدرة عمل افضل) والتي لا تستطيع ان تحتويها التروسس المعدنية. من خلال اجراء تحليل لاجهادات و التشوهات الحاصلة لمسنن الاصم تحت تاثير ظروف الاستخدام القوى الساكنة والمتحركة باستخدام طريقة العناصر المحددة (FEM) باستخدام 200 عنصرو340 نقطة لثلاث درجات من الحرية للنقطة الواحدة. كذلك تم دراسة الفشل المرتبط بنظام بناء المواد المركبة وبنفس ظروف التحميل السابقة ووجد ان (الترددات الطبيعية وشكل الطوار). للمسنن المصنع من المواد المركبة تحت تاثير قوة متمركزة واخرا متحركة على امتدا سطح المسن اقل مماهو عليه في المسنن المعدني.

ان الدراسة المفصلة بالجزئين العملي والنظري اثبتت ان التروس المصنعة من المواد المركبة اكثر قدرة على تحمل الاجهادات باتجاه الالياف من التروس المعدنية و اصبح بالامكان من استخدام المواد المركبة كبديل عن المعادن.

Keywords: composite, spur gear, glasses/graphite/epoxy, numerical static and dynamic stresses analysis, aircrafts gear pump.

INTRODUCTION

In the past century, there have been major developments in the technology of power transmission by gears. One particular field of research which plays a key role by assessment of mesh stiffness of orthotropic material gear because of, it can be rebuilt the macrostructures of materials to create new mechanical properties of combination of (low noise, oil-les running, light weight, and high strength) using for power transmission.

***So the metallic gear is; heavy but difficult to use oil-less condition. Also the plastic gear; less in weight but low loading capability, and weaker impact loading, Thus composite gear are attention (to meet market requirement)*[Toshiki H. 2006]**, Which is a part of orthotropic material and achieved their entire gear problem because it lighter materials are desired or required without sacrificing strength. They have even become essential for many gear applications.

In a general sense, the word composite means constituted of two or more different parts in practice, the term of composite is used in a more restrictive sense, as a material constituted by the assemblage of two or more materials of different natures with complementary properties leading to a material which have better properties than the properties of the composite components considered separately **[Jean-Marie Berthelot 2003]**. So composite preferred in places because of:-

1) Two or more materials combined on a ***macroscopic*** scale to form a useful material.
2) Ideal for structural applications ***"high strength-to-weight and stiffness-to-weight ratio"***.
3) Conventional composites limited to in-plane distributed loads.
4) The properties of composite materials are result from:

a -The properties of constituent materials,

b- Their geometrical distribution,

c- Their interaction.

Some transmission gears make use of composite materials in many different places such as watches, instruments, washing machine, gear pumps, etc. It has been reported **[Vijayarangan and N. Ganesan 1992]** that the life of stainless-steel gear pump was prolonged when the gear made from glass-fiber reinforced epoxy was exchanged and when an injection moulding compound, reinforced with 30% by weight carbon fibers, was used for the gears. This pump recorded 1000 hours of extra life. Because of the overwhelming advantages of composite materials and its existing use for high power or kinematic applications, that lead to be interested to know the feasibility of usage of composite materials for power transmission gearing. The literatures available on metallic (isotropic) gears both on experimental and on theoretical studies is enormous. However, the authors could trace very little literature about composite gears.

But here will be investigate a practical model of composite material and studying its behavior comprehensively, {numerically by FEM, when an attempt has been made to study ***the variation of tensile and compressive stresses***, ***on the load and unloaded sides of tooth surface***, which are responsible for the catastropic failure of gear tooth made of composite material}, and then made a comparison between the composite spur gear with isotropic one.

The finite element method [FEM] is a numerical technique in which governing equations are represented in matrix form and as such are well suited to solution by advance mathematical programming using [maple calculator package Ver. (11)].

From the results obtained by analyzing a spur gear made of orthotropic material, which is found that these composite materials may also be thought of as a material for power transmission gearing, from a stress point of view.

FINITE ELEMENT MODELING OF COMPOSITE GEAR TOOTH SECTOR

Since the three dimensions, namely the tooth height, tooth thickness and tooth face width, of a gear tooth in three mutually perpendicular directions are comparable with each other it is more appropriate to use ***3D modeling***. Table 1 show the standard parameters used in this work. The gear tooth sector developed in 3D figure was extrapolated in the perpendicular (Z-axis) direction as it is only a spur gear, the same configuration as in the front exists all through the Z-axis. ***A fine mesh closer to the root section was chosen to get better results of root stresses in total of 200 elements with 340 nodes were used for the analysis*** Fig.1. Each gear tooth sector subtends to an angle of 360°/z, where z is the number of teeth in the gear. This is chosen for ***cyclic symmetry*** is applied [**S. Mohamed Nabi & N. Ganesan, 1993**] later on.

An external normal force (F) of amplitude (245.25 N) is applied at a single point in the tip of the tooth (concentrated loads) this uniformly distributed load was lumped at the nodes. The value of the applied force is selected such that the expected maximum stress is less than the yield strength of the composite materials and mild steel (Hereafter called as Gl/Ep, Gr/Ep and Ms, respectively) present in the Table 2.

FORMULATION OF CHARACTERISTICS MATRICES AND VECTORS

Consider three coordinates x, y and z to be associated with element in Cartesian plane as shown in Fig. 1. It is useful to employ a local system which is simple, unique and independent of the global system, such a system is known as an intrinsic system and its coordinates are the intrinsic coordinate's ζ, η and τ.

The problem now reduces to one of obtaining the equation of the transformation from the Cartesian plane. It can be assumed that x, y and z is field functions defined as follows:

$$\left.\begin{aligned} X(\zeta,\eta,\tau) &= \textstyle\sum_{i=1}^{n=8} x_i N_i(\zeta,\eta,\tau) \\ y(\zeta,\eta,\tau) &= \textstyle\sum_{i=1}^{n=8} y_i N_i(\zeta,\eta,\tau) \\ z(\zeta,\eta,\tau) &= \textstyle\sum_{i=1}^{n=8} z_i N_i(\zeta,\eta,\tau) \end{aligned}\right\} \quad (1)$$

In which x_i, y_i and z_i are nodal coordinates and $N_i(\zeta, \eta, \tau)$ are functions of ζ ,η and τ called shape function .For any point in the intrinsic plane with known values of ζ ,η and τ the Cartesian x ,y and z coordinates can be found once the functions Ni(ζ , η , τ) are known.

$$\left.\begin{aligned} N_1 &= \tfrac{1}{2}(1-\zeta)(1-\eta)(1-\tau) \\ N_2 &= \tfrac{1}{2}(1-\zeta)(1+\eta)(1-\tau) \\ N_3 &= \tfrac{1}{2}(1+\zeta)(1-\eta)(1-\tau) \\ N_4 &= \tfrac{1}{2}(1+\zeta)(1+\eta)(1-\tau) \\ N_5 &= \tfrac{1}{2}(1-\zeta)(1-\eta)(1+\tau) \\ N_6 &= \tfrac{1}{2}(1-\zeta)(1+\eta)(1+\tau) \\ N_7 &= \tfrac{1}{2}(1+\zeta)(1-\eta)(1+\tau) \\ N_8 &= \tfrac{1}{2}(1+\zeta)(1+\eta)(1+\tau) \end{aligned}\right\} \quad (2)$$

Displacement and Force Fields

The nodal displacement vector {δ} and the force vector {F} can be defined as follows:-

$$\left.\begin{aligned} \{\delta\} &= \{u_1 v_1 w_1 u_2 v_2 w_2 \ldots\ldots\ldots u_8 v_8 w_8\} \\ \{F\} &= \{f x_1 f y_1 f z_1 f x_2 f y_2 f z_2 \ldots\ldots\ldots f x_8 f y_8 f z_8\} \end{aligned}\right\} \quad (3)$$

The displacements components at any point can be expressed in terms of displacements and shape function:-

$$\left.\begin{aligned} u(x,y,z) &= \textstyle\sum_{i=1}^{n=8} u_i N_i(x,y,z) & u(\zeta,\eta,\tau) &= \textstyle\sum_{i=1}^{n=8} u_i N_i(\zeta,\eta,\tau) \\ v(x,y,z) &= \textstyle\sum_{i=1}^{n=8} v_i N_i(x,y,z) & v(\zeta,\eta,\tau) &= \textstyle\sum_{i=1}^{n=8} v_i N_i(\zeta,\eta,\tau) \\ w(x,y,z) &= \textstyle\sum_{i=1}^{n=8} w_i N_i(x,y,z) & w(\zeta,\eta,\tau) &= \textstyle\sum_{i=1}^{n=8} w_i N_i(\zeta,\eta,\tau) \end{aligned}\right\} \quad (4)$$

Where, u(x,y,z) ,v(x,y,z,) ,w(x,y,z) represents the displacement components at any point (x,y,z) inside the element, $N_i(x,y,z)$ represents the shape function at node, i and n represents the number of element nodes. Finally, the displacement vector {q} at any point (x, y and z) inside the element can be defined as follows:-

$$\{q\} = \begin{bmatrix} N_1 & 0 & 0 & N_2 & 0 & 0 & \dots N_8 & 0 & 0 \\ 0 & N_1 & 0 & 0 & N_2 & 0 & \dots 0 & N_8 & 0 \\ 0 & 0 & N_1 & 0 & 0 & N_2 & \dots 0 & 0 & N_8 \end{bmatrix} \{\delta\}$$

$$\text{Hence } \{q\} = [N]\,\{\delta\} \qquad (5)$$

Strain Field

From the strain-displacement relations it is very useful to form the shape functions expressed in terms of intrinsic coordinates (ζ, η and τ) for initial calculation.

$$\begin{Bmatrix} \varepsilon_x \\ \varepsilon_y \\ \varepsilon_z \\ \gamma_{xy} \\ \gamma_{xz} \\ \gamma_{yz} \end{Bmatrix} = \begin{Bmatrix} \frac{\partial u}{\partial x} \\ \frac{\partial v}{\partial y} \\ \frac{\partial w}{\partial z} \\ \frac{\partial u}{\partial y}+\frac{\partial v}{\partial x} \\ \frac{\partial u}{\partial z}+\frac{\partial w}{\partial x} \\ \frac{\partial v}{\partial z}+\frac{\partial w}{\partial y} \end{Bmatrix} = [J] \begin{Bmatrix} \frac{\partial u}{\partial \zeta} \\ \frac{\partial v}{\partial \eta} \\ \frac{\partial w}{\partial \tau} \\ \frac{\partial u}{\partial \eta}+\frac{\partial v}{\partial x} \\ \frac{\partial u}{\partial z}+\frac{\partial w}{\partial x} \\ \frac{\partial v}{\partial z}+\frac{\partial w}{\partial y} \end{Bmatrix} \qquad (6)$$

Here [J] is the Jacobean matrix.

Since that the nodal displacement vector in terms of intrinsic co-ordinates is;

$$\frac{\partial u}{\partial \zeta} = \begin{bmatrix} \frac{\partial N_1}{\partial \zeta} & 0 & 0 & \frac{\partial N_2}{\partial \zeta} & 0 & 0 \dots\dots\dots & \frac{\partial N_8}{\partial \zeta} & 0 & 0 \end{bmatrix} \{\delta\}$$

$$\frac{\partial v}{\partial \eta} = \begin{bmatrix} 0 & \frac{\partial N_1}{\partial \eta} & 0 & 0 & \frac{\partial N_2}{\partial \eta} & 0 \dots\dots\dots & 0 & \frac{\partial N_8}{\partial \eta} & 0 \end{bmatrix} \{\delta\}$$

$$\frac{\partial w}{\partial \tau} = \begin{bmatrix} 0 & 0 & \frac{\partial N_1}{\partial \tau} & 0 & 0 & \frac{\partial N_2}{\partial \tau} \dots\dots\dots & 0 & 0 & \frac{\partial N_8}{\partial \tau} \end{bmatrix} \{\delta\}$$

And

$$\frac{\partial u}{\partial \eta}+\frac{\partial v}{\partial \zeta} = \begin{bmatrix} \frac{\partial N_1}{\partial \eta} & \frac{\partial N_1}{\partial \zeta} & 0 & \frac{\partial N_2}{\partial \eta} & \frac{\partial N_2}{\partial \zeta} & 0 \dots\dots\dots & \frac{\partial N_8}{\partial \eta} & \frac{\partial N_8}{\partial \zeta} & 0 \end{bmatrix} \{\delta\}$$

$$\frac{\partial u}{\partial \tau}+\frac{\partial w}{\partial \zeta} = \begin{bmatrix} \frac{\partial N_1}{\partial \tau} & 0 & \frac{\partial N_1}{\partial \zeta} & \frac{\partial N_2}{\partial \tau} & 0 & \frac{\partial N_2}{\partial \zeta} \dots\dots\dots & \frac{\partial N_8}{\partial \tau} & 0 & \frac{\partial N_8}{\partial \zeta} \end{bmatrix} \{\delta\}$$

$$\frac{\partial v}{\partial \tau}+\frac{\partial w}{\partial \eta} = \begin{bmatrix} 0 & \frac{\partial N_1}{\partial \tau} & \frac{\partial N_1}{\partial \eta} & 0 & \frac{\partial N_2}{\partial \tau} & \frac{\partial N_2}{\partial \eta} \dots\dots\dots & 0 & \frac{\partial N_8}{\partial \tau} & \frac{\partial N_8}{\partial \eta} \end{bmatrix} \{\delta\}$$

Hence, it can be deduced that; $\underset{6\times1}{\{\varepsilon\}} = \underset{6\times24}{[B]}\ \underset{24\times1}{\{\delta\}}$, Where $\{\varepsilon\}$ is a strain vector, {δ} is the nodal displacement vector and [B] is the strain displacement matrix all of them in terms of intrinsic co-ordinates.

$$\begin{bmatrix} \frac{\partial u}{\partial \zeta} \\ \frac{\partial v}{\partial \eta} \\ \frac{\partial w}{\partial \tau} \\ \frac{\partial u}{\partial \eta}+\frac{\partial v}{\partial \zeta} \\ \frac{\partial u}{\partial \tau}+\frac{\partial w}{\partial \zeta} \\ \frac{\partial v}{\partial \tau}+\frac{\partial w}{\partial \eta} \end{bmatrix} = \begin{bmatrix} \frac{\partial N_1}{\partial \zeta} & 0 & 0 & \frac{\partial N_2}{\partial \zeta} & 0 & 0 & \cdots & \frac{\partial N_8}{\partial \zeta} & 0 & 0 \\ 0 & \frac{\partial N_1}{\partial \eta} & 0 & 0 & \frac{\partial N_2}{\partial \eta} & 0 & \cdots & 0 & \frac{\partial N_8}{\partial \eta} & 0 \\ 0 & 0 & \frac{\partial N_1}{\partial \tau} & 0 & 0 & \frac{\partial N_2}{\partial \tau} & \cdots & 0 & 0 & \frac{\partial N_8}{\partial \tau} \\ \frac{\partial N_1}{\partial \eta} & \frac{\partial N_1}{\partial \zeta} & 0 & \frac{\partial N_2}{\partial \eta} & \frac{\partial N_2}{\partial \zeta} & 0 & \cdots & \frac{\partial N_8}{\partial \eta} & \frac{\partial N_8}{\partial \zeta} & 0 \\ \frac{\partial N_1}{\partial \tau} & 0 & \frac{\partial N_1}{\partial \zeta} & \frac{\partial N_2}{\partial \tau} & 0 & \frac{\partial N_2}{\partial \zeta} & \cdots & \frac{\partial N_8}{\partial \tau} & 0 & \frac{\partial N_8}{\partial \zeta} \\ 0 & \frac{\partial N_1}{\partial \tau} & \frac{\partial N_1}{\partial \eta} & 0 & \frac{\partial N_2}{\partial \tau} & \frac{\partial N_2}{\partial \eta} & \cdots & 0 & \frac{\partial N_8}{\partial \tau} & \frac{\partial N_8}{\partial \eta} \end{bmatrix} \begin{Bmatrix} u_1 \\ v_1 \\ w_1 \\ u_2 \\ v_2 \\ w_2 \\ \vdots \\ u_8 \\ v_8 \\ w_8 \end{Bmatrix} \qquad (7)$$

That led to differentiation the shape function with respect to intrinsic coordinate as follow;

$$\begin{aligned}
\frac{\partial N_1}{\partial \zeta} &= -\tfrac{1}{2}(1-\eta)(1-\tau) \\
\frac{\partial N_2}{\partial \zeta} &= -\tfrac{1}{2}(1+\eta)(1-\tau) \\
\frac{\partial N_3}{\partial \zeta} &= \tfrac{1}{2}(1-\eta)(1-\tau) \\
\frac{\partial N_4}{\partial \zeta} &= \tfrac{1}{2}(1+\eta)(1-\tau) \\
\frac{\partial N_5}{\partial \zeta} &= -\tfrac{1}{2}(1-\eta)(1+\tau) \\
\frac{\partial N_6}{\partial \zeta} &= -\tfrac{1}{2}(1+\eta)(1+\tau) \\
\frac{\partial N_7}{\partial \zeta} &= \tfrac{1}{2}(1-\eta)(1+\tau) \\
\frac{\partial N_8}{\partial \zeta} &= \tfrac{1}{2}(1+\eta)(1+\tau)
\end{aligned}$$

$$\begin{aligned}
\frac{\partial N_1}{\partial \eta} &= -\tfrac{1}{2}(1-\zeta)(1-\tau) \\
\frac{\partial N_2}{\partial \eta} &= \tfrac{1}{2}(1-\zeta)(1-\tau) \\
\frac{\partial N_3}{\partial \eta} &= -\tfrac{1}{2}(1+\zeta)(1-\tau) \\
\frac{\partial N_4}{\partial \eta} &= \tfrac{1}{2}(1+\zeta)(1-\tau) \\
\frac{\partial N_5}{\partial \eta} &= -\tfrac{1}{2}(1-\zeta)(1+\tau) \\
\frac{\partial N_6}{\partial \eta} &= \tfrac{1}{2}(1-\zeta)(1+\tau) \\
\frac{\partial N_7}{\partial \eta} &= -\tfrac{1}{2}(1+\zeta)(1+\tau) \\
\frac{\partial N_8}{\partial \eta} &= \tfrac{1}{2}(1+\zeta)(1+\tau)
\end{aligned}$$

$$\begin{aligned}
\frac{\partial N_1}{\partial \tau} &= -\tfrac{1}{2}(1-\zeta)(1-\eta) \\
\frac{\partial N_2}{\partial \tau} &= -\tfrac{1}{2}(1-\zeta)(1+\eta) \\
\frac{\partial N_3}{\partial \tau} &= -\tfrac{1}{2}(1+\zeta)(1-\eta) \\
\frac{\partial N_4}{\partial \tau} &= -\tfrac{1}{2}(1+\zeta)(1+\eta) \\
\frac{\partial N_5}{\partial \tau} &= \tfrac{1}{2}(1-\zeta)(1-\eta) \\
\frac{\partial N_6}{\partial \tau} &= \tfrac{1}{2}(1-\zeta)(1+\eta) \\
\frac{\partial N_7}{\partial \tau} &= \tfrac{1}{2}(1+\zeta)(1-\eta) \\
\frac{\partial N_8}{\partial \tau} &= \tfrac{1}{2}(1+\zeta)(1+\eta)
\end{aligned} \qquad (8)$$

The Stress-Strain Matrix

To determine the elasticity or (stress-strain) matrix from the normal stresses and the shear stresses relationships where E_1, E_2, E_3 are the elastic modules, G_{12}, G_{23}, G_{13}, are shear modules and υ_{12}, υ_{23}, υ_{13} are Poisson's ratio in the L, T, Z directions of the fiber and LT, TZ and ZL planes. ***"Assuming that the reinforcing fibers in an element are all in a radial direction"***:-

$$\left.\begin{array}{ll} \varepsilon_x = \frac{\sigma_x}{E_1} - \upsilon_{12}\frac{\sigma_y}{E_2} - \upsilon_{13}\frac{\sigma_z}{E_3} & \tau_{xy} = \gamma_{xy}G \\ \varepsilon_y = -\upsilon_{21}\frac{\sigma_x}{E_1} + \frac{\sigma_y}{E_2} - \upsilon_{23}\frac{\sigma_z}{E_3} & \tau_{xz} = \gamma_{xz}G \\ \varepsilon_z = -\upsilon_{31}\frac{\sigma_x}{E_1} - \upsilon_{32}\frac{\sigma_y}{E_2} + \frac{\sigma_z}{E_3} & \tau_{yz} = \gamma_{yz}G \end{array}\right\} \quad (9)$$

Hence $\{\varepsilon\} = [S]\{\sigma\}$, where $\{\varepsilon\}$ is strain vector, $\{\sigma\}$ is stresses vector, and [S] is the compliance matrix. But the compliance matrix it is the inverse of the elasticity matrix, so $[S]^{-1}= [D]$. Or;

$$\begin{Bmatrix} \sigma_x \\ \sigma_y \\ \sigma_z \\ \tau_{xy} \\ \tau_{xz} \\ \tau_{yz} \end{Bmatrix} = \begin{bmatrix} C_{11} & C_{12} & C_{13} & 0 & 0 & 0 \\ C_{12} & C_{22} & C_{23} & 0 & 0 & 0 \\ C_{13} & C_{23} & C_{33} & 0 & 0 & 0 \\ 0 & 0 & 0 & C_{44} & 0 & 0 \\ 0 & 0 & 0 & 0 & C_{55} & 0 \\ 0 & 0 & 0 & 0 & 0 & C_{66} \end{bmatrix} \begin{Bmatrix} \varepsilon_x \\ \varepsilon_y \\ \varepsilon_z \\ \gamma_{xy} \\ \gamma_{xz} \\ \gamma_{yz} \end{Bmatrix} \quad (10)$$

Where [D] is the elasticity or (stress-strain) matrix ***for an orthotropic material.***

Where C_{ij} is the elasticity constant explaining by the relation down as follows ;

$$\begin{array}{l} C11=E_1\,(1-\upsilon_{23}.\,\upsilon_{32})/\,(1-(\upsilon_{12}\upsilon_{21}-\upsilon_{32}\upsilon_{23}-\upsilon_{31}\upsilon_{13})-2\upsilon_{13}\upsilon_{32}\upsilon_{21} \\ C12=E_1\,(\upsilon_{21}+\upsilon_{23}.\,\upsilon_{32})/\,(1-(\upsilon_{12}\upsilon_{21}-\upsilon_{32}\upsilon_{23}-\upsilon_{31}\upsilon_{13})-2\upsilon_{13}\upsilon_{32}\upsilon_{21} \\ C13=E_1\,(\upsilon_{31}+\upsilon_{23}.\,\upsilon_{32})/\,(1-(\upsilon_{12}\upsilon_{21}-\upsilon_{32}\upsilon_{23}-\upsilon_{31}\upsilon_{13})-2\upsilon_{13}\upsilon_{32}\upsilon_{21} \\ C22=E_2\,(1-\upsilon_{13}.\,\upsilon_{31})/\,(1-(\upsilon_{12}\upsilon_{21}-\upsilon_{32}\upsilon_{23}-\upsilon_{31}\upsilon_{13})-2\upsilon_{13}\upsilon_{32}\upsilon_{21} \\ C23=E_2\,(\upsilon_{32}+\upsilon_{12}.\,\upsilon_{31})/\,(1-(\upsilon_{12}\upsilon_{21}-\upsilon_{32}\upsilon_{23}-\upsilon_{31}\upsilon_{13})-2\upsilon_{13}\upsilon_{32}\upsilon_{21} \\ C33=E_3\,(1-\upsilon_{12}.\,\upsilon_{21})/\,(1-(\upsilon_{12}\upsilon_{21}-\upsilon_{32}\upsilon_{23}-\upsilon_{31}\upsilon_{13})-2\upsilon_{13}\upsilon_{32}\upsilon_{21} \\ C44=G_{12} \\ C55=G_{23} \\ C66=G_{31} \end{array} \quad (11)$$

***properties achieved by simple tensile test the entire elasticity constant in terms of mechanical* Stress Field**

Referring to the Eq. (10) it can be deduced that:-

$$\{\sigma\} = [D]\,\{\varepsilon\}$$

Where $\{\sigma\}$ is the stress vector,

From Eq. (7) and Eq. (10) it can be found that:-

$$\{\sigma\} = [D]\,[B]\,\{\delta\} \quad (12)$$

Formulation of the Transformation Matrix

The fiber orientation angle (α) measured from ***the vertical direction (X -axis)*** is given as $\alpha = \tan^{-1}(XX\,/\,YY)$, where XX and YY are the X and Y co-ordinates of the geometric centre of any element under consideration. The transformation of elastic properties E_L, E_T, E_Z, G_{LT}, G_{LZ}, G_{TZ}, υ_{LT}, υ_{lZ}, υ_{TZ} with

respect to local x, y, z co-ordinates were performed using an appropriate transformation matrix. The transformation matrix used in this case is:-

$$[T]= \begin{bmatrix} S^2 & C^2 & 0 & -2CS & 0 & 0 \\ C^2 & S^2 & 0 & 2CS & 0 & 0 \\ 0 & 0 & 1 & 0 & 0 & 0 \\ CS & CS & 0 & S^2-C^2 & 0 & 0 \\ 0 & 0 & 0 & 0 & S & -C \\ 0 & 0 & 0 & 0 & C & S \end{bmatrix}$$

Where $S = \sin\alpha$ and $C = \cos\alpha$. (13)

Formulation of Element Stiffness Matrix

Three degrees of freedom per node, namely displacements u, v, w in the X, Y, and Z co-ordinates were assumed. The Cartesian co-ordinates x, y and z describing the elemental continuum, the intrinsic co-ordinates ζ, η and τ ranging from -1 to $+1$ on element boundaries and the intrinsic node numbering are all shown in Fig. 1.

The element stiffness matrix is found from the ***total potential energy*** of the element **P**. This energy can be expressed as follows:-

$$P = U - W$$

Where U is the strain energy can be shown as: -

$$U = \frac{1}{2}\iiint_{element}\{\sigma\}^t\,\{\varepsilon\}\,dx\,dy\,dz$$

Work done by the external force is:-

$$W = \{\delta\}^t\{F\}$$

From eq. (12), it is clear that:-

$$\{\sigma\}^t = \{\delta\}^t[B]^t[D]^t$$

Thus the composite material stiffness matrix [D*] was obtained as:-

$$[D^*] = [T]\,[D]\,[T]^T \qquad (14)$$

Hence,

$$U = \frac{1}{2}\iiint_{element}\{\delta\}^t\,[B]^t[D^*][B]\{\delta\}\,dx\,dy\,dz$$

Then

$$P = \frac{1}{2}\{\delta\}^t\left[\iiint_{element}[B]^t[D^*][B]\,dx\,dy\,dz\right]\{\delta\} - \{\delta\}^t\{F\}$$

Apply the minimum total potential energy theorem:- $\frac{\partial P}{\partial\{\delta\}} = 0$

$$\left[\iiint_{element}[B]^t[D^*][B]\,dx\,dy\,dz\right]\{\delta\} = \{F\}$$

But; - [K] $\{\delta\}$= {f}, then finally the element stiffness matrix is:-

$$[K] = \iiint_{element}[B]^t[D^*][B]\,dx\,dy\,dz$$

By converting the Cartesian coordinate to intrinsic coordinate, the eq. become:-

$$\left[\underset{24\times24}{K}\right] = \iiint_{element}\left[\underset{24\times6}{B}\right]^t\left[\underset{6\times6}{D^*}\right]\left[\underset{6\times24}{B}\right]|J|\,d\zeta\,d\eta\,d\tau \qquad (15)$$

The integration in Eq. (15) is evaluated numerically using the modified Gauss-quadratic. where [J] is the Jacobean matrix

$$\begin{Bmatrix} \frac{\partial u}{\partial \zeta} \\ \frac{\partial v}{\partial \eta} \\ \frac{\partial w}{\partial \tau} \\ \frac{\partial u}{\partial \eta}+\frac{\partial v}{\partial \zeta} \\ \frac{\partial u}{\partial \tau}+\frac{\partial w}{\partial \zeta} \\ \frac{\partial v}{\partial \tau}+\frac{\partial w}{\partial \eta} \end{Bmatrix} = \underset{Jacobean\ 6\times9}{\begin{bmatrix} \frac{\partial X}{\partial \zeta} & \frac{\partial Y}{\partial \zeta} & \frac{\partial Z}{\partial \zeta} & - & - & - & - & - & - \\ - & - & - & \frac{\partial X}{\partial \eta} & \frac{\partial Y}{\partial \eta} & \frac{\partial Z}{\partial \eta} & - & - & - \\ - & - & - & - & - & - & \frac{\partial X}{\partial \tau} & \frac{\partial Y}{\partial \tau} & \frac{\partial Z}{\partial \tau} \\ \frac{\partial X}{\partial \tau} & \frac{\partial Y}{\partial \eta} & \frac{\partial Z}{\partial \eta} & \frac{\partial X}{\partial \zeta} & \frac{\partial Y}{\partial \zeta} & \frac{\partial Z}{\partial \zeta} & - & - & - \\ \frac{\partial X}{\partial \tau} & \frac{\partial Y}{\partial \tau} & \frac{\partial Z}{\partial \tau} & - & - & - & \frac{\partial X}{\partial \zeta} & \frac{\partial Y}{\partial \zeta} & \frac{\partial Z}{\partial \zeta} \\ - & - & - & \frac{\partial X}{\partial \tau} & \frac{\partial Y}{\partial \tau} & \frac{\partial Z}{\partial \tau} & \frac{\partial X}{\partial \eta} & \frac{\partial Y}{\partial \zeta} & \frac{\partial Z}{\partial \zeta} \end{bmatrix}} \begin{Bmatrix} \frac{\partial u}{\partial X} \\ \frac{\partial u}{\partial Y} \\ \frac{\partial u}{\partial Z} \\ \frac{\partial v}{\partial X} \\ \frac{\partial v}{\partial Y} \\ \frac{\partial v}{\partial Z} \\ \frac{\partial w}{\partial X} \\ \frac{\partial w}{\partial Y} \\ \frac{\partial w}{\partial Z} \end{Bmatrix}$$

Finally every term in Jacobean matrix can expression as a shape function from Eq. (1).

I.e. ($x = N_1x_1 + N_2x_2 + N_3x_3 \ldots\ldots\ldots . N_8x_8$),

So $\frac{\partial x}{\partial \zeta} = \frac{\partial N_1}{\partial \zeta}x_1 + \frac{\partial N_2}{\partial \zeta}x_2 + \frac{\partial N_3}{\partial \zeta}x_3 \ldots + \frac{\partial N_8}{\partial \zeta}x_8$,

And by use the shape function derivatives Eq. (8) will be find all the independent.

Formulation of Mass Matrix

For anybody of infinitesimal mass dm and velocity vector $\{\dot{q}\}$, the kinetic energy [K, E] can be defined as:

$$K.E = \frac{1}{2}\int\{\dot{q}\}\{\dot{q}\}dm$$

But $dm = \rho dvol = \rho dxdydz$ Referring to Eq. (5) and relation $\{\dot{q}\} = [N]\{\dot{\delta}\}$;-

$$K.E = \frac{1}{2}\{\dot{\delta}\}^t[\iiint \rho[N]^t[N]dxdydz]\{\dot{\delta}\}$$

Then the element mass matrix can be written as:-

$$[M] = \iiint \rho[N]^t[N]dxdydz$$

Using the intrinsic coordinates the eq. can be written as:-

$$[M] = \rho\int_{-1}^{1}\int_{-1}^{1}\int_{-1}^{1}[N]^t[N]\,|J|\,d\zeta d\eta d\tau \qquad (16)$$

In which, ρ is the mass density

Determination of Damping Matrix

In general, the damping matrix may be of the form **[N. Ganesan and T. C. Ramesh, 1992]**;

$$[C] = [M]\sum_{i=1}^{m} a_i[[M]^{-1}[K]]^i \quad (17)$$

Where m is the number of degrees of freedom.

$$\{a\} = 2[Q]^{-1}\{\zeta\} \quad (18)$$

$$\{a\} = \begin{Bmatrix} a_1 \\ a_2 \\ \vdots \\ a_m \end{Bmatrix},$$

$$\{\zeta\} = \begin{Bmatrix} \zeta_1 \\ \zeta_2 \\ \vdots \\ \zeta_m \end{Bmatrix} \quad \&$$

$$[Q] = \begin{bmatrix} \omega_1 & \omega_1^3 & \omega_1^5 & \cdots & \cdots & \omega_1^{2m-1} \\ \omega_2 & \omega_2^3 & \omega_2^5 & \cdots & \cdots & \omega_2^{2m-1} \\ \vdots & \vdots & \vdots & \cdots & \cdots & \vdots \\ \omega_m & \omega_m^3 & \omega_m^5 & \cdots & \cdots & \omega_m^{2m-1} \end{bmatrix}$$

Where ω_1, ω_2 …ω_m are the natural frequencies of the system and ζ_1, ζ_2 …ζ_m are the damping ratios, by considering that the damping ratio is taken as (0.07) **[H. Vinayak, R. Singh, 1995].** Finally the damping matrix [C] is obtained by substituting Eq. (18) into Eq. (17).

SOLUTION OF FINITE ELEMENT EQUILIBRIUM EQUATION [Time History Analysis]

The general equation of motion can be written as **[Singireu S. Rao, 1967]**:-

$$[M]\{\ddot{U}\} + [C]\{\dot{U}\} + [K]\{U\} = \{R\} \quad (19)$$

Where [M], [C] and [K] are mass, damping and stiffness matrices respectively, {R} is the external load vector; {U}, $\{\dot{U}\}$ and $\{\ddot{U}\}$ are the displacement, velocity and acceleration vectors respectively. All of them are being time–dependent. Therefore in dynamic analysis, in principles, static equilibrium at time (t), which includes the effect of acceleration dependent inertia forces and velocity-dependent damping forces, is considered. Time history analysis; is a technique used to determine the dynamic response of a structure under the action of any general time dependent loads. This analysis can be used to determine the time-varying displacement, strain, stresses and force in a structure as it responds to any type time dependent loads. So can be considering the Houbolt method is reference to a multi degree of freedom system **[Singireu S. Rao, 1967]**, the following finite difference expansions are employed;

$$\dot{x}_{i+1} = \frac{1}{6\Delta t}(11x_{i+1} - 18x_i + 9x_{i-1} - 2x_{i-2}) \quad (20)$$

$$\ddot{x}_{i+1} = \frac{1}{(\Delta t)^2}(2x_{i+1} - 5x_i + 4x_{i-1} - x_{i-2}) \quad (21)$$

To drive Eq. (20) & (21), consider the function (x_t). Let the values of x at the equally spaced grid points $t_{i-2}=t_{i-2}.\Delta t$, $t_{i-1}=t_i-\Delta t$, t_i and $t_{i+1}=t_i+\Delta t$ be given by x_{i-2}, x_{i-1}, x_i and x_{i+1} respectively, The Taylor`s series expansion, with backward step gives the following;

With step size=Δt;

$$x_{(i)} = x_{(i+1)} - \Delta t\,\dot{x}_{(i+1)} + \frac{1}{2!}(\Delta t)^2\ddot{x}_{(i+1)} - \frac{1}{6}(\Delta t)^3\dddot{x}_{(i+1)} \quad (22)$$

With step size=2Δt;

$$x_{(i-1)} = x_{(i+1)} - 2\Delta t\,\dot{x}_{(i+1)} + 2(\Delta t)^2\ddot{x}_{(i+1)} - \frac{4}{3}(\Delta t)^3\dddot{x}_{(i+1)} \quad (23)$$

With step size=3Δt;

$$x_{(i-2)} = x_{(i+1)} - 3\Delta t\,\dot{x}_{(i+1)} + \frac{9}{2}(\Delta t)^2\ddot{x}_{(i+1)} - \frac{9}{2}(\Delta t)^3\dddot{x}_{(i+1)} \quad (24)$$

By considering terms up to $(\Delta t)^3$ only, Eq. (22) to (24) can be solved to express $\dot{x}_{(i+1)}$, $\ddot{x}_{(i+1)}$ and $\dddot{x}_{(i+1)}$ in terms of $x_{(i-2)}$, $x_{(i-1)}$, $x_{(i)}$ and $x_{(i+1)}$.

This gives $\dot{x}_{(i+1)}$ and $\ddot{x}_{(i+1)}$ as the Eq. of motion;

$[M]\ddot{x} + [C]\dot{x} + [K]x = F.$

And to find the solution at step i+1 ($x_{(i+1)}$), we consider Eq. of motion at t_{i+1}, so that;

$$[M]\,\ddot{x}_{(i+1)} + [C]\,\dot{x}_{(i+1)} + [K]\,x_{(i+1)} = F_{(i+1)} = F\,(t = t_{i+1}) \qquad (25)$$

By substituting Eq. (20) & (21) into Eq. (25), we obtain;

$$\left(\frac{2}{(\Delta t)^2}[M] + \frac{11}{6\Delta t}[C] + [K]\right)x_{(i+1)} = F_{(i+1)} + \left(\frac{5}{(\Delta t)^2}[M] + \frac{3}{\Delta t}[C]\right)x_{(i)} - \left(\frac{4}{(\Delta t)^2}[M] + \frac{3}{2\Delta t}[C]\right)x_{(i-1)} + \left(\frac{1}{(\Delta t)^2}[M] + \frac{1}{3\Delta t}[C]\right)x_{(i-2)} \qquad (26)$$

A. Determine x_{-1} using Eq. (22).

B. Find x_1 and x_2 using the central difference relationship;

$$x_{(i+1)} = \left[\frac{1}{(\Delta t)^2}[M] + \frac{1}{2\Delta t}[C]\right]^{-1} \times \left[F_{(i)} - \left([K] - \frac{2}{(\Delta t)^2}[M]\right)x_{(i)} - \left(\frac{1}{(\Delta t)^2}[M] - \frac{1}{2\Delta t}[C]\right)x_{(i-1)}\right]$$

D. Compute x_{i+1}, starting with i=2 and using Eq. (26).

$$x_{(i+1)} = \left(\frac{2}{(\Delta t)^2}[M] + \frac{11}{6\Delta t}[C] + [K]\right)^{-1} \times \left\{F_{(i+1)} + \left(\frac{5}{(\Delta t)^2}[M] + \frac{3}{\Delta t}[C]\right)x_{(i)} - \left(\frac{4}{(\Delta t)^2}[M] + \frac{3}{2\Delta t}[C]\right)x_{(i-1)} + \left(\frac{1}{(\Delta t)^2}[M] + \frac{1}{3\Delta t}[C]\right)x_{(i-2)}\right\}$$

The step-by-step procedure to be used in the Houbolt method is giving below;

Form the known initial conditions at t=0 x_0 and $\dot{x}_0$ to find $\ddot{x}_0$ by using Eq. of motion;

$\ddot{x}_0 = [M]^{-1}(f_0 - [C]\,\dot{x}_0 - [K]\,x_0)$.

C Select a suitable time of step Δt.

FORMULATION OF GLOBAL MATRICES & IT`S EVALUATION

The individual element stiffness's were assembled in the usual way. The global stiffness matrix was of size 24×24. The half band width was obtained.

A uniform load of 245.25 N/mm was assumed to act at the tip as shown in Fig. 1 this uniformly distributed load was lumped at the nodes.

Strategy for Determining the Stiffness Matrix

A. Compute the nodal coordinate in the real element in meters {in this work we have just (68) nod in x-y plane and (340) nod for holly tooth body}

B. Form strain displacement matrix [B], by apply the master element coordinate (ζ,η,τ) of the gauss point use Eq. (8) to find the independent of Eq. (7).
Differentiation of Eq. (1) with respect to (ζ, η, and τ) and put the shape function derivatives formula Eq. (8), to create the Jacobean matrix. Integrate the stiffness formula Eq. (15) by gauss four point to form matrix of size 24×24.

Strategy for Determining the Inertia & Damping Matrix

A. Integrate by gauss quadratic formula Eq. (16) but the value of mass to be in term of density depending on the type of the orthotropic material that use.

B. Apply the natural frequencies, the mass matrix, and damping ratio in Eq. (17), to determine the damping matrix for each material that considered in the current work.

DISCUSSION

Static Analysis

It was observed that the variations of displacements U, V, W, the normal stresses in L, T, Z directions, and the shear stresses in the LT, TZ, ZL planes both along the involute profile on the load surface and across the root those of mild steel gear. The trend of these variations indicates that orthotropic material gears also behave similarly to isotropic material gears.

The maximum stress near the root along the fiber is 10% and 21.5% more for Gl/Ep and Gr/Ep than the Ms Gear, Fig. 5-a. Whereas, the maximum stresses, in the other two directions, are very much lower. In the T direction it is 56% and 70% less Fig. 5-b. And in the Z -direction 74% and 87% less for

Gl/Ep and Gr/Ep gears respectively than Ms gear Fig. 5-c.

Similarly the shear stresses near the root in the LT plane, for orthotropic material gears is much less than that of isotropic gear, even though at the tip they are 24.5% and 43% more for Gl/Ep and Gr/Ep than Ms gear Fig. 6-a. The shear stress, in the other two planes TZ and ZL, even though the graph indicates some amount of dispersion, magnitude wise they are negligibly small Fig. 6-b and Fig. 6-c. All the figure shown the variations of stresses along the gear tooth profile on the load surface

It is reported by many investigators that the stresses on the compression side of the gear tooth are slightly more than those on the tension side **[Lewis, W., 1892]**. In this investigation also, along the fiber orientation direction, for Ms-Gear the maximum compressive stress is 11.75% more than the maximum tensile stress, whereas the maximum compressive stress is only 7% and 0.3% for Gl/Ep and Gr/Ep gears. These variations are shown in Fig. 7-a, Fig. 7-b, Fig. 7-c, Fig. 7-d, Fig. 7-e, Fig. 7-f.

Although the stresses are in a favorable direction, the displacements are relatively large for orthotropic materials. At the critical section, displacement U in the radial (L) direction is 7.5 times larger and 2.16 times larger Fig. 8-a. And displacement V in the tangential (T) direction is 11.6 times and 5.3 times larger Fig. 8-b. For the Gl/Ep and Gr/Ep gears than their corresponding values for the Ms gear.

The displacements W in (Z) direction along the face width of the gear are negligibly small in all the three cases as they are of the order of 10^{-6} Fig. 8-c.

In a similar way the displacements across the root thickness are also more for Gl/Ep and Gr/Ep gears. This is shown on Fig. 9-a, Fig. 9-b, and Fig. 9-c.

From Fig. 5 to Fig. 9 it may be observed that the performance of Gr/Ep gear is very much closer to Ms-Gear than Gl/Ep gear. Hence it may be concluded that Gr/Ep is a better material compared to Gl/Ep as an alternate for Ms for power transmission gears.

Dynamic {Time History} Analysis

The evaluation of dynamic stresses present by using maple calculator to solve the finite element equation motion for transient dynamic analysis and their procedures of the eigenvalues and eigenvectors for various modes wear obtained. These eigenvalues and eigenvector were then used in anther calculation {Houbolt method} in which the mode superposition technique was used to evaluate the dynamic stresses. The dynamic loads that act on the gear tooth sector can be considered as ***one half of a sinusoidal type impulse load*** Fig. 2 which represented by **[Kazunor, 1974];-** $F_t = F \sin\left(\frac{\pi t}{tf}\right)$

A- Time History Analysis of Concentrated Load on the Tip of the Gear Tooth

One half of a sinusoidal type impulse load will be concentrated in the tip of the gear tooth as shown in Fig.3 to studies the decay of vibration of the gear tooth, from calculate the displacement and stresses were carried out for (90-micro-sec) with (1.8- micro-sec) time step.

B- Time History Analysis of Moving Line Load on Gear Tooth Profile

The maximum normal load F_n acting on the gear tooth sector was assumed to be 245.25 N per mm length of face width. The load distribution on the tooth profile, when the load moved from the tip to the bottom, was assumed to be of the form shown in Fig. 4 in accordance with the theory of gearing **[Ramamurti, V., and Ananda, M., 1988]**.this normal load was considered in terms of its components in the radial and tangential direction with account taken of the pressure angle at any point under consideration; that is, the tangential load is

$F_t=F_n \cos \alpha_i$ And the radial load is $F_r=F_n \cos \alpha_i$, where α_i is the pressure angle at the point under consideration.

Discussion of Time History Analysis for Concentrated Load Response

The time history of tooth tip displacement for two types of spur gears made of composite material (Gl/Ep and Gr/Ep), represent low dynamic response in there modes shape with respect to mild steel gear, where the maximum deflection in the tip is (33%) and (16.6%) less for Gl/Ep and Gr/Ep than the Ms Gear Fig. 10-a, whereas, the maximum deflection in the other two

directions, are very much lower Fig. 10-b, and Fig. 10-c.

The maximum fillet stress along the fiber direction (σ_L) is (38%) and (41.5%) more for Gl/Ep and Gr/Ep than the Ms Gear, whereas, the maximum stresses, in the other two directions, are slightly more. In the (σ_T) direction it is (21%) and (28%) more .And in the (σ_Z) direction (11%) and (16%) more for Gl/Ep and Gr/Ep gears respectively than Ms gear Fig. 11.

Similarly the shear fillet stresses in the (τ_{TZ}) plane, they are (35%) and (20%) more for Gl/Ep and Gr/Ep than Ms gear. The shear stress, in the other two planes (τ_{LT})and (τ_{ZL}), even though the graph indicates some amount of deference's between the orthotropic gears and isotropic one in the magnitude these shear stresses wise they are negligibly small Fig. 12.

Recorded that the amplitude of dynamic displacement exceeds the static displacement by (48%), (60%) for Gl/Ep and Gr/Ep respectively for application of sinusoidal concentrated load. In a similar way the dynamic stresses exceeds the static stresses by (20%), (35%) for Gl/Ep and Gr/Ep respectively for the same application of load.

Discussion of Time History Analysis for Moving Line Load Response

The total time taken for the load to move from top to bottom was obtained as (6.25×10^{-3}) Sec. **[K. J. Huang, and T. S. LIU, 2000]**. This time was divided into **1000** intervals, each of (6.25) μs, the proportionate number of intervals during which the load moves form one node to the other was calculated. The load was moved down the profile at each interval of (6.25) μs and the corresponding loads shared by the adjacent nodes were calculated. Thus the new load vector for each interval was calculated and fed into the dynamic calculation by use of Houbolt method, and the corresponding respectively, but for the isotropic material Ms is 84.372Mpa Fig. 13, but the root stresses under static load condition for the same cases is 122.72Mpa, 101.36Mpa, 87.52Mpa for Ms, Gr/Ep, and Gl/Ep respectively, which is more than the dynamic load condition. The reason is that in the static analysis case the full load was assumed to act at the tip, whereas in the case of dynamic analysis only half of the load acts at the tip.

When the full load at the tip is considered as a moving load then the corresponding maximum dynamic root stresses obtained was 194.95Mpa, 183.72Mpa, and 164.19Mpa for Ms, Gr/Ep, and Gl/Ep respectively [by put the equivalent load in the tip of the tooth profile].

Also the mode shape of the point on the tip will be calculated for Ms, Gr/Ep, and Gl/Ep in Fig. 14-a, Fig. 14-b, and Fig. 14-c, which represent the deformation of the tooth tip under the moving line of load. thickness for the two orthotropic material gears were very similar to

displacements and stresses were thus obtained.

It is reported by many investigators that the variation of dynamic root stresses with time to that the dynamic stresses at the root when the load is at the tip is less, and greater when the load is at the mid-height. This is obvious since the dynamic stresses is greater when the full load is impressed on only one tooth, even though the bending moment arm is slightly less.

In this work will be found that the peak stresses for two orthotropic materials Gl/Ep and Gr/Ep is 98.468Mpa and 75.719Mpa

CONCLUSION

1. The behavior of orthotropic material gears and mild steel gears (i.e. the variations of stresses and displacements both along tooth profile and across the tooth thickness) are very similar.
2. The maximum normal stress in the fibre (L) direction in orthotropic material gears is little more than the maximum stress in mild steel gear.
3. The maximum normal stresses in the other two perpendicular (T and Z**)** directions for orthotropic material gears are much smaller than that of mild steel gear.
4. The shear stress in the LT plane alone for orthotropic material gears is slightly more than that for mild steel gear, whereas the other two perpendicular (TZ and ZL) planes are negligibly less.
5. The displacements in the radial and tangential directions of orthotropic material gears are considerably more than that of mild steel gear, even along the face width it is almost zero.
6. For orthotropic material gears the maximum stress decreases with decreasing rim thickness, in the range of analysis made.
7. The Ms gear represent more response respect to the concentrated dynamic load then the Gl/Ep and Gr/Ep gears where it gives a little mode shapes and natural frequencies values for same load
8. The amplitude of dynamic stresses exceeds the static stresses for sinusoidal concentrated load.
9. The peak root stresses inhibit in the gear tooth that made of composite material respect to the dynamic moving load on the surface profile is slightly less than the concentrated load on tip.
10. Also that is found the spur gear that made from composite (graphite/epoxy) also comes very much closer to mild steel gear behavior, may definitely be thought of for power transmission.

REFERENCES

H. Vinayak, R. Singh, and C. Padmanabhan, (Linear Dynamic Analysis of Multi-Mesh Transmission Containing External, Rigid Gear) Journal of Sound and Vibration (1995) 185(1) 1-32.

Jean-Marie Berthelot, (Mechanical Behaviour of Composite Materials and Structures), Book ISMANS Institute for Advanced Le Mans, France Materials and Mechanics.

Kazunori and Fujio, (Dynamic Behavior of Heavy-Loaded Spur Gears), Transaction of ASME, Journal of Engineering for Industry, PP.373-381, May 1974.

K. J. Huang, and T. S. LIU, (Dynamic Analysis of A Spur Gear by the Dynamic Stiffness Method), Journal of Sound and Vibration (2000) 234(2), 311)329; http://www.idealibrary.com

Lewis, W., (Investigation of the Strength of Gear Teeth), Proceeding Engineers, Club, Philadelphia, October 1892.

N. Ganesan and T. C. Ramesh, (Free Vibration Analysis of Composite Wheels), Journal of Sound and Vibration (1992) 153(l), I13-124, Elsevier Science Publishers Ltd.

Ramamurti, V., and Ananda, M., (Dynamic Analysis of Spur Gear Teeth), Indian Institute of Technology, India, Journal of Computers and Structures, Vol.29, No.5, PP.831-843, 1988.

Singireu S. Rao, (Mechanical Vibrations)

Third Edition, Addiso-Wesley Publishing Company

S. Mohamed Nabi & N. Ganesan, (Static Stress Analysis of Composite Spur Gears Using 3D-Finite Element and Cyclic Symmetric Approach), Composite & Structures Vol. 46, No. 5, pp. 1993

Toshiki H., Eiichi A. Tsutao K. (Development of Design System for Composite Gears for Power Transmission), 2006 Elsevier, Science Direct, Japan Doshisha Univ.

Vijayarangan and N. Ganesan ,(Stress Analysis of Composite Spur Gears Using 3D-Finite Element Approach), Computers & Structures Vol. 46, No. 5, pp. 869475, 1993 Elsevier Science ltd.

Table 1 gear tooth parameter.

NO.	Design Parameter	Value
1.	*Pressure angle*	*20^o*
2.	*Module , mm*	*10*
3.	*Addendum*	*1m*
4.	*Dedendum*	*$1.25m_o$*
5.	*Root fillet radius*	*$0.3m_o$*
6.	*Rim thickness*	*$1.25m_o$*
7.	*Number of teeth*	*20*
8.	*Face width*	*$11m_o$*
9.	*Loading Condition*	*β=31.1684^o*

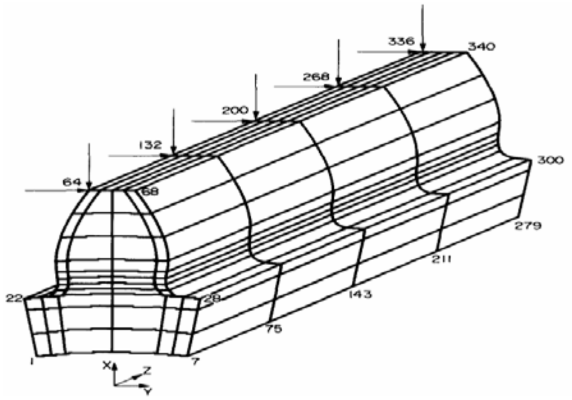

Fig. 1 gear meshing and tooth sector.

Table 2 mechanical properties for studying case.

PROPERTIES	MS	Gl//Ep	Gr/Ep
1. E_1,N/mm^2	20.60100	37.86660	180.99450
2. E_2,N/mm^2	20.60100	8.11290	10.70270
3. E_3,N/mm^2	20.60100	8.09990	10.51276
4. G_{12},N/mm^2	79.2354	4.06130	7171.10
5. G_{13},N/mm^2	79.2354	1.07711	0.90724
6. G_{23},N/mm^2	79.2354	1.12361	0.91132
7. ν_{12}	0.3	0.26	0.28
8. ν_{12}	0.3	0.0366	0.11
9. ν_{12}	0.3	0.0363	0.105
10. Density,Kg/mm^2	781E-10	1.81E-10	1.46E-10
11. X_T,N/mm^2	353.2	981.00	1079.10
12. Y_T,N/mm^2	353.2	34.40	34.40
13. Z_T,N/mm^2	353.2	40.87	42.54
14. S,N/mm^2	176.6	88.30	88.30
15. ν_{21}	Isotropic	0.065	0.0167
16. ν_{13}		0.009	0.0063
17. ν_{32}		0.036	0.103
18.The weight of model	9.413547	3.7674	2.2135

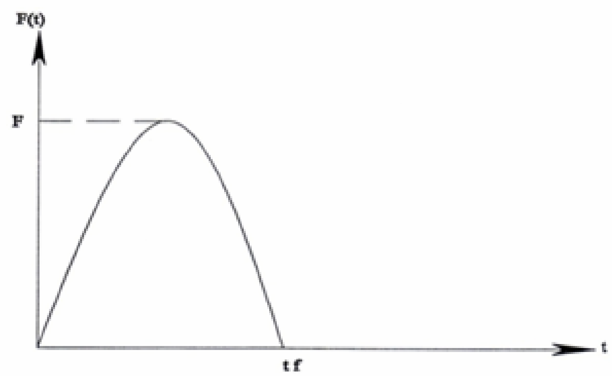

Fig. 2 The time history of one half of sinusoidal type impulse loads.
F=Amplitude of the applied load
F= (245.25 N) per (mm) of tooth face width.
tf =Total duration of the load, which is taken as (30) microsecond.

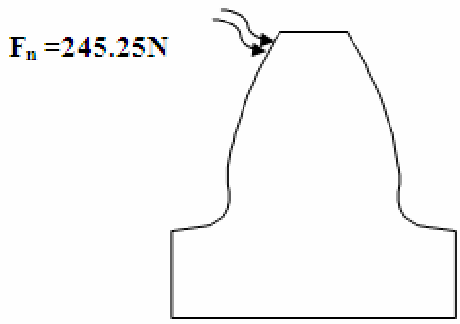

Fig. 3 one half sinusoidal type impulse concentrated load.

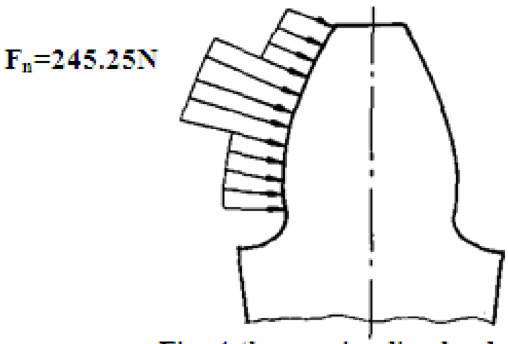

Fig. 4 the moving line load on tooth profile.

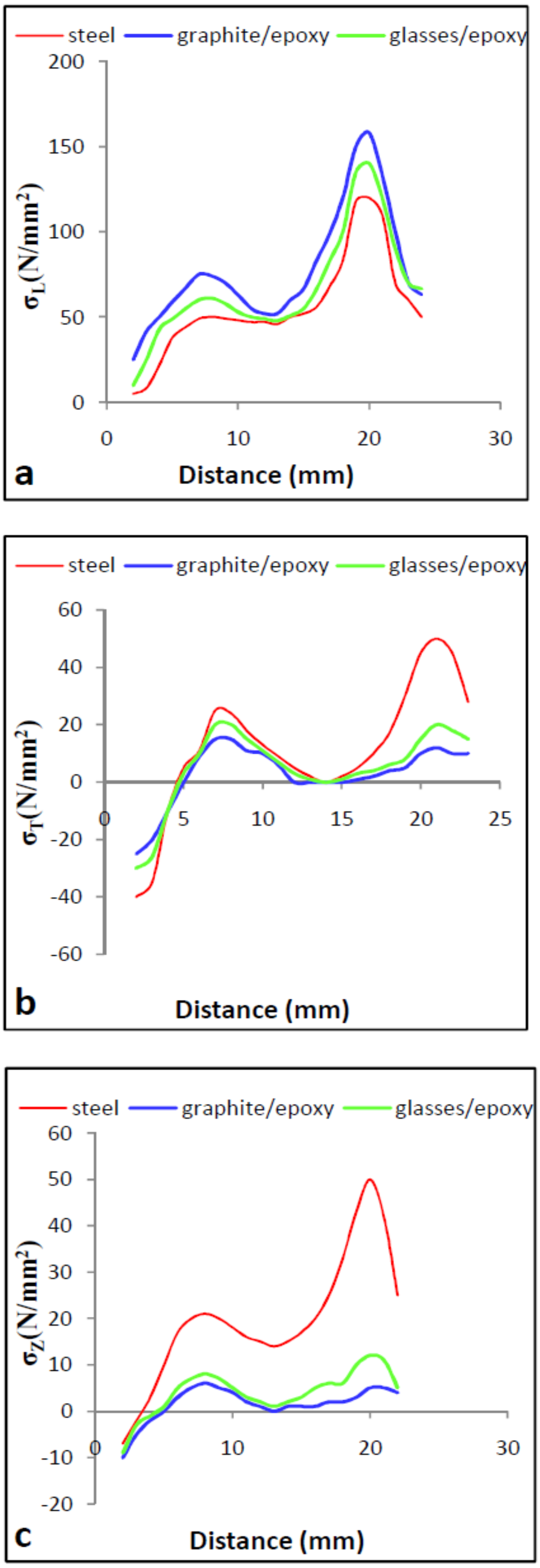

Fig. 5.a-b-c the maximum stress near the root.

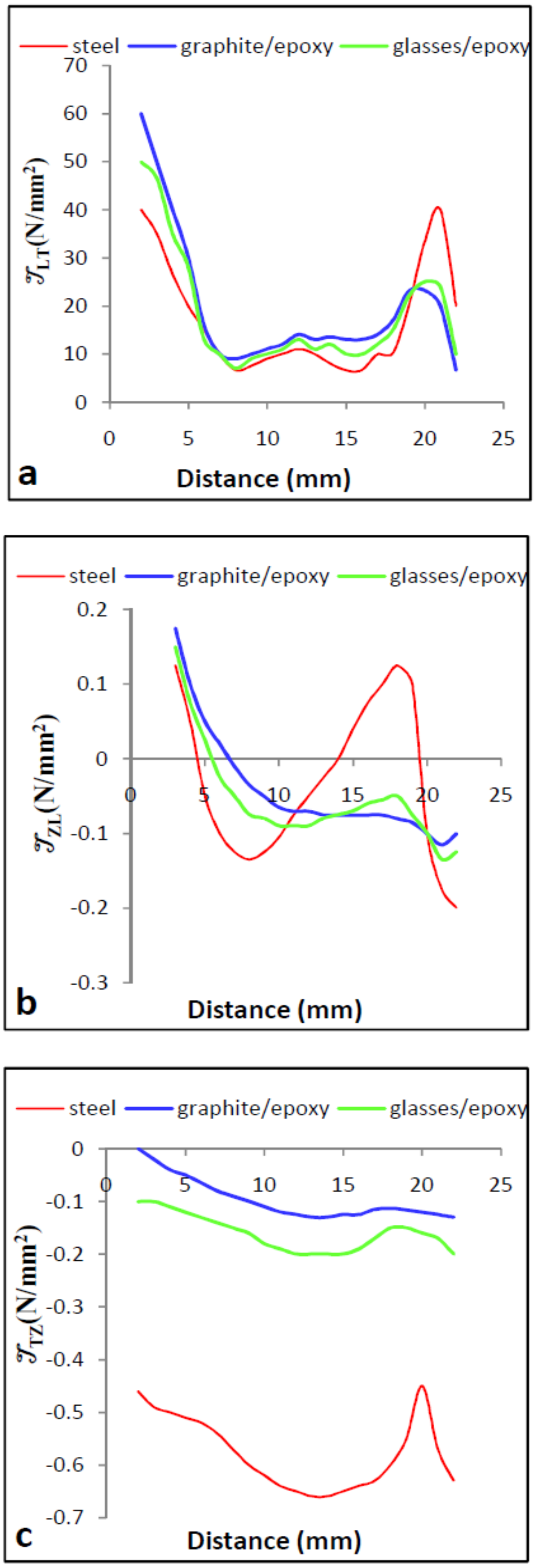

Fig. 6.a-b-c the shear stresses near the root.

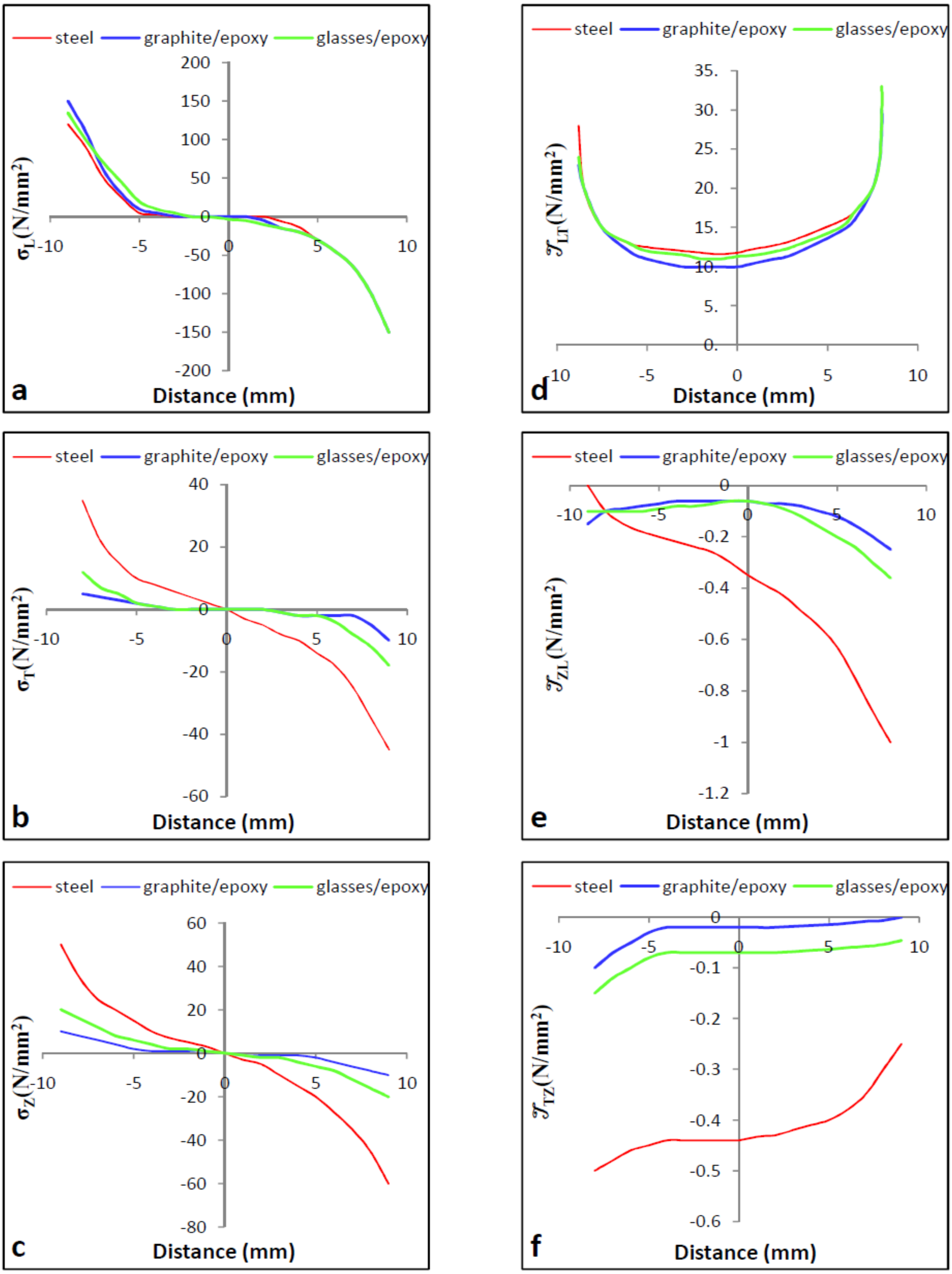

Fig. 7.a-b-c-d-e-f maximum stresses a cross root thickness.

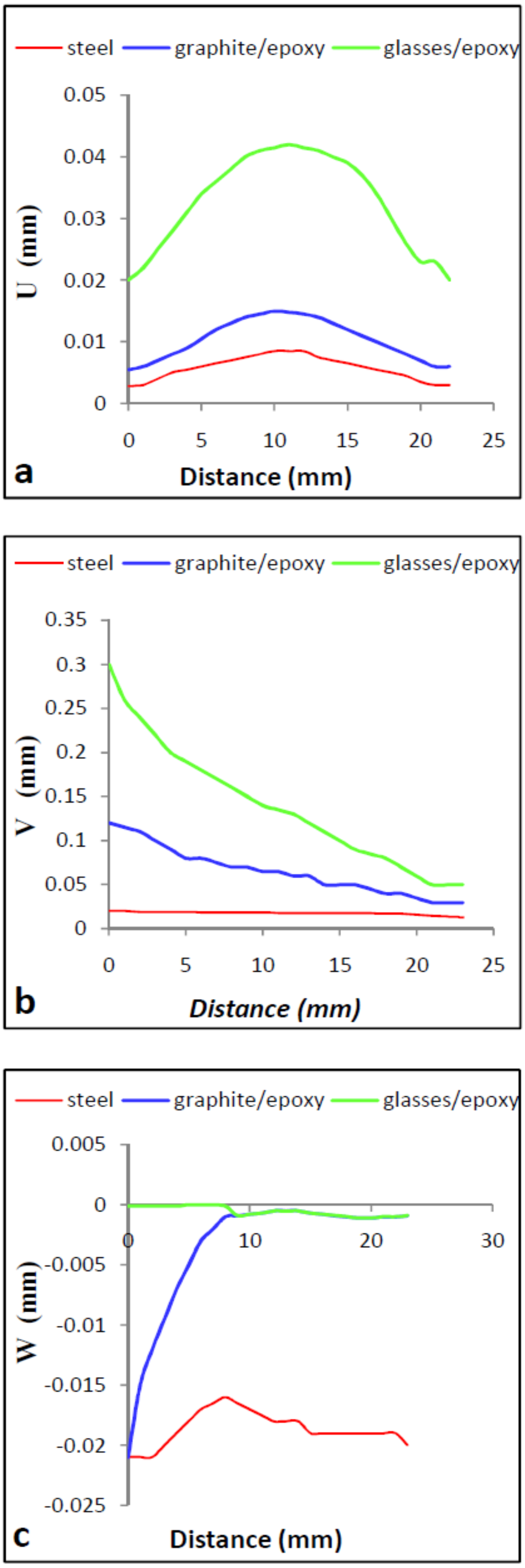

Fig. 8.a-b-c displacement along surface profile.

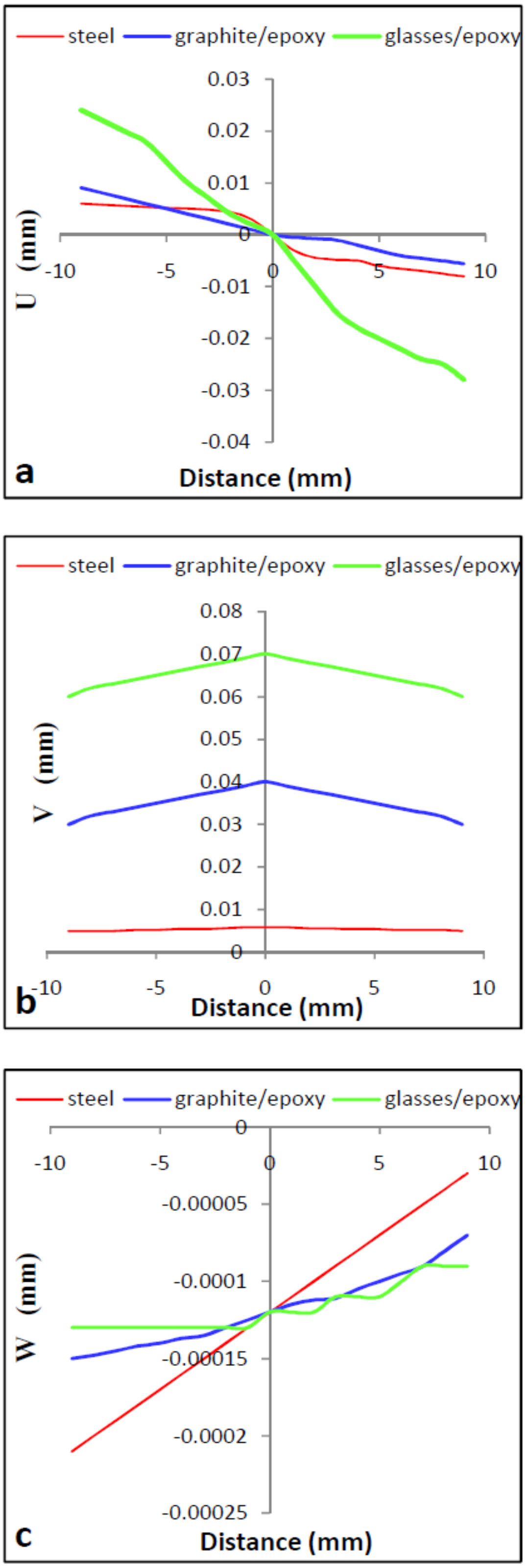

Fig. 9.a-b-c displacement a cross root thickness.

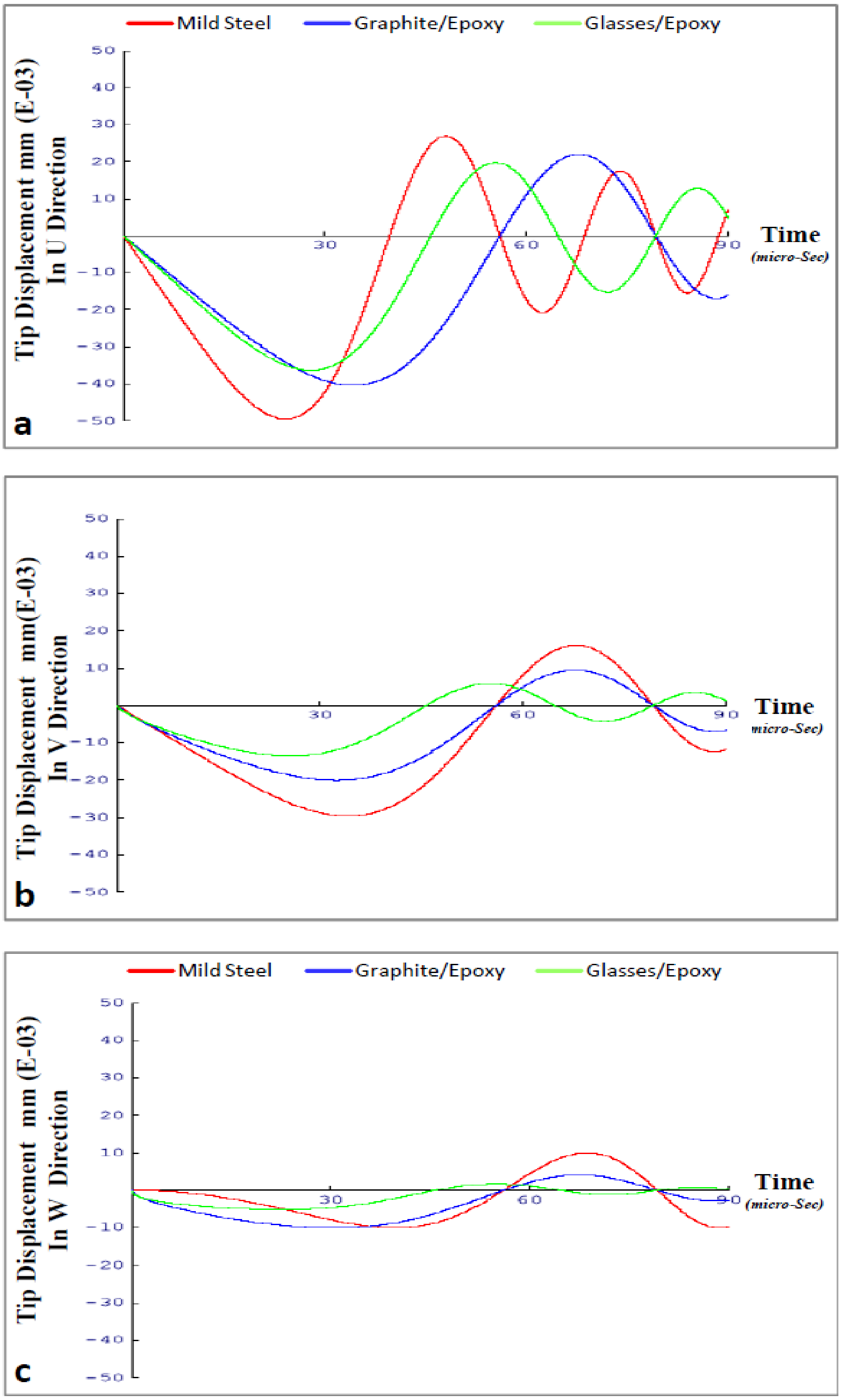

Fig. 10.a-b-c the maximum deflection in the tip

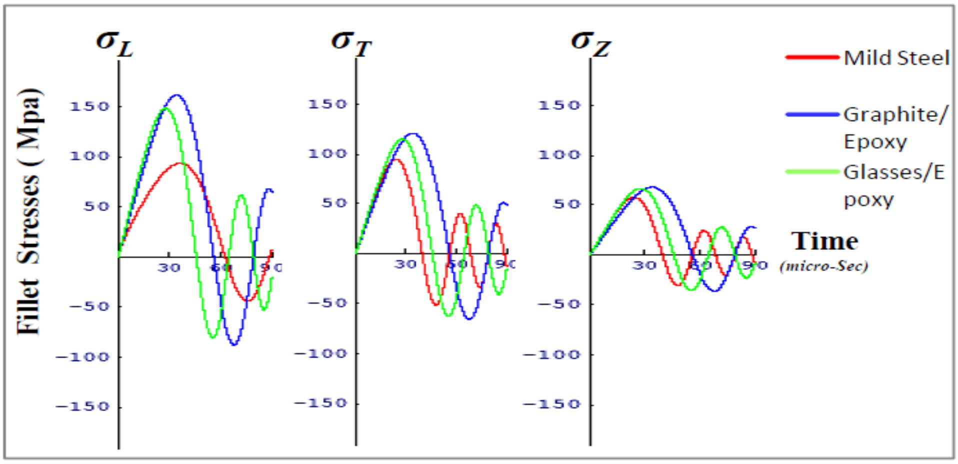

Fig. 11 fillet normal stresses due to the sinusoidal conetrated load.

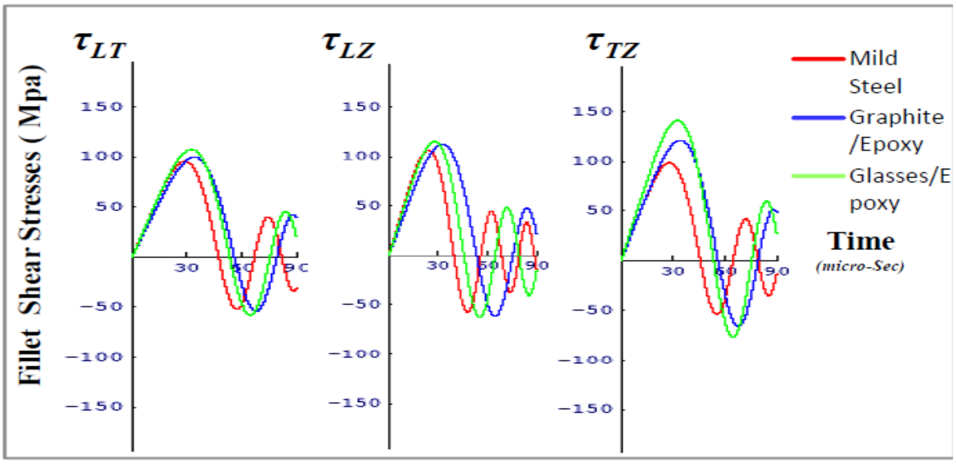

Fig. 12 fillet shear stresses due to the sinusoidal conetrated load.

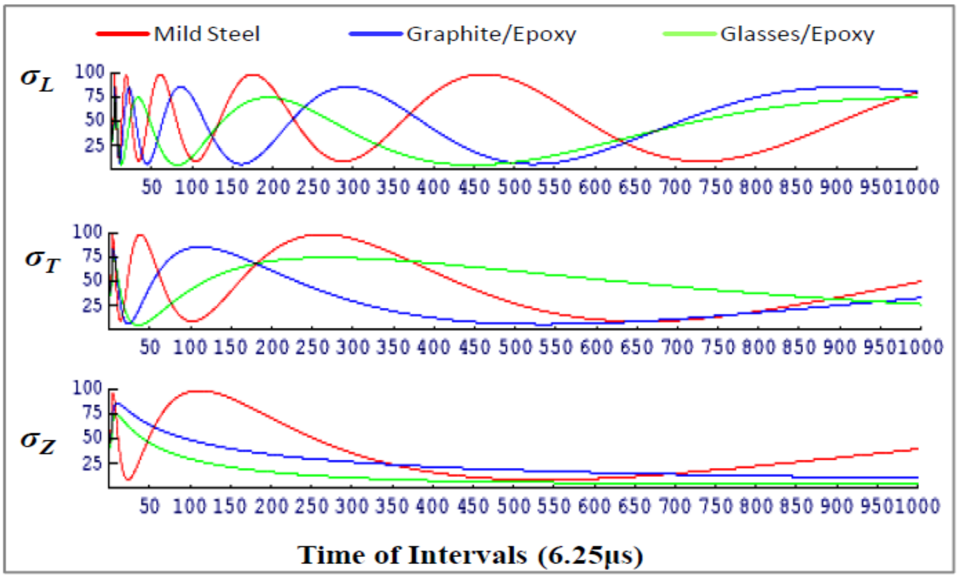

Fig. 13 fillet stresses due to the moving line load.

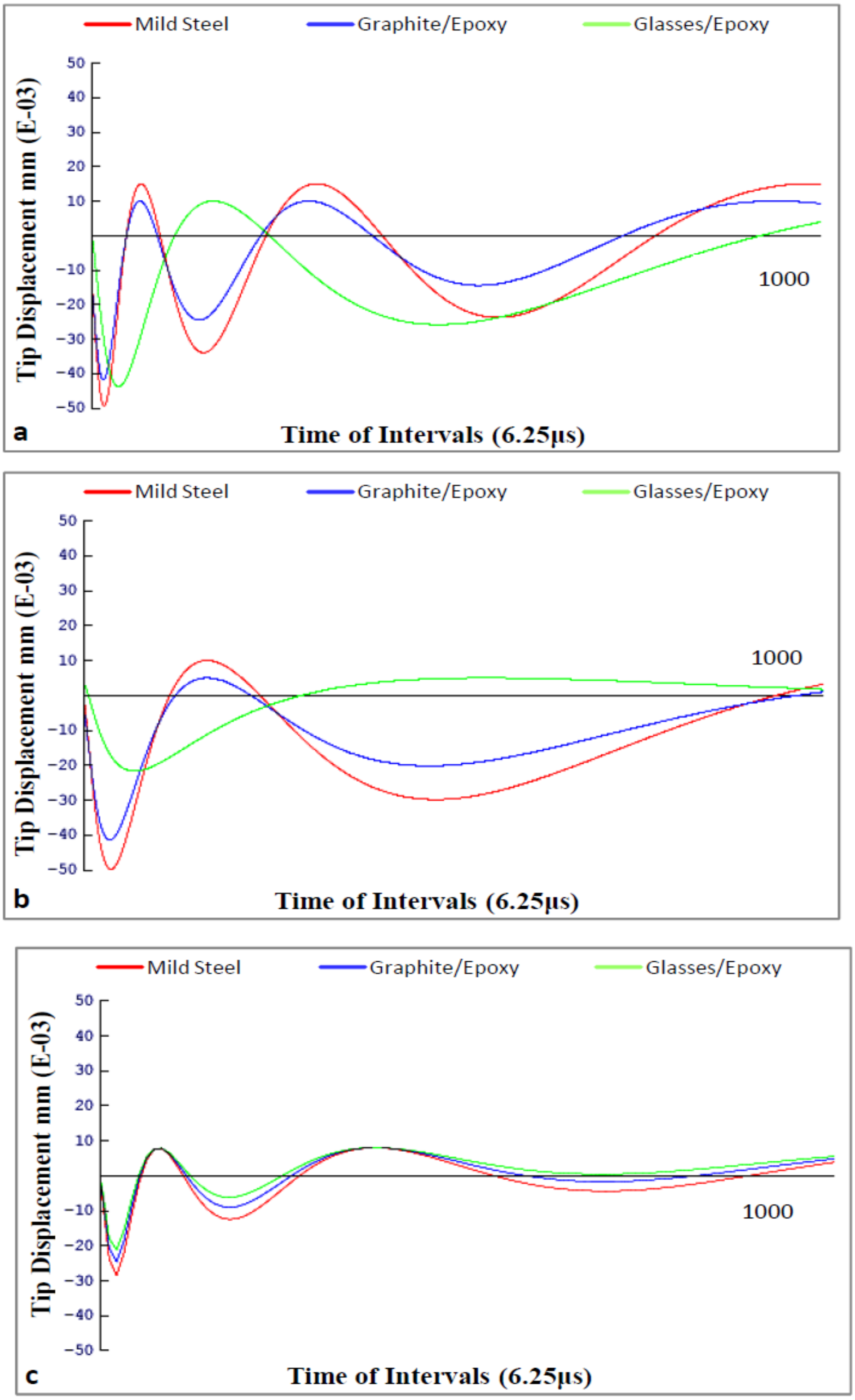

Fig. 14.a-b-c the mode shape of the gear tooth tip in W direction.

RHEOLOGICAL PROPERTIES OF IRAQI ASPHALT BINDERS MEASURED USING SUPERPAVE SYSTEM AND SHELL SOFTWARE

Alaa H. Abed
University of AL-Nahrain, Baghdad-

Prof. Hamed M. Hamdou
University of Baghdad, Baghdad-Iraq

Ass. Prof. Dr Namir G. Ahmed
University of AL-Mustansiriya, Baghdad-Iraq

ABSTRACT

The performance grading system (superpave) has provided means to incorporate binder characteristics with pavement failure types. It's a comprehensive system that relates climate, traffic conditions and aging with critical pavement distress. The objective of this paper is to develop an improved asphalt binder grading system for Iraq based on the principal of superpave. The country was divided into different zones according to the highest and lowest temperature ranges and traffic loading. The Performance graded binder proposed for each zone was compared with some States of USA that have same hot weather of Iraq by using Long Term Pavement Performance (LTPP v3.1) software. Iraqi asphalt samples were tested using the Superpave technology in Wisconsin University and the results were compared with those estimated using Shell pavement design software packages (BANDS 2) at different loading time and frequency. In general, the performance grade of binders produced from the three refineries in Iraq (Daurah, Basrah and Baiji) is PG 64-16. The m- value (slope of log creep stiffness versus log frequency curve at specified temperature) determined by DSR (Dynamic Shear Rheometer) and Shell software was compared.

Keywords: Superpave; Performance Grading; Phase Angle; BANDS; Shell software.

الخلاصة

إن نظام درجة الأداء (التبليط الفائق) يدمج بين صفات الإسفلت والأنواع الرئيسية لفشل الخرسانة الاسفلتية، لذلك يعتبر نظام شامل لربط الظروف المناخية والأحمال وعمر التبليط مع انواع الفشل الحرجة. إن الهدف الرئيسي من هذا البحث هو إيجاد وتحسين نظام الأداء للإسفلت العراقي مبنياً على مبادىء التبليط الفائق.تم تقسيم العراق الى عدة مناطق حسب اقصى واقل درجة حرارية وأحمال المرور. لقد تم مقارنة نظام الأداء المقترح مع بعض الولايات الأمريكية ذات امناخ الحار المشابه لحرارة مناخ العراق. لقد تم فحص الاسفلت العراقي في ولايات وسكونسن الامريكية اعتمادا على تكنلوجيا التلبط الفائق ومقارنة النتائج مع برنامج شركة شيل. وبصورة عامة نظام الأداء للأسفلت المنتج في مصافي الدورة والبصرة وبيجي هو 16 -64. ولقد تم مقارنة قيمت م (الميل بين لوغاريتم متانة الاسفلت ولوغاريتم التردد لدرجحة حرارة ثابتة) الناتجة من فحص الداينمك شير ريوميتر مع قيمة م الناتجة من برنامج شيل.

Alaa H. Abed

Prof. Hamed M. Hamdou

Ass. Prof. Dr Namir G. Ahmed

RHEOLOGICAL PROPERTIES OF IRAQI ASPHALT BINDERS MEASURED USING SUPERPAVE SYSTEM AND SHELL SOFTWARE

INTRODUCTION

Conventional measurements of asphalt physical properties cannot be considered reliable to characterize asphalt properties that are critical for pavement performance because of the engineering complications related to the method by which there are interpreted (Asphalt Handbook, 2007)

Performance grading could be defined as "a system in which fundamental mechanical properties that are related to pavement performance are used to select binder to minimize critical failure, rutting, fatigue cracking and low temperature crack, at critical conditions of pavement temperatures and traffic characteristics".(Roberts et al 1996)
The Superpave binder specifications, also called Performance Grading (PG) System has effectively achieved this by using advanced rheometers in which temperature and loading rate are easily controlled. This achievement is arguable one of the most important advancements in asphalt binder quality control technologies during the last 60 years.
The Superpave performance grading system has provided means to contribute binder resistance with pavement failure type. It's comprehensive system related climate, traffic conditions and aging with critical pavement distress.
The specifications of the local asphalt binder are based on the conventional methods "empirical single point–measurements" viscosity measures and susceptibility parameters, climate and failure modes are not directly recognize. In this study samples were collected from the three refineries and tested at the university of Wisconsin-Madison testing lab to determine the physical properties according to the Penetration grading system and the Superpave system. The results were used to study the difference between the two systems and to trying various methods to estimate the performance grading from simple measurements. Based on the results, a map of PG binders was established for Iraq and the binders tested form the Iraqi refineries were fitted for the PG zones. Because it was clear that some of the climatic zones in Iraq will need better grades than what is produced, the study was extended to include modification for the available binders.

PERCENTAGE OF ASPHALTEN

The percentage of asphaltenes has been measured for different types of local asphalt binder according to ASTM (D3279, 2007); Figure (1) shows experimental work to find the percentage of asphaltenes. The results for different asphalt binder are tabulated in Table (1).

Fig. 1 Tools used to find percentage of asphaltenes.

Table 1 Percentage of asphaltenes for local asphalt binders

Type of Asphalt	Daurah PG 64-16	Daurah PG 58-22	Basrah PG 64-16	Baiji PG 64-16
% Asphaltenes	14	15	14	17

SUPERPAVE RHEOLOGICAL PROPERTIES FOR THE LOCAL ASPHALT BINDERS

In the superpave system the physical properties remain constant for all performance grades (PG), but the temperature at which these properties must be achieved varies from grade to another depending on the climate in which the asphalt binder is expected to perform. The stiffness of asphalt can vary by as much as eight orders in magnitude, and their phase angle (relative distribution of response between elastic and viscous behavior) by as much as 85^o between peak summer and peak winter conditions. These binders can also vary by similar amounts in response to standing traffic and high-speed traffic (Anderson et al.1994). At any combination of time and temperature, viscoelastic behavior, within the linear range, must be characterized by at least two properties: the total resistance to deformation and the relative distribution of that resistance between an elastic part and a viscous part (Bahia and Anderson, 1995). Although there are many methods of characterizing viscoelastic properties, dynamic (oscillatory) testing is one of the best techniques to represent the behavior of this class of materials. In the shear mode, the dynamic modulus denoted as G* and phase angle (δ) are measured. G* represents the total resistance to deformation under load, while δ represents the relative distribution of this total response between an in-phase component and an out-of-phase component. The in-phase component is an elastic component and is related to energy stored in a sample for every loading cycle, while the out-of-phase component represents the viscous component and is related to energy lost per cycle in permanent flow. The relative distribution of these components is a function of the composition of the material, loading time, and temperature.

RESULTS AND ANALYSIS

In this study the binders collected from refiners in Iraq were tested in the lab. Also, the BANDS2 program, which is based on the vander Poel nomograph (Van der Poel 1954) was used to compare directly measured values with the estimated values. Figure (2) shows a snap shot of a typical screen that displayed of the original binder that estimated using BANDS2. Tables (2) and (3) show results of rheological properties measured for the binders from the Iraqi Refiners. The testing included the rotational viscometer (RV), dynamic shear rheometer (DSR) and bending beam rheometer (BBR) for binders after different aging conditions, following the Superpave PG grading requirements. The tables also include comparison of these measurements with estimated stiffness by van der poel nomograph using (BANDS2) software. The estimated results depends on time of loading (1.59 Hz), which is assumed to correlate G*/sinδ at 10 rad/sec, bitumen temperature, softening point and penetration value at different aging film. To determine creep stiffness at minimum temperature the same procedure of superpave is used by raising test temperature 10ºC to simulate two hour loading time) (Bahia, 2009). Table (4) presents summary of the performance grade of different binders produced in Iraq.

In addition to the testing required for the PG grading, frequency sweep testing was conducted at constant strain (1%) and different temperatures (34 ºC, 31 ºC, 28 ºC, 25 ºC, and 19 ºC) for pressure aging film to measure G* at different frequency, m-value (slope between log complex modulus versus log frequency curve at specified temperature) that calculated from these tests were compared with m-value estimated by shell software at different frequency and temperature for pressure aging film also, Figure (3) and (4) depicted m-value for different types of asphalt binder measured and estimated at different temperature.

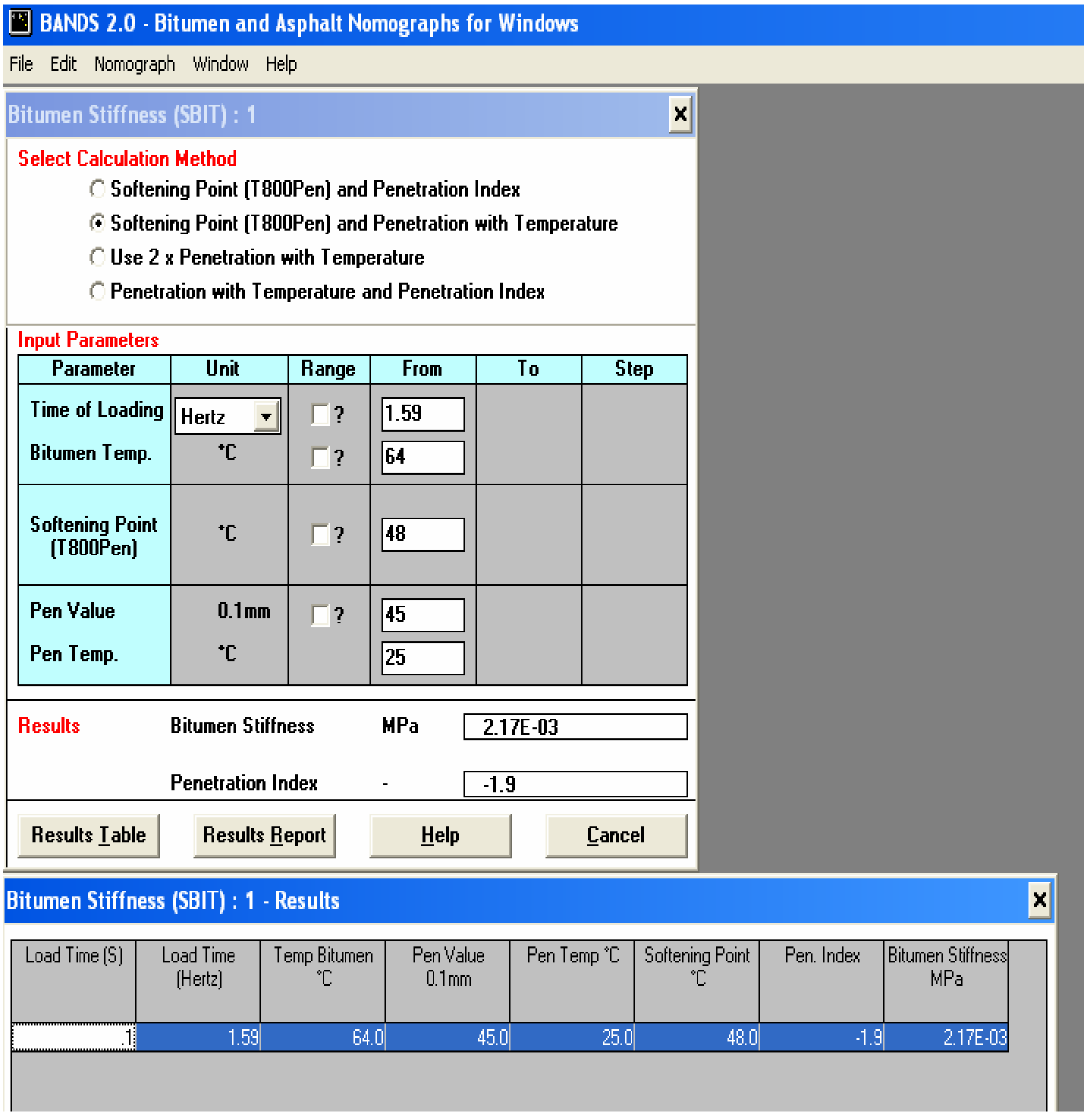

Fig. 2 Snap shot of the displayed screen in BANDS2.

Table 2 Measured (Estimated- BANDS 2) for Daurah Binder

Type of Asphalt	*Daurah 40-50 Pen. Grade*		*Daurah 85-100 pen. Grade*	
Aging	*Original*		*Original*	
Rotational Viscosity Pa.sec	@135 °C	0.516	@135 °C	0.33
G*/sin δ, kPa	@64 °C	2.37 (2.17)*	@58 °C	1.875 (2.61)
	@70 °C	0.958 (1.06)	@64 °C	0.886 (1.22)
True Grade	**69.83** °C	1	**63.32** °C	1
Penetration	@25°C	45	@25°C	88
Softening Point	48 °C		43°C	
Aging	*RTFO*		*RTFO*	
G*/sin δ, kPa	@64 °C	4.05 (4.04)	@58 °C	4.31 (4.34)
	@70 °C	1.887 (1.72)	@64 °C	1.91 (1.81)
True Grade	**69.13** °C	2.2	**63.27** °C	2.2
Loss (%)	0.73	< 1	0.77	< 1
Penetration	@25°C	29	@25 °C	47
Softening Point	52 °C		47 °C	
Aging	*PAV*		*PAV*	
δ	@25 °C	53°(63°)	@22 °C	53°(66.5°)
	@28 °C	59° (67°)	@25°C	59° (68.6°)
m-value	@25 °C	0.525(0.638)	@22 °C	0.53(0.688)
	@28 °C	0.578(0.692)	@25°C	0.586(0.73)
G*.sin δ, kPa	@25 °C	7320(22453)	@22 °C	7770(20633)
	@28 °C	4700 (12334)	@25 °C	4353(11358)
Creep Stiffness, MPa	@-16 °C	182 (200)	@-22°C	222(411)
	@-22 °C	426 (490)	@-28°C	369(839)
True Grade	**-18.9** °C	300	**-25** °C	300
Slop m-value	@-16 °C	0.399 (0.477)	@-22 °C	0.367 (0.349)
	@-22 °C	0.289 (0.269)	@-28 °C	0.26 (0.176)
True Grade	**-21.4** °C	0.3	**-25.8** °C	0.3
Penetration	@25°C	20	@25°C	30
Softening Point	57°C		52°C	

* **Estimated using BANDS 2 Software.**

Table 3 Measured (Estimated- BANDS2) for Basrah and Baiji Binder

Type of Asphalt	*Basrah 40-50 Pen. Grade*		*Baiji 40-50 pen. Grade*	
Aging	*Original*		*Original*	
Rotational Viscosity Pa.sec	@135 °C	0.444	@135 °C	0.444
G*/sin δ, kPa	@64 °C	1.26 (1.18)	@64 °C	1.32(1.79)
	@70 °C	0.605 (0.58)	@70°C	0.638(0.876)
True Grade	**66.36** °C	1	**66.8** °C	1
Penetration	@25°C	48	@25°C	46
Softening Point	45 °C		47 °C	
Aging	*RTFO*		*RTFO*	
G*/sin δ, kPa	@64 °C	2.93 (2.81)	@64 °C	2.41(3.27)
	@70 °C	1.24 (1.25)	@70 °C	1.13(1.43)
True Grade	**66.59** °C	2.2	**65** °C	2.2
Loss (%)	0.34	< 1	0.4	< 1
Penetration	@25°C	32.5	@25°C	29
Softening Point	50 °C		51 °C	
Aging	*PAV*		*PAV*	
δ	@25 °C	58.5°(66°)	@25 °C	54°(65°)
	@28 °C	63° (68.4°)	@28 °C	59° (66.7°)
m-value	@25 °C	0.577(0.685)	@25 °C	0.537(0.667)
	@28 °C	0.635(0.725)	@28 °C	0.578(0.692)
G*.sin δ, kPa	@25 °C	7192 (18728)	@25 °C	6830(20573)
	@28 °C	4340 (11010)	@28 °C	4153(11296)
Creep Stiffness, MPa	@-16 °C	159.5 (205)	@-16 °C	161(203)
	@-22 °C	391.5 (581)	@-22 °C	412(528)
True Grade	**-19.65** °C	300	**-19.3** °C	300
Slop m-value	@-16 °C	0.4 (.51)	@-16 °C	0.402(0.485)
	@-22 °C	0.26 (0.33)	@-22 °C	0.288(0.296)
True Grade	**-20.3** °C	0.3	**-21.4** °C	0.3
Penetration	@25 °C	22	@25 °C	21
Softening Point	55 °C		56 °C	

Table 4 Summary value for PG for different binder

Type of Asphalt	Penetration	Performance Grade
Daurah	40-50	PG 64-16
Daurah	85-100	PG 58-22
Basrah	40-50	PG 64-16
Baiji	40-50	PG 64-16

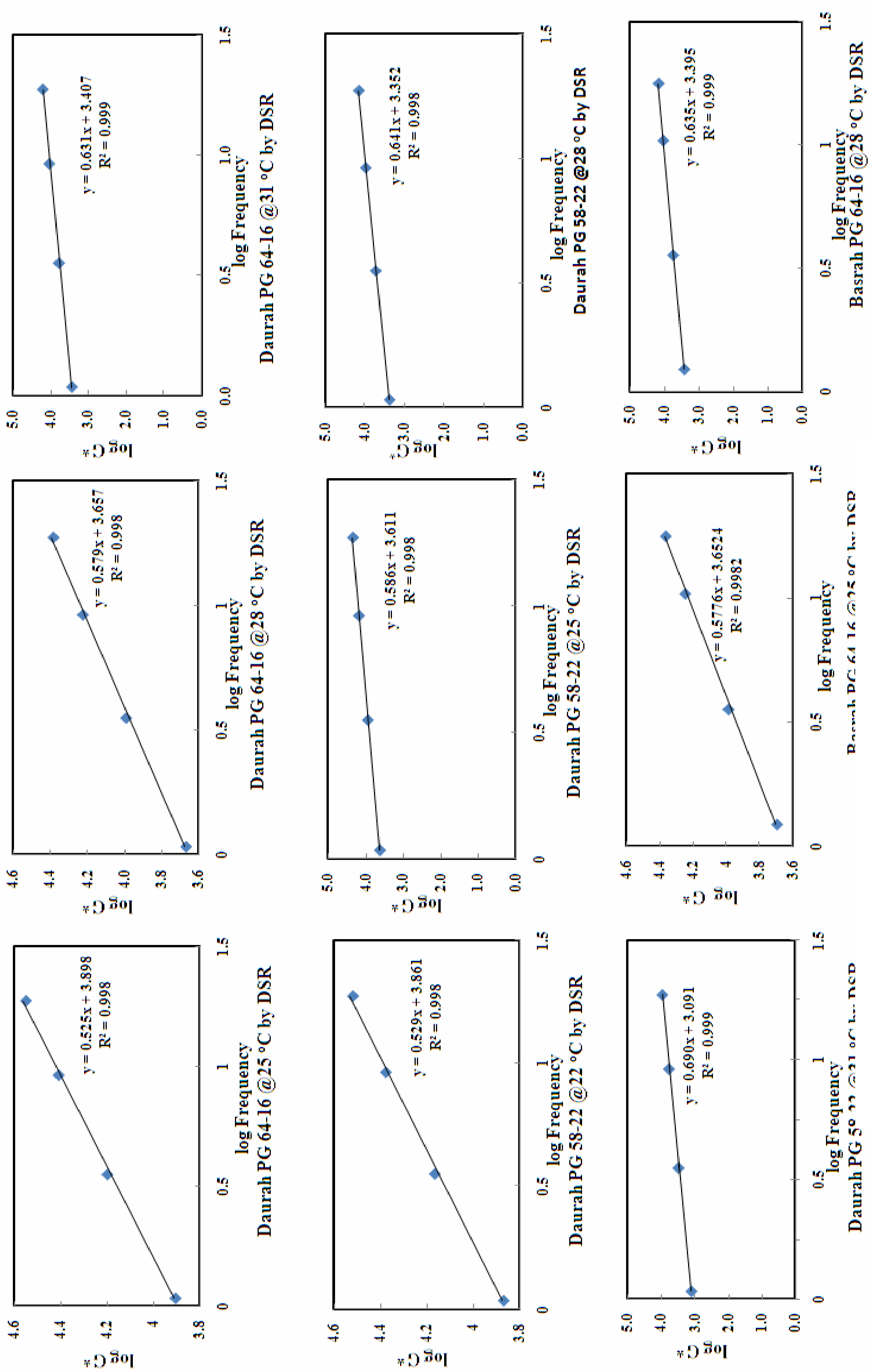

Fig. 3 Log G* versus log frequency measured by DSR

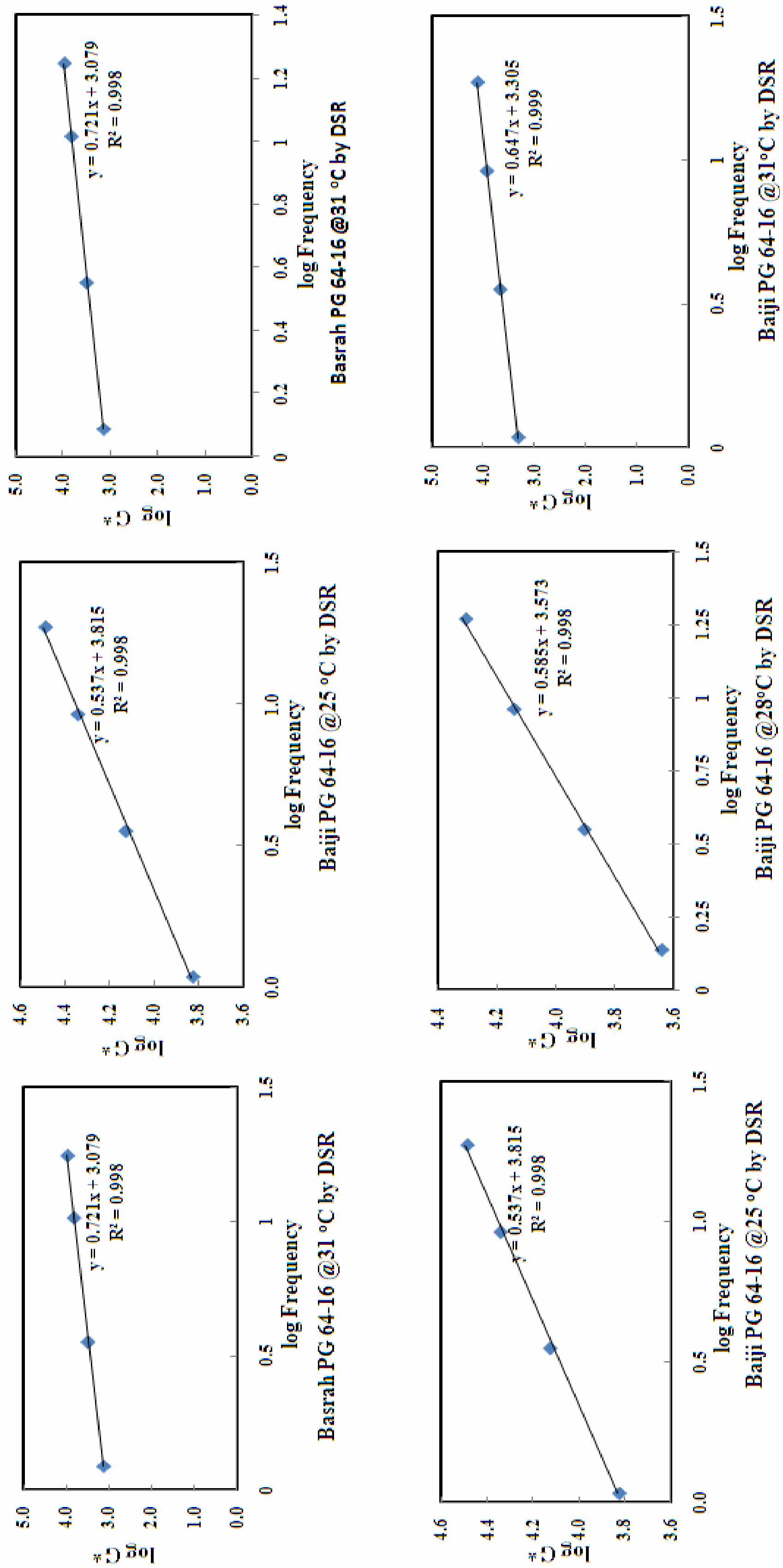

Fig. 3 Log G^* versus log frequency measured by DSR (continued)

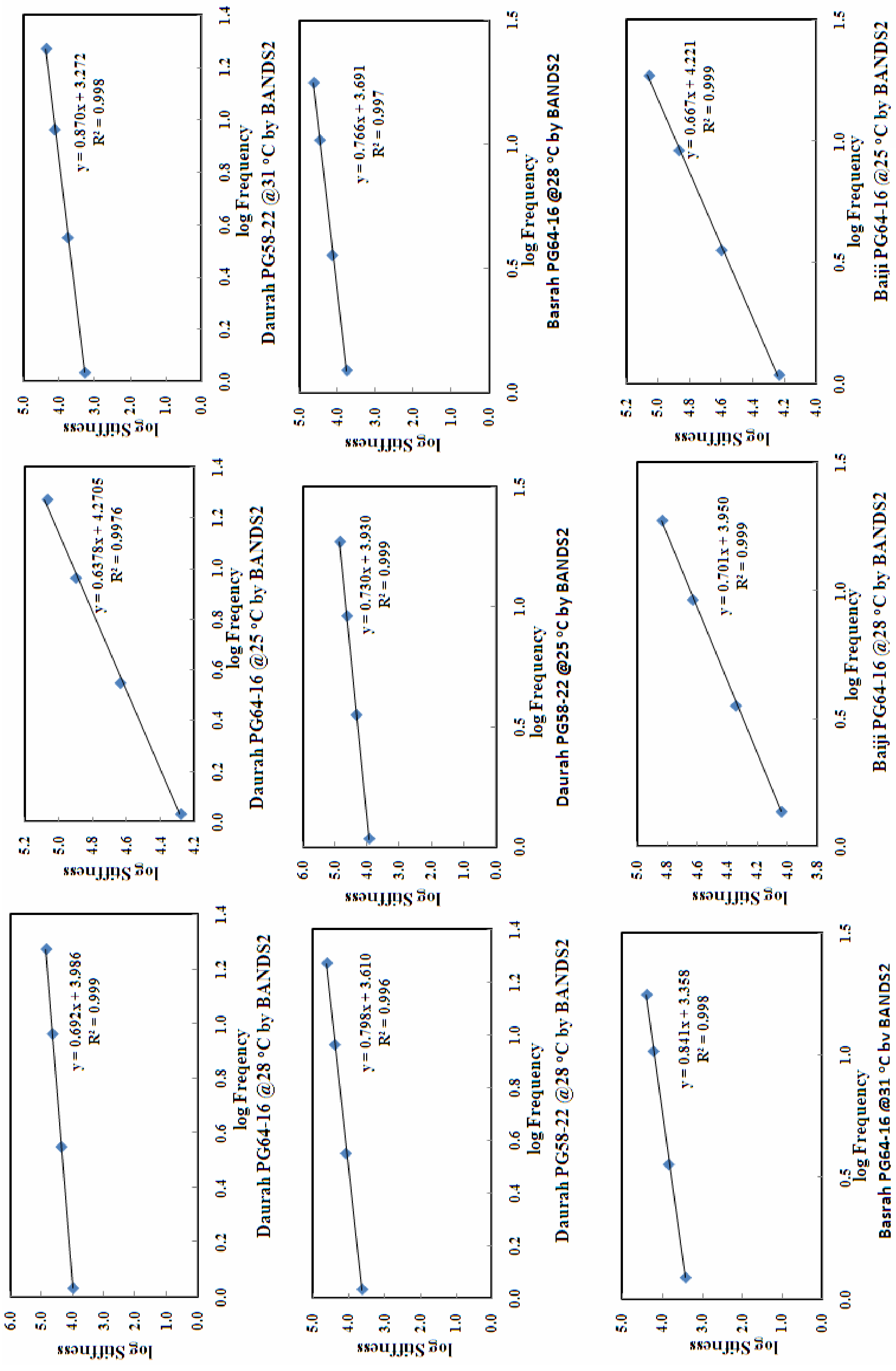

Fig. 4 Log stiffness versus log frequency estimated by BANDS2

When measure G^* /sinδ for original and rolling thin film by dynamic shear rheometer the phase angle dose not effects on results because sinδ almost one, but at intermediate temperature the effect of phase angle increase, since phase angle (δ) cannot calculated by using BANDS2, therefore, there is no indication to consider the elasticity and viscosity values of the binder. As presented in Figure (5), a good correlation for regression relations is obtained when compared m-value measured by DSR and estimated by BANDS2. Accordingly, it is proposed to use the relation in Figure (6) between tanδ and m-DSR to estimate the phase angle (δ) by substitute m-shell instead m-DSR.

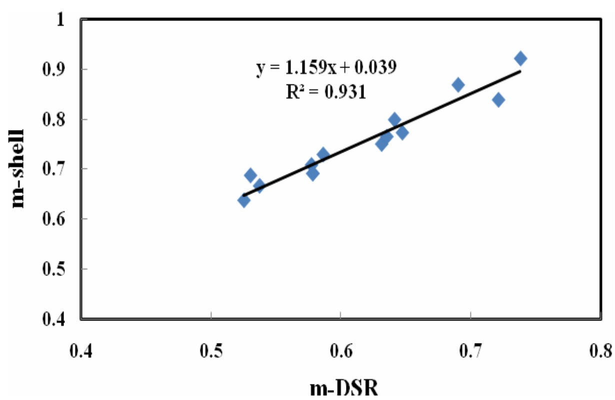

Fig. 5 Relation between m-DSR and m-Shell

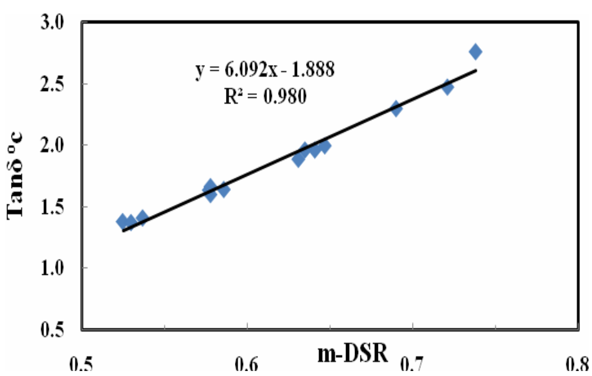

Fig. 6 Relation between m-value and tanδ obtain by DSR

Figures (7) and (8) illustration the relation between complex modulus measures by DSR using frequency sweeps test for rolling thin film at control strain (10%) and stiffness estimated by (BANS2) software for different frequency at softening point and penetration value of rolling thin film .

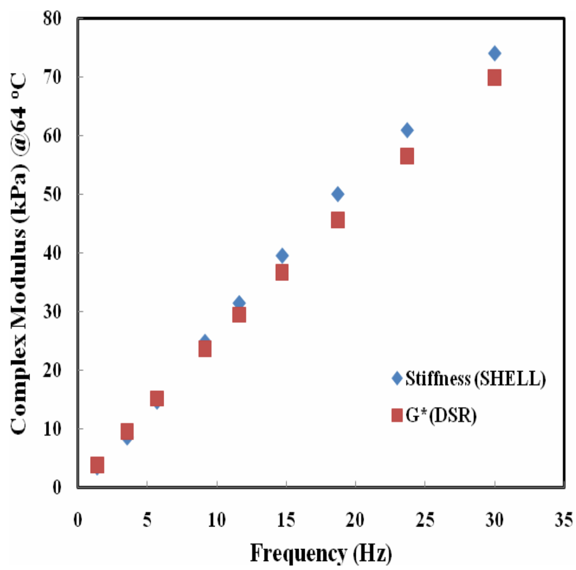

Fig. 7 Complex modulus versus frequency for Daurah PG 64-16

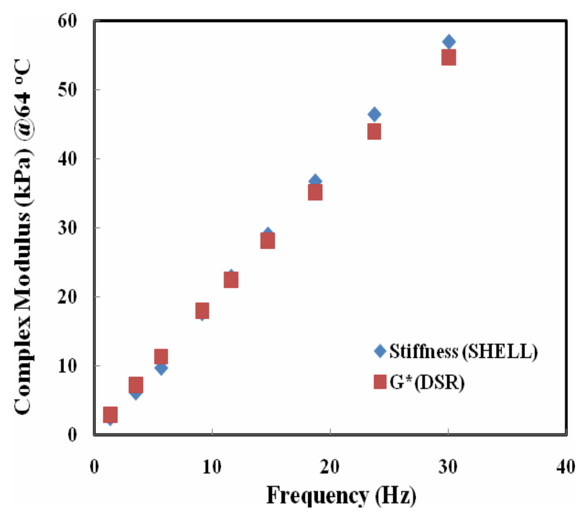

Fig. 8 Complex modulus versus frequency for Basrah PG 64-16

TEMPERATURE ZONING FOR IRAQ

Weather data are collected from five weather stations distributed across Iraq. Collected data from Iraqi Metrological Organization (IMO) is covered a minimum of 17 years of continuous temperature recording. The data are analyzed to obtain the annual minimum recorded air temperature. The annual average consecutive seven-day maximum air temperature, in addition to standard deviation of both high and low temperatures. Calculated average high-low air temperatures for 50% and 98% reliability are shown in Table (5).

Table 5 Average air temperature for Iraq

NO	Station	Latitude	50 % - Reliability				98 % - Reliability	
			High Air Temperature		Low Air Temperature			
			Mean	Standard Deviation	Mean	Standard Deviation	Avg. High Air Temp	Avg. Low Air Temp
1	BAGHDAD	33.23	47.5	1.18	-2.6	1.6	49.9	-5.9
2	BASRAH	30.57	48.3	1.15	1.8	1.76	50.6	-1.77
3	RUTBA	33.05	41.4	2.03	-3.4	2.03	45.46	-7.47
4	KARKUK	35.47	45.4	1.9	-1.4	4.53	49.2	-10
5	MOSUL	36.32	44.8	2.07	-3.4	1.49	48.9	-6.4

LTPPV3.1 Superpave software is used to investigate the performance grade for Iraq. This software has a database of weather information for about 7500 reporting weather stations in the U.S and Canada, Tables (6), (7), (8) and (9) show the data obtained by selected performance grade searching, 50% reliability (critical), to find weather information for these countries. Figure (9) depicted Iraq map which divided according to weather station after analyzing the obtained data as presented in the above tables and comparing them with the Iraqi database for weather information then converted to the pavement performance grade according to the superpave grade.

Selected performance grades have to be shifted up at least one grade for high numbers of heavy traffic loads (ESAL higher than 30 million) or slow, standing loads, Figure (10) shows Iraq map proposed and divided according to climate and traffic loading. Since refineries of Iraq product generally asphalt grade PG 64-16 as measured in Table (4), therefore to reach required grade, polymers should be added to modify binder for shifting grade.

Table 6 PG 70-10, 50% reliability, weather data information

NO	PG	State	No. of countries	Country which have Highest Average High Temperature				
				Station	Avg. High	Avg. Low	Latitude	Country
1	70-10	AZ	69	AZ6471	44.7	-3	36.1	COCONINO
2	70-10	CA	36	CA6699	44.8	0	34.28	SAN BERNAR.
3	70-10	FL	65	FL1986	36.3	-8.9	30.78	OKALOOSA
4	70-10	GA	13	GA4674	36.9	-7.3	31.65	WAYNE
5	70-10	NM	23	NM1153	39.5	-11.8	32.52	EDDY
6	70-10	LA	4	LA5527	36.9	-10.5	31.98	DESOTO
7	70-10	MS	2	MS5789	36.5	-9.8	30.98	GEORGE
8	70-10	NV	13	NV7925	44.8	-10.4	36.2	CLARK
9	70-10	OK	7	OK5509	40.5	-16.1	34.83	COMANCHE
10	70-10	PR	23	PR8881	34.7	11.6	18.35	AGUADILLA
11	70-10	TX	203	TX1524	42.9	-6.9	29.13	CUSTOLON
12	70-10	UT	4	UT7516	41.8	-10.7	37.12	WASHINGTON

Table 7 PG 76-10, 50% reliability, weather data information

NO	PG	State	No. of countries	Country /District that have Highest Average High Temperature.				
				Station	Avg. High	Avg. Low	Latitude	Country
1	76-10	AZ	18	AZ1050	47.1	-0.9	35.17	MOHAVE
2	76-10	CA	14	CA2319	49.4	-3.4	36.47	LNYO
3	76-10	NV	2	NV4480	47	-6.6	35.17	CLARK
4	76-10	TX	1	TX0950	43.2	-8.4	28.12	BREWSTER

Table 8 PG 70-16, 50% reliability, weather data information

NO	PG	State	No. of countries	Country /District that have Highest Average High Temperature.				
				Station	Avg. High	Avg. Low	Latitude	Country
1	70-16	NM	1	NM0992	39.1	-19.5	33.47	CHAVES
2	70-16	OK	1	OK1243	40.4	-19.9	36.83	HAPRER
3	70-16	UT	1	UT5733	39.9	-16.3	38.58	GRAND

Table 9 PG 64-22, 50% reliability, weather data information

NO	PG	State	No. of countries	Country /District that have Highest Average High Temperature.				
				Station	Avg. High	Avg. Low	Latitude	Country
1	64-22	CO	12	CO4834	38.6	-24.3	38.07	BENT
2	64-22	ID	1	ID9683	36.8	-22.3	44.23	WASHINGTON
3	64-22	KS	22	KS3897	39	-25.2	39.23	MITCHEL
4	64-22	MO	7	MO1759	37.1	-25.8	38.33	BENTON
5	64-22	NE	14	NE0640	38.8	-26.5	40.13	FURANS
6	64-22	NM	2	NM1647	34.9	-25.9	36.03	SANJUAN
7	64-22	NV	2	NV0691	37.2	-24.7	37.2	LANDER
8	64-22	OR	2	OR8797	38.2	-23.9	38.2	MALHEUR
9	64-22	UT	12	UT9152	37.6	-25.3	37.6	BEAVER

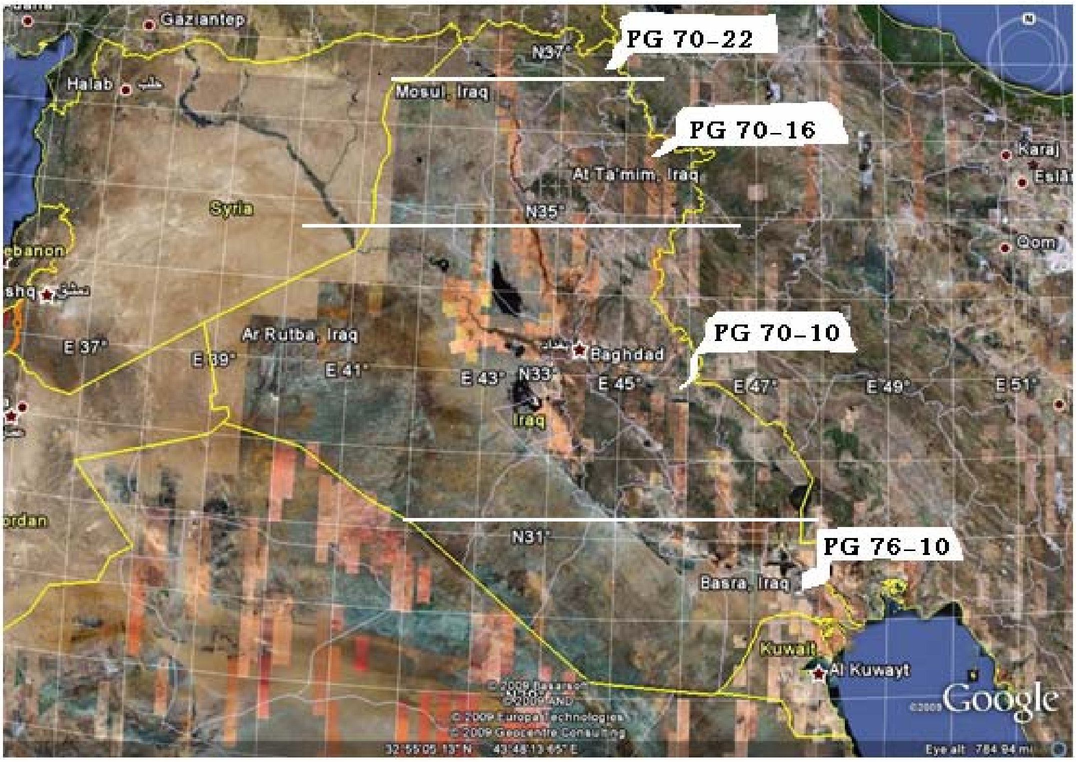

Fig. 9 Iraq map divided according to weather stations

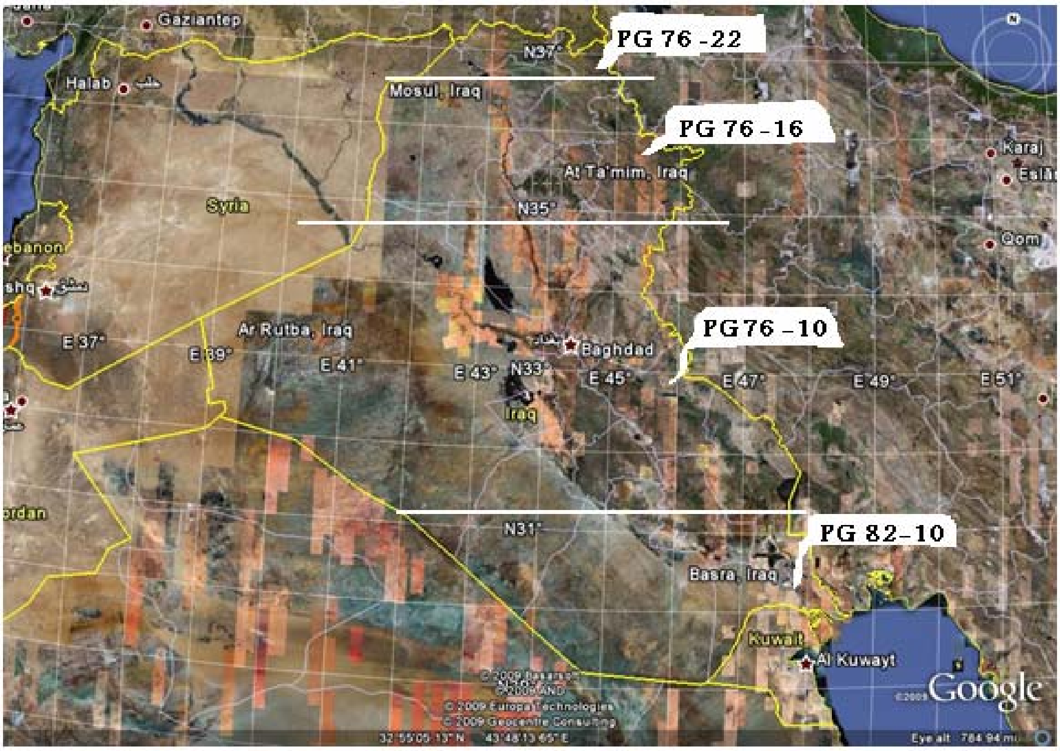

Fig. 10 Iraq map divided according to traffic loads

CONCLUSIONS

Based on the principal of superpave technology, the performance grade PG 64-16 represent asphalt binders produced in the following Iraq refineries; (Daurah, Basrah, Baiji)- (40-50) penetration grade while, PG 58-22 for Daurah (85-100) penetration grade.

The country is divided into different zones according to the highest and lowest temperature which that collected from Iraqi Metrological Organization (IMO) and converted to performance grade using SHRP temperature models as follows; PG 76-22 and PG 76-16 for the north, PG70-10 for the middle and PG 76-10 for the south.

The proposed performance grade divided according to climate and traffic condition, after compared with some states in the USA that have the same hot weather by using Long Term Pavement Performance (LTPPBind V3.1) software, the Iraqi map can be covered by the following PG's of asphalt binders : PG 76-22 for the north of N 36.5^{o} latitude (extreme north), PG 76-16 for the area between N35^{o} and N 36.5^{o} (north), PG 70-10 for the reign between N31^{o} and N 35^{o} (middle), and

PG 82-10 for the reign beyond N31^{o} (south).

The m- value (slope of log creep stiffness versus log frequency curve at specified temperature) determined by DSR (Dynamic Shear Rheometer) and (BANDS2) Shell software is compared .The estimated phase angle by the mentioned relation reflects good indication for binder elasticity at intermediate temperature.

Acknowledgements

The authors would like to acknowledge the Asphalt Research Group in the University of Wisconsin-Madison, Engineering College of Baghdad University, Engineering College of Al-Nahrain University and Ministry of Higher Education in Iraq for their support during the preparation of this research.

REFRENCES

Anderson, D., D. Christensen, H. Bahia, R. Dongre, Sharma M., and J. Button,(1994) “Binder characterization and evaluation”, Volume 3:“Physical characterization,” Report No. SHRP-A- 369, the Strategic Highway Research Program, national Research Council, Washington, D.C.

Asphalt Handbook, (2007), Asphalt Institute, MS-4, 7thEdition, Manual Series, Lexington, Kentucky.

ASTM, (2009), “Road and Paving Materals,” Annual Book of ASTM Standards, Volume 04.03, American Society for Testing and Materials,” West Conshohocken, USA.

Bahia H., Vivanco, “The transition to a PG grading system for asphalt binders in developing countries,” Conference Proceeding First Middle East International Conference on Advances in Civil, Mechanical and Materials Engineering, May 10-13, 2005, Amman-Jordan.

Bahia, H.U., (2009), “Materials for Constructed Facilities,” CEE/EMA 395, Lectures at University of Wisconsin-Madison during (March 3-August 12).

Bahia, H.U., and D.A. Anderson, (1995), “The New Proposed Rheological Properties of Asphalt Binders: Why are They Required and How Do They Compare to The Conventional Properties,” Physical Properties of Asphalt Binders, ASTM, STP 1241.

Roberts, F., Kandhal P., Brown et al. “Hot mix asphalt materials, mixture design, and construction”, NAPA education foundation, Second Edition, Maryland, USA, 1996.

Van de poel, (1954), “A General System Describing the Viscoelastic Properties of Bitumens and its Relation to Routine Test Data,” Journal of Applied Chemistry, Vol. 4, p.221.

DYE REMOVAL FROM TEXTILE WASTEWATER BY COAGULATION USING ALUM AND PAC

Nada N. Abdul-Razzaq
Chemical Engineering Department – College of Engineering – University of Baghdad – Iraq
nada.naom@baghdad-eng.org

ABSTRACT

Removal of solar brown and direct black dyes by coagulation with two aluminum based coagulants was conducted. The main objective is to examine the efficiency of these coagulants in the treatment of dye polluted water discharged from Al-Kadhymia Textile Company (Baghdad-Iraq). The performance of these coagulants was investigated through jar test by comparing dye percent removal at different wastewater pH, coagulant dose, and initial dye concentration. Results show that alum works better than PAC under acidic media (5-6) and PAC works better under basic media (7-8) in the removal of both solar brown and direct black dyes. Higher doses of PAC were required to achieve the maximum removal efficiency under optimum pH conditions for both dyes. It was observed that under optimum conditions of pH and dose values, PAC was significantly higher dye removal efficiency than alum for all dyes initial concentrations.

KEYWORDS

Dye removal, dye pollution, direct black, solar brown, coagulation.

ازالـة الالوان من الماء المطروح في الصناعـات النسيجيـة بالتخثيـر بواسطـة الشـب ومتعدد كلوريد الالمنيـوم

الخلاصـة

تم دراسة ازالة صبغة السوداء المباشرة والبني الشمسي بالتخثير باستخدام مختر الشب ومتعدد كلوريد الالمنيوم لغرض معالجة الماء المطروح الحاوي على الصبغتين من معمل نسيج الكاظمية (بغداد-العراق). اداء كل من المخثرين تمت دراسته باستخدام اختبار الجرة وذلك بمقارنة نسبة الازالة اللونية من الماء المعامل تحت ظروف مختلفة من الدالة الحامضية وكمية المخثر والتركيز الابتدائي للصبغة. بينت النتائج بان الشب اثبت اداءً افضل من متعدد كلوريد الالمنيوم في الوسط الحامضي (5-6) بينما اثبت متعدد كلوريد الالمنيوم اداءً افضل من الشب في الوسط القاعدي (7-8). عند العمل في الظروف المثلى للدالة الحامضية تبين ان اقصى نسبة ازالة يمكن تحقيقها باستخدام متعدد كلوريد الالمنيوم عند جرعات اعلى من تلك اللازمة في حالة الشب. وتبين ان تطبيق الظروف المثلى من دالة الحامضية وجرعة المخثر بان متعدد كلوريد الالمنيوم افضل عمليا من الشب في حال تغير تركيز الصبغة في الماء الملوث المطروح ولكلا الصبغتين.

INTRODUCTION

Water pollution control is presently takes major area of scientific research. Automation and industrialization has resulted in rapid deterioration of water quality. Some of these industries such as textile, printing, leather, paint and so on are most of polluted resources (Joonghwan *et al*, 2005).

These processes use large amount of water and discharge colored wastewaters that are heavily polluted with dyes, hazard chemicals, and other toxic compounds. Presence of color has always been undesirable in water for either industrial or domestic needs. Even very small amounts of dyes in water (less than 1ppm for some dyes) are highly visible (Crini, 2006). These colored compounds causes reduction of sunlight penetration and depletion of dissolved oxygen. Additionally the majority of synthetic dyes are highly water-soluble which are toxic to some organisms and may pose serious health threat to human beings (Baoyou Shi *et al*, 2006). Thus dyes in wastewater have to be removed completely before discharging into receiving waters.

Since dye compounds are specifically designed to be recalcitrant with poor biodegradability, they are very stable and difficult to remove by conventional biological treatment, thus physicochemical techniques such as coagulation/flocculation, adsorption, membrane filtration and ozonation are usually used for the treatment (Ozer *et al*, 2006; Shi *et al*, 2007).

Each treatment method has its advantages and disadvantages. Generally adsorption process is the most common technique because of its effectiveness but it is an expensive process (Gutpvk *et al*, 2000). Membrane separation process is one of the popular methods used in textile treatment but this process has a problem of membrane fouling by the pollutants (Vrijenhoek *et al*, 2001). Ozonation improved the biodegradability of toxic substances but it may form toxic byproducts in the effluent after treatment (Pradeep *et al*, 2007).

Coagulation and flocculation processes have been widely used as pretreatments to remove suspended particles and coloring materials prior to biological treatment. It is one of most effective methods for dye removal from industrial wastewaters (Duk *et al*, 2005).

This work was mainly focused on the determination of the optimum conditions for the treatment of cotton textile dyeing wastewaters such as pH, coagulant dose, and initial dye concentration to study their effect on the dye removal efficiency using coagulation/flocculation process.

MATERIALS AND METHODS

Materials

Two direct dyes were used to simulate dye-polluted waters, direct black and solar brown. These dyes were procured from Al-khadimya Cotton Textile Company (Baghdad, Iraq). Two chemical coagulants: aluminum sulfate (alum, $Al_2(SO_4)_3$) and poly aluminum chloride (PAC) were selected in this study for the coagulation-sedimentation process since they represent the most widely used coagulants. 1M Solutions of

H_2SO_4 and NaOH were used to adjust pH.

Preparation of Synthetic Wastewater

Stock solutions of concentration 5000 mg/l for each dye were prepared and then diluted using deionized water to obtain the desired concentrations of 5, 10, 15, 20, and 25 mg/l for each dye. It is important to notice here that the natural effluent wastewater discharged from the company contains about 10 mg/l under normal conditions (Rasha, 2010).

Coagulation and Flocculation Experiments

A standard jar-test floc tester apparatus was used for the coagulation flocculation processes. Six beakers of 1 liter capacity were filled with synthetic wastewater and transferred to the jars. The pH of prepared synthetic wastewater was adjusted with H_2SO_4 and NaOH solutions using Thermo Fisher Scientific portable pH meter (model Orion 3 star, USA). The samples in the jars were rapidly mixed at a paddle speed of 200 rpm and inorganic coagulant (alum or PAC) was added during mixing. Rapid mixing at 200 rpm was continued for 2 min, followed by slow mixing for 10 min at 35 rpm, followed by settling for 45 min. After settling, samples were withdrawn for analysis using a pipette from 2-3 cm below the surface treated wastewater in each jar. All experiments were conducted between 27-30°C.

Measurement of Dye Concentration after Coagulation

The wavelength of maximum absorbency (λmax) of the two dyes in the background of deionized water were measured to be 419 nm for solar brown and 566 nm for direct black according to scanning patterns performed on a UV spectrophotometer (model Shimatatzu 160A, Japan). The absorbency of the two dyes was measured using Labomed Inc. spectrophotometer (model Spectro SC, USA) for different dye concentrations at the determined wavelengths. Linear relationships were obtained between dye concentrations and absorbency for each dye as shown in **Fig**.1 and **Fig**. 2. Measured absorbency for each dye was converted into units of concentration and further into removal percentage.

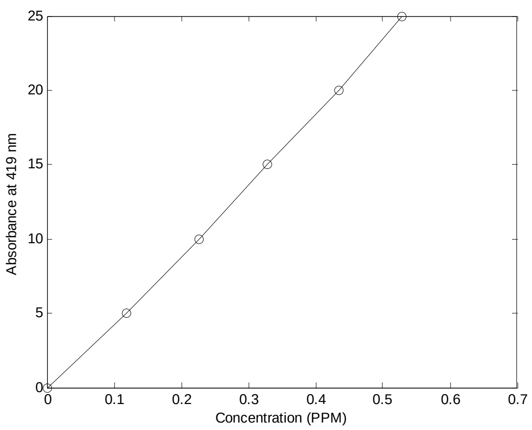

Fig. 1 Absorbency vs. concentration for solar brown dye

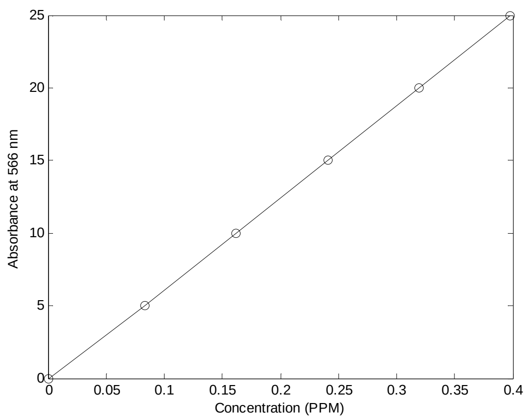

Fig. 2 Absorbency vs. concentration for direct black dye

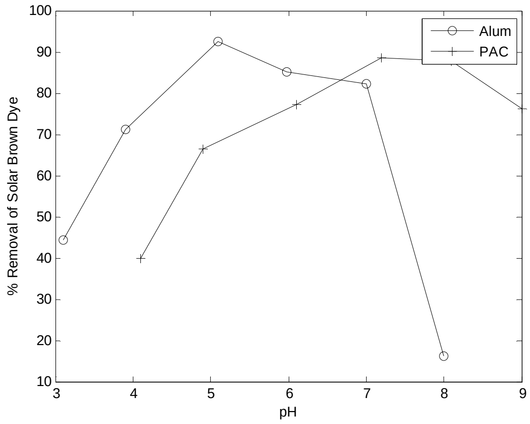

Fig. 3 Removal efficiency for solar brown dye at different pH values

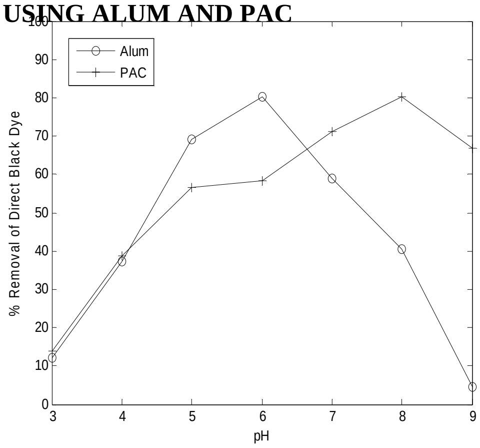

Fig. 4 Removal efficiency for direct black dye at different pH

RESULTS AND DISCUSSION

Effect of pH on Dye Removal

The effect of pH of the synthetic dye wastewater on the percentage of dye removal was studied since the pH plays an important role in determining coagulation efficiency. An optimum pH range in which metal hydroxide precipitates occur, should be determined to establish optimum conditions for coagulation (Duk *et al*, 2007; Maryam *et al*, 2008).

To study the effect of pH on dye removal, the dosages of alum and PAC were kept constant at 30 mg/l, while varying the pH of samples from 2 up to 9. Dye concentration was kept constant at 10 mg/l for all solutions during the experiments at this time. **Figs**. 3 and 4 show the removal efficiency of both solar brown and direct black dyes respectively at different values of PH using alum and PAC.

It was observed that alum is active in the acidic medium whereas PAC is more active in alkaline medium for the removal of both dyes. The reduction of dissolved organics (dyes) during coagulation with coagulants at different pH values follow two different mechanisms. At low pH the effluent containing anionic organic molecules coordinate with metal cation and form insoluble metal complexes at higher pH (alkaline range). The organics are adsorbed on or form flocs of metal hydroxide and then precipitated. The combined effect of two mechanisms show that the reductions of dissolved organics with different coagulants can occur at different pH. The maximum dye removal may thus occur where the combined effect of both the mechanisms is high (Pradeep *et al*, 2008). **Table** 1 shows the optimum pH obtained in which maximum dye removal occurred.

Table 1 Optimum pH and coagulant dose in which maximum dye removal can be obtained

	pH		Coagulant dose (mg/l)	
Coagulant type	Solar brown	Direct black	Solar brow n	Direct black
Alum	5	6	30	40
PAC	7	8	45	50

Effect of Coagulant Dose

The effect of coagulant dosage on dye removal efficiency was examined. Variable amounts of inorganic coagulant (alum and PAC) were dosed into the dye containing solutions. Dye concentration was kept constant at 10 mg/l and pH was adjusted to optimum values as indicated in **Table** 1. The results are shown in **Figs**. 5 and 6 as percent of dye reduction. It was observed that the reduction in color for both dyes was increased initially as the dose of both alum and PAC increased. For alum the removal efficiencies increased for the doses from 10 up to 30 mg/l for solar brown and from 10 up to 40 mg/l for direct black. For PAC the removal efficiencies increased form 10 up to 45 mg/l for solar brown and from 10 up to 50 mg/l for direct black. With further increase in coagulant dose the dye percent reduction decrease. However, it was observed that PAC is more effective relative to alum but with higher doses for the removal of both dyes. **Table** 1 show the optimum coagulant dose obtained in which maximum dye removal was occurred.

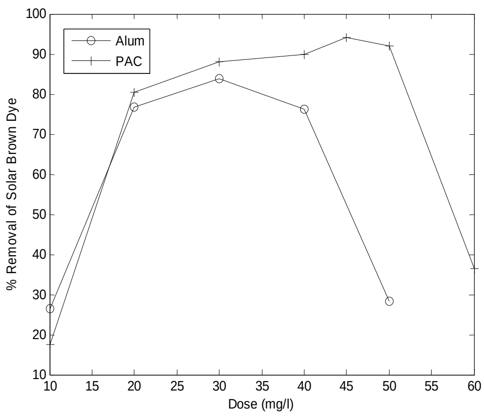

Fig. 5 Removal efficiency of solar brown dye at different

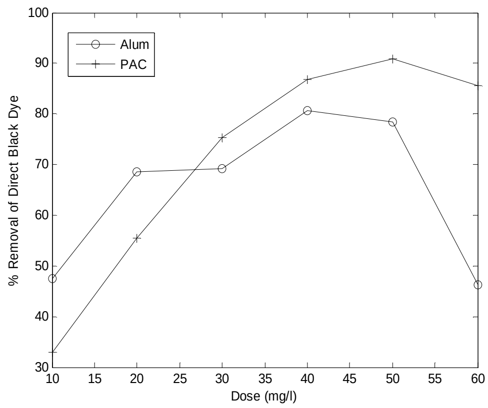

Fig. 6 Removal efficiency of direct black dye at different

Effect of Initial Dye Concentration

The influence of initial dye concentration on the dye removal efficiency was investigated. Optimum coagulant dosage (30 mg/l for alum and 45 mg/l for PAC) for solar brown and (40 mg/l for alum and 50 mg/l for PAC) direct black were used in which maximum dye removal occurs.

For alum, when the concentration of two dyes was increased from 5 mg/l to 10 mg/l, the removal efficiency increased to 84% for solar brown and to 87% for direct black. For dyes concentrations more than 10 mg/l the efficiency decreased and reached to 73% and 67% for solar brown and direct black respectively. Similar behavior was observed in the case of PAC. However the values of the removal efficiencies were superior for PAC for two dyes. Figs. 7 and 8 show the removal efficiency for both solar brown and direct black dyes under different initial dye concentrations.

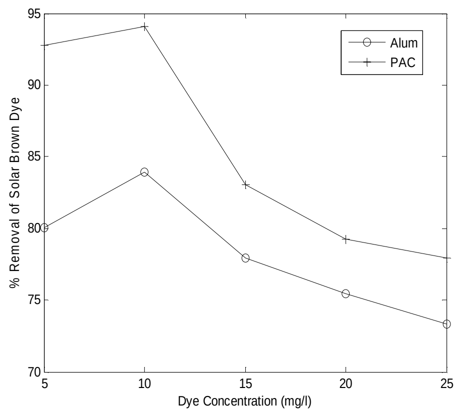

Fig. 7 Removal efficiency of solar brown dye at different dye

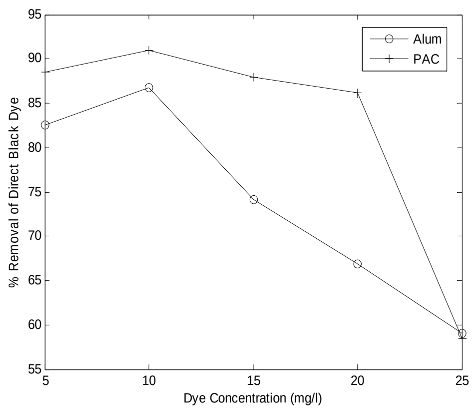

Fig. 8 Removal efficiency of direct black dye at different dye

CONCLUSIONS

1. Dye removal of direct black and solar brown dyes from textile wastewater can be achieved by coagulation using traditional coagulants of alum and PAC. Removal process was affected highly by pH. Changing coagulant dose should be accomplished at optimum pH to maximize the removal efficiency.
2. Maximum removal efficiency occurred when the pH was about 5 and 6 for solar brown and direct black respectively using alum coagulant.
3. Maximum removal efficiency occurred when the pH was about 7 and 8 for solar brown and direct black respectively using PAC coagulant.
4. Optimum coagulant dose was found to be 30 and 40 mg/l for solar brown and direct black respectively using alum coagulant.
5. Optimum coagulant dose was found to be 45 and 50 mg/l for solar brown and direct black respectively using PAC coagulant.

6. Generally, PAC gives more removal efficiency than alum at all dye concentrations from 5 up to 25 mg/l.

REFERENCES

Baoyou Shi, Guohong Li, Dongsheng Wang, Chenghong Feng, and Hangxiao Tang, *Removal of direct dyes by coagulation: the performance of preformed polymeric aluminum species*, Journal of Hazardous Materials 143 (2007) 567-574.

Cirini G., *Non-conventional low-cost adsorbent for dye removal: a review*. Bioresource Technology 97 (2006) 1061-1085.

Duk Jong Joo, Won Sik Shin, Jeong-Hak Choi, Sang June Choi, Myung-Chul Kim, Myung Ho Jan, Tae Wook Ha, and Young-Hun Kim, *Decolorization of reactive dyes using inorganic coagulants and synthetic polymer*, Dyes and Pigments 73 (2007) 59-64.

Gupta VK, Mohan D. Sharma S, and Sharma M., *Removal of basic dyes (rhodamine B and methylene blue) from aqueous solutions using bagasse fly ash*. Separation Science and Technology 35 (2005) 2097-2113.

Joonghwan Mo. Jeong-Eun Hwang, Jonggeon Jegal, and Laephil Kim, *Pretreatment of a dying wastewater using chemical coagulants*, Dyes and Pigments 72 (2007) 240-245.

Maryam Hasani Zonoozi, Mohammad Reza Alavi Moghaddam, and Mukhtar Arami, *Removal of acid red 398 from aqueous solutions by coagulation/flocculation process*. Environment Engineering and Management Journal 7 (2008) 695-699.

Ozer A. Akkaya G., Turabik M., *The removal of acid red 274 from wastewater: combined biosorption and biocoagulation with spirogyra rhizopus*, Dyes and Pigments 71 (2006) 83-89.

Pradeep Kumar, B. Prasad, I.M. Mishra, and Shri Chand, *Decolorization and COD reduction of dyeing wastewater from a cotton textile mill using thermolysis and coagulation*, Journal of Hazardous Materials 153 (2008) 635-645.

Rasha H. Salman, Removal of Dyes from Textile Effluent by Adsorption onto Oven Dried Alum Sludge, Journal of Engineering 16 Issue 2 (2010) 5249-5262.

Vrijenhoek EM, Hong SK, Elimelech M, *Influence of membrane surface properties on initial rate of colloidal fouling of reverse osmosis and nanofiltration membranes*. Journal of Membrane Science 188 Issue 1 (2001) 115-128.

EXPERIMENTAL OBSERVATIONS ON THE BEHAVIOR OF A PILED RAFT FOUNDATION

Dr. Mosa J. Al-Mosawi(1) **Dr. Mohammed Y. Fattah(2)**
Abbas A. O. Al-Zayadi(3)

(1) Professor, College of Engineering, Civil Eng. Dept., University of Baghdad, Iraq.
(2) Assistant Professor, Building and Construction Eng. Dept., University of Technology.
(3) Formerly graduate student, College of Engineering, Civil Eng. Dept, University of Baghdad.

ABSTRACT

The piled raft is a geotechnical composite construction consisting of three elements: piles, raft and soil. In the design of piled rafts, the load shared between the piles and the raft, and the piles are used up to a load level that can be of the same order of magnitude as the bearing capacity of a comparable single pile or even greater. Therefore, the piled raft foundation allows reduction of settlements in a very economic way as compared to traditional foundation concepts.

This paper presents experimental study to investigate the behavior of piled raft system in sandy soil. A small scale “prototype” model was tested in a sand box with load applied to the system through a compression machine. The settlement was measured at the center of the raft, strain gages were used to measure the strains and calculate the total load carried by piles. Four configurations of piles (2x1, 3x1, 2x2 and 3x2) were tested in the laboratory, in addition to rafts with different sizes. The effects of pile length, pile diameter, and raft thickness on the load carrying capacity of the piled raft system are included in the load-settlement presentation.

It was found that the percentage of the load carried by piles to the total applied load of the groups (2x1, 3x1, 2x2, 3x2) with raft thickness of 5 mm, pile diameter of 9 mm, and pile length of 200 mm was 28% , 38% , 56% , 79% , respectively. The percent of the load carried by piles increases with the increase of number of piles.

مشاهدات عملية على تصرف الأساس الحصيري المستند الى ركائز

الخلاصة:

يعتبر الأساس الحصيري المستند الى ركائز منشأ جيوتقنيا مركبا يتألف من ثلاثة عناصر هي الركائز و الحصيرة و التربة. عند تصميم الأسس الحصيرية المستندة الى ركائز تحصل مشاركة في الحمل بين الركائز و الحصيرة و تصمم الركائز لمستوى حمل يمكن أن يكون مساويا الى مقدار قابلية تحمل الركيزة المنفردة و ربما أكبر. و لذلك فان الأساس الحصيري المستند الى ركائز يسمح بتقليل الهبوط بطريقة اقتصادية مقارنة مع مبادئ تصميم الأسس التقليدية.

هذا البحث يعرض دراسة عملية لتحري تصرف منظومة الأساس الحصيري المستند الى ركائز في ترب رملية، حيث تم فحص نموذج مختبري مصغر في صندوق من الرمل ، و تم تسليط الحمل على المنظومة من خلال ماكنة الضغط. و قد قيس الهبوط في مركز الحصيرة فيما أستعملت مقاييس انفعال لقياس الانفعالات و حساب الحمل الكلي الذي تتحمله الركائز. و فحصت مختبريا أربعة أشكال لمجاميع الركائز (1x2 و 1x3 و 2x2 و 2x3) و ذلك باستعمال ركائز ذات أحجام مختلفة. و درس تأثير كل من طول الركائز و قطرها و سمك الحصيرة على قابلية تحمل منظومة الحصيرة المستندة الى ركائز من خلال عرض علاقات الحمل – الهبوط.

و قد وجد أن نسبة الحمل الذي تحمله الركائز من الحمل المسلط على مجاميع الركائز(1x2 و 1x3 و 2x2 و 2x3) عندما يكون سمك الحصيرة 5 ملم و قطر الركيزة 9 ملم و طولها 200 ملم تبلغ 28% و 38% و 56% و 79% على التوالي، و تتزايد نسبة الحمل الذي تحمله الركائز مع زيادة عدد الركائز.

INTRODUCTION

Raft and pile groups are the two alternative foundation options to support structures with heavy column loads. Raft is normally designed as rigid in order to withstand high moment and differential settlement, which is a function of intensity of load and relative stiffness of raft and soil. In the case of pile groups more number of piles is provided than required to cater the column load and to practically eliminate the settlement, which makes the foundation to be very expensive. The concept of pile raft was conceived and introduced about three decades back to overcome the difficulties stated above as well as for the effective utilization of the pile group.

A piled foundation system consists of three elements: raft, piles, and the subsoil. An external vertical load Q is equilibrated partly by the contact pressure between the raft and the soil (with resultant Q_R), and partly by the piles (with resultant Q_G). It is then possible to introduce a coefficient,

$$\alpha_P = \frac{Q_G}{Q} \qquad (1)$$

where α_P represents the portion of the load taken by the piles.

The case α_P = 0 represents a shallow foundation with no piles (or raft foundation), while the case α_P=1 represents a pile group with a raft clear from the ground. Piled raft foundations cover the range 0 < α_P<1. Every piled foundation behaves like a piled raft, with the exception of those cases where there is no contact between the raft and the soil as in offshore structures (de Sanctis and Mandolini, 2006).

Piled raft foundations are composite structures unlike classical foundation where the building load is either transferred by the raft or the piles alone. In a piled raft foundation, the contribution of the piles as well as the raft is taken into account.

The piles transfer a part of the building loads into deeper and stiffer layers of soil and thereby allow the reduction of settlement and differential settlement in a very economic way. Piles are used up to a load level which can be of the same order of magnitude as the bearing capacity of a comparable single pile or even greater (Hartmann and Jahn, 2001).

The adoption of piled raft foundations concept in the design of pile groups is by no means new, and has been described by several authors, including Zeevaert (1957), Davis and Poulos (1972), Hooper (1973), Burland et al. (1977), Katzenbach and Reul (1997), Prakoso and Kulhawy (2000), and Reul and Randolph (2003), among many others. In the early years, because of the limited availability of computers memory and processing speed, the use of numerical methods was confined to simple problems. In the last two decades due to the rapid development in computer technologies, numerical methods such as full three-dimensional methods are often used to solve complex problems.

EXPERIMENTAL WORK

Laboratory-scale investigations into piles behavior remain popular because of the high cost of field testing and the possibility of achieving specific soil characteristics in a laboratory environment. The monitored behavior of prototype structures has led to a better understanding of piles foundation and enables more reliable and economical design to be employed.

Model tests are relatively inexpensive and can be conducted under controlled laboratory conditions. This provides an efficient means of investigation. For instance, Cox et al. (1984) reported a study in which tests on 58 single piles and 41 pile groups were performed. They varied the geometric arrangement of piles within groups, the number of piles per group, and the spacing between piles (Mokwa, 1999).

The main purpose of the experimental research implemented in this paper is to study the load sharing mechanism between raft and piles, as well as the load settlement behavior of piled raft with different configurations, lengths of piles, and diameters. The following sections describe the test setup used to perform the model tests, the mechanical properties of the investigated soil, the configuration of model piled rafts, and the testing program and procedure. All the experimental works have been made in the laboratory of soil mechanics in the University of Baghdad.

Test Setup

All model tests were conducted using the setup shown in **Figure (1)**, which consists of a soil tank, model piled raft and loading machine. The vertical load was applied to the model piles by means of 10 ton compression test machine (Wykeham Farrance, England). It is a displacement controlled machine with rate capability in the range of (0.0001–59.99 mm/min), during all the experimental tests, the loading rate was kept constant with a value of 1 mm/min. The applied load was measured using a proving ring (Wykeham Farrance, England) of 5 kN and 10 kN capacity with 0.00434 and 0.00606 kN accuracy, respectively. A deformation dial gauge with 0.01 mm sensitivity was used for measuring displacements at the centerline of the piled raft model. Strain gages were adhered to the pile and connected to a strain indicator so as to measure the strains in the pile.

Soil Tank

The soil tank has 0.6 m length, 0.6 m width, and 0.7 m height supported by a relatively rigid steel framework stiffened with 3 lines of 25 mm steel angles, provided with a 0.28 x 0.22 m hatch for sand unloading. The base was stiffened with additional 3mm steel plates and 25mm steel angle frame and stiffeners, in order to prevent concentration of the load exerted from the position on a small area. The dimensions of the tank were chosen so that the tank can be put inside the testing machine and there will be no interference between the walls of the soil tank and the failure zone around the piled raft system. The internal sides of the tank were covered with polyethylene sheets in order to minimize friction that may develop between the steel tank surfaces and the soil. **Figure (2)** presents the soil tank fitted inside the compression machine.

Soil Properties

The soil used for the model tests is clean, oven-dried, uniform quartz (Kerbela) sand. The tests are performed on medium dense sand with maximum and minimum dry unit weights of the sand determined according to the ASTM (D4253-2000) and ASTM (D4254-2000) specifications, respectively. The specific gravity test is performed according to ASTM (D854-2005) and the grain size distribution is analyzed according to ASTM (D422-2001) specifications. **Figure (3)** shows the grain size distribution of the sand and Table (1) shows the physical properties of the tested sand. The angle of internal friction is determined using the direct shear test and found to be 38°.

Sand Deposit Preparation

The sand deposit was prepared using the sand raining technique. A special raining device similar to that recommended by Bieganousky and Marcuson (1976) was designed to obtain a uniform deposit with the desired density; this devise has been used by previous researchers (Al-Jebouri, 1986, and Jawad 2009). **Figure (2)** shows a schema for the raining device.

Table (1), Physical properties for the tested sand.

Property	Value
Grain size analysis	
Effective size, D_{10}	0.26 mm
Coefficient of uniformity, C_u	2.67
Coefficient of curvature, C_c	1.0
Classification (USCS)*	SP
Specific gravity, G_s	2.63
Dry unit weights	
Maximum unit weight, $\gamma_{d\,(max)}$	17.5 kN/m^3
Minimum unit weight, $\gamma_{d\,(min)}$	14.50 kN/ m^3
Test unit weight, $\gamma_{d\,(test)}$	16.30 kN/ m^3
Relative density, D_r	63%
Void ratio	
Maximum void ratio, e_{max}	0.82
Minimum void ratio, e_{min}	0.50
Test void ratio, e_{test}	0.62

* USCS refers to Unified Soil Classification System

The unit weight of the sand deposit in the raining method depends primarily on the drop height and the discharge rate of the sand (Turner and Kulhawy, 1987). The `height of the free fall of the sand can be controlled by adjusting the elevation of the raining device with respect to the sand tank while the discharge rate of the sand was kept constant.

Sand deposits were prepared with the sand tank resting on the loading platen of the testing machine so that the sand deposit was not disturbed and hence the desired unit weight of the sand is not altered.

Calibration curves similar to those prepared by Al-Jebouri (1986) to find the proper drop height related to the density, void ratio and relative density for maintaining a constant density of sand during all the experimental tests were made in this work. **Figure (4)** shows these calibration curves. The height of drop was chosen to be 50 cm, which corresponds to a placing unit weight of 16.3 kN/m^3 and a void ratio of 0.63 and a relative density of 63%.

Model Piled Rafts

The model piles used in this study are smooth aluminum pipe piles having three different outside diameters and thicknesses. The embedment (depth to diameter) ratio l/d = 20, 25, and 30, where l represents the pile length and d is the outside diameter of the pipe pile.
The spacing between piles is kept constant (S = 5 cm) in all tests.
model raft used in the test was also made of aluminum with The smooth surface and two different thicknesses 5 and 2.5 mm to study the effect of raft stiffness. Both piles and rafts were composed of ALUPCO alloy, which is supplied locally by ALUPCO Alloys Company. The technical specification and the mechanical properties of the used alloy are shown in table (2).

Table (2), Mechanical properties of the used Aluminum alloy.

Property	Value
Minimum yield strength (N/mm^2)	160
Minimum ultimate strength (N/mm^2)	215
Minimum % of elongation	10
Poisson's ratio	0.34

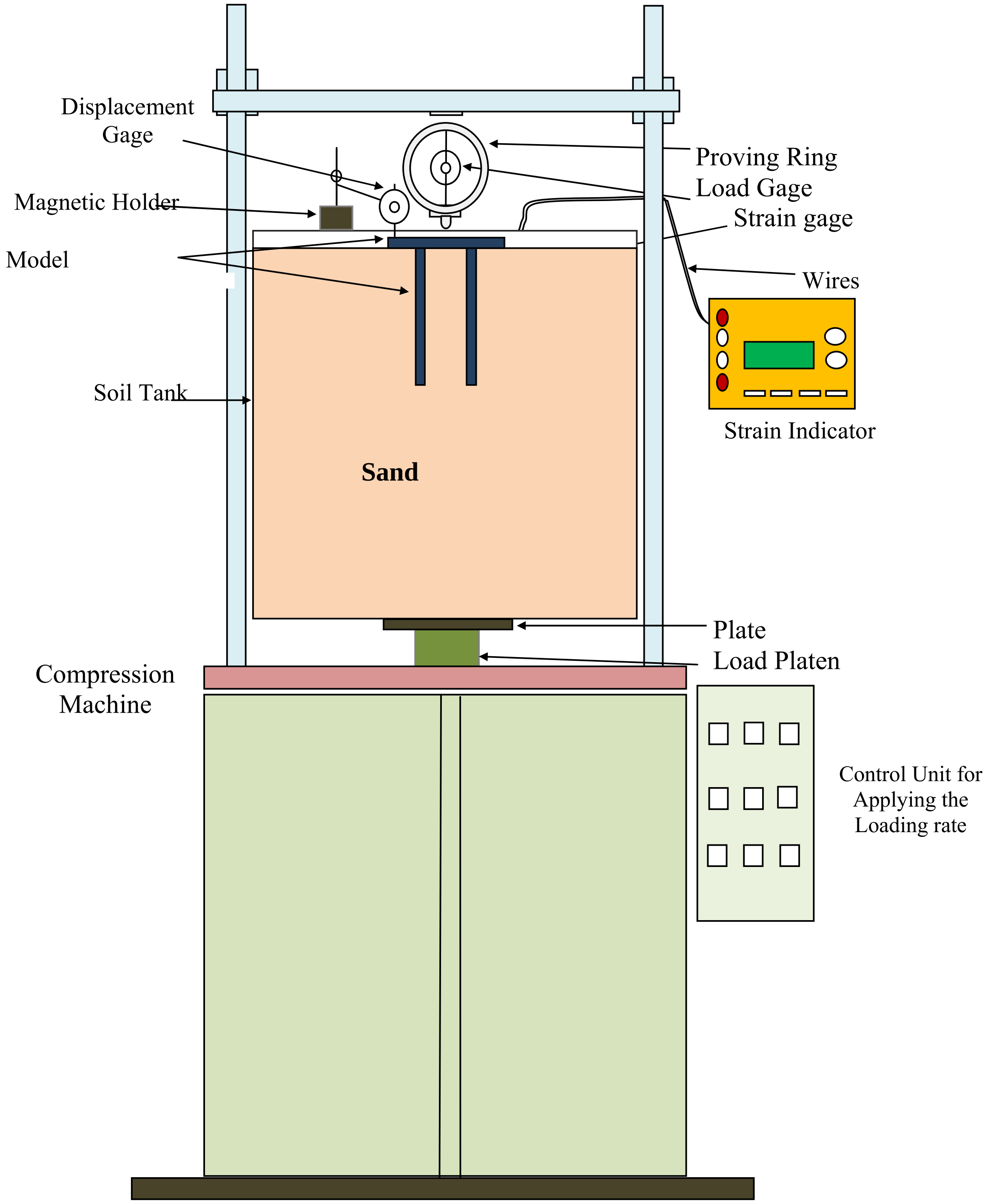

Fig. (1), Setup of the laboratory model.

a. Soil tank used in the experimental study.

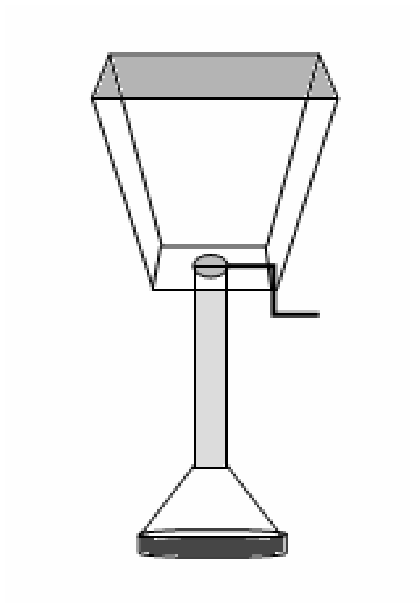

b. Sand hopper used in the raining technique.

Fig. (2), Test equipment.

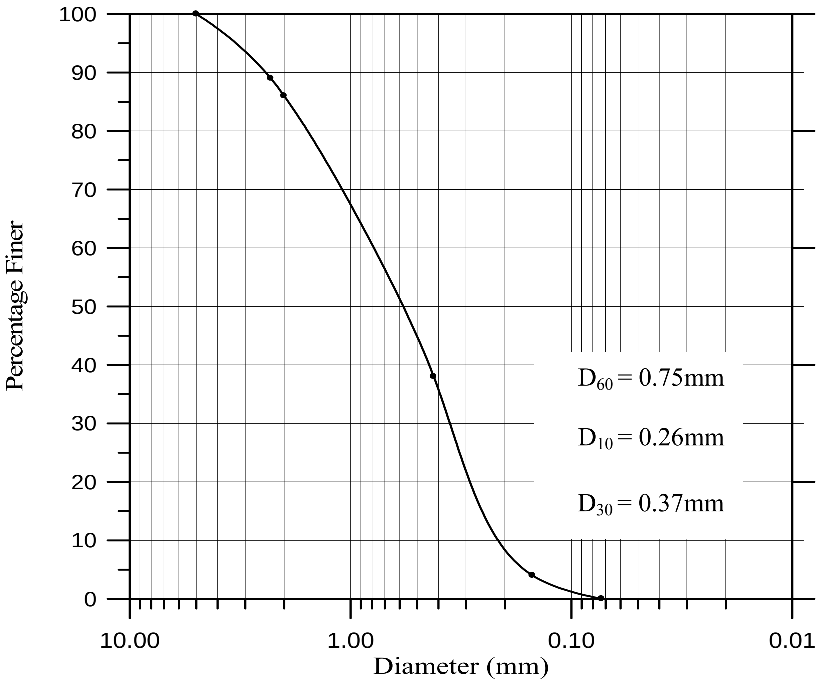

Fig. (3), Grain size distribution of the sand.

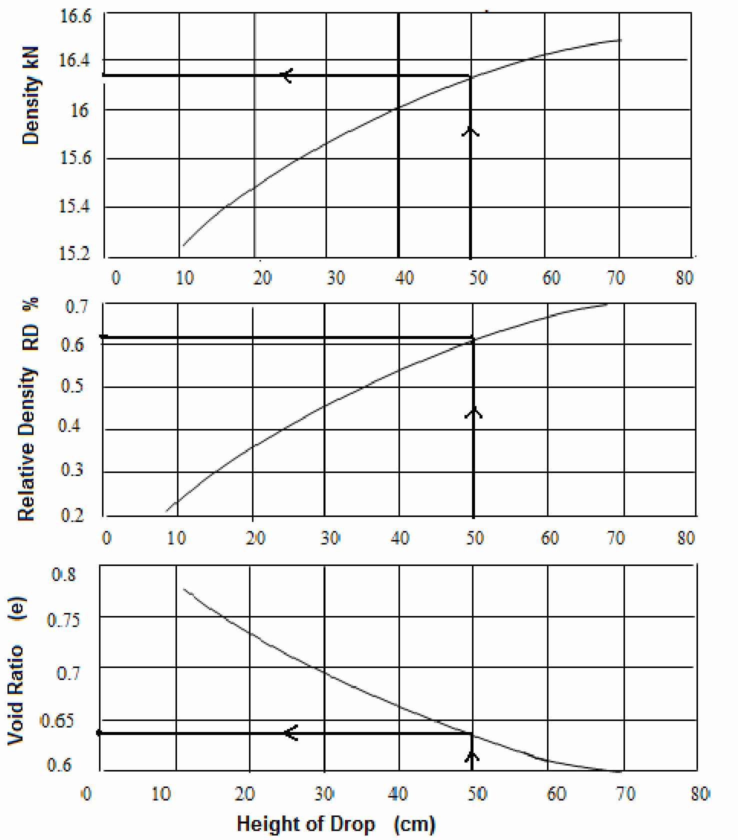

Fig. (4), Density calibration curves.

A laboratory test was carried out to find the modulus of elasticity for an Aluminum sample making use of the strain gage technique. A stress strain relationship was obtained in the laboratory from which the modulus of elasticity of the Aluminum was found to be 65 GPa.

A strain gage produced by Vishay Micro-Measurements was attached to the pile shaft and connected to a strain indicator to read the strain in the pile. Since the modulus of elasticity and the cross sectional area of the piles are known, then the amount of load carried by pile can be obtained. The load sharing mechanism between piles and raft can be well studied.

Strain Indicator

A 3800 Wide-Range Strain Indicator was used to read the strain initiated in the piles. This electronic instrument is highly versatile, specifically designed for use with strain gages. Its unique combination of “wide-range” features and easy-to- use controls makes the Model 3800 the right choice for many strain gage and transducers measurement applications.

The strain indicator of the model 3800 shown in **Figure (5)** can be used to obtain extremely accurate, high resolution strain measurements in a variety of circumstances. Resolutions of 0.10 $\mu\varepsilon$ (micro strain) are routinely possible if the excitation voltage kept above 5.0V, even higher resolution can be kept in the 10 to 15V range and the operation environment is relatively noise-free.

The used strain indicator was utilized with shunt calibration resistors across the internal 120Ω and 350Ω dummy gages for quarter bridge calibration. The calibration resistors can be used in conjunction with the gage factor potentiometer to compensate for leadwire resistance (Model 3800 Manual, 2002).

Before adopting the results obtained from the strain indicator, an external calibration was made by testing a steel bar with known modulus of elasticity twice, once by using the 3800 Vishay Model and then by using DMD-21 OMEGA strain indicator which was used only for the calibration purposes. The results of the two strain indicators were exactly the same, and the same modulus of elasticity of steel was obtained by the two devices.

TESTING PROCEDURE

The procedure followed in testing the piled raft model was divided into the following steps:

I. **Building the piled raft model:**
Aluminum pipe piles with different diameters and lengths, forming four configurations 2x1, 3x1, 2x2, and 3x2, were prepared to fulfill the testing program of the experimental study. The piles were fixed to approximately rigid rafts using strong epoxy. The epoxy was used as substitution for welding the piles to the raft since the aluminum may melt in the extremely high temperature of welding. The epoxy simulates a semi-fixed connection of piles to the raft.

II. **Attachment of strain gage:**
A strain gage was placed in the middle of the pile shaft**.** The strain gage was covered with a thin layer of sponge to protect it from damage, at the same time sponge does not bear any load.

III. **Preparation of sand deposit and placing of piled raft model:**
The sand was placed in the tank according to the raining techniques, i.e. maintaining a dropping height of 50 cm. After each test, the sand box should be emptied to a depth below the zone of influence (which was considered as 2L below the raft, where L is the pile length). During the process of sand raining, the piled raft model was placed at the center of the tank and under the loading ring, a bubble balance was used to insure

the level of the raft, then the raining was continued to a level of the lower surface of the raft. The final layer of the sand is leveled by a sharp edge ruler.

IV. Connection of wires to the strain indicator:

A quarter bridge connection was performed in the use of strain indicator, a gage factor of 2.03, excitation voltage of 10V and shunt calibration resistor of 120Ω was used to compensate for the leadwire resistant. Before starting the test, a reading of 0.00 was set in the strain indicator and waiting for 5 minutes to allow the system to be stable, then if the reading still around 0.00, the test can be started successfully.

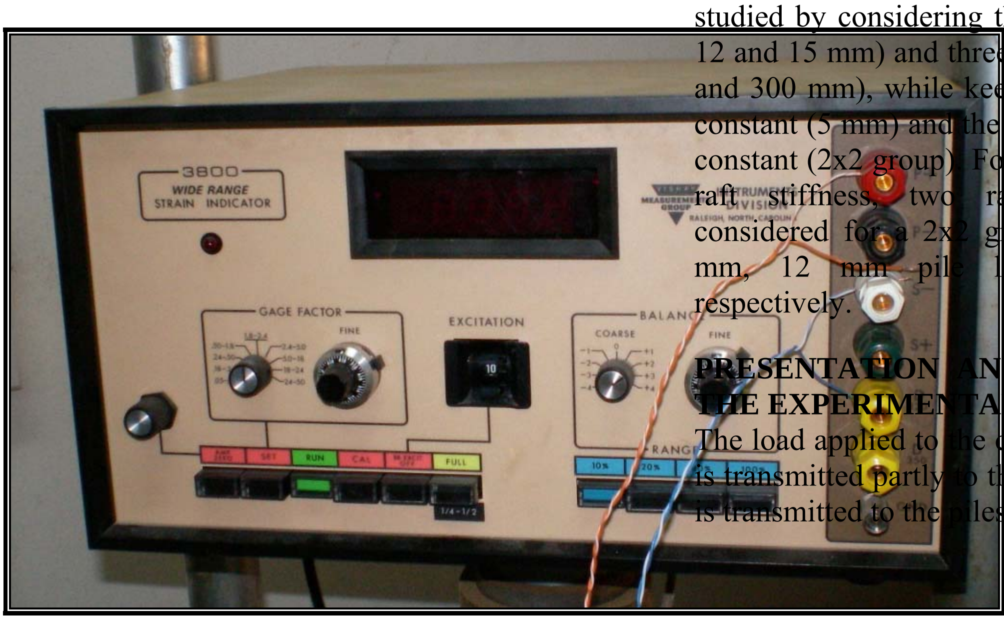

Fig. (5), Visahy 3800 strain indicator.

Testing Program

A program for performing a parametric study on piled raft model was carried out by testing four configurations with the same pile length (200 mm), diameter (12 mm), spacing (50 mm) and two raft thicknesses of 5 mm and 2.5 mm). The results were compared with rafts of the same sizes and thicknesses.

The effect of increasing the diameter of the pile as well as the effect of pile length on

V. Application of vertical load:

A vertical load was applied through a 5 or 10 kN proving ring, a constant loading rate of 1 mm/min was adopted in the entire testing program. The test was continued until recording a continuous displacement of the piled raft under constant load. The load was read from a dial gage fixed to the proving ring, while the central displacement of the raft was read by a dial gage of 0.01 mm sensitivity, and the strain in the pile was read from the strain indicator.

The above steps were repeated for each test. **Figure (6)** shows a piled raft model ready to be tested.

the load settlement and load sharing have been studied by considering three pile diameters (9, 12 and 15 mm) and three pile lengths (200, 250 and 300 mm), while keeping the raft thickness constant (5 mm) and the configuration also was constant (2x2 group). For studying the effect of raft stiffness, two raft thicknesses were considered for a 2x2 group of piles and 200 mm, 12 mm pile length and diameter, respectively.

PRESENTATION AND DISCUSSION OF THE EXPERIMENTAL RESULTS

The load applied to the center of the model raft is transmitted partly to the soil and another part is transmitted to the piles. The percent of load carried by piles to the total applied load can be determined in the laboratory through instrumentation of the piles with strain gages to find out the strain initiated in each pile. Due to the limited capabilities of the measuring devices in the laboratory, strain can be measured in only one pile in the group. To overcome this lack of devices, rigid rafts have been used to distribute the load equally to the piles, and by knowing the load in one pile, the total load carried by other piles can be obtained. By knowing the strain in a pile, one can calculate the load in that pile if the cross sectional area and the modulus of elasticity are known.

(a) Model piled raft with attached strain gage.

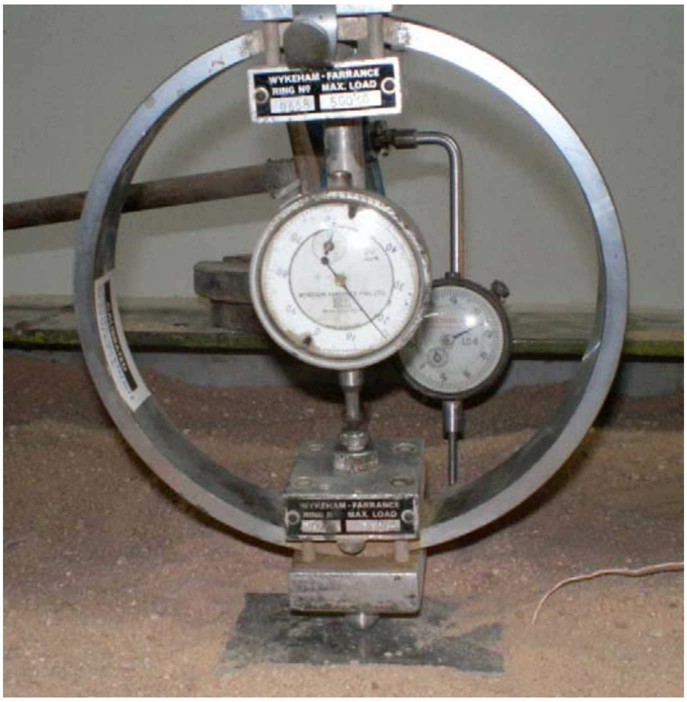

(b) Model piled raft and proving ring.

Fig. (6), Model piled raft ready to test.

Configurations of Piled Rafts

Piled raft configurations used maintain symmetrical shapes, especially where the differential settlement is expected to be of no major concern. Four different configurations of piles are used in the piled raft prototypes. The groups consist of (2x1), (3x1), (2x2) and (3x2) piles, a schematic diagram for the groups is shown in **Figure (7)**.

Load Carrying Capacity of Rafts and Piled Rafts

This section presents the load carrying capacity of the piles in each group as well as the load settlement behavior of the whole system with outside diameters having the values of 9, 12 and 15 mm, keeping the length of piles constant at 200 mm.

In the following figures, the settlement is plotted with the vertical applied load. In the same figures a curve representing the load settlement behavior of unpiled raft is added, where rafts are tested separately for the sake of comparison. The total load carried by piles is also shown in the same figure as calculated from strains measured through the use of strain gages.

Figures (8) to (10) show the load settlement behavior of piled rafts, and rafts of the same size and thicknesses and dimensions as well as the load carried by piles for the group of (2x1) with three different diameters (9, 12 and 15 mm), respectively. The pile length is kept constant (200 mm). **Figures (11) to (13)** are devoted for the groups of (3x1), while **Figures (14) to (16)** represent the groups of (2x2) piles. For the group of (3x2) only, one case having a pile diameter of (9 mm) and length of pile (200 mm) is shown in **Figure (17)**.

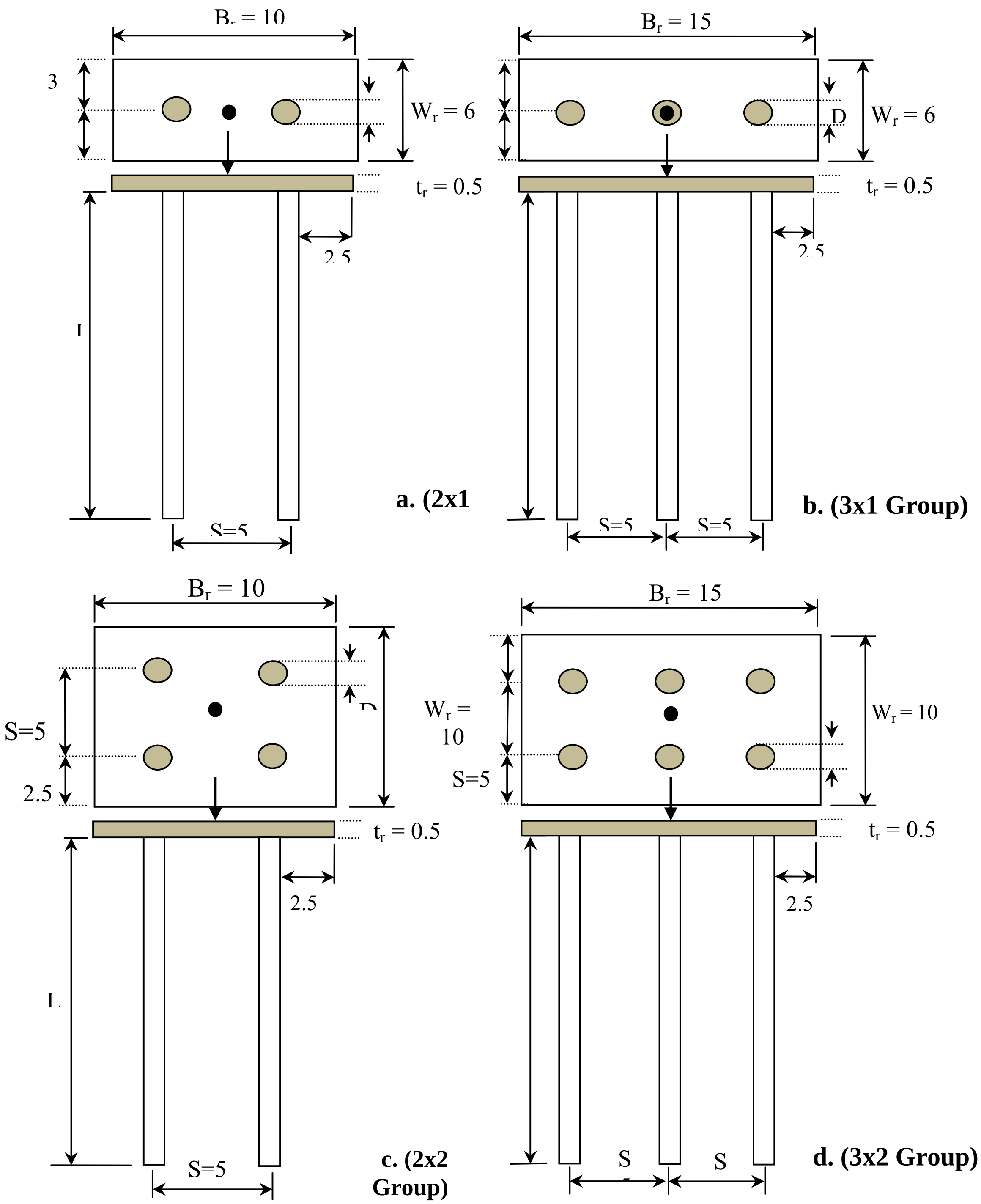

*Note: All dimensions are in cm.

Fig. (7), Piled raft configurations adopted in the experimental research.

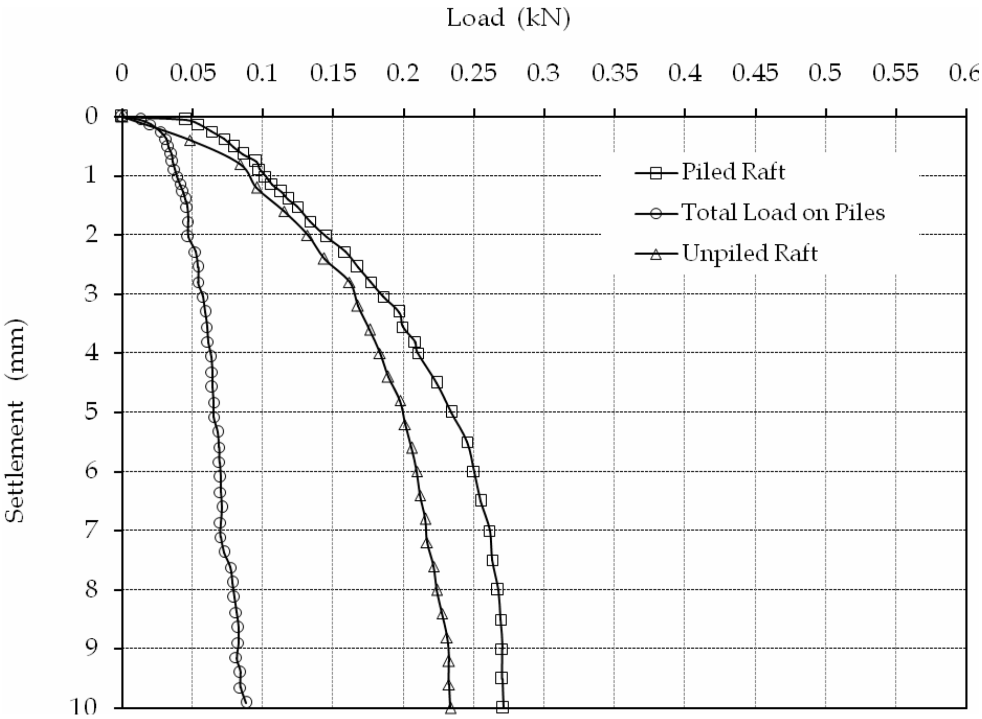

Fig. (8) Load –displacement curve for (**2x1**) piled raft, unpiled raft and total load on piles (L=200 mm, D=9 mm).

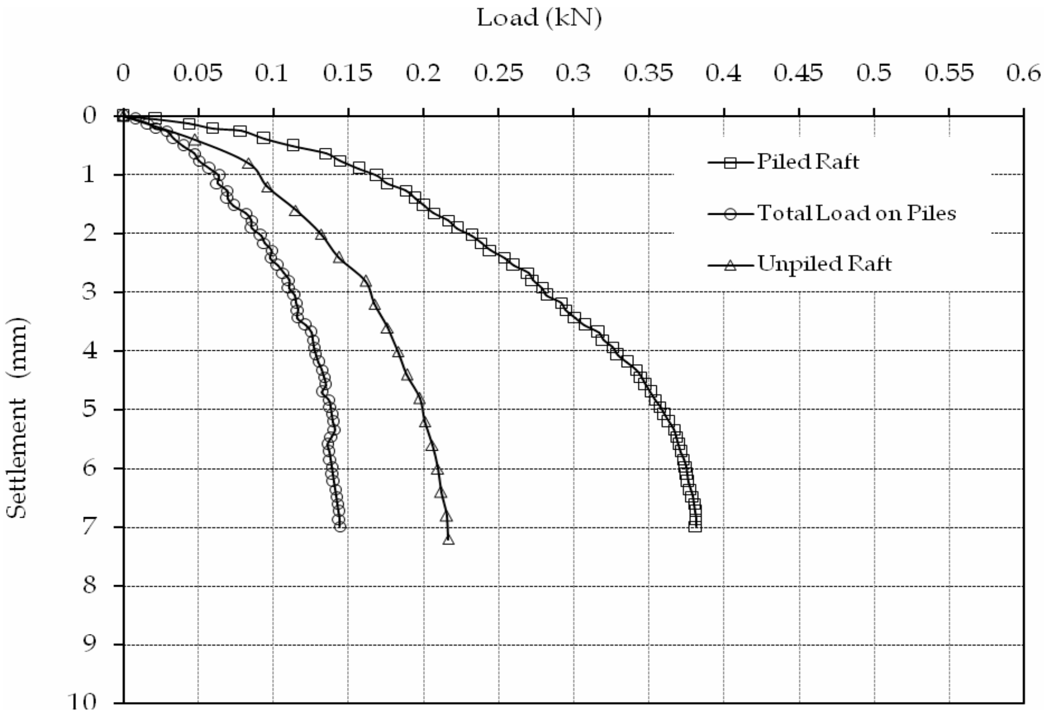

Fig. (9) Load – displacement curve for (**2x1**) piled raft, unpiled raft and total load on piles (L=200 mm and D=12 mm).

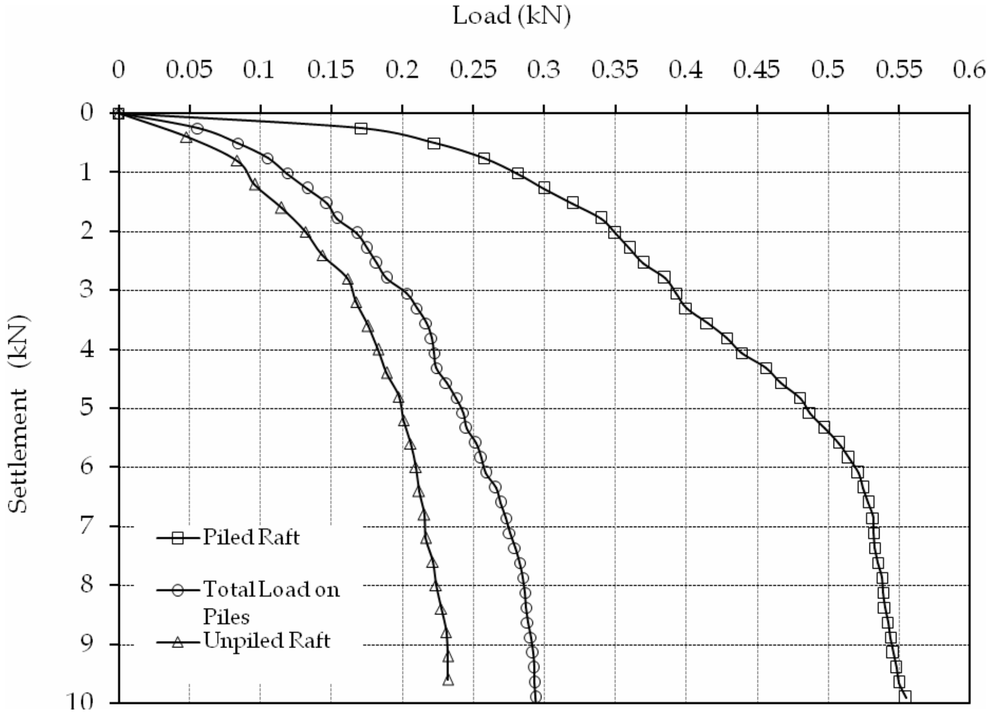

Fig. (10) Load – displacement curve for (**2x1**) piled raft, unpiled raft and total load on piles (L=200 mm and D=15 mm).

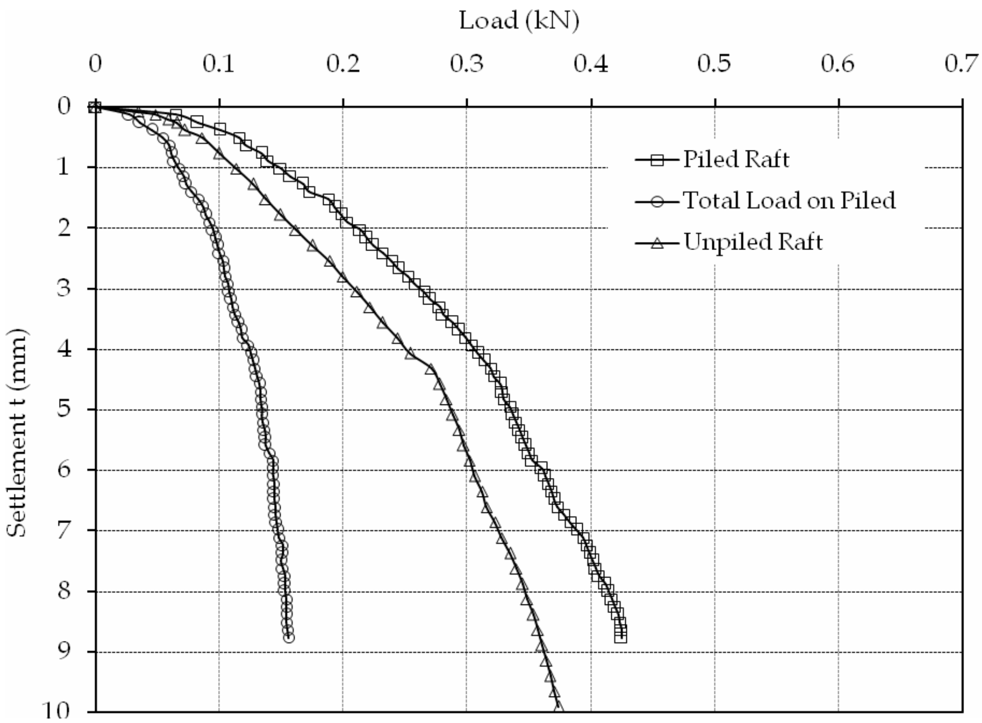

Fig. (11) Load – displacement curve for (**3x1**) piled raft, unpiled raft and total load on piles (L=200 mm, D=9 mm).

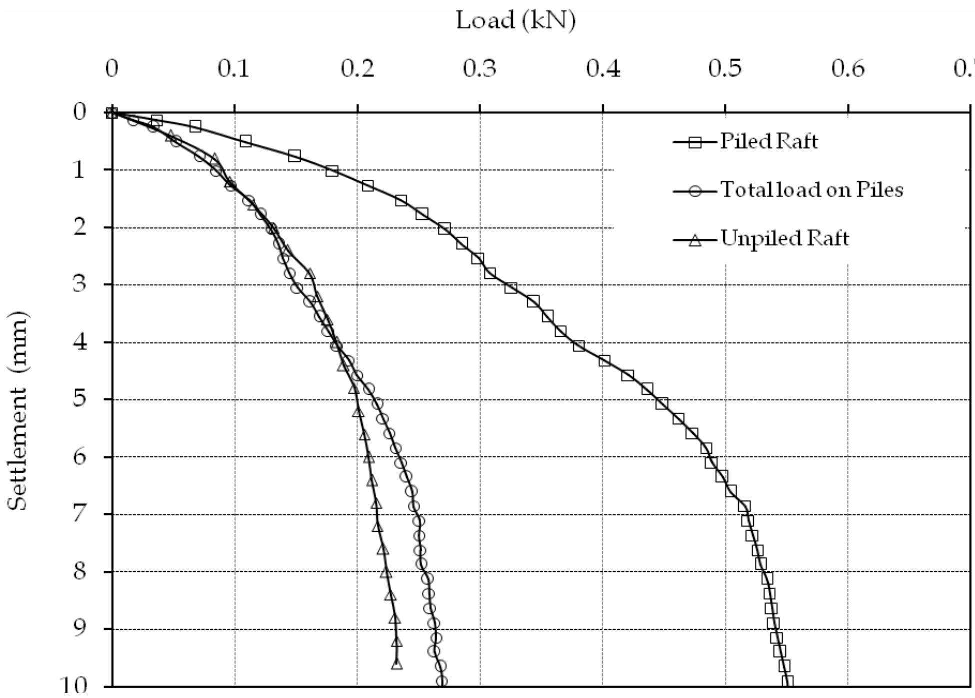

Fig. (12) Load – displacement curve for (**3x1**) piled raft, unpiled raft and total load on piles (L=200mm, D=12 mm).

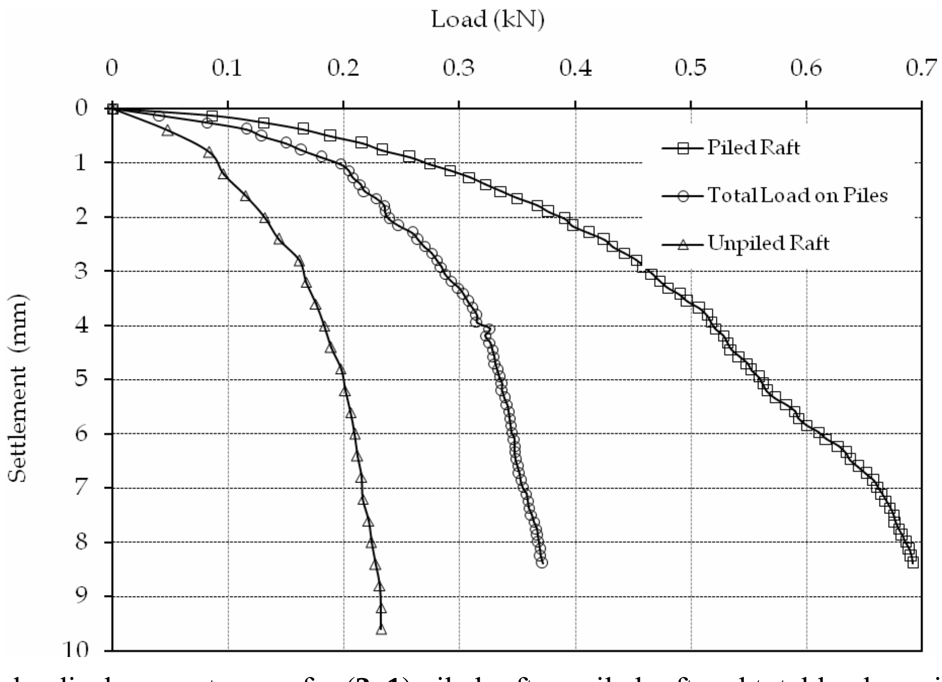

Fig. (13) Load – displacement curve for (**3x1**) piled raft, unpiled raft and total load on piles (L=200 mm, D=15 mm).

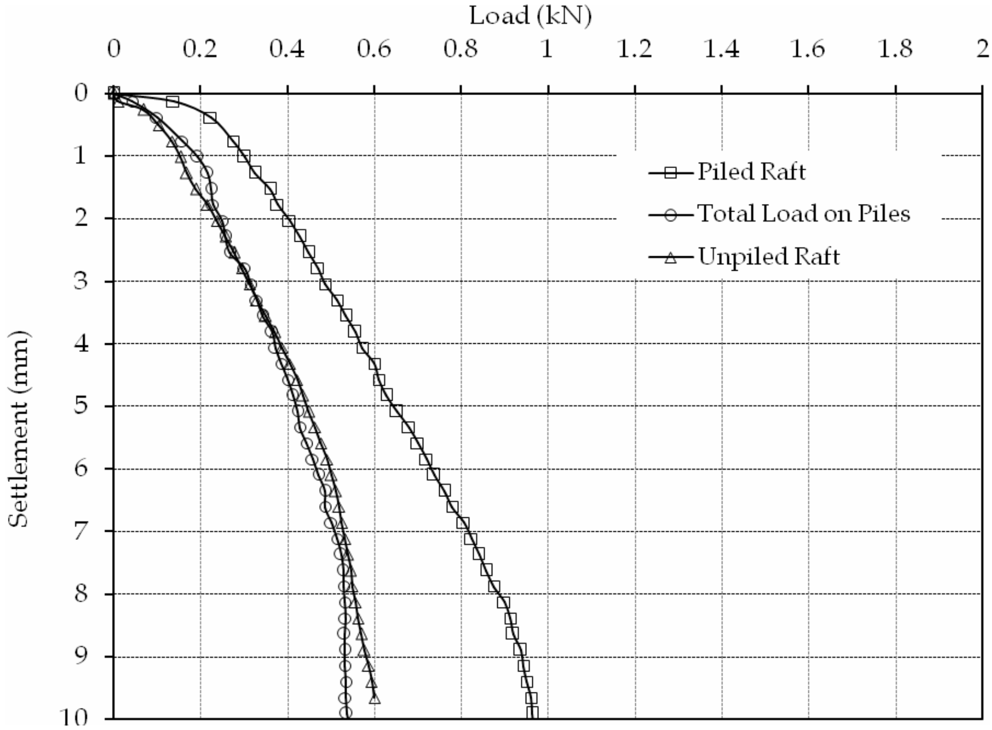

Fig. (14) Load – displacement curve for (**2x2**) piled raft, unpiled raft and total load on piles (L=200 mm, D=9 mm).

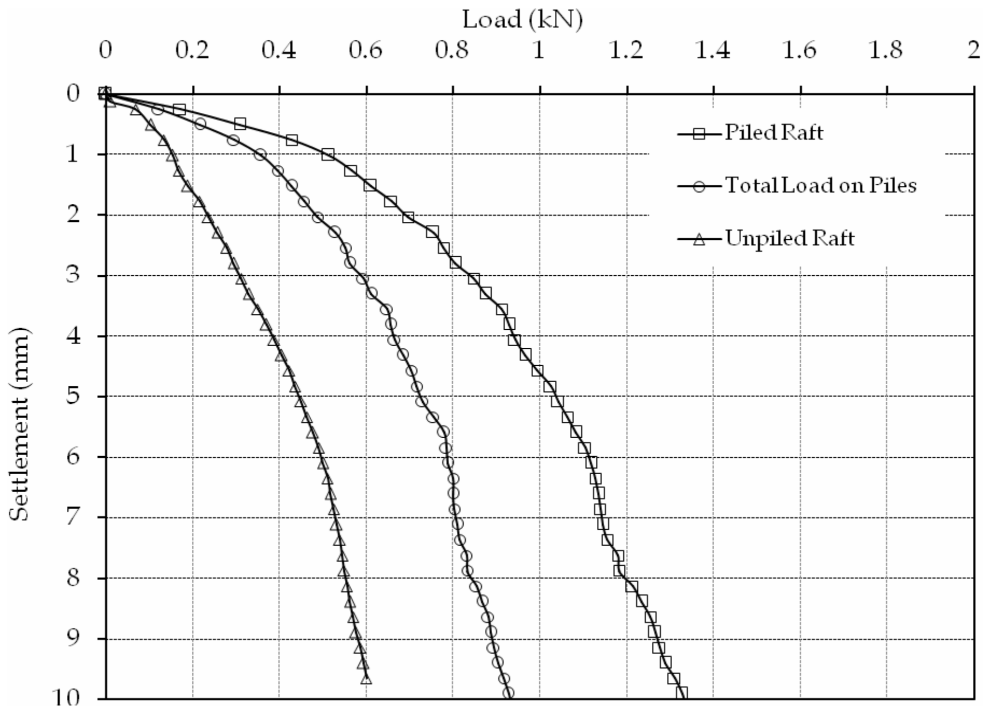

Fig. (15) Load – displacement curve for (**2x2**) piled raft, unpiled raft and total load on piles (L=200 mm and D=12 mm).

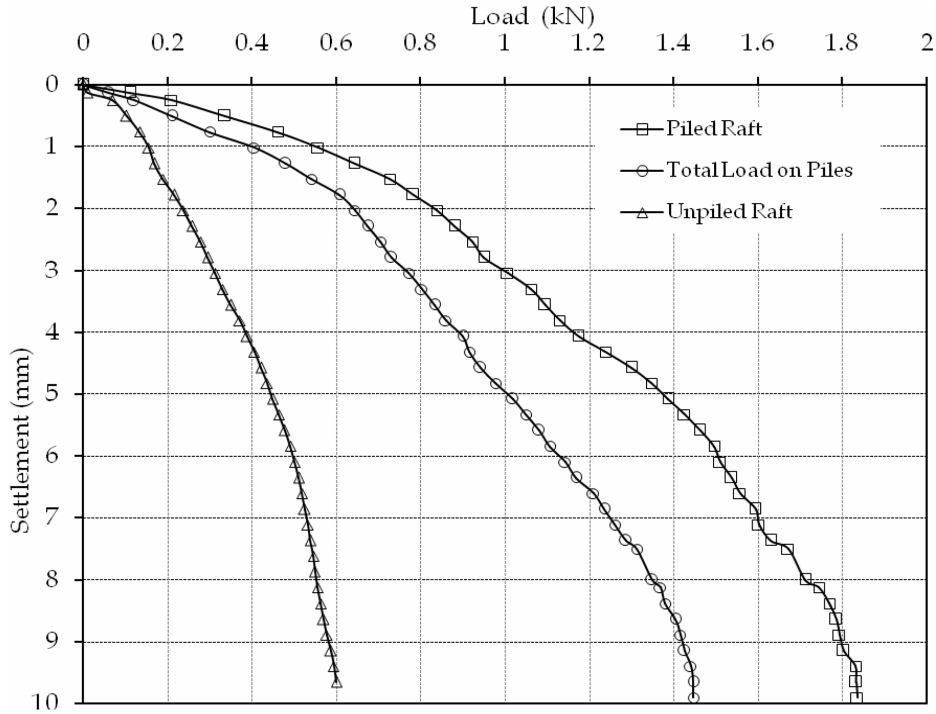

Fig. (16) Load – displacement curve for (**2x2**) piled raft, unpiled raft and total load on piles (L=200 mm and D=15 mm).

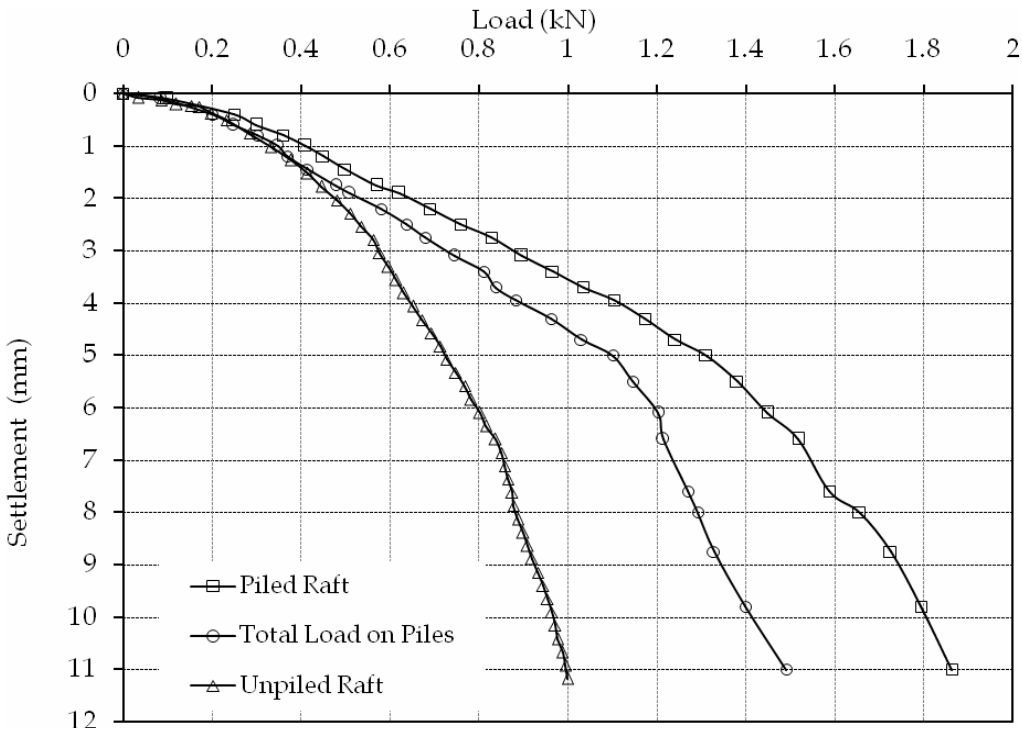

Fig. (17) Load – displacement curve for (**3x2**) piled raft, unpiled raft and total load on piles (L=200 mm, D=9 mm).

Selection of Failure Criterion

Several criteria have been proposed for defining the failure load of the piles. Some of these criteria are described by Fellenius (2006) as follows:

- **De Beer** in 1967 proposal. The bearing capacity is taken at break point of two intersecting straight lines of different slopes after plotting the load-settlement relationship in log-log plot. This break point represents failure.
- **Terzaghi** in 1947 proposal, where failure was defined as the load corresponding to dispalcment of 10% of the model footing width (or pile diameter).
- **Tangent** proposal, in which definition of failure based on the intersection of the two tangents of load-settelment curve while the second is tangent to the lower flatter portion of the curve.
- **Chin** in1970 proposal, this method assumes that the load-settlement curve is hyperbolic in shape when the failure load is approached. Each load value is divided by its corresponding settlement value and the resulting value is plotted against the settlement, the plotted value fall on a straight line, so the inverse of the slope of this line is the Chin failure load

After examining the previous proposals and by inspection of the behavior of the load-settlement relation for the piles in the present work, it was found that the tangent proposal can be adopted in specifying the ultimate piled raft capacity. The piles carrying capacity for the studied groups with different diameters are shown in table (3)

By checking **Figures (8) to (17)**, it can be noted that the piles carrying capacity increases with the increase of the pile diameter for all the studied groups. The total carrying capacity of the piles relative to the total applied load increases also with the increase in the number of piles in the group, whereas the group of (3x2) recorded the maximum piles capacity with 79% of the total applied load.

Effect of Raft Size and Thickness

The experimental study included implicitly the testing of rafts (unpiled rafts) of different sizes and thicknesses to compare the results with those of the piled raft system. The aluminum plates used for modeling the rafts are relatively of high stiffness which yields a uniform distribution of load between piles. Unpiled rafts with dimensions similar to the rafts used with groups of piles to form the piled raft system were testes separately. The load settlement curves are shown in **Figure (18)** for rafts having a thickness of (5) mm.

To study the effect of raft sized, the pressure under the raft is plotted against the settlement, as shown in **Figure (18)**. The pressure under the raft of size (15x10 cm) was (64 kN/m^2) corresponding to a settlement of 10 mm, this value is 30% greater than the pressure under a raft of size (6x10 cm) and corresponding to the same settlement. The case of raft with size (6x15 cm) showed the lowest values of pressure under the raft, and this may be attributed its relatively narrow width.

Table (3) Piles capacity for the studied cases.

Case	Pile Raft Capacity (kN)	Piles Capacity (kN)	% of Load Carried by Piles
(2x1) Group, L = 200 mm, D = 9 mm	0.25	0.068	27
(2x1) Group, L = 200 mm, D = 12 mm	0.365	0.14	38
(2x1) Group, L = 200 mm, D = 15 mm	0.5	0.26	52
(3x1) Group, L = 200 mm, D = 9 mm	0.4	0.144	36
(3x1) Group, L = 200 mm, D = 12 mm	0.51	0.25	49
(3x1) Group, L = 200 mm, D = 15 mm	0.62	0.325	52
(2x2) Group, L = 200 mm, D = 9 mm	0.83	0.45	54
(2x2) Group, L = 200 mm, D = 12 mm	1.15	0.78	68
(2x2) Group, L = 200 mm, D = 15 mm	1.6	1.25	78
(3x2) Group, L = 200 mm, D = 9 mm	1.62	1.275	79

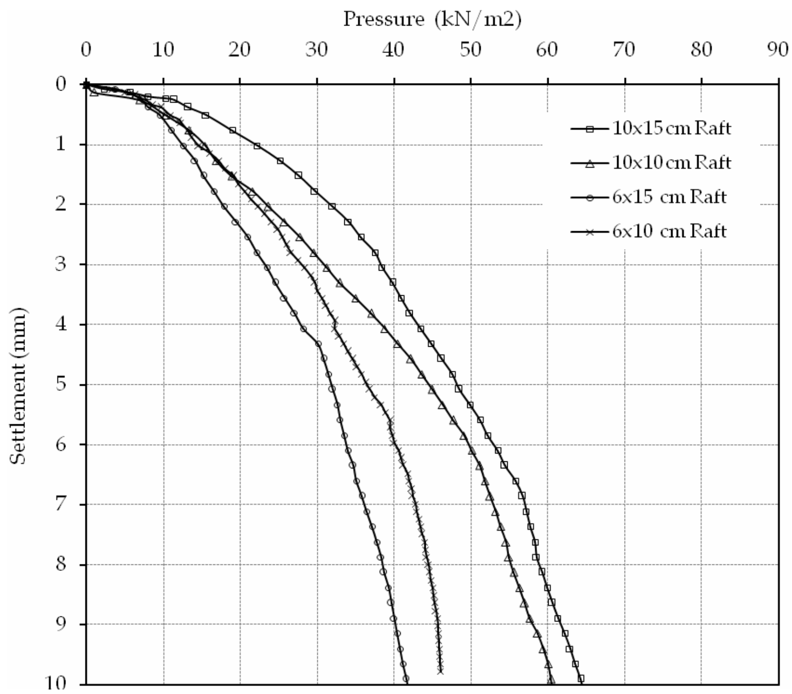

Fig. (18), Load – displacement of unpiled rafts of different sizes (t_r = 5 mm).

The effect of raft thickness is also studied for the case of piled raft system, a thickness of (2.5) mm tested with (2x2) group of piles, for L= (200) mm and D= (12) mm.

The results of load settlement curve and the load carrying capacity of piles are shown in **Figure (19)** in which the unpiled raft with the same thickness is also shown. The total bearing capacity of piled raft system is not much affected by the raft thickness, while the total load carried by piles is slightly reduced. The percent of load carried by piles is plotted against the raft thickness in **Figure (20)**.

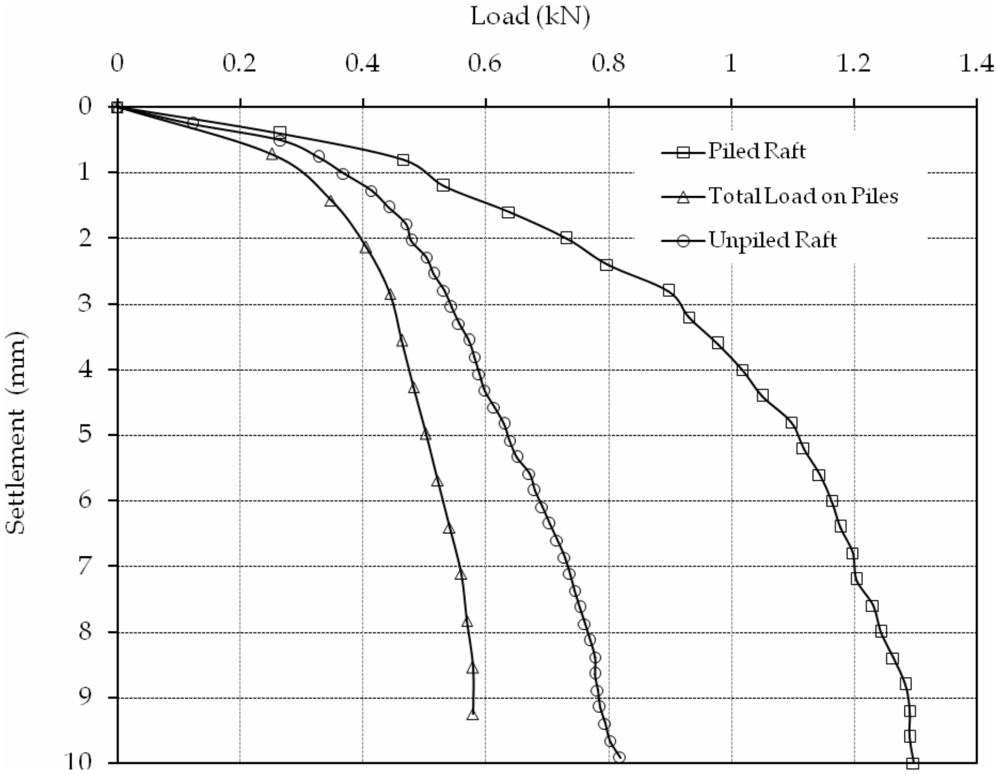

Fig. (19) Load – displacement curve for (2x2) piled raft, unpiled raft and total load on piles (L=200 mm, D=12mm, and t_r=2.5 mm).

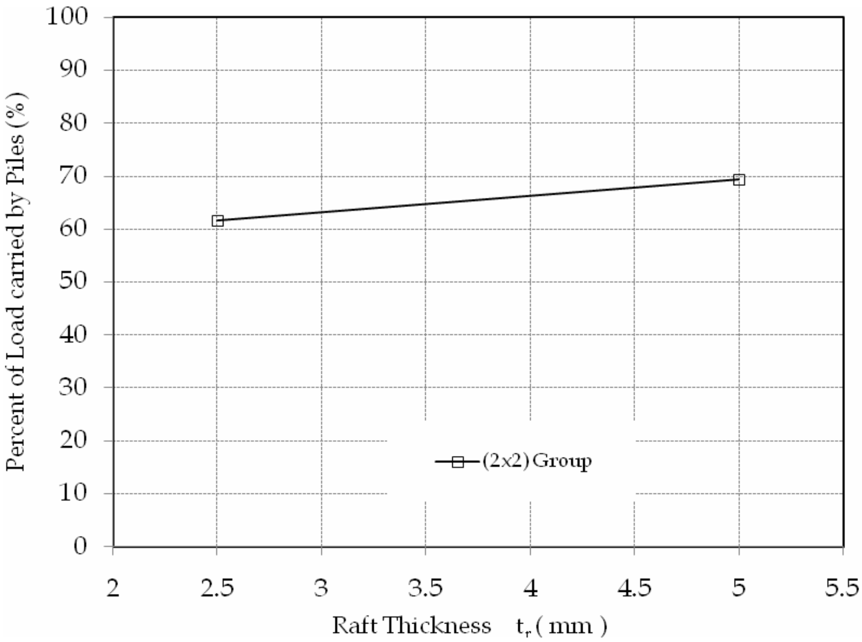

Fig. (20), Percent of load carried by piles for (2x2) group of piles (L=200 mm, D=12 mm) with raft thickness.

CONCLUSIONS

The experimental modeling implemented in this paper yielded the following conclusions:

1. The load carrying capacity of the unpiled raft increases with the increase of the size, while the raft thickness slightly affects the load carrying capacity. For the piled raft model, the total carrying capacity of the model increased with the increase of raft size, number of piles in the group, length of piles, and diameter of piles.
2. The percentage of the load carried by piles to the total applied load of the groups (2x1, 3x1, 2x2, 3x2) with raft thickness of 5 mm, pile diameter of 9 mm, and pile length of 200 mm was 28% , 38% , 56% , 79% , respectively. The percent of the load carried by piles increases with the increase of number of piles.

REFERENCES

- Al-Jebouri, J. M. (1986), "Bearing Capacity of Footing on Reinforced Sand" M.Sc. Thesis, University of Baghdad, Iraq.
- Bieganousky, W. N. and Marcuson, W. F. (1976),"Uniform Placement of Sand", Journal of Geotechnical Engineering Div., ASCE, Vol. 102, No. GT.3,pp.229-233.
- Burland, J.B., Broms, B.B. and de Mello, V.F.B. (1977), “Behaviour of Foundations and Structures”, Proc. 9th ICSMFE, Tokyo, Vol.2, pp. 495-546.
- Cox, W. R., Dixon, D. A., and Murphy, B. S. (1984), “Lateral-Load Tests on 25.4-mm (1-in.) Diameter Piles in Very Soft Clay in Side-by-Side and in-Line Groups” Laterally Loaded Deep Foundations: Analysis and Performance, ASTM STP 835, 122-139.

-
- Davis, E. H. and Poulos, H. G. (1972), Rate of Settlement under Two-and Three-Dimensional Conditions, Geotechnique, Vol.22, No.1, pp. 95-114.
- de Sanctis L., and Mandolini A., (2006), "Bearing Capacity of Piled Rafts on Soft Clay Soils", Journal of Geotechnical and Geoenvironmental Engineering, ASCE, Vol. 132, No. 12, pp. 1600-1610.
- Fellenius, B. H., (2006), "Basics of Foundation Design:, Electronic Edition. www.Fellenius.net, 275 p.
- Hartman, F. and Jahn, P. (2001), "Boundary Element Analysis of Raft Foundations on Piles", Meccanica Vol. 3, pp. 351–366, Kluwer Academic Publishers. Netherlands.
- Hooper, J.A., (1973), "Observations on the Behavior of a Piled Raft Foundation in London Clay", Proceeding of Institution of Civil Engineers, Vol.55, No.2, pp. 855-877.
- Jawad, W. F. (2009)," Improvement of Loose Sand Using Geogrids to Support Footing Subjected to Eccentric loads", M.Sc. Thesis, University of Baghdad, Iraq.
- Katzenbach, R. and Reul, O. (1997), "Design and Performance of Piled Rafts", Proceeding XIVth ICSMFE, Hamburg Vol. 4, pp. 2253-2256.
- Model 3800 Instruction Manual, (2002), "Wide Range Strain Indicator", USA, www.vishaymg.com.
- Mokwa, R. L. (1999), "Investigation of the Resistance of Pile Caps to Lateral Loading", Ph.D. Thesis, Virginia Polytechnic Institute and State University, USA.
- Prakoso, W.A. and Kulhawy, F.H., (2001), "Contribution to Piled Raft Foundation Design", Journal of Geotechnical and Geoenvironmental Engineering, ASCE, Vol.127, No.1, pp.17-24.
- Reul, O. and Randolph, M. F., (2003), "Piled Rafts in Overconsolidated Clay: Comparison of in Situ Measurements and Numerical Analysis", Geotechnique, Vol. 53, No. 3, pp. 301-315.
- Turner, J. P. and Kulhawy, F. H. (1987), "Experimental Analysis of Drilled Foundations Subjected to Repeated Axial Loads Under Drained Conditions", Report EL-5325, Electric Power Research Institute, Palo Alto, California.
- Zeevaert, L. (1957) "Compensated Friction-pile Foundation to Reduce the Settlement of Buildings on Highly Compressible Volcanic Clay of Mexico City", Proc. 4th ICSMFE, London, V.2.

EFFECT OF STEEL FIBERS ADDITION ON THE BEHAVIOR OF HIGH STRENGTH CONCRETE CIRCULAR SHORT COLUMNS

Yasir M. W. Al-Shamma
M.Sc. Student, Civil Eng. Dep., College of Engineering, Al-Mustansiriya University
Asst. Prof. Dr. Riyadh Jawad Aziz
Civil Eng. Dep., College of Engineering, Nahrain University
Lect. Dr. Zubidah Abdullateef Al-Bayati
Civil Eng. Dep., College of Engineering, Al-Mustansiriya University

ABSTRACT

This paper presents the effects of the addition of steel fibers on the behavior of concentrically loaded reinforced concrete circular short columns. An experimental investigation into the behavior of 24 short reinforced concrete columns with and without steel fibers was carried out. The columns had a circular section (200 mm diameter and 900 mm long). Test variables include concrete strength, spacing of spiral reinforcement, and inclusion of steel fibers. The axial stress and axial strains were obtained and used to evaluate the effects of the presence of steel fibers. It was found that the addition of steel fibers slightly improves the load carrying capacity of the tested columns whereas it significantly enhances the ductility of these specimens. Test results also indicated that for the same confinement parameter $\rho_s f_{sy}/f'_c$, specimens with steel fibers has higher strength enhancement compared to specimens without steel fibers. For confinement parameter of 0.1 the strength enhancement equal 1.7 for specimens with fibers while it is 1.4 for nonfibrous specimens. An empirical expression is proposed and used to predict the confined strength of columns. It was shown that the proposed formula predicts the load carrying capacity of the tested columns reasonably.

Keywords: short columns; compressive tests; confined concrete; high strength concrete; steel fibers.

تأثير إضافة ألياف الفولاذ على سلوك الأعمدة الخرسانية الدائرية عالية المقاومة و القصيرة

الخلاصة

يبين هذا البحث تأثير إضافة مادة ألياف الفولاذ على سلوك الأعمدة الخرسانية عالية المقاومة الدائرية و القصيرة و المفحوصة تحت تأثير أحمال انضغاط محورية. تضمن الجزء العملي من البحث تحضير وفحص 24 أنموذجاً لأعمدة خرسانية مسلحة دائرية المقطع بقطر 200 ملم و طول 900 ملم تحتوي نصفها على مادة ألياف الفولاذ. تشمل المتغيرات مقاومة الخرسانة للإنضغاط و المسافة الشاقولية لتوزيع حديد التسليح الحلزوني و وجود ألياف الفولاذ ضمن الخرسانة. أظهرت نتائج الفحص بأن ألياف الفولاذ المضافة حسنت بدرجة قليلة مقاومة التحمل القصوى للأعمدة في حين أن المطيلية ازدادت بشكل كبير مقارنة بالأعمدة غير الحاوية على ألياف الفولاذ. وكذلك وجد عند تثبيت معامل الحصر فأن تحسين المقاومه للأعمده الحاويه على الياف الفولاذ أعلى من تحسين المقاومه للأعمده غير الحاويه على الألياف. حيث وجد أن تحسين المقاومة بلغ 1,7 للأعمدة الحاوية على ألياف الفولاذ بينما بلغ 1,4 للأعمدة غير الحاوية على ألياف الفولاذ عندما يكون معامل الحصر مساوياً إلى 0,1. و كذلك فقد تم إقتراح علاقة تجريبية للتنبأ بالمقاومة القصوى لخرسانة الأعمدة المحصورة. و قد وجد أن المعادلة المقترحة تعطي نتائج جيدة مقارنة مع النتائج المختبرية.

INTRODUCTION

High strength concrete has been commonly used in reinforced concrete structures and particularly in columns. It leads to a reduction in column size due to higher load carrying capacity. It is well known that the mechanical behavior of high strength concrete is brittle under compression relative to lower strength concrete. Thus, confinement, ductility and deformability features of high strength concrete columns are important, especially under seismic loading conditions. Ductility of high strength reinforced concrete columns can be improved by effectively confining column core. It is widely accepted that concrete confinement can be provided by using small spacing of lateral ties and also adding steel fibers to concrete. The use of steel fiber composites in reinforced concrete structures has become very popular and found effective [Tokgoz, 2009].

High strength concrete with steel fibers does not fail even after high strain values under compression, thus the member behaves a ductile manner. Moreover, the addition of steel fibers into high strength concrete column not only improves ductility but also prevents premature cover spalling [Ganesan and Murthy 1990, Hsu et al. 1995, Foster and Attard 2001, and Foster 2001].

Ganesan and Murthy (1990) have presented an experimental investigation on the strength and behavior of reinforced concrete columns with and without steel fibers subjected to monotonic axial compression. The effect of steel fibers on the strength, confinement and ductility of reinforced concrete columns have been given, and an analytical model to describe the stress–strain behavior of confined steel fiber concrete has been proposed.

Hsu et al. (1995) have tested 14 square section slender high strength reinforced concrete columns with and without steel fibers to examine the experimental and theoretical load–deflection behavior of the columns under biaxially eccentric load. They found that the addition of steel fibers improved the ductility and confinement of high strength concrete columns. They also indicated that steel fibers do not affect the load carrying capacity of the columns significantly.

Foster and Attard (2001) have tested plain and steel fiber high strength concrete columns to examine the effects of steel fibers on strength and ductility. They have reported that cover spalling of the columns can be effectively prevented by adding steel fibers into the concrete, and the use of steel fibers improves the strength and ductility of high-strength concrete columns.

Foster (2001) has investigated the effect of steel fibers on the cover spalling and ductility of concrete columns. It has been concluded that steel fibers prevent premature cover spalling and improve ductility of high strength concrete columns. A model was developed to determine the quantity of steel fibers to ensure reasonable level of ductility.

Lima Junior and Giongo (2004) have investigated the experimental behavior of concentrically loaded steel fiber high strength concrete columns confined with low ratios of rectangular ties. They reported that steel fibers improve ductility and confinement and prevent premature concrete cover spalling of columns.

Campione et al. (2010) have tested 16 short, confined, reinforced concrete columns with and without steel fibers. The specimens were tested to failure at different strain rates under two loading schemes: concentric compression and eccentric compression with constant eccentricity. They concluded that the presence of steel fibers delay the spalling of concrete cover and increase the strain capacity and ductility; the eccentricity of the applied axial load cause substantial variation in the peak load, ultimate strength, and failure modes.

COLUMN DUCTILITY

Ductility is the ability of columns to deform without significant loss of strength. Since testing of columns was performed using load control procedure it was not possible to trace the response of the specimens after the peak load. For this reason the ductility of the tested columns were computed using the procedure developed by Foster and Attard (2001).

Foster and Attard (2001) used a technique involving an I_{10} ductility index which allows a comparison between the performance of fiber and non-fiber reinforced concrete columns. The method is based on the definition of flexural toughness as set out in ASTM C1018-97, where the level of ductility is defined using the I_{10} ductility index. The I_{10} factor "energy ductility" can be found by dividing the area under the load- deflection curve at 5.5 times the yield deflection by the area under the curve at yield deflection, as defined in Fig. 1.

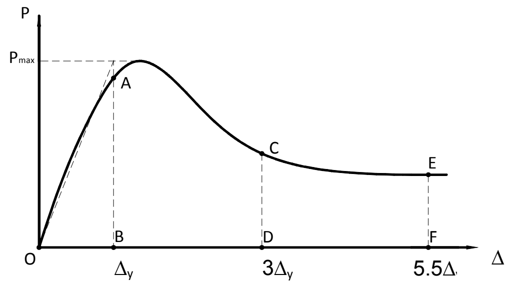

Fig.1 Determination of column ductility [Foster 2001]

A number of authors [Sheikh and Uzumeri 1980, Martinez et al. 1984, Mander et al. 1988, and Razvi and Saatcioglu 1994] have indicated that ductility is a function of the confinement parameter $k_e\rho_s f_{sy}/f'_c$, where ρ_s is the lateral reinforcement volumetric ratio, f_{sy} is the yield strength of the spiral reinforcement, f'_c is the concrete compressive strength, and k_e is a confinement effectiveness coefficient, which represents the efficiency of tie reinforcement arrangement. Martinez et al. (1984) shows that for columns confined by spirals k_e can be calculated using the following expression:

$$k_e = \frac{\left(d_s - \frac{s'}{2}\right)}{1-\rho_{cc}} \tag{1}$$

where

d_s : Diameter of the column core measured between the spiral centers,

s' : Clear vertical spacing between spiral bars,

ρ_{cc} : Ratio of longitudinal reinforcement area to concrete core area.

Foster and Attard (2001) suggested that the relationship between ductility and the confinement parameter $k_e\rho_s f_{sy}/f'_c$ for non-fiber spiral columns can be given by:

$$I_{10} = 1.9\,ln(1000k_e\rho_s f_{sy}/f'_c) \tag{2}$$

where

ρ_s : Volumetric ratio of spiral reinforcement,

f_{sy} : Yield strength of spiral steel.

Noting that the confinement parameter is related to the confining stress f_l which determined as $0.5\rho_s f_{sy}$, then Eq. (2) can be written as:

$$I_{10} = 1.9\,ln(1000 \times 2k_e f_l/f'_c) \tag{3}$$

For columns with both spirals and steel fibers, Foster and Attard (2001) supposed that the confinement due to each component can be summed to give a total confining stress. That is:

$$I_{10} = 1.9\,ln\left[1000\left((2k_e f_l/f'_c) + (2f_{lf}/f'_c)\right)\right] \tag{4}$$

Where f_{lf} is the lateral confinement stress provided by the steel fibers. Marti et al. (1999) assumed a constant bond shear τ_b along the length of the embedded fiber and found that the confining pressure applied to the section by the fibers is:

$$f_{lf} = \frac{3}{8}\alpha_f\rho_f\tau_b \tag{5}$$

where

α_f : Fiber aspect ratio = l_f/d_f , where l_f and d_f is the fiber effective length and diameter, respectively,

τ_b : Fiber-concrete bond shear strength = $0.6(f'_c)^{2/3}$ as an approximation suggested by Marti et al. (1999), in MPa.

EXPERIMENTAL PROGRAM

Specimens

A total of 24 short column specimens had an overall height of 900 mm with circular cross-section of 200 mm diameter were loaded concentrically. Half of the specimens were cast with the inclusion of steel fibers and the other half was without steel fibers. The concrete mix of fiber-reinforced samples contains 0.5% by volume (approx. 1.67% by weight) of end hooked steel fibers.

The column specimens were divided into three main groups depending on the concrete strength; low, normal and high strength concrete. Each group was subdivided into two subgroups depending on the inclusion of fibers. More details are given in reference [Al-Shamma, 2011].

Four columns were tested for each subgroup. The first column was plain without reinforcement, is used to establish the properties of unconfined concrete and to account for the difference between concrete strength in the column and that based on testing of concrete cylinder. The second column was reinforced with six longitudinal steel bars of 10 mm diameter only. The third column was reinforced with six longitudinal steel bars of 10 mm diameter and spirals of 6 mm diameter with spiral pitch equals to 50 mm. The fourth column was reinforced with the same reinforcement as the third column except for spiral pitch which was 100 mm. Fig. 2 shows reinforcement details of columns with spiral steel.

In all specimens the ratio of the gross area of the column cross section A_g to the core area A_c measured to the outside of the lateral reinforcement was 1.3. The columns were prepared for vertical casting using local PVC tubes cut to match the column height and then cut vertically to facilitate the removing of the mold later. Three clamps were used to support the mold throughout the casting process. The base of molds was constructed by cutting plywood panel into square pieces with dimensions 300×300 mm. Then, the fabricated steel cages were placed in the molds. The assembled steel cages for the tested columns are shown in Plate 1.

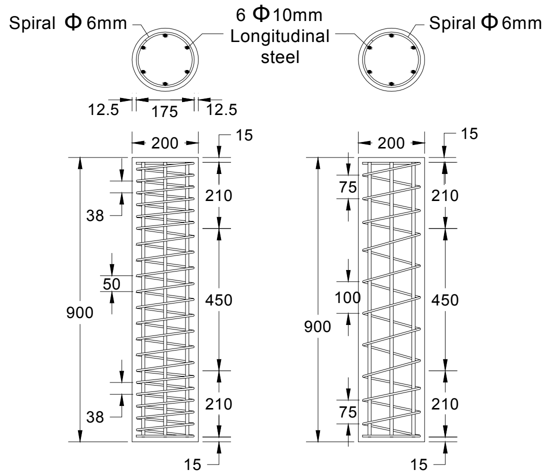

Fig. 2 Reinforcement details of spiral columns

Column specimens are identified with a series of numbers and letters. For example, column specimen LSC-F-100 is a column with low strength concrete, fiber reinforced, and 100 mm pitch of spiral reinforcement. Table 1 shows various properties of longitudinal and transverse reinforcement of the tested columns. The concrete strength f'_c given in Table 1 represents standard cylinder compressive strength obtained at the day of test of the specimens, ρ_l, s, and ρ_s are respectively longitudinal steel ratio, spacing and volumetric ratio of spiral steel. The volumetric ratio of spiral reinforcement, ρ_s varied between 0.6% and 1.3%.

Table 1 Details of test specimens

Column ID	Volumetric Ratio of Steel Fibers	Concrete Compressive Strength	Longitudinal Reinforcement (Deformed Bars)		Lateral Reinforcement (Plain Bars)		
	ρ_f (%)	f'_c (MPa)	No. & Size (mm)	(%) ρ_l	Size (mm)	Pitch, s (mm)	ρ_s (%)
LSC-F-50	0.5	28.71	10ϕ6	1.5	6	50	1.3
LSC-F-100					6	100	0.6
LSC-F-L					--	--	--
LSC-F-P			--	--	--	--	--
NSC-F-50		41.36	10ϕ6	1.5	6	50	1.3
NSC-F-100					6	100	0.6
NSC-F-L					--	--	--
NSC-F-P			--	--	--	--	--
HSC-F-50		64.46	10ϕ6	1.5	6	50	1.3
HSC-F-100					6	100	0.6
HSC-F-L					--	--	--
HSC-F-P			--	--	--	--	--
LSC-N-50	--	27.68	10ϕ6	1.5	6	50	1.3
LSC-N-100					6	100	0.6
LSC-N-L					--	--	--
LSC-N-P			--	--	--	--	--
NSC-N-50		40.59	10ϕ6	1.5	6	50	1.3
NSC-N-100					6	100	0.6
NSC-N-L					--	--	--
NSC-N-P			--	--	--	--	--
HSC-N-50		59.13	10ϕ6	1.5	6	50	1.3
HSC-N-100					6	100	0.6
HSC-N-L					--	--	--
HSC-N-P			--	--	--	--	--

Table 2 Longitudinal and transverse reinforcing bar properties*

Bar Size (mm)	Tensile Strength (MPa)	Yield Strength (MPa)	Elongation (%)
6	418	317	23.2
10	590	495	15.3

* Test results for each type of reinforcement are average values of three coupons.

Plate 1 Assembled reinforcement cages for columns

Material Properties

The materials consisted of Ordinary portland cement (Type I) produced by United Cement Company (TASLUJA), maximum size of 10 mm local gravel brought from Al-Nibaee region, well graded natural sand obtained from Al-Ukhaider region, tap water for mixing and curing, silica fume produced by Sika Corporation and TufFlow SP603 superplasticizer admixture to maintain good workability of the mix. 10 mm diameter deformed steel bars and 6 mm diameter plain steel bars are used for longitudinal and spiral reinforcement, respectively. The main data obtained for testing bars are shown in Table 2.

Fibrous concrete was obtained by adding hooked end steel fibers in fresh concrete. The steel fibers are Dramix® ZC 50/50 type and manufactured by Bekaert Corporation (Plate 2). The fiber had a length of 50 mm, a diameter of 0.5 mm, and a tensile strength (declared by the manufacturer) of 1000 MPa (Fig. 3). The fiber percentage adopted was 0.5% by volume of concrete, corresponding to 40 kg/m^3.

Plate 2 Dramix® ZC 50/50

Fig. 3 Steel fiber dimensions end hooked steel fibers

Three target concrete strengths, 21 MPa, 42 MPa, and 63 MPa, are considered in this study and obtained using several laboratory trial batches. Low water-cement ratio w/c and high cement content were used to achieve the strength level required. The corresponding water to cementitious material ratios w/c was 0.5, 0.4, and 0.3 for LSC, NSC and HSC respectively. Different mix designs for the three target concrete strengths were used for six batches of concrete. Table 3 shows details of concrete mix design for each of the targeted strengths.

Material	Target Strengths (MPa)		
	21	42	63
	Mix1	Mix2	Mix3
Cement (Type I) (kg/m^3)	400	450	500
Silica Fume (kg/m^3)	-	-	40
Sand (kg/m^3)	600	680	700
Gravel (kg/m^3)	1200	1150	1100
Water (kg/m^3)	200	180	162
Superplasticizer (SP603) (L/100 kg)*	-	1.5	2.5
w/c	0.5	0.4	0.3

* Liter per 100 kg of cementitious materials (Cement + Silica Fume).

Table 3 Details of the concrete mix design

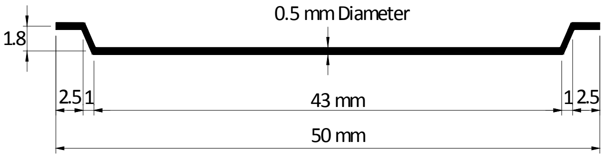

Table 4 Mechanical properties of hardened concrete

Mix design ID	Volumetric Ratio of Fibers (%)	f'_c (MPa)	f_{ct} (MPa)	E_c (GPa)	f_r (MPa)
LSC (Mix 1)	0	26.37	4	22.34	4
NSC (Mix 2)		38.66	5.30	28.94	4.71
HSC (Mix 3)		56.32	6.65	36.91	5.26
LSC (Mix 1)	0.5	27.35	4.59	24.53	5.4
NSC (Mix 2)		39.93	5.77	31.83	7.1
HSC (Mix 3)		61.39	7.14	36.17	7.52

Twelve standard cylinders 150×300 mm and two standard prisms 100×100×500 mm with each batch were tested to determine the mechanical properties of hardened concrete. In Table 4 values of concrete compressive strength f'_c, modulus of elasticity E_c, splitting tensile strength f_{ct}, and modulus of rupture f_r, at an age of 28 days are given for both ordinary and fibrous concrete. The stress-strain curves of the reinforcing bars and the concretes are shown in Figs. 4 and 5, respectively.

Columns Casting

A total of six batches of concrete were used to cast the columns. All columns were cast vertically to simulate typical construction practice of columns. Concrete was discharged in the columns directly from 0.1 m^3 capacity horizontal pan mixer in approximately 2 or 3 lifts. The mixing time was about 5-8 minutes; the dry constituents were well mixed for about 2 minutes to insure proper distribution of the ingredients and to disperse any agglomeration of the fine materials in the pan. For batches with superplasticizers, the added water was premixed with superplasticizer and mixed for 3 minutes. Batches contain steel fibers, the fibers were added carefully (to prevent balling) and mixed for another 3 minutes. An electric table vibrator was used to consolidate the concrete and to remove air bubbles at each of the lifts. The column formworks were stripped and de-molded approximately two days after casting and covered by fresh water inside the curing tanks at ambient temperature in the laboratory for about four weeks. After that the specimens were removed from the water and left to dry under laboratory conditions until testing.

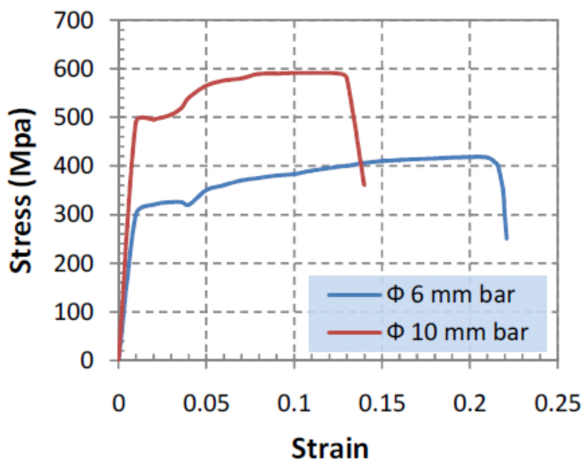

Fig. 4 stress-strain curves of reinforcing bars

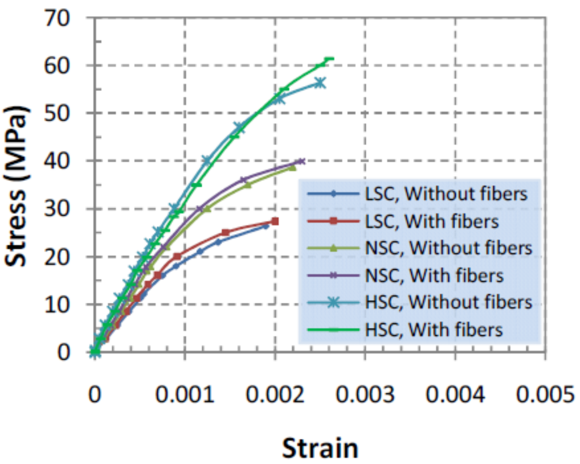

Fig. 5 stress-strain curves of concrete

Instrumentation and Testing Procedure

The columns gross axial shortening was measured using dial gauge of 0.01mm/div. sensitivity, located at the bottom surface of testing machine. Also, Demec points are used to measure the surface strains of concrete. They were mounted along the concrete surfaces within the test region of the tested samples. Two demec gauge points were mounted at spacing of 100 mm at the column mid-height along the column vertical axis to measure longitudinal compressive strains at two opposite directions of the column.

A 3000 kN capacity compression testing machine (MFL SYSTEME) located at Structures Laboratory of Al-Mustansiriya University, was used to apply the compression load monotonically until failure. Details of test set-up, distribution of demec points and location of dial gauge are shown in Fig. 6.

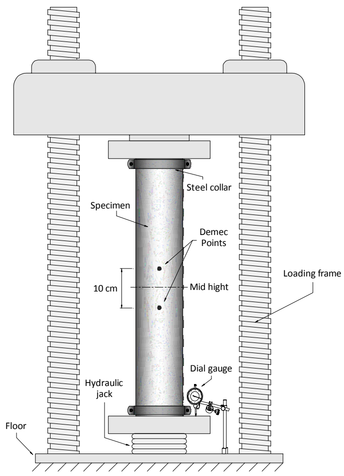

Plate 3 Failure mode of fibrous and nonfibrous columns

Fig. 6 Test set-up, distribution of demec points and location of dial gauge

FAILURE MODE OF COLUMN SPECIMENS

During testing of column specimens up to failure, it was observed that failure of unconfined columns is by the formation of the longitudinal cracks at certain location followed by cracks which propagated to other sides. It was also noticed that for unconfined high strength concrete specimens a sudden type of failure occurs, unless steel fibers were used. When columns cast with steel fibers the failure was ductile, small crack width and much less cover spalling was observed. It was also observed that, addition of steel fibers to high strength concrete columns resulted in small crack width, and crack propagation was gradual and premature concrete cover spalling of the columns was delayed. It could be noticed that the addition of steel fibers resulted in bulging of the central part of the columns relative to concrete columns without steel fibers, as shown in Plate 3.

For fiber reinforced columns, it can be seen that the steel fibers played a significant role in preventing concrete cover from early spalling. This is because steel fibers crosses the cracks and preventing from further widening and allowing other cracks to form at other locations. It seems that the presence of steel fibers is highly effective at load stages after peak where it was also observed then that the column bulging continues to increase without loss of column integrity which resulted in increasing the tensile stresses in the spirals leading to rupture of some of these spirals, as shown in Plate 4.

STRESS-STRAIN RELATIONSHIP OF THE TESTED COLUMNS

The stress strain curve of the column specimens consists of two main parts; ascending and descending.

Plate 4 Spiral rupture occurs before complete spalling of concrete cover (HSC-F-100)

divided into two distinct stages of behavior. The first stage is characterized by an approximately linear relationship between stress and strain. This behavior continued until the initiation of longitudinal cracks. The second stage begins when the concrete cover starts to spall out. At this stage the stiffness of the column decreased as indicated by the reduced slope of the stress-axial strain curves. The final stage occurred when the longitudinal reinforcement starts to bend and the core of concrete carries all the axial loading while the concrete cover is completely spall out at failure regions.

In Fig. 7 the relation between stress and strain of columns for various types of concrete are presented. A stiffer response in the pre-cracking stage is noted for columns with higher concrete compressive strength. Also, the ascending part of the curves for HSC specimens is nearly linear in comparison to both NSC and LSC specimens which shows a nonlinear response.

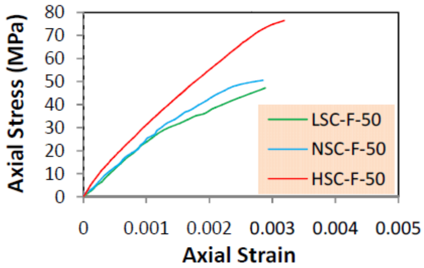

(a) Reinforced with 0.5% steel fibers

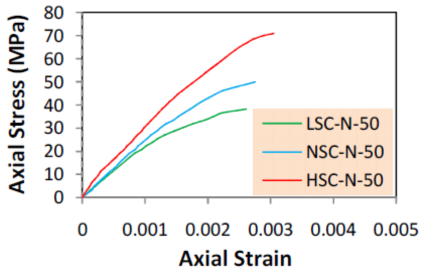

(b) Non-fiber concrete

Fig. 7 Effect of concrete strength on the stress-strain curves of column specimens

TEST RESULTS AND DISCUSSION

Axial Load Capacity of the Tested Columns

Fig. 8 shows the ultimate load capacity for all the tested columns. For fiber reinforced concrete columns, no significant variation in the peak load was observed compared to that of ordinary concrete columns.

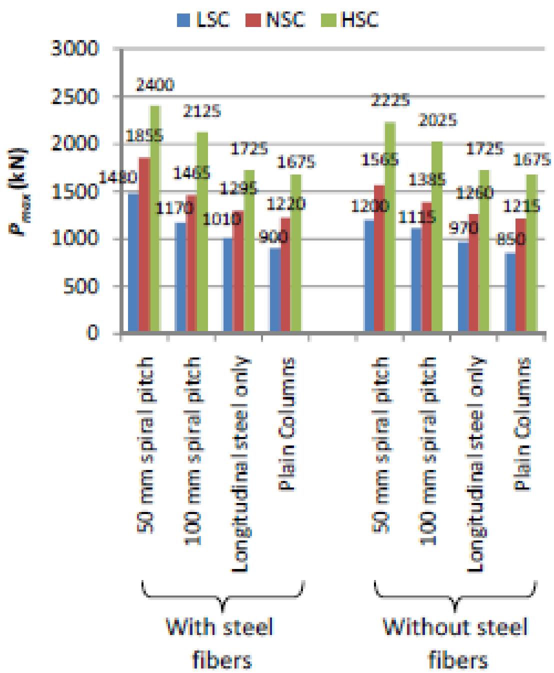

Fig. 8 Ultimate experimental load capacities P_{max} for tested columns

From Fig. 8 it can be seen that for nonfibrous columns, reducing the spacing of spiral steel from 100 mm to 50 mm increased the load capacity by about 8%, 13%, and 10% for LSC, NSC, and HSC respectively. Whereas for fibrous columns the load capacity increased by about 27%for LSC and NSC and 13% for HSC. It was also observed that the addition of steel fibers to concrete does not enhance the load capacity of unconfined columns, while little increase in load capacity is observed for confined columns. For columns with 50 mm spacing spirals, the increase in capacity is about 23%, 19%, and 8% for LSC, NSC, and HSC respectively. Test results showed that increasing concrete strength from 26 MPa to 60 MPa the load capacity of columns with 50 mm spacing spirals increased by about 85% or nonfibrous columns and 62% for fibrous columns.

Confined Concrete Strength by Spiral Reinforcement

Kim (2007) have indicated that the confined concrete strength f'_{cc} of columns can be determined by subtracting the calculated load carried by longitudinal reinforcement from the measured maximum load Pmax of the column, divided by the area of concrete core as follows:

$$f'_{cc} = \frac{P_{max} - (A_s f_y)}{A_c - A_s} \qquad (6)$$

where

f'_{cc} : Confined concrete strength of column,

P_{max}: Measured maximum load of column,

A_s : Total area of longitudinal reinforcement,

f_y : Yield strength of longitudinal steel,

A_c : Area of core measured to outside diameter of spiral steel.

In this paper Eq. (6) is used to calculate the confined concrete strength of the tested columns. The ratio of the confined strength of the tested reinforced concrete columns to the unconfined strength of similar column f'_{cc}/f'_{co} represents the strength enhancement of concrete. This enhancement of concrete strength was shown to be affected by the confinement parameter $\rho_s f_{sy}/f'_c$ as illustrated in Fig. 9.

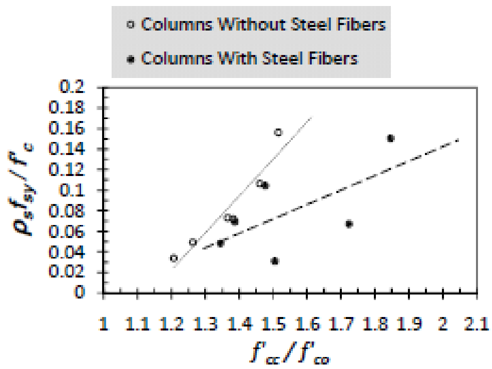

Fig. 9 Relationship between confinement parameter $\rho_s f_{sy}/f'_c$ and strength enhancement f'_{cc}/f'_{co}

Fig. 9 indicates that by increasing the confinement parameter $\rho_s f_{sy}/f'_c$ the strength enhancement f'_{cc}/f'_{co} considerably increased. Therefore, if the same level of strength enhancement f'_{cc}/f'_{co} is desired, columns with higher concrete strength should be reinforced with more lateral steel than those with lower concrete strength. Thus, the lateral confinement pressure required for high-strength concrete may be significantly higher than that for normal strength concrete. Saatcioglu and Razvi (1998) have also indicated that this requirement is usually met by using higher grades of spiral steel rather than increasing the volumetric ratio of reinforcement to avoid congestion of the column cage.

Fig. 9 also indicates that for the same confinement parameter $\rho_s f_{sy}/f'_c$ specimens with steel fibers posses higher strength enhancement compared to specimens without steel fibers. For confinement parameter of 0.1 the strength enhancement equal 1.7 for specimens with fibers while it is 1.4 for nonfibrous specimens. (i.e. an increase of about 20% relative to nonfibrous concrete columns).

An empirical expression was developed for the confined concrete strength f'_{cc} using regression analysis of 42 columns based on current test data and data of other researchers [Razvi 1995, Li 1994]. The obtained expression is a function of unconfined concrete strength and confining stresses provided by the spiral steel and steel fibers, as follows:

$$f'_{cc} = f'_{co} + 6.9(f_l + f_{lf})^{0.8} \qquad (7)$$

where

f'_{cc} : Axial compressive strength of confined concrete,

f'_{co} : Axial compressive strength of unconfined concrete,

f_l : Lateral confining stress provided by the spiral steel = $0.5\rho_s f_{sy}$,

f_{lf} : Lateral confining stress provided by steel fibers, Eq. (5).

The numbers 6.9 and 0.8 shown in Eq. (7) are constants obtained from nonlinear multiple stepwise regression analysis using Data Fit 9.0 software.

Comparison between the strength obtained using Eq. (7) and the experimental strength values based on Kim's Eq. (6) are presented in Fig. 10. The results indicate good agreement between the analytical and experimental strength values.

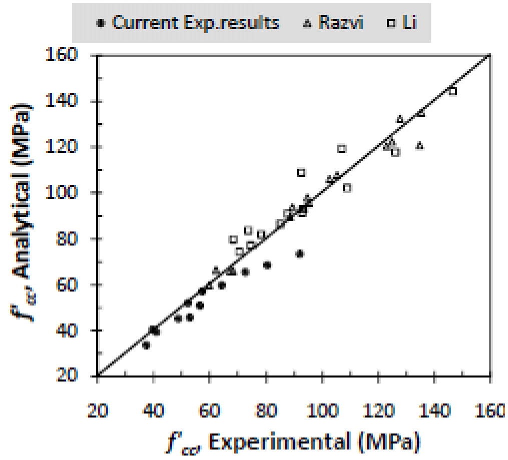

Fig. 10 Comparison between analytical confined strength using Eq. (7) and experimental strength values using Eq. (6)

Ductility of the Tested Columns

Since testing of columns was performed using load control procedure it was not possible to trace the response of the specimens after the peak load. For this reason the ductility of the tested columns were computed using the procedure developed by Foster and Attard (2001). It was observed that the addition of steel fibers significantly enhances the ductility of the tested columns. The tested columns with steel fibers were found to be able to deform lateral without loss of strength and the final failure was precipitated by large numbers of cracks and high lateral deformation.

For the above reasons an attempt has been made to separate the effect of spiral reinforcement contribution from steel fibers contribution in the equation developed by Foster and Attard (2001). This has been made by separating the equation into two parts and add them algebraically, as shown below:

$$(I_{10})_{Spiral} = 1.9\,ln(1000 \times 2k_e f_l/f'_c) \qquad (8)$$

$$(I_{10})_{Fibers} = 1.9\,ln(1000 \times 2f_{lf}/f'_c) \qquad (9)$$

$$I_{10} = (I_{10})_{Spiral} + (I_{10})_{Fibers} \qquad (10)$$

$$I_{10} = 1.9[\ln(1000 \times 2k_e f_l / f'_c) + \ln(1000 \times 2f_{lf} / f'_c)] \quad (11)$$

The ductility index I_{10} for various specimens was computed using Eq. (11) and the results are presented in Fig. 11.

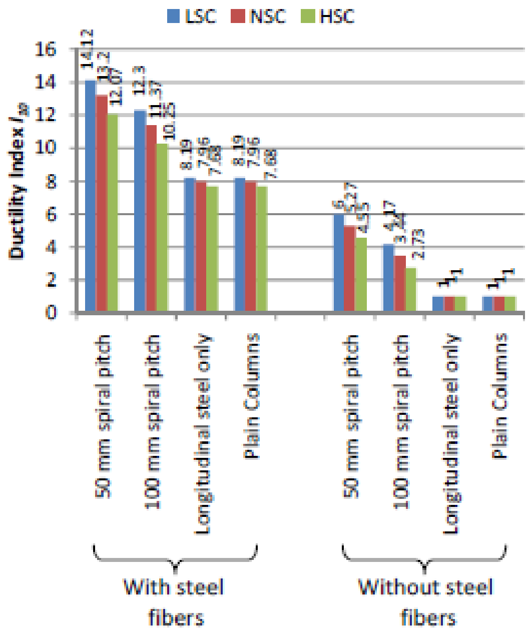

Fig. 11 Computed ductility Index I_{10} for columns using Eq. (9)

For columns confined by 50 mm spacing spirals, the addition of 0.5% by volume of steel fibers increases the ductility index I_{10} by about 135%, 150%, and 165% for LSC, NSC, and HSC respectively. Fig. 11 shows that for nonfibrous columns, increasing the confining stress by reducing the pitch of spirals from 100 mm to 50 mm cause an increase in column ductility index I_{10} by about 44%, 53%, and 67% for LSC, NSC, and HSC respectively. Test results showed that increasing concrete strength from 26 MPa to 60 MPa for columns with 50 mm spacing spirals resulted in reduction of ductility index I_{10} by about 24% for nonfibrous columns and 15% for fibrous columns.

CONCLUSIONS

1. Experimental tests show that columns without confinement failed shortly after the formation of vertical cracks, while columns confined with closely spaced spirals or having steel fibers shows a gradual bulging before failure takes place.
2. It was observed that the addition of steel fibers to concrete does not enhance the load capacity of unconfined columns, while little increase in load capacity is observed for confined columns. For columns with 50 mm spacing spirals, the increase in capacity is about 23%, 19%, and 8% for LSC, NSC, and HSC respectively.
3. The addition of steel fibers significantly enhances the ductility of the tested columns. For columns confined by 50 mm spacing spirals, the addition of 0.5% by volume of steel fibers increases the ductility index I_{10} by about 135%, 150%, and 165% for LSC, NSC, and HSC respectively.
4. Test results indicate that for the same confinement parameter $\rho_s f_{sy} / f'_c$, specimens with steel fibers has higher strength enhancement f'_{cc}/f'_{co} compared to specimens without steel fibers. For confinement parameter of 0.1 the strength enhancement equal 1.7 for specimens with fibers while it is 1.4 for nonfibrous specimens.
5. The proposed strength of confined columns given in Eq. (7), could predict the confined strength (f'_{cc}) of short concrete columns with good degree of accuracy.

REFERENCES

Al-Shamma Y. M. W., *"Strength and Ductility of Confined Concrete Short Columns,"* M.Sc. Thesis, Al-Mustansiriya University, Baghdad, Iraq, 2011, (presented and will be evaluated by the examining committee).

ASTM C1018, *"Standard Test for Flexural Toughness and First-Crack Strength of Fiber-Reinforced Concrete (Using Beam with Third-Point Loading),"* Annual book of ASTM standards, Vol. 04.02, pp. 8, 1997.

Campione G., Fossetti M., and Papia M., *"Behavior of Fiber-Reinforced Concrete Columns under Axially and Eccentrically Compressive Loads,"* ACI Structural Journal, Vol. 107, No. 3, pp. 272-281, May-June 2010.

Foster S. J. and Attard M. M., *"Strength and Ductility of Fiber-Reinforced High-Strength Concrete Columns,"* Journal of Structural Engineering, ASCE, Vol. 127, No. 1, pp. 28-34, January 2001.

Foster S. J., *" On Behavior of High-Strength Concrete Columns: Cover Spalling, Steel Fibers, and Ductility,"* ACI Structural Journal, Vol. 98, No. 4, pp. 583–589, 2001.

Ganesan N. and Murthy J. V. R., *"Strength and Behavior of Confined Steel Fiber Reinforced Concrete Columns,"* ACI Materials Journal, Vol. 87, No. 3, pp. 221-227, May 1990.

Hsu C. T. T., Hsu L. S. M., and Tsao W. H., *"Biaxially Loaded Slender High-Strength Reinforced Concrete Columns with and without Steel Fibers,"* Magazine of Concrete Research, Vol. 47, No. 173, pp. 299–310, 1995.

Kim S., *"Behavior of High-Strength Concrete Columns,"* PhD thesis, North Carolina State University, Raleigh, North Carolina, pp. 205, 2007.

Li B. *"Strength and Ductility of Reinforced Concrete Members and Frames Constructed Using High Strength Concrete."* Res. Rep. No. 94-5, University of Canterbury, Christchurch, New Zealand, pp. 389, 1994.

Lima Junior H.C., Giongo J.S., *"Steel Fibre High Strength Concrete Prisms Confined by Rectangular Ties under Concentric Compression,"* Materials and Structures, Vol. 37, No. 10, pp. 689–697, 2004.

Mander J. B., Priestley M. J. N., and Park R., *"Theoretical Stress-Strain Model for Confined Concrete,"* Journal of Structural Engineering, ASCE, Vol. 114, No. 8, pp. 1804-1826, August 1988.

Marti P., Pfyl T., Sigrist V. and Ulaga T., *"Harmonized Test Procedure for Steel Fibre-Reinforced Concrete,"* ACI Materials Journal, Vol. 96, No. 6, pp. 676-685, 1999.

Martinez S., Nilson A. H., and Slate F. O., *"Spirally Reinforced High-Strength Concrete Columns,"* ACI Journal, Vol. 81, No. 5, pp. 431-442, Sep. 1984.

Razvi S. R. and Saatcioglu M., *"Strength and Deformability of Confined High-Strength Concrete Columns,"* ACI Structural Journal, Vol. 91, No. 6, pp. 678-687, 1994.

Razvi S., *"Confinement on Normal and High Strength-Concrete Columns,"* PhD Thesis, University of Ottawa, Ottawa, Canada, pp. 416, 1995.

Saatcioglu M. and Razvi S. R., *"High-Strength Concrete Columns with Square Sections under Concentric Compression,"* Journal of Structural Engineering, ASCE, Vol. 124, No. 12, pp. 1438-1447, Dec. 1998.

Sheikh S. A. and Uzumeri S. M., *"Strength and Ductility of Tied Concrete Columns,"* Journal of Structural Engineering, ASCE, Vol. 106, No. 5, pp. 1079-1102, May 1980.

Tokgoz S., *"Effects of Steel Fiber Addition on the Behavior of Biaxially Loaded High Strength Concrete Columns,"* Journal of Materials and Structures, Vol. 42, No. 8, pp. 1125-1138, 2009.

NOTATION

A_c	Area of the column core: the area enclosed inside the perimeter of the centre lines of spirals or ties
A_g	Gross sectional area of the column
d_f	Fiber diameter
d_s	Diameter of the column core measured between the spiral centers
E_c	Modules of elasticity of concrete
f'_c	Cylinder compressive strength of

concrete

f'_{cc} Axial compressive strength of confined concrete

f'_{co} Plain concrete strength in a member

f_{ct} Splitting tensile strength of concrete

f_l Lateral confinement stress provided by the spiral steel

f_{lf} Lateral confinement stress provided by the steel fibers

f_r Modulus of rupture of concrete

f_{sy} Yield strength of spiral steel.

f_y Yield strength of longitudinal reinforcement

I_{10} Ductility index

k_e Confinement effectiveness coefficient ($k_e \leq 1$)

l_f Fiber effective length

P_{max} Measured maximum load of column

s Spacing or pitch of spiral

s' Clear spacing between spiral or hoop bars

α_f Fiber aspect ratio = l_f/d_f

Δ_y Deflection at yield stress

Δ_{85} Deflection at 85 % of the maximum axial load on the descending branch of the axial load - deflection curve

ρ_{cc} Ratio of longitudinal reinforcement area
to concrete core area

ρ_f Volumetric ratio of steel fibers

ρ_l Ratio of longitudinal reinforcement area to concrete gross area

ρ_s Volumetric ratio of spiral reinforcement

τ_b Fiber-Concrete bond shear strength

EXHAUST ANALYSIS AND PERFORMANCE OF A SINGLE CYLINDER DIESEL ENGINE RUN ON DUAL FUELS MODE

Miqdam Tariq Chaichan
Lecturer-Mechanical Eng. Dep.-University of Technology

ABSTRACT

Generally fossil based fuels are used in internal combustion engines as an energy source. Excessive use of fossil based fuels diminishes present reserves and increases the air pollution in urban areas. This enhances the importance of the effective use of present reserves and/or to develop new alternative fuels, which are environment friendly. Use of alternative fuel is a way of emission control. The term "Alternative Gaseous Fuels" relates to a wide range of fuels that are in the gaseous state at ambient conditions, whether when used on their own or as components of mixtures with other fuels.

In this study, a single cylinder diesel engine was modified to use LPG in dual fuel mode to study the performance, emission, and combustion characteristics. The primary fuel, liquefied petroleum gas (LPG), was mixed with air, compressed, and ignited by a small pilot spray of diesel. Dual fuel engine showed a reduction in oxides of nitrogen in the entire load range. The brake thermal efficiency improved by 3% in dual fuel mode, especially at low load, and also reduced the hydrocarbon, carbon monoxide, and CO_2 emissions.

تحليل أداء وملوثات محرك ديزل أحادي الاسطوانة يعمل بنظام وقود ثنائي

الخلاصة

يستخدم الوقود الاحفوري بشكل عام كمصدر طاقة لمحركات الاحتراق الداخلي، وتسبب الاستخدام المفرط لهذا الوقود بنضوب معظم مصادرة اضافة الى تلوث الهواء في المساحات المدينية، ولهذا تركز الأهتمام على الاستخدام الفعال للمصادر الحالية للطاقة أو تطوير مصادر وقود جديدة، تكون صديقة للبيئة. إن استخدام الوقود البديل هو طريقة للسيطرة على التلوث، وتعبير " الوقود الغازي البديل" يرتبط بعدة أنواع من الوقود تكون بالحالة الغازية في ظروف الجو الأعتيادية، سواء استخدمت بمفردها أو مشتركة ومخلوطة مع وقود أخر.

في هذة الدراسة، تم تحوير محرك ديزل أحادي الاسطوانة ليستخدم الغاز النفطي المسال باسلوب الوقود الثنائي، لدراسة خصائص الأحتراق كأداء وملوثات المحرك. يتم خلط الغاز النفطي المسال (الوقود الابتدائي) بالهواء، يضغط بعدها ثم يشعل بواسطة كمية صغيرة من وقود ديزل محقون. أظهر محرك الوقود الثنائي نقصانا في ملوثات أكاسيد النيتروجين لكافة الاحمال المستخددمة، كما تحسنت الكفاءة الحرارية بمقدار 3% في هذة الحالة، كما قلت ملوثات الهيدروكاربونات غير المحترقة وأول أكسيد الكاربون وثاني أكسيد الكاربون.

KEY WORDS

Diesel engine; Dual fuel engine; Liquefied petroleum gas (LPG), Exhaust emissions; Alternative fuel, reduction in pollutant emissions and fuel consumption

INTRODUCTION

Global pollution caused by transport consists primarily of the emissions from transport systems during manufacture, operation and disposal of the greenhouse gases. These gases include the direct greenhouse gases such as carbon dioxide and methane, the ozone precursors such as hydrocarbons and the nitrogen oxides, and carbon monoxide which have an indirect effect on greenhouse gas production. The problem of global pollution from transport activities is centered on the use of fossil fuels for transport. These fuels are mainly in the form of gasoline and diesel oil for road transport, kerosene for air transport, and diesel oil for rail transport, industrial application, shipping etc (Selim, 2005 and Lakshmanan, 2009).

Gaseous fuels promise to be suitable for higher compression ratios engines, since it is known that they resist knock more than conventional liquid fuels, as well as producing less polluting exhaust gases if appropriate conditions are satisfied for its mixing and combustion (Yousufuddin, 2008). Therefore, it is more economical and of environmental advantage to use gaseous fuel in diesel engines that use the dual fuel concept. There have been many published works on the use of gaseous fuels in dual fuel engines. Natural gas use in dual fuel engines has been studied from the combustion duration and ignition delay point of view (Stanislav, 2001) and from the performance and emissions point of view (Abd Alla, 2002). Combustion and thermal loading and temperature distribution have also been studied for dual engines (Karim, 1991). Pure methane has also been studied in dual fuel engines from the flame spread limits point of view (Papagiannakis, 2003) and performance and emissions point of view (Selim, 2004).

The potential benefits of using LPG in diesel engines are both economical and environmental. In the dual fuel engines, the gaseous fuel is inducted along with the air, and this mixture of air and gas is compressed like in conventional diesel engines. A small amount of diesel, usually called the pilot, is sprayed near the end of the compression stroke to initiate the combustion of the inducted gas air mixture (Vijayabalan, 2009). With reduced energy consumption, the dual fuel engine shows a significant reduction in smoke density, oxides of nitrogen emission, and improved brake thermal efficiency. The combustion of this pilot diesel leads to flame propagation and combustion of the gaseous fuel. The engine can be run in the dual fuel mode without any major modification, but is usually associated with poor brake thermal efficiency and high HC & CO emissions at low loads (Ma, 2007 and Salman, 2004).

The increase in pilot diesel improves the brake thermal efficiency at low loads. At higher loads, it reduces efficiency due to rapid combustion. Low efficiency and poor emissions at light loads can be improved significantly by advancing injection timing of the pilot fuel. Any measures that lower the effective lean flammability limit of charge and promote flame propagation will improve part load performance (Heng, 2008).

According to the characteristics of LPG (table 1) there are following specialties in the engine:

- LPG high ignition temperature and safety: In the normal temperature it can be liquefied at 1.6MPa 2Mpa which makes it easy to use.
- LPG has high heat value, with its gaseous state makes it easy to mix with air. It has perfect combustion redounds to improve power output, as well as, good antiknock because of high octane (Saleh, 2008).
- Soot can be obviously reduced because low carbon compound. Also the accumulative soot layer can be reduced in combustion chamber (Benea, 2007).
- Gas fuel will not dilute the engine lubrication oil. The replacement period of lubrication oil could be longer (Qi, 2007).

But ignition time delay of LPG is longer because the low cetane number. Moreover the volumetric efficiency of LPG is lower. It must make fully use of advantages of LPG and improve the power and economy of engine and reduce the pollutant. In order to reach this object, it must optimize structure and operating parameters of the engine (Sethi, 2004).

The present study is concerned with the reduction of diesel engine exhaust emissions. For this purpose, a single cylinder, indirect injection diesel engine was modified to operate with dual fuel. During the experimental study the engine was run with (30% and 60%) LPG and (70% or 40%) diesel fuel (by volume) and changes in engine performance and exhaust emissions were observed.

EXPERIMENTAL TECHNIQUE

The test rig used in the present study is the Ricardo E6 single cylinder variable compression indirect injection diesel engine. The specifications of the engine are listed in **Table 2**. The engine cylinder head has a Ricardo Comet Mk V compression swirl combustion chamber. This type of combustion system consists of two parts. The swirl chamber in the head has a top half of spherical form and the lower half is a truncated cone which communicates with the cylinder by means of a narrow passage or throat. The second part consists of special cavities cut into the crown of the piston. The engine is capable to run on 100% diesel fuel or dual fuel. The engine is converted to run on dual fuel by introducing the gaseous fuel, LPG in the present work, in the intake manifold by means of a gas adapter. The gas is injected at a pressure slightly higher than atmospheric pressure.

The schematic diagram for the engine test rig is shown in **Fig. 1**. The engine is loaded by an electrical dynamometer rated at 22 kW and 420 V. The engine is fully equipped for measurements of all operating parameters. The liquid fuel flow rate is measured by means of two tanks, main tank (9 liters) and secondary tank (1 liter), with a set of valves to close and open fuel line, and a fuel flow measurement devise. The gaseous fuel flow rate is measured by using an orifice meter connected to electronic partial pressure transducer that is connected to a digital pressure meter.

The Multigas mode 4880 emissions analyzer was used to measure the concentration of nitrogen oxide (NOx), unburned total hydrocarbon (HC), CO_2 and CO. This divice was calibrated at Central Organization for Standardization and Quality Control in Baghdad-Iraq.

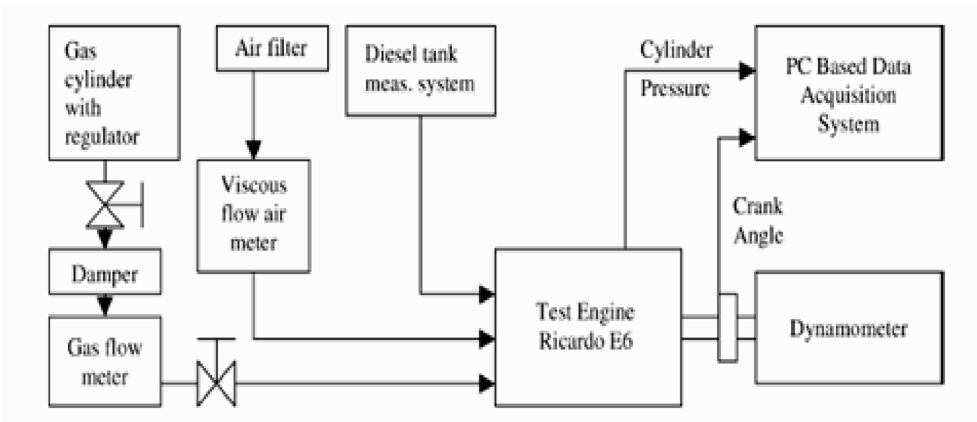

Fig. 1, Schematic diagram of the engine test rig.

Experiments have been carried out after running the engine for some time until it reaches steady state and oil temperature is at 60 ^{o}C±5, and cooling water temperature is at

70 ^{o}C±5. The engine design and operating parameters have been varied at the following levels:

1. Type of fuel included pure diesel fuel (base case as normal diesel engine), dual fuel of diesel and LPG.
2. The engine load was varied from no load to full load.
3. The pilot diesel fuel injection timing was varied from 20 to 45 ^{o}BTDC in steps of 5^{o}.
4. The engine speed was varied from 1000 to 2100 rpm.

In the first case, engine was operated with liquefied petroleum gas (LPG), which was mixed with suction air having 30 and 60% LPG on volume basis along with the pure diesel through timed cylinder injection. The fuel injection system was adjusted to supply lesser diesel during the operation with air-LPG mixture for smooth operation. Tests of engine performance and exhaust emissions on diesel fuel alone were conducted as a basis for comparison. Engine was run on no load condition and its speed was adjusted to 1500 rpm + 20 rpm by adjusting the screw provided with the fuel injector pump. The engine was run to attain uniform speed, and then it was gradually loaded. The experiments were conducted at full load level, and the engine was run for at least 3 min at that load. The experiments were replicated three times.

A simple, low cost air-LPG mixing device, designed as shown in **Fig. 2**, was used to mix LPG with inlet air during suction stroke.

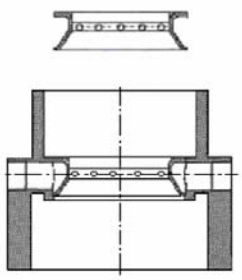

Fig.2 The cross sectional drawing of the mixer

RESULTS and DISCUSSIONS

LPG introduced as gas in the combustion chamber, so its proportion took a part of air share, this reduction in air volume reflected as a reduction in volumetric efficiency of duel engine compared with diesel engine, as **Fig. 3** represents.

For the load characteristics at 1500 rpm, a comparison between the bsfc of LPG–diesel dual fuel and diesel is shown in **Fig. 4**. The bsfc of both engines are almost equal when the load ratio is less than 35 per cent, when the load ratio is larger than 35 per cent, the bsfc of dual fuel is slightly less than that of diesel. The dual-fuel can be electronically controlled that the engine is fuelled with dual fuel when its load ratio is larger than 35 percent and with diesel when its load ratio is less than 35 percent.

Fig. 5 shows the relationship of brake thermal efficiency and brake power for the two fuel systems. Increasing LPG portion to 60% increased indicated thermal efficiency, due to high calorific value of LPG with low mass used in this mode, compared with diesel fuel.

Fig. 6 represents the relationship between exhaust gas temperatures and bp. Exhaust gas temperatures increased with load increase, and reduced with increasing LPG in mixture. Engine operation at optimum injection timing with LPG presence, gave fast and efficient combustion, so when the piston run down in power stroke, all the fuel had been burned, and all burned gases would be cooled in this stroke before exhaust valve opened, emitting lower exhaust gas temperatures.

The comparison between bmep of the external characteristics of LPG–diesel dual fuel and diesel at variable engine speeds is shown in **Fig. 7**. The bmep of the dual fuel is slightly less than that of diesel at low speeds, so the dynamic characteristic of the dual-fuel engine almost does not decline. Although the LPG pre-mixture causes a small decrease in the engine's intake air amount, the torque of dual fuel is almost equal to that of diesel which makes the heat value of the mixture in the cylinder recover, and dual fuel has a higher combustion efficiency than diesel.

The comparison between the bsfc's of LPG–diesel dual fuel and diesel is shown in **Fig. 8**. The bsfc of dual fuel is less than that of diesel. Because of the good quality of the mixture and high combustion efficiency of dual fuel, the bsfc of dual fuel at full load is low.

During the experiment, injection timings were adjusted based on the opening time of the needle 5^{o}crank angle (CA) before top dead center (BTDC) each time. **Fig. 9** shows engine brake specific fuel consumption versus fuel injection timings fueled with two duel fuels and neat diesel. The results show that the brake specific fuel consumption decreases remarkably when operating on the duel mode. The brake specific fuel consumption of the fuels has the minimum value at the fuel injection timing of 27^{o}BTDC (in 60% LPG case) and at 30^{o}BTDC (in 30% LPG cases). The brake specific fuel consumption increased sharply while retarding the fuel injection timing. It is noted that further retarding fuel injection timing was not appointed in this study due to the rapid increase in brake specific fuel consumption under the speed conditions. The brake specific fuel consumption decreased with the increase of LPG proportion in the mixture and the decreasing trend becomes gentle.

Fig. 10 shows the bmep versus the fuel injection timings. Retarding injection timing increases the cylinder air temperature at the timing of fuel injection beginning. This will Cause high increament in vaporization of injected fuel inside the cylinder. This leads to decrease in both the physical preparing time and the chemical reaction time before ignition starts, resulting in shortening the ignition delay. Advancing injection timing in the other hand will improve combustion, especially for LPG mixtures, causing higher bmep.

Retarding injection timing increased exhaust gas temperatures, as well as, increasing the LPG proportion in the blends, as **Fig. 11** indicates. Retarding injection timing decreases the ignition delay and leading the fuel to burn after the piston move from TDC, resulting in increaments in the exhaust gas temperatures. The good mixing of LPG in air increases the combustible mixture available during the ignition delay period. This leads to increase heat released in the premixed combustion phase, and increases the peak cylinder pressure and maximum heat release rates at combustion period. These gases will run out at lower temperatures after the results are being cooled at power stroke, and at exhaust stroke.

CO concentrations for duel mode approached the resulted concentrations for diesel with little reductions at some F/A ratios, as **Fig. 12** shows, the reason for lower emission is the increased burning temperature which created local turbulence and increased flame velocity.

The effect of engine speed on CO emissions is shown in **Fig. 13**. At full load, The CO concentrations of dual fuel is almost exceeded to that of diesel fuel at low speeds, and reduced away from them at medium and high speeds. The formation of CO is related to the mixture concentration and fuel composition.

Fig. 14 shows the effect of fuel injection timings on exhaust CO emission. Exhaust CO emission increased while retarding the fuel injection timings, and decreased with increasing the LPG proportion in the blends. Retarding the fuel injection timing decreases the amount of fuel burned in the premixed combustion phase and increases the amount of fuel burned in the subsequent diffusive combustion phase. The latter phase always takes place in a rich mixture environment and easily produces the incomplete burning product CO. Increasing the LPG proportion in the blends decreases the carbon fraction in the blends.

CO_2 concentrations reduced with duel mode for all examined F/A ratios, as **Fig. 15** represents. LPG existence increased hydrogen to carbon percentage in the fuel, which improved the combustion and reduced resulted CO_2.

Fig. 16 shows the effects of fuel injection timings on exhaust CO_2 emissions. CO_2 emission increased while retarding the fuel injection timings and it decreased with increasing the LPG proportion in the fuel mixture, and when working with optimum injection timing. The molecular structure of LPG is simpler than that of diesel fuel and can be oxidized more easily, as well as increasing the LPG proportion in the blends decreased the carbon fraction in the blends.

The variation of NOx emission with load at variable fuel- air ratios is shown in **Fig. 17**. It increased marginally in the case dual fuel operation as well as in case of neat diesel fuel, but for duel mode the resulted concentrations were less than that for diesel. LPG fuel forms a homogeneous mixture with air, and it leads to nearly complete combustion, resulting in high temperature inside the engine during combustion. It increases the possibility of NOx formation, but high temperatures leads to high dissociation rates. The resultants of these reactions will freeze when the piston goes down in power stroke, and combustion chamber cooled by cooling water. Also, the pre-chamber combustion figure improves turbulence and complete burning. Moreover working with OIT reduced the time available for NOx formation. The resultant NOx concentrations were the outcome of all these parameters.

The comparison between the nitrogen oxides (NOx) emissions of the dual fuel and diesel at variable engine speeds is shown in **Fig. 18**. The NOx emission of dual fuel is almost less than that of diesel at many speeds ranges. The change in the creation of NOx is determined by factors such as the mixture concentration and the combustion temperature, which are slightly changed. Therefore, the NOx emission is slightly changed.

The effect of fuel injection timings on NOx emission is given in **Fig. 19**. The study shows that both the fuel injection timing and LPG proportion in the mixtures affect exhaust NOx emission remarkably. The concentration of NOx decreased while retarding the fuel injection timings and increased with increasing the LPG proportion in the blends. Retarding the fuel injection timing reduces ignition delay period, causin reductioins in the amount of heat released, cylinder gas temperature and the exhausted NOx. Increasing LPG proportion increases the ignition delay period, the amount of heat release, and the cylinder gas temperatures. This will contribute to increase NOx emission. The emitted NOx concentration will be the resultant of these two parameters. So, some measures need to be implemented to reduce NOx emission when operating with the diesel-LPG blends such as exhaust gas recirculation.

Fig. 20 shows unburned hydrocarbons (UBHC) concentrations for tested fuels at variable fuel-air ratios, the results prove that using LPG in duel mode reduced UBHC for all tested ratios, contrary to reference (Gunea, 1998) who demonstrated increase in HC emissions with duel mode, may be because the researchers didn't use optimum injection timing for tested fuels as took place in this study.

The comparison between the HC emissions of the dual fuel and diesel for variable engine speeds is shown in **Fig. 21**. At full load, the HC emission of dual fuel is higher than that of diesel, which is caused by two key factors; the first is that the LPG pre-mixture is scavenged to outside from the cylinder in the overlap period of the valves. The second is that the LPG pre-mixture that is pressed into the cooled crevices during compression stroke is difficult to burn.

Fig. 22 shows the effects of fuel injection timings on exhaust HC emission. HC emission increases while retarding the fuel injection timings and it decreases with increasing the LPG proportion in the fuel mixture. Over-lean and over-rich mixtures will increase exhaust HC emission. The high cylinder gas temperature will promote the post flame HC oxidation. Furthermore, the molecular structure of LPG is simpler than that of diesel fuel and can be oxidized more easily. The total HC emission decreases while increasing the LPG proportion in the blends. The study also indicates that the effect of LPG in the mixtures on the reduction of HC emission is stronger than that from advancing the fuel injection timing. Thus, diesel-LPG duel fuel is beneficial to the reduction of HC emission.

CONCLUSIONS

Experiments were conducted to study the performance and emission characteristics of IDI diesel engine in dual fuel mode of operation. Liquefied petroleum gas was introduced in the inlet manifold for various loads, with diesel as an ignition source. The following conclusions have been arrived at,

1. Dual fuel operation of LPG exhibits lower exhaust gas temperatures as compared to diesel operation.
2. A perceivable reduction in HC, CO and CO_2 emissions was observed with LPG operated dual fuel mode.
3. The brake specific fuel consumption of the engine fueled with diesel-LPG blends is lower than that of diesel fuel under the optimum injection timings.
4. At the same engine speed and brake mean effective pressure, engine exhausts HC, CO, and CO_2 emissions increased and exhaust NOx emission decreased while retarding the fuel injection timing. Exhaust HC, CO, and smoke emissions decreased and exhaust NOx emission increased while increasing the LPG proportion in the mixtures.

The exhaust emissions (NOx and UBHC) were improved in dual fuel operation. This indicates that fuel property is one of the most important parameters, which affects the exhaust emissions. Diesel powered engines can be converted to operate with dual fuel. So the air quality will be better. LPG can be introduced to the intake manifold to obtain the precise control of the amount of fuel, admitting to the cylinder. Also, by increasing the LPG proportion in dual fuel operation a further improves in exhaust emissions can be obtained.

REFERANCES

Abd Alla G H, Soliman H A, Badr O A and Abd.Rabbo M F, Effect of injection timing on the performance of a dual fuel engine, Energy Conversion and Management, vol. 43, No.2, pp: 269-277, 2002.

Benea B C and Soica A O, Researches regarding using LPG on diesel engine, Fascicle of Management and Technological Engineering, vol. VI (XVI), 2007.

Heng T Y, Briggs H G, Mustafa K F, Performance Characterization of a Direct Injection LPG Fuelled Two-Stroke Motorcycle Engine, SAE paper No.2008-32-0045, 2008.

Karim G A, An Examination of some measures for improving the performance of gas fuelled diesel engine at light load. SAE Transactions, 912366, 1991.

Lakshmanan T and Nagarajan G, Performance and Emission of Acetylene-Aspirated Diesel Engine, Jordan Journal of Mechanical and Industrial Engineering, vol. 3, No. 2, 2009.

Ma Z, Huang Z,Li C,Wang X, and Miao H, Effects of Fuel Injection Timing on Combustion and Emission Characteristics of a Diesel Engine Fueled with Diesel-Propane Blends, Energy & Fuels,vol. 21, pp:1504-1510, 2007.

Papagiannakis R G and Hountalas D T, Experimental investigation concerning the effect of natural gas percentage on performance and emissions of a DI dual fuel Diesel engine, Applied Thermal Engineering, vol. 23, No. 3, pp: 353-365, 2003.

Qi D H, Bian Y ZH, Ma ZH Y, Zhang CH H and Liu SH Q, Combustion and exhaust emission characteristics of a compression ignition engine using liquefied petroleum gas-Diesel blended fuel. Energy Conversion and Management, vol. 48, No.2, pp: 500 -509, 2007.

Saleh H E, Effect of variation in LPG composition on emissions and performance in a dual fuel diesel engine. Fuels, vol. 87, No.13-14, pp: 3031-3039, 2008.

Salman S, Çinar C, Hasimoglu C, Topgul T and Civiz M, The effects of duel fuel operation on exhaust emissions in diesel engines, TEKNOLOJİ, vol. 7, Issue 3, pp: 455-460, 2004.

Selim M Y E, Sensitivity of dual fuel engine combustion and knocking limits to gaseous fuel composition, Energy Conversion and Management, vol.45, pp: 411–425, 2004.

Selim M Y E, Effect of engine parameters and gaseous fuel type on the cyclic variability of dual fuel engines, Fuel, vol. 84, pp: 961–971, 2005.

Sethi V P and Salariya K S, Exhaust Analysis and Performance of a Single Cylinder Diesel
Engine Run on Dual Fuels, IE (I) Journal.MC vol. 85, April, 2004.

Stanislav B, The development of gas (CNG, LPG and H_2) engines for buses and trucks and their emission and cycle variability characteristics. SAE Transactions, 2001-01-0144, 2001.

Vijayabalan P and Nagarajan G, Performance, Emission and Combustion of LPG Diesel Dual Fuel Engine using Glow Plug, Jordan Journal of Mechanical and Industrial Engineering, vol. 3, No. 2, 2009.

Yousufuddin S and Mehdi S N, Performance and Emission Characteristics of LPG-Fuelled Variable Compression Ratio SI Engine, Turkish J. Eng. Env. Sci., 32, 7 – 12, 2008.

Table 1 Properties of fuels used

Property	Diesel	LPG
Calorific value , kJ/kg	44500	50000
Self ignition temperature, ºC	725	525
Boiling point range , ºC	260-320	-34
Ignition delay period, s	0.002	-
Flame propagation rate, cm/s	10.5	83.7
Flame temperature, ºC	1715	1985
Surface tension, dynes	32	-
Viscosity at 39 ºC, centistokes	2.7	-
Specific gravity at 32 ºC	0.83	0.43
Sulpher content by weight, %	0.8	0.0112

Table 2 Engine characteristics

Model	Ricardo E6
Type	IDI with the pre-combustion chamber
Number of cylinders	1
Bore × Stroke (mm)	76.2×111.1
Cycle	4-stroke
Compression ratio	From 5 to 22
Maximum power (kW)	9 naturally aspirated
Maximum speed (rpm)	3000
Injection timing	Variable

Nomenclature

ATDC	After top dead center
BTDC	Before top dead center
ºCA	Crank angle degrees
CO	Carbon monoxide
CO_2	Carbon dioxide
CR	Compression ratio
FAR	Fuel-air ratio
OIT	Optimum injection timing
NOx	Nitrogen oxides
UBHC	Unburned hydrocarbons
bmep	Brake mean effective pressure
bp	Brake power
bsfc	Brake specific fuel consumption

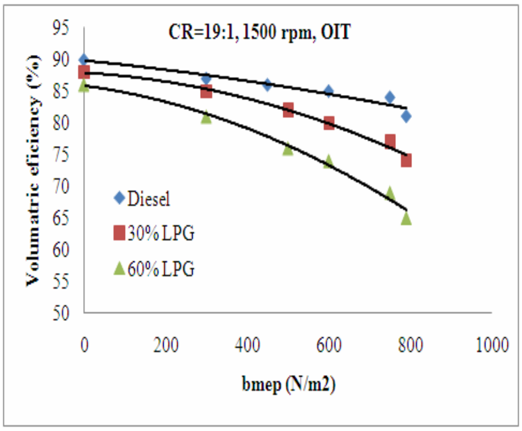

Fig. 3, Effect of LPG addition on volumetric efficiency at variable loads

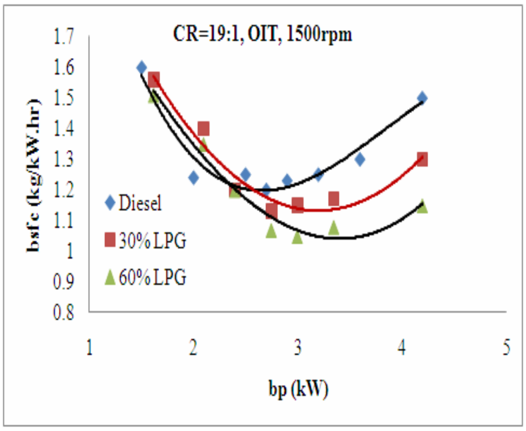

Fig. 4, Effect of LPG addition on bsfc at variable brake powers

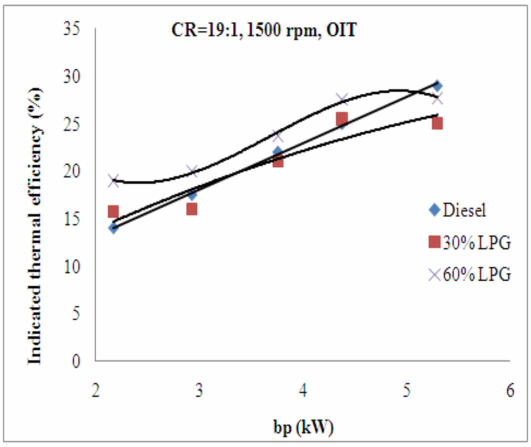

Fig. 5, Effect of LPG addition on indicated thermal efficiency at variable brake powers

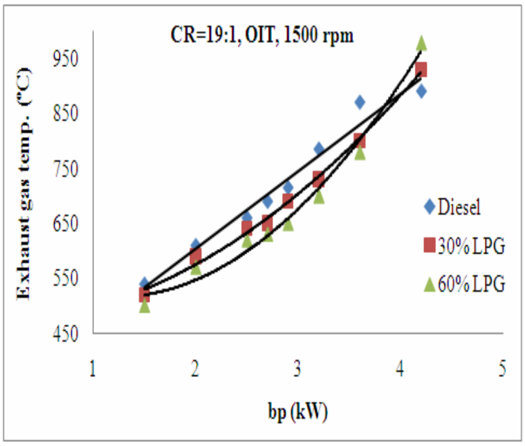

Fig. 6 Effect of LPG addition on exhaust gas temperatures at variable loads

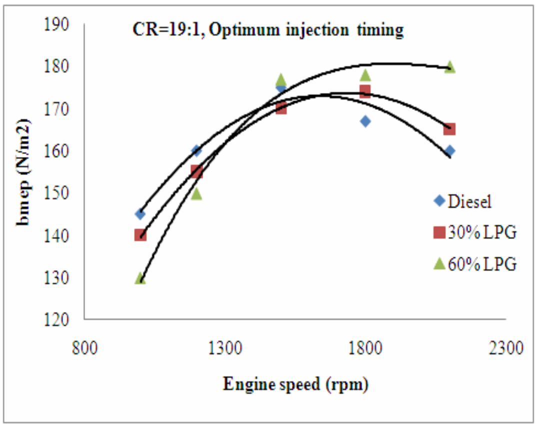

Fig. 7, Effect of LPG addition on bmep at variable engine speeds

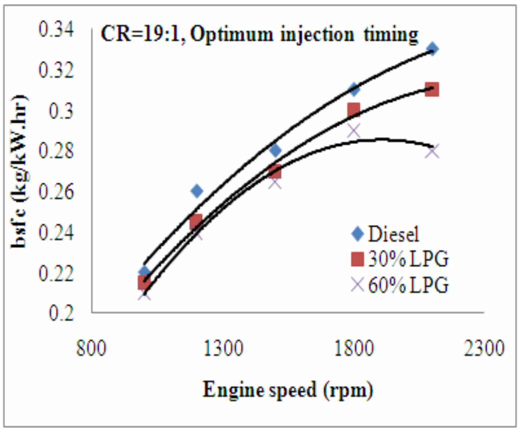

Fig. 8, Effect of LPG addition on bsfc at variable engine speeds

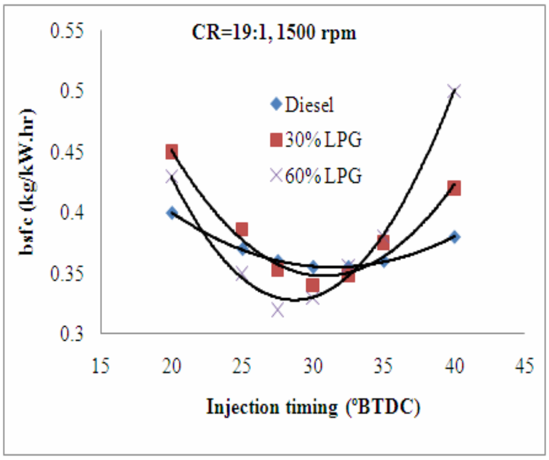

Fig. 9, Effect of LPG addition on bsfc at variable injection timing

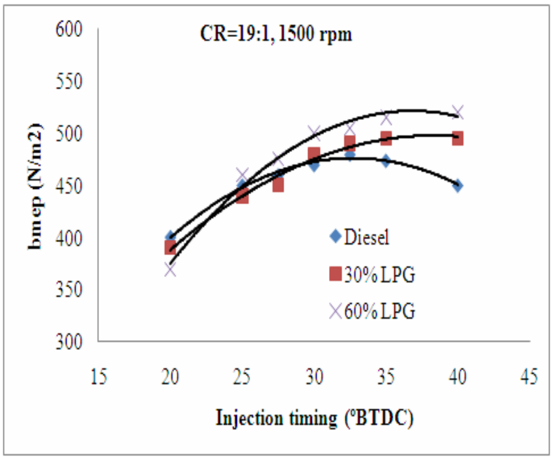

Fig. 10, Effect of LPG addition on bmep at variable injection timing

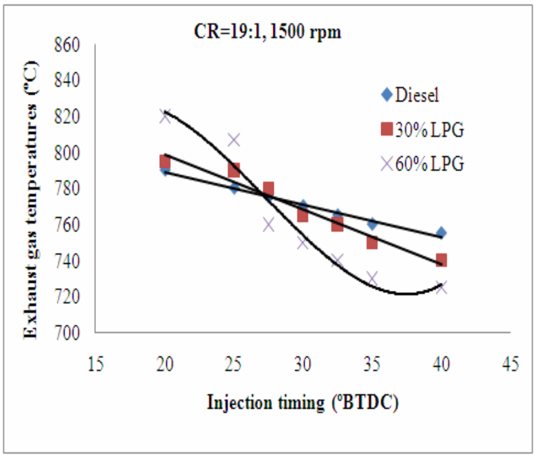

Fig. 11, Effect of LPG addition on exhaust gas temperatures at variable injection timing

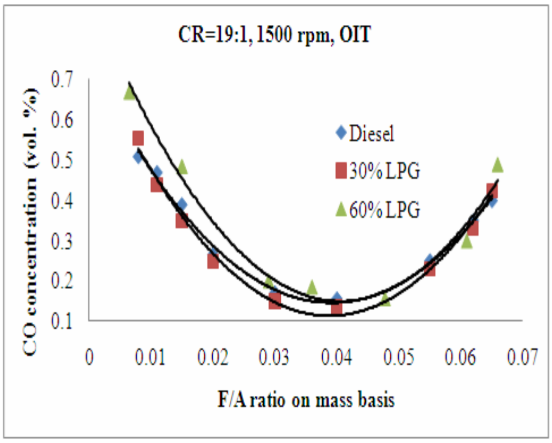

Fig. 12, Effect of LPG addition on CO concentrations at variable fuel-air ratios

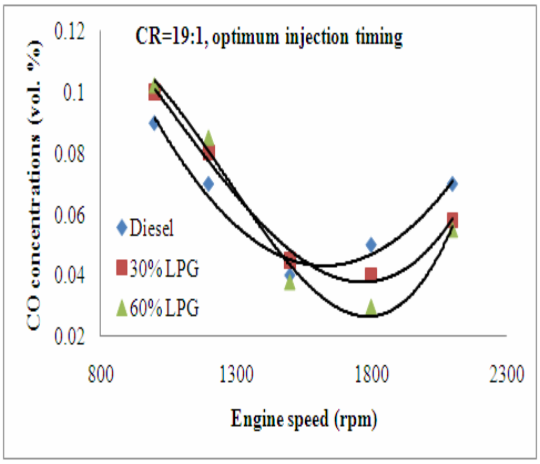

Fig. 13, Effect of LPG addition on CO at variable engine speeds

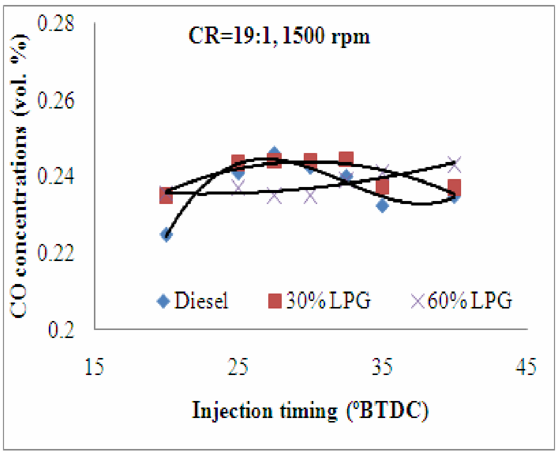

Fig. 14, Effect of LPG addition on CO at variable injection timing

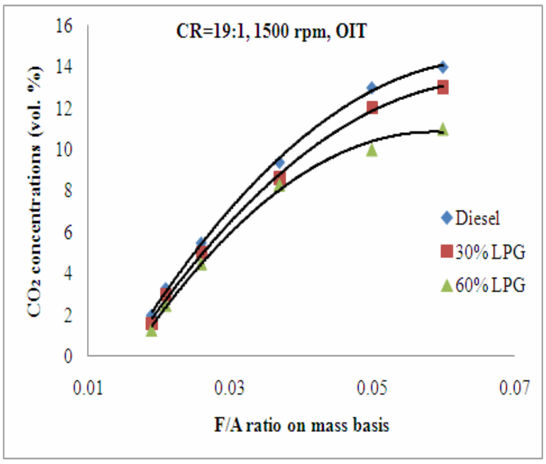

Fig. 15, Effect of LPG addition on CO_2 concentrations at variable fuel-air ratios

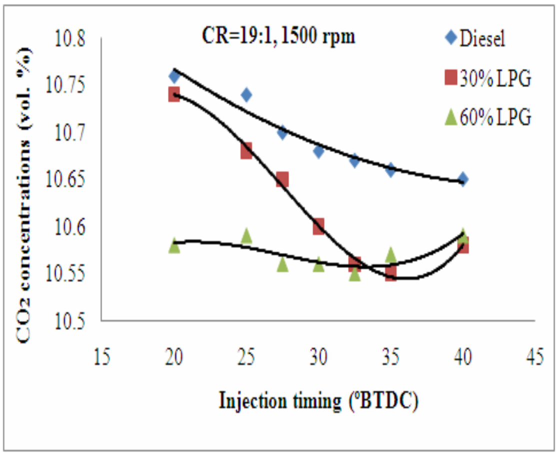

Fig. 16, Effect of LPG addition on CO_2 at variable injection timing

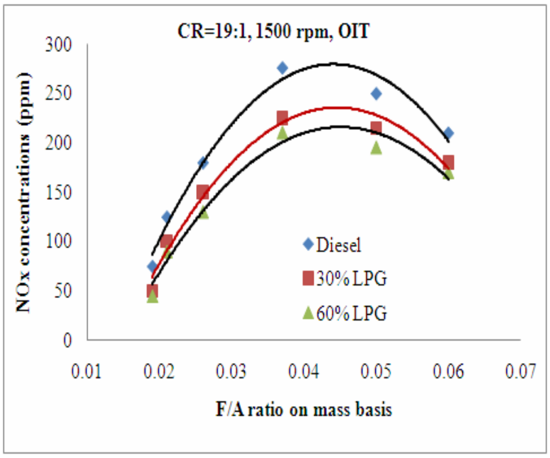

Fig. 17, Effect of LPG addition on NOx concentrations at variable fuel-

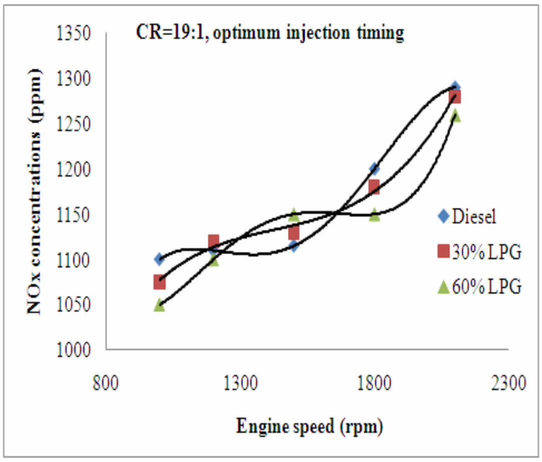

Fig. 18, Effect of LPG addition on NOx at variable engine speeds

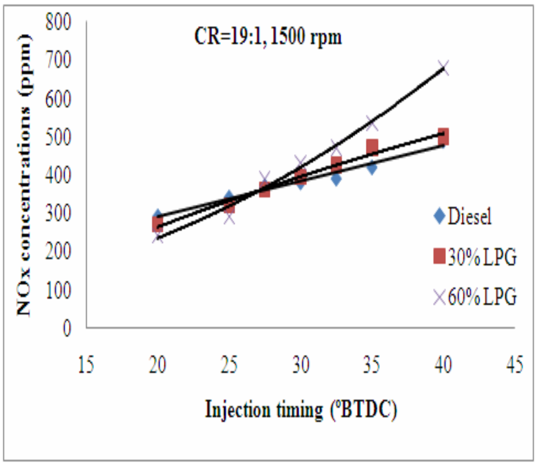

Fig. 19, Effect of LPG addition on NOx at variable injection timing

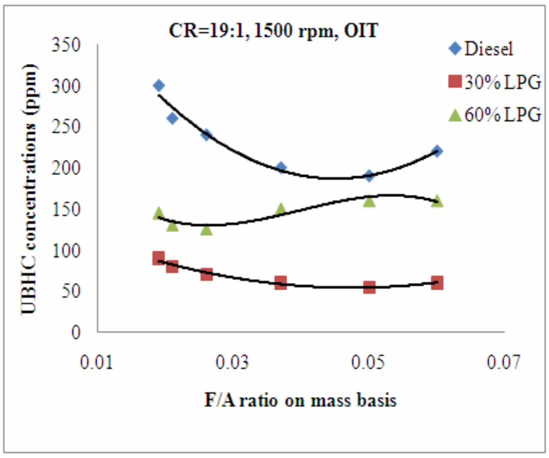

Fig. 20, Effect of LPG addition on UBHC concentrations at variable fuel-air ratios

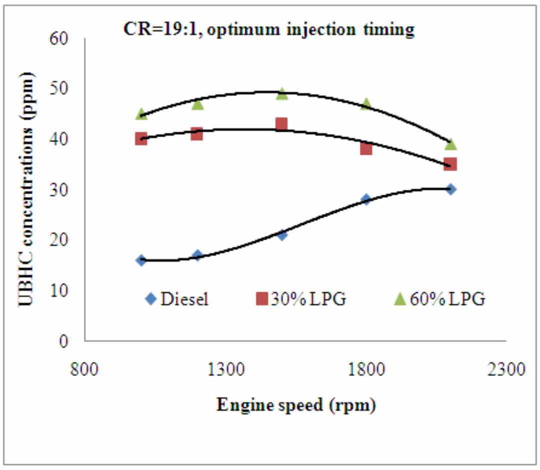

Fig. 21, Effect of LPG addition on UBHC at variable engine speeds

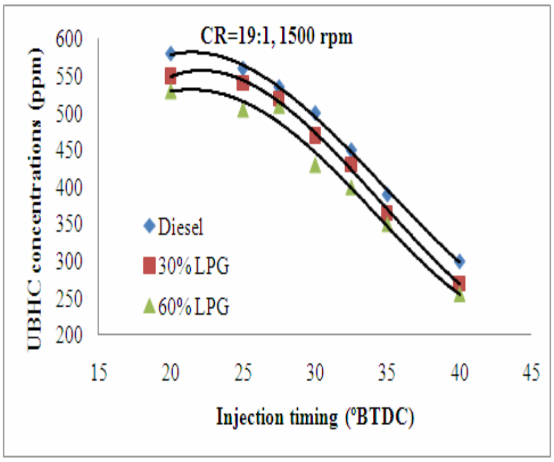

Fig. 22, Effect of LPG addition on UBHC at variable injection timing

PHOTO DYNAMIC THERAPY (PDT) WITH BIOLOGICAL TISSUES USING ND:GLASS LASER

Assistant Lecturer
Eng. Hadeel Kassim AL-Jobouri
Medical Engineering Department / College of Engineering /Al-Nahrain University, Baghdad, Iraq.
E-mail: hadeel_bme77@yahoo.com

Dr. Anwaar A. Al Dergazly
Laser and Optoelectronics Engineering Department / College of Engineering / Al-Nahrain University, Baghdad, Iraq.
E-mail: anlaser@hotmail.com

ABSTRACT:

A Photo Dynamic Therapy (PDT) is a technique which is used with Laser to treat many of cancer tissues. This paper deals with the relatively new therapeutic technique (PDT) with pulsed Nd:glass Laser which was applied to human soft tissues (Ovary and Kidney tissues), and to the hard tissues (freshly extracted human teeth), with power density of 280 watt/mm^2 and exposure time 330 *u*sec. Different dyes (Blue, methylene, eosin, and orange) were applied to the area before irradiation to study the effect of the pigments on the laser interaction with biological tissues. The zone of treatment (Z-necrosis) with aid of MATLAB was determined. The relationship of zone of treatment with exposure time, accumulated damage and fraction of oxidative radicals was obtained.

الخُلاصة:

أن تقنية العلاجَ الصورّي الديناميكي تستخدم مع الليزر لعلاجَ العديد مِنْ ألانسجةِ السرطانية. يتناول هذا البحث اهمية هذه التقنية بأستعمال ليزر النيديوم الزجاجي النبضي المسلط على أنسجة بشرية لينة (أنسجة الكلية والمبيضَ)، وإلى الأنسجةِ الصلبةِ (أسنانَ بشرية منتزعة جديدا)، بقدرة كثافية 280واط/مليمتر^2 ووقت التعرّض 330ميكروثانية. صباغات مختلفة (أزرق, ميثالين، أيوسين، وبرتقالي) أُطبقتْ على مساحة الانسجة قبل التعرض للاشعاع وذلك لغرض دِراسَة تأثيرِ هذه الصبغاتِ في تفاعلات الليزرَ مع الأنسجةِ الحيويةِ. منطقة المعالجةِ وجدت ووضحت بمساعدة برنامج المحاكاة بالتعامل مع الماتلاب . أن علاقة منطقةِ المعالجةِ بوقتِ التعرّض، الاضرار المجمّعَة وتكسرَ الأكسدة الراديكاليي قد حُصِلَ عليها.

Keywords:
Photo Dynamic Therapy (PDT) technique, a pulsed Nd:glass Laser, Z-necrosis, Dyes with human tissues, Photosensitizers.

1. INTRODUCTION:

Photodynamic therapy (PDT) is the most modern and important method in the therapy of both neoplastic and non-neoplastic diseases because of its safe treatment approach for superficial human cancers and selection benign conditions. When radiant energy is absorbed by tissue, four basic types of interactions are occurring: photo chemical, photo thermal, photo mechanical, photo electrical. (PDT) involves light activation chemotherapy in the presence of molecular oxygen, of certain dyes (photosensitizers) that are taken up by the target tissue.

A photon is absorbed by a photosensitive drug which moves the drug into an excited state. The excited drug can then pass its energy to oxygen to create a chemical radical called "singlet oxygen". Singlet oxygen attacks cellular structures by oxidation. Such oxidative damage might be oxidation of cell membranes or proteins. When the accumulation of oxidative damage exceeds a threshold level, the cell begins to die, as shown in **Fig.1.1**.

The PDT treatment window is shown in the **Fig.1.2**. There must be enough photosensitizing DRUG and activating LIGHT to achieve effective PDT treatment. A threshold dose is defined as:

LIGHT x DRUG = threshold dose

Too much drug may lead to "dark toxicity." Too much light can lead to photo destruction or "photo bleaching" of the drug (Patterson MS, 1990).

In the clinic, one doctor must be sure that there is sufficient DRUG in the tissue and sufficient light penetrating the tissue to the desired depth so as to enter the PDT treatment window (**Fig.1.2**).

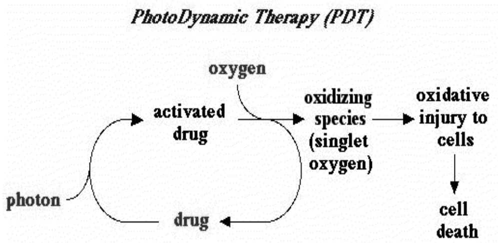

Fig.1.1 *The PhotoDynamic Therapy [PDT]* (Patterson MS, 1990).

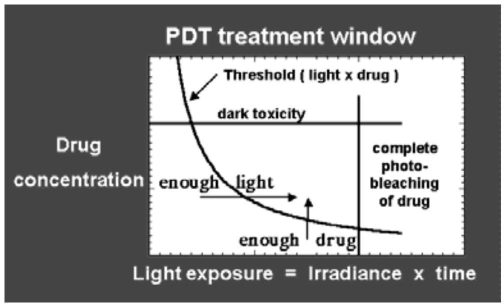

Fig.1.2 *PDT treatment* window (Patterson MS, 1990).

1.1. The Mathematics of PDT Dosimetry for Cancer Treatment:

This section provides a working description of PDT dosimetry using definitions summarizing PDT with a flow diagram as shown in **Fig.1.3**.

As illustrated in this figure, PDT depends on the amount of light delivered (**L**), the amount of photosensitizing drug (**D**) in the tissue, and the amount of oxygen (**O^2**) in the tissue. Absorption of light converts **D** into an activated drug (**D***). Reaction of **D*** with oxygen yields oxidizing radicals (**R***, primarily singlet oxygen). A fraction (**f**) of these radicals attacks critical sites within the cell causing an accumulated oxidative damage (**A**). When the accumulated damage exceeds a threshold, (**$A > A_{th}$**), then cell death occurs (Foster TH, 1991).

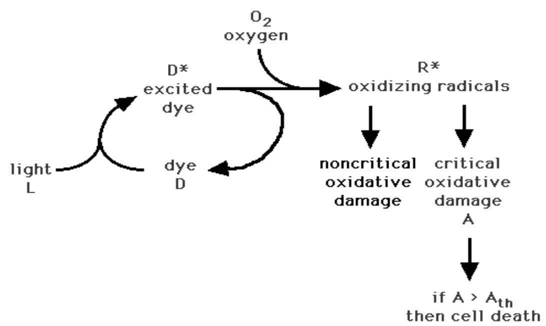

Fig.1.3 *Schematic diagram for PDT* (Allison RR, 2004).

The light provided by a delivered fluence rate (ϕ) can be expressed in units of photon concentration:

$$L = \frac{\phi}{c}\frac{\lambda}{hc}\frac{1000}{6x10^{23}} \quad , [\text{moles/liter}] \qquad \textbf{(1.1)}$$

where:

ϕ **:** is the fluence rate of light [W/cm^2] or [J/ (cm^2.s)].

λ**/(hc) :** is number of photons per J of energy [ph/J].

λ **:** is the photon wavelength in [cm].

c **:** is the speed of light, 3.0x10^{10} [cm/s].

h **:** is Planck's constant, 6.6x10^{-34} [J s].

The rate constant (**k$_1$**) for drug activation (**D >D***) is:

$$\text{rate constant for drug activation} \quad k_1 = c\varepsilon \quad , [s^{-1}\,(\text{moles/liter})^{-1}] \qquad \textbf{(1.2)}$$

where:

ε **:** is the extinction coefficient of the photosensitizing drug [(cm^{-1}) / (moles/liter)].

The rate of production of activated drug is:

$$\text{rate of drug activation} = k_1 LD \quad , [(\text{moles/liter})\, s^{-1}] \qquad \textbf{(1.3)}$$

The total amount of activated drug (**D***) produced per unit volume of tissue is:

Where:

T **:** is the time of light exposure in second.

The probability that an activated drug (**D***) will transfer its excited state energy to oxygen to yield an oxidative radical (**R***) is specified by the quantum yield (Φ) which depends on the oxygen concentration in the tissue. The total amount of **R*** produced is:

$$\text{total amount of oxidative radicals } R^* = \Phi D^* \quad , [\text{moles/liter}] \qquad \textbf{(1.5)}$$

A fraction (**f**) of **R*** succeeds in oxidative damaging critical sites in the cell which contributes to cell death. The remaining fraction (**1 - f**) will attack relatively inert or no critical sites. The accumulation (**A**) of critical oxidative damage is:

$$\text{accumulation of critical oxidative damage} =$$

$$A = f\Phi\varepsilon\phi DT \frac{\lambda}{hc}\frac{1000}{6x10^{23}} \quad , [\text{moles/liter}] \qquad \textbf{(1.6)}$$

If the accumulated damage exceeds a threshold, **A > A$_{th}$**, then cell death occurs.

$$\text{if} \quad A > A_{th} \quad \text{then} \quad \text{cell death} \qquad \textbf{(1.7)}$$

1.2. <u>Photodynamic Dose (D*):</u>

Currently, few laboratories concerned with rigorous PDT dosimetry routinely document the light reaching a tissue site (Φ), the amount of photosensitizing drug that accumulates in that tissue site (**D**), and the light exposure time (**T**), then calculate the total amount of drug activated during the light exposure period (Tromberg BJ, 1990).

This factor is quantifiable and therefore a practical dosimetric parameter which has been called the **"photodynamic dose"**. We have used the symbol **D*** and the units of [moles/liter] to describe the "photodynamic dose", Which have described as the number of photons absorbed by photosensitizing drug per gram of tissue [ph/g].

$$\text{"photodynamic dose"} \quad D^* = \varepsilon D\phi T \frac{\lambda}{hc\,\rho} \quad , [\text{ph/g}] \qquad \textbf{(1.8)}$$

where:

ρ **:** is the density of tissue [g/cm^3].

The "photodynamic dose" (**D***) does not consider the quantum yield (Φ) of oxidative radicals, the effect of oxygen on (Φ), or the fraction (**f**) of radicals that oxidize critical sites. However, "photodynamic dose" is the dosimetric parameter most commonly documented. There is logic in this choice since light (**L**), drug (**D**), and exposure time (**T**) are parameters under experimental or clinical control. Experimental determination of the margins of necrosis induced by a well-defined **D*** can specify the threshold dose (**D*$_{th}$**). The criteria for necrosis are then:

$$\text{if} \quad D^* > D^*_{th} \quad \text{then} \quad \text{cell death} \tag{1.9}$$

1.3. Treatment Zone:

Consider a treatment using topical irradiation of a tissue surface with a broad beam of light a couple (cm) in diameter (Jacques, 1992). The light penetration into the tissue can be described by the one-dimensional expression:

$$\phi = E\, k_s \exp(-z/\delta) \tag{1.10}$$

where:

E : irradiance at tissue surface [W/cm^2].
ks : the backscattering factor which accounts for how reflected light from the tissue augments delivered light [dimensionless]
z : depth into the tissue [cm]
δ **:** the optical penetration depth [cm], the path length which causes the concentration of light to drop to 1/e or 37% of its initial concentration.

Assume that the depth of necrosis from such a topical PDT treatment is located at **z_necrosis** which corresponds to the depth at which the threshold accumulation of oxidative damage, **A$_{th}$**, occurs. Then combining equations (1.9) and (1.10) and inserting **z_necrosis** and **A$_{th}$** yields:

$$A_{th} = f\Phi\varepsilon DT \frac{\lambda}{hc} \frac{1000}{6\times10^{23}} Ek_s \exp(-z_{necrosis}/\delta) \text{ , [moles/liter]} \tag{1.11}$$

Finally, rearrange equation (1.11) to solve for **z_necrosis**:

$$z_{necrosis} = \delta \ln\left[\frac{f\Phi\varepsilon\phi DTEk_s}{A_{th}} \frac{\lambda}{hc} \frac{1000}{6\times10^{23}}\right] \text{ , [cm]} \tag{1.12}$$

Eq. (1.12) shows how the depth of necrosis depends on all the various parameters that affect PDT. Notice that **z_necrosis** is linearly related to the optical penetration depth δ but logarithmically related to all other parameters.
Again consider the practical dosimetry based on **D***, the "photodynamic dose". If the irradiance at the tissue surface yields a **D*$_{surface}$** at the surface, then the depth of necrosis can be expressed:

$$z_{necrosis} = \delta \ln\left[\frac{D^*_{surface}}{D^*_{th}}\right] \text{ , [cm]} \tag{1.13}$$

$$\text{where} \quad D^*_{surface} = \varepsilon DTEk_s \frac{\lambda}{hc} \frac{1}{\rho}$$

2. EXPERIMENTAL WORK:

2.1 Method:

The Nd:glass laser system which was used in this experiment (in the Institute of Laser for Postgraduate Studies / Baghdad University) is a homemade laser (**Fig.2.1**). It operates in the pulsed mode giving a single pulse for each shot. This system gives a beam of (1064 nm) wavelength. The active medium of the system is a glass rod Silicate type ED-2 doped with (2.83x10^{20} cm^{-3}) concentration of Nd^{+3} ions. The rod length is 20 cm with 1.25 cm in diameter. The Nd:glass rod is optically pumped with a xenon filled flash lamp to pump the laser rod. The flash lamp supported with voltage pulse by using pulsing power supply in which connected with a charge capacitor to give out a voltage pulse within about (4–6 KV) to the flash lamp. The out-put laser energy increases with

increasing the charging of the capacitor "flash lamp power". The output laser energy was measured by using a joulemeter which is a thermal detector (Orazio Svelto, 1998), (W.T. Silfvast, 2004).
The joulmeter was connected to an oscilloscope to measure the voltage generated by the joulmeter as a result of the incidence of the laser beam on its surface .The calibration of the output voltages displayed in the oscilloscope were divided by the detector factor which is about 10.3 Volt/joule, to obtain the amount of incidence energy "in joule" of the laser beam on the detector. The output laser power is obtained by dividing the output laser energy to the pulse width "330 microseconds". In order to calculate the power density, the spot diameter is controlled partly by the focal length of the lens of 10 cm to focus the beam (**Table.2.1**).

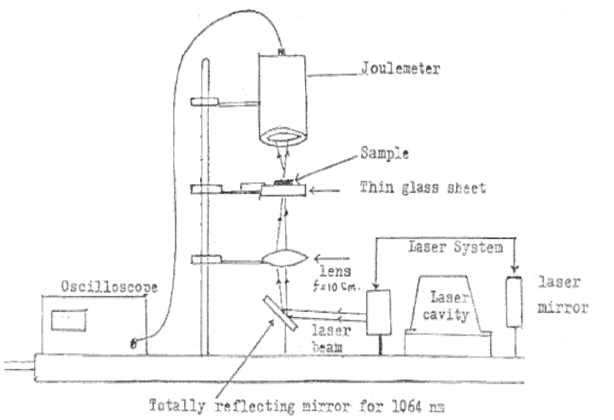

Fig.2.1 *Schematic diagram of Nd:glass laser.*

Table.2.1 *The physical properties of the glass-rod.*

Glass type	Silicate
Nd-ion concentration	2.83 x 1020
Density	2.547 gm/cm^3
Refractive index	1.555
Wavelength	**1064 nm**
Photon energy "for single photon"	1.88 x 10^{-19} J
Thermal conductivity	**1.35 x 10^{-2} w.cm^{-1}.k^{-1}**
Pulse width	330 micro-second

2.1.1 Experiment (1):

Soft tissues were obtained, from human kidney and ovary, and served as homogeneous biological test media. The samples were taken from Pathology Department / College of Medicine / Baghdad University. All samples used were fixed with 10% formalin. Each sample was supported along its length by two razor blades, each mounted and cut into a few millimeters in thickness, 3-5 mm. The soft tissue is almost perfectly colorless in its intrinsic state, and served as control. The other samples were stained with different dyes, methylene-blue, eosin and orange dye.
Dyes and Stains are frequently used in biology and medicine to highlight structures in biological tissues for viewing. Stains may be used to define and examine bulk tissues (highlighting, for example, muscle fibers or connective tissue), cell populations (classifying different blood cells, for instance), or organelles within individual cells. In biochemistry it involves adding a class-specific (DNA, proteins, lipids, carbohydrates) dye to a substrate to qualify or quantify the presence of a specific compound (Horobin RW, 2002).
The samples were irradiated with pulses of Nd:glass laser at 1064 wavelength, emission energy 0.0184 joule, and pulse duration 330 μsec.

2.1.2 Experiment (2):

Freshly extracted human teeth were obtained from Surgery Department/College of Dentistry/Baghdad University. These samples were chosen because of their inhomogeneous appearance; represent bones as hard tissues and with inclusions of caries. All extracted teeth were washed with fresh water immediately and fixed with 10% formalin. The tooth without staining "carries existing" served as a control. While the other teeth stained with methylene blue, orange and eosin dye, were irradiated with pulses of Nd:glass laser, emission energy 0.0184J, beam diameter 0.5 mm , and pulse duration 330 μsec.

2.2 Readings:

The used laser parameters:

- Incident energy "E_o" = 0.0184 joule.
- Spot diameter = 0.5 mm
- Spot radius = 0.25 mm = 0.025 cm
- Spot size in "cm^2"= $3.14x(0.025)^2$ = $2.0x10^{-3}$ cm^2

2.2.1 Fluence:

Table.2.2 shows the measurements of the transmitted joulemeter in term of "Joule", of the control and stained samples with different dyes. Where **Table.2.3** shows the calculations of the transmitted fluence "Energy Density (J/cm2)" of the control and stained samples with different dyes.

- Energy density or Fluence = $\frac{0.0184 \text{ J}}{2 \times 10^{-3}} = 9.2\, Joul \ / cm^2$
- Pulse duration = 330 μsec.

Table.2.2 *Measurements of the Joulemeter in term of "Joule".*

Sample	*Control "J"*	*Orange "J"*	*Eosin" J"*	*Blue "J"*
Ovary	0.00854	0.00504	0.00103	0.0066
Kidney	0.01456	0.01514	0.01456	0.01553
Intact tooth	0.00543	0.00737	0.00348	0.00691
Caries-tooth	0.00407	0.00427	0.00485	0.00582

Table.2.3 *Calculations of the Transmitted Fluence "Energy Density (J/cm^2)".*

Sample	*Control "J/cm^2"*	*Orange" J/cm^2"*	*Eosin" J/cm^2"*	*Blue"J /cm^2"*
Ovary	4.27	2.52	0.515	3.3
Kidney	7.28	7.57	7.28	7.77
Intact tooth	2.72	3.69	1.74	3.1
Caries-tooth	2.04	2.14	2.43	2.91

2.2.2 Power:

Table.2.4 shows the calculations of the power densities of the control and stained samples with different dyes.

- $power = \frac{\text{Energy} \quad \text{(Joule)}}{\text{Time} \quad \text{(sec)}}$
- Incident power = $\frac{0.0184 \quad \text{J}}{330 \times 10^{-6}} = 55.8 Watt$
- Incident power density =

$$\frac{\text{Power}}{\text{Area}} = \frac{Watt}{cm^2} = \frac{55.8}{2 \times 10^{-3}} = 28 \times 10^3 Watt \ / cm^2$$
$$= 280 Watt \ / mm^2$$

Table.2.4 *Calculations of the Power Densities.*

Sample	*Control "W/mm 2"*	*Orange "W/mm2 "*	*Eosin "W/mm2 "*	*Blue "W/mm 2"*
Ovary	129	76	16	100
Kidney	221	230	221	235
Intact-tooth	112	112	53	91
Caries tooth	62	65	74	88

2.2.3 Transmission Coefficient:

Transmission coefficient is defined as the percentage ratio of the transmitted energy density (J/cm2) to the incident energy density (J/cm2). **Table.2.5** shows the transmission coefficient calculations of the control and stained samples with different dyes.

Table.2.5 *Calculations of the Transmission Coefficient.*

Sample	*Control %*	*Orange %*	*Eosin %*	*Blue %*
Ovary	46	27	6	36
Kidney	79	82	79	85
Intact-tooth	30	40	19	34
Caries-tooth	22	23	26	32

2.2.4 Optical Density:

Table.2.6 shows the calculations of the optical densities "OD" of the control and samples coated with different dyes. The depth of laser light transmission is governed by the wavelength dependent optical density "OD" of the tissue which is defined as:

$$Optical Density = \log \frac{\text{Incident Fluence}(J/cm^2)}{\text{Transmitted fluence}(J/cm^2)}$$

Table.2.6 *Calculations of the Optical Densities "OD".*

Sample	*Control*	*Orange*	*Eosin*	*Blue*
Ovary	0.333	0.562	1.252	0.445
Kidney	0.102	0.084	0.102	0.073
Intact-tooth	0.529	0.396	0.723	0.472
Caries-tooth	0.654	0.633	0.578	0.499

The optical density is directly proportional to the concentration of light absorbing chromophores and the tissue thickness or light path length [8].

3. SOFTWARE AND RESULTS:

In this work, the zone of treatment (z_necrosis) is determined by using a simulation program which was dealt with MATLAB. The relationship of zone of treatment with exposure time, accumulated damage and fraction of oxidative radicals is obtained. As well as the calculations of the penetration depth, by using the eq.s (1.10), (1.11) and (1.13). **Fig.3.1** shows the flow chart of the program for PDT technique.

In this work, the values of parameters which used to calculate the Penetration depth (Z-necrosis) are taken from **Table.3.1**.

The curves which obtained from execution this program with the readings from the above experiments are shown in figures below.

Fig.3.2 shows that the zone of treatment (Z-necrosis) will change with exposure time .When the exposure time increased Z-necrosis will be increased quickly until reached to 12cm after this point the Z-necrosis is increased slowly with increasing exposure time. Then from this curve Z-necrosis is linear proportional with exposure time.

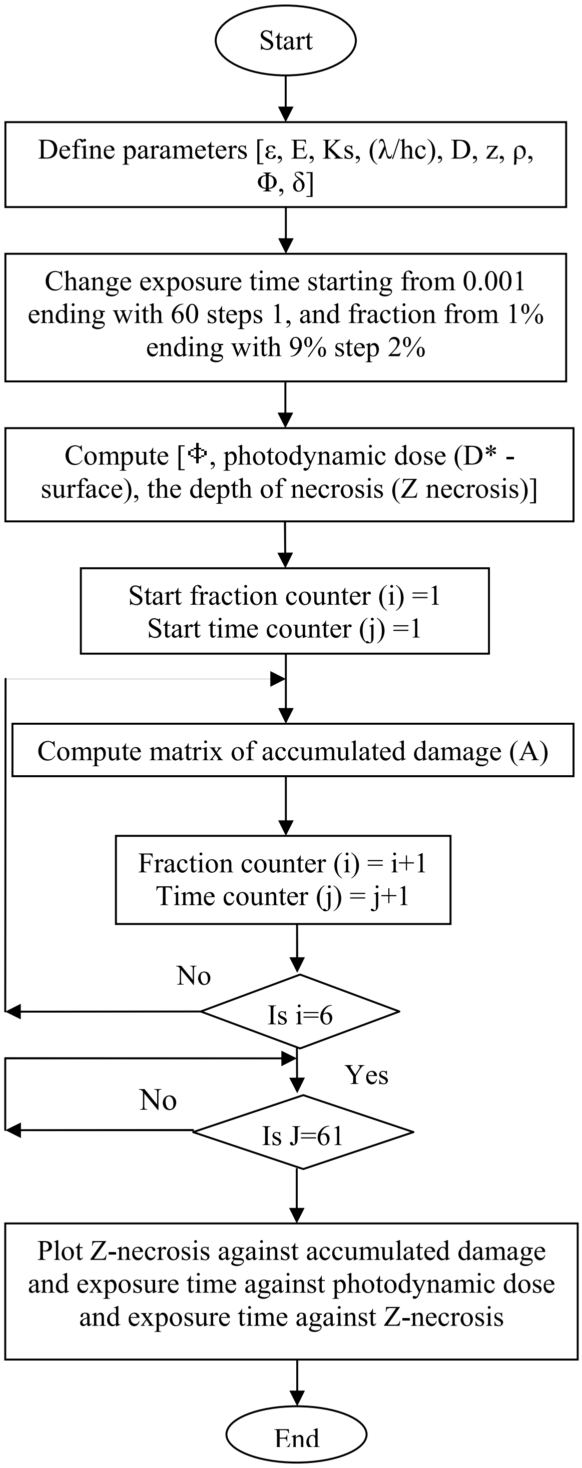

Fig.3.1 *Flow chart of the program of determining penetration depth.*

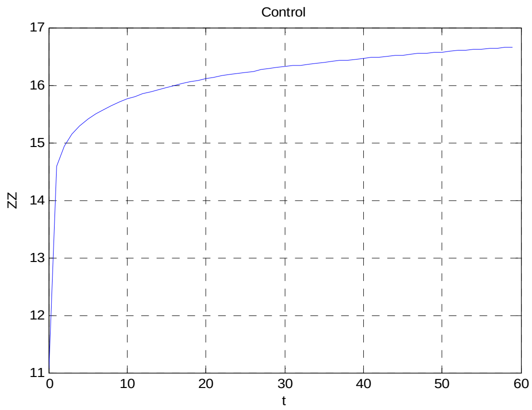

(a)

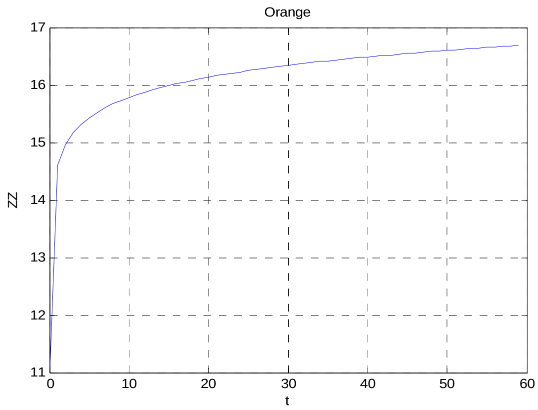

(b)

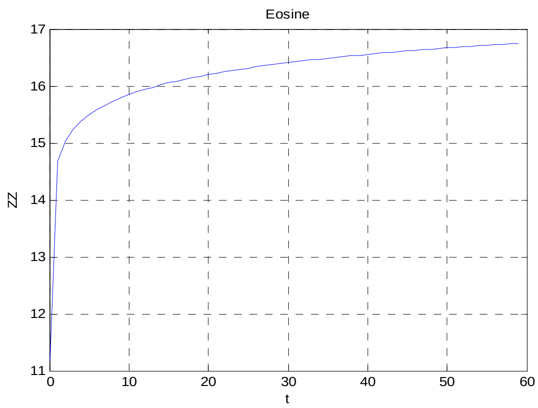

(c)

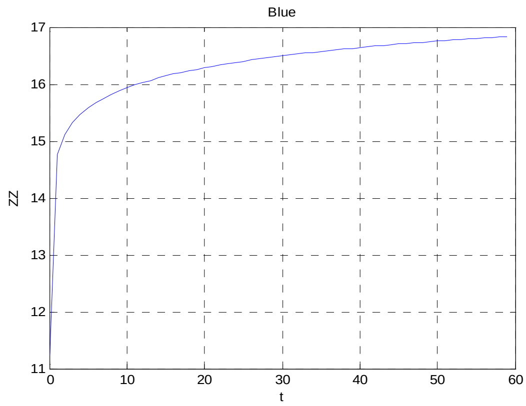

(d)

Fig. 3.2 *The relationship between Z-necrosis and exposure time of the* ***(a)*** *Control,* ***(b)*** *Orange,* ***(c)*** *Eosin and* ***(d)*** *Blue.*

Table.3.1 *The parameters that used in Z-necrosis.*

photon		
Wavelength	λ	1064 nm = 1.064 *u*m
Irradiance	E	From Table. 2.2 & 2.3
Exposure time	T	10 min = 600 s
Optical penetration depth	δ	0.51 cm
Optical backscatter factor	ks	4.4 [dimensionless]
Conversion constant	λ/hc	3.2x10^18 photons/J
Photosensitive drug		
Administered drug dose	-	5 mg/kg body weight = 5 ug/g.tissue

Molecular weight of drug	MW	600 g/mole
Tissue density	ρ	1 g.tissue/cm^3
Tissue concentration of drug	D	3 ug/g.tissue = (3x10^-6 g/g.tissue)(1 mole/600 g)(1 g.tissue/cm^3)(1000 cm^3/liter) = 5x10^-6 moles/liter
Extinction coefficient of drug	ε	10^4 (cm^-1)/(mole/liter)
Quantum efficiency of activating radicals	Φ	0.1 [dimensionless]
"Photodynamic dose" at surface	D*_surface	8.4x10^19 ph/g = 143 mmoles/liter
Tissue treatment zone		
Threshold toxic product	D*th	10^19 ph/g = 17 mmoles/liter
Zone of treatment	z_necrosis	1.1 cm

Fig. 3.3 explains that the relationship between the photodynamic dose and exposure time was linear.

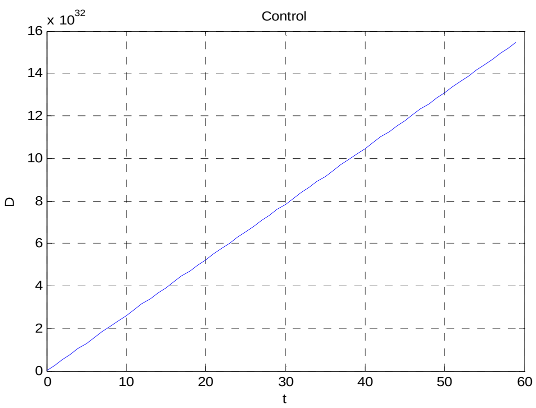

(a)

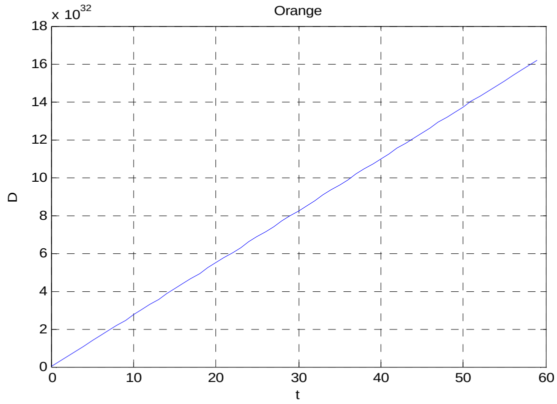

(b)

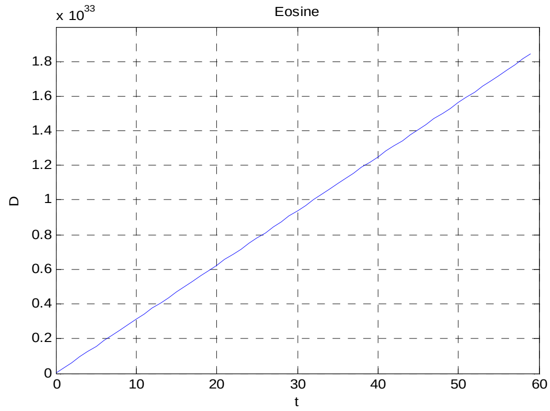

(c)

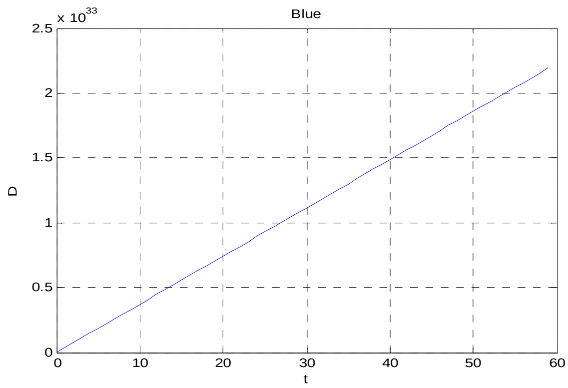

(d)

Fig. 3.3 *The relationship between D*_Surface and exposure time of the* ***(a)*** *Control,* ***(b)*** *Orange,* ***(c)*** *Eosin and* ***(d)*** *Blue.*

Fig. 3.4 shows that the accumulated damage remained constant when Z-necrosis increased, but when change the fraction of oxidative radicals the accumulated damage increased and remained constant with Z-necrosis.

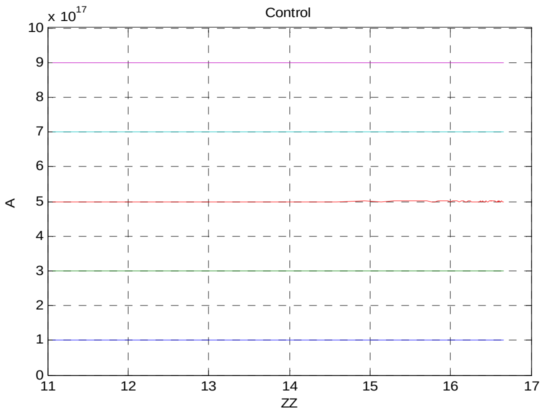

(a)

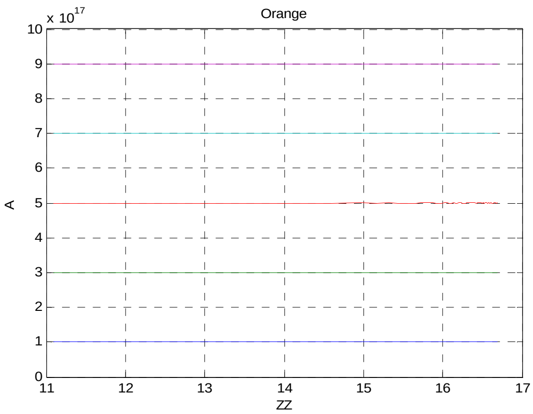

(b)

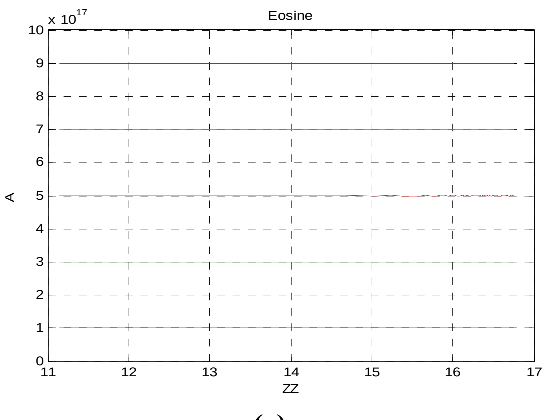

(c)

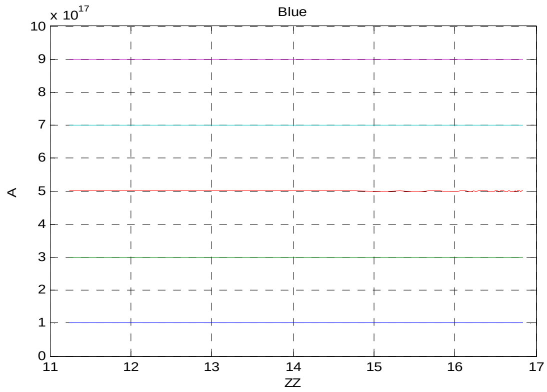

(d)

Fig. 3.4 *The relationship between accumulated damage and different fractions with Z-necrosis of the* ***(a)*** *Control,* ***(b)*** *Orange,* ***(c)*** *Eosin and* ***(d)*** *Blue.*

All the above results showed that the samples coated with blue stain increased the power density and reduced the scattering effect, whereas the effect of eosin dye was to increase the scattering effect.

4. DISCUSSION:

Laser light Incident on tissue can be reflected, transmitted or absorbed. The distribution of light in tissue is governed by wavelength dependent, optical properties of the target, primarily absorption and scattering, as well as by physical parameters of the incident laser beam "e.g., energy, power density, exposure time and spot size ".

The optical properties of tissue may be altered by exposure to laser light, such that the distribution of light during or after an Initial exposure may be completely different.

4.1 The Soft Tissues:

In **Table.3**, the transmitted fluences of the ovary tissues stained with different dyes were less than the control samples. The significant reduction of the output light was in eosin-ovary tissue as well as with orange dye. These results might indicate that the orange and eosin dyes were increase the

volume of the target in which interact with Incident laser, and reduced the result of energy density. The effects of the dyes were noticed in **Table.5**, where the transmittance of the stained samples with eosin, orange, and blue dyes were 6.0%, 27%, and 36% respectively. All of these coefficients were less than the control.
Since the optical properties of tissue may be altered by exposure to laser light, **Table.6**, clearly indicated that the optical densities of the stained-ovary samples were more than the control that might be due to the concentration of light-absorbing chromospheres and the depth of the light within the targets during the exposure. Mean while, there were a little change of optical density in stained kidney samples, that might be reflected to the amount of chromospheres present in tissue targets (Chromospheres: any substance that absorbs light).

Scattering Effect:
Scattering has the effect of increasing the volume of tissue in which the photons of the incident laser beam are distributed and may eventually be absorbed (Jon H, 2004). This effect actually increases the spot size of the laser beam within the target tissue and thus decreases the concentration of photons per unit volume tissue; (i.e, decreases power density). Scattering, particularly backscattering, along with absorption contributes to the exponential decrease in light intensity with increasing depth in the target tissue. The amount of scattered light reflected from or transmitted through tissue depends on internal reflectance and on the absorption properties of the tissue.
Table.4 showed a significant reduction in transmitted power density of the eosin-ovary sample than the other dyes and control sample; that's, because of the strong scattering of the light within the target. While the effect of the blue dye was less scattering, this might be was due to the selective absorption of pulses Nd-laser. The power density of the blue-kidney samples was more than the other samples with orange, eosin and control samples, that; indicated the blue dye was increased the absorption of the light by reducing the amount of scattering effect .

4.2 The Hard Tissues:
In **Table.3**, there was reduction in the amount of the transmitted fluence in the intact tooth tissues stained with eosin dye, whereas, the effect of the other dyes were to improve the amount of light to the tissue targets. The transmission coefficients of eosin and blue dyes were less than the control, where there was a significant enhancement of transmission of the light in the orange dye. These results explain the physical and biological interaction of these dyes with the targets due to the ability of these dyes or biological stains to react or concentrate in different parts of a cell or tissue, and these properties are used to advantage to reveal specific parts or areas (Horobin RW, 2002). **Table.6**, showed these effects, where the optical density of the eosin sample was more than control sample. The power density of the eosin sample was less than the control, that’s due to the scattering effect, while there was significant power density in the orange-dye samples, that’s due to the selective absorption effect.
Determination of the reflection and absorption of laser light by tooth tissues showed that the absorption of Nd-laser radiation in unstained sections of teeth varies and depending on the present or absence of caries.

5. CONCLUSIONS:
Photodynamic therapy (PDT) technique has been successfully applied in various biomedical and clinical applications; like in the treatments of head and neck, lung and skin cancers. In this work when the program of determined the penetration depth is written and execution, there are three curves are obtained which are explained the relationship between exposure time, accumulated damage, fraction of oxidative radicals and Z-necrosis.
The relationship between Z-necrosis and exposure time is linear as well as the relationship between photodynamic doze and exposure time is linear.

When the fraction of oxidative radicals is constant, accumulated damage is remained constant when Z-necrosis is changed. While when fraction is changed then the accumulated damage is changed too but remained constant with changing in Z-necrosis.
This work also showed that the tooth tissues with caries and for all dyes have effect of increase the amount of laser to the target tissues, whereas the power density of the blue dye sample was more than the control and other dyes samples.
The results showed that from all dyes that was used; blue dye gave the greatest potentiating of the effect.

6. REFERENCES:

Allison RR, Downie GH, Cuenca R, Hu XH, Childs C, Sibata CH., **"Photosensitizers in clinical PDT"**. Photodiagn Photodyn Ther 1:27–42, 2004.

Foster TH, RS Murant, RG Bryant, RS Knox, SL Gibson, R. Hilf, **"Oxygen consumption and diffusion effects in photodynamic therapy"**, Radiation Research 126:296-303, 1991.

Jacques, S.L., **"Laser-tissue interactions: photochemical, photothermal, and photomechanical mechanisms"**, Surgical Clinics of North America, 72:531-558, 1992.

Jon H, Robertson, W.Ciaig Clark., **"Laser in neurological"** Kluwer Academic Publishers, Boston Dordrecht Lancaster, 2004.

Horobin RW, Kiernan JA Conn's Biological Stains, **"A Handbook of Dyes Stains and Fluorochromes for Use in Biology and Medicine"**, 10th ed. Oxford: BIOS. ISBN: 1859960995, 2002.

Orazio Svelto, **"Principles of Lasers",** Springer Science & Business Media, Inc., 1998.

Patterson MS, BC Wilson, R Graff, **"In vivo tests of the concept of photodynamic threshold dose in normal rat liver photosensitized by aluminum chlorosulphonated phthalocyanine"**, Photochem Photobiol 51:343-349, 1990.

Tromberg BJ, A Orenstein, S Kimel, SJ Barker, J Hyatt, JS Nelson, MW Berns, **"In vivo tumor oxygen tension measurements for the evaluation of the efficiency of photodynamic therapy"**, Photochem Photobiol 52:375-385, 1990.

William T. Silfvast, "Laser **Fundamentals ",** William T. Silfvast, 2004.

.

DISSOLUTION OF BENZENE IN THE SATURATED POROUS MEDIA

By

Prof. Dr. Abbas H. Sulaymon
Environmental Engineering Department /College of Engineering/University of Baghdad.

Dr. Hatem Asal Gzar
Environmental Engineering Department /College of Engineering/University of Baghdad.

ABSTRACT:

The aim of the present research is to study the dissolution and transport process of benzene as a light nonaqueous phase liquid (LNAPL) in saturated porous media. Unidirectional flow at water velocities ranged from 0.90 to 3.60 cm/hr was adopted to study this process in a three dimensional saturated sand tank (100 cm×40 cm×35 cm). This tank represents a laboratory-scale aquifer. The aquifer was constructed by packing homogeneous sand in the rectangular tank. The experimental results were used to characterize the dissolution behavior of an entrapped nonaqueous phase benzene source in a three dimensional aquifer model. The time invariant average mass transfer coefficient was determined at each interstitial velocity, the values of this coefficient were ranged from 0.016 to 0.061 cm/hr. It was increased proportionally with velocity toward a limiting value. The results show that the concentration of the LNAPL reduces as the distance increased in *x* and/or *z* direction from the source of pollution. In most cases the benzene concentration declines with velocity more than 2.34 cm/hr at downstream of the LNAPL pool.

الخلاصة:

ان الهدف من هذا البحث دراسة عملية ذوبان وانتقال البنزين الذي يعتبر سائل عضوي اخـف مـن المـاء و يسمى Light nonaqueous phase liquid (LNAPL) في وسط مسامي مشبع بالماء. تم اعتمـاد جريـان المـاء احادي الاتجاه عند سرع تغلغل تتراوح قيمها من 0.90 الى 3.60 سم/ساعة لدراسة هذه العملية في خزان رملي مشبع بالماء ثلاثي الابعاد (100 سم × 40 سم × 35 سم). ان هذا الخزان يمثل مكمن مختبري . تم تكوين هذا المكمن من خلال حشو رمل متجانس في الخزان المستطيل .ان النتائج العملية تم من خلالها وصف سلوك عملية ذوبان البنزين في نموذج المكمن الثلاثي الابعاد.

استخدمت النتائج العملية لتشخيص او وصف سلوك عملية ذوبان البنزين في المكمن الثلاثي الابعاد.

تم ايجاد معدل معامل انتقال الكتلة عند كل سرعة تغلغل، حيث كانت قيم هذا المعامل تتراوح من 0.016 الى 0.061 سم/ساعة وتزداد طردياً مع السرعة وصولاً الى قيمه محدده. اوضحت النتائج ان تركيز البنزين يخفض كلمـا ازدادت المسافة بالاتجاه الافقي والعمودي ابتعاداً عن مصدر التلوث. ايضاً اوضحت نتائج البحث ان في اغلب الحالات قيم التركيز تنخفض عندما تكون سرعة التغلغل اكثر من 2.34 سم/ ساعة.

Key wards: Light nonaqueous phase liquid, saturated porous media, dissolution, transport, contamination.

1. INTRODUCTION:

The contamination of soil and ground-water by petroleum hydrocarbons has been of major concern over the last two decades. The most frequent cause of contamination is leakage from underground storage tanks, pipelines, spillages from overfilling or accidents during transferring fuel (Moore et al., 1992). When pollution occurs, a number of dangerous substances may migrate through ground-water, enter into the food and water chain, and finally directly or indirectly harm man (Hiscock, 1995; Makri et al., 2006).

Nonaqueous phase liquids are hydrocarbons that exist as a separate, immiscible phase when in contact with water and/or air. Difference in the physical and chemical properties of water and nonaqueous phase liquid (NAPL) resulted in the formation of a physical interface between the liquids which prevents the two fluids from mixing. Nonaqueous phase liquids are typically classified as either light nonaqueous phase liquids (LNAPLs) which have densities less than that of water, or dense nonaqueous phase liquids (DNAPLs) which have densities greater than that of water. The most common LNAPLs related ground-water contamination problems result from the release of petroleum products .These products are typically multicomponent organic mixture composed of chemicals with varying degrees of water solubility. Examples of LNAPLs include gasoline, jet fuel and heating oils. Gasoline is made up of mono-aromatic compounds such as benzene, toluene, ethylbenzene, and xylenes (including ortho-xylenes, meta-xylenes, and para-xylenes), which are collectively called BTEX compounds .These compounds make up about 18 % by weight of gasoline. The effective solubilities of BTEX compounds are lower than their single - compound aqueous solubilities. BTEX represent potential long-term sources for continued ground-water contamination at many sites (Newell et al, 1995; Phophi, 2004).

When the BTEX compounds enter the water or food chain, this can be fatal for human life, causing harm in the short or long term. However, benzene is considered as carcinogenic and mutagenic as well as a priority pollutants according to the Environmental Protection Agency (EPA) and National Primary Drinking Standards (Christensen and Elton, 2005 ; Makri et al., 2006).

A NAPL in physical contact with ground-water will dissolve (solubilize, partition) into the aqueous phase. The solubility of an organic compound is the equilibrium concentration of the compound in water at a specified temperature and pressure. For all practical purposes, the solubility represents the maximum concentration of that compound in water (Newell et al, 1995).

The aqueous-phase concentrations of dissolved NAPLs in ground-water are primarily governed by interphase mass transfer processes that often are slow and rate-limited (Mackay et al. 1985).

Only a limited number of experimental studies have focused on characterizing the NAPL dissolution process under three-dimensional flow conditions (Clement et al. 2004; Lee and Chrysikopoulos 2006).

The objective of the present study is study the dissolution of benzene as a LNAPL in three dimensional homogeneous, isotropic, and saturated porous media.

2. EXPERIMENTAL DESIGN:

2.1. Design of the Experimental Aquifer:

The dissolution experiments were conducted in a three dimensional intermediate-scale sand tank model. The tank was made of 1 cm thick Perspex plates with dimensions of 100 cm long by 40 cm wide by 35 cm high. Two perforated Perspex plates were used, each one located 10 cm away from both sides dividing the tank into three chambers. The middle chamber was filled with saturated porous sand, and the chambers at both sides were filled with water to maintain constant heads. A filtration cloth was fixed on the perforated plates to prevent passing the sand into the chambers at both sides of the aquifer. Figure (1) shows a schematic diagram of the laboratory-scale aquifer and the other auxiliary equipments. The auxiliary equipments consists of a 125 liter storage tank contains tap water, two constant head reservoirs of 20 liter and 3 liter volumes, respectively, and a flowmeter (Cole-Parmer Instrument Co.; Chicago, Illinois 60648).

2.2. LNAPL Pool Formation and Aquifer Packing:

A circular plastic bowl of 15 cm inner diameter and 5 cm height was used to confine the LNAPL (benzene) pool at the surface of the experimental aquifer. The aquifer tank was filled with sand to a height 23 cm, the water cover all the sand. The bowl was inversely placed on the upper surface of the water-saturated sand, so the open side of the bowl directly faced the sand. The aim of this configuration is to keep the pool within 15 cm of the porous media. The bowl fixed by four screws with the Perspex cover of tank (figure 1). The LNAPL was dyed with Sudan III which is a powdered, nonvolatile organic dye of red color, soluble in hydrocarbons and insoluble in water. The addition of the red dye is to assist in the visual observation of the LNAPL pool. The thickness of the floating LNAPL pool in the bowl is 1 cm. The pool is injected at a rate of 18 ml/hr.

Karbalaa's sand was used as a porous medium. The 1 mm sand was packed into the tank to height 23 cm. This configuration resulted in a packed volume of about 92,000 cm^3 (100×40×23 cm). The tank was then filled with water (several cm above the upper level of sand) and left overnight to settle and saturate the sand. The system was then flushed at maximum velocity until the effluent water was free of suspended fine material. After ending each experiment, the used sand removed from the tank. The tank was washed and cleaned very well and then fills with new sand in order to be ready for a new experiment.

A small stream of 200 mg/l sodium azide solution was introduced to the influent water at the chamber in the left side of aquifer to inhibit biological growth.

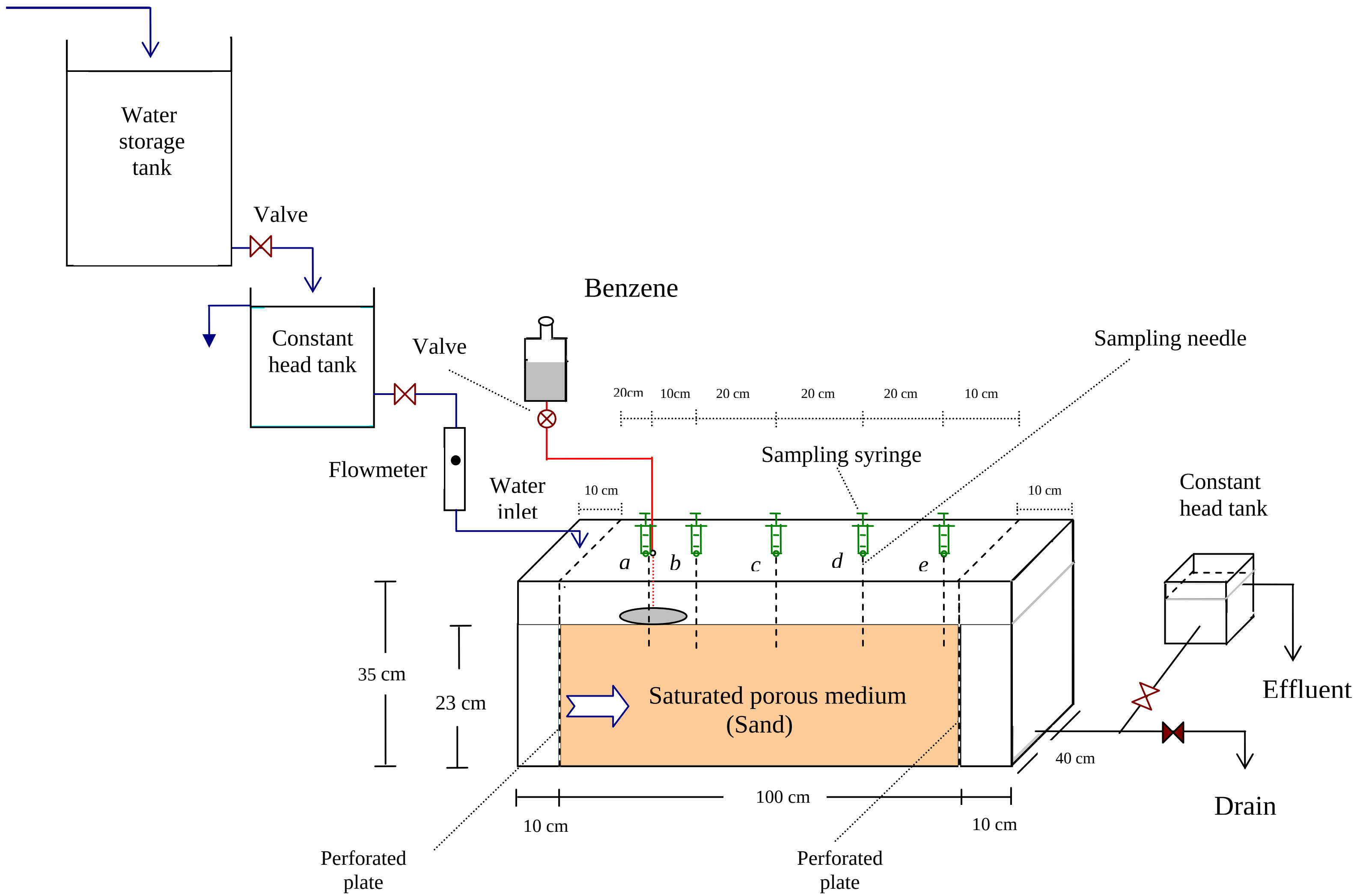

Figure 1: A schematic diagram of the laboratory-scale aquifer (three dimensional sand tank 100×40×35 cm).

2.3. Porous Medium Properties:

Karbalaa's sand (this type of the soil was taken from the land of Karbalaa's Governorate in Iraq) was used in the present study as a porous medium. The sand passing through 1 mm mesh was used. Samples were tested for measurement of particle size distribution by mechanical sieve analysis, porosity, as well as the permeability coefficient. All these measurements were achieved at the Soil Laboratory in Civil Engineering Department/College of Engineering/ University of Baghdad.

2.3.1. Particle Size Distribution:

The particle size distribution was obtained by using mechanical sieve analysis as shown in figure (2). The uniformity coefficient (*Cu*), gives an indication of the range of grain sizes presented in a given soil sample (Bowels, 1978; Al-Khafaji and Andersland, 1992). This coefficient was found to be 2.22. The bulk density of the dry sand is 1.6 g/cm^3, and the porosity is 0.345.

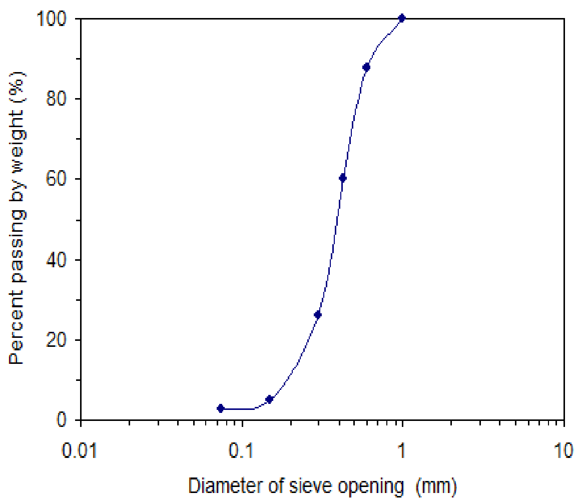

Figure 2: Particle size distribution curve for the Karbalaa's sand.

2.3.2. Interstitial Velocity:

The Interstitial velocity within the model aquifer was determined by using the following equation (Chrysikopoulos et al, 2000):

$$V_x = \frac{Q}{whn} \tag{1}$$

where Q is the water volumetric flowrate , w is the aquifer width, h is the head of water in the aquifer, and n is the porosity of porous medium. Five interstitial velocities 0.90, 1.80, 2.34, 2.70, and 3.60 cm/hr were used in the present study.

2.4. Dissolution Experiments:

Five sampling ports (a to e) were conducted on the cover of sand tank. For collecting samples a 15-gauged stainless-steel needles (manufactured by Sherwood Medical St. Louis, Mo, 63103 USA) were inserted into the ports and pushed into the porous medium. Wire inserted inside the needle during the placement process prevented clogging.

Ten dissolution experiments were conducted in the three dimensional bench scale aquifer. These experiments divided into two sets of samples; each one was collected from five selected points within the aquifer downstream from the LNAPL pool at a selected interstitial velocity. The first set was at depth z =1 cm, the sampling points located at (-7.5,20,1), (2.5,20,1), (22.5,20,1), (42.5,20,1), and (62.5,20,1) respectively. The second set of the samples were at depth z = 3 cm , the sampling points located at (-7.5,20,3), (2.5,20,3), (22.5,20,3), (42.5,20,3), and (62.5,20,3) respectively. The sampling point (-7.5,20,1) and (-7.5,20,3) refers to the sampling point below the LNAPL pool at depth 1 cm and 3 cm respectively.

The flow of water from the storage tank and the constant head tank was by gravity. A flowmeter was used to measure the water flow from the constant head tank to the aquifer. For all experiments the flowrate was ranging from 5 to 20 ml/min. These flowrates yields an interstitial velocity range of 0.90 to 3.60 cm/hr. All experiments were conducted at temperature of 20 ± 1°C. The water elevation in the aquifer was maintained at the desired level by using two constant head reservoirs one before the inlet and the other after the outlet of the aquifer.

2.5. Sample Collection and Analysis:

Aqueous phase LNAPL concentrations were collected only when steady-state concentrations were observed at sampling port (*e*), which is the sampling port farthest away from the LNAPL pool. Interstitial water samples were collected from ports of the sand tank using syringe-needles (figure 1). The volume of syringe used was 5 ml. 1 ml of sample was withdrawn from each location and stored in a glass vial, sealed with teflon-lined septa. The number of collected samples from the five ports in the porous medium was 200 samples at depth 1 cm and 200 samples were at depth 3 cm from the top (figure 3). The samples were analyzed in the Center of Chemical Research and Petrochemical industries/Ministry of the Science and Technology, using Gas Chromatograph equipped with flame ionization detector (Gas Chromatograph GC-2014, Shimadzu Corporation, Analytical & Measuring Instrument Division, KYOTO, Japan).

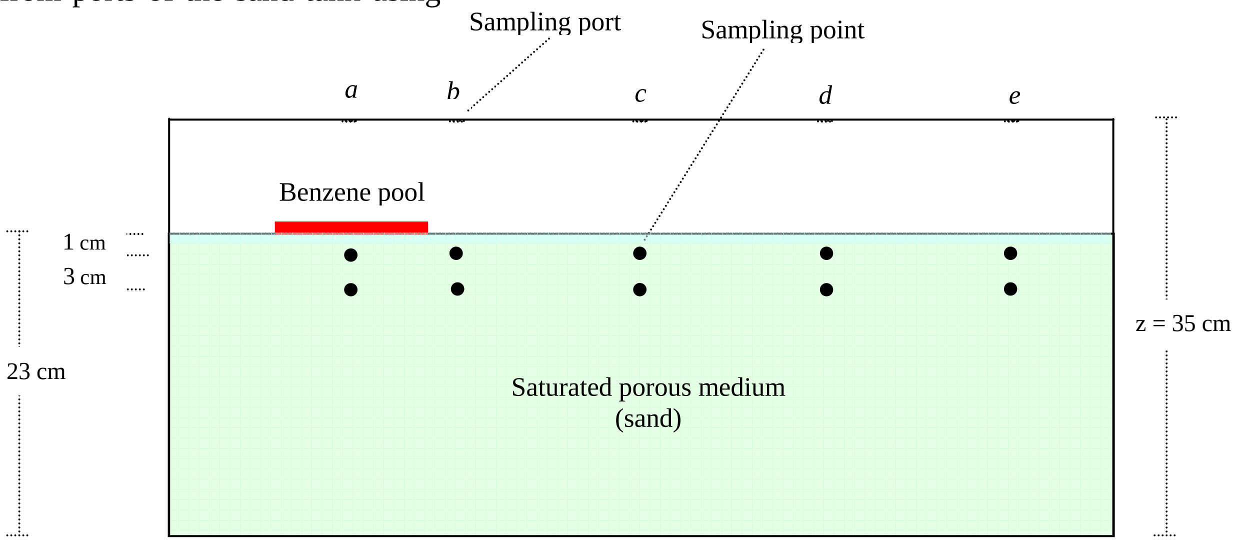

Figure 3: Sketch illustrate *side view* of the model aquifer sampling points location, the points located at depths (z) of 1 cm and 3 cm.

3. RESULTS AND DISCUSSION:

Figures (4) and (5) show the change of the measured benzene concentration with distance (*x*) below and downstream of the benzene pool at sampling times of 1 , 4 , and 8 day. The lateral distance y = 20 cm, and at depths (*z*) 1cm and 3 cm, respectively. In general the concentration values decreased with distance. In figure (4), at time 1 day and velocities approximately equal or less than 2.7 cm/hr, the concentrations were increased within the distance -7.5 cm (below the center of benzene pool) to 2.5 cm and then declined to the lower limits, while other profiles have the same behavior which are decreased with distance from upper to lower limits. In figure (5) which show the concentration versus distance at depth 3 cm, all concentration profiles declined with distance from upper to lower values; except at velocity 3.60 cm/hr; the concentration profile of time 8 day increased within the distance -7.5 cm to 2.5 cm and then continue to decline to the lower limit.

In figure (4), approximately there is no significant difference between the concentration values at time 1 , 4 , and 8 day with horizontal distance (*x*) except those at the distance between -7.5 cm and

2.5 cm. While in figure (5), a significant difference in concentration was noticed especially at the horizontal distance equal or less than 22.5 cm. The interpreting of this phenomenon may be attributed to effect of many parameters which are collectively effect on the on dispersion and transport of contaminant, these parameters are hydrodynamic conditions such as interstitial velocity (V_x) and dispersion coefficients, and horizontal and vertical (depth) distances.

The effect of the interstitial water velocity on benzene concentration is shown in figures (6) and (7). In these figures; except at distance -7.5 cm, and at distance 2.5 cm in figure (7); the measured concentrations declined at velocities more than about 2.34 cm/hr. The interpretation for this behavior is the increasing of interstitial velocity led to increasing the value of horizontal advection which means that the amount of concentration downstream will be reduced. At the distances -7.5 cm and 2.5 cm where the sampling points situated in holes *a* and *b* ;under and near the benzene pool (at x= -7.5 cm, y=20 cm, z=1 cm; x= -7.5 cm, y=20 cm, z=3 cm; and x= 2.5 cm, y=20 cm, z=3 cm); the behavior of concentration was differ than that of the other figures. In figure (6) at distance -7.5 cm where the sampling point located at the center line below the benzene pool, for the times 1 day and 4 day the concentration increased with increasing velocity; while at the time of the 8 day, the concentration decreased until the velocity reach about 2.34 cm/hr then it is increased with increasing the velocity. In figure (7) at distance -7.5 cm, the concentrations at time 1 day were increased with increasing velocity but then decreased after velocity of 2.34 cm/hr. At times 4 day and 8 day in this figure, and at all times at distance 2.5 cm, the concentration profiles are fluctuated and unstable with increasing velocity.

Clement et.al. (2004) reported that at high velocity, the net flow through the system will increase and therefore the overall dispersion and dilution rates would have also increased; this should have had a negative influence on the downstream concentration levels. On the other hand, the high velocity conditions would have increased the overall dissolution rate because of the presence of high concentration gradient and better mixing conditions near the LNAPL-water boundary; this should have had a positive influence on the downstream concentration levels. Further, high velocities might have also influenced the time-dependent variations in the morphology of the LNAPL source. It is difficult to conceptualize the combined influence of all these complex processes that have offsetting effects.

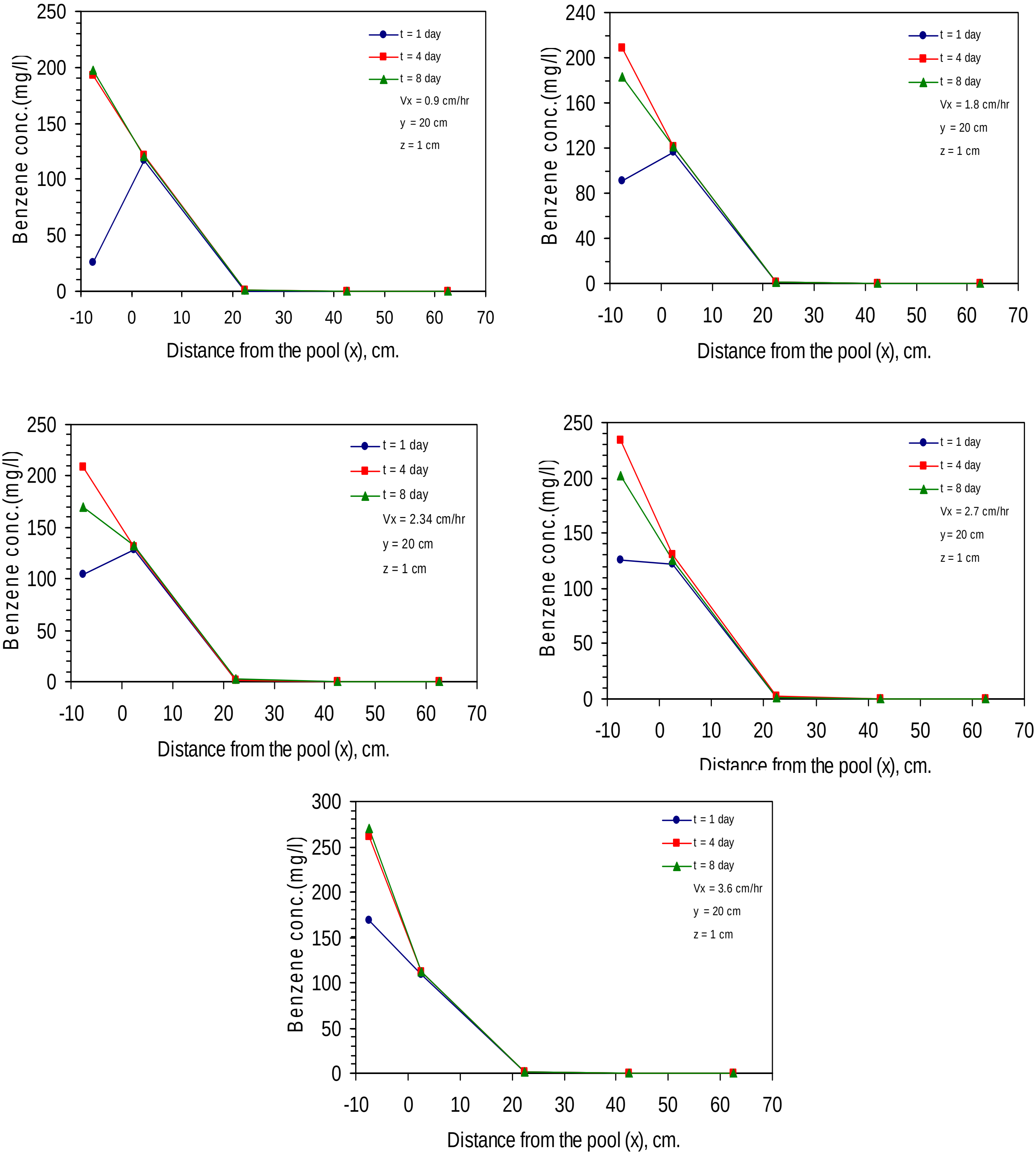

Figure 4: The measured concentration of benzene versus distance from the pool (x) at *interstitial velocity 0.90, 1.80, 2.34, 2.70, and 3.60 cm/hr*, *depth (z) = 1 cm* , y = 20 cm, and times 1 , 4 , 8 day.

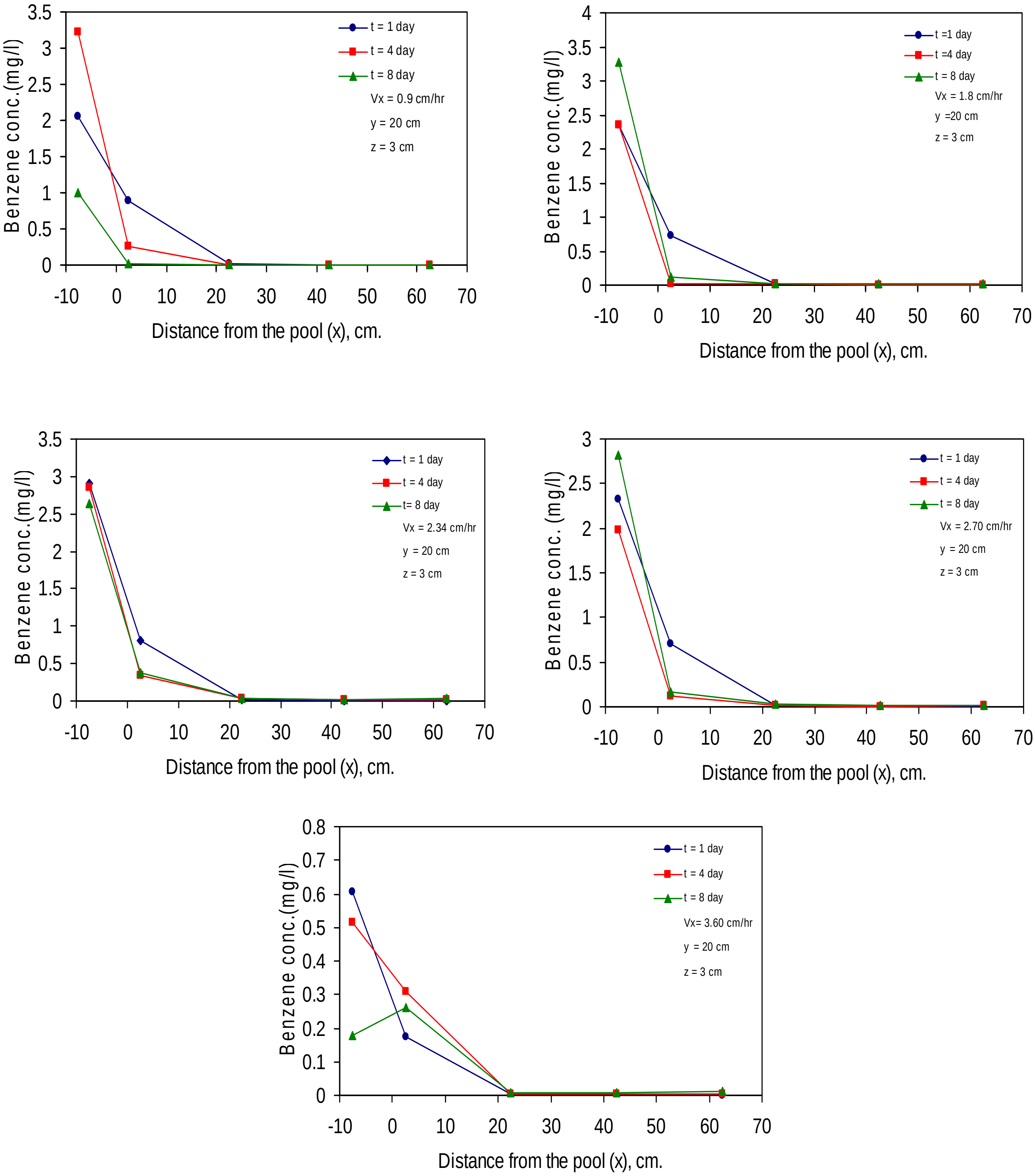

Figure 5: The measured concentration of benzene versus distance from the pool (*x*) at *interstitial velocity 0.90, 1.80, 2.34, 2.70, and 3.60 cm/hr, cm/hr, depth (z) 3 cm , y* = 20 cm, and times 1 , 4 , 8 day.

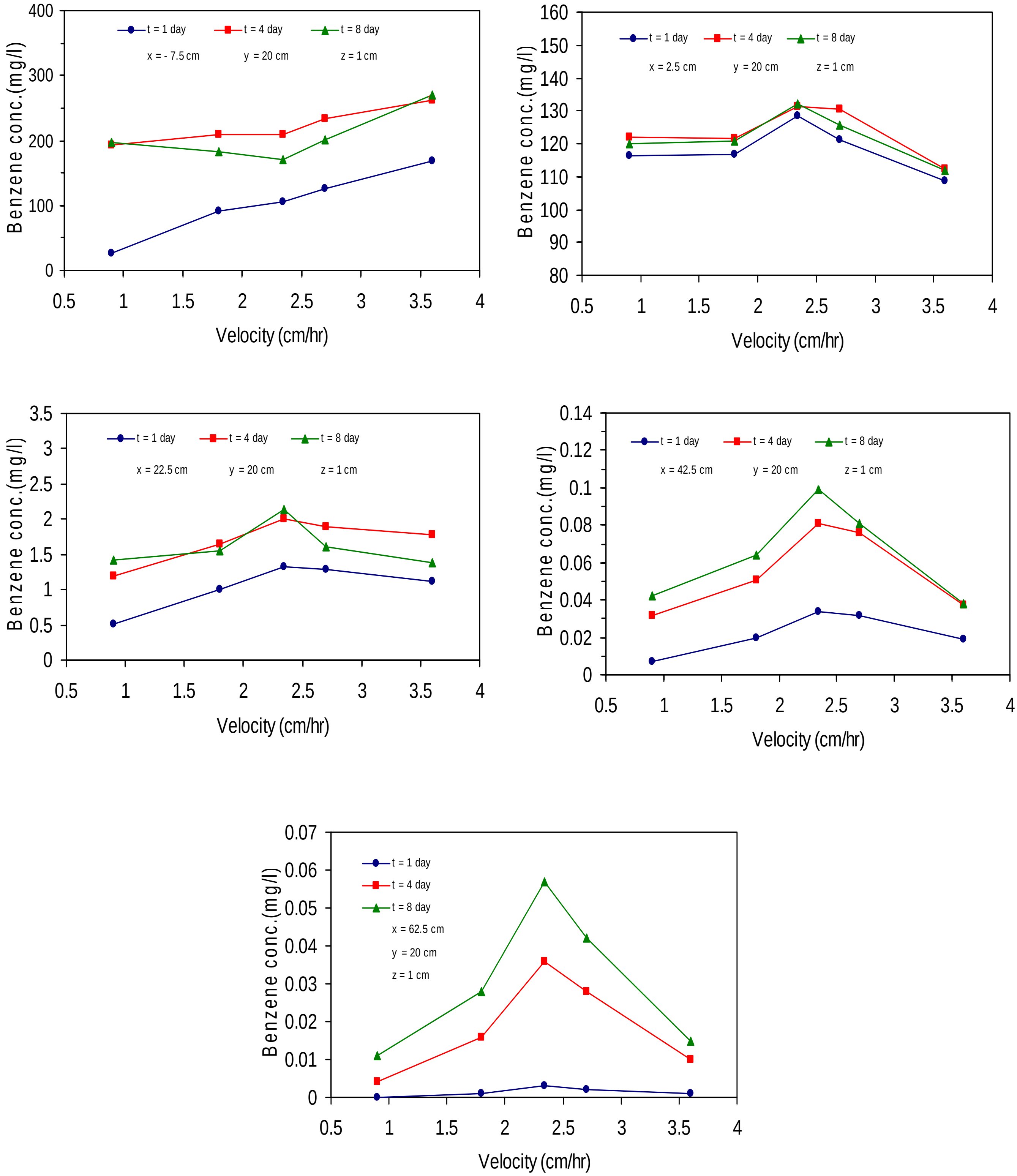

Figure 6: The measured concentration of benzene versus the interstitial velocity (*Vx*) at *depth (z) 1 cm, The distance from the pool (x) – 7.5,2.5 , 22.5 , 42.5 ,and 62.5 cm, y* = 20 cm, and times 1, 4, 8 day.

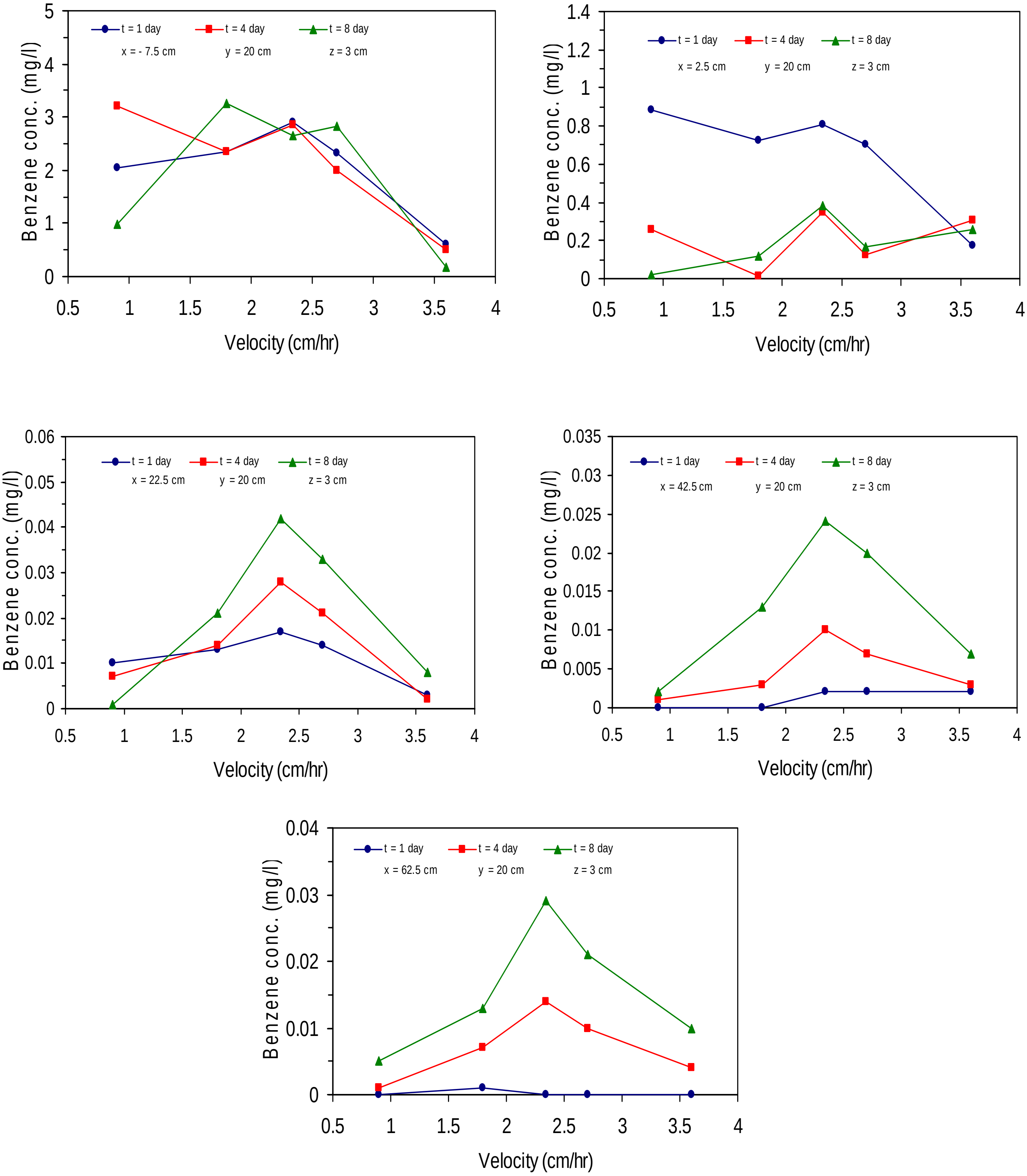

Figure 7: The measured concentration of benzene versus the interstitial velocity (*Vx*) at *depth (z) 3 cm, distance from the pool (x) -7.5 cm, 2.5 , 22.5 , 42.5 ,and 62.5 cm, y* = 20 cm, and times 1, 4, 8 day.

4. MASS TRANSFER CORRELATION:

Power and Heermann (1999) reported that the average mass-transfer coefficient (k^*) can be computed from the following equation:

$$k^* = n\sqrt{\frac{4D_z V_x}{\pi L}} \qquad (2)$$

where L is the length of interface.

Time invariant, average mass transfer correlations for NAPL pool dissolution in saturated porous media were developed by Kim and Chrysikopoulos (1999), based on numerically determined average mass transfer coefficients evaluated for interstitial fluid velocities of 0.3,0.5,0.7, and 1.0m/day.

The time invariant average mass transfer coefficient (k^*) was experimentally determined using equation (2) for each velocity. The vertical dispersion coefficient (D_z) is 2.84×10^{-2} , 5.53×10^{-2} , 6.96×10^{-2}, 7.80×10^{-2}, and 1.014×10^{-1} cm^2/hr at the velocities 0.90, 1.80, 2.34, 2.70, 3.60 cm/hr respectively (Gzar, 2010). Figure (8) indicates that k^* is proportional to the interstitial velocity (V_x). This behavior is attributed to increasing the concentration gradients at the NAPL-water interface with increasing V_x .The best fit relation of the time invariant average mass transfer coefficient (k^*) as a function to interstitial velocity (V_x) is:

$$k^* = 0.0166 V_x + 0.0016 \qquad (3)$$

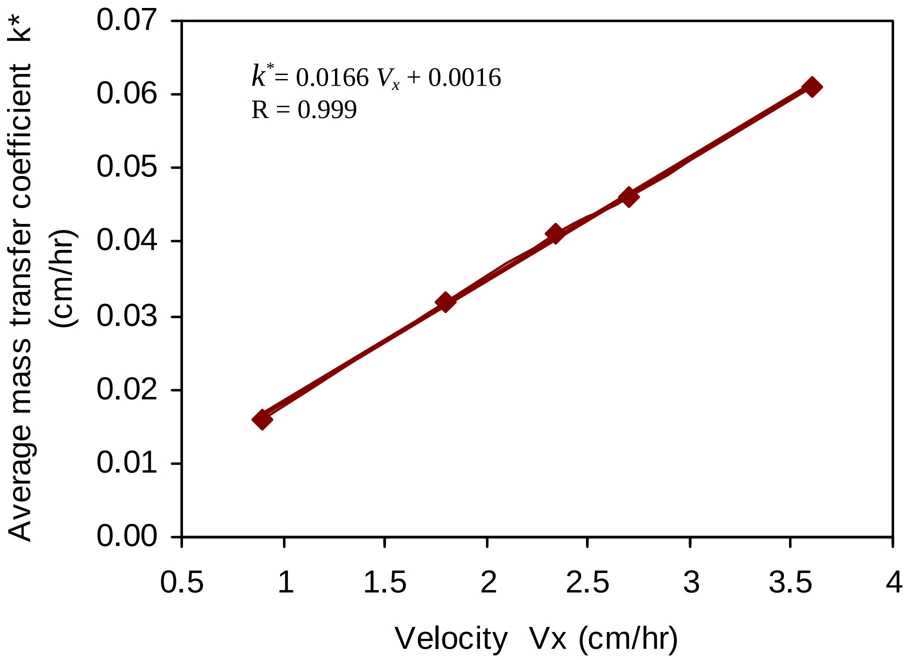

Figure 8: The change of the average mass transfer coefficient (k^*) with the interstitial velocity (V_x).

The dimensionless mass transfer behavior is summarized in terms of the modified Sherwood number, $Sh^*_{(e)} = k^* \, l_{c(e)}/D_e$, (figure 9), where the characteristic length ($l_{c(e)}$) employed here is the square root of the pool area. The computed $l_{c(e)}$, and D_e for the present research were 13.29 cm and 2.47*10^{-2} cm^2/hr respectively.

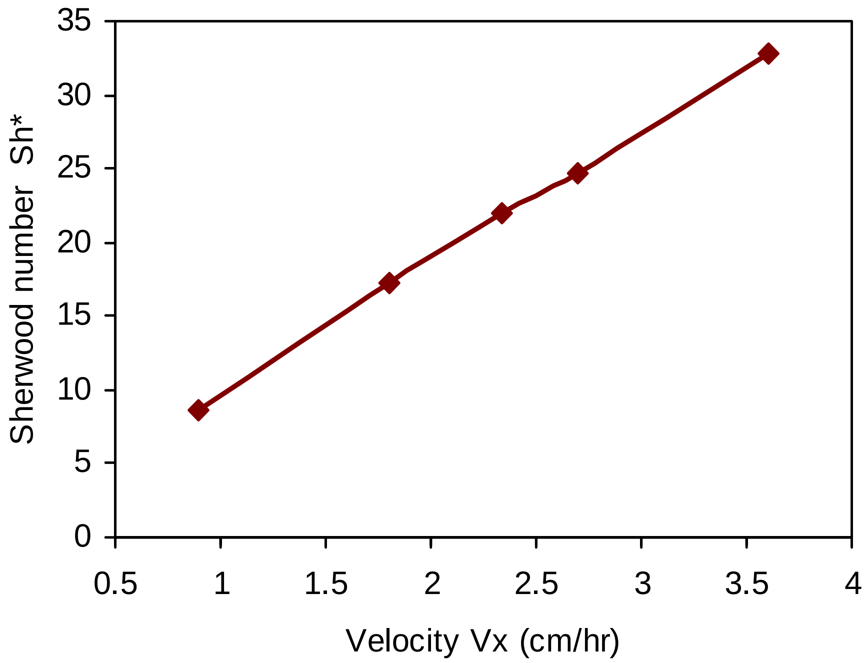

Figure 9: The dimensionless mass transfer (modified Sherwood number $Sh^*_{(e)}$) behavior with the interstitial velocity (V_x).

5. CONCLUSIONS:

A three dimensional bench-scale aquifer has been designed and constructed for dissolution experiments. The concentration profile with time is determined at different distances near the water table at different values of the interstitial velocity. A relationship is found between the time invariant average mass transfer coefficient and the interstitial velocity. The values of this coefficient are ranged from 0.016 to 0.061 cm/hr. It is increased proportionally with velocity toward a limiting value. The results show that the concentration of the LNAPL reduces as the distance increased in *x* and/or *z* direction from the source of pollution. In most cases the concentration declines with velocity more than 2.34 cm/hr at distances downstream of the LNAPL pool.

References:

Al-Khafaji A.W., and Andersland O.B., "Geotechnical engineering and soil testing", Saunders College Publishing, 1992.

Bowles J.E., " Engineering properties of soils and their measurement ", McGraw-Hill Kogakusha, Ltd., 1978.

Christensen, J.S., and J. Elton, "Soil and ground-water pollution from BTEX". www.cee.vt.edu/prorgram_areas/environmental/teach/gwprimer/btex/btex.html, 2005.

Chrysikopoulos C.V., and Kim T-J, "Local mass transfer correlations for nonaqueous phase liquid pool dissolution in saturated porous media", *Transp. Porous Media*, 38, 167-187, 2000.

Clement T.P. , Kim Y.C., Gautam T.R., and Lee K.K, "Experimental and numerical investigation of DNAPL dissolution process in a laboratory aquifer model", *Journal of Ground water Monitoring & Remediation* , 24(4), 88-96, 2004.

Gzar H. A., "Experimental investigation and numerical modeling of benzene dissolution and transport in a saturated zone of the soil", Ph.D. thesis, College of Engineering/ University of Baghdad, 2010.

Hiscock K., " Ground-water pollution and protection", Environmental Science for Environmental Management, O'Riordan (eds),1995.

Kim T-J, and Chrysikopoulos C.V., "Mass transfer correlations for nonaqueous phase liquid pool dissolution in saturated porous media", *Water Resour. Res.* , 35 449-459, 1999.

Lee K.Y. and Chrysikopoulos C.V., "Dissolution of a multicomponent DNAPL pool in an experimental aquifer", *Journal of Hazardous Materials*, B128, 218-226, 2006.

Mackay D.M., Roberts P.V., Cherry J.A., "Transport of organic contaminants in ground-water: distribution and fate of chemicals in sand and gravel aquifers", *Environ. Sci. Technol*., 19 (5), 384-392, 1985.

Makri P., Kalivas D.K., Bathrellos G., and Skilodimou H., "Spatio-temporal analysis of ground-water pollution from BTEX in Thriassio Field, Attica, Greece", *IAEG*, paper number 409, 2006.

Moore G.S., Villenave J.H., and Hickey J.C., "Characterization of petroleum contaminants in ground-water and soils", Hydrocarbon contaminated soil In: Kostecki P., Calabrese E., and Bonazountas M. (eds).Chelsea Lewis Publishers, USA, 1992.

Newell C.J., Acree S.D.,Ross R.R., and Huling S.G.,"Light nonaqueous phase liquids", EPA Ground Water Issue,EPA/540/S-95/500, September 1995.

Phophi T.S., "The occurrence and evaluation of LNAPLs contamination in urban areas of South Africa", Master thesis, University of the Free State, Bloemfontein, South Africa, 2004.

Power S.E. and Heermann S.E., " Potential ground and surface water impacts, appendix B: Modeling interface mass-transfer processes" presented in "A critical review: the effect of ethanol in gasoline on the fate and transport of BTEX in the subsurface", Editors Cannon G. and Rice D. , UCRL-AR-135949 Vol.4, chapter 2, 1999.

Forward and Reverse Osmosis Process for Recovery and Re-use of Water from Polluted Water by Phenol

Ahmed Faiq Al-Alawy
Chemical Engineering Department – College of Engineering – University of Baghdad – Iraq.

ABSTRACT

The research aims to apply the novel forward osmosis (FO) process to recover pure water from contaminated water. Phenol was used as organic substance in the feed solution, while sodium chloride salt was used as draw solution. Membranes used in the FO process is the cellulose triacetate (CTA) and polyamide (thin film composite (TFC)) membrane. Reverse osmosis process was used to treatment the draw solution, the exterior from the forward osmosis process. In the FO process the active layer of the membrane faces the feed solution and the porous support layer faces the draw solution and this will show the effect of dilutive internal concentration polarization and concentrative external concentration polarization.

In the FO process was a run-time for five hours, and the concentration of phenol 100 and 1000 mg/l, and for the NaCl the concentration was 10000 and 30000 mg/l. It was found that recovery percent increases with increasing time, while water flux through membrane decreases with increasing time. Also, it was found that recovery and water flux increases with increasing draw solution concentration, on the contrary, water flux and the percentage of recovery decreases with increasing the concentration of phenol (feed solution). Increase in draw solute (NaCl) concentration has more effect on the water flux in FO process compared with increase in the concentration of phenol. Outlet phenol concentration increases with time, while the outlet salt concentration decreases with increasing the time. The results showed that the cellulose triacetate membrane gave the highest recovery ratio from the thin film composite membrane. The highest recovery was reached in five hours is 51.33%, while using CTA membrane recovery rate increase, by 23% compared with TFC membrane. The value of the resistance to solute diffusion within the membrane porous support layer is 36.83 h/m. Reverse osmosis is perfect method for removal of dissolved salts from water, thus its suitable process for reducing the content of NaCl in draw solution; therefore the sodium chloride rejection percentage was 91.6 – 96 % for polyamide membrane (TFC). Within two hours of work of the reverse osmosis system the recovery percentage of pure water is 58%.

عملية التناضح الامامي والعكسي لاسترجاع واعادة استخدام الماء من المياه الملوثة بالفينول

الخلاصة

يهدف البحث الى تطبيق عملية التناضح الامامي (FO) الجديدة لاسترجاع الماء النقي من المياه الملوثة. تم استخدام الفينول كمادة عضوية في محلول التغذية، بينما تم استخدام ملح كلوريد الصوديوم كمحلول سحب. الاغشية المستخدمة في عملية التناضح الامامي هي غشاء الأسيتات الثلاثي السليلوزي (CTA) وغشاء البولي امايد (البوليمر الرقيق المركب (TFC)). تم استخدام عملية التناضح العكسي لمعالجة محلول السحب الخارج من عملية التناضح العكسي. في عملية التناضح الامامي الطبقة الفعالة للغشاء تقابل محلول التغذية وطبقة الدعم المسامية تقابل محلول السحب وهذا سوف يظهر تاثير استقطاب التركيز الداخلي المخفف واستقطاب التركيز الخارجي المركز.

في عملية التناضح الامامي كان وقت التشغيل لمدة خمس ساعات ، وتركيز الفينول المستخدم 100 و 1000 ملغ \ لتر ، وبالنسبة لتركيز NaCl كان 10000 و 30000 ملغم \ لتر. لقد وجد بأن نسبة الاسترجاع تزداد بزيادة الزمن ، في حين تدفق

الماء خلال الغشاء يتناقص مع زيادة الوقت. وكذلك، لقد وجد بان الاسترجاع وتدفق الماء يزداد بزيادة تركيز محلول السحب، وبالعكس، تدفق الماء ونسبة الاسترجاع تقل بزيادة تركيز الفينول (محلول التغذية). الزيادة في تركيز مذاب السحب (NaCl) له تأثير اكثر على معدل تدفق الماء في عملية التناضح الامامي مقارنةً بالزيادة في تركيز الفينول. تركيز الفينول الخارج يزداد مع الزمن، بينما تركيز الملح الخارج يقل بزيادة الزمن. وأظهرت النتائج أن غشاء الأسيتات الثلاثي السليلوزي أعطى أعلى نسبة استرجاع من الغشاء الرقيق المركب. اعلى نسبة مئوية للاسترجاع تم التوصل اليها في خمس ساعات هي 51,33% ،بينما استخدام غشاء CTA الاسترجاع زاد بنسبة 23% مقارنةً باستخدام غشاء TFC. قيمة المقاومة لانتشار المذاب داخل الطبقة الداعمة المسامية للغشاء هي 36،83 ساعة \ م. التناضح العكسي هي طريقة مثالية لأزالة الاملاح الذائبة من الماء، لهذا تعتبر عملية مناسبة لتقليل محتوى ملح كلوريد الصوديوم في محلول السحب، ولهذا النسبة المئوية لرفض كلوريد الصوديوم كانت 91,6 – 96 % لغشاء البوليمر (TFC). خلال ساعتين من عمل نظام التناضح العكسي نسبة استرجاع الماء النقي هي 58 ٪.

Keywords: Forward Osmosis; Reverse Osmosis; Recovery of Water; Wastewater; Phenol; Membranes.

INTRODUCTION

The problem of considerable contamination of the aqueous environment with organic pollutants still requires the development of quick and simple methods for the removal, separation and determination of these compounds. The main classes of organic compounds that most of the industries use and discharge into the effluents is phenol, surfactant and dye. All these compounds are troublesome contaminants which pose not only to toxicity and health hazards but also hamper the environmental treatment processes (John et al., 2005). In particular, the removal of phenol is of great interest in wastewater treatment. With a global production of 8 million tons nearly each year, phenol is one of the most important intermediates in chemical industry. Phenol contaminated effluents arise, for example, during the production processes of bisphenol A, phenol formaldehyde resins, and the Hock process (Kujawski et al., 2004). Methods for the recovery of phenols include membrane processes (Ray et al., 1997 and Hoshi et al., 1997), solvent extraction (Krishnakumar and Sharma, 1984 and Shejiao et al., 2001), activated carbon and polymer adsorption (Bercie et al., 1996).

Water scarcity problems in recent years and ground water contamination due to floods have been increasing alarmingly. The aim of wastewater treatment cannot be limited merely on achieving permissible discharge limits; rather its objectives should also focus on possible recycle options within the treatment schemes (Mahesh and Sukumar, 2008). Membrane separation processes are quite useful in concentration, separation and purification. So far, the most widely used membrane processes for water treatment include microfiltration (MF), ultrafiltration (UF), nanofiltration (NF), and reverse osmosis (RO). All of these are pressure-driven processes, which require energy to pressurize the system. While pressure-driven membrane processes, such as reverse osmosis, have dominated for several decades, new desalination processes are now appear, such as forward osmosis (FO) (Ahmed, 2007 and Hasan 2008).

Reverse osmosis (RO) is a technology that uses pressure to separate the salt (as NaCl) from the water and is capable of reducing water salinity. With this technology, the pressure is increased above the osmotic pressure, which allows the water to pass through semi-permeable membranes, but retains the solid salt particles (George, 1997 and Sourirajan, 1970). The reverse osmosis technology was introduced in the 1970's. After the multi-stage flash distillation (MSF) technology, it is the most-used technology in all the Gulf countries. Reverse osmosis is considered the best alternative to distillation, due primarily to its low energy consumption, low deposition rate, smaller required space compared to other desalination facilities, and lower costs. This technology is generally very suitable for desalinating brackish water. Most currently available RO membranes fall into two categories: asymmetric membranes containing one polymer, and thin-film composite membranes consisting of two or more polymer layers. There are four main types of membrane modules: plate-and-frame, tubular, spiral wound, and hollow fiber. The most popular module in industry for nanofiltration or reverse osmosis membranes is the spiral wound module (Merten, 1966 and Schutte, 2003). The main advantage of this design is the large surface area of the membrane that is packaged into a relatively small volume of the cylindrical membrane element. The efficiency of water production with this method depends on the salinity level of the feed water and the number of desalination stages (number of membranes). Most reverse osmosis membranes allow less than 1% of the salt content in a single stage. With additional costs, the salinity can be further reduced with second-stage membrane desalination (Ahmed, 2000 and James et al., 2010).

Forward (or direct) osmosis is a process in which osmosis is used to pull water from feed solution (wastewater), through a semi-permeable membrane, into an osmotic agent solution (draw solution or NaCl – H_2O solution in this search). The semi-permeable membrane is permeable to water, but essentially impermeable to other species. Osmotic transfer of water from the feed solution into the draw solution occurs because of the high concentration of dissolved solids maintained in the draw solution (Kravath and Davis, 1975). This gives the draw solution a very high osmotic potential, causing it to pull water through the membrane from the feed. Forward osmosis membranes reject organics, metals and other solids similar to reverse osmosis but resist typical fouling problems (Holloway et al., 2007).

Forward osmosis has several unique benefits of technology. Firstly, FO process overcomes fouling, comparison with other membranes separation processes (such as RO, NF, UF, and MF). Secondly, FO can be treated different feed streams; the water source is dirty or contaminated, which contains high levels of suspended solids (Mi and Elimelech, 2010). Thirdly, in membranes separation processes which using pressure as driving force; all components of a feed are compulsorily forced against the membrane surface. Fourthly, in FO process using different concentration on sides of membrane surface as driving force, this leads to selectively draws molecules through the membrane avoiding membrane fouling and compaction (Yip et al., 2010). And finally, forward osmosis is a process normally occurring in nature, so, requires little or no electricity or external power source (i.e. low cost). The draw solution solute (or osmotic agent) must have very specific characteristics such as highly soluble in water and low molecular weight; from these characteristics obtain a high osmotic pressure which it leads to higher water flux and feed water recovery. Also, osmotic agent solution solute must be nontoxic and probably the solute is edible in some cases. Ideal draw solution does not interact with the membrane or degrade the membrane. It should be noted, the solute in a draw solution non-edible must be separated easily and economically to be used again (McCutcheon et al., 2006).

The present study includes two parts, the first stage application novel method (forward osmosis) to recovery of water from wastewater by phenol. Membranes used in the paper are cellulose triacetate (CTA) and thin film composite (TFC) membranes. Draw solution that was used is sodium chloride solution (NaCl - H_2O) because it has an ideal specification for draw solution solute. The effect of time, feed solution concentration and draw solution concentration for two types of membranes on recovery percentage, water flux, outlet concentration of phenol and sodium chloride have been determined. The second stage, a technically viable reverse osmosis process has been employed to treat the draw solution outlet from forward osmosis process, and then recycle draw solution to FO process to be used again.

THEORY AND METHODS

Concentration polarization is a significant problem in pressure-driven membrane desalination processes and has thus been the target of several investigations. Concentration polarization takes place when species that are retained or rejected by the membrane accumulate at the membrane surface. The concentration increases as they approach the membrane surface. The effect of this accumulation depends on the solute concentration (International Atomic Energy Agency, 2004 and Baker, 2004). Below, these two concentration polarization phenomena are quantitatively described.

External Concentration Polarization

Concentrative external concentration polarization occurs in forward osmosis when the feed solution is placed against the active layer of the membrane. To account for this phenomenon, the extent of concentration polarization was calculated from film theory. The Sherwood number, Sh, was first determined by using either the laminar or turbulent flow correlation for a rectangular channel (McCutcheon and Elimelech, 2006):

$$sh = 1.85\left(\mathrm{Re}\,\mathrm{Sc}\,\frac{d_h}{L}\right)^{0.33} \quad \text{(Laminar Flow)} \tag{1}$$

$$sh = 0.04\,\mathrm{Re}^{0.75}\,\mathrm{Sc}^{0.33} \quad \text{(Turbulent Flow)} \tag{2}$$

Here, Re is the Reynolds number, Sc is the Schmidt number, d_h is the hydraulic diameter, and L is the length of the channel. The mass transfer coefficient, k, is related to Sh by

$$k = \frac{\mathrm{Sh}\,D}{d_h} \tag{3}$$

Where D is the solute diffusion coefficient. The concentrative external concentration polarization moduli at each permeate flux, J, could be calculated using

$$\frac{\pi_{F,m}}{\pi_{F,b}} = \exp\left(\frac{J}{k}\right) \tag{4}$$

Where J is the experimental permeate water flux, and $\pi_{F,m}$ and $\pi_{F,b}$ are the osmotic pressures of the feed solution at the membrane surface and in the bulk, respectively. Note that the exponent is positive, indicating that $\pi_{F,m} > \pi_{F,b}$.

The draw solution in contact with the permeate side of the membrane is being diluted at the permeate–membrane interface by the permeating water (Moody and Kessler, 1976). This is called dilutive external CP. Both concentrative and dilutive external CP phenomena reduce the effective osmotic driving force. A dilutive external CP modulus can be defined as above, except that in this case, the membrane surface concentration of the draw solute is less than that of the bulk (i.e. $\pi_{D,b} > \pi_{D,m}$) (Cath et al., 2006):

$$\frac{\pi_{D,m}}{\pi_{D,b}} = \exp\left(-\frac{J}{k}\right) \tag{5}$$

Where $\pi_{D,m}$ and $\pi_{D,b}$ are the osmotic pressures of the draw solution at the membrane surface and in the bulk, respectively.

To model the flux performance of the forward osmosis process in the presence of external concentration polarization, we start with the flux equation for forward osmosis, given as

$$J = A\,(\pi_{D,b} - \pi_{F,b}) \tag{6}$$

Here, A is the pure water permeability coefficient. We assume that salt does not cross the membrane, the osmotic reflection coefficient (σ), has a value of 1. Equation 6 predict flux as a function of driving force only in the absence of concentrative or dilutive external concentration polarization, which may be valid only if the permeate flux is very low. When flux rates are higher, this equation must be modified to include both the concentrative and dilutive external concentration polarization:

$$J = A\left[\pi_{D,b}\exp\left(-\frac{J}{k}\right) - \pi_{F,b}\exp\left(\frac{J}{k}\right)\right] \tag{7}$$

Figure 1a show this phenomenon with a dense symmetric membrane (McCutcheon and Elimelech, 2006).

Internal Concentration Polarization

If the porous support layer of an asymmetric membrane faces the feed solution, as in pressure retarded osmosis (PRO), a polarized layer is established along the inside of the dense active layer as water and solute propagate the porous layer (Figure 1b). This is referred to as concentrative internal concentration polarization, this phenomenon is similar to concentrative external concentration polarization, except that it takes place within the porous layer, and therefore, cannot be minimized by cross flow. Lee et al., (1981) derived an expression modeling this phenomenon in pressure retarded osmosis, which Loeb et al., (1997) later described for osmosis. This equation describes internal concentration polarization (ICP) effects and how they relate to water flux (J), salt permeability coefficient (B) and water permeability coefficient (A):

$$K=\left(\frac{1}{J}\right)\ln\frac{B+A\pi_{D,m}-J}{B+A\pi_{F,b}} \tag{8}$$

Where K is the resistance to solute diffusion within the membrane porous support layer, K is defined as

$$K=\frac{t\tau}{D\varepsilon} \tag{9}$$

Where D is the diffusion coefficient of the solute, and t, τ, and ε are the thickness, tortuosity, and porosity of the support layer, respectively. K is a measure of how easily a solute can diffuse into and out of the support layer and thus is a measure of the severity of ICP. We maintain the use of the K term due to convention established in previous studies on internal concentration polarization. Salt permeability coefficient (B) is negligible compared to the other terms in Equation 8. Therefore, we ignore salt flux in the direction of water flux and any passage of salt from the permeate (draw solution) side (Gray et al., 2006). Thus, flux can be solved for implicitly from Equation 8:

$$J=A\left[\pi_{D,m}-\pi_{F,b}\exp(JK)\right] \tag{10}$$

The exponential term in equation 10 is a correction factor that can be considered the concentrative internal concentration polarization modulus, defined as

$$\frac{\pi_{F,i}}{\pi_{F,b}}=\exp(JK) \tag{11}$$

Where $\pi_{F,i}$ is the osmotic pressure of the feed solution on the inside of the active layer within the porous support. The positive exponent indicates that $\pi_{F,i} > \pi_{F,b}$, or that the effect is concentrative. Substitute Equation 5 into 10 to obtain an analytical model for the effect of internal and external concentration polarization on water flux:

$$J=A\left[\pi_{D,b}\exp\left(-\frac{J}{k}\right)-\pi_{F,b}\exp(JK)\right] \tag{12}$$

All the terms in Equation 12 are readily determined through calculations or experiments. From equation we can calculate the water flux through an asymmetric membrane where the feed solution is placed against the support layer and the draw solution against the active layer.

In forward osmosis applications for desalination and water treatment, the active layer of the membrane faces the feed solution and the porous support layer faces the draw solution (Kessler and Moody, 1976). As water permeates the active layer, the draw solution within the porous substructure becomes diluted. This is referred to as dilutive internal concentration polarization (Figure 1c). Loeb et al., (1997) similarly described flux behavior in the forward osmosis mode:

$$K=\left(\frac{1}{J}\right)\ln\frac{B+A\,\pi_{D,b}}{B+J+A\,\pi_{F,m}} \tag{13}$$

When assuming that B = 0, σ = 0 (i.e., the salt permeability is negligible) and the equation 13 is rearranged, an implicit equation for the permeate water flux is obtained:

$$J=A\left[\pi_{D,b}\exp(-JK)-\pi_{F,m}\right] \tag{14}$$

Here, $\pi_{D,b}$ is now corrected by the dilutive internal concentration polarization modulus, given by

$$\frac{\pi_{D,i}}{\pi_{D,b}}=\exp(-JK) \tag{15}$$

Where $\pi_{D,i}$ is the concentration of the draw solution on the inside of the active layer within the porous support. The negative exponent because the water flux is in the direction away from the membrane active layer surface. In other words, the concentration polarization effect in our case is dilutive, meaning that $\pi_{D,i} < \pi_{D,b}$ by substituting Equation 4 into 14, we get

$$J = A\left[\pi_{D,b}\exp(-JK) - \pi_{F,b}\exp\left(\frac{J}{k}\right)\right] \qquad (16)$$

The terms in Equation 16 are measurable system conditions and membrane parameters. Note that here; dilutive internal concentration polarization is coupled with concentrative external concentration polarization, whereas in the Equation 12, concentrative internal concentration polarization was coupled with dilutive external concentration polarization.

In each of these cases, the external concentration polarization and internal concentration polarization moduli all contribute negatively to the overall osmotic driving force. The negative contribution of each increases with higher flux, which suggests a self limiting flux behavior. This implies that increasing osmotic driving force will provide diminishing increases in flux (Tang et al., 2010).

In this search for ideal state, assuming that the salt permeability coefficient (B) is equal to zero and the small value of the flux (J) compared to osmotic pressure of draw solution (π_{NaCl}), therefore the Equations 8 and 13 it can simplify as follows:

$$K = \frac{1}{J}\left(\ln\frac{\pi_{D,b}}{\pi_{F,b}}\right) \quad \text{or} \quad J = \frac{1}{K}\left(\ln\frac{\pi_{NaCl}}{\pi_{phenol}}\right) \qquad (17)$$

Osmotic Pressure

Osmotic pressure magnitude is proportional to the amount of dissolved substances in the solution, dissociated ions per molecule and to the temperature of the solution, and is completely independent of the membrane. In 1886, van't Hoff formulated an equation to calculate osmotic pressure (π), based on data for sugar solution and the similarity of dilute solutions to ideal gases (Thain, 1967 and Ahmed, 2007):

$$\pi = \Phi\, i R_g T C \qquad (18)$$

Where C is the concentration of solute, T is the temperature of solution, R_g is the gas constant, i is number of dissociated ions per molecule, and Φ is osmotic coefficient.

Rejection Percentage

The measure of membrane selectivity is solute rejection, the ratio of solute rejected by a membrane to the solute in the feed. It is the most common method of evaluating a membrane's ability to separate solute, because the determination is simple and can be done as accurately in the field as in the laboratory (Hasan 2008 and Yip et al., 2010).

$$R = \left(\frac{C_F - C_P}{C_F}\right)\times 100 \qquad (19)$$

Where C_F is the concentration of a specific component in the feed solution to the membrane process and C_P is the concentration of the same specific component in the product stream leaving the membrane system.

Recovery Percentage

The recovery factor measures how much of the feed is recovered as permeate. It is reported as a percentage (Ahmed, 2000). Recovery, or conversion, is defined by:

$$Y = \left(\frac{V_P}{V_F}\right)\times 100 \qquad (20)$$

Where V_P is the permeate (or product) volume of water and V_F is the volume of water in feed vessel.

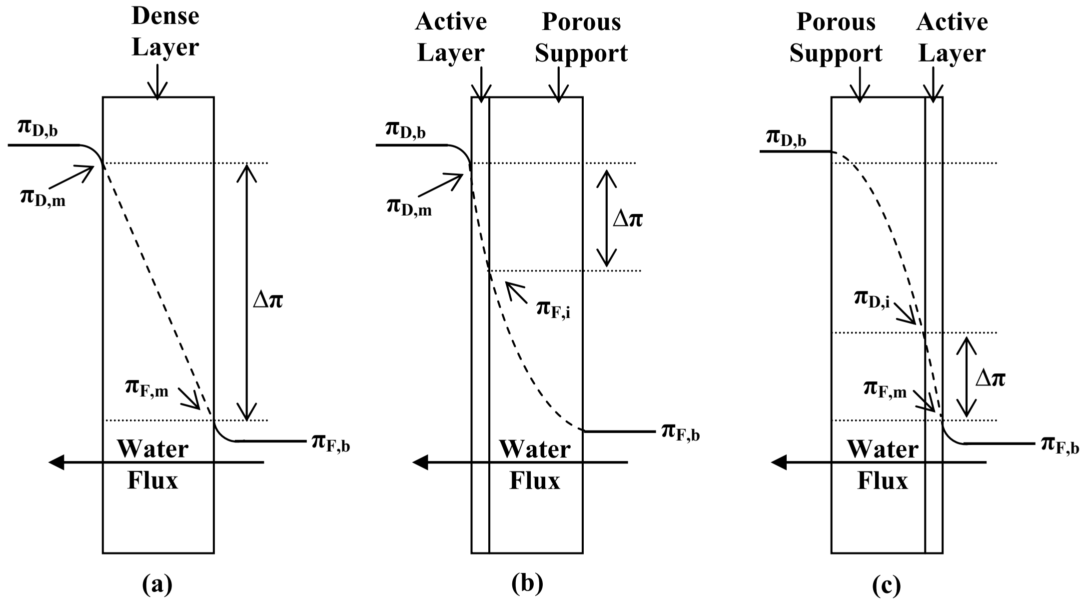

Fig. 1 Illustration of osmotic driving force profiles for osmosis through several membrane types and orientations, incorporating both internal and external concentration polarization. (a) The profile illustrates concentrative and dilutive external CP. (b) PRO mode; the profile illustrates concentrative internal CP and dilutive external CP. (c) FO mode; the profile illustrates dilutive internal CP and concentrative external CP (McCutcheon and Elimelech, 2006).

EXPERIMENTAL

Forward Osmosis

- **Draw and Feed Solutions**

The concentrated draw solution is made by dissolving sodium chloride salt (NaCl) in demineralized water, of 10 – 20 µS/cm conductivity, used for preparing concentrations of 10000 and 30000 mg/l in a QVF glass vessel (25 liter). The high solubility in conjunction with a relatively low molecular weight of the NaCl salt leads to a very high osmotic pressure (i.e. high water flux). As for the preparation of feed solution, it accomplished by dissolving small amounts of phenol in water, to produce concentrations (100 and 1000 mg/l). The chemical analysis of the draw and feed solutions are given in Table 1.

- **The Membranes**

In this study, two types of membranes used. First membrane is cellulose triacetate (CTA) forward osmosis membrane (X-Pack^{TM} supplied by Hydration Technology Inc., Albany, OR) was used for the osmosis experiments. The thickness of the CTA membrane is less than 50 µm and membrane consists of a woven fabric mesh embedded within a continuous polymer layer. The CTA membrane has high sodium chloride rejection 95 – 99%.

The second membrane is thin film composite membrane (TFC) which is commonly used in the process of reverse osmosis, but in this research was used in the two processes (FO and RO). TFC membrane is an aromatic polyamide consisting of three layers: polyester support web (120 µm), micro porous poly sulphone interlayer (40 µm), and ultra thin polyamide barrier layer on the top surface (0.2 µm). The specifications of the TFC membrane are salt rejection (96 – 99 %), maximum operating pressure (6 – 9 Mpa), maximum operating temperature 45 ^{o}C and pH range for continuous operation (2 – 11). The structure of forward osmosis membrane (CTA) is quite different from standard reverse osmosis membranes (TFC).

Table 1 Chemical Specification of Draw and Feed Solutions

Substance	Properties
Phenol (C_6H_6O) MW = 94.11 Scharlab S.L. Made in Spain Solubility (8.2 g/ 100 ml H_2O)	Phenol, crystallized, reagent grade, ACS Assay 99.5% min. Identity (IR-Spectrum) passes test Chlorides 0.0005% Iron 0.0001% o-cresol 0.05% m-cresol 0.05% p-cresol 0.05% Non- volatile matter 0.01% Water 0.2%
Sodium Chloride (NaCl) MW = 58.44 Fluka chemika Solubility (35.7 g/ 100 ml H_2O)	Assay 99.5% min. Max. limits of impurities (%) Ammonia 0.002 Iron 0.002 Lead 0.0005 Potassium 0.02 Sulphate 0.02

- **The Unit Setup**

Figure 2 describes the forward osmosis apparatus used in laboratory of chemical engineering department – University of Baghdad. The osmosis cell is a plate and frame designed with a rectangular channel on each side of the membrane. The channel has dimensions of 19.7 cm length, 4 cm width, and 10 cm height, providing an effective membrane area of 197 cm^2. The draw solution ($NaCl – H_2O$) is flowing on the permeate side and the feed solution (phenol) on the feed side. Co-current flow is used to reduce strain on the suspended membrane. Mesh spacers are also inserted for support within both channels, and it serve to increase turbulence and hence mass transport on both sides of the membrane. The feed and draw solutions were pumped by means of a centrifugal pump (11.4 – 54.6 l/min, 3 – 13.7 m. H, 210 Watt, STUART TURNER LTD. HENLEY ON THAMES ENG, England) to pass through channels of osmosis cell. Two submersible electrical coil (220 Volt, 1000 Watt) and thermostat of range from 0 to 80 °C were used to control on the solutions temperature. The flow rate of draw and feed solutions was regulated by means of globe valve connected at the discharge of the pumps, and measure with a calibrated rotameters with range flow (0 – 100 l/hr). Both the draw and feed solutions were held at the same temperature and flow rate during the FO tests. Concentration of phenol was measured by UV-ultraviolet/visible spectrophotometer (Shimadzu model UV-160 A). While, the concentration of NaCl was measured by digital laboratory conductivity meter (inoLab Cond 720, range (0 – 2 * 10^6 μS/cm), operating temperature (0 – 55 ^oC), accuracy is ± 0.5% full scale, the electrode material is graphite, and made in Germany (WTW)) and digital total dissolved solid (TDS) meter (Waterproof TDSTestr High+, range (0 – 1 * 10^4 mg/l), operating temperature (0 – 50 ^oC), accuracy is ± 1% , and Oakton instruments).

- **Experimental Procedure**

In the forward osmosis process, the phenol solution and draw solution flow tangent to the membrane in a cross flow mode. In the typical orientation of forward osmosis process, the draw solution is placed against the support layer and the feed solution is on the active layer. Through osmosis, water transports from the feed solution (low concentration) across the phenol rejecting membrane and into the draw solution (high concentration). The outlet streams of feed and draw solutions, recycled back to the main vessels. For every one hour, the concentrations of phenol and NaCl were measured and the water flux through membrane. The water flux was calculated by dividing the permeate volume by the product of effective membrane area and time. After recording the results, the solution (remaining in feed vessel), was drained by means of a drain valve. The whole system was washed by distilled water.

Reverse Osmosis

To yield pure water, the diluted draw solution exterior from forward osmosis process is sent to a reverse osmosis unit. An experimental rig of reverse osmosis unit was constructed in the laboratory as shown schematically in Figure 3. The devices used in forward osmosis unit itself was used in reverse osmosis unit, except the selected membrane used a TFC membrane constructed as spiral - wound module (type SSRO50G, length = 12 in., diameter = 2 in., and membrane area = 0.483 m^2). Also, in RO we need to high pressure pump (santoprene and polypropylene materials, maximum pressure = 120 psi, and power = 220 – 240 V) to overcome on osmotic pressure for salt NaCl in water. The process is carried out in a system where the draw solution flows across the RO membrane and pure water and a very reduced amount of the NaCl will pass through the membrane. Produce from the reverse osmosis two streams, the first contains pure water can be used, while the second contains the concentrate draw solution, which be recycled to forward osmosis process. For every quarter hour, the conductivities and concentrations of the reject draw solution (concentrate) and product solution were measured by the conductivity and TDS meters, and the flow rate of the product (permeate) solution for each run was recorded.

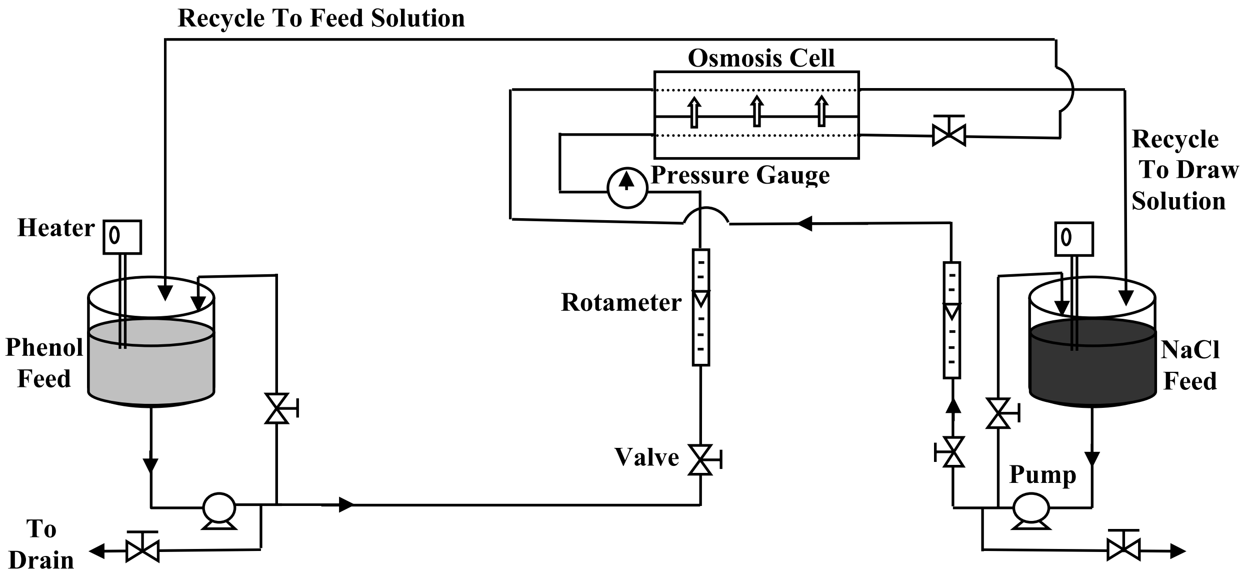

Fig. 2 Schematic Diagram of Forward Osmosis Process

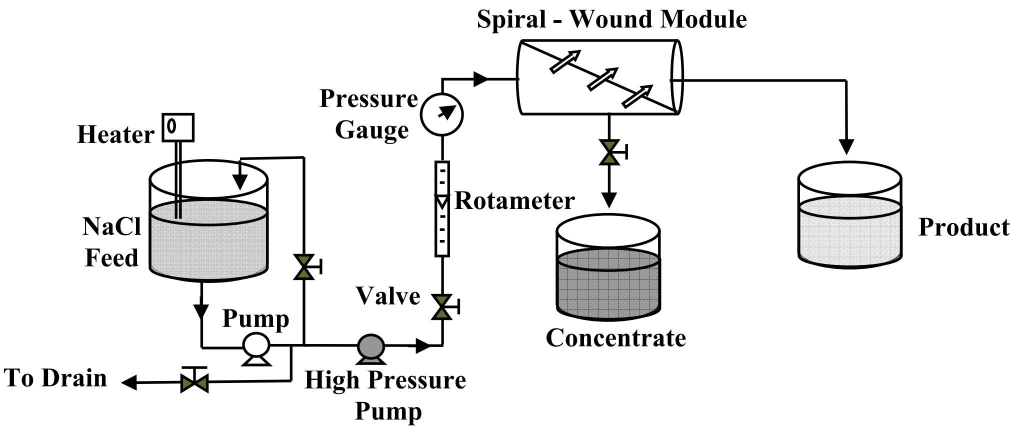

Fig. 3 Schematic Diagram of Reverse Osmosis Process

RESULTS AND DISCUSSION

Forward Osmosis

The effect of operating time (for 5 hour) on recovery percentage (Y%) and water flux (J) is shown in Figure 4. The increase in percentage recovery with increase in time might be due to an increase in the volume of pure water transfer from feed solution (phenol) to the draw solution across the membrane. The water flux decrease with time due to an increase of phenol concentration in feed vessel and decrease of draw solution concentration in feed, subsequently the osmotic power (or the driving force) across the membrane decreased. The water flux calculated by dividing the volume of pure water which transfers from feed to draw solution on time and active area of membrane. The phenol concentrations in these experiments are 100 and 1000 mg/l at the time zero, the recovery and water flux decrease with increasing phenol concentration in feed because the driving force decreased. Figure 5 shows the concentration of phenol in feed vessel and osmotic pressure of phenol versus time. The concentration and osmotic pressure of sodium chloride with time is shown in Figure 6. The solution of phenol loses quantities of pure water and this leads to increased concentration of phenol. The same quantities of pure water transferred across the membrane to the draw solution, as a result, decrease the concentration of sodium chloride. Thus, increases or decreases in concentrations of sodium chloride and phenol are linked to each other.

The Figures 7, 8 and 9 show the effect of NaCl concentration (10000 and 30000 mg/l at t = 0 h) on the recovery percentage, water flux, and outlet concentrations of phenol and sodium chloride respectively. The effect of the change in salt concentration (NaCl) has a greater effect on the water flux through the membrane because the sodium chloride has a high osmotic pressure. The increase in draw solution concentration while the concentration of feed solution (phenol) remains constant this leads to the difference increase in osmotic pressures on sides of membrane ($\pi_{NaCl} - \pi_{phenol}$), subsequently the flux (J) increased according to the Equation 6. These observations are well agreed with the results of McCutcheon et al., 2006.

The discrimination between cellulose triacetate membrane CTA and thin film composite membrane TFC in forward osmosis process illustrated in Figures 10, 11 and 12. The CTA membrane gives higher water flux than TFC membrane, thus we note that the percentage of recovery for the CTA membrane higher than the TFC membrane and this is evident in Figure 10. The CTA membrane better than TFC membrane because the CTA membrane was originally manufactured for the forward osmosis process, in addition the TFC membrane is composed of several layers and has a supportive layer to withstand the high pressures in the reverse osmosis process. Therefore, the concentration of phenol is more concentrate in the case of the use of CTA membrane, while the concentration of NaCl is high in the case TFC membrane used, and this is due to the high efficiency of the CTA membrane in the forward osmosis process. This is shown in Figures 11 and 12. Practical experiments of the FO process showed that the highest recovery ratio has been reached is 51.33% and this means that it has been recovered 7.7 liter of pure water from contaminated water by phenol, which was the size of 15 liter. Also, by using the CTA membrane increased recovery percentage of water by 23% compared to using the TFC membrane at the same conditions. These results correspond with the results of the researcher Rana, 2011.

The Analysis of Concentration Polarization

In Figures 13, 14, and 15 water flux is presented as a function of the osmotic pressure difference ($\pi_{NaCl} - \pi_{phenol}$) between the bulk feed and draw NaCl solutions. Osmotic pressure was calculated according to the equation 18 where i = 2 for NaCl, i = 1 for phenol and $\Phi = 1$ for an ideal solution. In these figures the membrane was oriented in the forward osmosis mode and also indicates flux under the influence of dilutive internal concentration polarization in the presence of concentrative external concentration polarization. The relationship between driving force and the rate of transfer of water through the membrane is a linear relationship for the membranes which used in this search. This behavior is agreement with standard equation for forward osmosis process (Equation 6). Therefore, increase in difference between the osmotic pressure of phenol and sodium chloride leads to an increase in the water flux.

Figure 16 show the flux (J) versus $\ln(\pi_D/\pi_F)$, we find the slope of line in figure 16 which represent the inverse of K (Equation 17). The value of resistance to solute diffusion within the membrane porous support layer (K) is 36.83 h/m. This equation considers another way of evaluating the flux behavior and confirming the presence of internal concentration polarization is by normalizing the driving force. These calculations are well agreed with the results of Tang et al., 2010.

Reverse Osmosis

In the second stage of research has been taking the sample of the draw solution to see the possibility of treatment by reverse osmosis process. Also, know specifications of the product water from reverse osmosis process. According to this process the draw solution is separated into two parts, the first part consists of pure water and contain small amounts of salt can be used in several applications, while the second part consists of too salty water and can be retrieved to the forward osmosis process as draw solution.

The recovery percent and water flux from reverse osmosis unit are plotted versus time, as shown in Figure 17. By increasing time, the pure water quantities which transfer across the membrane increased, therefore the recovery percent increase according to Equation 19. While, the flux decreased with increase in operating time. The flux of a reverse osmosis system decrease as fouling occurs, because the foulants on the membrane surface retard the back diffusion of the salt into the bulk solution to cause concentration polarization at the membrane surface. The increase in concentration polarization causes a decrease in the product rate (i.e. water flux), an increase in the concentration of NaCl in concentrate stream and a decrease in the concentration of sodium chloride in permeate stream. The rejection of salt decreased with increase in operating time. This is shown in Figure 18. The increasing of salt concentration in permeate will decrease the rejection percentage and vice versa. The reason, which was discussed before, for the effect of time on NaCl concentration, can be explain the decreasing of rejection percentage with increase in operating time. These results are similar behavior with the results of the Ahmed, 2000.

The concentration of NaCl in concentrate stream (or reject stream) versus time is shown in Figure 19. The decrease in salt concentration and the osmotic pressure in the reject stream with time due to a decrease in the transfer of pure water across the membrane with time. After two hours of work of the reverse osmosis system we get a recovery ratio of 58%, means it has been obtained 11.6 liters from feed vessel which it has volume is 20 liters.

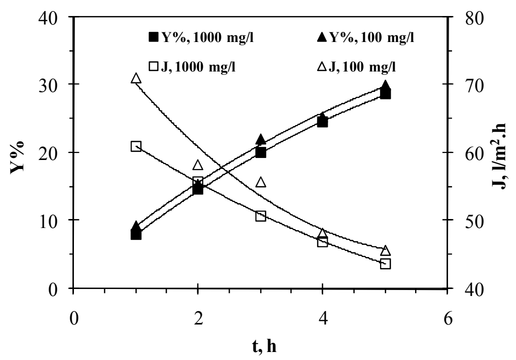

Fig. 4 Effect of Time on Recovery Percent and Flux for different Phenol Concentration (CTA Membrane, C_{NaCl} = 10000 mg/l, Q_{NaCl} = 50 l/h, Q_{phenol} = 50 l/h, P = 0.3 bar and T = 25 °C)

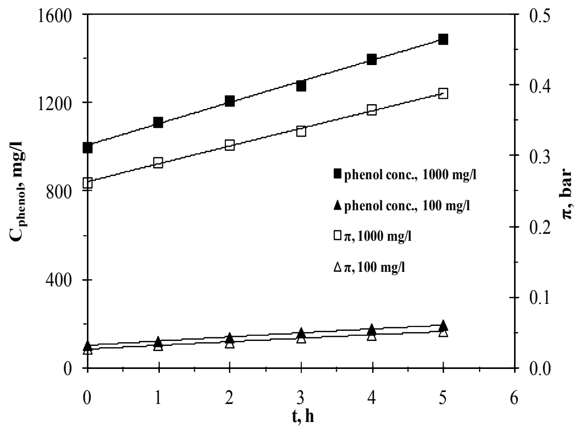

Fig. 5 Effect of Time on Phenol Conc. and Osmotic Pressure of Phenol for different Phenol Concentration (CTA Membrane, C_{NaCl} = 10000 mg/l, Q_{NaCl} = 50 l/h, Q_{phenol} = 50 l/h, P = 0.3 bar and T = 25 °C)

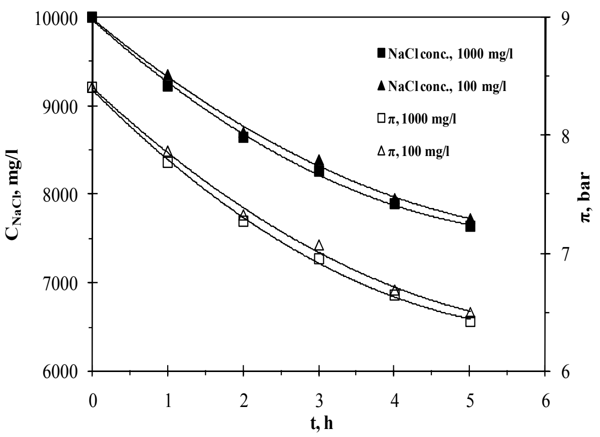

Fig. 6 Effect of Time on NaCl Conc. and Osmotic Pressure of NaCl for different Phenol Concentration (CTA Membrane, C_{NaCl} = 10000 mg/l, Q_{NaCl} = 50 l/h, Q_{phenol} = 50 l/h, P = 0.3 bar and T = 25 °C)

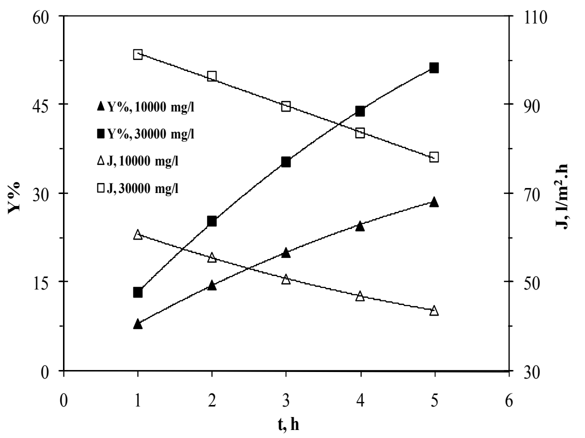

Fig. 7 Effect of Time on Recovery Percent and Flux for different NaCl Concentration (CTA Membrane, C_{phenol} = 1000 mg/l, Q_{NaCl} = 50 l/h, Q_{phenol} = 50 l/h, P = 0.3 bar and T = 25 °C)

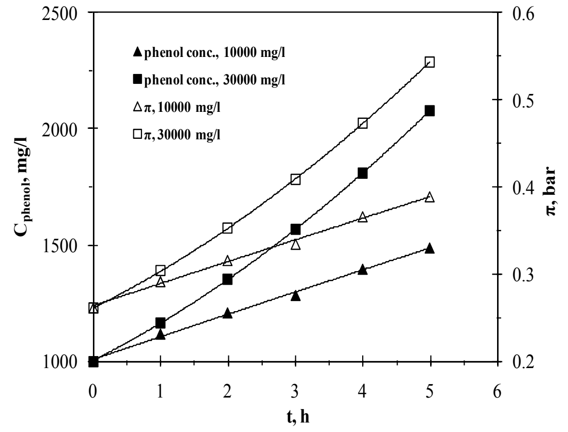

Fig. 8 Effect of Time on Phenol Conc. and Osmotic Pressure of Phenol for different NaCl Concentration (CTA Membrane, C_{phenol} = 1000 mg/l, Q_{NaCl} = 50 l/h, Q_{phenol} = 50 l/h, P = 0.3 bar and T = 25 °C)

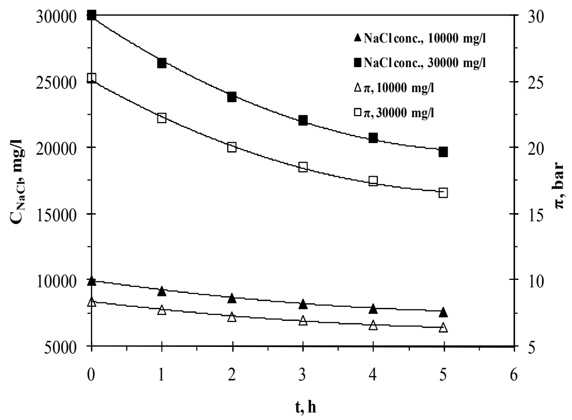

Fig. 9 Effect of Time on NaCl Conc. and Osmotic Pressure of NaCl for different NaCl Concentration (CTA Membrane, C_{phenol} = 1000 mg/l, Q_{NaCl} = 50 l/h, Q_{phenol} = 50 l/h, P = 0.3 bar and T = 25 °C)

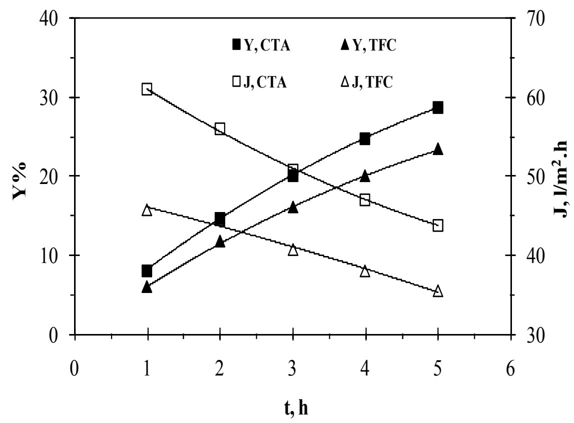

Fig. 10 Effect of Time on Recovery Percent and Flux for CTA and TFC Membranes (C_{NaCl} = 10000 mg/l, C_{phenol} = 1000 mg/l, Q_{NaCl} = 50 l/h, Q_{phenol} = 50 l/h, P = 0.3 bar and T = 25 °C)

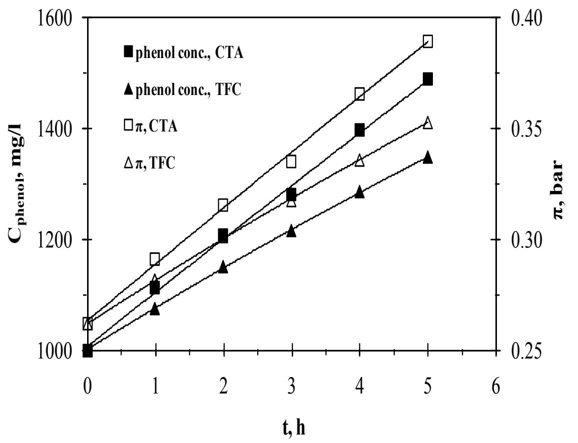

Fig. 11 Effect of Time on Phenol Conc. and Osmotic Pressure of Phenol for CTA and TFC Membranes (C_{NaCl} = 10000 mg/l, C_{phenol} = 1000 mg/l, Q_{NaCl} = 50 l/h, Q_{phenol} = 50 l/h, P = 0.3 bar and T = 25 °C)

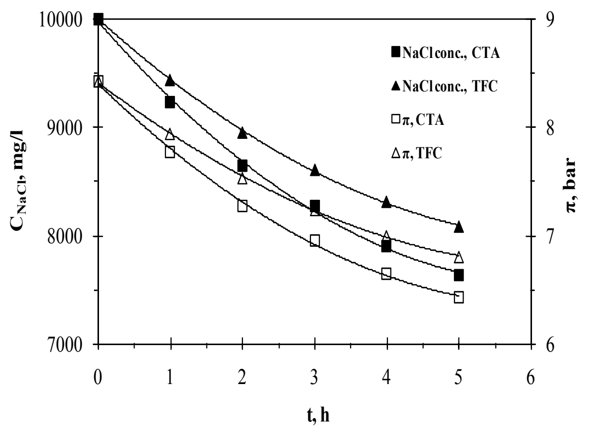

Fig. 12 Effect of Time on NaCl Conc. and Osmotic Pressure of NaCl for CTA and TFC Membranes (C_{NaCl} = 10000 mg/l, C_{phenol} = 1000 mg/l, Q_{NaCl} = 50 l/h, Q_{phenol} = 50 l/h, P = 0.3 bar and T = 25 °C)

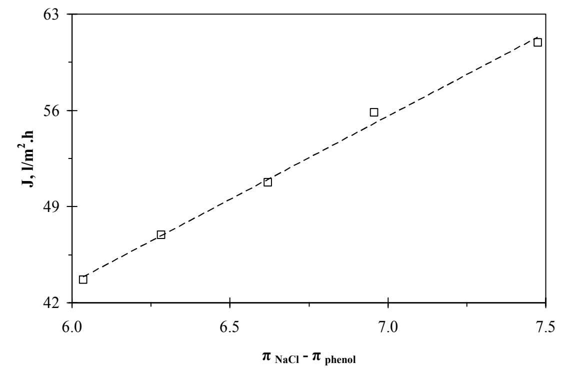

Fig. 13 Effect of Driving Force on Water Flux for CTA Membrane (C_{NaCl} = 10000 mg/l, C_{phenol} = 1000 mg/l, Q_{NaCl} = 50 l/h, Q_{phenol} = 50 l/h, P = 0.3 bar and T = 25 °C)

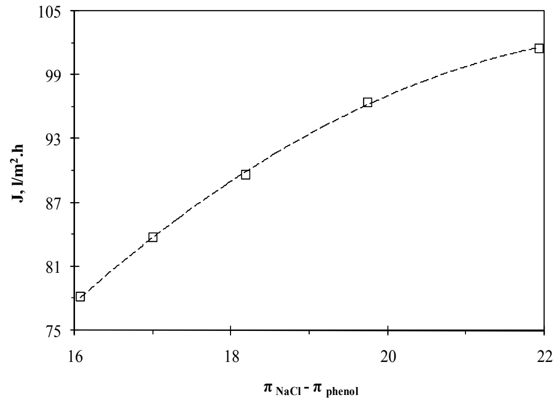

Fig. 14 Effect of Driving Force on Water Flux for CTA Membrane (C_{NaCl} = 30000 mg/l, C_{phenol} = 1000 mg/l, Q_{NaCl} = 50 l/h, Q_{phenol} = 50 l/h, P = 0.3 bar and T = 25 °C)

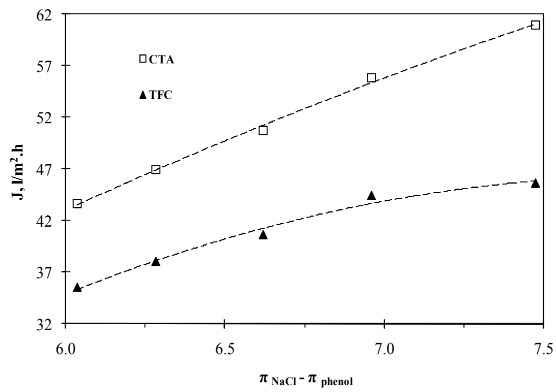

Fig. 15 Effect of Driving Force on Water Flux for CTA and TFC Membranes (C_{NaCl} = 10000 mg/l, C_{phenol} = 1000 mg/l, Q_{NaCl} = 50 l/h, Q_{phenol} = 50 l/h, P = 0.3 bar and T = 25 °C)

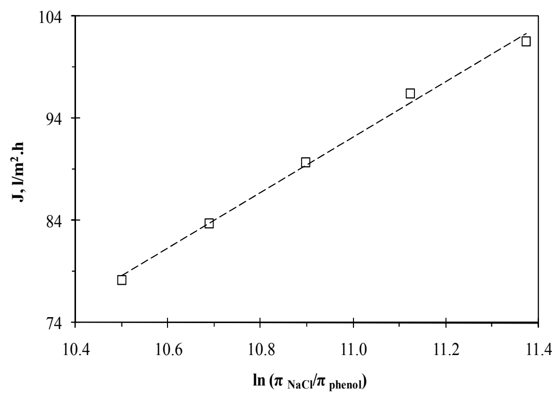

Fig. 16 Water Flux Data Plotted Against the Logarithm of the Ratio of Feed and Draw Solution Osmotic Pressures for Calculate K,

Equation 20 (CTA Membrane, C_{NaCl} = 30000 mg/l, C_{phenol} = 1000 mg/l, Q_{NaCl} = 50 l/h, Q_{phenol} = 50 l/h, P = 0.3 bar and T = 25 °C)

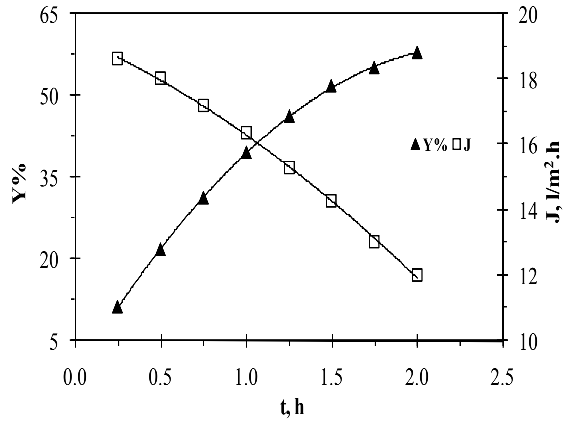

Fig. 17 Effect of Time on Recovery Percent and Flux in RO Process (C_{NaCl} = 7500 mg/l, Q_{Feed} = 20 l/h, pH = 6.5, P = 8.5 bar, V_F = 25 l and T = 25 °C)

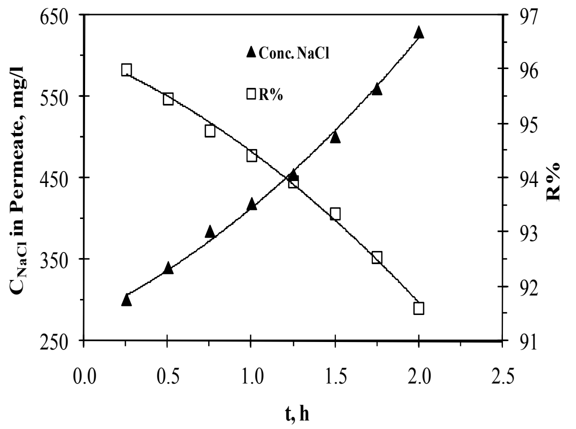

Fig. 18 Effect of Time on Product NaCl Concentration and Rejection Percent in RO Process (C_{NaCl} = 7500 mg/l, Q_{Feed} = 20 l/h, pH = 6.5, P = 8.5 bar, V_F = 25 l and T = 25 °C)

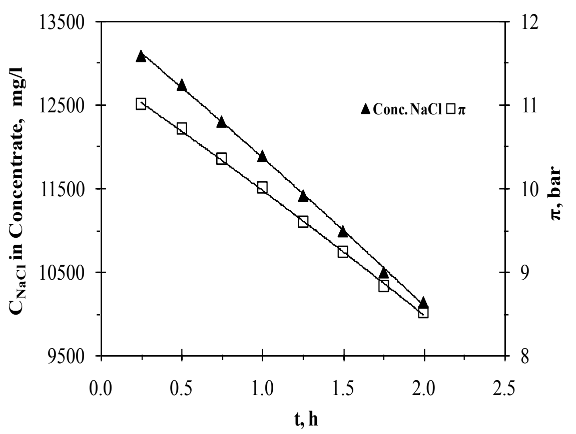

Fig. 19 Effect of Time on Rejected NaCl Concentration and Osmotic Pressure in RO Process (C_{NaCl} = 7500 mg/l, Q_{Feed} = 20 l/h, pH = 6.5, P = 8.5 bar, V_F = 25 l and T = 25 °C)

CONCLUSION

- Forward osmosis process is a convenient method for recovery of water from wastewater by phenol.
- Cellulose triacetate membrane (CTA) gave better results than the thin film composite membrane (TFC). Therefore, membrane CTA prefers more in the forward osmosis process.
- The recovery percentage for water through membrane increases with increasing operating time. Water flux decreases with time due to the decrease in driving force.
- The recovery percentage and water flux increases with increasing concentration of draw solution (i.e. osmotic pressure). While, the recovery and flux decreases with increasing concentration of feed solution.
- Outlet concentration of each of salt and phenol is associated with the amount of pure water transfer through the membrane, where the increase in water flux cause increase in concentration of phenol and decrease the salt concentration.
- The highest recovery ratio is 51.33%. Using CTA membrane recovery rate increase by 23% compared to using TFC membrane.
- The influence of dilutive internal concentration polarization and concentrative external concentration polarization appeared in forward osmosis process. Numerical value was calculated for the resistance to solute diffusion within the membrane porous support layer (K) is 36.83 h/m. .
- Reverse osmosis process is a good method to treatment of draw solution to

be used again. Recovery percentage from pure water is 58% after the operating time of two hours.

- In the RO process, the TFC membrane has high salt (sodium chloride) rejection 91.6 – 96 %. This leads to improve the performance of the forward and reverse osmosis processes together to recover the pure water from wastewater.

REFERENCES

- Ahmed, F. H., 2007, "Performance of Manipulated Direct Osmosis in Water Desalination Process", Ph.D. Thesis, Baghdad University.
- Ahmed, F.H., 2000, "Study of The Factors Affecting the Efficiency of Reverse Osmosis Process", M.Sc. thesis, Baghdad University.
- Baker, R.W., 2004, "Membrane Technology and Applications", Wiley, West Sussex.
- Bercie, G., Pintar, A., and Levee, J., 1996, "Adsorption of phenol from activated carbon by hot water regeneration: desorption isotherms", Ind. Eng. Chem. Res. (35), 4619.
- Cath, T.Y., Childress, A.E., and Elimelech, M., 2006, "Forward osmosis: principles, applications, and recent developments", Journal of Membrane Science, (281), 70.
- George, S., 1997, "Basic water Treatment", Britain.
- Gray, GT., McCutcheon, JR., and Elimelech, M., 2006, "Internal concentration polarization in forward osmosis: role of membrane orientation", Desalination, (197), 1–8.
- Hasan, F. M., 2008, "Investigating Polyamide Membrane in Direct Osmosis Process in Cooling Towers", Ph.D. Thesis, Baghdad University.
- Holloway, R.W., Childress, A.E., Dennett, K.E., and Cath, T.Y., 2007, "Forward osmosis for concentration of anaerobic digester centrate", Water Research, (41), 4005–4014.
- Hoshi, M., Kogure, M., Saitoh, T., and Nakagawa, T., 1997, "Separation of aqueous phenol through polyurethane membranes by pervaporation", J. Appl. Polym. Sci. (65), 469.
- International Atomic Energy Agency, 2004, "Application of Membrane Technologies for Liquid Radioactive Waste Processing", Technical Reports Series No. 431, IAEA, Vienna.
- James E. R. Couper, Rafiq Islam and Norman Lieberman, 2010, "Reverse Osmosis Design, Processes, and Applications for Engineers", John Wiley & Sons, Inc. Hoboken.
- John, C.C., Rhodes, R.T., David, W.H., Kerry, J.H., and George, T., 2005, “Water Treatment: Principles and Design”, John Wiley & Sons, Inc., 2nd Ed.
- Kessler, JO., and Moody, CD., 1976, "Drinking-water from sea-water by forward osmosis", Desalination, (18), 297–306.
- Kravath, R.E., and Davis, J.A., 1975, "Desalination of seawater by direct osmosis", Desalination, (16), 151–155.
- Krishnakumar, V.K., and Sharma, M.M., 1984, "A new method of recovering phenolic substances from aqueous alkaline waste streams", Ind. Eng. Chem. Process Des. Dev. (23), 410.
- Kujawski, W., Warszawski, A., Ratajczak, W., Pore bski, T., Capała, W., and Ostrowska, I., 2004, "Removal of phenol from wastewater by different separation techniques", Desalination (163), 287–296.
- Lee, K.L., Baker, R.W., and Lonsdale, H.K., 1981, "Membranes for power-generation by pressure-retarded osmosis", Journal of Membrane Science, (8), 141–171.

- Loeb, S., Titelman, L., Korngold, E., and Freiman, J., 1997, "Effect of porous support fabric on osmosis through a Loeb-Sourirajan type asymmetric membrane", Journal of Membrane Science, (129), 243–249.
- Mahesh Kumar, and Sukumar Roy, 2008, "Recovery of Water from Sewage Effluents using Alumina Ceramic Microfiltration", Membranes Separation Science and Technology, (43), 1034 – 1064.
- McCutcheon, J.R., McGinnis, R.L., and Elimelech, M., 2006, "Desalination by ammonia–carbon dioxide forward osmosis: influence of draw and feed solution concentrations on process performance", Journal of Membrane Science, (278), 114–123.
- McCutcheon, JR, and Elimelech M., 2006, "Influence of concentrative and dilutive internal concentration polarization on flux behavior in forward osmosis", Journal of Membrane Science, (284), 237–247.
- Merten, U., 1966, "Desalination by Reverse Osmosis", M.I.T. Press, Cambridge, Mass.
- Mi, B., and Elimelech, M., 2010 "Organic fouling of forward osmosis membranes: fouling reversibility and cleaning without chemical reagents", Journal of Membrane Science, (348), 337–345.
- Moody, CD, and Kessler, JO, 1976, "Forward osmosis extractors", Desalination, (18), 283–295.
- Rana, R.S., 2011, "Forward Osmosis Process for the Treatment of Wastewater from Textile Industries", M.Sc. thesis, Baghdad University.
- Ray, S.K., Sawant, S.B., Joshi, J.B., and Pangarkar, V.G., 1997, "Perstraction of phenolic compounds from aqueous solution using a nonporous membrane", Sep. Sci. Technol. (32), 2669.
- Schutte, F.C., 2003, "The rejection of specific organic compounds by reverse osmosis membranes", Desalination, (158), 285 – 294.
- Shejiao Han, Frederico Castelo Ferreira, and Andrew Livingston, 2001, "Membrane aromatic recovery system (MARS) — a new membrane process for the recovery of phenols from wastewaters", Journal of Membrane Science (188), 219–233.
- Sourirajan.S, 1970, "Reverse Osmosis", Academic, New York.
- Tang, C.Y., She, Q.H., Lay, W.C.L., Wang, R., and Fane, A.G., 2010, "Coupled effects of internal concentration polarization and fouling on flux behavior of forward osmosis membranes during humic acid filtration", Journal of Membrane Science, (355), 158–167.
- Thain, J.F., 1967, "Principles of Osmotic Phenomena", W Heffer & Sons Ltd, London.
- Yip, N.Y., Tiraferri, A., Phillip, W.A., Schiffman, J.D., and Elimelech, M., 2010, "High performance thin-film composite forward osmosis membrane", Environmental Science & Technology, (44), 3812–3818.

NOMENCLATURE

Symbol	Definition	Units
A	Pure Water Permeability Coefficient	$l/m^2.h.bar$
B	Salt Permeability Coefficient	m/s
C	Concentration of Solute	mg/l
C_F	Feed Concentration	mg/l
C_P	Product Concentration	mg/l
CP	Concentration Polarization	
D	Solute Diffusion Coefficient	m^2/s

d_h	Hydraulic Diameter	m
J	Water Flux	$l/m^2.h$
k	Mass Transfer Coefficient	m/s
K	Resistance to Solute Diffusion	m/h
P	Pressure	bar
Q	Flow Rate	l/h
L	Length	m
R	Rejection Percentage	
Re	Reynolds Number	
R_g	Gas Constant	bar. l/gmol. k
Sc	Schmidt Number	
Sh	Sherwood Number	
t	Time	h
T	Temperature	°C
V_F	Volume of Water in Feed Vessel	l
V_P	Product Volume of Water	l
Y	Recovery Percentage	

reek Symbols

Symbol	Definition	Units
π	Osmotic Pressure	bar
$\pi_{D,b}$	Osmotic Pressure of the Draw Solution in the Bulk	bar
$\pi_{D,i}$	Osmotic Pressure of the Draw Solution on the Inside of the Active Layer	bar
$\pi_{D,m}$	Osmotic Pressure of the Draw Solution at the Membrane Surface	bar
$\pi_{F,b}$	Osmotic Pressure of the Feed Solution in the Bulk	bar
$\pi_{F,i}$	Osmotic Pressure of the Feed Solution on the Inside of the Active Layer	bar
$\pi_{F,m}$	Osmotic Pressure of the Feed Solution at the Membrane Surface	bar
σ	Osmotic Reflection Coefficient	
Φ	Osmotic Coefficient	

OPTIMIZATION OF RESOURCE ALLOCATION AND LEVELING USING GENETIC ALGORITHMS

Assist. Prof.: Dr. Sawsan Rasheed Mohammed
University of Baghdad
College of Engineering
Department of Civil Engineering

Ameer Ahmed Abdul Ameer
University of Baghdad
College of Engineering
Department of Civil Engineering

ABSTRACT

Resource allocation and leveling are of the top challenges in project management, due to the complexity of projects. This research aims to develop an optimization model for resource smoothing, so that.

The proposed model is formulated using C++ program for resource smoothing. The project management software MS-Projects is adopted hereto perform resource leveling to facilitate achieving the optimal solution.

The proposed model utilizes a system that depends on Genetic Algorithms (GAs) procedure built in C++ program to find the optimum solution.

This research reach concludes that it is possible to smooth resources using Genetic Algorithms program and compares then with MS-Project when the GA results are better than MS-Project.

Three case studies have been applied in this research and the application results come identical with research objectives, to form the conclusion.

Then comes the recommendations regarding adopting and using the research results in construction planning and project management. Further suggestions related to the research subject are proposed for future works.

الخلاصة

ان تعيين وتسوية الموارد هي من اكثر التحديات في ادارة المشروع بسبب تعقيد المشاريع.

يهدف هذا البحث الى بناء نموذج امثل لتسوية الموارد. لقد تم بناء النموذج المقترح باستخدام برنامج ++C لتسوية الموارد وكما تم اعتماد برنامج لادارة المشاريع (MS-Project) لاجراء تسوية الموارد لتسهيل الوصول الى الحل الامثل. يعتمد النموذج المقترح على اسلوب الخوارميات الجينية حيث تم بناؤه باستخدام برنامج (++C) للبحث عن الحل الامثل.

توصل البحث الى امكانية تسوية الموارد باستخدام الخوارزميات الجينية ومقارنتها مع برنامج MS-Project ولقد وجد ان نتائج الخوارزميات الجينية افضل من نتائج MS-Project وطبقت نتائج البحث على ثلاث حالات درست وكانت نتائج التطبيق مطابقة لما هدف اليه البحث. وتم التوصل الى عدد من الاستنتاجات كما وضعت عدد من التوصيات والمقترحات بشان تبني نتائج البحث في حقل التخطيط وادارة المشاريع كما وضعت عدد من المقترحات لبحوث لاحقة ذات صلة بموضوع البحث.

INTRODUCTION

Resource allocation and leveling have been dealt with as two distinct subproblems solved mainly using heuristic procedures that cannot guarantee optimum solutions. In this research, improvements are proposed to resource smoothing and leveling heuristics, and the Genetic Algorithms (GAs) technique is used to search for near-optimum solution.

In dealing with project resources, two main types of techniques have been used: resource allocation and resource leveling. Resource allocation (sometimes referred to as Constrained-Resource Scheduling) attempts to schedule the project tasks so that a limited number of resources can be efficiently utilized while keeping the unavoidable extension of the project to a minimum. Resource leveling (often referred to as resource smoothing), on the other hand, attempts to reduce the sharp variations among the peaks and valleys in the resource demand histogram while maintaining the original project duration [Mselhi 1993].

Genetic Algorithms (GAs) are search procedures that combine an artificial survival of the fittest strategy with genetic operators abstracted from nature [Michell 1998]. GAs are optimization search procedures inspired by the biological system improved fitness through evolution. GAs employ a random yet directed search for locating the globally optimal solution. [Goldberq 1989]

SCHEDULING DEFINITION & OBJECTIVES

Scheduling deals with time order in which project activities are to take place, and also the manpower, material machinery and money (the 4m’s) required at every stage of production that should be shown in the scheduling. [Senupta 1995]

Schedule development means determining the start and finish dates for project activities. If the start and finish dates are not realistic, the project is unlikely to be finished as schedule. The schedule development process must be iterated (along with processes that provide inputs, especially duration estimating and cost estimating) prior to the determination of the project schedule. [Project Management Institute 1996]

The basic objectives of the scheduling process are as follows:[Callahan 1992]

a. To find out how long the total project duration is. Timely completion of the project is particularly important when fails to complete within the time required by contract that carries a financial penalty or liquidated damages;
b. evaluating the early and late times at which activities start and finish.
c. Identifying the group of critical activities so that special care is taken to make sure they are not delayed;
d. since the construction environment is always exposed to constraints and changes, it is important to be able to evaluate the implications of changes in start and/or finish times of activities on the overall project duration;
e. the follow up execution of the project;
f. to monitor the usage of Resources;
g. to Expect the stoppage in the execution and reasons behind;
h. to prepare the financial requirements and cost control of work; and

to control the sub-contractors work and their interference.

SCHEDULING TECHNIQUES

There are many types of schedules which can be used for many construction project. The choice of which type of planning to be used depends on the characteristics of each project.

Several tools and techniques assist in the planning development process.

- Gantt Chart (Bar Chart)
- Network Analysis
- Program Evaluation and Review Technique PERT
- Line of Balance

OPTIMIZATION SCHEDULING METHODS (MODELS)

Modeling can be defined as the process of producing a model; model is a representation of the construction and working of some system of interest. [Maria 1997]

Modeling is one of the most powerful tools that have ever been employed in various research disciplines. Often it's the typical way and some times the only way to conduct experiments on a wide range of systems of various types.

- Linear Programming Model
- Simulation Model
- Monte Carlo Simulation
- Genetic Algorithms Techniques

RESOURCE SMOOTHING

Resource smoothing attempts to reduce peak requirements and smooth out period-to-period fluctuations in resource assignment without changing project duration. The objective of resource leveling procedures is to schedule project activities so that the project duration does not exceed a specific limit and the variation in the projects demand for a resource from one time period to another is held to a minimum. [Harris 1990]

The project managers' objective to hire the minimum number of resources, to reduce resource fluctuation and to ensure better utilization of resources. Typical situations include full utilization of a rented piece of equipment that needs to be returned early, also reducing the number of skilled workers who need to be hired for the job. Project managers have desired resource profiles that they try to get their resource profiles to match.

A well-known heuristic algorithm is the minimum moment algorithm that assumes limited project duration and unlimited resources [Hiyassat 2001]. The objective in this algorithm is to minimize daily fluctuations in resource use while keeping the total project duration unchanged. As a proxy to this objective the Algorithm minimizes the moment of the resource histogram around the horizontal axis. [Harris 1978]

The moment MX is calculated by summing the daily moments as follows: [Haider 1999]

$Mx = \sum [1*\text{Resource Demand}_i)*1/2\text{Resource Demand}_1]$

$$Mx = 1/2 \sum (\text{Resource Demand}_i)^2 \qquad (1)$$

Where n is the working day number of the projects finish date. Equation – to be a minimum becomes:

$$Mx = \sum (\text{Resource Demand}_i)^2 \qquad (2)$$

GENETIC ALGORITHMS DESCRIPTION

Genetic Algorithms are search algorithms based on the mechanics of natural selection and natural genetics. They combine survival of the fittest among string structures with a structured yet randomized information exchange to form a search algorithm with some of the innovative flair of human search. In every generation, a new set of artificial creatures (strings) is created using bits and pieces of the fittest of the old; an occasional new part is tried for good measure. While randomized, genetic algorithms are no simple random walk. They efficiently exploit historical information to speculate on new search points with expected improved performance.

The central theme of research on genetic algorithms has been robustness, the balance between efficiency and efficacy necessary for survival in many different environments. The implications of robustness for artificial systems are manifold. If artificial systems can be made more robust, costly redesigns can be reduced or eliminated. If the higher levels of adaptation can be achieved, existing systems can perform their functions longer and better. Designers of artificial systems – both Software and hardware, whether Engineering Systems, Computer systems, or Business systems – can only marvel at the robustness, the efficiency, and the flexibility of biological systems. Features for self-repair, self-guidance, and reproduction are the rule in Biological systems, whereas they barely exist in most sophisticated artificial systems.

Genetic Algorithms are now finding more widespread application in Business, Scientific, and Engineering circles. The reasons behind the growing numbers of applications are clear. These algorithms are computationally simple yet powerful in their improvement. Furthermore, they are not fundamentally limited by restrictive assumptions about the search space (assumptions concerning continuity, existence of derivatives, unimodality, and other matters).[Baker 1985]

THE WORK OF GAS

GAs work with a family of solutions, known as the "current population" from which the "next generation" of solutions is obtained, better solutions from one generation to the next are progressively obtained [Harmanani 2001]. GAs procedure begins by generating an initial collection (referred to as population) of random solutions that are encoded in the form of strings called Chromosomes.

Each individual Chromosome represents one solution that is better or worse than others in the population. The fitness of each solution is determined by evaluating its performance with respect to an objective function. To stimulated the natural survival of the fittest process, best Chromosomes (potential solutions) exchange information to produce offspring that are evaluated and can replace less fir members in the population. Usually, this solutions replace unfit solutions), until criterion is met (e.g. one solution becomes satisfactory). At the end of the process, the member of the population with the best performance becomes the optimum solution [Tarek 1999]. Figure (1) illustrates the basic cycle of genetic algorithm operations.

STEPS OF GENETIC ALGORITHM SYSTEM

The following points illustrate the principle work of genetic algorithm:

Encoding the Application of GA

GAs require a representation scheme to encode feasible solutions to the Optimization problem. Each Chromosome represents one member, i.e., one solution, which is better or worse than other members in a population.

A Chromosome represents a sequence of genes that require Optimization.

There are two basic chromosome formats in GAs,

a. Binary Coding.
b. Ordinary Coding.

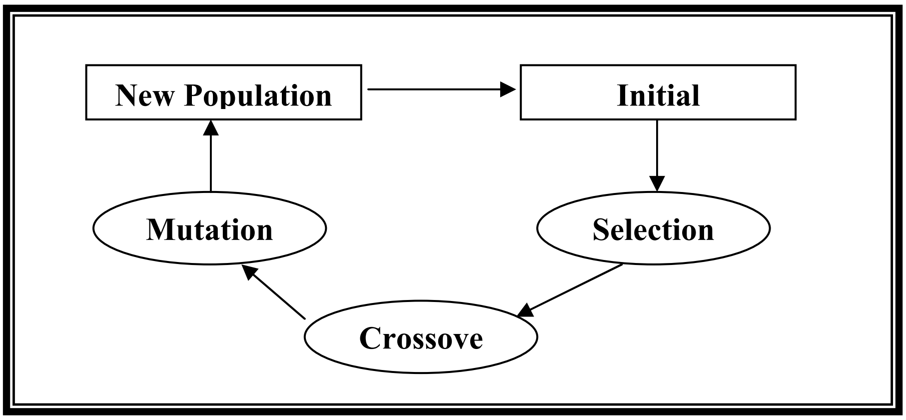

Figure 1 Basic Cycle of GA Operations [Tarek 1999]

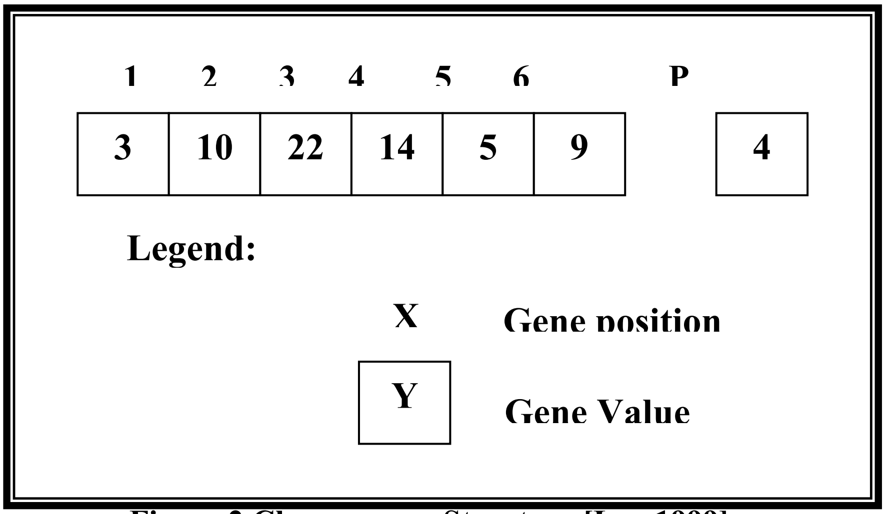

Figure 2 Chromosome Structure [Lue 1999]

Generating an Initial Population of Chromosomes

The process of genetic algorithms starts with a randomly created first generation of population. Every individual in a generation represents one solution and consists of one Chromosome with a number of genes. [Haider 1999]

Deciding the Chromosome Evolution Criterion (Objective Function)

The performance of the strings is often called fitness, and the fitness of each string (Chromosome) in the population is evaluated with respect to an Objective Function.

Selection

A pair of parent Chromosome from the current population is selected. Each of the two parent Chromosomes is randomly selected in a manner such that its probability of being selected is proportional to its relative merit.

Crossover

Crossover is the process of combing the chromosomes of two potentially good solutions to form two offsprings [Kevin 2003]. Crossover is performed by randomly selecting two members from the Population and exchanging their chromosomal information.

Figure (3) illustrates that two Chromosomes (parents 1 and 2) are randomly selected and broken at a random point (at gen 5), and after the exchange at genetic material two new Chromosomes (Offspring 1 and 2) are generated.

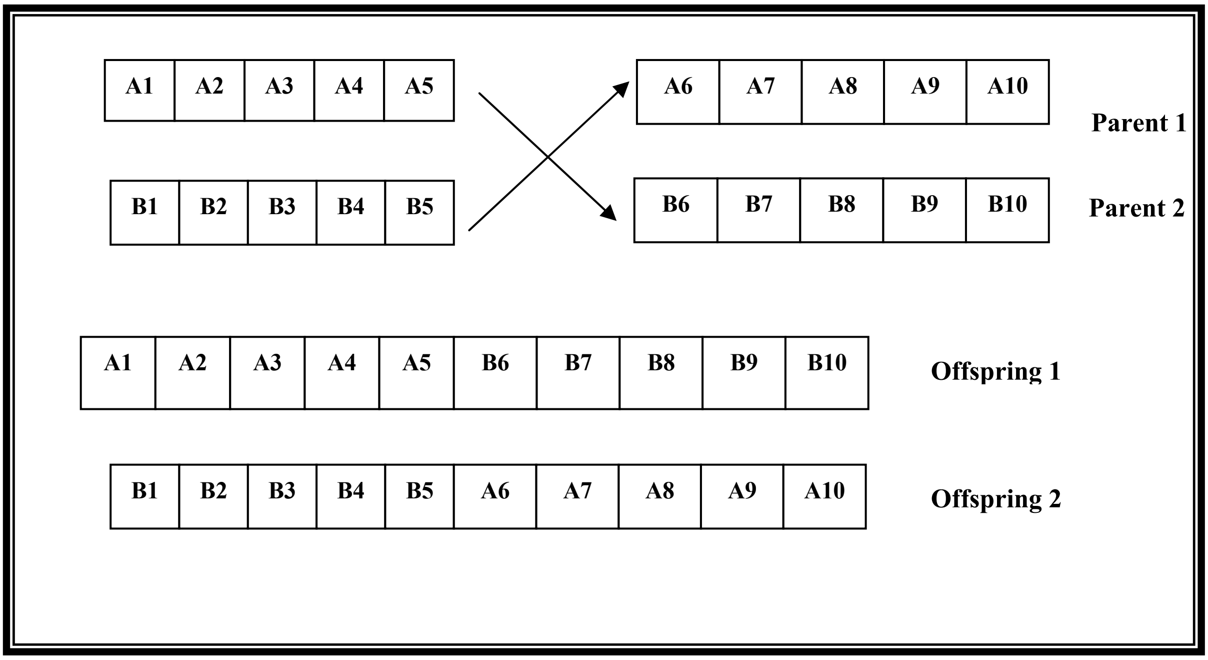

Figure 3 Crossover [Kevin 2003**]**

Mutation

Mutation is a rare process that resembles the process of a sudden generation of an odd offspring that turns out to be a genius. This can be done by randomly selecting one Chromosome from the population and then randomly changing some of its information. The benefit of the mutation process is that it can break any stagnation in the evolutionary process and avoid sub optimal solutions. Figure (4) displays some forms of mutation [Goldberg 1989]. In this figure characters have mutation operation.

1 1 0 0 1 1 0 1 0 1 ⟶
1 0 0 1 1 1 1 0 1

A B D A C E ⟶
G B D A N E

4 5 1 8 11 1 7 3 ⟶
4 20 1 8 2 1 7 3

Figure 4 Some Examples of Mutation in GA [Goldberg 1989**]**

PARAMETERS OF GAS

To implement GAs, its Parameters must be set having: [Michell 1998]

a. Population Size: is the number of population to be generated randomly. Population size is an important factor that affects the solution and processing time it takes. Large Population size (in the order of hundreds) increases the likelihood of obtaining a Global Optimum solution, however, it substantially increases processing time.
b. Chromosome Length: A solution is represented as a linear string called a Chromosome whose length varies with each application.
c. Crossover Probability (Pc): A rate to perform Crossover between any pairs of two selected Chromosomes (strings). Pc is real number from 0 to 1 and the mostly used of Crossover probability are from 0.3 to 0.95. [Tarek 2000]
d. Mutation Probability (Pm): A rate to randomly alter one or more genes of a selected string (Pm) is real number

e. from 0 to 0.1 and the mostly used values of mutation probability are from 0.001 to 0.1. [Tarek 2000]

Stopping Criteria: There are two types of stopping criteria included in GAs. The first one is in state of meaning the value of objective function, and the second is the number of Offspring generations. The two types above can be used as a termination criterion for the GA process. [Tarek 1999]

BENEFITS OF GAS IN CONSTRUCTION

GAs are particularly suited for Optimization problems in Construction Scheduling because:

a. They do not experience combinatorial explosion: [Que 2002] GAs perform well on problems whose complexity increases exponentially with the number of input Parameters. Such problems are called NP-Complete. The Resource Leveling problem could be defined as a (NP-Complete) problem. That is computational time which grows exponentially as the size of the problem increases. [Son 1999]
b. They are Robust: GA has the feature of robustness because of its ability to evaluate many possible solutions simultaneously and use the Chromosome fitness to direct the search.

COMPUTER IMPLEMENTATION

GAs procedure can be implemented on a Visual C++ Program.

C++ is more faster than any Programming languages to reach the Optimal solution because it is deeply treat with computer and upon of this feature it is object oriented.

Always C++ depends on specifying the object to get a specific class (or specific character) then create other target (object) from that specific character which have the same characters of that class. Each class should have some functions, each of it do special work depend on that variables. [De Jon 1980]

The objective of our program of C++ is getting the minimum of MX, are equal $\sum R^2$ whereas R is the resource of each activity. The target of that is getting specific project.

The aim of this project is to get knowledge the optimum resources to get the minimum $\sum R^2$ for each project and the early start of each activity which only has TF.

This work does not happen by isolated the activity from the other one because the activities is interfusion, therefore $\sum R^2$ is cumulative.

Any programmer sees this idea thought to move the first activity and calculate $\sum R^2$ and then the second activity, this way is correct and it is long. But in the event of using Genetic Algorithm we will adapt this concept and make the movement which depend on correct programming grammars used in our program which is called cumulative test procedure and relation movement.

The Activities Features are as Follows:

a. Each activity has duration.
b. Each activity has early start that is important.
c. Each activity has total float that is more important. Then we will make the permutation and calculate the fitness function ($\sum R^2$).
d. It's noted there are critical activities without movement and uncompatible with the permutation because of the total float is equal zero.

Every time in our project we are keep generated the offsprings to get the best cumulative resources of each day of project duration. The visual C++ program illustrates the optimum solution.

APPLICABILITY OF GENETIC ALGORITHMS TO RESOURCE LEVELING

The minimum resource moment algorithm was improved using both Mx and My resource moments. The moment Mx (Moment of the resource histogram about the x-axis) represents the resource fluctuation and the moment My (Moment of the resource histogram about y-axis) represents the resource utilization. The minimum value of these two combined moments serves as a good indicator of efficiently utilized resources where fluctuations from period to another are avoided. The random activity priorities and the combined moments approach form the basis of the optimization process. [Tarek 1999]

The detailed GA Procedure is outlined in Figure (5)

PROPOSED RESOURCE SMOOTHING SYSTEM

The proposed model comprises two main sections: processing project data in MS and optimizing resource leveling using genetic algorithms program.

Figure (6) illustrates process chart diagram of the proposed model.

MINIMIZING RESOURCE MOMENTS

The minimizing resource moments objective represents the optimization of the resource smoothing procedure. Which involves the process of optimally minimizing resource fluctuations and resource utilization moments. This process is executed under unlimited resources Figure (7) illustrates process chart of resource smoothing.

The optimization parameters associated with this process are outlined as follows:

a. Objective function which will minimize the fluctuation and/or utilization moments;
b. optimization variables which consist of activity TF values, which range accepts integers between zero and the maximum TF value obtained from Microsoft project before applying resource smoothing;
c. optimization constraints which state that the project duration should be equal to the project deadline.

d.

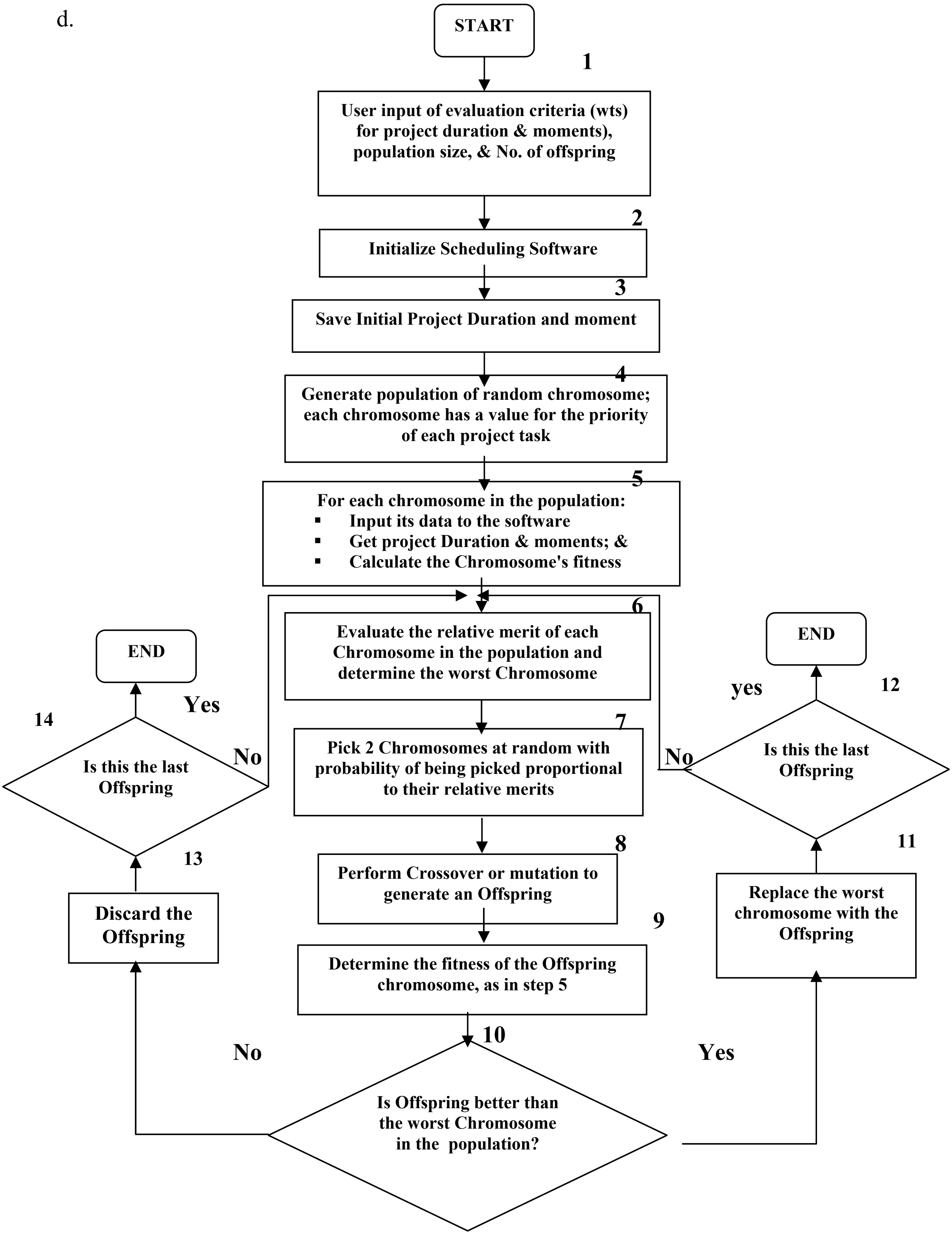

Figure 5 Genetic Algorithm Procedure [Tarek 1999]

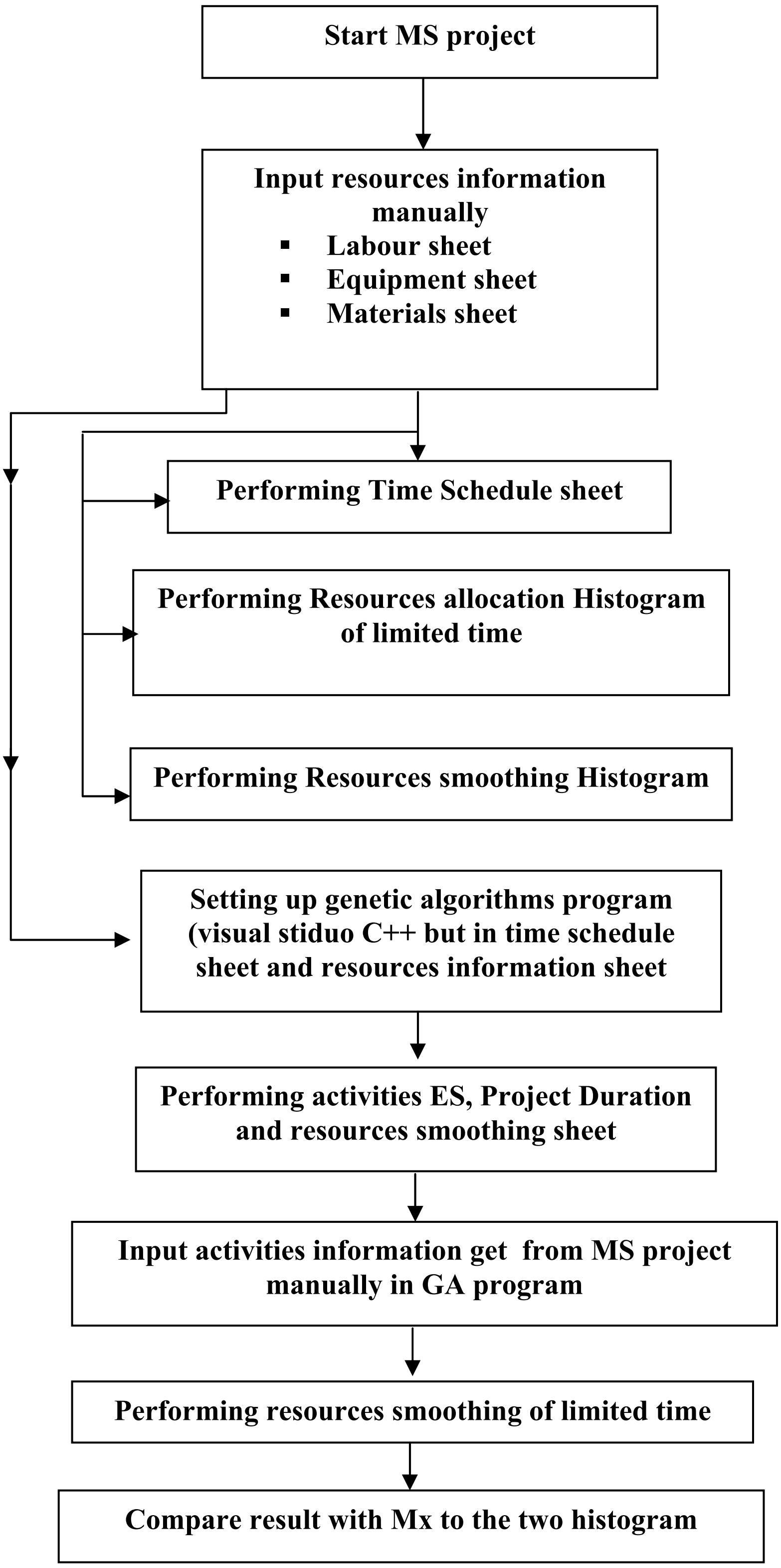

Figure 6 Process Chart Diagram of the Proposed Model [researcher]

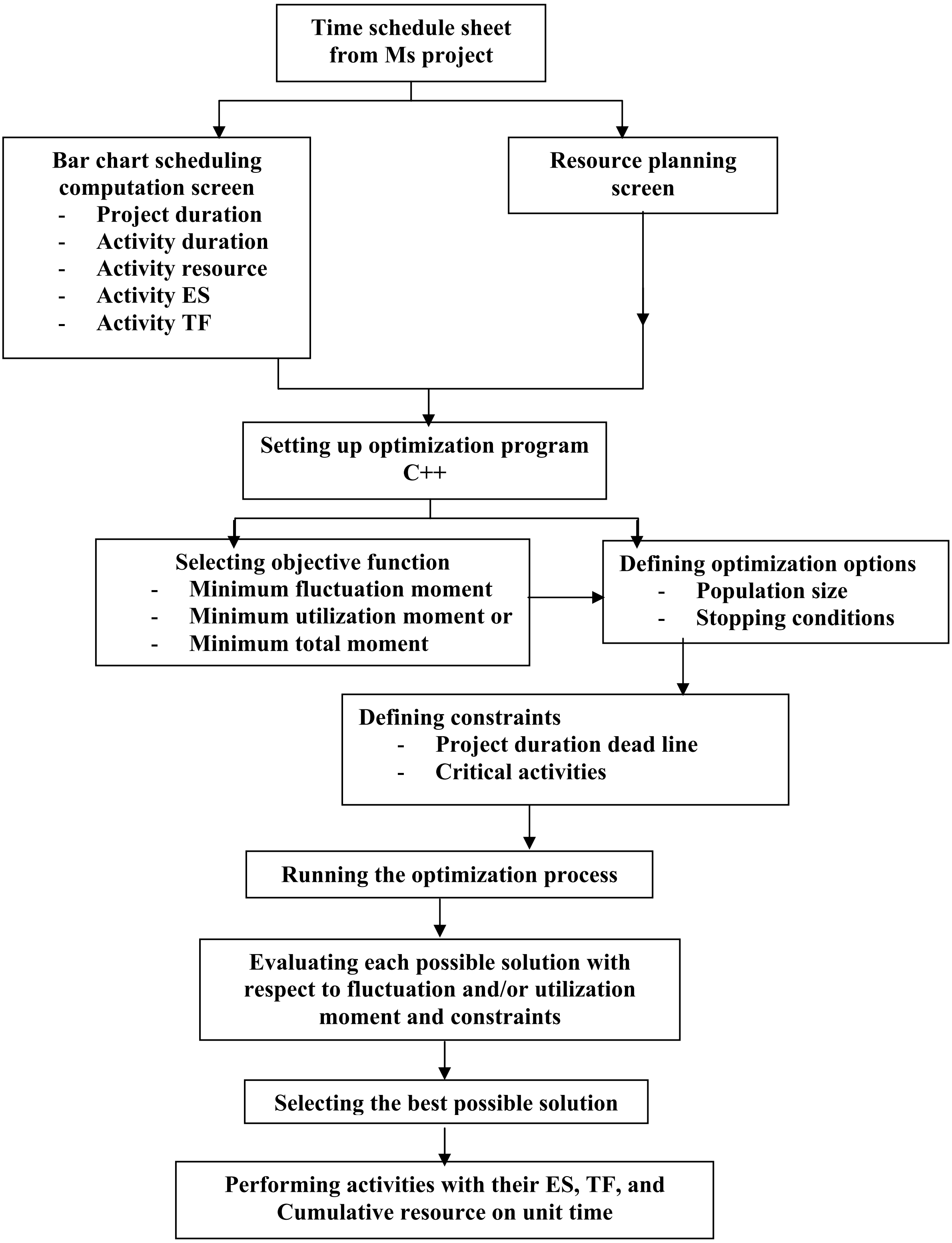

Figure 7 Optimization Process Chart of the Resource smoothing [researcher]

OPENING AND USING C++

when C++ screen appears follows these steps:

1. File
2. Open
3. Write the file name contains the code
4. Press F7
5. Press Yes
6. Press Ctrl+F5

After the above steps GA input screen which we will input the number of activity, duration of project, for each activity input we will input:

a. Duration
b. Early start (ES)
c. Total Float (TF)
d. Resources (R)
e. Is it critical or not
f. When Click Enter the GAs is operate and give us Resource of each day and the minimum of (Mx)

These steps illustrate in Figure (8) that input the data of one activity

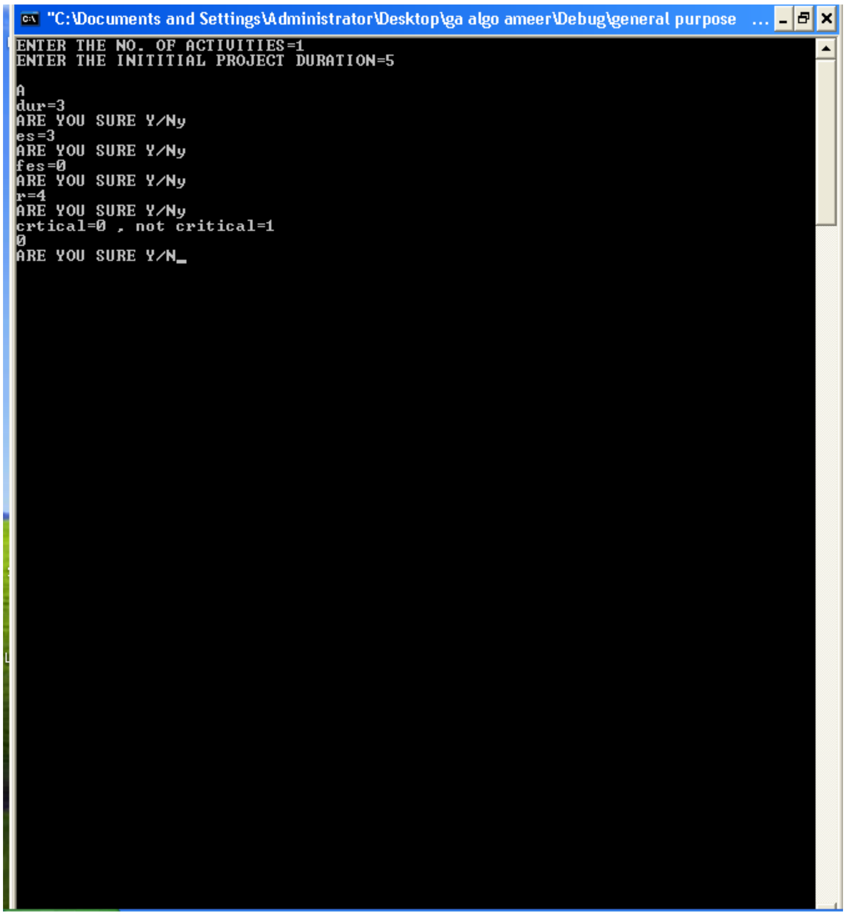

Figure 8 GA Input Screen

MODEL APPLICATION

Case Study1 of 7 Activity (Description and Data)

A summary of the case study data is demonstrated in Table (1)

Table 1 Case Study Data of 7 activity

Activity	Duration	Labour (R)	Predecessors
A	2	2	-
B	6	4	A
C	3	3	A
D	1	1	B
E	6	3	B
F	3	3	C,D
G	2	2	E,F

From MS Project we get figure (9) and (10) show a hypothetical case study of 7 activities in the form of activity on node (AON) network and a bar chart representation respectively.

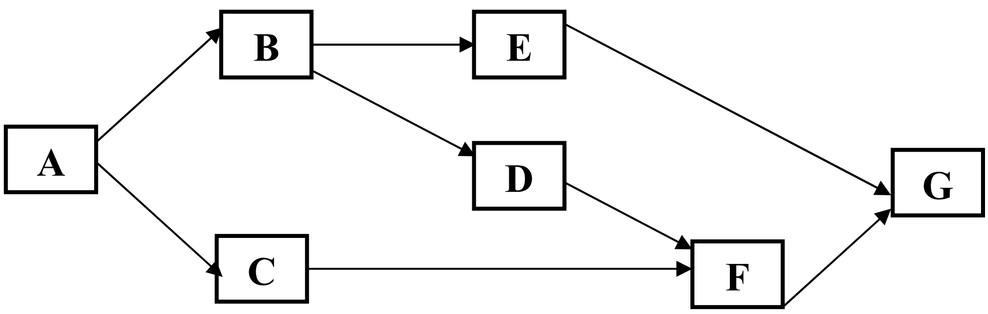

Figure 9 AON Network of 7 Activity

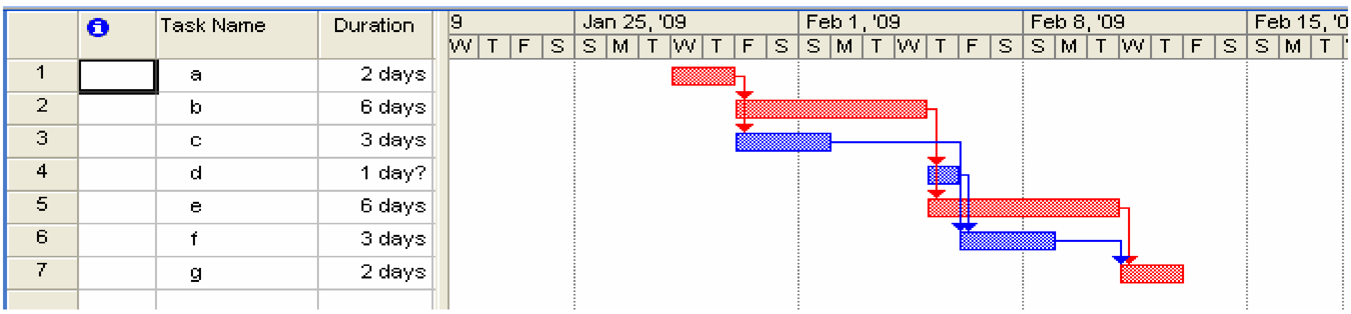

Figure 10 Bar Chart of 7 Activity Project

Figure (11) illustrate the Resource Histogram before Smoothing where Mx = 353

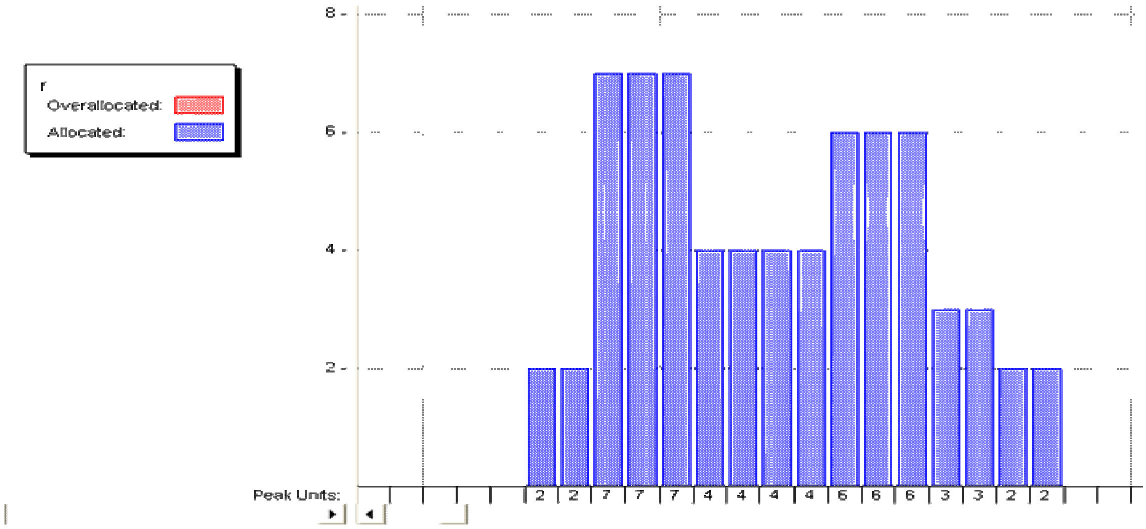

Figure 11 Resource Histogram Before Smoothing

Figure (12) illustrate resource Histogram after Smoothing in MS Project where Mx = 353

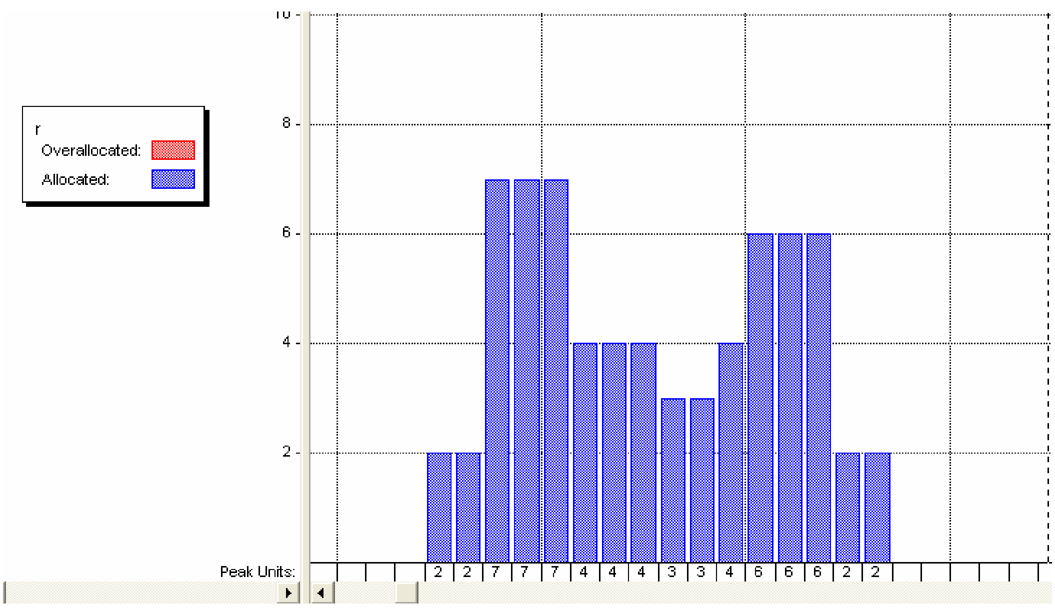

Figure 12 Resource Histogram After Smoothing

Table (2) show the information needed to GA Resource Smoothing System which get it from MS Project before Smoothing and Table (3) show the information after Smoothing.

Table 2 Activity Information Before Smoothing

Act	Dur	E.S	T.F.	R	Prec.	Critical or not
A	2	0	0	2	-	Cri
B	6	2	0	4	A	Cri
C	3	2	6	3	A	Non-Cri
D	1	8	2	1	B	Non-Cri
E	6	8	0	3	B	Cri
F	3	9	2	3	C,D	Non-Cri
G	2	14	0	2	E,F	Cri

Table 3 Activity Information After Smoothing in MS-Project

Act	Dur	E.S	T.F.	R	Prec.	Critical or not
A	2	0	0	2	-	Cri
B	6	2	0	4	A	Cri
C	3	2	6	3	A	Non-Cri
D	1	10	0	1	B+2day[FS]	Cri
E	6	8	0	3	B	Cri
F	3	11	0	3	C,D	Cri
G	2	14	0	2	E,F	Cri

It is noted that MS-Project after smoothing make the activity D,F is critical and the Total Float = 0 while the moment of resources (Mx) is not changed and equal (Mx = 353).

Performing Optimization Process

This application is perform to compare the proposed model results with manual solution of the case study. Optimization options are set as follow:

- Population size: After initial experimentation with different population size (chromosomes) = No. of duration of any project.
- Crossover rate = No. of total float of each non-critical activity.
- Stopping condition: as GA gives results that show no further improvements.

Performing Resource Smoothing

This application demonstrates the proposed model ability to optimize the process of resource smoothing to compare the results with MS-project program and manual results.

The optimization parameters associated are as follows:

- Objective function: minimizes fluctuation moment (Mx).
- Change TF, ES to non-critical activities.
- Constraints:
  Project duration = deadline duration (16)
  ES = early start to critical activity.

The results of resource smoothing in GA are illustrated in table (4)

Table 4 Activity Information of Resource Smoothing in GA

Act	Dur	E.S	T.F.	R	Prec.	Critical or not
A	2	0	0	2	-	Cri
B	6	2	0	4	A	Cri
C	3	8	0	3	A,B	Cri
D	1	8	2	1	B	Non-Cri
E	6	8	0	3	B	Cri
F	3	11	0	3	C,D	Cri
G	2	14	0	2	E,F	Cri

And the bar chart after smoothing in GA as shown in Figure (13)

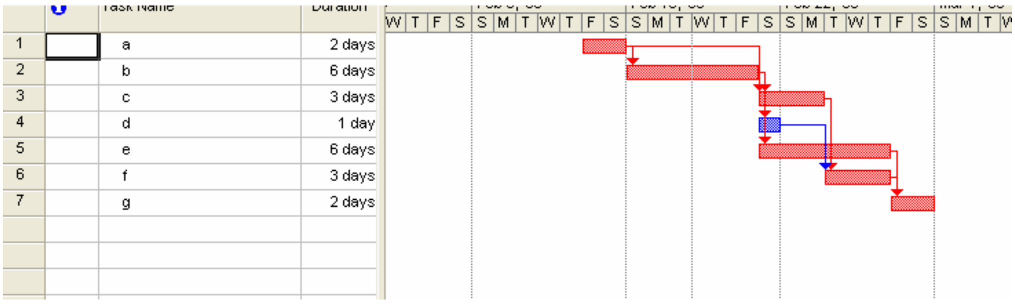

Figure 13 Bar Chart of 7 Activity After Smoothing in GA

We conclude from the above that the MS project made the activity D,F is critical where Mx = 353 but GA is made the activity C,F is critical and activity D is still non-critical where Mx = 341 and it is less than the calculated Mx from MS project and equal mx from manual solution and the Histogram because its small project where the Mx from GA equal Mx from manual solution.

It's noted No. of peak and No. of changes = 2 and highest peak = 7 from Ms results while No. of changes and No. of peak = 1 from GA results

Figure (14) show resource smoothing histogram from GA results where Mx = 341

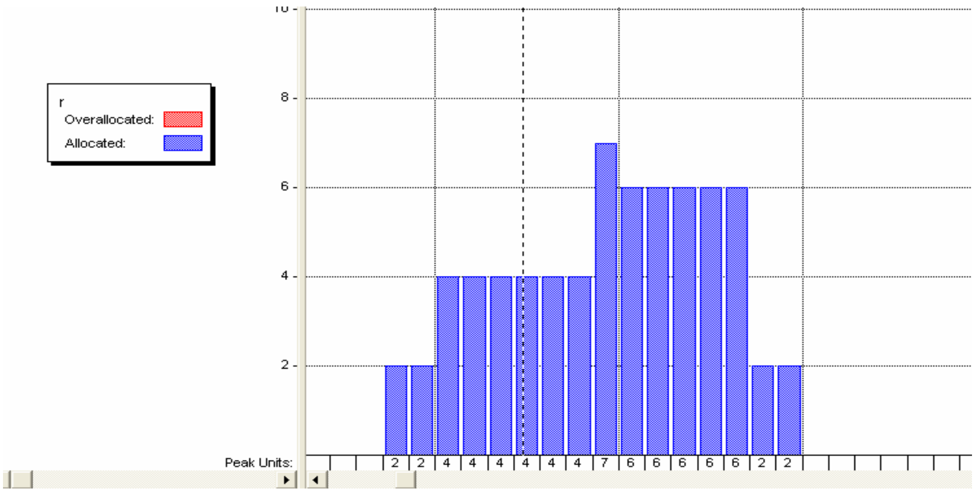

Figure 14 Resource Histogram After Smoothing From GA Results

Figure (15) show the GA output screen from C++

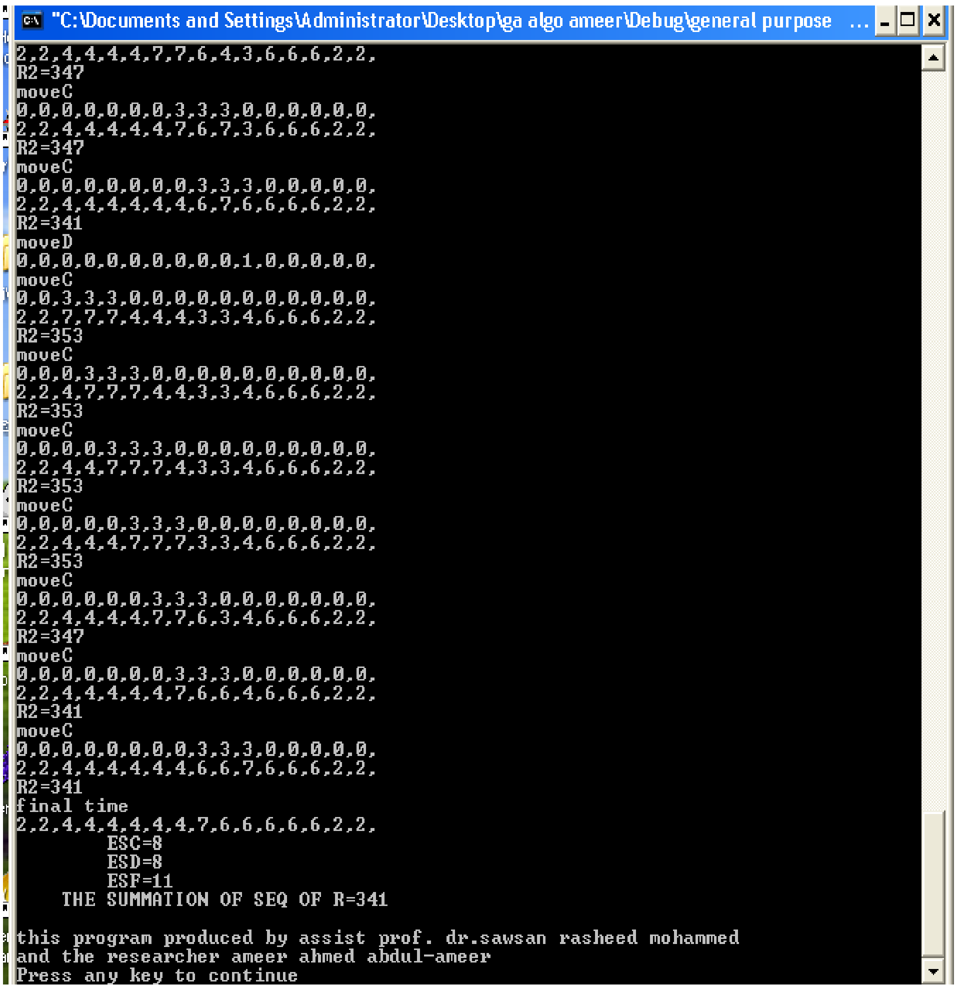

Figure 15 GA Output Screen

CONCLUSIONS

Through the research work, there are groups of conclusions that can be summarized by the following points:

1. Through the literature review, the researcher found that :
   a- There are no researches or studies accomplished in Iraq deal with the subject of Resource Leveling in spite of the importance of this part of Management.
   b- GA can be utilized in the other areas of Project Management such as Productivity, Value Engineering, Scheduling…etc.
2. Through the development of Resource Smoothing Model using GA, the following points are concluded:
   a- GA have demonstrated to be a promising tool for use in the initial stages of Construction Projects.
   b- The scheduling model has the capability to obtain optimum solution for performing resource smoothing. Genetic algorithms program searches for the optimum set of activities methods of constructions that minimize the moment of resources (MX). The purpose model can perform resource leveling is better than the Microsoft project program (MS-project). We also find that the calculated moment of resources (MX) of proposed model (C++) is less than the results of (MS-project) and given better smoothing. Resource smoothing can be applied with the proposed model to obtain results identical (improved further) to that obtained from adopting Microsoft project software.

RECOMMENDATIONS

1. Despite the good performance of GA in this work and in many situations in civil engineering, it suffer from a number of shortcomings, notably, the lack of theory to help with it development, the fact that success in finding a good solution is usually achieved by optimize project plan during planning stage.
2. For the future work, it is suggested to transfer the information automatically (to perform Resource Smoothing).

It is suggested to adopt the research findings in the application field throughout using the model in the planning and managing of construction project in Iraqi construction industry.

REFERENCES

Baker, J.E. (1985). Adaptive Selection Methods for Genetic Algorithms. Proceedings of an International Conference on Genetic Algorithms and Their Applications, 101-111.

Callahan, M. T., Enbush. D.G.Q. and Rowings, J. E., 1992, "Construction Project Scheduling", McGraw-Hill, Inc.

De Jon, K.A. (1980b). “A Genetic-Based Global Function Optimization Technique” Pittsburgh: University of Pittsburgh. Department of Computer Science.

GOLDberq, D. E., 1989, "Genetic Algorithms in search optimization and Machine Learning", Addision Wesley Publishing Co.

Haider, A., Naoum, S., Howes, R and Tah, J., 1999, "Genetic Algorithms Application and Testing for Equipment Selection", ASCE Journal of Construction Engineering and Management, vol. 125, No.1.

Harmanani, H., Zouein, P., Hajar, A., 2000, "An Evolutionary Site Layout" , ASCE, Journal of Construction Engineering and Management, vol. 128, No.6.

Harris, R. B., 1990, "Packing Method for Resource Leveling (PACK)", Journal of Construction Engineering and Management, vol. 116, No. 2.

Harris, R. B., 1978, "Precedence and Arrow Networking Techniques Press, London, England.

Hiyassat, A. M., 2001, "Applying Modified Minimum Moment Method to Multiple Resource Leveling", ASCE, Journal of Construction Engineering and Management, vol. 127, No. 3.

Kevin, P. and Tarek, H., 2003, "Genetic Optimization for Dynamic project Control", ASCE journal of Construction Engineering and Management, vol. 129, No.4.

Leu, S. and Yang, C. H.,1999, "GA-Based Multicriteria in Optimal Model for Construction Scheduling", ASCE, Journal of Construction Engineering and Management, vol. 125, No. 6.

Maria, A., 1997 "Introduction to Modeling and Simulation" Proceedings of the 1997 Winter Simulation Conference, Atlanta, Georgia, USA.

Michell,M.,1998,"An Introduction to Genetic Algorithms", MIT press, London, England.

Moselhi, A., and Lorterapong, P. (1993). “Least Impact Algorithm for Resource Allocation.” ” Can. J. Civ. Engrg., CSCE, 20(2).

Project Management Institute, 1996, " A guide to the Project Management Body of Knowledge" USA.

Que, B. C., 2002, "Incorporating Practicability into Genetic Algorithms-Based Time-Cost Optimization", Journal of Construction Engineering and Management.

Senupta, B. and Guha, H.,1995, "Construction Management and Planning", Tata Mc Gra-Hill.

Son, J. and Skibuiewski, M. J., 1999, "Multi Heuristic Approach for Resource Leveling Problem in Construction Engineering and Management", Journal of Construction Engineering and Management ASCE, vol. 125, No. 1.

Tarek, H, 1999 "Optimization of Construction Time-Cost Trade off Analysis Using Genetic Algorithms", Canadian Journal of Civil Engineer, Vol. 26.

Tarek, H. 1999 "Optimization of Resource Allocation and Leveling Using Genetic Algorithms", ASCE, Journal of Construction Engineering and Management, Vol. 125, No. 3.

Tarek, S. A., 2000, "conjugation and Controlled Mutations New Operatos in Genetic Algorithms", Ph. D. Thesis, Computer Science and Information System, University of Technology.

DAMAGE DETECTION AND LOCATION FOR IN AND OUT-OF-PLANE CURVED BEAMS USING FUZZY LOGIC BASED ON FREQUENCY DIFFERENCE

Asst. Prof. Dr. Nabil H. Hadi 1*and M. Sc. Hayder S. Ashoor 2**
*University of Baghdad / College of Engineering / Mechanical Engineering Department
**University of Baghdad / College of Engineering / Mechanical Engineering Department

ABSTRACT

In this study, structures damage identification method based on changes in the dynamic characteristics (frequencies) of the structure are examined, stiffness as well as mass matrices of the curved (in and out-of-plane vibration) beam elements is formulated using Hamilton's principle. Each node of both of them possesses seven degrees of freedom including the warping degree of freedom. The curved beam element had been derived based on the Kang and Yoo's thin-walled curved beam theory in 1994. A computer program was developing to carry out free vibration analyses of the curved beam as well as straight beam. Comparing with the frequencies for other researchers using the general purpose program MATLAB. Fuzzy logic system (FLS) applied in two stages to calculate the damage extent and location in simply in and out-of- plane curved beam, the damage deduce by reduction in stiffness for three levels (20%, 40%, 60%). At the first stage the output faults of the fuzzy system represented by four levels of damage in curved beam (undamaged, slight, moderate, and severe), and at second stage indicate damage location at element with two defuzzification methods (centroid and middle of maximum).

The results show that the frequency difference method is efficient to indicate and quantify damage with accuracy about (99.5%) for slight and moderate damage about (100%) for severe damage. Consequently fuzzy logic performs well for detecting, locating and quantifying damage in curved beam.

الخلاصة

في هذا البحث يتم التعرف على الضرر في الهياكل من خلال فحص التغيير في الصفات الديناميكية (الترددات) للهيكل،تم صياغة مصفوفتي الجساءة والكتلة لعنصر العتبة المقوسة (بالاتجاه الموازي والعمود على المستوي) باستعمال مبدأ هاملتون. كل عقدة تحوي على سبع درجات من الحرية مع الاخذ بنظر الاعتبار الاعوجاج (warping).أشتق عنصر العتبة المقوسة بالإعتماد على نظرية كانك وياو (1994) للعتبة المقوسة ذات الجدران الرقيقة، وطور برنامج ماتلاب (MATLAB) ليستعمل للعتبة المقوسة كذلك المستقيمة مع مقارنة الترددات المستخرجة مع باحثين اخرين. طبق نظام المنطق الضبابي(Fuzzy logic system) على مرحلتين لحساب كمية الضرر وموقعه،يتم الاستدلال على الضرر من خلال عمل تخفيض في جساءة الهيكل وبثلاث مستويات (20%،40%،60%). في المرحلة الاولى نوع الضرر المستخرج من نظام المنطق الضبابي عبارة عن اربع مستويات من الضرر(غير متضرر،خفيف،متوسط و عالي)، اما في المرحلة الثانية فالقيم المستخرجة من النظام تحدد موقع الضرر في اي عنصر من العتبة وباستعمال طريقتان (centroid and middle of maximum).
النتائج المستخرجة اوضحت كفاءة طريقة الفرق في التردد في تحديد كمية وموقع الضرر وبدقة بحدود (99.5%) بالنسبة للضرر الخفيف والمتوسط وبحدود (100%) بالنسبة للضرر العالي. وبالنتيجة فأن نظام المنطق الضبابي أنجز وبشكل جيد في تحديد كمية وموقع الضرر في العتبة المقوسة.

Keywords: curved beam; fuzzy logic; damage detection

1. INTRODUCTION

It is easily accepted that when damage occurs, a structure would suffer a decrease in stiffness. And as a consequence, there was a decrease in natural frequencies of vibration. For a beam structure a loss in stiffness would imply an increase in curvature of the elastica which can be used for damage detection **[1]**. In the most general terms damage can be defined as changes introduced into a system that adversely affect the current or future performance of that system. Implicit in this definition is the concept that damage is not meaningful without a comparison between two different states of the system, one of which is assumed to represent the initial, and often undamaged, state. Structural damage identification based on change dynamic characteristics provides a global way to evaluate the structural condition. These methods are based on the premise that modal parameters (i.e., natural frequencies, mode shapes, modal damping ratios, etc.) are a function of the physical properties of the structure (stiffness, damping, mass and boundary conditions). The approach is based on the fact that natural frequencies are sensitive indicators of structural integrity. Thus, an analysis of periodical frequency measurements can be used to monitor structural condition. Since frequency measurements can be cheaply acquired, the approach could provide an inexpensive structural assessment technique. **Ju and Mimovich [2]** used changes in modal frequencies to locate damage occurring at sections of a beam to within 3% of the length. It was found that the accuracy of the damage localization was improved to less than 1% of the length when the built-in end of the experimental beam was represented by a torsion spring. **Cawley and Adams [3]** study the sensitivity concept and it is based on the premise that the ratio of frequency changes in two modes is a function of the location of the damage only, if changes in stiffness are independent of frequency. To locate the defect, theoretical frequency shifts, due to damage at selected positions on the structure, are calculated and compared with measured values. **Uzgider and Sanli [4]** proposed a damage location method which uses measured natural frequencies to identify stiffness parameters. The natural frequencies of the selected modes are then used to identify the stiffness parameters. The relative magnitudes of the differences between the identified parameters and prior estimates are used to indicate the presence of structural damage. **H. R. Öz and M. T. Das [5]** studied the in- plane vibrations of cracked circular curved beams, the beam is an Euler-Bernoulli beam. Only bending and extension effects are included, the curvature was in a single plane. An in-plane vibration is analyzed using FEM. In the analysis, elongation, bending and rotary inertia effects are included, four degrees of freedom for in-plane vibrations is assumed. Increasing the crack depth decreases the frequencies. At the recent years many researchers used artificial intelligence likes "neural network, genetic algorithm, fuzzy logic" to detect damage for structure. Fuzzy logic systems have been widely used in engineering applications; because of the flexibility they offer designers and their ability to handle uncertainty and has a natural way of dealing with paradoxes **[6]** another important feature is that fuzzy behavior was shown to produce good results, even in cases with incompletely defined dependencies **[7].** Finally, an important advantage of a fuzzy system over a “classic” expert system is that a fuzzy system usually has significantly fewer rules **[8],** so we take fuzzy logic in this study as the all below researchers use it. **RANJAN GANGULI [9]** study the rotor blade which modeled as an elastic beam undergoing transverse (flap) and in plane (lag) bending, axial and torsion deformations. A finite element model of the rotor blade is used to calculate the change in blade frequencies (both rotating and no rotating) because of structural damage. The measurement deviations due to damage are then fuzzified and mapped to a set of faults using a fuzzy logic system. **Prashant M and Ranjan [10]** propose a genetic fuzzy system used to find the location and extent of damage. A finite element model of a cantilever beam is used to calculate the change in beam frequencies. The genetic fuzzy logic system in this study is proposed as a method for automatic rule generation in fuzzy systems for structural damage detection. **M. Chandrashekhar, Ranjan Ganguli [11]** a fuzzy logic system (FLS) with a new sliding window defuzzifier is developed for damage detection. The effect of changes in the damage evaluation parameter (frequency) due to uncertainty in material properties is explored and the results of the probabilistic analysis are used to develop a robust FLS for damage detection. The FLS also accurately classifies the undamaged condition in presence of the mentioned uncertainties reducing the possibility of false alarms. From an algorithmic standpoint, this paper connects the disparate areas of probability and fuzzy logic to alleviate uncertainty issues in damage detection.

In this study, it had been used a fuzzy logic system for damage detection and location in (in and out-of-plane) curved beam based on frequency difference, the method apply in two stages; the first stage used to detect the damage extent along beam and the second used to detect the damage at any element of beam.

2. INTRODUCTION TO FUZZY LOGIC

Fuzzy logic deals with reasoning with inexact or fuzzy concepts **[12]**. Fuzzy logic has two different meanings. In a narrow sense, fuzzy logic is a logical system, which is an extension of multivalued logic. However, in a wider sense fuzzy logic (FL) is almost synonymous with the theory of fuzzy sets, a theory which relates to classes of objects with unsharp boundaries in which membership is a matter of degree **[13].**

2.1 Membership Function

A membership function is a curve that defines how each point in the input space is mapped to a membership value (or degree of membership) between 0 and 1. The input space is sometimes referred to as the universe of discourse. The simplest membership functions are formed using straight lines. In this work three types of membership function were used (triangular, trapezoidal and gaussian).

2.2 Fuzzy Rules

Fuzzy sets and fuzzy operators are the subjects and verbs of fuzzy logic. Usually the knowledge involved in fuzzy reasoning is expressed as rules in the form:

If x is A Then y is B

Where x and y are fuzzy variables and A and B are fuzzy values defined by fuzzy sets. The if-part of the rule "x is A" is called the antecedent or premise, while the then-part of the rule "y is B" is called the consequent or conclusion. Statements in the antecedent (or consequent) parts of the rules may well involve fuzzy logical connectives such as ‘AND’ and ‘OR’.

2.3 Fuzzy Inference System

Fuzzy inference is the process of formulating the mapping from a given input to an output using fuzzy logic. The fuzzy inference system was consisting of parts as shown in Fig.1 **[13]**.

- **Fuzzification**. Convert crisp set to fuzzy set.
- **Rule evaluation**. Consist of two parts; fuzzy operators and conditional statement.
- **Aggregation.** Combine all output fuzzy sets from rule evaluation to a single fuzzy set.
- **Defuzzification.** Reduction of fuzzy set to singleton. There are five defuzzification methods as shown in Fig.2. In this study takes two defuzzification methods (Centroid and Middle of Maximum (Mom)).

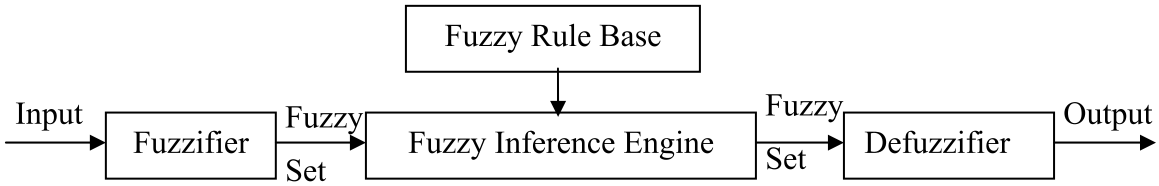

Fig.1. Schematic representation of a fuzzy inference system

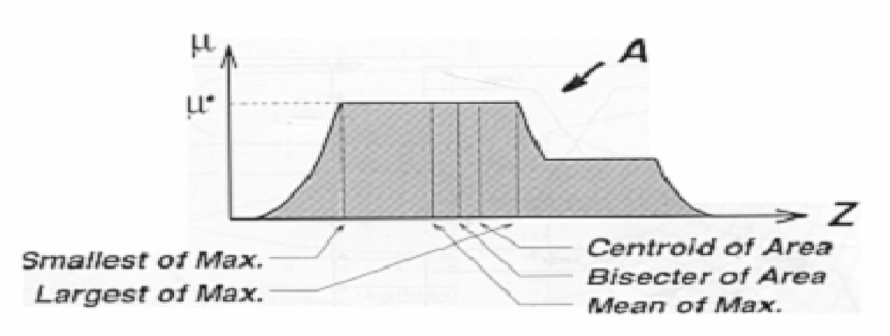

Fig.2. Defuzzification methods

3. MODELING THE DAMAGED BEAM

In this study the equation of motion for simply curved beam acquired from Kang and Yoo's theory of thin- walled curved beams **[14]** to drive the element stiffness and mass matrices respectively. The curved beam element is shown in Fig.3 in curvilinear coordinate system. Each node of the curved beam element possesses seven degrees of freedom including the warping degree of freedom. Using Hamilton's principle, the dynamic equilibrium can be expressed in the variation form as following **[15]**.

$$\int_{t1}^{t2}(\delta T + \delta U + \delta \forall)dt = 0 \qquad (1)$$

Where δT is the variation kinetic energy, δU is the variation strain energy, and $\delta \forall$ is the variation potential energy loss due to applied loads. The symbol (δ) means the first variation. For the linear elastic body, the variation of strain energy stored in the body is

$$\delta U = \int_V \tau_{ij}\, \delta\varepsilon_{ij} dV \qquad (2)$$

Where τ_{ij} refers to the components of the stress tensor and ε_{ij} to those of the strain tensor. The variation in kinetic energy of a thin-walled curved beam is

$$\delta T = \int_V \rho \frac{\partial^2 u_i}{\partial t^2} \delta u_i dV \qquad (3)$$

Where ρ is the mass density, u_i is the displacement components of the curved beam, and t is time. The variation potential energy loss due to applied loads with body forces neglected is

$$\delta \forall = -\int_l q_i\, \delta u_i dz \qquad (4)$$

Where q_i stands for distributed loads applied on the line of shear center and l is the length of the element. Substituting the strain-displacement relationship and the stress resultant–displacement relationship into eqs. (1), (2), (3) and (4) and carrying out the conventional procedure of the calculus of variation, the following set of equations of motion is obtained **[15].**

$$\rho\left(A\ddot{u}_o - I_y\ddot{u}_o'' - \frac{2I_y}{R}\ddot{w}_o'\right) - \frac{EA}{R}\left(w_o' - \frac{u_o}{R}\right) + EI_y\left(u_o^{IV} + \frac{2}{R^2}u_o'' + \frac{1}{R^3}w_o'\right) = q_x - m_y'$$

(5a)

$$\rho\left[A\ddot{v}_o\left(I_x+\frac{I_\omega-2K_{xy\omega}}{R^2}\right)\ddot{v}_o''-\frac{I_y}{R}\ddot{\beta}-\frac{I_\omega-K_{xy\omega}}{R}\ddot{\beta}''\right]+EI_x\left(v_o^{IV}-\frac{1}{R}\beta''\right)+\frac{EK_{xy\omega}}{R}\left(\beta^{IV}+\frac{2}{R}v_o^{IV}-\frac{\beta''}{R^2}\right)+\frac{EI_\omega}{R}\left(\beta^{IV}+\frac{v_o^{IV}}{R}\right)-\frac{GK_T}{R}\left(\beta''+\frac{v_o''}{R}\right)=q_y+m_x'$$

(5b)

$$\rho\left[\left(A+\frac{3I_y}{R^2}\right)\ddot{w}_o+\frac{2I_y}{R}\ddot{u}_o\right]+E\left(\frac{I_y}{R^2}-A\right)\left(w_o''-\frac{1}{R}u_o'\right)=q_z$$

(5c)

$$\rho\left[\left(I_x+I_y\right)\ddot{\beta}-I_\omega\ddot{\beta}''-\frac{I_y}{R}\ddot{v}_o-\frac{I_\omega-K_{xy\omega}}{R}\ddot{v}_o''\right]-\frac{EI_x}{R}\left(v_o''-\frac{1}{R}\beta\right)+\frac{EK_{XY\omega}}{R}\left(v_o^{IV}-\frac{2}{R}\beta''-\frac{1}{R^2}v_o''\right)+EI_\omega\left(\beta^{IV}+\frac{1}{R}v_o^{IV}\right)-GK_T\left(\beta''+\frac{1}{R}v_o''\right)=m_z+m_\omega'$$

(5d)

Where the reference displacements u_o, v_o, w_o, and β are displacements of the centroid in the x, y, and z directions and a rotation of the cross-section about z-axis, respectively. Displacement components u_o and w_o are associated with in-plane of curvature displacement field while displacement components v_o and β are referenced with out-of plane of curvature displacement field. The linear equations of motion given in equations (5a), (5b), (5c), and (5d) are partially, if not completely, uncoupled. It is observed that u_o and w_o appear only in eqs. (5a) and (5c) whereas v_o and β are present only in eqs. (5b) and (5d), which means that two displacement fields related with in-plane of curvature and out-of-plane of curvature, respectively are fully separated each other.

Only equations that are most related to the modeling of curved beams by straight-beam elements will be presented herein by consider a curved beam as comprising an infinitesimal straight beam. This assumption is consistent with those used by **[16]**. Theory of curved members developed can be reduced to that of straight beam simply by letting the radius of curvature approaches to infinity in eqs. (5a), (5b), (5c), and (5d) **[15].**

$$\rho A\ddot{u}_o-\rho I_y\ddot{u}_o''+EI_yu_o^{IV}=q_x-m_y' \qquad (6a)$$

$$\rho A\ddot{v}_o-\rho I_x\ddot{v}_o''+EI_xv_o^{IV}=q_y-m_x' \qquad (6b)$$

$$\rho A\ddot{w}_o-EAw_o'=q_z \qquad (6c)$$

$$\rho\left(I_x+I_y\right)\ddot{\beta}-\rho I_\omega\ddot{\beta}''+EI_\omega\beta^{IV}-GK_T\beta''=m_z'+m_\omega'$$

(6d)

Where every displacement fields, u_o, v_o, w_o, and β, are not coupled with one another hence can be formulated separately. In the present study, the third order Hermit polynomials are employed as shape functions about u_o, v_o, and β. The axial displacement w_o is represented by a linear function.

A linear stiffness matrix and a consistent mass matrix are developed so that various analyses such as linear and free vibration analyses can be performed. Using shape functions, the dynamic equilibrium given in eq. (1) yields a set of simultaneous equations

$$\delta T+\delta U+\delta V=\delta d^T[\mathrm{M}\ddot{d}+\mathrm{K}d-\mathrm{f}]=0 \qquad (7)$$

From which one obtains by letting f equal zero.

$$\mathrm{M}\ddot{d}+\mathrm{K}d=0 \qquad (8)$$

Where K, M, d, and f are the linear stiffness matrix, the consistent mass matrix, the nodal displacement vector, and the applied

force vector of a global structural system, respectively. The nodal forces and the corresponding nodal displacements are shown in Fig.3 in the positive senses. The nodal forces are seven components $(F_z, M_x, M_y, B, T_T, V_x, \text{and } V_y)$. The corresponding nodal displacements are $(w_o, \gamma, -v_o', -\tau, \beta, u_o, and\ v_o)$ where γ and τ are defined as

$$\gamma=u_o' \qquad (9a)$$

$$\tau=\beta' \qquad (9b)$$

w_o, u_o, and γ describe the in-plane displacements whereas v_o, $-v_o'$, β, and $-\tau$ are the out-of-plane displacements. These two parts of displacement fields are not coupled with each other and can be formulated separately. Then, the displacement fields can be expressed in terms of nodal displacements as following **[15].**

$$\begin{Bmatrix} u_o \\ v_o \\ w_o \\ \beta \end{Bmatrix} = \begin{bmatrix} N_u & & & \\ & N_v & & \\ & & N_w & \\ & & & N_\beta \end{bmatrix} \begin{Bmatrix} d^u \\ d^v \\ d^w \\ d^\beta \end{Bmatrix} \quad (10)$$

Where the shapes function, N is defined as.

$$N_u = [1 - 3\xi^2 + 2\xi^3 \quad \iota(\xi - 2\xi^2 + \xi^3) \quad 3\xi^2 - 2\xi^3 \quad \iota(-\xi^2 + \xi^3)] \quad (11a)$$

$$N_v = N_\beta = [1 - 3\xi^2 + 2\xi^3 \quad \iota(-\xi + 2\xi^2 - \xi^3) \quad 3\xi^2 - 2\xi^3 \quad \iota(-\xi^2 + \xi^3)] \quad (11b)$$

$$N_w = [1 - \xi \quad \xi] \quad (11c)$$

Where $\xi = z/\iota$

Where the nodal displacement, d is represented

$$d^u = [u_{oi} \quad \gamma_i \quad u_{oj} \quad \gamma_j]^T \quad (12a)$$

$$d^v = [v_{oi} \quad -v'_{oi} \quad v_{oj} \quad -v'_{oj}]^T \quad (12b)$$

$$d^w = [w_{oi} \quad w_{oj}]^T \quad (12c)$$

$$d^\beta = [\beta_i \quad -\tau_i \quad \beta_j \quad -\tau_j]^T \quad (12d)$$

From the variation of strain energy presented in eq. (2) and the shape function in eqs. (11a), (11b), and (11c) the element stiffness matrix for curved beam is derived as shown **[15].**

$$[k_u] = \begin{bmatrix} EI_y K_a & 0 & 0 & 0 \\ 0 & EI_x K_b & 0 & 0 \\ 0 & 0 & EAK_c & 0 \\ 0 & 0 & 0 & EI_\omega K_d + GK_T K_e \end{bmatrix} \quad (13)$$

From the variation kinetic energy presented in eq. (3) and following the similar procedure as used for the element stiffness matrix for curved beam formulation, the mass matrix is derived **[15].**

$$[m_u] = \rho \begin{bmatrix} AM_a + I_y M_e & & & \\ & AM_b + I_x M_b & & \\ & & AM_c & \\ & & & (I_x + I_y) M_a + I_\omega M_f \end{bmatrix} \quad (14)$$

Where $[k_u]$ $[m_u]$ represented undamaged stiffness and mass matrices respectively, but for damage cases it had been taken reduction for stiffness matrix at any element of curved beam.

4. FREQUENCY DIFFERENCE

The difference between the frequency of the damaged and undamaged for simply curved beam is that used as the system indicator for damage and is referred to as a ‘‘summation deltas’’ since the reduction in stiffness for a damaged simply supported curved beam decreases the frequency. The summation deltas is expressed as follow.

$$\sum \Delta\omega = \sum_{i=1}^{m} (\omega_{ui} - \omega_{di}) \quad (15)$$

Where
$\sum\Delta\omega$: summation delta.
i: mode number (i=1,2,3,….,m)
ω_{ui}: Frequency undamaged.
ω_{di}: Frequency damage.

A finite element approach is used to calculate the natural frequencies of the simply curved beam. Each beam finite element has seven degrees of freedom. Damage is modeled as a reduction in element stiffness of (20, 40 and 60%) respectively. These damage sizes are classified as ‘‘slight damage’’, ‘‘moderate damage’’ and ‘‘severe damage’’, respectively. Damage sizes below ‘‘slight damage’’ are classified as undamaged. Damage sizes greater than ‘‘severe damage’’ are classified as ‘‘catastrophic damage’’.

5. FORMULATION OF FUZZY LOGIC SYSTEM

5.1. Input and Output

Inputs to the FLS are summation deltas, at the first stage; it has been taken the least number of modes which realize minimum interference between damage extent values, so the chosen number of modes is fifteen for in-plane and twenty-six for out-of-plane with use eq. (15), and outputs are structural damage faults (SLD,MOD and SVD). We have three summation deltas represented by y and five fault quantity represented by x. The objective is to find a functional mapping between y and x. mathematically this can be represented as:

$$x= f(y) \tag{16}$$

Where x= {damage extent} and $y = \{\sum\Delta\omega_1, \sum\Delta\omega_2, \sum\Delta\omega_3\}$.

At second stage represents the FLS input is frequency difference for eight modes for in-plane and nine modes for out-of-plane, and the damage element indicator as output, here x represented element number x={damage at element} and y represented frequency difference y=$\{\Delta\omega_1, \dots, \Delta\omega_9\}$.

5.2 Fuzzification

Here the structural damages are crisp numbers. To get a degree of resolution of the extent of damage, each of this damage extent is allowed several levels of damage and split into linguistic variables. For example, at first stage consider ''beam" as a linguistic variable. Then it can be decomposed into a set of terms T(beam) = {Undamaged,Slight Damage,Moderate Damage, Severe Damage, Catastrophic Damage}.where each term in T(beam) is characterized by a fuzzy set in the universe of discourse U(beam)={0, 70} as shown in Fig.4. The summation deltas ∑Δω also treated as fuzzy variables. For example, at first stage consider ∑Δω as a linguistic variable. It can be decomposed into a set of terms T(∑Δω)={Negligible, Low,Medium, High, Very High}.where each term in T(∑Δω) is characterized by a fuzzy set in the universe of discourse U (∑Δω)= {0,max} as shown in Fig.5 for in-plane and Fig.6 for out-of-plane. The other two summation deltas are defined using the same set of terms. Summation deltas larger than covered by the universe of discourse will represent an extensive structural damage indicative of a catastrophic failure. Fuzzy sets with Trapezoidal membership functions are used for the first stage input variables and triangular membership functions are used for the first stage output variables. Tables (1) and (2) give the linguistic measure and rules associated with each fuzzy set at first stage. The values mentioned in the Tables (1) and (2) were indicate by substituting summation deltas ∑Δω for each element along curved beam in three damaged extent and then using fuzzy logic tool box to construct membership functions and rules.

The second stage FLS is the same manner as previous, fuzzy sets with gaussian membership functions are used for the second stage input variables. These fuzzy sets can be defined using the following equation **[13]**.

$$\mu(x) = e^{-0.5(x-\frac{m_0}{\sigma})^2} \tag{17}$$

Where m_0 is the midpoint of the fuzzy set and σ is standard deviation associated with the variable. Fig. 7 and Fig.8 represent the input fuzzy sets for in and out-of-plane respectively at second stage which consist of ten gaussian membership functions (N=negligible, VVL=very very low, VL=very low, L=low, LM=low medium, M=medium, MH=medium high, H=high, VH=very high and VVH=very very high) where each term in T(Δω) is characterized by a fuzzy set in the universe of discourse U(Δω) ={-68.75,550}, and output represented by thirteen triangular membership functions for in-plane and fifteen triangular membership functions for out-of-plane which represent element number as shown in Fig. 9 and Fig.10 respectively where each term in T(damage at element) is characterized by a fuzzy set in the universe of discourse U(damage at element) ={0,1,2,…,15}

5.3 Rules Generation

Rules for the fuzzy system are obtained by fuzzification of the numerical values obtained from the finite element analysis using the following procedure.

1. A set of summation deltas and frequency difference corresponding to a given structural fault is input to the FLS and the degrees of membership of

the elements of ($\sum\Delta\omega$) and ($\Delta\omega$) are obtained.

2. Therefore, each summation deltas has five degrees of memberships for first stage and each frequency difference has ten degrees of memberships for second stage.
3. Each summation deltas and frequency difference is then assigned to the fuzzy set with the maximum degree of membership.
4. One rule is obtained for each fault by relating the summation deltas and frequency difference with a fault.

These rules can be read as follows for the first stage:
IF $\Sigma\Delta\omega$ Is Low THEN Slight Damage.
IF $\Sigma\Delta\omega$ Is Medium THEN Moderate Damage.
IF $\Sigma\Delta\omega$ Is High THEN Severe Damage.

Then for example at second stage the rule for in-plane of "Severe Damage" fault is shown below,
IF
$\Delta\omega_1$ Is Very Very Low AND
$\Delta\omega_2$ Is Very Very Low AND
$\Delta\omega_3$ Is Low AND
$\Delta\omega_4$ Is Low AND
$\Delta\omega_5$ Is Very Very Low AND
$\Delta\omega_6$ Is Low AND
$\Delta\omega_7$ Is Medium AND
$\Delta\omega_8$ Is Medium High
Then damage at element No.5.

The same procedure applies to slight and moderate damage except the rules are different. These rules are tabulated in Tables (3) and (4) (these rules were indicate to damage extent 20%, 40% and 60% at second stage and results represented damage location at any element along the curved beam)

6. NUMERICAL RESULTS

In the present work we consider a simply (in and out-of-plane) curved beam for illustrating the fuzzy logic system for the damage detection problem; the fuzzy rules are automatically generated. Dimensions and material properties for the simply supported in and out-of-plane curved beam are shown in Tables (5) and (6) respectively

The simply in-plane curved beam is divided into 25 finite elements of equal length and out-of-plane is divided into 30 finite elements. The selection of number of element is justified in Fig. 11 and Fig.12 respectively to minimize FEM modeling error, in this figure the ratio of the eighth mode which is the highest mode used in the numerical results for in-plane and nine for out-of-plane with the first mode are shown. From the graph, it appears that 25 elements for in-plane and 30 elements for out-of-plane give a good resolution. The undamaged beam is uniform. Therefore, the frequency predictions from the FEM model of undamaged beam are validated by comparing with other researchers as shown in Tables (7) and (8) respectively

The generated rules are selected for first stage of summation deltas; by taking the appropriate modes here in this study take fifteen modes for in-plane and twenty-six modes for out-of-plane (the selected modes chosen according to minimize interference between damage extent for three cases) . At the second stage of frequency difference will be taken the eight input deltas for in-plane and nine input deltas for out-of-plane represent the highest natural frequencies used (these values were taking as mention in Fig. 11 and Fig. 12 which declare the difference between). The linguistic forms will remain constant for different structure but the numerical values of midpoints and standard deviation will change.

7. RESULTS AND DISCUSSION

After construct the fuzzy engine and check all damage elements under the test it could be calculated the error between proposed and predict values for all elements using two defuzzification methods (Centroid and Middle of Maximum) to compare and evaluate results product from fuzzy logic system. We chose these two methods because they had been already approval that they represent damage with the least error percentage, and this didn't mean we compare between them.

For in-plane curved beam as shown in the Fig.13, from charts it could be seen the middle of maximum defuzzification method is the best for detect slight (D=20%) and moderate (D=40%) damage but at severe (D=60%) damage the centroid defuzzification method is the best.

For out-of-plane curved beam as shown in the Fig.14, from charts it could be seen the middle of maximum defuzzification method is the best for detect slight (D=20%) and moderate (D=40%) damage but at severe (D=60%) damage the centroid defuzzification method is the best. Each value in Fig. 13 and Fig. 14 represented damage location because input and output values to fuzzy engine represent crisp set, referring that this study has been used theoretical results (FEM) as input data instead of experimental data.

The accuracy for detection damage at in and out-of-plane curved beam tabulated in Table (9) it could be seen the accuracy approach to (99.4%) for slight damage, (99.52%) for moderate damage and (100%) for severe damage.

8. CONCLUSIONS

The present study declares that a fuzzy logic depends on one of the well-known methods for damage detection as a base to generate rules, but here we use frequency difference as a new application as a base for fuzzy logic system. The results show that the fuzzy logic system presented in this paper provided a reliable and accurate outcome in recognition of different damage extent and appear more efficient when using summation for frequency difference once taking the fifteen modes for in-plane and twenty-six modes for out-of-plane at first stage, and taking the eight modes for in-plane and nine modes for out-of-plane at second stage. This method were used to detect damage at one location in beam but when we want to locate multi damage in beam we need to apply anther methods together like "strain energy, sensitivity, etc". The other advantage of this method is used to detect damage at low extent (less than 20%) with a good accuracy.

NOTATION

A Sectional area (m^2)
B_i Bimoment (N .m)
E Young modulus (N/m^2)
G Shear modulus (N/m^2)
I_y Area moment of inertia about y-axis (m^4)
I_x Area moment of inertia about x-axis (m^4)
I_ω Warping moment of inertia (m^6)
J Area polar moment of inertia (m^4)
K_T St Venant constant of a straight member(m^4)
l Length of the finite element (m, cm)
m_x, m_y, m_z Uniform distributed moments about x-, y-, and z-axis
m_ω Uniform distributed bimoment
M_x, M_y Moment about x- and y-axis (N.m)
q_x, q_y, q_z Uniform distributed forces about x-, y-, and z-directions
R Radius of initial curvature (m)
T Kinetic energy (N.m)
U Strain energy (N.m)
u_o, v_o Displacement components of the shear center in x- and y- directions, respectively
V Volume of body (m^3)
V_x, V_y Transverse shear forces (N)
w_o Average longitudinal displacement of cross-section

GREEK LETTERS

ρ Mass density (Kg/m^3)
β Rotation of the cross-section about z-axis
θ Subtended angle (degree)
ε_{ij} Components of strain tensor
δ Variation
γ, τ Nodal displacements
τ_{ij} Components of stress tensor

REFERENCES

[1] O. S. Salawu, "Detection of structural damage through changes in frequency: a review", Engineering Structures, Vol. 19, 1997.

[2] Ju, F. D. and Mimovich, M. "Modal frequency method in diagnosis of fracture damage in structures" in Proceedings, 4th International Modal Analysis Conference, Los Angeles, 2, pp 1168-1174, 1986.

[3] Cawley, P. and Adams, R. D. "The location of defects in structures from measurements of natural frequencies", Journal of Strain Analysis, 4 (2), pp 49-57 (1979).

[4] Uzgider, Z., Sanli, A. K., Piroglu, F. and Caglayan, D. B. "Identification of railway bridges using locomotive-induced vibrations "in Bridge Management 2 (edited J. E. Harding, G. A. R. Parke and M.J. Ryall), Thomas Telford, London, pp 833-841, 1993.

[5] H. R. Öz and M. T. Das, "In-plane vibrations of circular curved beams with a transverse open crack", Mathematical and Computational Applications, Vol. 11, No. 1, pp. 1-10,(2006).

[6] Hajek, P., Paris, J. and Shepherdson, J. (2000) "The liar paradox and fuzzy logic", J. Symb. Logic 65, 339–346.

[7] Raju, K. and Majumdar, "Fuzzy functional dependencies and lossless join decomposition of fuzzy relational database systems", ACM Trans. Database Syst. 13(32), 129–166, (1988).

[8] Juuso, Esko K. "Intelligent systems design with linguistic equations", Dortmund, Germany. (Dortmund University), pp 177–196, (1999).

[9] RANJAN GANGULI, "A Fuzzy Logic System for Ground Based Structural Health Monitoring of a Helicopter Rotor using Modal Data". Journal of intelligent material system and structures, Vol. 12, (2002).

[10] Prashant M and Ranjan, "Genetic fuzzy system for damage detection in beams and helicopter rotor blades". Journal of computer methods in applied mechanics and engineering .Vol. 192, Pages 2031–2057, (2003).

[11] M. Chandrashekhar, Ranjan Ganguli," Uncertainty handling in structural damage detection using fuzzy logic and probabilistic simulation" Journal of Mechanical Systems and Signal Processing, pp 1-21(2007).

[12] M. Ganesh, "Introduction to Fuzzy Sets and Fuzzy Logic". Prentice-Hall of India Private Limited, New Delhi (2006).

[13] Fuzzy Logic Toolbox 2 User's Guide, The Math Works, Inc, 1995–2007.

[14] Kang YJ, Yoo CH."Thin-walled curved beams. I: formulation of nonlinear equations". ASCE. Journal of Engineering Structures, Vol. 120, Pages 2072–2101 (1994).

[15] Ki-Young Yoona, Young-Jong Kangb, Young-Joon Choic, and Nam-Hoi Parkb. "Free vibration analysis of horizontally curved steel I-girder bridges". Journal of Thin-Walled Structures. Vol. 43, Pages 679–699(2005).

[16] Shyh Rong Kuo and Yeong Bin Yang," New theory on buckling of curved beams". ASCE. Journal of Engineering Mechanics, Vol. 117, Pages 1698–1717 (1991).

[17] Ki-Young Yoon, Nam Hoi Park, Young Joon Choi, and Young-Jong Kang "Natural frequencies of thin-walled curved beams" Journal of Finite Elements in Analysis and Design. Vol. 42, Pages 1176 – 1186(2006).

Faults	Summation Deltas (ΣΔω)	Numeric value
SLD	Low	351 - 687
MOD	Moderate	900 - 1657
SVD	High	1900 - 3137

Table 1 Rules for fuzzy system in-plane curved beam (first stage)

Faults	Summation Deltas (ΣΔω)	Numeric value
SLD	Low	162.5 - 356
MOD	Moderate	427 – 848.5
SVD	High	925 - 1580

Table 2 Rules for fuzzy system out-of-plane curved beam (first stage)

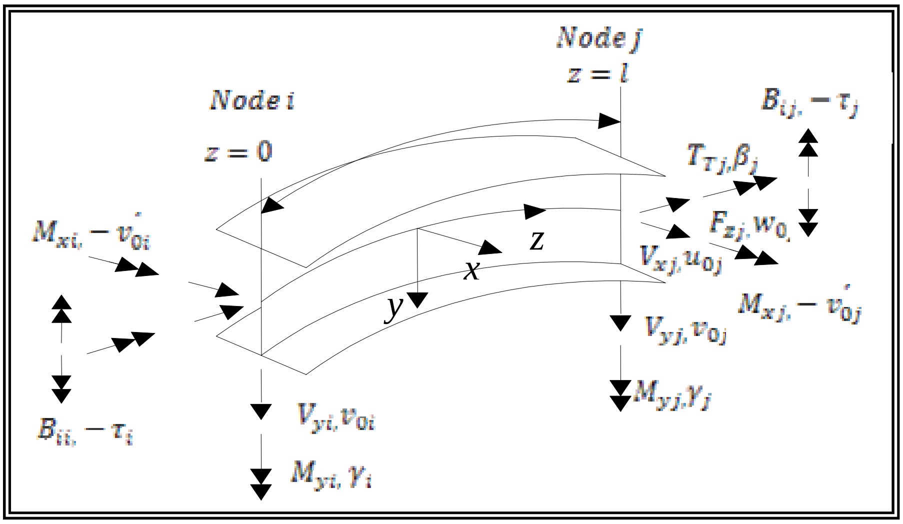

Fig.3. Curved beam element

.

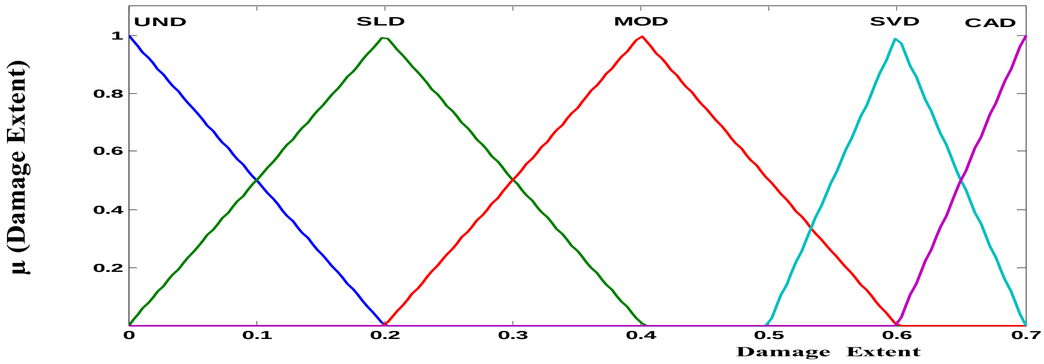

Fig.4. Input fuzzy sets representing damage levels (first stage)

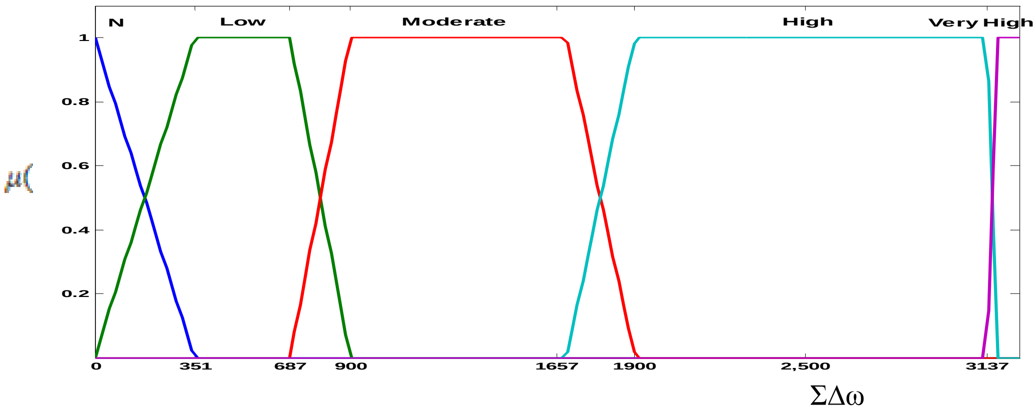

Fig.5. Input Fuzzy sets representing summation deltas for in-plane curved beam (first stage)

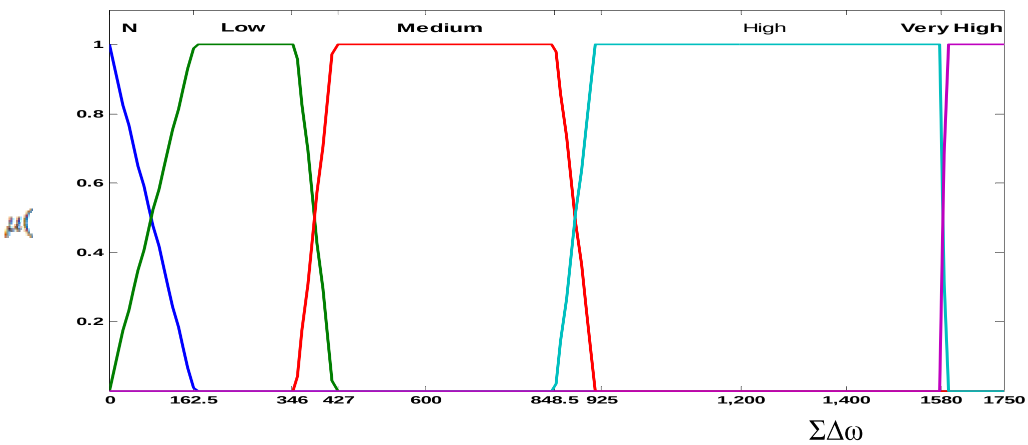

Fig.6. Input Fuzzy sets representing summation deltas for out-of-plane curved beam (first stage)

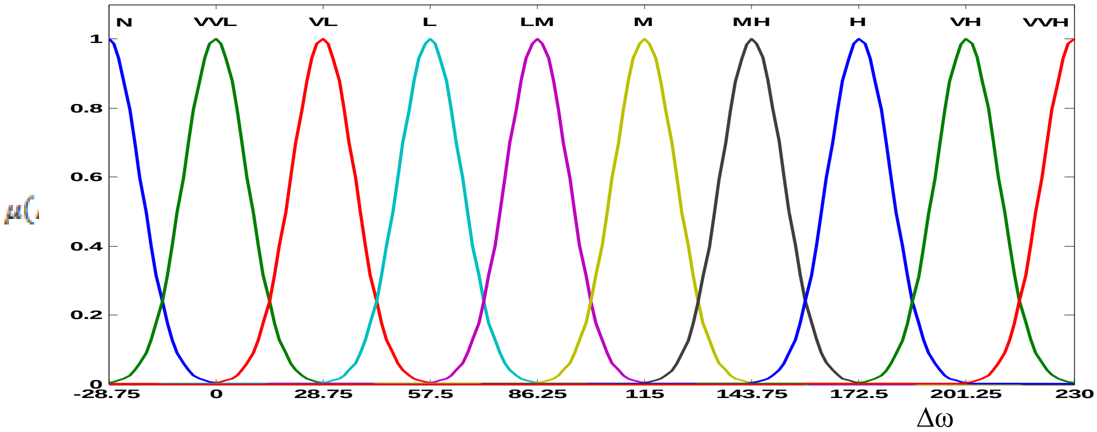

Fig.7. Input fuzzy sets for in-plane curved beam (second stage)

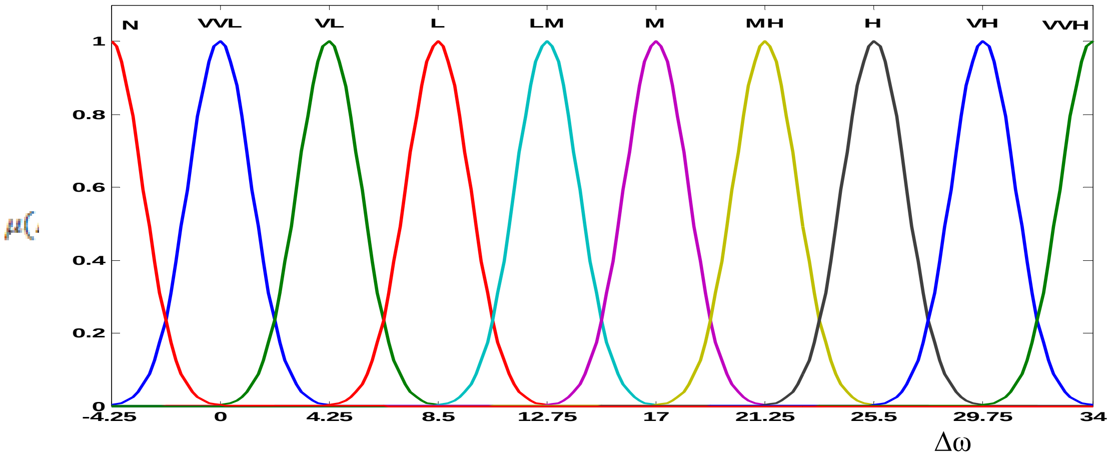

Fig.8. Input fuzzy sets for out-of-plane curved beam (second stage)

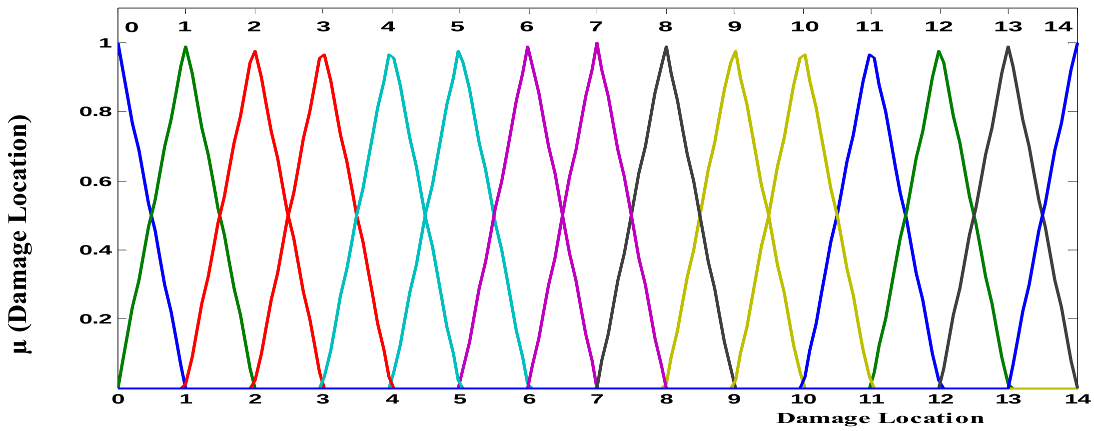

Fig.9. Output fuzzy sets for in-plane curved beam (second stage)

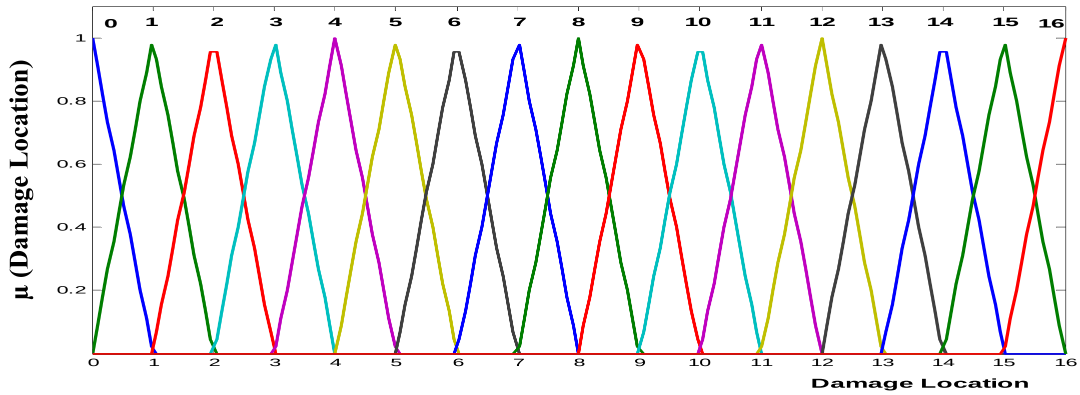

Fig.10. Output fuzzy sets for out-of-plane curved beam (second stage)

Table 3 Rules for fuzzy system of in-plane curved beam damaged cases (second stage)

Damaged at element No.	0	1	2	3	4	5	6	7	8	9	10	11	12	13
D=0.2														
$\Delta\omega1$	N	VVL	VVL	VVL	VVL	VVL	VVL	VVL	VVL	VVL	VVL	VVL	VVL	VVL
$\Delta\omega2$	N	VVL	VVL	VVL	VVL	VVL	VVL	VVL	VVL	VVL	VVL	VVL	VVL	VVL
$\Delta\omega3$	N	VVL	VVL	VL	VL	VVL	VVL	VVL	VVL	VL	VL	VVL	VVL	VVL
$\Delta\omega4$	N	VVL	VVL	VVL	VVL	VVL	VVL	VVL	VVL	VVL	VVL	VVL	VVL	VVL
$\Delta\omega5$	N	VVL	VL	VL	VL	VVL	VVL	VL	VL	VL	VVL	VL	VVL	VL
$\Delta\omega6$	N	VL	VL	VL	VVL	VVL	VL	VL	VVL	VVL	VL	VVL	VVL	VVL
$\Delta\omega7$	N	VL	VL	VL	VL	VL	VL	VL	VL	VVL	VVL	VVL	VVL	VVL
$\Delta\omega8$	N	VVL	L	VL	VVL	VL	L	VL	VVL	L	VL	VVL	VL	L
D=0.4														
$\Delta\omega1$	N	VVL	VVL	VVL	VVL	VVL	VVL	VVL	VVL	VVL	VVL	VVL	VVL	VVL
$\Delta\omega2$	N	VVL	VVL	VL	VL	VL	VL	VVL	VVL	VVL	VVL	VVL	VL	VL
$\Delta\omega3$	N	VVL	VL	VL	VL	VL	VVL	VVL	VL	VL	VL	VL	VVL	VVL
$\Delta\omega4$	N	VL	VL	VL	VL	VL	VL	VL	VL	VL	VL	VL	VL	VL
$\Delta\omega5$	N	VVL	L	L	L	VVL	VVL	L	L	L	VVL	VVL	L	L
$\Delta\omega6$	N	L	LM	LM	VL	VL	L	LM	VL	VVL	L	L	VL	VVL
$\Delta\omega7$	N	LM	M	M	LM	L	L	L	L	VL	VL	VL	VVL	VVL
$\Delta\omega8$	N	VL	M	LM	VVL	LM	M	VL	VL	M	LM	VVL	L	M
D=0.6														
$\Delta\omega1$	N	VVL	VVL	VVL	VVL	VL	VL	VL	VL	VVL	VVL	VVL	VVL	VVL
$\Delta\omega2$	N	VVL	VL	VL	L	VL	VL	VL	VVL	VVL	VVL	VL	VL	L
$\Delta\omega3$	N	VVL	L	LM	LM	L	VVL	VVL	VL	LM	LM	L	VL	VVL
$\Delta\omega4$	N	L	L	L	L	L	L	L	L	L	L	L	L	L
$\Delta\omega5$	N	VL	M	MH	LM	VL	VL	LM	M	LM	VL	VL	LM	M
$\Delta\omega6$	N	M	H	MH	LM	L	MH	MH	L	VL	LM	MH	L	VVL
$\Delta\omega7$	N	H	VVH	VH	H	M	MH	MH	LM	L	L	L	VL	VVL
$\Delta\omega8$	N	LM	VVH	MH	VL	MH	VH	LM	L	VH	H	VL	M	VVH

Table 4 Rules for fuzzy system of out-of-plane curved beam damaged cases (second stage)

Damaged at element No.	0	1	2	3	4	5	6	7	8	9	10	11	12	13	14	15
D= 20%																
Δω1	N	VVL	VVL	VVL	VVL	VVL	VVL	VVL	VVL	VVL	VVL	VVL	VVL	VVL	VVL	VVL
Δω2	N	VVL	VVL	VVL	VVL	VVL	VVL	VVL	VVL	VVL	VVL	VVL	VVL	VVL	VVL	VVL
Δω3	N	VVL	VVL	VVL	VVL	VVL	VVL	VVL	VVL	VVL	VVL	VVL	VVL	VVL	VVL	VVL
Δω4	N	VVL	VVL	VVL	VL	VL	VVL	VVL	VVL	VVL	VVL	VL	VL	VVL	VVL	VVL
Δω5	N	VVL	VL	VL	VL	VL	VVL	VVL	VL	VL	VL	VL	VVL	VVL	VL	VL
Δω6	N	VVL	VVL	VVL	VVL	VVL	VVL	VL	VL	VL	VL	VL	VL	VL	VL	VL
Δω7	N	VVL	VVL	VVL	VL	VL	VL	VL	VL	VL	VL	VL	VL	VVL	VVL	VVL
Δω8	N	VVL	VVL	VL	VL	L	L	VL	VL	VVL	VVL	VVL	VVL	VL	VL	L
Δω9	N	VVL	VL	L	VL	VVL	VL	VL	L	VL	VVL	VVL	VL	L	VL	VVL
D= 40%																
Δω1	N	VVL	VVL	VVL	VVL	VVL	VVL	VVL	VVL	VVL	VVL	VVL	VVL	VVL	VVL	VVL
Δω2	N	VVL	VVL	VVL	VVL	VVL	VVL	VVL	VVL	VVL	VVL	VVL	VVL	VVL	VVL	VVL
Δω3	N	VVL	VVL	VVL	VL	VL	VL	VVL	VVL	VVL	VVL	VVL	VVL	VVL	VL	VL
Δω4	N	VVL	VL	VL	VL	VL	VL	VVL	VVL	VVL	VL	VL	VL	VL	VL	VVL
Δω5	N	VL	L	LM	LM	L	VL	VL	L	LM	LM	L	L	L	L	LM
Δω6	N	VVL	VVL	VVL	VL	VL	VL	L	L	L	LM	LM	L	L	LM	LM
Δω7	N	VVL	VVL	VL	L	L	LM	LM	LM	LM	L	L	VL	VL	VVL	VVL
Δω8	N	VVL	VL	L	LM	M	M	LM	L	VL	VVL	VVL	VL	L	LM	M
Δω9	N	VL	LM	M	LM	VL	VL	LM	M	LM	VL	VL	LM	M	LM	VL
D= 40%																
Δω1	N	VVL	VVL	VVL	VVL	VVL	VVL	VVL	VVL	VVL	VVL	VVL	VVL	VVL	VVL	VVL
Δω2	N	VVL	VVL	VVL	VVL	VVL	VVL	VVL	VVL	VVL	VVL	VVL	VVL	VVL	VVL	VVL
Δω3	N	VVL	VVL	VL	VL	VL	VL	VL	VL	VVL	VVL	VVL	VVL	VL	VL	VL
Δω4	N	VL	VL	LM	LM	LM	L	VL	VVL	VL	L	LM	LM	L	VL	VVL
Δω5	N	VL	LM	MH	MH	LM	LM	MH	H	VH	VH	VH	VH	VH	VH	VVH
Δω6	N	VVL	VVL	VL	L	LM	L	L	M	MH	MH	M	L	L	M	H
Δω7	N	VVL	VL	L	M	MH	MH	MH	MH	M	M	LM	L	VL	VL	VVL
Δω8	N	VVL	L	MH	VH	VVH	VH	MH	LM	L	VVL	VVL	L	M	H	VH
Δω9	N	L	VH	VVH	MH	VL	L	H	VVH	MH	VL	L	H	VVH	MH	L

Table 5 Material properties of the in-plane curved beam

Area of cross section (A)	$4.071 \times 10^{-3}\ m^2$
Radius of the arch (R)	2.438 m
Mass density (ρ)	$7855\ {kg}/{m^3}$
Subtended angle (θ)	97°
Modules of Elasticity (E)	206.8 GPa
Modules of Rigidity (G)	77.9 GPa
Moment of inertia (I)	$6.456 \times 10^{-6} m^4$

Table 6 Material properties of the out-of- plane curved beam

Area of cross section (A)	$9.292 \times 10^{-3}\ m^2$
Length (L)	10.16 m
Mass density (ρ)	$7855\ kg/m^3$
Subtended angle (θ)	89°
Modules of Elasticity (E)	200 GPa
Modules of Rigidity (G)	77.2 GPa
Moment of inertia (Ix)	$1.134 \times 10^{-4} m^4$
Moment of inertia (Iy)	$3.886 \times 10^{-5} m^4$
Warping moment of inertia ($I\omega$)	$5.559 \times 10^{-7} m^6$
Venant constant (K_T)	$5.386 \times 10^{-7} m^4$

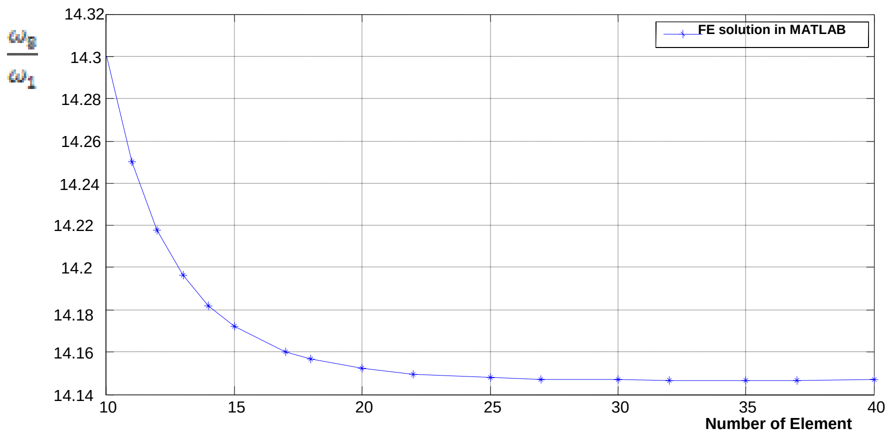

Fig.11. Convergence test for in-plane curved beam

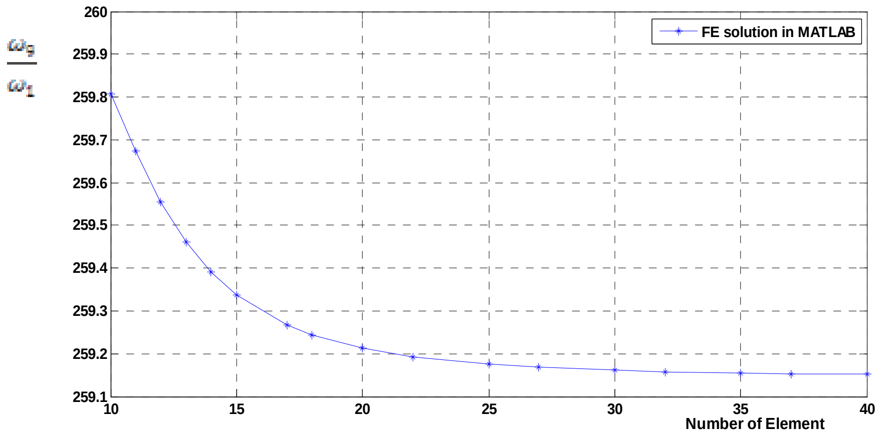

Fig.12. Convergence test for out-of-plane curved beam

Table 7 Comparisons of modal frequencies for in-plane curved

Mode No.	Natural Frequency(Hz)		Error (%)
	[Ki. Young et al] Results[17]	Present Numerical Results	
1	63.18	63.22	0.0633
2	148.21	148.38	0.1147
3	286.05	286.19	0.0489

Table 8 First natural frequencies for the simply supported out-of- plane curved beam

Subtended Angle (degree)	Natural Frequency (rad/sec)			Error (%)
	Analytical Results[17]	Numerical Results[17]	Present Numerical Results	
0	53.3000	53.3000	53.266	0.06379
10	31.8648	31.8669	31.863	0.0056
20	19.9616	19.9614	19.9592	0.01202
30	13.9944	13.9931	13.9915	0.0207
40	10.5386	10.5372	10.5343	0.0408
50	8.2946	8.2888	8.28753	0.08523
60	6.7121	6.7012	6.70043	0.1739
70	5.5270	5.5090	5.50836	0.33725
80	4.5991	4.5707	4.57020	0.62838
90	3.8479	3.8048	3.87485	0.70038

Table 9 Accuracy for in and out-of-plane curved beam (second stage)

Damage Extent (D)	Accuracy (%)			
	In-plane		Out-of-plane	
	Centroid	Mom	Centroid	Mom
SLD	71.01	99.40	88.8	99.27
MOD	99.42	99.52	99.34	99.47
SVD	100	99.33	99.74	99,15

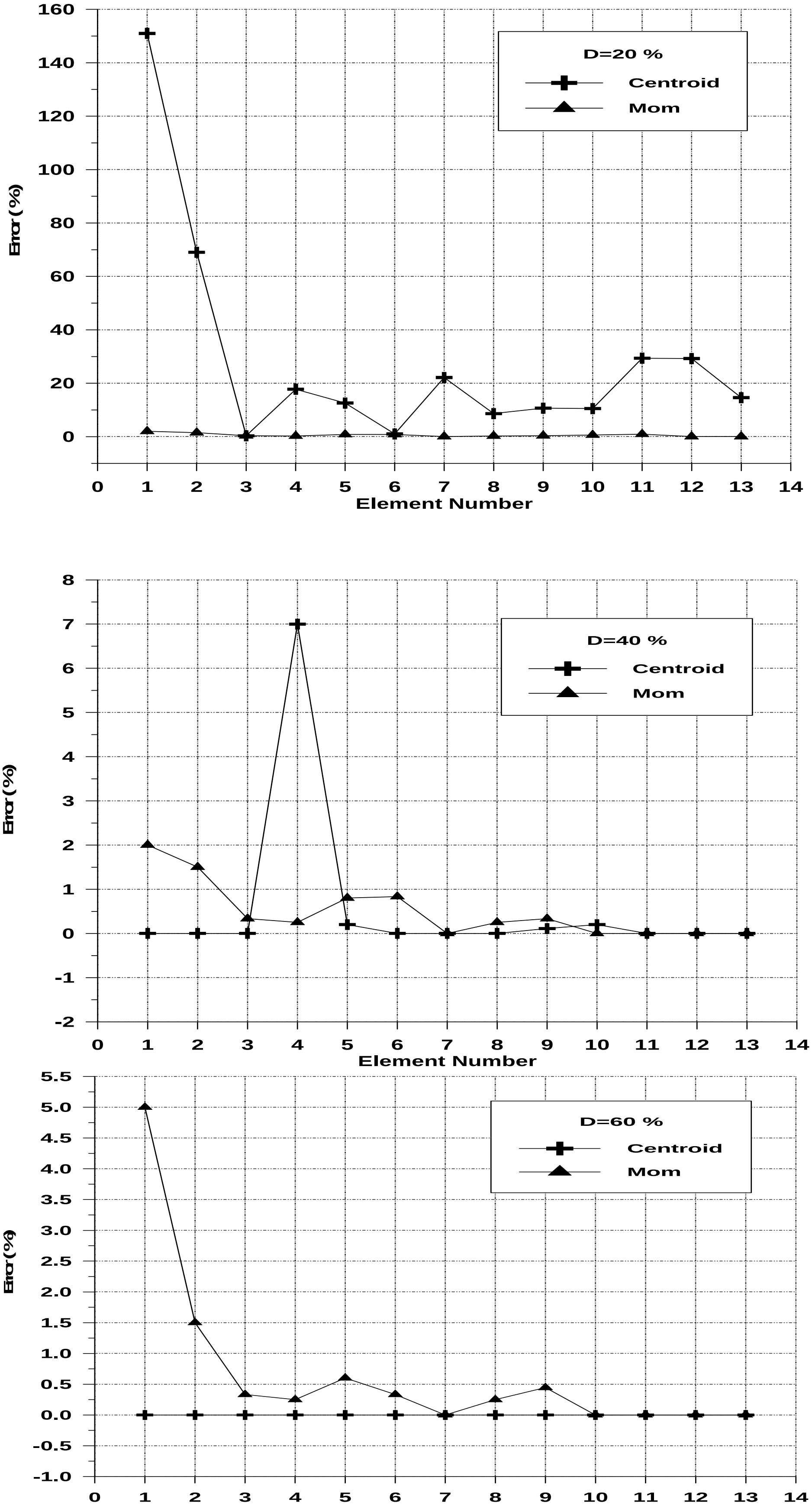

Fig.13. Error between proposed and predict damage at each element for in-plane curved beam

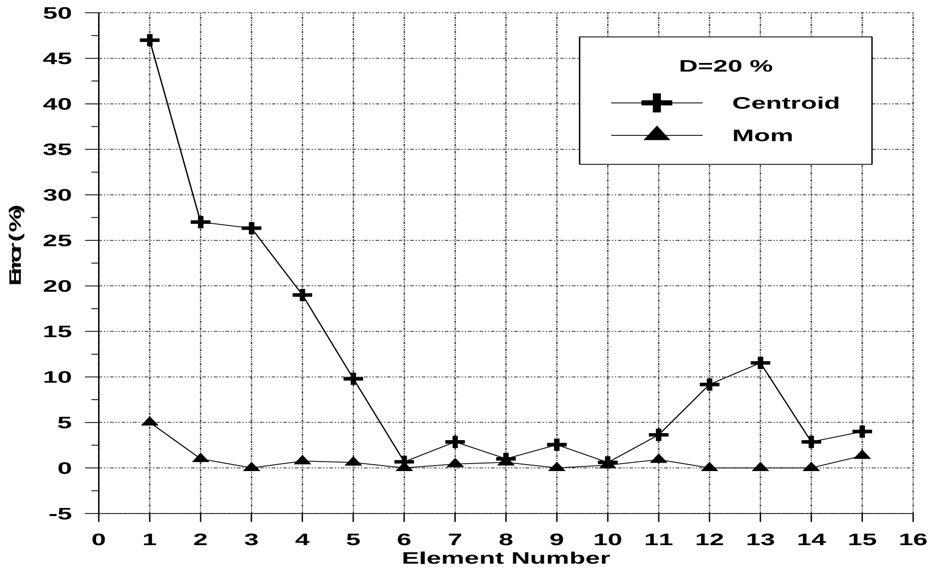

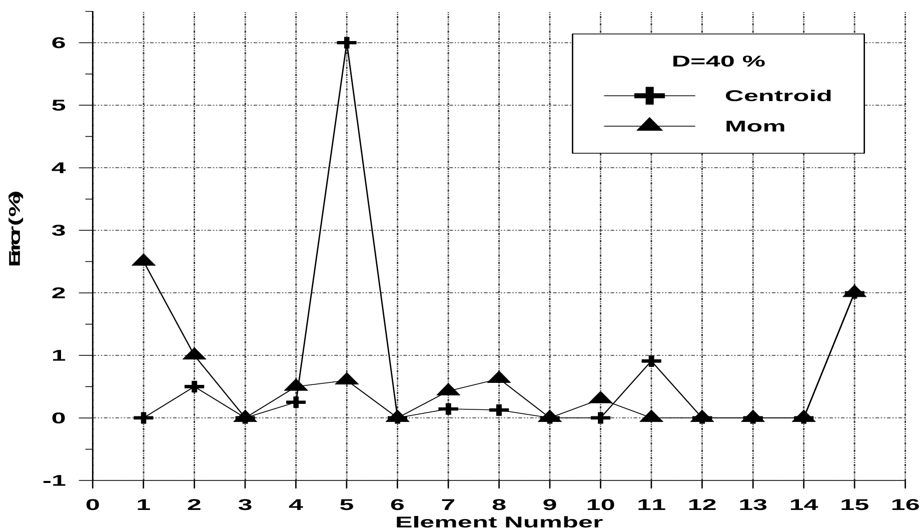

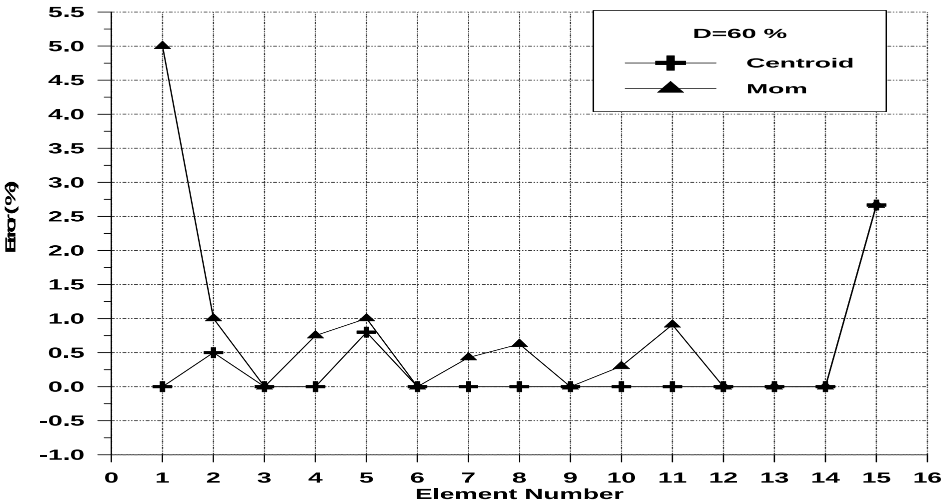

Fig.14. Error between proposed and predict damage at each element for out-of-plane curved beam

IMPLEMENTATION OF ROOT FINDING ALGORITHM OF MINIMUM PHASE FILTER USING VHDL

Zainab Noori Ghanim **Buthaina Mosa Omran**

Malathe Salah Al-Deen

University of Baghdad College of Engineering Electronics & Communications Department

ABSTRACT

Root-finding is an oldest classical problem, which is still an important research topic, due to its impact on computational algebra and geometry. In communications systems, when the impulse response of the channel is minimum phase the state of equalization algorithm is reduced and the spectral efficiency will improved. To make the channel impulse response minimum phase the prefilter which is called minimum phase filter is used, the adaptation of the minimum phase filter need root finding algorithm. In this paper, the VHDL implementation of the root finding algorithm introduced by Clark and Hau is introduced.

VHDL program is used in the work, to find the roots of two channels and make them minimum phase, the obtained output results are similar in accuracy to the past work results, which is built by using MATLAB program. Using VHDL is necessary in FPGAs for building hardware of the root finding algorithm in lower cost and time. MATLAB program is used only for displaying the input and output discrete signals of tested channels.

الخلاصة

ايجاد الجذور هي مسالة قديمة وتبقى محور بحثي مهم . ان في انظمة الاتصالات عندما تكون عينات الاستجابة للقناة ذات طور اصغر فانه يختصر عمل المعادل ويحسن كفائته . ان مرشحا يستعمل لجعل عينات الاستجابة للقناة ذات طور اصغر ، يسمى بالمرشح ذو الطور الاصغر. عملية تحديث المرشح تحتاج طريقة خاصة لايجاد الجذور .

في هذا البحث فان VHDL تم استعماله لايجاد هذه الجذور باستعمال طريقة Clark and Hau . برنامج VHDL تم استعماله لايجاد جذور قناتين و تحويلهما الى قناتين ذاتي طور اصغر و كانت النتائج مشابهة في دقتها و تحقيقها الغرض المطلوب لنتائج عمل سابق باستخدام برنامج MATLAB . استخدامVHDL هو ضروري في FPGA لبناء دائرة الكترونية لايجاد الجذور بكلفة و وقت اقل. لقد تم استخدام برنامج MATLAB فقط لغرض عرض عينات الاستجابة للقناتين قبل تحويلهما الى طور اصغر و بعد التحويل.

1. Introduction

The minimum-phase and the all-pass filters have over the years attracted much attention due to their broad applicability in signal processing. One area where the minimum-phase filter is widely used is in digital communications over multipath channels where higher-order modulation schemes are employed. In such scenarios the optimal symbol-by-symbol or sequence detector will often require a very high complexity, due to its exponential growth in complexity as a function of the filter length. Furthermore, in multi user detection the complexity grows further, since the number of users will also influence the complexity exponentially. Thus, suboptimal schemes, such as delayed decision feedback or reduced-state sequence estimation will often be applied in such systems instead. However, in order to ensure acceptable performance of these schemes, both the minimum-phase filter and the associated all pass filter are usually needed, since the minimum-phase filter provides the highest possible energy concentration in the beginning of the filter impulse response.[1].

For any suboptimum trellis based equalizer, a discrete time minimum-phase overall impulse response is essential for high performance. In general, this necessitates the introduction of a discrete time prefilter in front of the equalizer, which changes the channel impulse response into its minimum phase equivalent [2]. The, the shape of the impulse response of the channel is very important in the detection process. The first sample of sampled impulse response of the channel must be relatively large. The effect of adaptive linear filter on the channel is such that the resultant response of the channel and filter becomes minimum phase with essence that the energy of the pulse is concentrated towards the front portion of the pulse [3]. The adjustment of the linear filter is the sum of the time taken for the algorithm to find all (or some) of the roots outside the unit circle and the time required to form the filter [3].

In the cases where the linear phase property is not strictly required, much lower time delay can be achieved with the use of minimum phase (MP) filters that satisfy the same amplitude specifications. Having designed the high-order LP filter it is necessary to find its Z-plane roots, and fold all zeros that lie outside the unit circle to their reciprocal radius position [4].

Finding the root of a function is arguably the oldest and the most important problem in numerical mathematics. An interesting situation occurs when we do not know this function and can only observe the values of it with some error. This problem has numerous applications in science and engineering. The problem becomes very complicated when the true relationship is highly nonlinear and the measurements are extremely noisy. Some other applications of stochastic root finding include the quantile estimation problem in bio-assay experiments, quality and reliability improvement, sensitivity experiments and adaptive control and signal processing. [5]

Often it will not be possible to solve nonlinear equation root-finding problems analytically. When this occurs we turn to numerical methods to approximate the solution. The methods employed are usually *iterative*. Generally speaking, algorithms for solving problems numerically can be divided into two main groups: *direct methods* and *iterative methods*. Direct methods are those which can be completed in a predetermined finite number of steps. Iterative methods are methods which converge to the solution over time. These algorithms run until some convergence criterion is met. When choosing which method to use one important consideration is how quickly the algorithm converges to the solution or the method's *convergence rate*.[6].

In this paper the root finding algorithm introduced by Clark and Hau [7] is considered and implemented using VHDL program. FPGA is on the verge of revolutionizing digital signal processing and VHDL program help us to build the components of the FPGAs. Many front-end digital signal processing algorithms are now most often replaced by FPGA. This allows users to by pass the hardware design engineer leading to a significant reduction in development time and cost [8]. Two wireless channels are tested, which they have non-minimum phase response and have roots outside the unit circle. After applying the root finding algorithm these roots are replaced by their complex conjugate and the channels become minimum-phase channels.

2. MINIMUM PHASE FILTER

The block diagram of the system with minimum phase filter is shown in fig. (1). [2] Consider the z-transform of the 'sampled impulse response' of the channel [9]:

$$Y(z) = y_0 + y_1 z^{-1} + \ldots\ldots\ldots\ldots + y_g z^{-g} \quad (1)$$

Suppose now that:

$$Y(z) = Y_1(z)\, Y_2(z) \quad (2)$$

where

$$Y_1(z) = \eta\, (1 + \alpha_1 z^{-1})\, (1 + \alpha_2 z^{-1}) \ldots\ldots\ldots\ldots (1 + \alpha_{g-m} z^{-1}) \quad (3)$$

and

$$Y_2(z) = z^{-m}\, (1 + \beta_1 z)\, (1 + \beta_2 z) \ldots\ldots\ldots\ldots (1 + \beta_m z) \quad (4)$$

It is assume here that no roots (zeros) of Y(z) lie exactly on the unit circle in the z-plane. Also $|\alpha_i| < 1$ and $|\beta_i| < 1$, where α_i is the negative of a root Y(z), β_i is the negative of the reciprocal of a root of Y(z), and η is the appropriate complex value needed to satisfy equation (2), (3) and (4). $|\alpha_i|$ and $|\beta_i|$ are absolute values of α_i and β_i respectively. In applications where Y(z) has one or more roots on the unit circle, these are taken to be roots of $Y_1(z)$, such that in each case $|\alpha_i| = 1$.

The adaptive linear filter is always confined to be an all pass filter and, in its ideal form, adjust the sample impulse response of the channel and filter to be minimum phase such that in the z-transform of the resultant sampled impulse response, all the roots (zeros) lie inside the unit circle in the z-plane [3].

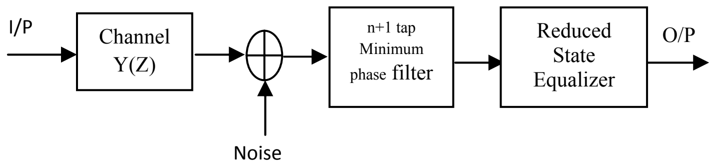

Fig. (1): Block Diagram of the System with Minimum Phase Filter

The adaptive linear transversal filter has n+1 taps. It will, for convenience, be assumed here that the filter is adjusted to its ideal form. The z-transform of the sampled impulse response of the filter is now approximately [3]:

$$M(z) = z^{-n} Y_2^{-1}(z) Y_3(z) \quad (5)$$

where

$$Y_3(z) = (1 + \beta_1^* z^{-1})(1 + \beta_2^* z^{-1}) \ldots\ldots\ldots\ldots\ldots\ldots (1 + \beta_m^* z^{-1}) \quad (6)$$

and β_i^* is the complex conjugate of β_i. Thus, the z-transform of the channel and linear filter is approximately [3]:

$$F(z) = Y(z)M(z)$$

$$= z^{-n}Y_1(z)Y_3(z) \qquad (7)$$

Clearly, all roots of F(z) lie inside the unit circle in the z-plane, which means that the channel and the linear filter together have a response that is minimum phase. The roots of $Y_3(z)$ are the complex conjugate of the reciprocal of the roots of $Y_2(z)$, so that the linear filter replaces all roots of Y(z) that lie outside the unit circle by the complex conjugate of their reciprocals, leaving the remaining roots unchanged. Since the receiver is assumed to know Y(z), it can in principle evaluate M(z) and hence F(z). This involves the determination of the roots of Y(z) that lie outside the unit circle, with no restriction in time or complexity, which would achieved by any conventional root finding algorithm[3].

Clark and Hau introduced an algorithm to determine the wanted roots of Y(z) and at the same time evaluate M(z) and F(z) [7]. The algorithm is discussed in the next section.

3.Root finding algorithm [3, 7, 9]

- First the receiver holds in store the sequence Y and an estimate λ_i of the quantity β_1. The first estimate of β_1 at the start of the process is one of a number of different starting points. The nine starting points given in Table (A1) are having been found to be the optimal starting points.
  Having determined λ_i the receiver appropriately adjusts the one tap feedback transversal filter shown in fig. (2) with z-transform:

$$A_i(z) = (1 + \lambda_i z)^{-1} \qquad (8)$$

- The stored sequence Y is now reversed in order, so that it starts with the component y_g and it is fed through the feedback transversal filter. The sequence Y passing though the filter in reverse order, is taken to be moving backwards in time starting with the component y_0 at time t=0. The delay of one sampling interval T in the feedback filter now becomes an advance of T with z-transform z. Thus, the effective z-transform of the feedback filter becomes $A_i(z)$ and the output from the filter is the sequence of the $\{e'_{i,h}\}$, only the g+1 components of this sequence are in fact generated. An improved estimate of β_1 is now given by:

$$\beta_1 \cong \lambda_i + \frac{e'_{i,0}}{\varepsilon_i} \qquad (9)$$

where

$$\varepsilon_i = e'_{i,1} - e'_{i,2}\lambda_i + e'_{i,3}\lambda_i^2 ....e'_{i,g}(-\lambda)^{g-1} \qquad (10)$$

This means that if c is a positive constant in the range of 0 to 1, then

$$\lambda_{i+1} = \lambda_i + c\frac{e'_{i,0}}{\varepsilon_i} \qquad (11)$$

This gives a new tap feedback transversal filter, with λ_i replace by λ_{i+1}. The effective z-transform of this filter, when operating on the sequence Y in reverse order is:

$$A_{i+1}(z) = (1 + \lambda_{i+1} z)^{-1} \qquad (12)$$

and the coefficients of z^{-h} in $Y(z)A_{i+1}(z)$ is $e'_{i+1,h}$. The iterative process continues in this manner until the term $e'_{i,0}/\varepsilon_i$ in equation (11) satisfies:

$$\left|\frac{e'_{i,0}}{\varepsilon_i}\right|^2 < d \qquad (13)$$

where d is an appropriate small positive real constant or else until either i=40 or $|\lambda_i| < 1$ and in each case the process is terminated. When equation (13) is satisfied the iterative process is taken to have converged. Let the value of i at convergence be k so that:

$$\lambda_k \approx \beta_1 \qquad (14)$$

β_1 is the negative of the reciprocal of the first root of Y(z) to be processed by the system and of course $|\beta_1| < 1$. Since the filter with z-transform is not limited to zero and negative power of z. At the end of iteration process, when i =k, the z-transform of the filter is:

$$A_k(z) = (1+\beta_1 z)^{-1} \qquad (15)$$

- The receiver next appropriately adjusts the two-tap feedforward transversal filter shown in fig. (3), which has the z-transform:

$$B_k(z) = 1 + \lambda_k^* z^{-1} \qquad (16)$$

The sequence of the $\{e'_{i,k}\}$ for h=0, 1,…..g is now fed through this filter in the correct order. This gives the output sequence (g+2) components with the z-transform:

$$f_{1,-1} + f_{1,0}z^{-1} + ... + f_{1,g}z^{-g-1} \qquad (17)$$

Which is approximately equal to $Y(z)A_k(z)B_k(z)$ and where $f_{1,-1} = 0$. The resultant effect on the sequence Y of the two filters giving the sequence of the $\{f_{1,h}\}$ approximately to that of a single filter with Z-transform:

$$C_1(z) = A_k(z)B_k(z) \approx (1+\beta_1 z)^{-1}(1+\beta_1^* z^{-1}) \qquad (18)$$

- The output sequence of $\{f_{1,h}\}$ is advanced by one place (sampling interval) and the first component $f_{1,-1}$ discarded to give the sequence F_1 with z-transform:

$$F_1 = f_{1,0} + f_{1,1}z^{-1} + ... + f_{1,g}z^{-g} \approx zC_1(z)Y(z) \qquad (19)$$

For practical purposes the linear factor $(1+\beta_1 z)$ is replaced in F(z) by the linear factor $(1+\beta_1^* z^{-1})$. Thus, the root $(-1/\beta_1)$ of Y(z) is replaced by the root $(-\beta_1^*)$, which is the complex conjugate of its reciprocal and lies inside the unit circle. $F_1(z)$ contains, in addition an advance of one sampling interval. The sequence F_1 (with z-transform $F_1(z)$) is an estimate of the sampled impulse response of the channel and adaptively linear transversal filter, when the z-transform of the latter is $zC_1(z)$. The iterative process is repeated with Y replaced by F_1 for the tracking of moor roots.

- The whole procedure is now repeated, but using $F_1(z)$ in place of Y(z). At the end of the iterative process $\lambda_k \approx \beta_2$ and the value of λ_k and $F_1(z)$ determines $F_2(z)$ which is used in place of $F_1(z)$ for processing β_3.

- The system continues in this way until, on the h^{th} repetition of the whole procedure, no roots of $F_h(z)$ outside the unit circle are found, starting from any of the nine possible values of λ_i. In the case where, from each starting point, $|\lambda_i| > 1$ for some value of i, or i reaches 40, it will be assumed that h=m. This being so, all the roots of Y(z) that lie outside the unit circle are replaced by the complex conjugate of their reciprocals, in the z-transform of the channel and adaptive filter.

The estimate of the sampled impulse response of the channel and the adaptive filter that are employed by the detector is the sequence F_m with z-transform:

$$F_m(z) = f_{m,0} + f_{m,1}z^{-1} + ... + f_{m,g}z^{-g}$$

$$\approx zF(z) \approx Y_1(z)Y_3(z) \qquad (20)$$

Table (1): The Nine Possible Starting Points

Root No.	Root Value
No.1	0.01
No.2	0.909
No.3	-j0.909
No.4	j0.909
No.5	-0.909
No.6	0.643-j0.643
No.7	0.643+j0.643
No.8	-0.643-j0.643
No.9	-0.643+j0.643

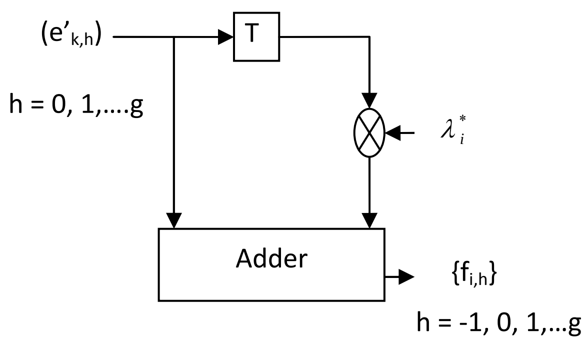

Fig. (2): One-Tap Feedback Transversal Filter

4. Design of Finding Roots in Minimum Phase

VHDL program provides language constructs for parametrizing and customizing designs, and for definition and usage of design libraries. These constructs enable a designer to generate a functional design independent of the specific technology and customize this generic design at a later stage. Specifically, library, use clause, package, and configuration declarations of VHDL are used for grouping or categorizing various components into design libraries and for customizing designs to use components in these libraries [10, 11].

The design is processed by using VHDL program. The main finding roots part of minimum phase component is shown in fig.(4).

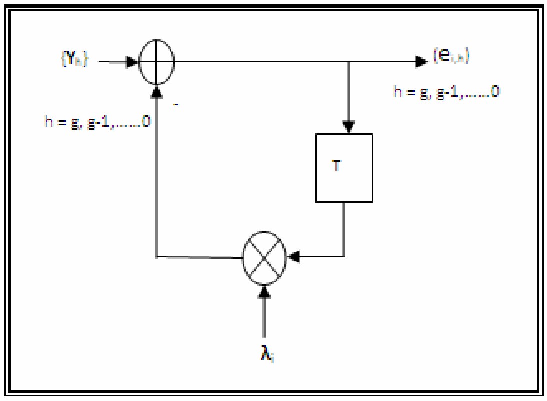

Fig. (3):Two-Tap Feedforward Transversal Filter.

This component reads the channel impulses from a text file (input data text file) and converts the complex numbers of channel impulses to binary values by specified procedure. This main level gives binary values of channel to the second level and receives edited channel impulses from the second level to be the output of this component. The edited channel impulses are converted from binary values to complex numbers and written in a text file (output data text file).

The second level has three components as shown in fig.(5). These components are:

A. First Part Finding Roots component :

The internal structure of this component is shown in fig.(6) and its algorithm as follows :

- Take the channel impulses (Y) from the first level with clock to start new operation with each clock.
- Read lamda (λ_i) initial value in each time from look up table, which has nine initial values for lamda.
- The Y and λ_i are used as inputs to three internal components in the first part component, see fig.(6). The internal components compute error matrix ($e'_{i,h}$) , epsilon (ε_i) and new lamda (λ_{i+1}) as output data.
- Check if $\left|\frac{e'_{i,0}}{\varepsilon_i}\right|^2 < 10^{-10}$ .If the condition is true the first part is stopped and gives output data (error matrix, lamda value and clock) to other second level components (Find Conjugate and Two Tap) to begin its work. But if the condition is false the first part repeats the operation of computing new error matrix, epsilon and new lamda, where new lamda is used as input with channel impulses to the three components in new iteration. The condition is checked in each iteration. This continues iteration process is stopped if the absolute value of lamda is more than one or the number of iterations be fourty, where new initial value of lamda is taken in this case to repeat the same process by using the second value of look up table of initial values until the first condition will be true or ending the look up table without finding any roots.
- Give restart signal to the three components at each new iteration.

The three internal components of the First Part component are:

1. One Tap: this component applied eq.(8) in its work. Channel impulses Y,

λ_i, clock and restart are the inputs for this component. Error matrix $e'_{i,h}$ and clock to the second component are the output of it. Its internal structure is shown in fig.(7) and its algorithm as follows:

- Start work when clock signal, Y and λ_i are received.
- Subtract feedback value from each value of Y in each time to obtain error value related to this value of Y until the error matrix is obtained with the same size of Y. Subtraction component is used for this purpose.
- Each value of error will be delayed by D_latch component.
- The old value of error is multiplied with λ_i by a multiplier component to obtain feed back value.
- The error matrix and a clock signal will be the output of One Tap component and are the inputs to the next component (Epsilon Computing component).

2. Epsilon Computing: this component finds the value of epsilon ε_i as in eq.(10). The component internal structure is shown in fig. (8). Its algorithm is as follows:

- Start new work when clock signal and new error matrix are received from One Tap.
- Find the value of powered lamda by computing lamda to the power **i** as in eq. (10) by a specified procedure.

- Multiply powered lamda with each value of error in error matrix (0-9) by a multiplier component.
- Add the result value of multiplier to the recent value of epsilon to obtain a new value of epsilon by using an adder component.
- The previous steps are repeated for each value of error to find the final value of epsilon to be an output of Epsilon Computing component.
- Clock signal and ε_i are given to the next component (Lamda Computing).

3. Lamda Computing: this component finds the new value of lamda λ_{i+1}, where the new value of lamda will be an old value in the next iteration as in eq.(11). Its internal structure is shown in fig.(9) and its algorithm is as follows :

- Divide the first value of error matrix (the output of One Tap) by the epsilon (output of Epsilon Computing) by using a divider component.
- The divider output will be multiplied with the constant c as in eq.(11). A multiplier component is used to find the multiplication result.
- The output of multiplier will be added to the recent value of lamda by an adder component to find new lamda. New lamda λ_{i+1} will be the output of Lamda Computing component.

B. Find Conjugate component:

This component is designed to find the conjugate value of any complex number and it's used here to find the conjugate of lamda, which realizes the previous condition. The output conjugate value will be the input to the Two Tap component.

C. Two Tap component:

This component has three inputs, which are error matrix, conjugate of lamda λ^*_i and clock and has one output. The edited channel impulses matrix (F) is the output of this component. Eq.(16) explains the work of this component. The internal structure of this component is shown in fig. (10) its algorithm is as follows:

- Multiply the lamda conjugate with the first value of error matrix by a multiplier component.
- Add the result of multiplication to the next value of error matrix by an adder component to find the first value of edited channel impulses matrix.
- Repeat the previous steps until the whole matrix of channel is found by taking the whole error matrix.
- The Two Tap begins new work with each received clock

The main finding roots component repeat the work ten times as minimum by taking Y matrix from the text value at first time, but when the root is found and Two Tap component works as a result, F the output of two tap will be the input in the next time instead of Y from file.

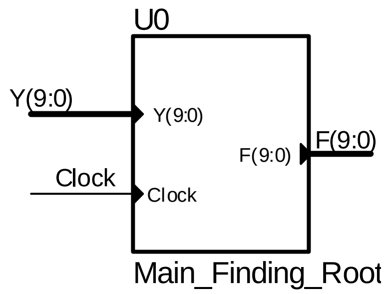

Fig.(4): Main Finding Root component architecture

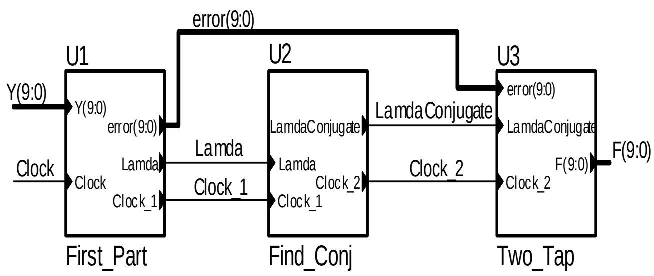

Fig.(5): Internal structure of Main Finding Root component

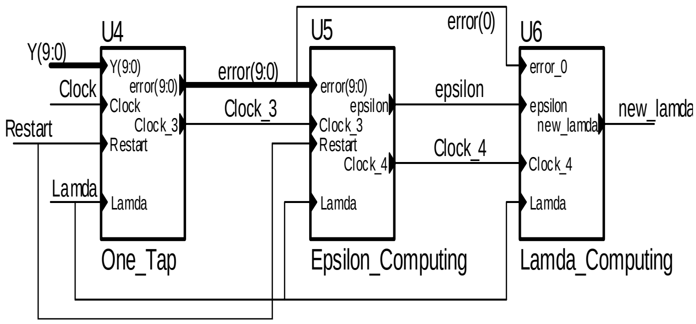

Fig.(6): Internal structure of First Part component

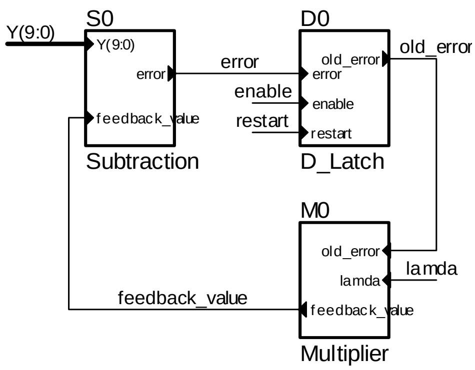

Fig.(7): Internal structure of One Tap.

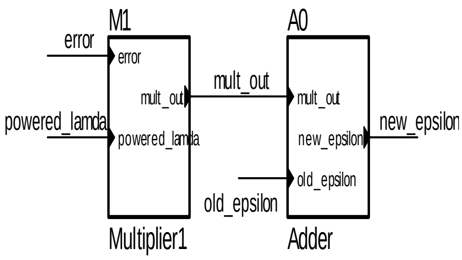

Fig.(8): Internal structure of Epsilon Computing component

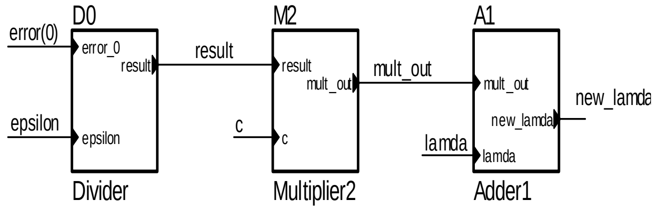

Fig.(9): Internal structure of Lamda Computing component.

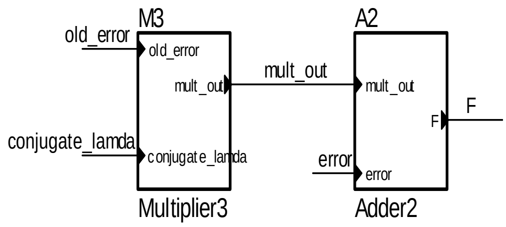

Fig.(10): Internal structure of Two Tap.

5. Results

Two non-minimum phase channels are used in the test, each of them has ten taps. The impulse response of them is shown in figs. (11) and (13). The roots of them are shown in figs. (15) and (17). All roots of the first channel are outside the unit circle, while the second channel has eight roots outside the unit circle and only one root inside the unit circle. The impulse responses of the two channels after using the minimum phase filter are shown in figs. (12) and (14). The proposed VHDL circuit reflects the roots of the two channels from outside the unit circle to inside it as shown in figs. (16) and (18). The input and output impulse response, which are written in input data text file and output data text file are plotted using MATLAB program.

6. Conclusion

The work with VHDL program gives good output signals by reflecting the roots from outside to inside the unit circle. The synchronization among the components is necessary in this work and the VHDL program offers the methods to synchronize the system.

As in any high level language, VHDL allows the definition and usage of functions and procedures. In addition to the important hardware implications of subprograms, these language constructs greatly improve readability and organization of a hardware description.

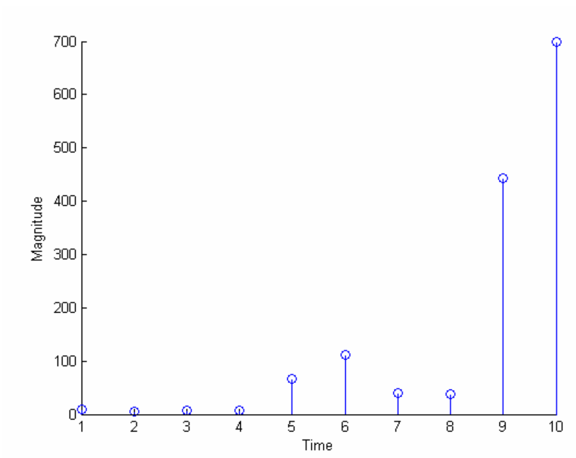

Fig.(11) Impulse response of channel 1

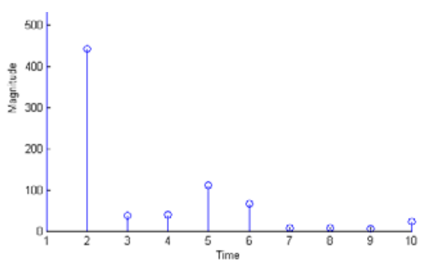

Fig. (12): Impulse response of combined channel 1 and minimum phase filter.

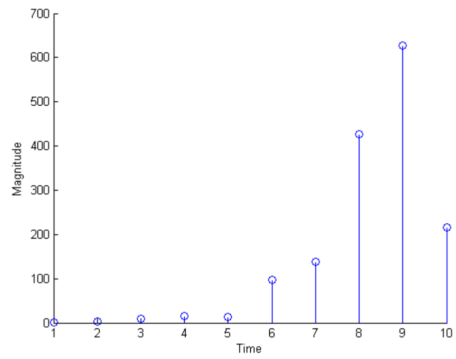

Fig. (13): Impulse response of channel 2

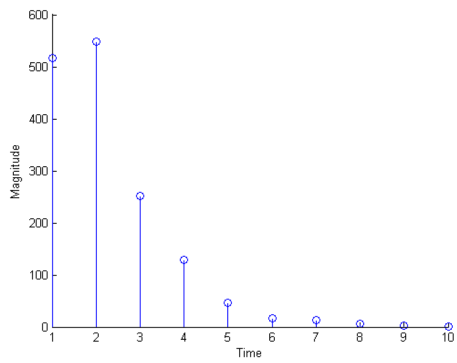

Fig. (14) Impulse response of combined channel 2 and minimum phase filter

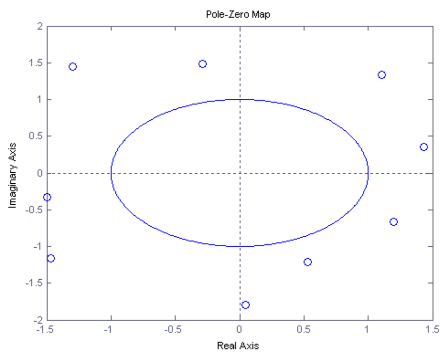

Fig. (15): Roots of channel 1

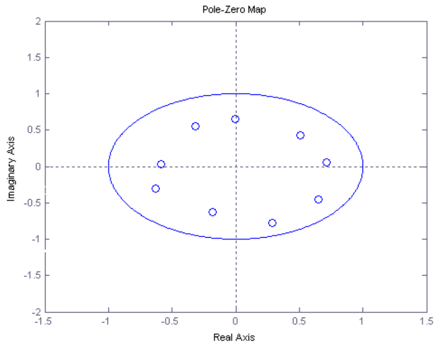

Fig. (16): Roots of channel 1 after minimum phase filter

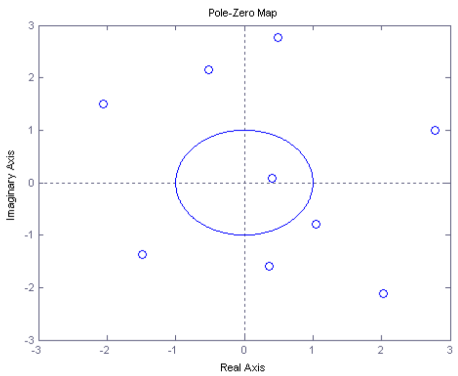

Fig. (17): Roots of channel 2.

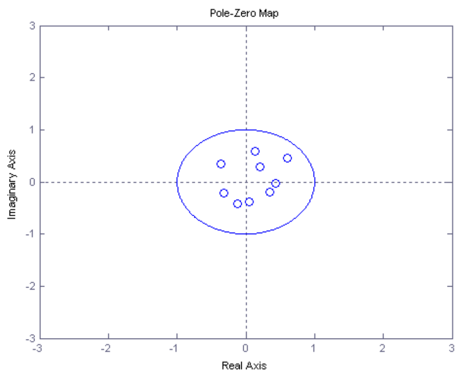

Fig. (18): Roots of channel 2 after minimum phase filter

References:

[1] Morten Hansen, Lars P. B. Christensen, and Ole Winther "**Computing the Minimum-Phase Filter Using the QL-Factorization**", IEEE Transaction on Signal Processing, Vol. 58, No. 6, June 2010.

[2] Wolfgang H. Gerstacker, Frank Obernosterer, Raimund Meyer, and Johannes B. Huber, " **On Prefilter Computation for Reduced-State Equalization**", IEEE Transaction on Wireless Communications, Vol. 1, No. 4, October 2002'

[3] Hau,S.F. **"Adaptive Adjustment of Modern Receiver for HF Radio Links"**, Ph.D. Thesis, Loughborough University of Technology, 1986.

[4] Gordana Jovanovic-Dolecek and Vlatko Dolecek, "**Narrowband Minimum Phase Filter Design Using Sharpened Comb Filter",** ECCTD'01 - European Conference on Circuit Theory and Design, August 28-31, 2001, Espoo, Finland.

[5] V. Roshan Joseph, Yubin Tian nd C. F. Jeff Wu,**" Adaptive Designs For Stochastic Root-Finding",** Statistica Sinica 17(2007), 1549-1565**.**

[6] KAREN A. KOPECKY," **Root-Finding Methods**", Lecture Notes ECO 613/614 FALL 2007.

[7] Clark, A.P and Hau, S.F, **"Adaptive adjustment of receiver for distorted digital signals"**, IEE Proc. 1984,131, pt. F. pp.526-536.

[8] Uwe Meyer-Baese[a], A. Vera[b], A. Meyer-Baese[a], M. Pattichis[b], R. Perry[a], [a]FAMU-FSU, **"Discrete Wavelet Transform FPGA Design using Matlab/simulink",** ECE Dept., 2525 Pottsdamer Street, Tallahassee, FL

USA-32310; [b] University of New Mexico, ECE Dept., Albuquerque, NM 87131, 2006.

[9] Buthaina Mosa Omran, **"Improvement Techniques for Satellite Digital Video Broadcasting Using OFDM",** Ph.D. Thesis, University of Baghdad, 2007.

[10] Zainalabedin Navabi, **"VHDL Analysis and Modeling of Digital Systems",** McGraw-Hill Series in Electrical and Computer Engineering, 1993.

[11]Mark Zwolinski, "**Digital System Design with VHDL**", Prentice Hall, 2000.

List of Abbreviations:

FPGAs : Field Programmable gate arrays.
VHSIC : Very High Speed Integrated Circuit.
VHDL : VHSIC Hardware Description Language.

EXPERIMENTAL STUDY OF AIR FLOW RATE EFFECTS ON HUMIDIFICATION PARAMETERS WITH PREHEATING AND DEHUMIDIFICATION PROCESS CHANGING

Assistant Lecturer Ayad Tareq Mustafa
University of Nahrain, College of Engineering, Mechanical Department

ABSTRACT

This research study experimentally the effect of air flow rate on humidification process parameters. Experimental data are obtained from air conditioning study unit T110D. Results obtained from experimental test, calculations and psychometrics software are discussed. The effect of air flow rate on steam humidification process parameters as a part of air-conditioning processes can be explained according to obtained results. Results of the steam humidification processes (1,2) with and without preheating with 5A and 7.5A shows decreasing in dry bulb temperature, humidity ratio, and heat add to moist air with increasing air flow rate, but humidification load, and total energy of moist air increase with increasing air flow rate in the testing tunnel. The steam humidification process (1) with dehumidifying coil shows increase in dry bulb temperature, humidity ratio, humidification load, and heat add to moist air with increasing air flow rate in the testing tunnel, but the total energy decrease as air flow rate increase. These obtained results can be beneficial for controlling comfort air-conditioning processes in buildings.

الخلاصة

هذا البحث يدرس تأثير نسبة جريان الهواء عمليا على معاملات عملية الترطيب. البيانات التجريبية تم الحصول عليها من جهاز وحدة دراسة تكييف الهواء T110D. تم مناقشة نتائج الحسابات والبرنامج الحسابي المصردي. تأثير نسبة جريان الهواء على معاملات عملية الترطيب بالبخار يمكن توضيحها في النتائج المستحصلة كجزء من عمليات تكييف الهواء. نتائج الترطيب بالبخار (2,1) مع/ بدون تسخين ابتدائي 5A و 7.5A اظهرت نقصان في درجة حرارة البصلة الجافّة، نسبة الترطيب، والحرارة المضافة للهواء الرطب بازدياد نسبة جريان الهواء، ولكن حمل الترطيب والطاقة الكلية للهواء الرطب تزداد بازدياد نسبة جريان الهواء في قناة الاختبار. عملية الترطيب بالبخار (1) مع وجود ملف سحب الرطوبة اظهرت زيادة في درجة حرارة البصلة الجافّة، نسبة الترطيب، حمل الترطيب، والحرارة المضافة للهواء الرطب بازدياد نسبة جريان الهواء في قناة الاختبار، ولكن نقصان الطاقة الكلية بازدياد نسبة جريان الهواء. هذه النتائج المستحصلة يمكن الاستفادة منها في نظام سيطرة عمليات تكييف الهواء في الابنية.

Keywords: Humidification process; Air flow rate; Total Energy; Preheating; dehumidifying coil.

INTRODUCTION

The indoor air environment of modern buildings is customarily extremely airtight and highly controlled, though may still exhibit inadequate ventilation. The controlling system must regulates temperature, relative humidity (RH), air flow, and concentration of dusts. The air flow rate in air conditioning system must change due to changing of temperature and relative humidity (RH) between summer and winter.

The humidity parameters contains Humidity ratio (*W*) (alternatively, the moisture content or mixing ratio) of a given moist air sample is defined as the ratio of the mass of water vapor to the mass of dry air contained in the sample: $W = M_w / M_{da}$

The humidity ratio (*W*) is equal to the mole fraction ratio x_w/x_{da} multiplied by the ratio of molecular masses, namely, 18.01528/28.9645= 0.62198: $W = 0.62198 X_w / X_{da}$

Relative humidity (Φ) is the ratio of the mole fraction of water vapor X_w in a given moist air sample to the mole fraction X_{ws} in an air sample saturated at the same temperature and pressure:

$$\Phi = (X_w / X_{ws})_{t,p}$$

Thermodynamic wet-bulb temperature t* is the temperature at which water (liquid or solid), by evaporating into moist air at a given dry-bulb temperature *t* and humidity ratio *W*, can bring air to saturation adiabatically at the same temperature *t** while the total pressure *p* is maintained constant. Dew-point temperature (t_d) is a temperature of saturated moist air at the same pressure and humidity ratio as the given mixture [ASHRAE - 2009].

Humidification processes is the transfer (addition) of water vapor to air**.** This process is usually accomplished by introducing water vapor or by spraying fine droplets of water that evaporate into the circulating air stream. Moisture can be added to air by injecting steam, i.e. water which is already in vapor form and does not require the addition of latent heat. Under these conditions, the air will not be cooled and will stay at about the same dry bulb temperature. The steam will be at 100°C when released to the atmosphere (or may be slightly superheated), and so raises the final temperature of the mixture [A. R. Trott and T. Welch - 2000].

A natural concomitant of dropping the temperature of the air is removing moisture from it. In cooling the air in a low-temperature refrigerated warehouse the dehumidification process form frost on the coil, which is usually an undesirable by product of the temperature-reduction process. In a comfort or industrial air-conditioning application the dehumidification is usually a desirable objective [Stoeker W.F. – 1982].

Humidification processes with air flow, preheating, and a dehumidification effect has been the subject of various previously experimental studies:

S.A. El-Agouz, M. Abugderah (2008), presented an experimental investigation of humidification process by air passing through seawater. The main objective of their work was to determine the humid air behavior through single-stage of heating-humidifying processes. Two cases of different inlet conditions of ambient and heated air cases were studied. The experimental results show that, the vapor content difference and the humidification efficiency of the system is strongly affected by the saline water temperature in the evaporator chamber, headwater difference and the air velocity.

Hongbin Zhao, Pengxiu Yue et al (2009), showed a new humid air turbine cycle that uses low- or medium-temperature solar energy as assistant heat source was proposed for increasing the mass flow rate of humid air. The effects of some parameters such as pressure ratio, turbine inlet temperature, and solar collector efficiency, specific work, and solar energy to electricity efficiency were discussed. Compared with the conventional HAT cycle, because of the increased humid air mass flow rate in the new system, the humidity and the specific work of the new system were increased.

Mikiya Sato, Shingo Fukayo et al (2003),

explained that relative humidity (RH) shows the lowest achievement rate among the various general air quality standards for work environment. It has been mainly contributed by airtight design of modern buildings and occurrence of dry outdoor air in winter.
Furthermore, an ultra-dry air environment of nearly 0% RH is often required in sophisticated industries. In order to assess the adverse health effects of the ultra-dry air environment, using a self-reported questionnaire, they have undertaken a study of over 200 employees of a high-tech device developing laboratory having a room at 2.5% RH (ultra-dry room).

Paraya A., Faud M. B. et al (2000), showed a developed method for measuring the temperature and relative humidity of air prior to and after nasal conditioning and used it to study the effect of treatment with ipratropium bromide on the ability of the nose to condition cold, dry air.

Anton TenWolde, lain S. Walker (2001), focuses in their paper on interior moisture design loads for residences and proposes a procedure to estimate the design indoor humidity for both winter and summer conditions. The interior humidity is a function of moisture release, ventilation, dehumidification, and moisture storage in the materials in the building. If the home is not air conditioned or dehumidified, the weekly or monthly average design indoor humidity can be calculated from design ventilation and moisture release.

Tony Evans (2008), showed the control of humidity in information technology environments is essential to achieving high availability. His paper explains how humidity affects equipment and why humidity control is required.

Mohamed Mahmoud Gouda (2005), showed that the fuzzy ventilation control strategy aims to use the free cooling and dehumidification available due to differences in zone and ambient conditions. This can achieve by changing the proportion of fresh air entering the heating, ventilation and air conditioning (HVAC) system and hence the controlled zone.

The goal of this work is to study experimentally the effect of air flow rate on humidification process parameters; dry bulb temperature, humidity ratio, relative humidity, humidification load, heat added and total energy of the processes.

EXPERIMENTAL WORK

The operating principle of Air conditioning study unit T110D is as follow: a stream of air generated by a centrifugal fan is made to pass through a tunnel via a fluid thread rectifier. As it goes through the tunnel the air undergoes a series of treatments until it reaches a final chamber representing the environment to be conditioned. The air is initially preheated then humidified by means of steam diffusers then cooled by means of R22 evaporator and finally conveyed into the end chamber which enabling to vary the greatest possible quantity of parameter for understanding of climate control, Figure (1) describe the parts of the study unit.

The test procedure of steam humidification processes consists of turning the centrifugal fan on with mass flow rate (1) of steam humidifier, test air velocity inside circular testing tunnel vary from 2.6 m/s to 21 m/s, and test RH & Td after steam humidifier for each velocity. By using manual control valve over the steam boiler, the prior steps be repeated for mass flow rate (2) of humidification steam which is double mass of flow rate (1).

Before each test were the ambient RH & Td entering the testing tunnel, read as well as turn the preheater on for 5A and 7.5A current individually for preheating and steam humidification processes with mass flow rate (1,2) of steam, and finally turning dehumidifying coil (evaporator) on for the process of steam humidification and dehumidifying coil with mass flow rate (1) of steam. Individual steam humidification processes, preheating with steam humidification processes, and steam humidification with dehumidifying coil processes be achieved all in a space consider great enough to prevent mixing between outlet air conditions and inlet air conditions for any test process.

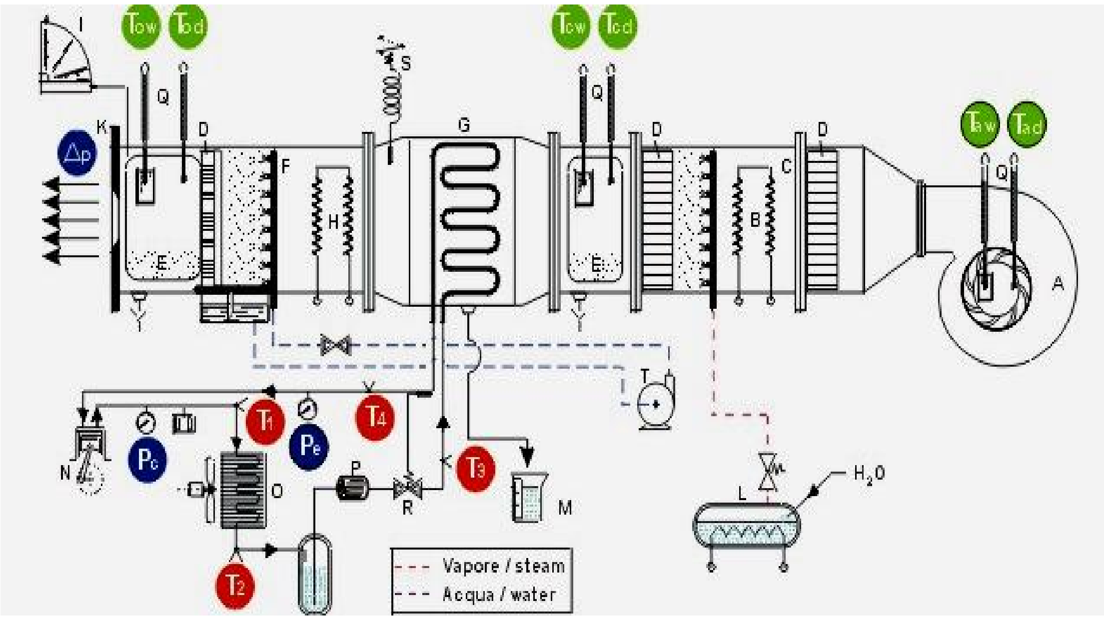

Figure (1): Schematic Diagram of Air-Conditioning Study Unit T110D

Key of drawing Fig. (1):

A. Variable speed centrifugal fan
B. Variable power pre-heater
C. Steam diffuser
D. Fluid thread rectifier
E. Inspection window
F. Water diffuser
G. R22/air evaporator
H. Variable power heater
I. Tilting scale differential micro manometer
K. Calibrated diaphragm
L. Automatic steam boiler
M. Extracted moisture measuring Device
N. Close type compressor
O. Ventilated R22/air condenser
P. Dehydrating filter
Q. Dry and wet bulb psychomotor
R. Isenthalpic thermostatic expansion valve
S. Electronic thermostat
T. Water circulation electro pump

Test Meters

1-Humidity and Temperature Meter:

Specifications

Temperature range: -10 °C to 50 °C

Relative humidity range: 5.0% RH to 98%RH

Accuracy

Temperature: ±1°C

Relative humidity: ±3.5%RH

2-Remote Vane Digital Anemometer:

Specifications

Air flow range: 0.4 m/s to 35 m/s

Temperature: -10 °C to 50 °C

Fan diameter: 70 mm

Accuracy

Air flow range: ±2%

Temperature: ±0.6°C

THEORY

The results obtained from the experimental work were relative humidity and dry bulb temperature with various air velocities are used in calculations, the calculations of humidification parameters are:-

1. Humidity ratio difference between air entering and air leaving the processes (Wo-W_i).

2. The amount of heat added in each process per kilogram of dry air is

$$\textbf{Heat added} = (h_o – h_i) \qquad (1)$$

$$\textbf{OR} \quad \textbf{Heat added} = C_p (T_o – T_i)$$

3. Humidification load which is given by

$$\textbf{Humidification load} = m_{air} (W_o - W_i) \qquad (2)$$

Where: $m_{air}=\rho V A$

ρ: density of air at entering the process
V: velocity of air at entering the process
A: cross suction area of the tunnel ($A=\pi d^2/4$)
d: diameter of tunnel (d = 0.1 m)

4. Total energy for each process could be obtained from the difference between outlet conditions and inlet conditions for individual steam humidification and compound steam humidification processes. At first, the total energy of steam humidification process calculated by the summation of sensible and latent energy through the process from psychrometrics software which equal to air mass flow rate multiplying by enthalpy difference at same process, as well as for steam humidification with preheating processes and steam humidification with dehumidifying coil processes.

The Psychrometrics software by LG air-conditioning system PRODUCT DATA has complete properties of psychrometrics chart of dry and wet bulb temperatures, relative humidity, humidity ratio, specific volume, and enthalpy. The software have ability to get the total properties of moist air from two properties only, and calculate the sensible and latent energy for total process which can drawn on the psychrometrics chart, then the total energy of the process can be achieved. The processes performed at psychrometrics software are; steam humidification process (1), steam humidification process (2), steam humidification process (1) with 5A preheating, steam humidification process (2) with 5A preheating, steam humidification process (1) with 7.5A preheating, steam humidification process (2) with 7.5A preheating, and steam humidification process (1) with dehumidifying coil. The seven processes have ten calculation points for each and the software used seventy times. Figures (2), (3), and (4) show three samples of psychrometric calculations.

RESULTS AND DISCUSSION

Air properties

Figure (5) shows the variation of air dry bulb temperature leaving the humidification process with air flow rate. The results show that when steam humidification (1, 2) decrease, air flow rate increase. Furthermore, steam humidification (1, 2) with 5A and 7.5A preheating decrease when air flow rate increase because of increasing of air velocity and heat loss which leads to a decrease in dry bulb temperature. For steam humidification (1) with dehumidifying coil the dry bulb temperature of air increases with air flow rate because of the increase in heat gain from the moist air itself in the testing tunnel.

Figure (6) shows the variation of relative humidity of air leaving humidification process with air flow rate. The relative humidity of steam humidification (1, 2) with and without 5A and 7.5A preheating decrease with an increase in the air flow rate till a value of (0.071) m^3/s after which the relative humidity increase with air flow rate. The relative humidity of steam humidification (1, 2) with 5A preheating is greater than that with 7.5A preheating because of heating the air then decreases RH. Relative humidity of steam humidification (1) with dehumidifying coil increase with air flow rate till a value of (0.111) m^3/s; after which it decreases with air flow rate because of comparatively fixed humidity ratio with an increase in dry bulb temperature. This is in contrast to the steam humidification (1, 2) with and without preheating because of the difference between heat added and heat removed at humidification process. The steam humidification (1, 2) with and without preheating leads to an increase in the air temperature and decrease in relative humidity for low air flow rate then they increase with air flow rate. The steam humidification with dehumidifying coil cause an increase in relative humidity for low air flow rate then it decreases with air flow rate. Steam humidification (2) with dehumidifying coil could not be performed because the relative humidity reached a value of 100% because of double mass of steam humidification with heat removed.

Humidification load

Figure (7) shows the variation of humidity ratio of air leaving the process with air flow rate. The humidity ratio of steam humidification (1,2) with and without preheating decrease as the air flow rate increases, but steam humidification (1) with dehumidifying coil increase as the air flow rate increases because of increase in the mole fraction ratio of humidity, which is in contrast to steam humidification with preheating.

Figure (8) shows the variation of humidification load with the air flow rate calculated from equation (2). The humidification load of steam carried out with air flow rate shows increase in the ability of carrying steam with increasing the flow rate of air. The negative values of humidification load for dehumidifying coil means a decrease in the humidity ratio of air leaving the process with respect to entering air because of dehumidifying coil use.

Heat added and total energy

Figure (9) shows the variation of heat added by the processes with air flow rate which is calculated from equation (1). The heat added of steam humidification (1,2) with and without preheating decrease as air flow rate increases because of the increase in air velocity while heat exchange decrease as the air flow rate increases from a value of (0.071) m^3/s to (0.165) m^3/s. The heat added at steam humidification (1) and (2) processes become very close after a flow rate of (0.071) m^3/s. Heat added at steam humidification process (1) with dehumidifying coil increase as air flow rate increases. The negative values of heat added are caused by using of dehumidifying coil.

Figure (10) shows the variation of total energy of the processes with air flow rate which is the sum of the sensible energy and the latent energy for each part participate in these processes. The total energy for steam humidification (1,2) without preheating increase slightly with air flow rate , but the total energy for steam humidification (1,2) with preheating increase strongly with air flow rate. This clearly means that the energy of steam with heating increase as air flow rate increases. The total energy of the process with dehumidifying coil decrease slightly as air flow rate increases; because of varying the sensible and latent energy between steam added in humidification process and steam removed in dehumidifying coil with increase in the air flow rate.

Analysis of Experimental Data Error

Error will creep into all experiments; an error in a measurement is defined as the difference between the true value of a quantity and its measured value. Uncertainty analysis method used for total energy results is the statistical bound of error (ΔE). The uncertainty of total energy of the processes is as follow:

Process of steam humidification (1) $\Delta E= \pm 0.1021\%$

Process of steam humidification (2) $\Delta E= \pm 0.1077\%$

Process of steam humidification (1) with preheating 5A $\Delta E= \pm 0.0961\%$

Process of steam humidification (2) with preheating 5A $\Delta E= \pm 0.1017\%$

Process of steam humidification (1) with preheating 7.5 A $\Delta E= \pm$ 0.0.0810%

Process of steam humidification (2) with preheating 7.5 A $\Delta E= \pm 0.0928\%$

Process of steam humidification (1) with dehumidifying coil $\Delta E= \pm 0.0368\%$

CONCLUSIONS

The following conclusions may be drawn from this study:

- The steam humidification process with and without preheating with 5A and 7.5A shows decreasing in dry bulb temperature, humidity ratio, and heat add to moist air with increasing air flow rate, but humidification load, and total energy of moist air increase with increasing air flow rate in the testing tunnel.

- The steam humidification process with dehumidifying coil shows increase in dry bulb temperature, humidity ratio, humidification load, and heat add to moist air with increasing air flow rate in the testing tunnel, but the total energy decrease as air flow rate increase.
- The relative humidity shows a different variation with increasing air flow rate. For low air flow rate, steam humidification process with and without preheating decrease till 0.071 m^3/s then increase for high flow rate; and steam humidification process with dehumidifying coil increase till 0.111 m^3/s then decrease for high flow rate.
- Humidification load, relative humidity, dry bulb temperature, and air velocity are the main parameters for controlling comfort air-conditioning processes in buildings.

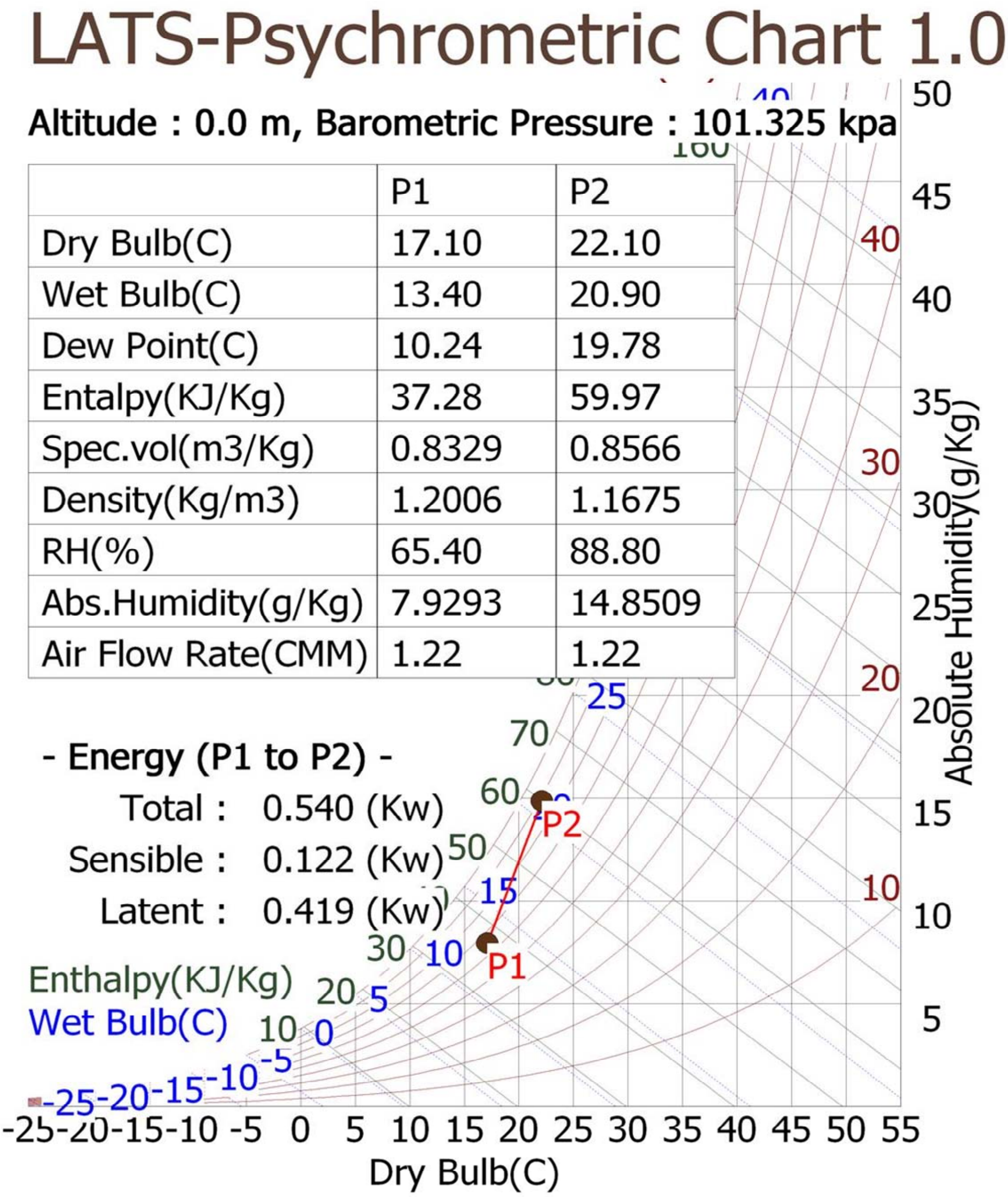

Figure (2): Psychrometric total calculations of steam humidification process (1) for points (1 – 2)

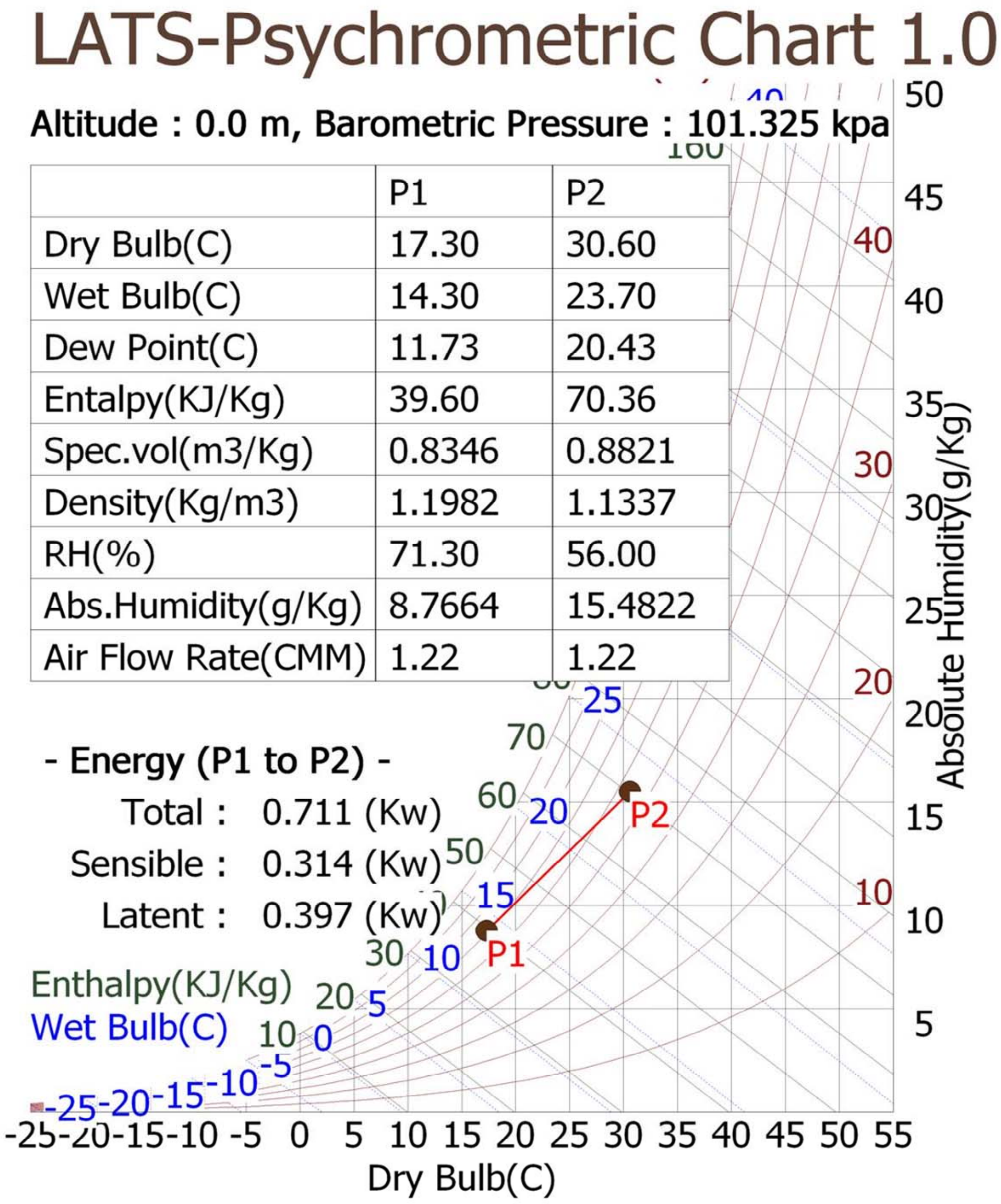

Figure (3): Psychrometric total calculations of steam humidification process (1) with 7.5A preheating for points (1 – 2)

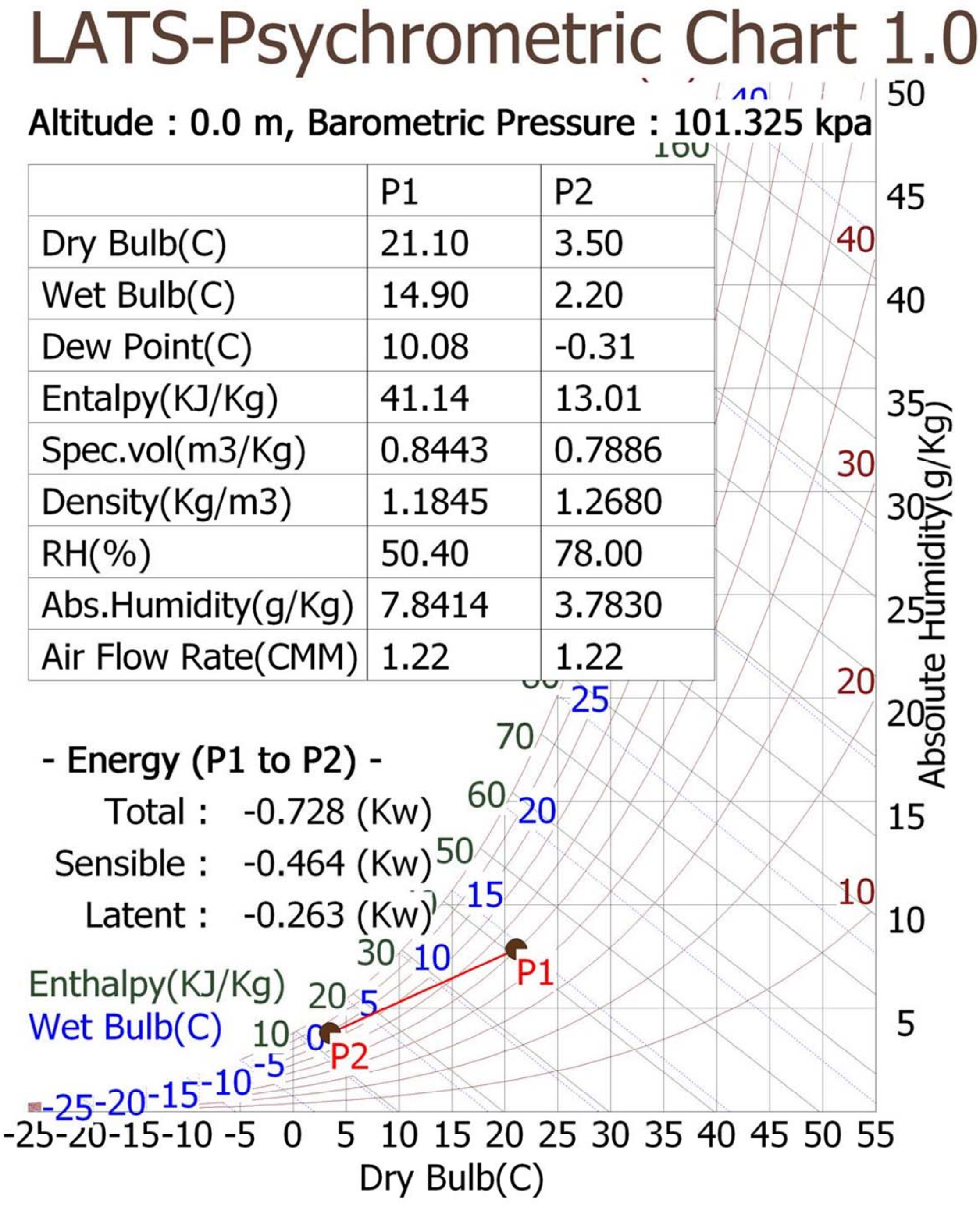

	P1	P2
Dry Bulb(C)	21.10	3.50
Wet Bulb(C)	14.90	2.20
Dew Point(C)	10.08	-0.31
Entalpy(KJ/Kg)	41.14	13.01
Spec.vol(m3/Kg)	0.8443	0.7886
Density(Kg/m3)	1.1845	1.2680
RH(%)	50.40	78.00
Abs.Humidity(g/Kg)	7.8414	3.7830
Air Flow Rate(CMM)	1.22	1.22

Figure (4): Psychrometric total calculations of steam humidification process (1) with dehumidifying coil for points (1 – 2)

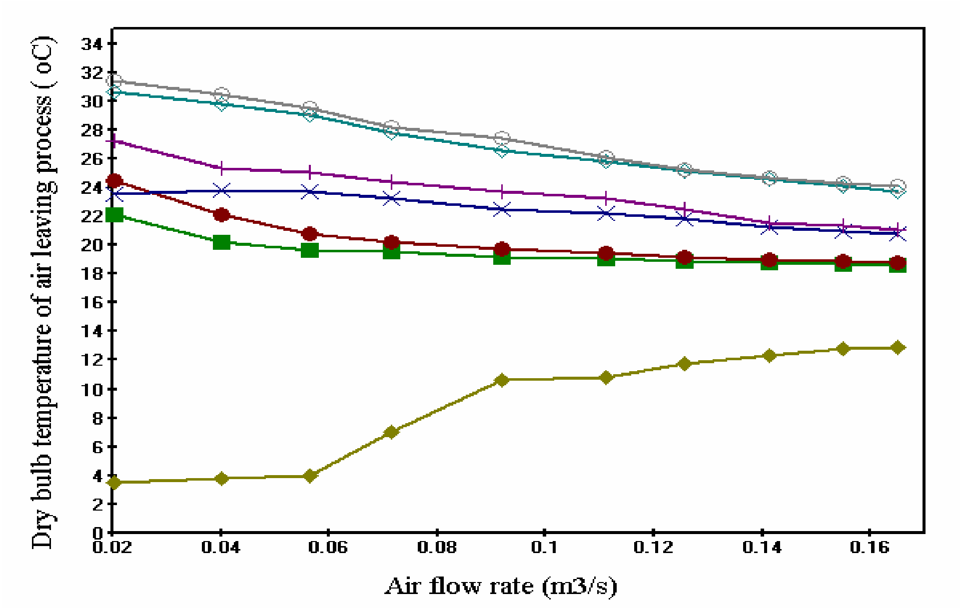

Figure (5): The variation of dry bulb air temperature leaving the processes for different air flow rate

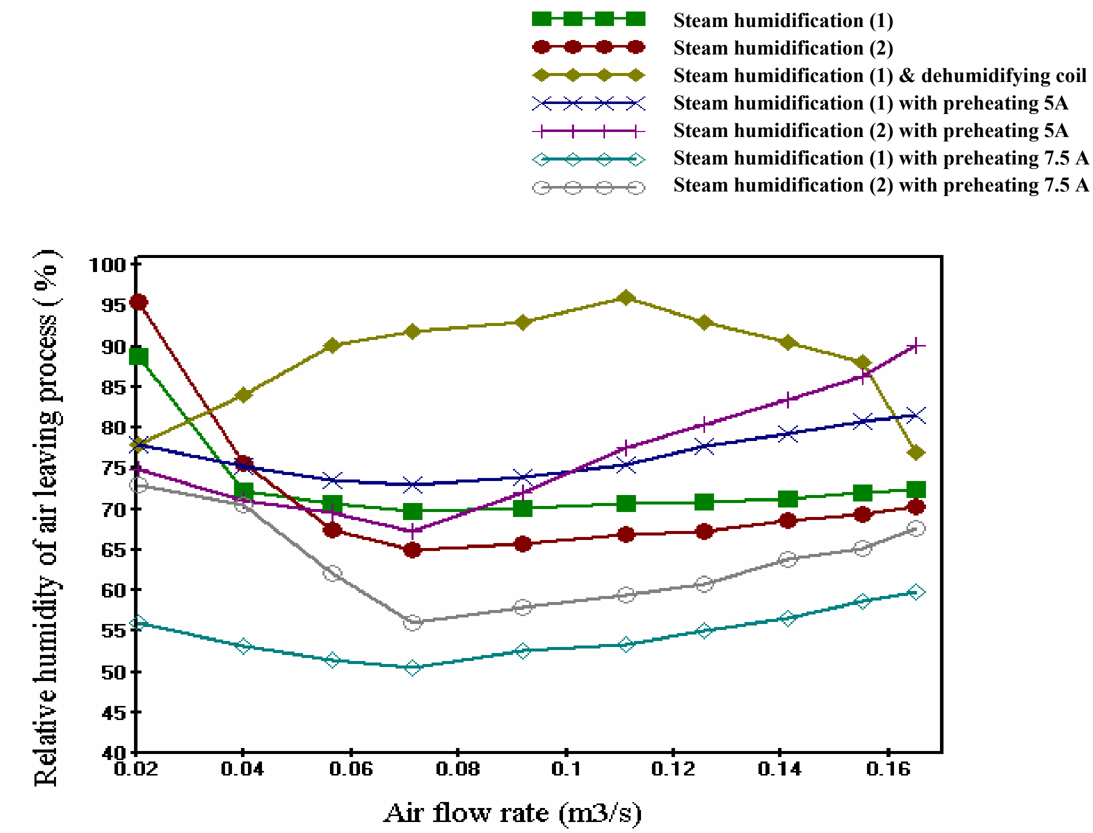

Figure (6): The variation of relative humidity of air leaving the processes for different air flow rate

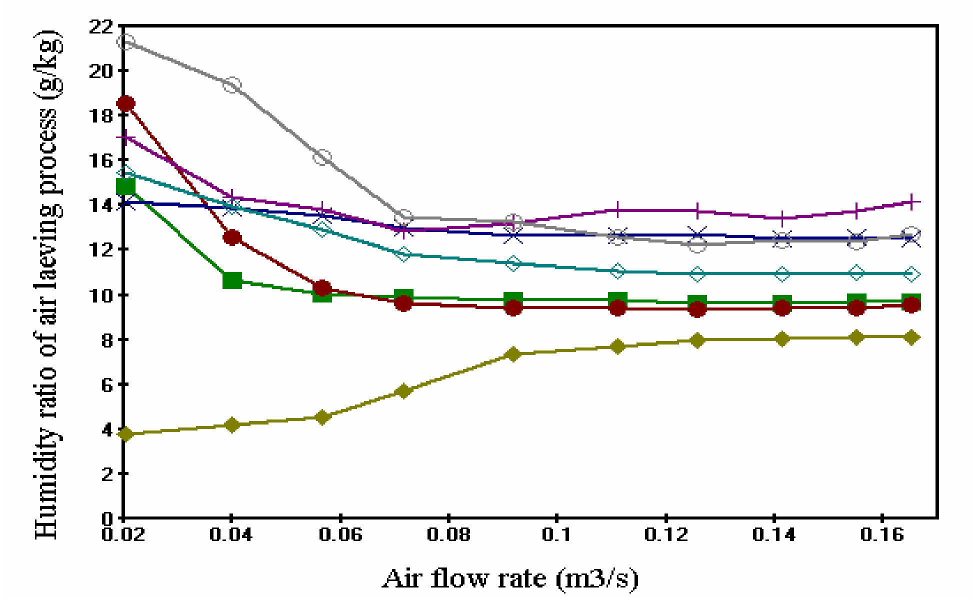

Figure (7): The variation of humidity ratio of air leaving the processes for different air flow rate

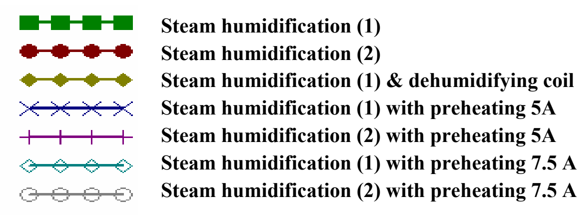

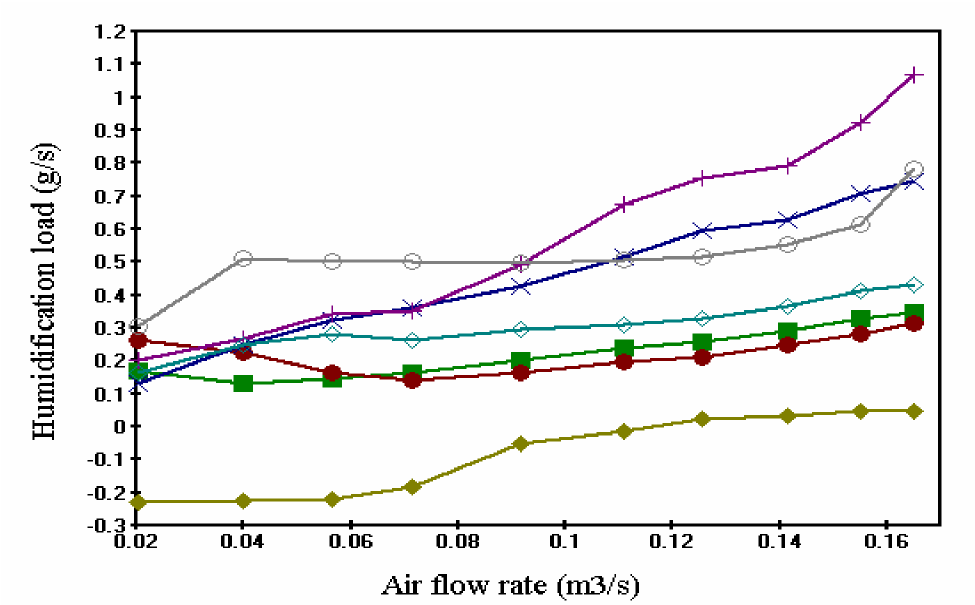

Figure (8): The variation of humidification load of the processes for different air flow rate

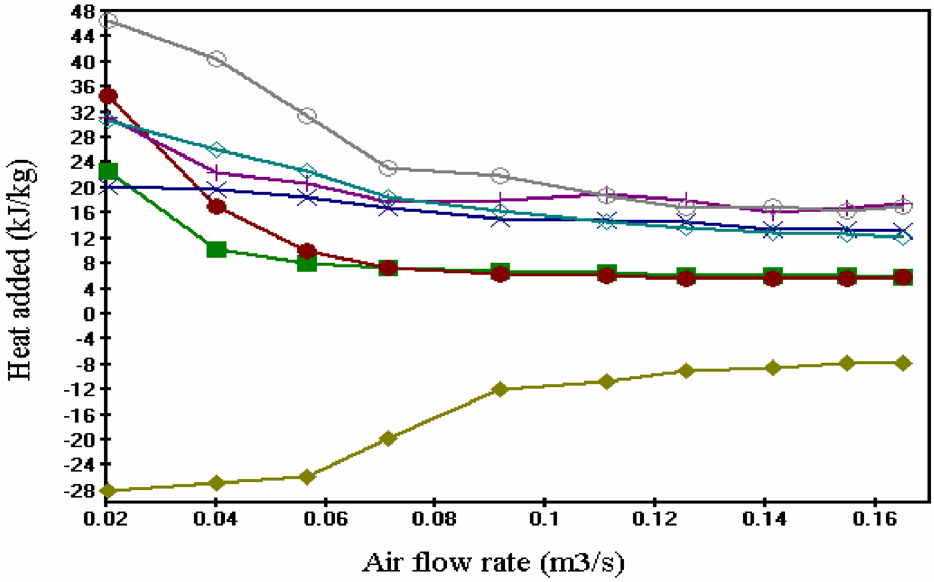

Figure (9): The variation of heat added at the processes for different air flow rate

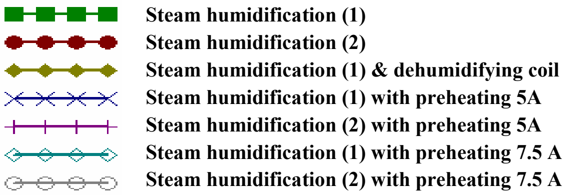

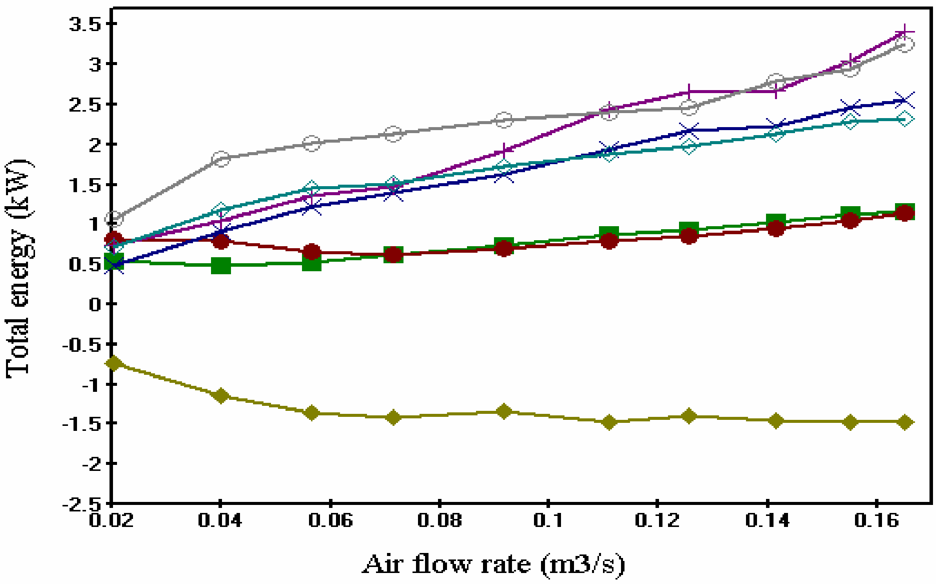

Figure (10): The variation of total energy of the processes for different air flow rate

REFERENCES

- Anton Tenwolde, and Iain S. Walker:" Interior moisture design loads for residences", Buildings VIII, American Society of Heating, Refrigerating and Air-Conditioning Engineers, Inc., (2001).

- Trott A. R. and T. Welch: "Refrigeration and Air Conditioning", 3rd Edition; chapter (24), Butterworth-Heinemann, (2000).

- ASHRAE Handbook Fundamentals: Chapter (1); American Society of Heating, Refrigeration, and Air Conditioning Engineers, (2009).

- Hongbin Zhao, Pengxiu Yue, and Ling Cao: "Analysis of Humid Air Turbine Cycle with Low- or Medium-Temperature Solar Energy'', Hindawi Publishing Corporation International Journal of Photo energy, Article ID 672627, doi:10.1155/2009/672627 Volume (2009).

- Mikiya Sato, Shingo Fukayo and Eiji Yano:" Adverse Environmental Health Effects of Ultra-low Relative Humidity Indoor Air", Journal of Occupational Health, Volume 45, PP 133–136 (2003).

- Mohamed Mahmoud Gouda, Member IEEE:" Fuzzy Ventilation Control for Zone Temperature and Relative Humidity", June 8-10, 2005. Portland, OR, American Control Conference, (2005).

- Paraya Assanasen, Faud M. Baroody, Philip Rouadi, Edward Naureckas, Julian Solway, and Robert M. Naclerio:" Ipratropium Bromide Increases the Ability of the Nose to Warm and Humidify Air ", American Journal of Respiratory and Critical Care Medicine, VOL. 162 (2000).

- S. A. El-Agouz, and M. Abugderah:"Experimental analysis of humidification process by air passing through seawater'', Energy Conversion and Management Volume 49, Issue 12, December (2008), PP 3698-3703.

- Stoeker W.F.: "Refrigeration and Air Conditioning", McGraw-Hill Publishing Company Ltd., (1982).

- Tony Evans:" Humidification strategies for data centers and network rooms", Wight Paper, American Power Conversion (2008).

NOMENCLATURE

A cross suction area of the tunnel (m^2)
C_p specific heat of moist air (kJ/kg.K)
d diameter of the tunnel (m)
h_i ambient air enthalpy entering process (kJ/kg)
h_o enthalpy of air leaving the process (kJ/kg)
m_{air} mass flow rate of air
$\dot{m}_{da}$ mass flow of dry air, per unit time
$\dot{m}_w$ mass flow of water (any phase), per unit time
M_{da} mass of dry air in moist air sample
M_w mass of water vapor in moist air sample
t_d dew-point temperature of moist air (°C)
T_i temperature of air entering process (°C)
T_o temperature of air leaving the process (°C)
V air velocity (m/s)
W humidity ratio of moist air (g/kg)
W_i ambient air humidity ratio (g/kg)
W_o humidity ratio of air leaving process (g/kg)
x_{da} mole-fraction of dry air, moles of dry air per mole of mixture

Greek symbols

Φ relative humidity
ρ air density (kg/m^3)
π 3.14159

CORRELATIONS OF POINT LOAD INDEX AND PULSE VELOCITY WITH THE UNIAXIAL COMPRESSIVE STRENGTH FOR ROCKS

Muhammad Abdul Jabbar
College of Engineering/ University of Baghdad

ABSTRACT:

Rock engineers widely use the uniaxial compressive strength (UCS) of rocks in designing surface and underground structures. The procedure for measuring this rock strength has been standardized by both the International Society for Rock Mechanics (ISRM) and American Society for Testing and Materials (ASTM), **Akram and Bakar(2007)**.

In this paper, an experimental study was performed to correlate of Point Load Index ($I_{s(50)}$) and Pulse Wave Velocity (V_p) to the Unconfined Compressive Strength (UCS) of Rocks. The effect of several parameters was studied. Point load test, Unconfined Compressive Strength (UCS) and Pulse Wave Velocity (V_p) were used for testing several rock samples with different diameters.

The predicted empirical correlations based on various test results indicate that the UCS could be obtained directly from measured (V_p), and then the Index $I_{s(50)}$ can be calculated by back substitution.

الخلاصة:

إن مهندسي الصخور يستخدمون بشكل واسع مقاومة الانضغاط المحوري للصخور (UCS) في تصميم المنشات المقامة فوق و تحت سطح الأرض. إن الطريقة الرئيسية لقياس مقاومة الصخور تمت معايرتها دولياً من قبل المجتمع الدولي لميكانيك الصخور (ISRM) و المجتمع الأميركي للفحوص و المواد(ASTM)، **أكرم و بكر(2007)**.

في هذا البحث تم إجراء برنامج عملي لغرض معرفة العلاقة بين دليل الحمل النقطي لنماذج ذو قطر 50 ملم ($I_{s(50)}$) و سرعة الموجات الطولية المارة بالنموذج(V_p) مع مقاومة الانضغاط اللا محصور (UCS) للصخور. الفحوص دليل الحمل النقطي($I_{s(50)}$)، سرعة الموجات الطولية المارة بالنموذج(V_p) و مقاومة الانضغاط اللا محصور(UCS) تم إجراءها على نماذج مختلفة من الصخور ذو أقطار مختلفة.

إن العلاقات التجريبية المستنتجة و المستندة على الفحوص المذكورة سابقاً تدل على أن مقاومة الانضغاط اللا محصور يمكن حسابها مباشرة من سرعة الموجات الطولية المقاسة للنماذج و بالتالي يمكن حساب دليل الحمل النقطي لنماذج ذو قطر 50 ملم بالتعويض العكسي.

KEY WORDS:- Rocks, Uniaxial Compressive Strength (UCS), Modulus of Elasticity(E_s), Point Load Index ($I_{s(50)}$), Pulse Wave Velocity (V_p).

INTRODUCTION:

The most two important engineering characteristics of a rock mass are its strength and the discontinuity spacing. In engineering terms, rock strength may be defined as the inherent strength of an isotropic rock under specific conditions, notably wet or dry, Hawkins(1998). The UCS is the geotechnical property that is most often quoted in rock engineering practice.

These methods are time consuming and expensive. Indirect test such as point load index ($I_{s\ (50)}$) as a quick estimation of the UCS is used. The test is easier to carry out because it does not need sample preparation and the testing equipment is less sophisticated, **Akram and Bakar(2007).**

Scope of the Study:

Unconfined compression tests and point load tests were carried out on different samples taken from Taq Taq Dam project and were used to obtain correlations between unconfined compressive strength UCS versus point load index, and UCS versus longitudinal wave velocity, V_P.

The researcher has been done all the tests including Point load index, unconfined compressive strength and ultra sonic waves on different rock core samples.

Engineering Properties of Rock:

Strength Test:

1. **Point-Load Index:**

   Definitions and Calculations:

   Broch and Franklin (1972) started with a simple formula taking an idealized failure plane of a diametric core sample into account **Fig. (1)**.

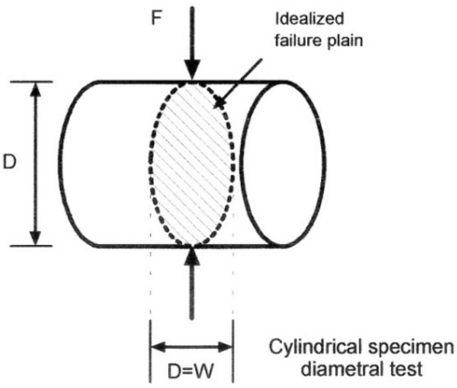

Fig.(1): Core specimen's dimensions for a diametric point load test.

$$I_s = \frac{F}{D_e^2} \qquad \text{Eq. (1)}$$

Where:

I_s = point load strength
F = load
D_e = equivalent core diameter

Since then, this formula varied little. Taking into account the cross sectional area of the core, the formula rewritten as:

$$I_s = \frac{4F}{\pi D^2} \qquad \text{Eq. (2)}$$

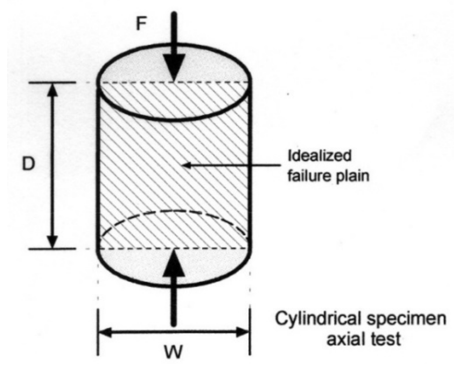

Fig.(2): Core Specimen dimensions for an axial point load test.

Users of this test noticed, that the results of a diametric test **Fig.(2)** were about 30% higher the results for an axial test using the same specimen dimensions. **Brook (1985)** and the **ISRM (1985)** suggest a size correction and introducing the "equivalent core diameter":

$$I_s = \frac{F}{D_e^2} = \text{ And}$$

$$W.D = A = \quad \text{Eq. (3)}$$

Where

I_s = point load strength
F = load
D_e = equivalent core diameter
D = thickness of specimen
W = width of specimen
A = minimum cross sectional area of a plane through the platen contact points.

Using the simple physical law σ = F/A, the formula for determining point load strength **(ASTM D 5731-95)** should be:

For cores:

$$I_s = \frac{4F}{\pi D^2} \quad \text{Eq. (4)}$$

And for blocks and irregular lumps:

$$I_s = \frac{F}{W.D} \quad \text{Eq. (5)}$$

Given the deficiencies in the derivation by the quoted authors, **Eq. (3)** used for determining the point load index for sake of comparisons.

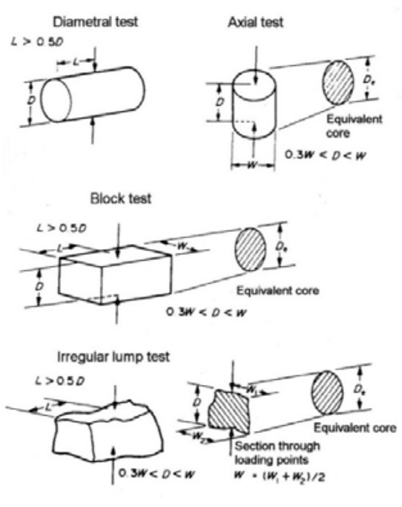

Fig.(3): Specimen shape requirements for different test types after **Brook (1985),ISRM (1985)**and **ASTM (D 5731-95).**

Approaches to Overcome Scale Effects:

Known from the onset of testing, the point load strength is highly dependent on the size of the specimen as well as the shape.

Using thick instead of tall specimens for the block and the irregular lump test and standardizing the general shape of the specimens were steps forward **Broch and Franklin (1972)**, **Brook 1985**. Specimen shape requirements are given in **Fig.(3)** to obtain more reliable testing results with a smaller standard deviation. However, analysis and evaluation were limited by size variation and the lack of a reliable and easy-to-comprehend method for size correction.

Broch and Franklin (1972) offered a Size Correction Chart with a set of curves to standardize every value of the point load strength I_s to a point load strength index ($I_{(50)}$) at a diameter of D = 50 mm. The purpose of the function was to describe the correlation between I and D and to answer the question, whether this function is uniform for all rock types or if it depends on the rock type together with grain size, composition of mineral bonds, grain cleavage etc.

Brook (1985) and the **ISRM (1985)** suggest three options to evaluate the results of a test set:

1. Testing at D=50 mm only (most reliable after **ISRM (1985)**).
2. Size correction over a range of D or D_e using a log-log plot, **Fig.(4)**. The most reliable method of size correction is to test the specimen over a range of D or D_e values and to plot graphically the relation between P and D_e. If a log-log plot is used, the relation is a straight line (see **Fig. 4**). Points that deviate substantially from the straight line may be disregarded (although they should not be deleted). The value of $Is_{(50)}$ corresponding to D_e =50 mm can be obtained by interpolation and use of size-corrected point load strength index calculated as shown in Eq.(7).**ASTM (D 5731-95)**.
3. when testing single-sized core at a diameter other than 50 mm or if only a few small pieces are available, size

correction may be accomplished using the formula containing the“Size Correction Factor” *f*:

$$I_s = f.\frac{F}{D_e^2} = f.\frac{\pi.F}{4.W.D} \quad \text{Eq. (6)}$$

Where:

$$f = \left(\frac{D_e}{50}\right)^{0.45} = \left(\frac{D_e}{2500}\right)^{0.225} \quad \text{Eq. (7)}$$

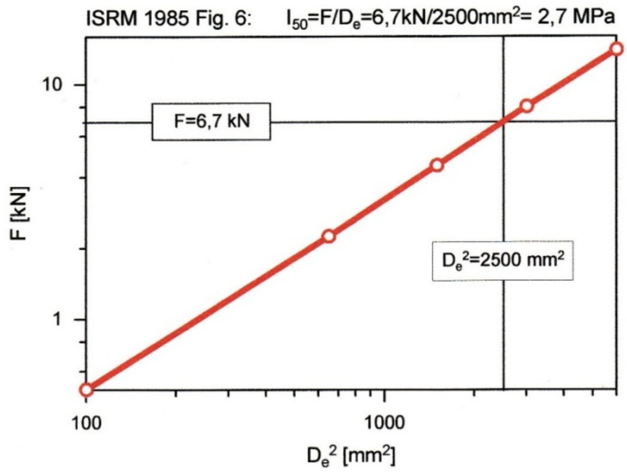

Fig.(4): Procedure for graphical determination of I $_{(50)}$ from a set of results at D_e values other than 50 mm **(ISRM 1985).**

2. Unconfined Compressive Strength Test (UCS):

Intact rock strength is mostly defined as the strength of the rock material between the discontinuities. Strength values used are often from unconfined compressive strength (UCS) tests **(ASTM D 2938-95)**. **Hack, R and Huisman, M.(2002)** stated the Problems caused by the definition of intact rock strength and using strength values based on UCS laboratory tests are:

1. The UCS includes discontinuity strength for rock masses with small discontinuity spacing. The UCS test sample is most often about 10 cm long and if the discontinuity spacing is, less than 10 cm the core may include discontinuities.
2. Samples tested in the laboratory tend to be of better quality than the average rock because poor rock is often disregarded when drill cores or samples break **(Laubscher, 1990)**, and cannot be tested.
3. The intact rock strength measured depends on the sample orientation if the intact rock exhibits anisotropy.

Unconfined Compression test is the most frequently used strength tests for rocks, yet it is simple to perform properly and results can vary by a factor of more than two as procedures are varied. The test specimen should be a rock cylinder of length to width ratio in the range 2 to 2.5 with flat, smooth, and parallel ends cut perpendicularly to the cylinder axis, **Goodman(1980)**. In the standard laboratory compression test, however, cores obtained during site exploration are usually trimmed and compressed between the crosshead and platen of a testing machine. The compressive strength (q_u) is expressed as the ratio of peak load (p) to initial cross-sectional area (A).

$$q_u = \frac{P}{A} \quad \text{Eq. (8)}$$

Strength – Deformation Characteristics:

1. Elastic Modulation:

For an isotropic and elastic material, the relation between shear and bulk module and Young’s modulus and Poisson’s ratio are:

$$G = \frac{E}{2(1+\upsilon)} \quad \text{Eq. (9)}$$

$$k = \frac{E}{3(1-2\upsilon)} \quad \text{Eq. (10)}$$

Where:

G = shear modulus,
k = bulk modulus,
E = Young’s modulus, and
υ= Poisson’s ratio.

The engineering applicability of these equations is not good if the rock is anisotropic. When possible, it is desirable to conduct tests in the plane of foliation, bedding, etc., and at right angles to it to determine the degree of anisotropy. It is noted that equations developed for isotropic materials may give only approximate calculated results if the difference in elastic module in any two directions is greater than 10 % for a given stress level.

The axial Young's modulus, E, (**ASTM D 3148 – 02)** may be calculated using any of several methods employed in engineering practice. The most common methods are as follows:

1. Tangent modulus at a stress level that is some fixed percentage (usually 50 %) of the maximum strength.
2. Average slope of the more-or-less straight-line portion of the stress-strain curve. The average slope may be calculated either by dividing the change in stress by the change in strain or by making a linear least squares fit to the stress-strain data in the straight-line portion of the curve.
3. Secant modulus, usually from zero stress to some fixed percentage of maximum strength.

2. Ultrasonic Testing

Measurement of velocity of sound waves (longitudinal and shear waves) in core specimen **(ASTM D2845-00)** is relatively simple and done by means of Pundit apparatus as shown in **Plate (1).**

Plate (1): Ultrasonic testing Apparatus (Pundit Apparatus).

The most popular method pulses one end of the rock with a piezoelectric crystal and receives the vibrations with a second crystal at the other end. The travel time is determined by measuring the phase difference with an oscilloscope equipped with a variable delay line. It is also possible to resonate the rock with a vibrator and then calculate its sonic velocity from the resonant frequency, known dimensions, and density. Both longitudinal and transverse shear wave velocities can be determined.

However, the index test described here requires the determination of only the longitudinal velocity, V_p, which proves the easier to measure. **ASTM D2845-00 (2003)** describes laboratory determination of pulse velocities and ultrasonic elastic constants of rock.

Theoretically, the velocity with which stress waves are transmitted through rock depends exclusively upon their elastic properties and their density. In practice, a network of fissures in the specimen superimposes and overriding effect. This being the case, the sonic velocity can serve to index the degree of fissuring within rock specimens.

Correlation Between uniaxial compressive strength and point load index for rocks:

The point load test has been reported as an indirect measure of the compressive or tensile strength of the rock. **D'Andrea et al (1964)**, performed uniaxial compression and the point load tests on a variety of rocks. They found the following linear regression model to correlate the UCS and $I_{s\,(50)}$:

$$q_u=16.3+15.3I_{s(50)} \qquad \text{Eq. (11)}$$

Where:

q_u = Uniaxial Compressive Strength of rock.

$I_{s(50)}$ = Point load index for 50 mm diameter core.

Broch and Franklin(1972) reported that for 50 mm diameter cores the uniaxial compressive strength is approximately equal to 24 times the point load index. They also developed a size correction chart so that core of various diameters could be used for strength determination.

$$UCS=24I_{s(50)} \qquad \text{Eq. (12)}$$

Bieniawski(1975)suggested the following approximate relation between UCS, I_s and the core diameter (D).

$$UCS=(14+0.175D)I_{s(50)} \qquad \text{Eq. (13)}$$

Pells (1975) showed that the index-to-strength conversion factor of 24 could lead to 20% error in the prediction of compressive strength for rocks such as Dolerite, Norite, and Pyroxenite.

According to **ISRM** commission on standardization of laboratory and field test report **(1985)**, the compressive strength is 20-25 times I_s. However, it is also reported that in tests on many different rock types the range varied between 15 and 50, especially for anisotropic rocks. So errors up to 100% should be expected if an arbitrary ration value is chosen to predict compressive strength from point load tests.

Hassani et al(1985)performed the point load test on large specimens and revised the size correlation chart commonly used to reference point load values from cores with differing diameters to the standard size of 50mm. with this new correction, they found the ration of UCS to $I_{s(50)}$ be approximately 29.

The dependence of the UCS versus $I_{s(50)}$ correlation on rock types was demonstrated by **Cargill and Shakoor (1990)**. They found the following correlation equation:

$q_u=13+23I_{s(50)}$ Eq. (14)

$q_u=9.08I_s+39.32$ Eq. (17)

Akram and Baker(2007)confirm from their study that UCS estimation equations are rock dependent. The UCS was found to be into two groups according to rocks types:

Group A: (Jutana Sandstone, Banghanwala Sandstone , Siltstone, Sakessar Massive Limestone, Khewra Sandstone and Dolomite).

$UCS=22.7921Is_{(50)}+13.295$ $R^2=0.88$ Eq. (18)

Group B: (Dandot Sandstone, Sakessar Nodular Limestone and Marl)**.**

$UCS=11.076Is_{(50)}$ $R^2=0.8876$ Eq. (19)

Chau and Wong (1996) proposed a simple analytical formula for the calculation of the UCS based on corrected I_s to a specimen diameter of 50mm $I_{s(50)}$. The index-to-strength conversion factor (k) relating UCS to $I_{s(50)}$ was reported to depend on the compressive to tensile strength ratio, the Poisson's ratio, the length and the diameter of the rock specimen.

Their theoretical prediction for k = 14.9 was reasonably close to the experimental observation k = 12.5 for Hong Kong rocks.

Rusnak and Mark (2000) reported the following relations for different rocks:

For coal measure rocks:

$q_u=23.62I_{s(50)}–2.69$ Eq. (15)

For other rocks:

$q_u=8.41I_{s(50)}+9.51$ Eq. (16)

Fener et al. (2005) reported the following relation between Point load index and UCS:

$UCS=143.000\times e^{-0.035t}$ Eq. (20)

Where:
UCS in psi and t is the travel time of the P-wave in micro sec/ft.

Vp (Longitudinal Waves) with UCS Tests:

Sonic logging has been routinely used for many years in Australia to obtain estimates of coalmine roof rock strength for use in roof support design **(McNally, 1987 and 1990)**. The estimates are obtained through measurements of the travel time of the compression or P wave, determined by running sonic geophysical logs in core holes, which are then correlated with uniaxial compressive strength measurements made on core samples form the same holes.

In **McNally's** classic original study, conducted in **1987**, sonic velocity logs and drill core were obtained from 16 mines throughout the Australian coalfields.

The overall correlation equation **McNally** obtained from least-squares regression was:

David et.al(2008),for the entire data set of coal mine roof rocks in Australia, the relationship between UCS and sonic travel time is expressed by the following equation, where UCS is in psi and t is the travel time of the P-wave in micro sec/ft.

$$UCS=468.000\times e^{-0.054t} \qquad \text{Eq. (21)}$$

The r-squared value(R^2) for this equation is 0.87, indicating that a strong correlation between sonic travel time and UCS can be achieved with this technique.

Experimental Work:

General

Rock core samples were taken from Taq Taq Dam project and used for mechanical properties tests (Point- load, Unconfined Compressive strength, and Ultrasonic Pulse velocity). The project was done between August and November of 2006. This dam site is situated in Lesser Zab River, upstream from Taq Taq Dam, and the roadway from Kirkuk to KoisanjEq.

1. Point load tests Data:

Point load tests were carried out and the results were listed in **Table (1)**. This table illustrates Bore hole No., Depths, Diameter and I_{50}. An attempt was made to correlate (I_{50}) with many variables such as Depth, water content and Diameter. The following **Figures (5), (6),** and **(7)** which shows the relations between (I_{50}) and water content, (I_{50}) and depths, (I_{50}) and diameter. For each graph R^2-values was taken into account.

2.Unconfined compressive strength tests Data:

Unconfined compressive strength tests were carried out and the results were listed in **Table (2)**. This table illustrates Borehole No., Depths, Unconfined compressive strength, and Modulus of Elasticity. In addition, an attempt was made to correlate (UCS) with many variables such as depths, water content, (I_{50}) and Modulus of elasticity. The following **Figures(8),(9)** and **(10)** show the relations between(UCS) and water content, (UCS) and depths, (UCS) and Modulus of elasticity, (UCS) and (I_{50}).

3.Ultrasonic Pulse Velocity tests Data:

Ultrasonic Pulse velocity tests were carried out and the results are listed in **Table(3)**. This table illustrates Borehole No., Depths, water content, and Pulse velocity.

Here, an attempt was made to correlate. (V_p) with many variables such as Depths, water content and UCS. The following **Figures (11), (12),** and **(13)** which show the relations between V_P and water content, V_P and Depths, V_P and UCS.

Table (1): Point Load Index of Rock Cores.

Borehole No.	Depth(m)	P(kN)	D(mm)	w_n,%	γ_t(kN/m³)	I_s, MPa	Factor*	$Is_{(50)}$, MPa
BR-5	10-12	4.5	85	3.80	22.80	0.623	1.2697	0.791
	12-14	4.71	81.33	0.54	22.40	0.712	1.2447	0.886
	37-39	3.299	78.86	5	22.97	0.530	1.2276	0.651
	67-69	4.71	67.50	4.5	21.51	1.034	1.1446	1.183
BR-6	30-33	5.298	77.73	4.44	22.66	0.877	1.2196	1.069
	40-42	5.892	84.6	3.03	22.75	0.823	1.2670	1.043
	48-50	4.223	82.72	10.4	22.33	0.617	1.2543	0.774
	53-55	5.298	83.89	2.85	23.02	0.753	1.2622	0.950
BR-9	28-29	6.484	82.86	9.25	21.84	0.944	1.2552	1.185
	48-50	3.299	82.17	2.17	22.85	0.489	1.2505	0.611
	87-89	1.33	83.26	2.56	20.29	0.192	1.2579	0.241
BR-10	12.5-14.45	1.489	79.75	4.83	21.32	0.234	1.2337	0.289
	22-24	1.112	80.27	6	20.87	0.172	1.2374	0.213
	58.8-61	0.5776	69.62	9.5	21.37	0.119	1.1606	0.138
BR-12	52.5-54.3	4.806	62.70	6.06	23.00	1.222	1.1072	1.353
	58-60	1.501	62.70	11.25	22.00	0.382	1.1072	0.423
	61.5-63	2.376	65.70	5	24.30	0.550	1.1307	0.622
	75.4-76.7	6.188	66.80	3.4	23.10	1.387	1.1392	1.579
	84.3-85.7	6.188	68.70	11.1	23.38	1.311	1.1537	1.513
BR-14	26-28	3.421	81.79	1.449	21.89	0.511	1.2479	0.638
	30-32	3.8159	78.45	1.33	22.574	0.620	1.2247	0.759
	46.3-48	5.133	82.88	1.17	22.914	0.747	1.2553	0.938
	52-54	4.5877	82.75	3	22.237	0.669	1.2545	0.840
BR-15	9.5-12	4.709	74.90	12.85	21.94	0.839	1.1994	1.007
	13.2-14.2	3.445	81.92	2.86	22.44	0.513	1.2488	0.641
	19-21	3.202	79.38	4.41	21.95	0.508	1.2312	0.626
	25-27	5.8918	81.76	5	21.49	0.881	1.2477	1.099
	40-42	2.522	78.80	9.21	20.88	0.406	1.2271	0.498
BR-16	6-8	1.1609	78.37	13.33	20.14	0.189	1.2241	0.231
	9-11	6.485	82.58	5.80	22.74	0.951	1.2533	1.192
	34.5-35.9	8.857	81.90	7.30	23.87	1.320	1.2486	1.649
BR-18	13-15	2.206	76.60	4.54	22.5	0.376	1.2116	0.455
	21.2-23	9.747	84.90	5.35	23.56	1.352	1.2690	1.716
	27-28.5	1.088	80.40	7.5	22.5	0.168	1.2383	0.208
BR-19	12-14	5.892	67.92	3.389	22.76	1.277	1.1478	1.466
BR-21	25.6-27	4.223	78.48	6.55	22.93	0.686	1.2249	0.839
	36.5-38.6	4.7056	82.0	9.09	24.457	0.699	1.2493	0.874
	40-41.7	2.7163	78.6	8.75	23.28	0.440	1.2257	0.539
	43.6-45	1.744	77.78	8.823	22.68	0.288	1.2199	0.352
	48-50	2.424	85.7	8.57	22.56	0.330	1.2744	0.421
BR-26	12-13.35	1.403	62.54	8.57	22.05	0.359	1.1059	0.397
	24-27	4.5148	64.49	3.16	23.274	1.085	1.1213	1.217
BR-28	27-30	3.105	65.5	3.33	21.98	0.724	1.1292	0.817
BR-29	10.5-12.5	1.696	78.00	8.196	22.41	0.279	1.2215	0.340
	21-22.9	6.485	79.40	4.225	22.81	1.029	1.2313	1.267
	40.6-42.6	0.893	71.40	1.29	19.03	0.175	1.1739	0.206
BR-30	21-22.6	14.195	80.60	1.56	24.13	2.185	1.2397	2.709
	34-35.4	10.637	84.00	1.90	23.35	1.507	1.263	1.904

*: Factor was calculated using Eq.7.

Table (2): Unconfined Compressive Strength of Rock Cores.

Borehole No.	Depth(m)	w_n,%	γ_t(kN/m^3)	UCS(kPa)	Modulus of Elasticity, E_s, kPa
BR-5	10-11	3.80	20.65	10601.35	76821.37
	11-12	4.68	21.613	12216.58	143724.47
	12-14	0.54	22.23	9846.05	209490.42
	12-14	1.163	22.20	9211.22	237708.87
	37-39	3.45	25.84	12531.81	305653.90
	67-69	4	22.736	16711.25	263169.29
	67-69	4.477	22.87	19312.88	603527.5
BR-6	30-33	8.33	22.608	13517.72	318064.0
	40-42	5.8	22.76	13600.85	261554.8
	48-50	8.5	22.74	13052.8	326320.0
	53-55	6.25	22.65	8739.387	268904.2
BR-9	28-30	5.45	22.32	11663.4	466536.0
	48-49	8.69	22.82	12461.32	377615.75
	49-50	5.71	22.61	7228.94	301205.9
	87-88	2.439	19	3473.011	231534.06
	88-89	2.56	20.56	3301.016	165050.8
BR-10	22-24	6	22.15	11395.02	245054.19
	58.8-60	9.09	21.034	1160.17	45274.77
	60-61	8.5	23.69	8203.99	468799.43
BR-12	52.5-54.3	8.62	23.076	7896.64	382867.2
	58-60	10.526	21.98	9707.13	351707.6
	61.5-63	5	24.46	7229.68	444903.26
	75.4-76.7	5.4	21.91	5024.56	341806.66
	75.4-76.7	3.389	23.695	19246.80	466589.09
	84.3-85.7	8.51	23.50	6216.40	382547.4
	84.3-85.7	6.25	24.12	6769.08	338453.95
BR-14	26-28	2.3	22.138	13005.44	394104.24
	30-32	2.0408	24.107	17772.37	253891.0
	46.3-48	2.0408	22.5	8021.836	320873.44
		3.508	21.768	7969.121	306504.65
	52-54	3.1	22.906	19120.98	354092.22
BR-15	9.5-12	4.59	21.52	4170.99	196466.6
	19-21	4.3	22.306	16818.41	538188.8
	25-26	10.42	21.55	6841.88	273675.2
	26-27	5.36	21.81	14093.83	281876.6
	40-42	3.45	22.53	6639.58	295749.71
BR-16	6-8	12.90	20.14	7629.10	142068.93
	9-11	3.225	24.165	8189.46	314979.11
	34.5-35.9	7.31	22.083	9883.18	299490.5
BR-18	13-15	8.1	23.09	10772.89	319196.7
	21.2-23	5	22.44	10032.43	209008.9
	27-28.5	9.43	22.99	10224.75	176287.93
BR-19	12-14	3.846	22.60	20998.04	430729.02
BR-21	25.6-27	6.97	23.18	13175.71	274493.96
	25.6-27	7.69	23.07	2362.926	315056.8
	36.5-38.6	7.55	23.75	11395.77	633098.3
	40-41.7	9.302	22.95	12868.43	419168.73
	43.6-45	9.876	22.159	10717.26	297701.6
	48-50	9.305	22.905	12768.42	283742.67
BR-26	12-13.35	7.35	23.502	10149.36	563853.33
	24-27	5.714	23.96	12578.9	314472.5
BR-28	27-30	2.5	22.338	11355.99	239073.47
	27-30	2.23	21.988	11653.64	448216.92
BR-29	10.5-12.5	6.78	22.76	4544.37	186435.69
	21-22.9	5.88	21.96	8866.92	73891.0
	40.6-42.6	2.857	24.014	8503.94	219456.5
BR-30	21-22.6	1.4	22.66	18422.68	1842268.0
	34-35.4	1.56	23.75	14907.70	425934.28

Table (3): Ultrasonic Velocity of Longitudinal Wave.

Borehole No.	Depth(m)	L(mm)	D(mm)	w_n,%	γ_t (kN/m³)	V_p(km/s)
BR-5	10-12	168	83.9	3.80	22.70	1.486
	12-14	224	82.12	4.60	22.22	1.583
	37-39	202	79.81	3.50	23.22	1.909
	67-68	98.52	66.16	4.00	22.35	1.753
	68-69	147.47	65.26	4.50	22.62	1.559
BR-6	30-33	196.68	77.73	4.44	22.66	1.633
	40-42	194.12	84.6	3.03	22.74	1.596
	48-50	212	82.72	10.4	22.33	1.867
	53-55	202.28	83.89	2.85	23.02	2.015
BR-9	28-29	203.42	82.85	3.92	22.50	2.209
	29-30	193.43	82.86	9.25	21.84	2.203
	48-49	190.32	82.06	6.72	22.82	2.239
	49-50	201.68	81.79	8.69	22.74	2.112
	48-49	116.45	82.17	2.17	22.85	2.065
	87-88	197.82	83.32	2.56	20.49	1.199
	87-88	161.64	83.27	2.7	20.516	1.013
	88-89	145.32	83.26	2.6	20.298	1.056
BR-10	12.5-14.45	81.55	80.05	5	21.32	1.742
	22-24	140.46	80.27	6	20.87	1.027
	58.8-61	157.75	62.18	9.1	23.69	1.860
BR-12	52.5-54.3	15.3	62.7	6.3	23.1	0.245
	58-60	160	62.4	12	22.2	2.435
	58-60	160	62.7	12.7	22.3	2.363
	61.5-63	160	65.7	13	24.3	2.689
	75.4-76.7	160	66.8	6.4	24.1	2.488
	84.3-85.7	162	68.7	11.1	23.38	2.70
BR-14	26-28	201	81.79	1.45	21.89	1.595
	30-32	141.44	78.45	1.33	22.57	1.704
	46.3-48	195.03	82.88	1.17	22.914	1.923
	52-54	161.28	82.75	3	22.237	1.708
BR-15	9.5-12	148	74.9	13	21.94	1.465
		130	77.8	12.5	21.19	2.063
	13.2-14.2	75.99	81.92	2.85	22.695	2.524
	19-21	168.78	79.38	4.41	21.956	1.582
	25-27	166.75	81.76	5	21.497	1.799
	40-42	120	78.8	8.1	20.88	1.832
BR-16	6-8	130.44	78.37	13.4	20.136	0.162
	8-9	118.55	82.58	5.88	22.74	1.39
	11-12	127.53	83.63	6.12	21.99	0.658
	34.5-35.9	198.97	79.57	6.8	22.08	1.93
	34.5-35.9	199	81.9	7.1	23.875	2.149
BR-18	13-15	150	76.6	4.5	22.51	1.961
	21.2-23	195	84.9	5.1	23.56	2.281
	27-28.5	100	80.4	6.5	22.55	1.244
BR-19	12-14	171.35	67.92	3.39	22.76	1.875
BR-21	25.6-27	196.52	78.48	6.55	24.457	2.568
	36.5-38.6	200.5	82	9.09	22.93	2.724
	40-41.7	160.18	78.6	8.75	23.28	2.625
	43.6-45	169.25	77.78	8.82	22.68	1.6625
	48-50	200	80	8.57	22.56	2.164
BR-26	12-13.35	129.62	62.54	8.57	22.05	1.865
	24-27	150.44	64.49	3.16	23.27	1.97
BR-28	27-30	150.32	65.02	3.33	22.4	1.886
BR-29	10.5-12.5	128	78	8.33	22.41	1.164
	21-22.9	192.3	79.4	4.25	22.81	1.966
	21-22.9	207	77.4	6.25	22.95	1.026
	40.6-42.6	161.3	71.4	1.3	19.09	1.078
BR-30	21-22.6	190	80.6	1.45	24.14	2.378
	34-35.4	215	84	1.6	23.35	2.183

RESULTS AND DISCSSIONS:

1. **Relations between (I_{50}) and water contents, depths, and diameters:**

A. Relationship between Point-load Index and water content:

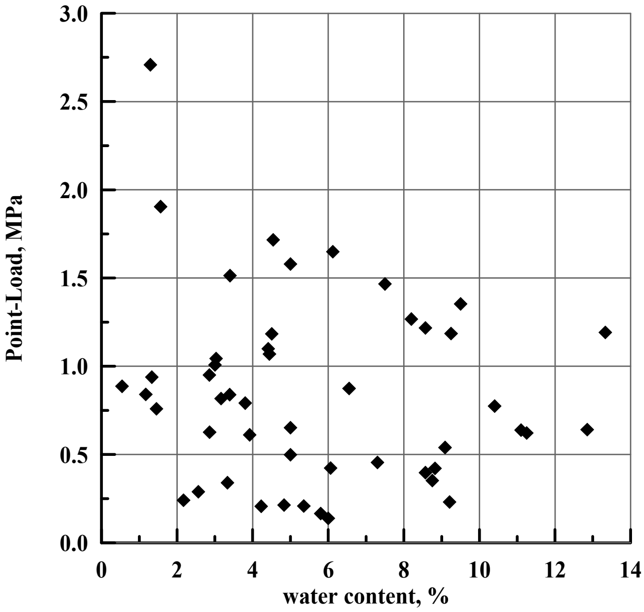

Fig.(5): Relationship between Point-load Index and water content.

B. Relationship between Point-load Index and depths:

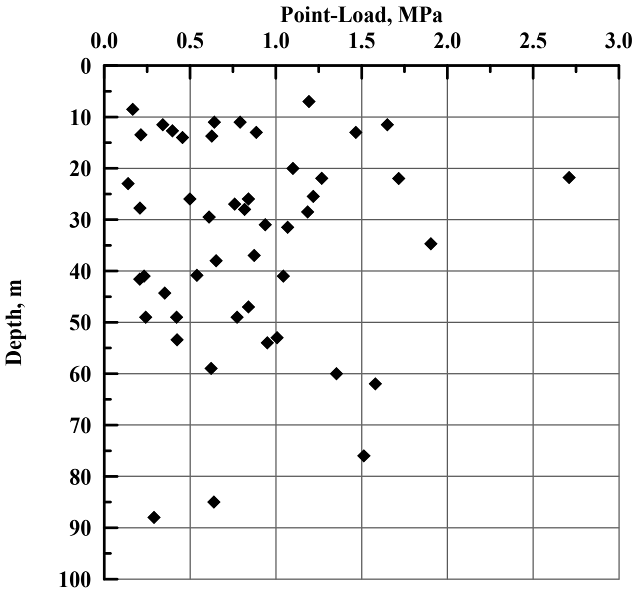

Fig.(6): Relationship between Point-load Index and depths.

From the previous graphs, despite the scatter in the data, the following points may be concluded:

1. There is a marked decrease in point load index with increasing water content up to 14% which reflect the field conditions as cited by **Hawkins(1986)**.
2. The point load index decreased with increasing depth.
3. The lower values of the point load index of all tested rock core samples are classified as sedimentary rocks which mainly consist of feldspar, Calcite, gypsum, chert, Mica,Biotite and Iron oxide.

2. **Relations between UCS and water contents, depths, and (I50):**

A. Relations between UCS and water content:

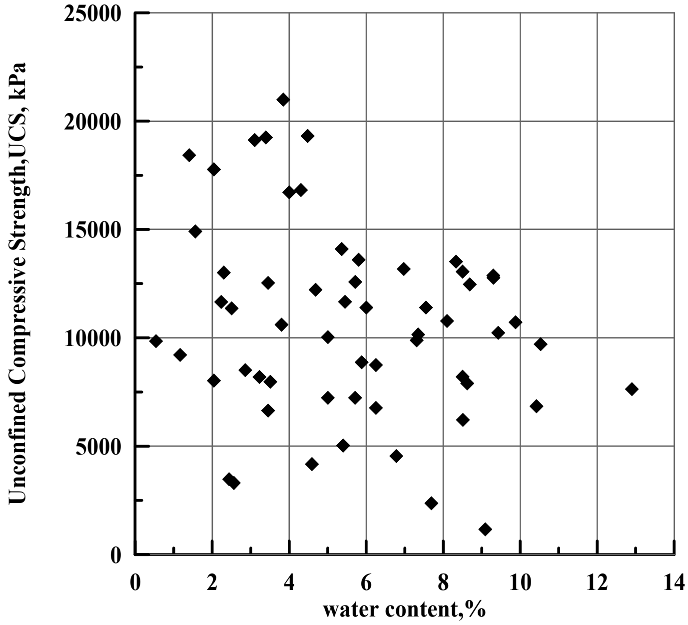

Fig.(7): Relationship between UCS and water content.

B. Relations between UCS and depth:

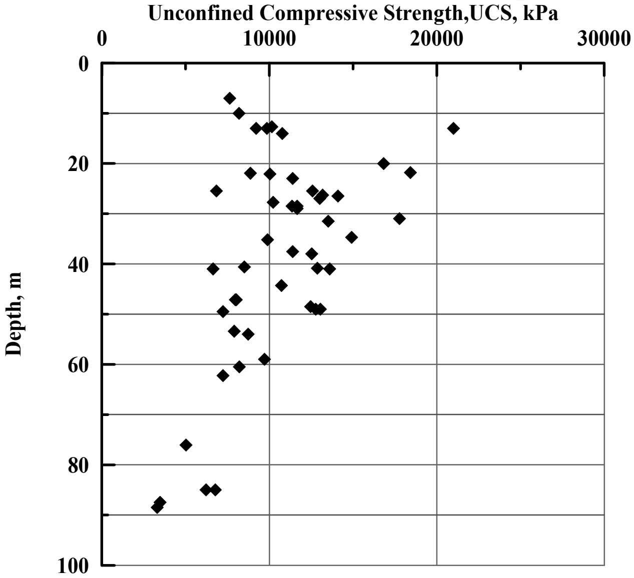

Fig.(8): Relationship between UCS and depth.

C. Relations between UCS and (I_{50}):

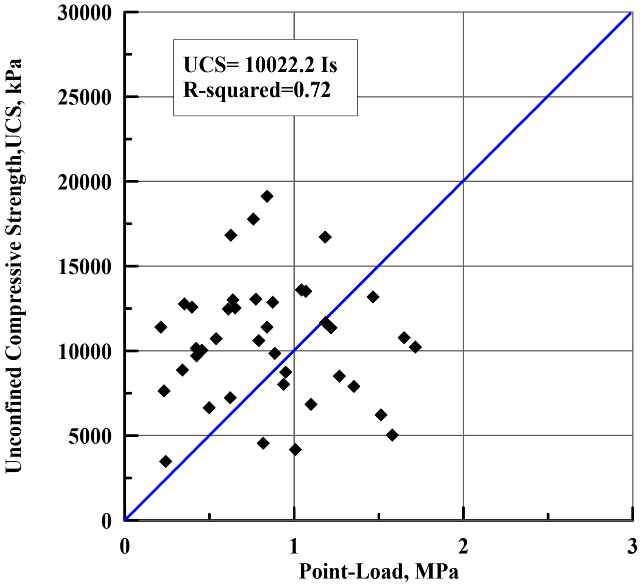

Fig.(9): Established Relationship between UCS and Point-load Index.

From the previous graphs, the following points may be derived:

1. The UCS decreased as the water content increased.
2. The UCS decreased as the depth increased which is similar to point load behaviour.
3. The UCS can be related with the point load index by:

UCS(kPa)=10022.2$I_{s(50)}$(MPa) R^2=0.72 Eq. (22)

This low strength range might be influenced by physical characteristics, such as size, saturation, weathering and mineral content. These results reveal that the sensitivity of rock strength due to changes in moisture content seems to vary from rock to rock. As cited by **Agustawijaya (2007)**,this sensitivity depends on the clay content of the rock being investigated. Also **Agustawijaya (2007)** pointed out that weaker sandstones are more sensitive to changes in moisture content than harder rocks and concluded that the texture of the rock, that is the proportion of grain contact, is responsible for reductions in the strength of sandstone. Further, he found that an increase in moisture content tends to decrease the range of elastic behaviour of sandstone.

It was concluded that variability in occurrences of quartz intragranular cracks and in Biotite percentage, distribution and orientation might have played a key role in accelerating or decelerating the failure processes, **Basu, Celestino and Bortolucci (2008)**.

3.Relations between V_p and water contents, depths, and UCS:

A. Relations between V_p and water contents:

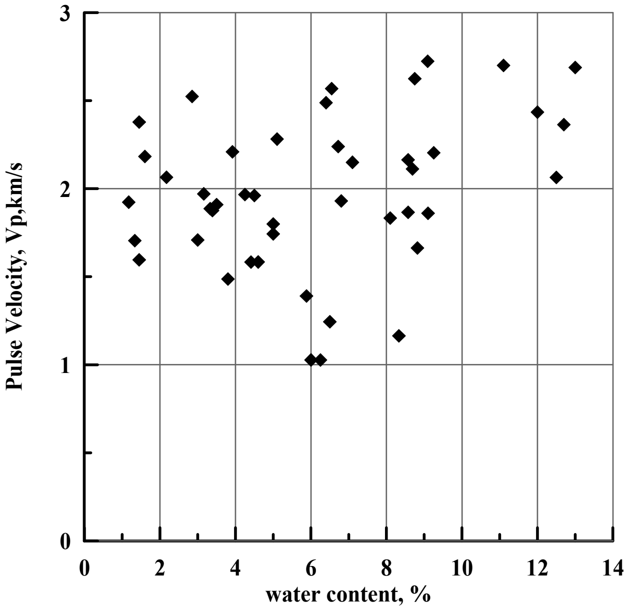

Fig.(10): Relationship between V_p and water content.

B. Relations between V_p and depths:

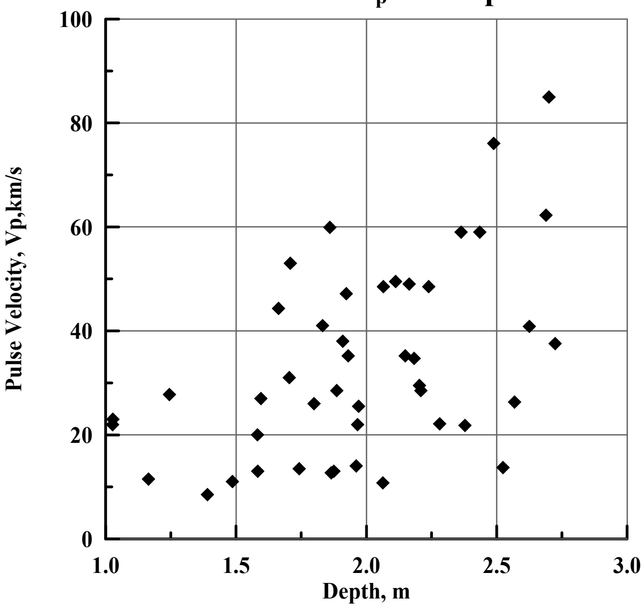

Fig.(11): Relationship between V_p and depths.

C. Relations between V_p and UCS:

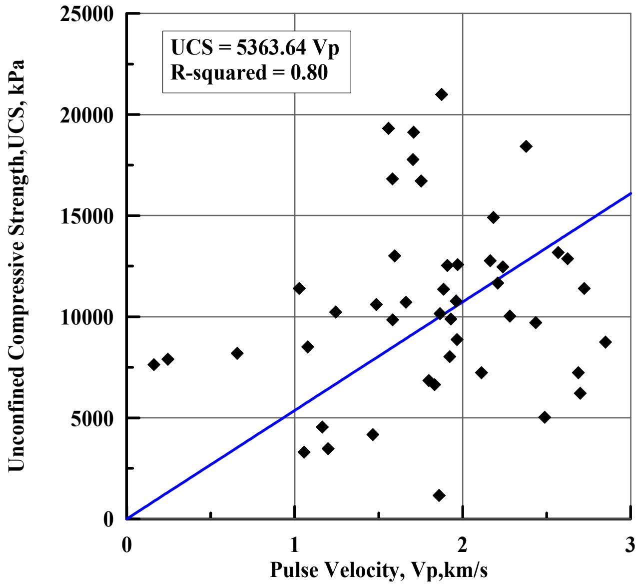

Fig.(12): Established Relationship between UCS and V_p.

From the previous graphs, the following points may be derived:

1. There is no obvious trend showing V_p, pulse velocity increase or decrease with increasing water content.
2. The pulse velocity, V_p increases with increasing depth due to densification and stratification of layered sedimentary rocks.
3. The UCS can be also related with pulse velocity:

UCS (kPa) = 5363.64 V_p (km/sec) R^2= 0.80 Eq. (23)

CONCLUSIONS AND RECOMMENDATIONS:

1. An attempt has been made to correlate UCS with (I_{50}).
2. The pulse velocity, V_p, increased with increasing water content and depths.
3. An equation has been found to correlate UCS with V_p.
4. For the correlations obtained, it is obvious that when V_p measured, the UCS can be calculated immediately, and then can be determined by back substitution of UCS in point load correlation.
5. There is no obvious trend for some relations.
6. Further study is needed to study the effect of discontinuity of rock on point load Index, UCS and V_p. Effect of saturation of rocks on engineering properties, and to study the possibility of using Schmidt hammer as an indication of UCS test result.

REFERENCES:

1. Akram,M.andBakar,M.Z.A.(2007): "Correlation between Uniaxial Compressive Strength and Point Load Index for Salt-Range Rocks". Pakistanian Journal of Engineering and Applied Science, Vol.1.
2. Agustawijaya,D.S.(2007):"The uniaxial compressive strength of soft rock". Civil engineering dimension.
3. Basu, A., Celestino, T.B. and Bortolucci, A.(2008):"Evaluation of rock mechanical behaviors under uniaxial compression with reference assessed weathering grade". Rock mechanics and rock engineering, Netherland.
4. Bieniawski,Z.T.(1975):Bulletin of Engineering Geology. 9(1), pages(1-11).
5. Broch, E. and Franklin, J.(1972) :Journal of Rock Mechanics and Mining Science 9 (6) pages (669-697).
6. Brook,N.(1985): "The equivalent core diameter method of size and shape correction in point load testing". International Journal of Rock Mechanics and Mining Science and Geomechanic. Abstract22:pages(61-70).
7. Cargill, J.S. and Shakoor, A.(1990): International Journal of Rock Mechanics and Mining Science and Geomechanic. Pages(495-503).
8. Chau,K.T.andWong,R.H.C.(1996): International Journal of Rock Mechanics and Mining Science. Pages(183-188).
9. D'Andrea, D.V., Fischer, R.L. and Fogelson, D.E. (1964); US Department of the Interior; Bureau of Mines, Report of Investigations, 6702. pages(1-23).
10. Fener, M., Kahraman, S., Bilgil, A. and Gunaydin, O.(2005). Rock Mechanics and Rock Engineering Austria, pages(1-15).
11. Goodman, R.E.(1980):"Introduction to Rock Mechanics". University of California at Berekly.
12. Hack, R and Huisman, M.(2002): "Estimating the Intact Rock Strength of a Rock Mass by Simple Means". Engineering Geology for Developing Countries. Proceeding of 9th Congress of the International Association for Engineering Geology and the Environment, Durban, South Africa.
13. Hassani, F.P., Scoble, M.J.J. and Whittaker, B.N.(1980): In Summers, D.A.(ed.) Proc.21st US Symposium, Rock Mech., Rolla, Missouri, pages: (543-553).
14. Hawkins AB (1986) Rock descriptions. In: Hawkins AB (ed) Site investigation practice: assessing BS 5930, Geological Society, pp 59–66.
15. Hawkins, A.B.(1998) :"Aspects of Rock Strength" Bull Eng Geol Env.

(1998) 57 : 17–30 7 Q Springer-Verlag.

16. ISRM (1985) Suggested methods for determining the point load strength. Int. Soc. for Rock Mech., Commission on Testing Methods; Working Group on Revision of the Point Load Test Methods. Int. J. Rock Mech. Min. Sci. Geomech. Abstr. 22 :51–60.
17. Laubscher,D.H.(1990). A geomechanics classification system for rating of rock mass in mine design.Journal South African Inst. of Mining and Metallurgy. 90, No. 10, pp. 257 - 273.
18. McNally,G.H.(1987):"Geotechnical Applications and Interpretation of Downhole Geophysical Logs".ACIRL Coal Research Report87-7, November, page 62.ISBN 0 86772 3297.
19. McNally,G.H.(1990):"The Prediction of Geotechnical Rock Properties from Sonic and Neutron Logs".Exploration Geophysics 21:pages(65-71).
20. Oyler,D.C.,Mark,C.andMolinda, G.M.(2008):NIOSH-Pittsburg Research Laboratory, Pittsburg,PA.
21. Pells ,P.J.N.(1975): Australian Geomechanic, G5 (N1) pages(54-56).
22. Rock Characterization Testing and Monitoring, International Society for Rock Mechanics Suggested Methods, Ed. E.T. Brown, Oxford, 1981.
23. Rusnak,J.andMark,C.(2000):19th Ground Control Conference in Mining, West Virginia University, pages(362-371).
24. Standard Test Method for Laboratory Determination of Pulse Velocities and Ultrasonic Elastic Constants of Rock. Standard Test Method for Rocks and Soils, ASTM Standards Vol.4.08, D2845-00 (2003).
25. Standard Test Method for Elastic Moduli of Intact Rock Core Specimens in Uniaxial Compression. Standard Test Method for Rocks and Soils, ASTM Standards Vol.4.08, D3148-02(2003).
26. Standard Test Method for Determination of the Point Load Strength Index of Rock. Standard Test Method for Rocks and Soils, ASTM Standards Vol.4.09,D 5731-95(2003).

ABBREVIATIONS AND NOTATIONS:

A	Minimum or initial cross sectional area
ASTM	American Society of Testing Material
D	Thickness of specimen or diameter
D_e	Equivalent core diameter
E	Young's Modulus
E_s	Modulus of elasticity
F	Force
G	Shear modulus
I_s	Point load strength
$I_{s(50)}$	Point load strength for 50 mm diameter core
ISRM	International Society for Rock Mechanics
k	Index to strength conversion factor
k	Bulk modulus
L	Length of specimen
P	Peak load
q_u	Compressive strength
R^2	The r-squared value
t	Travel time
UCS	Uniaxial compressive strength
V_p	Longitudinal wave velocity
W	Width of specimen
w_n	Natural water content
γ_t	Total unit weight
σ	Normal stress
υ	Poisson's ratio

EXPERIMENTAL INVESTIGATION OF LAMINAR NATURAL CONVECTION HEAT TRANSFER IN A RECTANGULAR ENCLOSURE WITH AND WITHOUT INSIDE PARTITIONS

Prof. Hussain Y. Mahmood
Mechanical Engineering Department
University of Baghdad

Ahmed Abdul Ameer Abdul Raheem
Mechanical Engineering Department
University of Baghdad

ABSTRACT

Experimental study has been conducted for laminar natural convection heat transfer of air flow through a rectangular enclosure fitted with vertical partition. The partition was oriented parallel to the two vertical isothermal walls with different temperatures, while all the other surfaces of the enclosure were insulated. In this study a test rig has been designed and constructed to allow studying the effect of Rayleigh number, aperture height ratio, partition thickness, the position of aperture according to the side walls and according to the height, the position of the partition according to the hot wall, and partition inclination. The experiments were carried out with air as the working fluid for Rayleigh number range ($5*10^7 – 1.3*10^8$) and aspect ratio of (0.5). 22 different configurations of partition were used in this study these are:

a) Undivided enclosure (no – partition).
b) (21) Cork partitions of different shapes.

Empirical correlations for average Nusselt number are obtained for the different cases tested. The results show that heat transfer is independent on the partition position according to the cold wall and according to the upper or lower walls, while it shows that heat transfer is sensitive to:

1. Rayleigh number (Ra), which increase with increasing Ra.
2. Aperture height ratio ($A_p=h_p/H$), which is found that when A_p= 5/6 (case 2,3), the reduction in heat transfer is 10.3%, while when A_p=1/2 (case 4,5), the reduction is 17.2% compared with the non partitioned enclosure.
3. Aperture position according to the height, which is found that when the aperture at the centre of the partition (case 13), the reduction in heat transfer is 16.7%, while when the aperture displaced to the upper surface (case 14), the reduction is 19% compared with the non partitioned enclosure.
4. Partition thickness (t), which is found that when t = 10 mm (case 4,5) the reduction in heat transfer is 17.2%, while when t = 150 mm (case 16) the reduction is 20.5% compared with the non partitioned enclosure.
5. Partition inclination (δ), which is found that the rate of heat transfer reduced with increasing δ as shown:
   a. For $\delta = 30^\circ$ toward the cold wall (case 22), the reduction in heat transfer is 18.2%.
   b. For $\delta = 45^\circ$ toward the cold wall (case 18), the reduction in heat transfer was 21.9%.
   c. For $\delta = 60^\circ$ toward the cold wall (case 20), the reduction in heat transfer is 30.2%.
   d. For $\delta = 30^\circ$ toward the hot wall (case 21), the reduction in heat transfer is 31.3%.
   e. For $\delta = 45^\circ$ toward the hot wall (case 17), the reduction in heat transfer is 40.7%.

f. For $\delta = 60^{\circ}$ toward the hot wall (case 19), the reduction in heat transfer is 42.1%.

الخلاصة

اجريتْ دراسة عملية لانتقال الحرارة بالحمل الطبيعي الطباقي لجريان الهواء في حيز مغلق بوجود حواجز ذات أشكال هندسية مختلفة وبعدم وجود حاجز، يتم وضع الحاجز بين سطحين أحدهما بارد والاخر ساخن بشرط ثبوت درجة الحرارة، بينما الاسطح الباقية معزولة حرارياً. الجانب العملي اشتمل على تصميم وبناء جهاز مختبري لدراسة تأثير رقم رايلي (Ra)، نسبة ارتفاع فتحة الحاجز الى ارتفاع الحيز (H_p)، سمك الحاجز (t)، موقع الفتحة في الحاجز، موقع الحاجز، و ميلان الحاجز. اجريت الدراسة العملية باستخدام الهواء كوسط ناقل للحرارة (مائع العمل) ولمدى عدد رايلي (٥×١٠^٧ – ١.٣×١٠^٨) ولنسبة ارتفاع الحيز الى طوله (النسبة الباعية) تساوي نصف. ولقد تم استخدام (٢٢) حاجزاً بمختلف الاشكال :

- ✓ غرفة مفردة بدون حاجز.
- ✓ حواجز من الفلين وعددها (٢١).

تم استنتاج علاقات تجريبية للحالات المختلفة التي درست، وقد بينت النتائج ان الحرارة المنتقلة لا تعتمد على موقع الحاجز نسبة الى الجدار البارد، بروز الحاجز من الاعلى او من الاسفل، وانما تعتمد على:

١) رقم رايلي (Ra) ، حيث وجد ان معدل انتقال الحرارة يزداد بزيادة رقم رايلي.

٢) نسبة ارتفاع فتحة الحاجز الى ارتفاع الحيز(A_p)، حيث وجد عندما تكون (A_p=5/6) (حالة ٢,٣)، ان الحاجز يقلل من انتقال الحرارة بنسبة %١٠.٣، بينما عندما (A_p=1/2) (حالة ٤,٥)، الحاجز يقلل من انتقال الحرارة بنسبة ١٧.٢%، مقارنة بانتقال الحرارة في الحيز بعدم وجود حاجز.

٣) موقع الفتحة نسبة الى الارتفاع، حيث وجد عندما تكون الفتحة في وسط الحاجز (حالة ١٣)، ان الحاجز يقلل من انتقال الحرارة بنسبة ١٦.٧%، بينما عندما تكون الفتحة قرب الجدار العلوي (حالة ١٤) الحاجز يقلل من انتقال الحرارة بمقدار ١٩%، مقارنة بانتقال الحرارة في الحيز بعدم وجود حاجز.

٤) سمك الحاجز (t)، حيث وجد عندما يكون سمك الحاجز ١٠ ملم (حالة ٤و٥)، ان الحاجز يقلل من انتقال الحرارة بمقدار ١٧.٢%، بينما عندما يكون سمك الجدار ١٥٠ ملم (حالة ١٦)، الحاجز يقلل من انتقال الحرارة بمقدار ٢٠.٥%، مقارنة بانتقال الحرارة في الحيز بعدم وجود حاجز.

٥) زاوية ميلان الحاجز (δ)، حيث وجد ان معدل انتقال الحرارة يقل بزيادة زاوية ميلان الحاجز.

- عندما يميل الحاجز بزاوية 30° باتجاه الجدار البارد (حالة ٢٢)، الحاجز يقلل من انتقال الحرارة بمقدار ١٨.٢%.
- عندما يميل الحاجز بزاوية 45° باتجاه الجدار البارد (حالة 18)، الحاجز يقلل من انتقال الحرارة بمقدار ٢١.٩%.
- عندما يميل الحاجز بزاوية 60° باتجاه الجدار البارد (حالة ٢٠)، الحاجز يقلل من انتقال الحرارة بمقدار ٣٠.٢%.
- عندما يميل الحاجز بزاوية 30° باتجاه الجدار الحار (حالة ٢١)، الحاجز يقلل من انتقال الحرارة بمقدار ٣١.٣%.
- عندما يميل الحاجز بزاوية 45° باتجاه الجدار الحار (حالة ١٧)، الحاجز يقلل من انتقال الحرارة بمقدار ٤٠.٧%.
- عندما يميل الحاجز بزاوية 60° باتجاه الجدار الحار (حالة ١٩)، الحاجز يقلل من انتقال الحرارة بمقدار ٤٢.١%.

Keywords: Laminar, Natural Convection, Rectangular Enclosure, Partitions.

INTRODUCTION

In the free convection, fluid motion is due to buoyancy effect, whereas in forced convection it is externally imposed. Buoyancy is due to the combined presence of a density gradient within the fluid and a body force that is proportional to the fluid density. As energy costs have escalated, there has been an increasing awareness of the impact that building design decisions can have an effect on energy consumption in the resulting structure. In addition to energy issue, the designer must also take into account aesthetic, economic, and functional requirements of the building. The most effective design solution depends on proper weighting of all relevant factors. In order for energy to have an appropriate weight in the decision, adequate accuracy in energy calculations must be provided. **Emery (1969)** studied experimentally free convection in a narrow vertical two – dimensional layer with a vertical baffle of variable height (l), (l/H = 0.25,0.5,0.75,0.9), the baffle was located, halfway between the hot and cold walls with equal spaces at the top and bottom. The experiments were carried out with pure glycerin (USP), the range of aspect ratio A=H/L = 10 - 40, and Rayleigh number (Ra_L) 1.5×10^6. Overall heat transfer measurements and temperature profiles were obtained; the result showed that there was no appreciable reduction of the overall free convection heat transfer although fairly significant changes do occurred in the local temperature profile. **Lin and Bejan (1983)** studied experimentally and analytically the phenomenon of heat transfer by natural convection in a rectangular enclosure fitted with an incomplete internal partition. The experiments were carried out in a water – filled enclosure with adiabatic horizontal walls and vertical walls maintained at different temperatures. Heat transfer measurements and flow visualization were conducted in the Rayleigh number range (10^9 – 10^{10}), for aperture height ratio h/H = 1, 1/4, 1/8, 1/16 and 0, where h and H were the height of the internal opening (in the partition) and the height of the enclosure, respectively. It was demonstrated that the aperture ratio h/H had a strong effect on both the heat transfer rate and the flow pattern. The heat transfer data were correlated satisfactorily by the equation:

$$Nu=\frac{0.366\times Ra^{0.25}}{Ap^{-0.75}+0.5} \qquad \text{............(1)}$$

The flow and temperature fields in this study were reported. **Sadiq Elias Abdullah (1997)** studied experimentally natural convection heat transfer in undivided and partially divided enclosures. The enclosure was fitted with vertical partition at midway between two vertical isothermal walls, one of which was heated and the other was cooled, while the other surface of the enclosure was insulated. Different configurations of partitions were used. The experiments were carried out using air as the working fluid over Rayleigh number range (Ra_H) of ($6*10^7$ – $1.22*10^8$), and aspect ratio of (0.5). The results showed that the location of the opening has a significant effect on the heat transfer together with the aperture height ratio, while a little effect of aperture width ratio was noticed. **Ahmed Fakhrey Khudheyer (1999)** investigated experimentally the heat transfer by natural convection in a rectangular enclosure fitted with a vertical adiabatic partition. The partition was oriented parallel to the two vertical isothermal walls. One of which was heated by heaters and the other cooled by water while all the other surfaces of the enclosure were insulated. The experiments were carried out with air as the working fluid for Rayleigh number range (Ra_H) (6×10^7 – 1.5×10^8) and an aspect ratio (height/ width) of 1/2, 14 different configurations of partition were used in this study.

For all these partitions the effect of their location was examined with respect to the hot wall by the ratio (x/L = 0.25, 0.5, 0.75), the results indicate that heat transfer was sensitive to the aperture height and it was independent of the aperture width and the upper or down extensions do not effect on the heat transfer. **Baïri, et-al (2007)** studied experimentally and numerically steady state natural convection in rectangular cavities filled with air. The active walls, hot and cold, of the cavity are maintained isothermal at temperatures T_h and T_c, respectively, and the other walls that close the cavity are adiabatic. Different angles of inclination $\emptyset$ of the cavity from 0º to 360º are considered. Two aspect ratios A= H/L = 0.75 and 1.5 are treated. The numerical study is carried out by means of the finite volume method and provides the thermal and dynamic maps of the fluid for several geometrical configurations obtained while varying $\emptyset$, A and $\Delta T = T_h - T_c$. the range of Rayleigh number, Ra_L from 10 to 10^8. The following relations was gotten for A=0.75 and 1.5, at different angles of inclination α, and $10^3 \leq Ra_L \leq 10^8$.

A (deg)	Correlation
0, 30, 360	$Nu_{ave}= 0.147\ Ra_L^{0.287}$
45, 135, 315	$Nu_{ave}= 0.130\ Ra_L^{0.305}$
60, 90	$Nu_{ave}= 0.133\ Ra_L^{0.304}$
270	$Nu_{ave}= 0.058\ Ra_L^{0.058}$

The main aim of the present investigation is to determine the effect of:

1. Rayleigh number (Ra) on heat transfer.
2. Different partition shapes on heat transfer.
3. Aperture height ratio (A_p) on heat transfer.
4. Partition thickness (t) on heat transfer.
5. The position of the aperture according to the side walls and according to the height on heat transfer.
6. The position of the partition according to the cold wall (L_p) on heat transfer.
7. Partition inclination (δ) on heat transfer.

EXPERIMENTAL APPARATUS AND PROCEDURE

A rig was designed and constructed to investigate the heat transfer by natural convection due to a temperature difference between hot and cold walls forming a rectangular cavity with air as the working fluid. Three individual heaters were used, each having a separate power control to maintain a uniform "isothermal" temperature over the entire hot wall surface. The apparatus dimensions were selected to simulate a living zone with inside dimensions of (300 mm) height, (300 mm) width, (600 mm) long, aspect ratio (A = H/L = 0.5), as shown in plate (1), and figure (1). The rig consists of the following parts:

1- Styrofoam enclosure
2- Plexiglas sheets
3- Hot wall assembly
4- Cold wall assembly
5- Different types and shapes of partitions
6- Instrumentation.

The Partitions

The partitions were inserted in the ceiling to divide the enclosure into two parts connecting each other by aperture at the partitions. 22 partitions classified into five groups as shown in figure (2).

Test Procedure:

The following steps were made in each test:

1- The required type of partition is positioned in place.
2- The power supply and water flow rate were set at the desired level.
3- The temperature of the heating plate was adjusted by varying the current supplied to the heaters with the help of a Rheostat for each heater.
4- During the transient condition, before reaching the steady state, the temperature of the hot wall was examined a number of times by means of thermocouples to check for a uniform temperature distribution over the hot wall, the current supplied to each heater was controlled for this purpose.
5- The steady state was identified by little or no change in the readings for (20-30) minuets.
6- After the experiments reaching steady state, the front and top insulations surfaces of the apparatus are removed.
7- Burning incense sticks are hung from the top of the enclosure near the cold wall to generate the smoke required for flow visualization technique.
8- A strong diffuse light was found to be the most appropriate light source for visualization the flow inside the enclosure. A diffuse light source was required to avoid light reflections from the enclosure walls. The enclosure was illuminated from the top, with the light diffusively reflected into the enclosure.
9- Capturing the smoke from the front surface.

A total of 110 tests were carried out for 22 different cases.

Calculation Procedure:

Analysis of Heat Transfer:

The electrical power input to the hot wall was measured by using the current and the voltage across each heater. The heat is transferred in the following ways:

1- Heat loss by conduction to the surrounding.
2- Heat exchange by radiation in the enclosure.
3- Heat transfer by natural convection in the enclosure.

Heat Loss by Conduction:

The conduction heat loss is assumed to consist of the following components:

A) Heat loss from the enclosure (excluding the hot and cold walls) to the surrounding.

Conduction shape factor method was used to estimate this loss. The following general equation, Bejan, A., (1994), was used.

$$q_{c1} = k\,(T_r - T_a)\left[\frac{2(H*L+W*L)}{X} + 2.16\,(L+H+W) + 1.2X\right] \qquad (2)$$

It is assumed that the wall was constructed from (50 mm) thick layer of Styrofoam with k =0.025 W/m.K.

$$q_{c1} = 0.025\,(T_r - T_a)\left[\frac{2(0.3*0.6+0.3*0.6)}{0.05} + 2.16\,(0.6+0.3+0.3) + 1.2*0.05\right]$$

$$q_{c1} = 0.4263 * (T_r - T_a) \quad W \qquad (3)$$

B) Heat loss from back side of the hot wall. The following equation was used to calculate this loss.

C) $q_{c2} = U.\,A_h\,(T_h - T_c)$ (4)

D) $$\frac{1}{U} = \frac{x_1}{k_1} + \frac{x_2}{k_2} + \frac{1}{h_\circ}$$

Where:

$h_\circ$ = Exterior convective heat transfer coefficient (ASHRAE 1981) = 3.08 W/m^2.K

x_1 = Styrofoam thickness = 50 mm

k_1 = Styrofoam thermal conductivity = 0.025 W/m.K

x_2 = Asbestos thickness = 20 mm

k_2 = Asbestos thermal conductivity = 0.17 W/m.K

$$\frac{1}{U} = \frac{0.05}{0.025} + \frac{0.02}{0.17} + \frac{1}{3.08}$$

q_{c2} = 0.0368 ($T_h - T_a$) W (5)

Total heat loss by conduction was

($q_c = q_{c1} + q_{c2}$) (6)

Heat Exchange by Radiation:

Absorption factor method was used in calculating the heat transfer by radiation from the hot wall to other walls. The general equation used was that given by Sucec, (1985):

$$(q_r)_j = E_j A_j - \sum_{i=1}^{n} B_{ij} * A_i * E_i \qquad (7)$$

Where:

A_i = Area of i_{th} surface (m^2)

$$E_i = \sigma \,.\, e_i \,.\, T_i^4$$

Where:

ϵ_i = Emissivity of i_{th} surface

T_i = Temperature of i_{th} surface (K)

B_{ij} = Absorption factor which is defined as the fraction of radiant energy emitted by the i_{th} surface which is eventually absorbed by the j_{th} surface after complex reflection pattern.

Absorption factor is obtained from solving the equation:

$[k_{ij}]$ $\{B_{ij}\}$ = { - ϵ_i F_{ij} }

Where:

$k_{ij} = F_{ij}\, \rho_i$

ρ_i = Reflectivity of i_{th} surface

ρ = 0.8 for Aluminum surfaces

ρ = 0.06 for Styrofoam surfaces

F_{ij} = Shape factor between walls

Heat Transfer by Natural Convection in the Enclosure:

The net heat transfer by natural convection between two walls was obtained from the following equation:

$q_{conv} = I * V^{-} - (q_c + q_r)$ (8)

The convection heat transfer coefficient was calculated as follows:

$q_{conv} = h.\, A_h\, (T_h - T_c)$ (9)

$$h = \frac{q_{conv}}{A_h(T_h - T_c)} \qquad (10)$$

Dimensionless Groups:

The results have been analyzed with the help of the well known dimensionless parameters given below:

Prandtl Number = $\dfrac{C_p \mu}{k_f}$

Rayleigh Number =

$$\frac{\beta * g * \Delta T * H^3}{\upsilon^2} * \frac{C_p * \mu}{K_f}$$

Nusselt Number = $\dfrac{h * H}{k_f}$

The properties were interpolated from table given by Sucec (1985), depending on a reference temperature given by:

$T_r = (T_h - T_c) * 0.5$

RESULTS AND DISCUSSION

A summary of the results and correlations of the present work are given in table (1). Natural convection heat transfer in enclosure is calculated by these empirical correlations. The general formula of these empirical correlations is:

$$Nu = C.Ra^n$$

Enclosure without Partition:

This case is the reference for the other cases. The heat transfer rate increases with increasing Rayleigh number due to increase temperature difference (ΔT). The present results are compared with those of **Sadiq Elias (1997)** since these studies are curried out in a small test cell using air as the working fluid and at the same range of Rayleigh number. The comparison is shown in figure (3). The comparison shows good agreement between the two experimental works, the percentage deviation was found to be about (0.5 %).

Group One:

The heat transfer results and correlations are shown in figure (4). The partition was found to reduce the heat transfer compared with the non partitioned room as shown:

A) Case (2,3); Ap = 5/6; Reduction = 10.3%
B) Case (4,5); Ap = 1/2; Reduction = 17.2%
C) Case (16); Ap = 1/2; Reduction = 20.5%

The reduction was produced as a result of relatively static pocket of hot fluid which was trapped in the upper zone of the hot zone of the test cell when the partition was at the upper wall. The trapped hot fluid inhibits convective heat transfer from upper zone of the hot wall, (see plate (2.a)). While when the partition was at the lower wall the cold fluid will trapped in the lower zone of the cold wall (see plate (2.b,c))

The comparison between case (2) and case (3), and between case (4) and case (5), explain that for the same distance between partition aperture and the upper surface or the lower surface, there is no effect on heat transfer.

The comparison between cases (2,3) and cases (4,5) represent the effect of the aperture height ratio (A_p) on natural convection heat transfer. It is found that the aperture height ratio has a significant effect on the heat transfer, the reason of that is the velocity of fluid is very low near the partition and it is larger at the aperture, therefore a part of fluid moving from the hot zone to the cold zone, heat is transferred with this moving fluid, due to buoyancy force which occurs because of the difference between hot and cold wall, because the amount of fluid transfer depends on aperture area so the amount of heat transfer also depends on aperture area on the partition.

The comparison between cases (4,5) and case (16) explain the effect of partition thickness on the convection heat transfer, the figure shows a little effect in heat transfer it shows that case (16), (t=150 mm) reduce heat transfer by about (3.3%) compared with cases (4,5), (t=10mm).

Group Two:

Figure (5) shows heat transfer results and correlations for group two.

The comparison between case (7) and case (8), explain the effect of the position of aperture according to the side wall it is found that for case (7) (aperture at side) the heat transfer reduction is about (23.2%) compared with case of non partition room, while for case (8) (aperture at centre) the reduction in heat transfer was about (20.1%). The drop in heat transfer in case (7) is larger than that for case (8), this reduction was expected since the blockage to air flow is greatest, in addition to the air trapped in the upper third of the hot zone of the test cell there is relatively static pocket of hot fluid which was trapped in opposed side of the aperture side.

In case (6) the partition found to reduce the heat transfer by about (9.1%) respect to the non partitioned room.

Group Three

Heat transfer results and correlations are shown in figure (6). The comparison between case (9) and case (10), and between case (13) and case (15) (in group four) represent the effect of aperture distribution according to the vertical axis for multi-aperture. It is found that for case (9) the heat transfer reduction is about 15.5%, while for case (10) the reduction was about 18% compared with the case of non partition. The reduction was expected since the fluid motion increase near the upper and lower surface and decrease near the centre of the enclosure.

Case (11) shows that the reduction in heat transfer is smaller than in case 9 and 10 it is about 12.2%, it is due to increase in aperture area.

Group Four:

Figure (7) shows the heat transfer results and correlations for this group. The partition was found to reduce the heat transfer compared with the non partitioned room as shown:

A) Case (15); Reduction = 10.6%

B) Case (12); Reduction = 13.5%

C) Case (13); Reduction = 16.7%

D) Case (14); Reduction = 19%

The comparison between case (13) and case (14), explain the effect of the distance between the aperture centre and the partition centre. The figure shows that the rate of heat transfer decreases when this distance increase. The reason of this effect is due to air falling and traps down in the cold zone.

Group Five:

Heat transfer results and comparison are shown in figure (8). This group explain the effect of the partition inclination at (δ = 30˚, 45˚,60˚) according to the hot wall, and at (30˚, 45˚, 60˚) according to the cold wall. The partition was found to reduce the heat transfer compared with the non partitioned room as shown:

- Case (22); Reduction = 18.2%
- Case (18); Reduction = 21.9%
- Case (20); Reduction = 30.2%
- Case (21); Reduction = 31.3%
- Case (17); Reduction = 40.7%
- Case (19); Reduction = 42.1%

The figure shows:

A- At the same angles [case (17, 18), case (19,20) and case (21, 22)] when the partition inclines toward the hot wall, the rate of heat transfer decrease more than that when the partition incline toward cold wall. Because in case when the partition inclines toward hot wall the partition obstructs the motion of fluid more than when the partition inclines to the cold wall. in addition to the air trapped in the upper part of the cold zone of the test cell there is relatively static pocket of cold fluid which was trapped in opposed side of the aperture side.

B- For cases when the partition inclines toward the hot wall, [case (17), case (19) and case (21)], the slope of the curve increase when the angle decrease. This mean that at low temperatures the rate of heat transfer is very low, and at high temperatures the rate of heat transfer become very high.

C- For cases when the partition inclines toward the cold wall, [case (18), case (20) and case (22)], the rate of heat transfer increase, when the angle decrease. The reason of that is due to the separation occured in the upper zone between the partition and the hot wall. And this separation increase when the angle increase (see plate 3, 4).

CONCLUSIONS

The conclusions of this investigation can be summarized as follows:

1- The aperture height ratio (A_p) have a significant effect on heat transfer. Its increase with increases aperture height, which is found that when A_p= 5/6 (case 2,3), the reduction in heat transfer was 10.3%, while when A_p=1/2 (case 4,5), the reduction was 17.2% compared with the non partitioned enclosure.

2- The position of the aperture near the upper surface or near the lower surface didn't affect on heat transfer for the same distance.

3- The partition's thickness has a little effect on heat transfer, and it is found that when t = 10 mm (case 4,5) the reduction in heat transfer was 17.2%, while when t = 150 mm (case 16) the reduction was 20.5% compared with the non partitioned enclosure.

4- When the aperture position change from the centre toward the side wall the natural convection heat transfer decreases, and it is found that when the aperture at the centre of the partition (case 13), the reduction in heat transfer was 16.7%, while when the aperture displaced to the upper surface (case 14), the reduction was 19% compared with the non partitioned enclosure.

5- Natural convection heat transfer depend on the position of the aperture according to the height. Its increases when the aperture near the centre.

6- For multi-apertures the rate of heat transfer increases when the apertures distributed near the upper and lower walls.

7- The position of the partition according to the hot wall didn't affect on heat transfer.

8- For the case of partition inclination:

A) Heat transfer increases when the partition inclined toward the cold wall for the same angle.

B) Increases the angle of inclination according to the upper wall decrease the heat transfer.

C) When the partition inclined toward the hot wall, its found that the slope of curve increases when the angle of inclination decrease.

which is found that the rate of heat transfer reduced with increasing δ as shown:

- For $\delta = 30^{\circ}$ toward the cold wall (case 22), the reduction in heat transfer was 18.2%.
- For $\delta = 45^{\circ}$ toward the cold wall (case 18), the reduction in heat transfer was 21.9%.
- For $\delta = 60^{\circ}$ toward the cold wall (case 20), the reduction in heat transfer was 30.2%.
- For $\delta = 30^{\circ}$ toward the hot wall (case 21), the reduction in heat transfer was 31.3%.
- For $\delta = 45^{\circ}$ toward the hot wall (case 17), the reduction in heat transfer was 40.7%.
- For $\delta = 60$ toward the hot wall (case 19), the reduction in heat transfer was 42.1%.

REFERENCES

Ahmed Fakhrey Khudheyer, "Experimental study into natural convection heat transfer coefficient in undivided and partially divided enclosures" M. Sc. Thesis, University of Technology, Mechanical Engineering Department, 1999.

Baïri A., Laraqi N., J. M. García J. M., "Numerical and experimental study of natural convection in tilted parallelepipedic cavities for large Rayleigh numbers", Experimental Thermal and Fluid Science, Vol. 31, pp. 309-324, 2007.

Bejan, A., "A synthesis of analytical results for natural convection heat transfer across rectangular enclosures", Int. J. Heat Mass Transfer, Vol. 23, pp. 723-726, 1979.

Emery A. F., "Exploratory studies of free convection heat transfer through an enclosed vertical liquid layer with vertical baffles", J. Heat Transfer, Vol. 91, pp. 163-165, 1969.

Lin N. and Adrian Bejan, "Natural convection in a partially divided enclosure", Int. J. Heat Mass Transfer, Vol. 26, No. 12, pp. 1867-1878, 1983.

Sadiq Elias Abdullah, "Buoyancy–driven convection in undivided and partially divided enclosures", M. Sc. Thesis, University of Technology, Mechanical Engineering Department, July 1997.

Sucec A., "Heat Transfer" WM. C. Broun publishers, Dubuque, Iowa,1985.

NOMENCLATURE

Latin Symbols

Symbol	Description	Units
A	Aspect ratio (H/L)	–
A_h	Area of hot wall = 0.09 m^2	m^2
A_c	Area of cold wall	m^2
A_p	Aperture height ratio (h_p/H)	–
A_w	Aperture width ratio (w_p/H)	–
E_i	Emissive power of i_{th} surface	W/m^2
g	Gravity acceleration	m/s^2
Gr_H	Grashof number	–
h	Heat transfer coefficient	$W/m^2.\,^oC$
h_p	Aperture height	m
H	Enclosure height	m
I	Current	Amp.
k	Thermal conductivity	$W/m.\,^oC$
L	length of enclosure	m
L_p	Distance between cold wall and partition	m
Nu_{ave}	Average Nusselt number	–
p	Pressure	N/m^2
Pr	Prandtl number	–
q_{conv}	Heat lost by convection	W
q_c	Rate of heat lost by conduction	W
q_r	Rate of heat lost by radiation	W
Ra_H	Rayleigh number	–

t	Partition thickness	m
T	Temperature	^oC
T_c	Temperature of cold wall	^oC
T_h	Temperature of hot wall	^oC
T_r	Reference temperature $(T_h+T_c)/2$	^oC
T_∞	Ambient temperature	^oC
U	The overall heat transfer coefficient	$W/m^2.\,^oC$
$\mathbf{V}^{-}$	Voltage	volt
w_p	Aperture width	m
W	Enclosure width	m
x,y	Cartesian coordinate	m

Creak Symbols

Symbol	Description	Units
α	Thermal Diffusivity	$[m^{2} s^{-1}]$
δ	Angle of partition inclination	degree
$\emptyset$	Angle of enclosure inclination	degree
β	Coefficient of volume expansion	1/K
μ	Dynamic viscosity	kg/m.s
υ	Kinematic viscosity	m^2/s
σ	Stefan Boltizmann constant	W/m^2K^4
Δ	Difference between two values	–

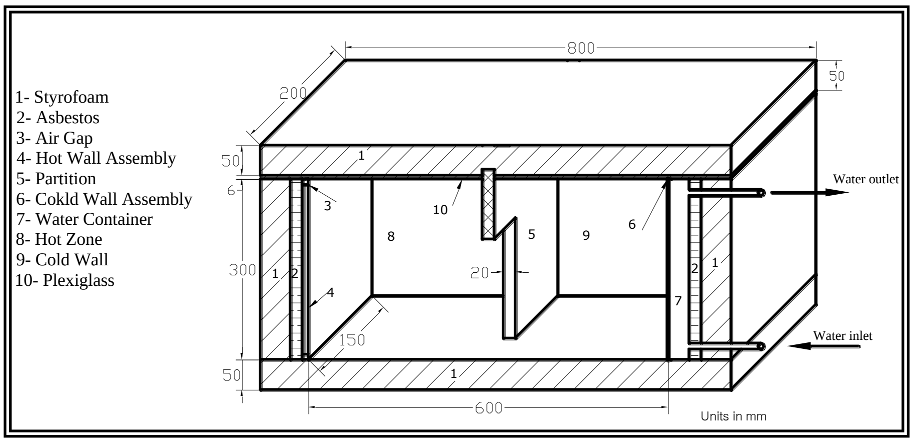

Fig.1: Cross Section of the Test Rig

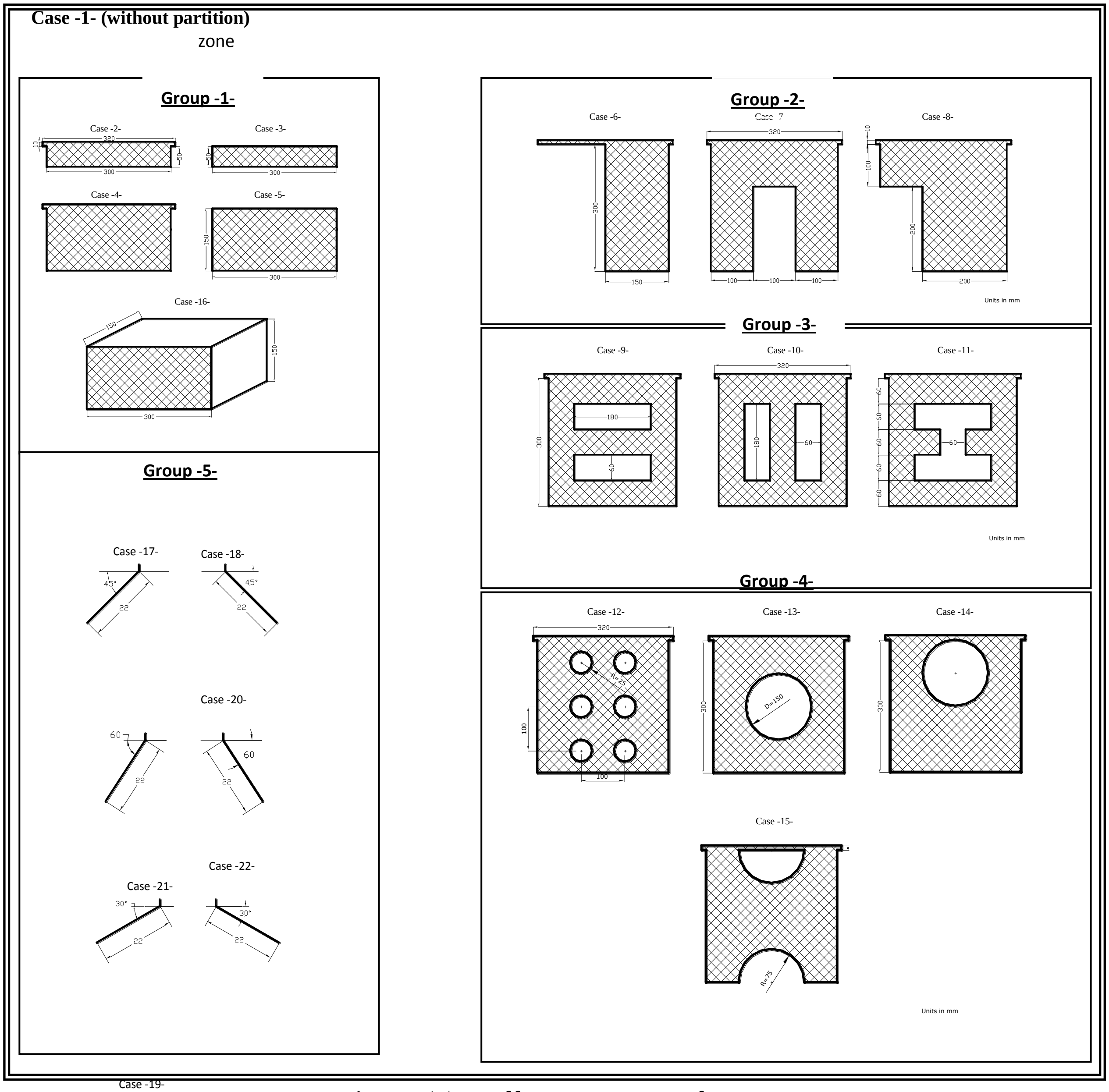

Figure (2): Different Patterns of Partitions

Table (1) Summary of Results

Case No.	Case Study	Nu = C.Ra^n		$A_p = \frac{h_p}{H}$	$A_w = \frac{w_p}{W}$
		C	n		
1	Without Partition	0.00282	0.5027	1	1
2,3		0.00045	0.5972	1/6	1
4,5	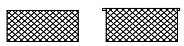	0.00031	0.6139	1/2	1
6	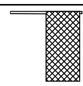	0.00097	0.5555	1	0.5
7	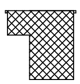	0.00011	0.6659	2/3	1/3
8	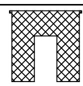	0.00018	0.6397	2/3	1/3
9	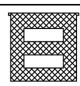	0.00101	0.5496	2/5	3/5
10	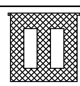	0.00132	0.5334	3/5	2/5
11	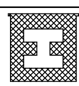	0.00078	0.5659	3/5	3/5
12	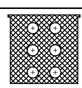	0.00329	0.4864	1/2	1/3
13	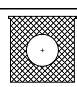	0.00159	0.5240	1/2	1/2
14	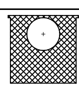	0.00166	0.5204	1/2	1/2
15	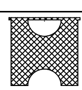	0.00172	0.5237	1/2	1/2

١٦	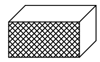	0.00036	0.6035	1/2	1
17	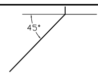	1.50638E-6	0.8860	1/2	1
18	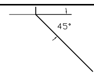	0.00044	0.5904	1/2	1
19	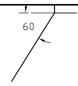	1.2276E-5	0.7702	2/3	1
20	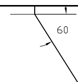	0.00017	0.6352	2/3	1
21	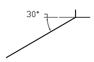	3.53956E-7	0.9733	1/3	1
22	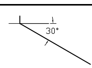	0.00055	0.5813	1/3	1

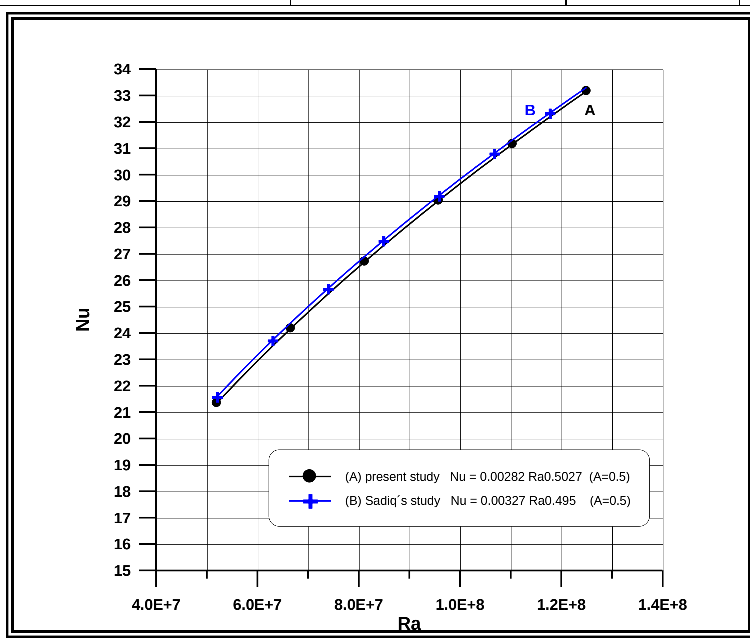

Figure (3) A comparison of average Nusselt Number Results in a single room

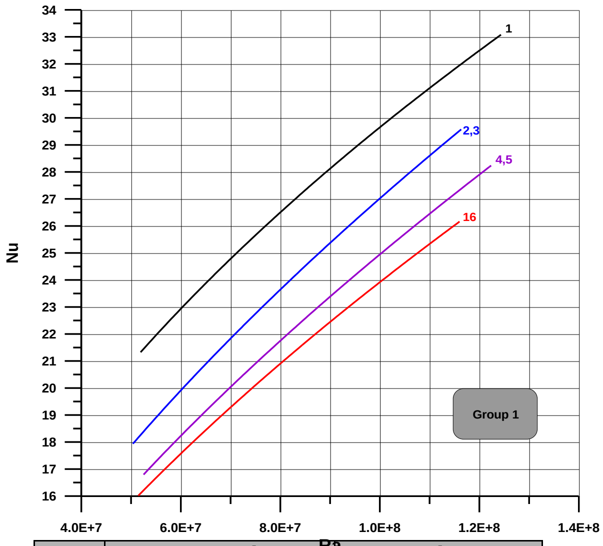

Case	Case Study	Correlation
1	Without Partition	Nu = $0.00282Ra^{0.5027}$
2,3	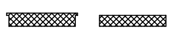	Nu = $0.00045Ra^{0.5972}$
4,5	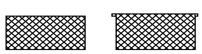	Nu = $0.00031Ra^{0.6139}$
16	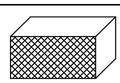	Nu = $0.00036Ra^{0.6035}$

Figure (4) a Comparison of Heat Transfer Results for Group One.

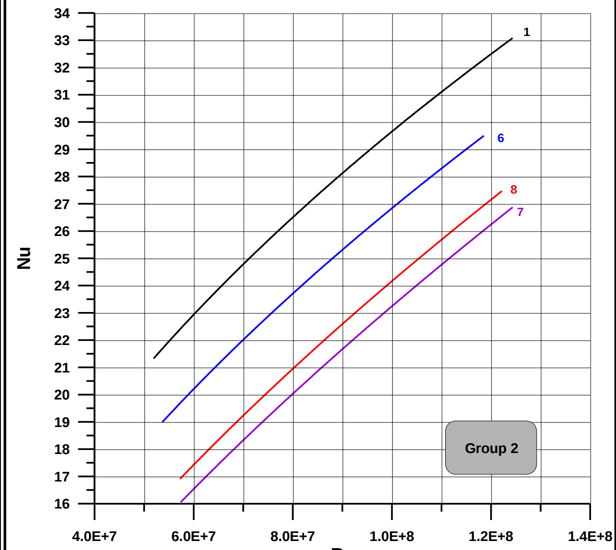

Case	Case Study	Correlation
1	Without Partition	Nu = $0.00282Ra^{0.5027}$
6	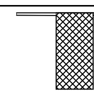	Nu = $0.00097Ra^{0.5555}$
8	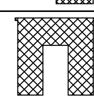	Nu = $0.00018\ Ra^{0.6397}$
7	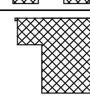	Nu = $0.00011\ Ra^{0.6659}$

Figure (5) a Comparison of Heat Transfer Results for Group Two.

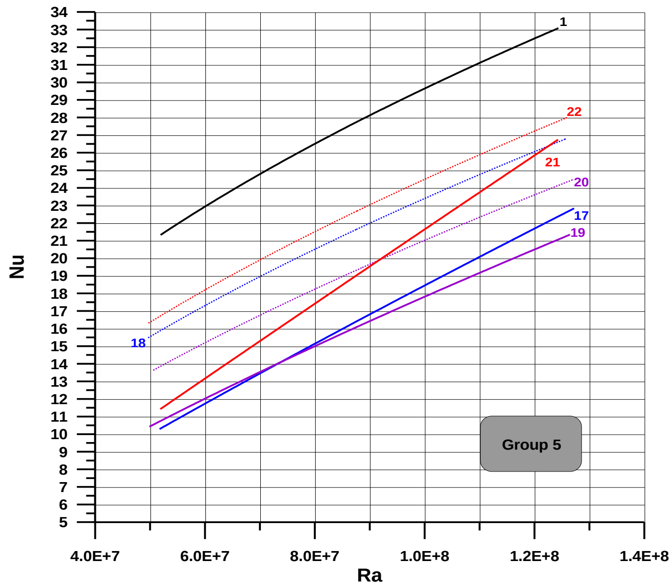

Case	Case Study	Correlation
1	Without Partition	$Nu = 0.00282Ra^{0.5027}$
22	30°	$Nu = 0.00055Ra^{0.5813}$
18	45°	$Nu = 0.00044Ra^{0.5904}$
20	60	$Nu = 0.00017Ra^{0.6352}$
21	30°	$Nu = 3.5396E\text{-}7Ra^{0.9733}$
17	45°	$Nu = 1.5064E\text{-}6Ra^{0.8860}$
19	60	$Nu = 1.2276E\text{-}5Ra^{0.7702}$

Figure (8) a Comparison of Heat Transfer Results for Group Five.

Plate (1) Experimental Apparatus

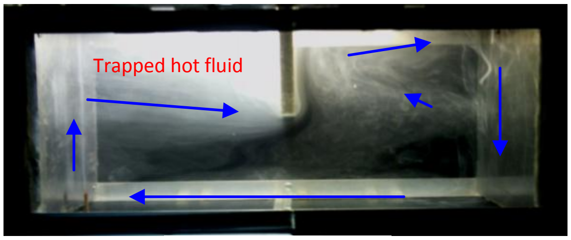

A) Ra = 8.24234*10^7

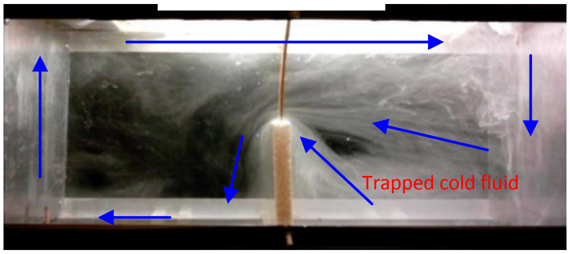

B) Ra = 5.25016*10^7

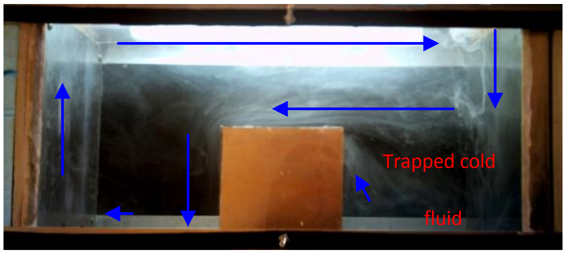

C) Ra = 4.97793*10^7

Plate (2) Flow Patterns using smoke visualization

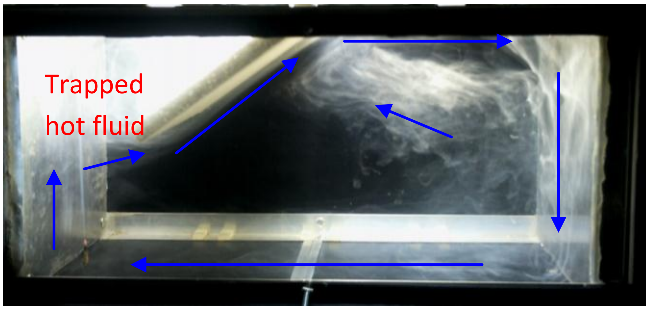

A) Ra = $5.18627*10^{7}$

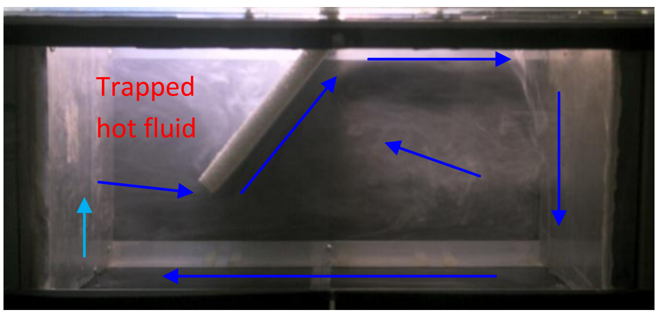

B) Ra = $8.84108*10^{7}$

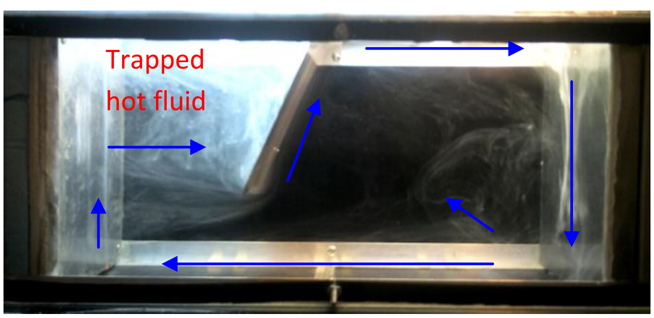

C) Ra = $4.98698*10^{7}$

Plate (3): Flow Patterns Using Smoke Visualization (Partitions Inclined Toward Hot Wall)

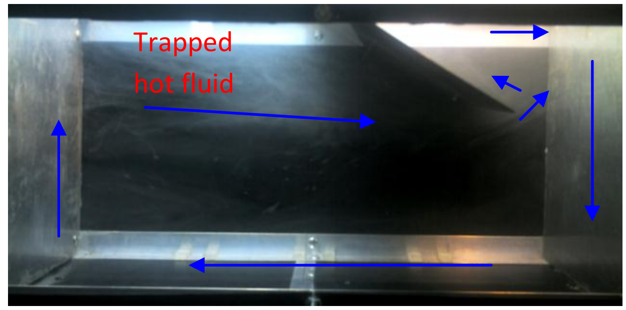

A) Ra = $4.96998*10^{7}$

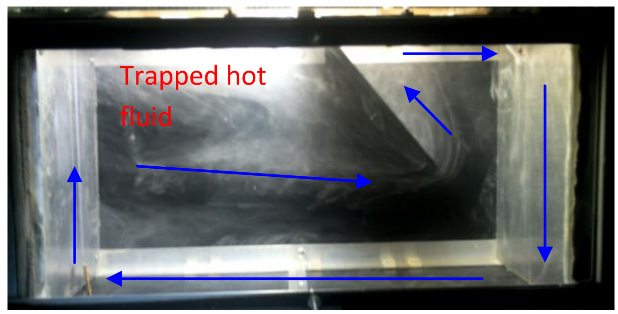

B) Ra = $7.2608*10^{7}$

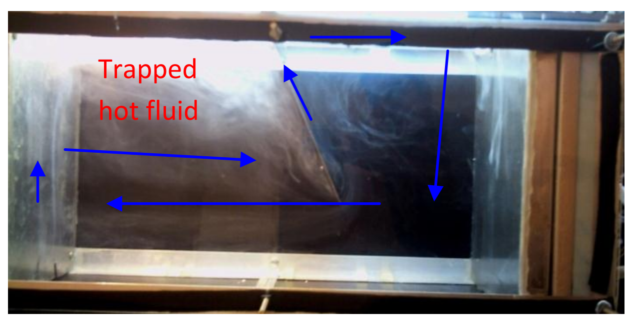

C) Ra = $8.97188*10^{7}$

Plate (4): Flow Patterns Using Smoke Visualization (Partitions Inclined Toward Cold Wall)

التكامل البيئي- الاجتماعي - الجمالي في تصميم المجمعات السكنية لنمط متعدد الاسر - تقويم التجربة العراقية –

أ.د. بهجت رشاد شاهين سنا لطيف أحمد
قسم الهندسة المعمارية – جامعة بغداد

المستخلص

يعد مبدأ التكامل البيئي- الاجتماعي - الجمالي من المبادىء المهمة في تصميم المجمعات السكنية لنمط متعدد الاسر لما لها من اهمية في وقتنا الحالي بسبب تفاقم ازمة السكن ، وللوصول الى تصاميم تقترب من نمط الاسكان منفرد الاسرة ، مع الاخذ بالمعلومات والمعطيات والحلول الناجعة والمتراكمة عبر خبرات سنين طويلة والموجودة في تراثنا العربي للمحلة السكنية التقليدية، على هذا الاساس اعتمد البحث في تقديمه للمشكلة البحثية المتمثلة في "**غياب المعرفة الشمولية وندرة وجود دراسات متخصصة بالتكامل البيئي - الاجتماعي - الجمالي في تصميم المجمعات السكنية لنمط متعدد الاسر** " ، حيث ان معظم الدراسات السابقة تخصصت في مقوم واحد من هذه المقومات واهملت البقية ولم توجد مراعاة لكون العملية التصميمية تحتاج لهذا التكامل لجميع هذه المقومات للوصول الى تصميم ينتمي للبيئة ويلبي احتياجات الساكنين ويعبر عنهم .و يفترض البحث **انه للوصول الى تصميم ناجح للمجمعات السكنية لنمط متعدد الاسر يجب مراعاة التكامل بين المقومات البيئية -الاجتماعية - الجمالية اثناء التصميم وللمنطقة التي نصمم فيها وان فقدان التكامل بين هذه المقومات سيسبب في عدة مشاكل للسكان.**

والهدف الاستراتيجي للبحث هو **الوصول الى بيان اهمية مفهوم التكامل بين العوامل البيئية - الاجتماعية - الجمالية في تصميم المجمعات السكنية المعاصرة لنمط متعدد الاسر** ويتفرع من هذا الهدف الاستراتيجي أهداف فرعية وهي:

1- بيان اهم مفردات القيم (البيئية- الاجتماعية - الجمالية) للمحلة السكنية التقليدية وصياغتها بشكل معاصر.

2- بعد معرفة اهم المفردات الفاعلة لكل ناحية من نواحي القيم وصياغتها بشكلها المعاصرسنستخدمها كمقياس تحليلي لتقويم التجربة العراقية.

ABSTRACT

The concept of (Environmental- social - aesthetical) integration is considered one of the most important concepts in any architectural design and any building, especially housing complexes The pattern of multi-family because of their importance at the present time due to the worsening housing crisis, and to reach out to the designs approaching a single family housing pattern, and that quite apart from what is happening now in our cities, where the designs of housing complexes have been taken from the formal imitation ,a curriculum, and ready technological solutions an easy way, that drifted it away from its special identity, and led to the neglect of information, data and solutions and expertise accumulated over many years, in the Arab heritage of the traditional residential district, and on this basis the problem of research based on the **"lack of inclusive knowledge and the scarcity of specialized studies of (Environmental – social - aesthetical) integration in designing housing complexes The pattern of multi-family ",** as most previous studies, specializing in one of these elements and neglected or passed by unnoticed the others and there have not taking into account the fact that the designing process needs the integration of all these elements to get to a design belongs to the environment and fulfill the needs of residents and reflects them.

The strategic objective of this research is to demonstrate the importance of the concept of **integration** of**(Environmental – social - aesthetical)aspects in designing housing complexes The pattern of multi-family** (through the global experience and local) and branches of this strategic objective, several sub-goals:

1 - Explain the most important items of(environmental, social, aesthetical) values of the traditional residential district and put it in contemporary form.

2 - After knowing the most important active vocabulary for each aspect of the values and put it in contemporary form we will use it as a measurement to evaluate the Iraqi experience .

ReSearch took from the traditional residential district a material for study and analysis to reach the main advantages and features of the environment for use in our contemporary designs not by formal imitation, but we must go to a deeper level to the thought associated with this traditional environment and try to simulate the characteristics of thought, which produced such architecture in our quest towards a design style housing complexes to multi-families reflect this heritage and continuing with it and fulfill the needs of residents and ensure the necessary integration among the(environmental- social - aesthetical) aspects, within the developments of our time and harness of techniques and technology, within the framework of thought integral.

- تمهيد

يعد التكامل من المفاهيم المهمة في تصميم المجمعات السكنية ولبيان هذه الاهمية سنتناول اولا مفهوم التكامل وبعدها سنتعرف على تأثيرات فقدان التكامل بين مفردات القيم (البيئية والاجتماعية والجمالية)على سكان المجمعات السكنية بشكل خاص وذلك لان فقدان التكامل سيتسبب باهمال احتياجات السكان وعدم تلبيتها في التصميم الناتج ، وكيفية تاثير ذلك على البيئة العمرانية للمدينة ككل عندما يتخذ السكان مسؤولية توفير المسكن الملائم والملبي احتياجاتهم على عاتقهم مما ينتج عنه مشاكل عمرانية والتي تتألف من اشكاليات كثيرة كلها تؤثر سلبا على المدينة والسكان ثم سنتعرف على اهم خصائص المحلة السكنية التقليدية ومن النواحي(البيئية- الاجتماعية - الجمالية) لاستخراج اهم المفردات الفاعلة لكل ناحية من نواحي القيم واستخدامها لتقويم التجربة العراقية .

1-1 مفهوم التكامل

لم يتم ادراك عملية التكامل في الفعالية البنائيـ ـ ـ ـة (بشطريها التصميمي والتنفيذي) الا مؤخرا فمفردة التكامل ليس لها معنى محدد ضمن الفعالية البنائية وكذلك لم تدرس بصورة واعية، ففعالية التكامل لها مدلول شامل كلي يعود الى المبنى ككل، فقد افترض (Rush 1986,P.5-16,) ان كل بناية في الوجود متكاملة ولكن نادرا ما يكون هذا التكامل واعيا ، حيث ان تصميم المبنى هو تحقيق التوازن بين مجموعة من الجوانب المؤثرة في الشكل الناتج ***(كالجوانب الوظيفية والاجتماعية والانشائية والبيئية والجمالية)*** تتكون العملية التصميمية للمبنى***(او المجمع السكني)*** من مجموعة من الانظمة التي لها متطلبات معينة وقد لايحصل التوافق في تحقيق المتطلبات ، فيصعب على التصميم ان يلبي متطلبات كل نظام بصورة كاملة ، الا ان التكامل النهائي الذي يصبح عليه تصميم المبنى يجب ان يحقق اكبر قدر من متطلبات تلك الانظمة، لذا فان التكامل نسق يحوي على انظمة(السهيري ، ايار ،1999) .

1-2 نتائج فقدان التكامل في التصميم

ان عملية تصميم المجمع السكني هي عملية معقدة تدخل فيها عدة جوانب والتي حاول البحث اختصارها في ثلاث قيم (القيم البيئية -الاجتماعية -الجمالية) وان اي عملية تصميمية يجب ان تكون فيها درجة معينه من التكامل وخصوصا تصميم المسكن الذي يجب ان يتمتع بافضل درجة من درجات التكامل للوصول الى اهم اهداف هذا التصميم وهو **تحقيق احتياجات السكان** ، حيث ان فقدان التكامل ينتج عنه مشاكل معقدة كما في الشكل (1) .

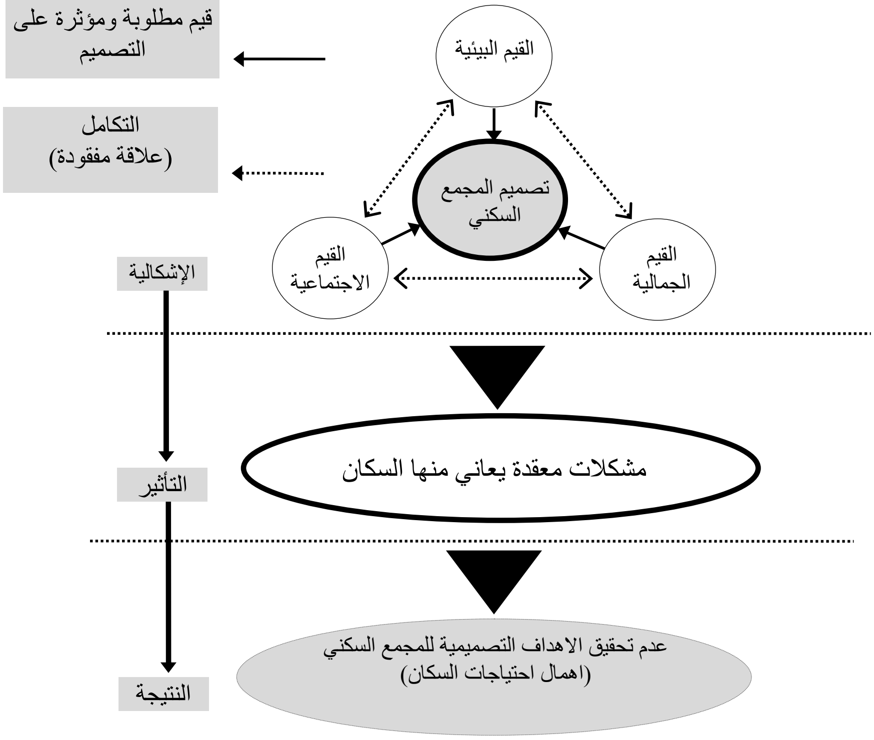

الشكل (1) تأثير فقدان التكامل (البيئي-الجمالي-الاجتماعي)على تصميم المجمعات السكنية
المصدر: الباحثة عن (الاكيابي ونوبي ،2002،ص115)

- وان النتائج السلبية عن عدم تحقيق احتياجات السكان نتيجة لفقدان التكامل ستؤدي الى ان يأخذ الافراد مسالة توفير المسكن الملائم لهم على عاتقهم مما سينتج مشاكل اخرى كما في الشكل (2).

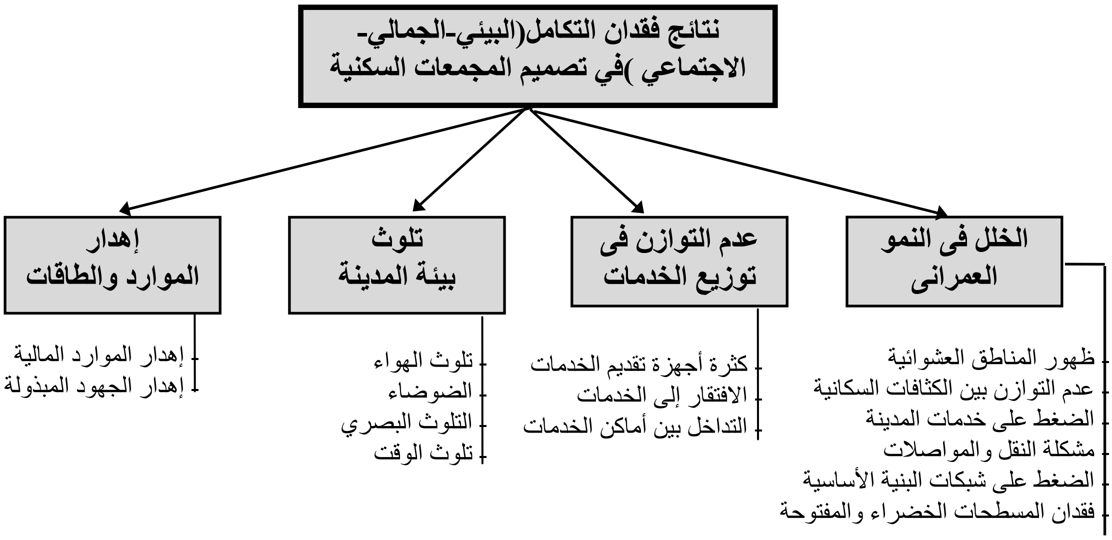

شكل (2) النتائج السلبية لفقدان التكامل (البيئي-الجمالي-الاجتماعي) في تصميم المجمعات السكنية المصدر: الباحثة عن (الاكيابي ونوبي ،2002،ص116)

1-2-1 الخلل فى النمو العمراني:

سعياً وراء الحصول على المسكن فى ظل الزيادة السكانية واتخاذ الافراد مسؤولية توفير المسكن على عاتقهم وبدون وجود ضوابط نمت المدن عمرانياً بشكل غير متوازن وبشكل يفتقر للتكامل بين القيم الاساسية التي يبحث عنها السكان، وقد أخذ النمو كلا الاتجاهين الاتيين:

* الاتجاه الأول: الامتداد العمراني الأفقي فى مناطق ملاصقة للمدن القائمة وعلى أطرافها.

* الاتجاه الثانى: الامتداد العمرانى الرأسى، وهو بناء العمارات السكنية إلى أقصى ارتفاع تسمح به قوانين البناء، وذلك فى كل مناطق المدينة المتاحة للبناء.

وقد نتج عن هذين الاتجاهين نمو عمرانى غير متوازن، أحدث خللاً فى عملية التنمية العمرانية للمدينة، وأدى إلى حدوث مشاكل فى المدينة من أهمها:

1- **ظهور المناطق العشوائية**
2- **عدم التوازن بين الكثافات السكانية على مستوى المدينة**
3- **الضغط على خدمات المدينة**
4- **فقدان المسطحات الخضراء والمفتوحة**

2-2-1 عدم التوازن فى توزيع الخدمات المختلفة بالمدينة:

يظهر قطاع الخدمات فى صورة مراكز متدرجة لها مستويات مختلفة طبقاً لنطاق تأثيرها وحجم ونوع الخدمات التى تؤديها لرواد هذا المركز وعدد السكان ونسبة ترددهم، فهناك مراكز للخدمات والمتطلبات اليومية والأسبوعية (فى مراكز المحلات السكنية)، ومراكز الخدمات الأسبوعية والشهرية (فى مراكز الأحياء)، ومراكز الخدمات الشهرية والسنوية (فى مراكز المدن الرئيسية)، ومراكز خدمات العابرين وليس المترددين (مراكز الخدمات الإقليمية على الطرق الرئيسية)، ومراكز الخدمات الموسمية للأنشطة السياحية(سعيد على 1993م.)

ويجب أن تتواجد المرافق الخدمية فى مواقع مناسبة وعلى مسافات قصيرة من المساكن، إذا أريد لسكانها أن يتمتعوا بمتطلبات الحماية عن طريق توفير وسائل الراحة والخدمات وسهولة الاتصال وسلامته، وذلك من خلال وجود تنسيق وظيفي بين الجهات القائمة على توفير الخدمات وإدارتها وبين الجهات المسؤولة عن توفير المساكن وفق المخطط العام الخاص بكل مدينة، فاذا اقام الافراد مساكنهم في مناطق غير مخصصة للسكن(المناطق العشوائية) فسيفقدون التمتع بهذه الخدمات (الشيخلى، 1986م،ص101)، ***والنتيجة الحتمية لعدم التنسيق بين هذه الأجهزة المختلفة هي اما كثرة أجهزة تقديم الخدمات وتضارب اختصاصاتها ، وبالتالي التأثير السلبي على كفاءة هذه الخدمات، أوالافتقار إلى الخدمات فى بعض المناطق وخصوصا المناطق العشوائية كما ذكرنا سابقا و بسبب غياب التنسيق والتكامل فى توفير الخدمات يحدث تداخل بين الخدمات*** مما يؤثر بشكل عكسي على الحياة فى المدينة ككل.

3-2-1 تلوث بيئة المدينة:

نظراً للامتداد العمراني المتضخم أفقياً ورأسياً يحدث الزحام فى الطرق والذى يؤدى إلى ضياع كثيراً من الوقت فى الحركة بين مناطق المدينة، كما يحدث كثافة فى السيارات على الطرق المختلفة الداخلية والخارجية والتى تعد السبب الرئيسى فى تلوث البيئة بالغازات الضارة والضوضاء.

ومن أهم عناصر تلوث بيئة المجمعات السكنية والمرتبطة بفقدان التكامل ما ياتي:

1- تلوث الهواء:

فقد أثبتت الأبحاث الخاصة بتلوث البيئة السكنية فى المدن أن التركيز الرأسي للعمران والمتمثل فى ظاهرة المباني المرتفعة والأبراج العالية من الأسباب المباشرة فى ارتفاع نسبة التلوث فى الهواء فى عناصره المعروفة بالرائحة والأبخرة المختلفة والغبار والغازات الضارة (كريم، مجلة جمعية المهندسين المصرية، المجلد 13، العدد4، 1974م) فهذه المباني اذا صممت باسلوب فردي ودون الاهتمام بالعوامل البيئية الخاصة بالمنطقة وكذلك استعمالات الارض وعدد السكان المتوقع ومع عدم وجود فراغات بينية مناسبة بالتالى ستزيد نسبة تلوث الهواء علاوة على كونه ملوثاً أصلاً.

2- التلوث السمعى (الضوضاء):

وهو ما ينتج بسبب الخلط في الاستعمالات داخل المناطق المختلفة فى المدينة نتيجة لعدم التنسيق بين أدوار الجهات التصميمية المختلفة، حيث توظف أي قطعة أرض شاغرة للاستعمال السكني من قبل مالكها فقط، دون مراعاة للظروف المحيطة بالموقع وطبيعة استعمال المنطقة، فتقام المجمعات السكنية بجانب الورش (وهى من المصادر القوية للضوضاء) ، أضافة إلى ذلك الضوضاء الصادرة من كثرة استعمال السيارات والازدحام فى مناطق العمران الرأسي والأفقي غير المخطط له.

3- التلوث البصري:

لقد تحولت الصورة الخارجية المرئية للمباني والمناطق المختلفة المدينة من ملكية عامة إلى خاصة بكل مالك والذى أصبح يتصرف فيها وفقاً لرغبة شخصية ودون مراعاة لقواعد الذوق العام، كما يحدث حاليا في مجمعاتنا السكنية فضلا عن الخلل فى الصورة البصرية والمقياس الإنساني في بعض المجمعات السكنية بسبب عدم ملائمتها للبيئة المحيطة بها (**الإكيابى ، محمودو نوبى محمد حسن، تكامل القطاعات المختلفة فى عملية التنمية العمرانية للمدينة العربية،2002 ،ص124**) .

1-2-4 إهدار الموارد والطاقات والوقت:

وهذه هى نتيجةلكل ماسبق أقرب من كونه انتيجةمستقلة بذاتها، فعدم التنسيق بين الجهود المبذولة فى عملية التنمية العمرانية وتصميم وانشاء المجمعات السكنية غير الملبية لحاجات الساكنين وغير متلائمة مع مفردات القيم الخاصة بالمنطقة على كافة مستوياتها من شأنه أن يؤدى إلى الهدر فى الموارد والوقت والطاقات الفعلية المبذولة لعدم تحقيقها الاهداف المرجوة منها.

1-3 استخراج المؤشرات (البيئية - الاجتماعية– الجمالية) من المدن التقليدية

اعتمدت المجتمعات التقليدية على وسائل وتقنيات متوارثة عبر التاريخ وتطويرها باستمرارعن طريق التجربة الميدانية و الممارسة اليومية اما تشكيل البيئة الحضرية في أيامنا فقد أصبح يعتمد كثيرا على التخطيط العلمي و منطق التصميم المعماري و العمراني من جهة و التطور التكنولوجي من جهة أخرى. (Golany G. S. (1996) Vol.30 .No.3, pp455-465). و هذا ما يؤدي بنا إلى محاولة الاستفادة من الخبرة البشرية القديمة و المتراكمة و تطويرها لتكون مادة لاستنباط الحلول لقضايا التخطيط و التصميم. ***و في هذا السياق يهدف البحث إلى استخراج مؤشرات بيئية واجتماعية وجمالية من البيئة الحضرية للمدن التقليدية يمكن استعمالها أو الاهتداء بها لتوجيه تصميم المجمعات السكنية للنمط متعدد الاسر خصوصا في المناطق الحارة وللاستفادة منها في تقييم نوعية التصاميم الموجودة من حيث استجابتها للمعطيات المناخية، ومتطلبات التنميةالبيئية المستدامة*.***

4-1 المعالجات المعمارية البيئية

أدرك المعماري المسلم ومنذ زمن بعيد أهمية تهيئة المناخ الملائم باستخدام الطاقة التى توفرها البيئة الطبيعية المحليه ، كما اتقن استغلال التهوية الطبيعية لغرض تبريد جسم الانسان ، فنرى بعمارتنا التقليدية العديد من المعالجات المعمارية التي يمكن ان تقسم الى نوعين:

1 - المعالجات المعمارية الاساسية للمناطق الحارة الجافة

2- المعالجات المعمارية المكملة

1 - المعالجات المعمارية الاساسية للمناطق الحارة الجافة

تمتازالمناطق الحارة الجافة بالحاجة للاحتفاظ بالرطوبة داخل الفضاءات مع خلق تيار هواء بارد وحماية الفضاءات الداخلية من انتقال الحرارة الخارجية لها ، وهذه الميزةهي اساس المعالجات المعمارية التي لجأ اليها المعمار العربى المبدع ومن خلال معرفته الدقيقة بعلم (aerodynamics) الديناميكا الهوائية استخدم مبدأين لضمان التحرك الهوائي الطبيعي خلال الفراغ الانسيابي

التكاملي لعموم المدينة العربية التقليدية وحسب الأتي:
- يعتمد **المبدأ الاول** على التباين في ضغط الهواء الناجم عن الاختلافات في سرعة الرياح (velocities)، الامر الذي يؤدي الى تدفق الهواء من منطقة الضغط العالي الى الضغط المنخفض ، اي حركة الهواء بفعل تباين الضغط وبالاعتماد على مبدأ (عملية فنتوري - Venturi action) المشتق اساسا عن ظاهرة تاثير(برنولي - Bernoulli effect) كأطار نظري هام لفهم كيفية حدوث حركة الهواء بفعل تباين الضغط الناتج عن حركة الرياح.وتتلخص نظرية (برنولي) بأن ضغط المائع المتحرك (moving fluid) يقل بازدياد سرعته (velocityist) ويعتمد **المبدا الثاني** على حركة الهواء بتاثير الحمل (Convection) الناتجة عن تسخن الهواء وصعوده الى الاعلى، بما يقتضي حلول هواء اكثر برودة منه في مكانه كما قد تؤدي العملية الى مايدعى (stack effect) مفعول المدخنة فعندما يرتفع الهواء الدافىء يجب ان يستبدل بهواء اكثر برودة من محيطه .وبوجود مصدر الحرارة المستمر تتولد حركة دائمة في الهواء (شاهين ، د.بهجت ، المجلة العراقية للهندسة المعمارية ،2006)

- **فنجد بهذه المدن الحارة الجافة المعالجات المعمارية الاتية :**

الفراغ الأنسيابي في النسيج العمراني التقليدي أعتمد اساسا على المبداين المذكورين اعلاه. حيث يبدأ بالساحات العامة القريبة من جامع المدينة او مركز التسوق وربما يشمل كذلك ساحات المدارس والحدائق العامة حيث يبدأ اول انخفاض واضح في الحمل الحراري الاجمالي المؤثر في عموم المنطقة ..وبما ان الساحات العامة في النسيج الحضري التقليدي تتكون من مساحات واحجام مختلفة منها المظللة ومنها المشمسة ومنها الغنية بالمزروعات والمسطحات المائية ومنها المبلطة والمخصصة

للتجمعات السكانية ..هذه المواصفة في التشكيل الفضائي المفتوح لجميع الساحات العامة تخلق بطبيعة الحال اختلافا واضحا في الضغط تفرضه مبادىء الاختلاف في درجات الحرارة مابين فضاء وفضاء لتنساب التيارات الهوائية عبر الازقة الضيقة المظللة والمتعرجة باتجاه الفناءات الداخلية المشمسة والمظللة لتخلق تيارا هوائيا لعموم النسيج العمراني التقليدي (شاهين ، د.بهجت ، المجلة العراقية للهندسة المعمارية ،2006)

2- المعالجات المعمارية المكملة :

أ- **الشناشيل** او كما يسميها المصريون **بالمشربيات** التي تعني في الأصل مكان الشرب ، حيث صممت في الماضي على شكل حيز بارد ذي فتحة منخلية (Lattice opening) توضع فيها جرار الماء الصغيره لتبرد بفعل التبخر الناتج عن تحرك الهواء عبر الفتحة .وتعتبر من اهم المفردات المعمارية المتميزة في واجهات الدور التقليدية المطلة على الازقة الضيقة او داخل فناءات الدار وتكون عادة بارزة عن الهيكل الأنشائي للدار ومرفوعة من خلال روافد معدنية او خشبية او عن طريق تدرج في منطقة القاعدة، تمثل الشناشيل حالة عناق مستمرة بين اجواء الغرف الداخلية والأجواء الخارجية من ناحية حصولها على التحرك الهوائي والضوء الطبيعي .

ب - الملاقف الهوائية او البادكيرات بأنواعها ويرجع ظهورها الى ازمنة تاريخية قديمة جدا فقد استعملها المصريون القدماء في مساكن تل العمارنة في مصر، وانتشرت بشكل واضح في العراق وفي كثير من البلدان العربية الأخرى ولازالت موجودة في وقتا هذا وقد كان ارتباطها تاريخيا بفضاءات السراديب لطابق او طابقين واحيانا يصل عمقها الى ثلاث طوابق تحت مستوى الأرض ، فالسرداب لايمكن ان تستكمل فاعليته في الحصول على التيار الهوائي الا اذا زود بملاقف هوائية (بادكيرات) وعادة توجه فتحة الملقف الهوائي باتجاه الرياح السائدة في اعالي الدار حيث تسمح بتمرير الهواء البارد صيفا (عندما تكون درجة حرارة الهواء الخارجي أقل من 33 درجة مئوية) والخالي من الغبار والرمال اللذين تحملها الرياح التي تهب على الأقاليم الحارة الجافة ، خاصة وان الرياح في اعالي المبنى تحوي على نسبة اقل من كمية المواد العالقة. ويتحرك الهواء البارد باتجاه السراديب من خلال مجرى هوائي بني داخل الجدران

السميكة للدار(shaft) والى اعمق نقطة في السرداب(المصدر السابق).

5-1 القيم الاجتماعية في المحلة السكنية التقليدية :

لكون البيئة السكنية التقليدية تحمل الكثير الذي يمكن الافادة منه في تصاميمنا المعاصرة فسنتناول ابرز القيم الاجتماعية المستخلصة من هذه البيئة وهي :

- **الخصوصية** :تمثل الخصوصية حاجة اساسية من الحاجات النفسية للانسان وهي مرتبطة بحاجات اخرى مثل الملكية واضفاء الطابع الشخصي وتعتمد درجة تحقيقها على مدى تلبية بقية الحاجات .

تعددت تعاريف الخصوصية ونذكر منها تعريف رابابورت (Rapoport ,1977) الذي يعرفها على انها :(القدرة على السيطرة على التفاعلات وامتلاك الخيارات وتحقيق التفاعلات المطلوبة) اي ان الخصوصية لاتعني بالضرورة الانعزال عن الاخرين.

وان متطلبات الخصوصية في مجتمعاتنا الاسلامية عالية جدا ونجد انها تحققت بعدة اشكال عبر المعالجات المعمارية للبيئة التقليدية وذلك عن طريق :

- التوجه نحو الداخل من اهم المعالجات التي تعزز الخصوصية وتمنع الاختراق البصري والسمعي ، حيث تمثل الجدران الخارجية قشرة سميكة عازلة للبيت عن محيطه الخارجي.

- قلة الفتحات في الجدران او انعدامها وخصوصا في الطابق الارضي حيث نجد ان الفتحات تكون مرتفعة وصغيرة ، وكذلك المداخل غالبا ما تكون منكسرة لمنع الاستمرارية البصرية بالاضافة الى عدم تقابل ابواب البيوت المتقابلة عبر الزقاق، اما الطابق العلوي فنجد ان معالجة الفتحات الخارجية هي بالشناشيل المزخرفة التي تسمح بالنظر باتجاه واحد فقط ، من الداخل الى الخارج، وكل هذه المعالجات وفرت للساكنين الخيارات المطلوبة للسيطرة على التفاعلات المرغوبة وغير المرغوبة مع المحيط الخارجي .

-اما في داخل المسكن الواحد فنجد ان جميع الفضاءات تفتح شبابيكها على الفناء الداخلي وهذه الشبابيك معالجة بزخارف ومشبكات تمنح بالاضافة الى الغنى البصري والاحساس بالبهجة شعورا بالخصوصية البصرية لكل فضاء ، كذلك فان سمك الجدران الداخلية يخفف من انتقال الاصوات بين الفضاءات .

- نجد في البيئة السكنية التقليدية ان المسكن يمثل الملكية الخاصة ، في حين يمثل الزقاق المجاور للبيت الفضاء شبه العام ، اما الفضاء العام فيتمثل بالجامع ، السوق ، المقهى والحمام ، اي اننا نلاحظ وجود تدرج وتسلسل واضح من العام الى الخاص ، حيث اننا كلما اقتربنا من الملكية الخاصة نجد الازقة تقل عرضا وتزداد تعرجا وانحناءا حتى تنتهي الازقة بنهايات مغلقة ، مما يعزز من خصوصية البيوت المفتوحة عليها ، ويزيد من التفاعل بين السكان ويمنحهم درجة عالية من الامان ، حيث يمكن التعرف على الغرباء بسهولة عند اختراقهم للمنطقة ، اي انه يشكل فضاء دفاعي .

- ومما يعزز الاحساس بالامان وجود الشناشيل التي تفتح على الازقة حيث تمثل اشرافا طبيعيا عليها ، لذلك نجد ان نسبة الجريمة كانت منخفضة بشكل كبير ، ويعود ذلك للاعراف الاجتماعية وتعاليم الدين الاسلامي .

- ونجد ان البيئة السكنية التقليدية ربما تكون متشابهة بشكل كبير من الخارج الا ان الطابع الشخصي نراه بشكل واضح في داخل المساكن من ناحية الزخارف والتفاصيل المختلفة كالتاثيث وتزيين الفناء الداخلي بالاشجار والمزروعات والاحواض المائية .

- نجد ان العلاقات الانسانية في المجتمعات التقليدية تمتاز بقوتها و ان السكان يميلون للتفاعل مع الجيران خصوصا ضمن الحي السكني الواحد ، ومما حفز هذه العلاقات والتفاعلات الاجتماعية هو وجود الازقة

بتعرجاتها وانحناءاتها التي تكون فيها عقد تحفز التفاعل الاجتماعي .

1-6 الخصائص الجمالية للبيئة السكنية التقليدية

- ابرز الخصائص الجمالية للمحلة السكنية التقليدية " **غياب القيم الجماليه المستعاره وحضور الجمال الحقيقي من منابعه الاصليه** "حيث امتازت المعالجات المعمارية للبيئة السكنية التقليدية باصالة جمالها ، لكون هذا الجمال يمتاز بالتكامل ، اي ان المعالجات المعمارية لم تاتي للحاجة الجمالية للمظهر الخارجي فقط ، وانما جاءت لتلبية حاجات الانسان بالدرجة الاولى ، لهذا هي تمتاز بالعمق وبكونها اساسية في التكوين اي انها تحقق (جمال الجوهر : وهو الجمال الناتج عن سلامة الأداء الوظيفي و جمال المظهر : وهو الجمال الناتج عن سلامة الاداء المرئي) ونلاحظ ذلك في كل مكونات البيئة ، وسندرس الموضوع في ثلاثة نواحي: (1) التخطيط والتجميع (2) البيئة الخارجية (3) البيئة الداخلية

<u>1- التخطيط والتجميع</u>

لو نظرنا لاي مخطط افقي سواءا للمحلة السكنية التقليدية او للمسكن التقليدي المنفرد فيها فسنجد عدة خصائص تنطبق عليهما وتتكامل بينهما ومن اهم هذه الخصائص والتي تعتبر كخاصية جمالية ومميزة رئيسية لهذه البيئة هي **التضام والاحتواء والاتجاهية والمحورية** فهي تعطي نسق يمتاز بجماله الشكلي وبتكامله والذي يوفر للمستخدم متعة جمالية فريدة من نوعها.

التضام و الاحتواء :

يقصد بالتضام في تجميع المدينة هو تقارب مباني المدينة بعضها مع بعض بحيث تتكتل وتتراص في صفوف متلاصقة لمنع تعرض واجهاتها للعوامل الجوية مثل اشعة الشمس المباشرة والرياح المحملة بالاتربة التي تؤدي الي رفع درجة الحـــــــرارة داخل المباني . (خير الدين ، 1997 ، ص864).

من هذه المفاهيم تنطلق فكرة المظهر والجوهر ، إذ ان المعالجات المعمارية للفناء من الداخل تعبر عن الجوهر والمضمون يكمن الثراء الحقيقي والشعور بالانتماء وتحقيق الذات . وهكذا انعكست ذاتية المسلم في داخل المبنى في حين تبرز البساطة المعمارية الخارجية المعبرةعن القيم الاجتماعية الاسلامية ، كالمساواة والتكافل والجوار .

اما مفهوم الاحتواء فهو السمة الاساسية المميزة للتكوين الفضائى والكتلي في المدينة العربية التقليدية .. وهو يعبر عن الاستجابة العقلانية للمتطلبات الانسانية التي اوجدتها قيم المجتمع الاسلامي . وقد ادى الفناء الداخلي مهمة اساسية في بلورة هذا المفهوم بوصفه خلية الاحتواء الاساسية في المدينة . وان شكل الكتلة البنائية غير محدد بوضوح ، الا ان شكل الفناء (فضاء الفناء) محدد ومعرف ومع هذا فهو لايحدد الشكل النهائي للمبنى ، اذ تحدده الطرق والمباني المجاورة . (الطالب ،1989 ،ص133).

الاتجاهية والمحورية :

ان الاتجاهية الاكثر تأثيرأ في التكوين الفضائي للنسيج الحضاري للمدينة العربية التقليديةهو توجيه المسجد الجامع نحو الكعبة، فالمحور الخفي الذي يتوجه نحو الكعبة يحدد توجيه المسجد وبالتالي يتحدد اتجاه واستقامة الشوارع الرئيسية التي تتقاطع في المركز عند المسجد الجامع .

تشكل البؤر البصرية محطات على الطريق او تعلن عن اهمية الحدث العمراني الحضري او المبنى الذي ترمز اليه ويختلف موقعها افقيا او عموديا بحسب طبيعتها ، ومن ابرزها ألمئذنة التي تشكل مع خط السماء الطريق العام بشكل ايحائي يعلن باهمية الحدث العمراني الملازم لها ،كما ان البناء الافقي للنسيج التقليدي يوفر امتدادا بصريا مريحا ولا يحجب الضوء و يعطي فرصة للتفاوت البصري . (كمونه ،10، كانون الاول ،1994) .

<u>2- البيئة الخارجية</u>

نجد ان الواجهات الخارجية كانت في معظم الاحيان صماء او تمتاز بفتحات قليلة، وهذا جاء نتيجة للبيئة القاسية ،لكن بالرغم من ذلك نجد بعض العناصر التي ميزت هذه الواجهات وجعلتها جميلة باصالة كون ان هذه العناصر جاءت كمعالجات بيئية واجتماعية في اغلب الاحيان ولكنها اضافت قيمة جمالية متاصلة كالتلاعب بالكتل والزخارف المحفورة عليها وكذلك الشناشيل والساباطات الممتدة والتي تعطي ايقاع متوازن ومتنوع يغني التجربة الجمالية للساكن والسائر كما في الشكل (4) .

الايقاع في التكوين الفضائي والكتلي :

ان التكوين الفضائي والكتلي للمدينة العربية الاسلامية يظهر درجة عالية من التوافق والانسجام والانتظام في التصميم،إذ يتكيف الفضاء مع الوظيفة التي يخدمها،والكتلة تتبع الفضاء في الاحساس والتفاعل وتبدو وكانها ترديدا له، فتحقق الايقاع بتلقائية حرة ضمن الالتزام التقليدي العام. والتنوع البصري ضمن الوحدة العامة فيضيق الفضاء تارة ويتسع تارة اخرى وينفتح وينغلق، ويمتد مستقيما وينحنى ويتغير اتجاهه، إذ تتعاقب الفضاءات من فضاء اتجاهي الى فضاء اخر لاتجاهي والتي تمثل محطات توقف واحتواء ضمن ايقاع طبيعى غير مفتعل .

ويعتبر الزقاق اهم عنصر من عناصر البيئة الخارجية، وخير من وصف الزقاق هو المعماري (رفعت الجادرجي) في مقاله اذ قال :(نحتية الزقاق نحتيه ديناميكيه مليئة بالعناصر الدافعة ، فالبروزات المتعاقبة تكون قوة دافعة باتجاه الايقاع ، ولكن الايقاع يتاكد ويتضخم في التكرار المتنوع من الايقاعات المتشابهة في البيوت المتجاورة والمقابلة والبيوت الاخرى التي تكون الزقاق ، مجموع هذه العناصر تبرز وترتد وترتفع فتكون سطوحا ونتوءات تتواثب فيها القوى من واحدة الى الاخرى الى ان تتلاشى في الظلال الداكنه لنهاية الزقاق والتي تؤكد ديناميكيته)(شاهين2006ص4-5)

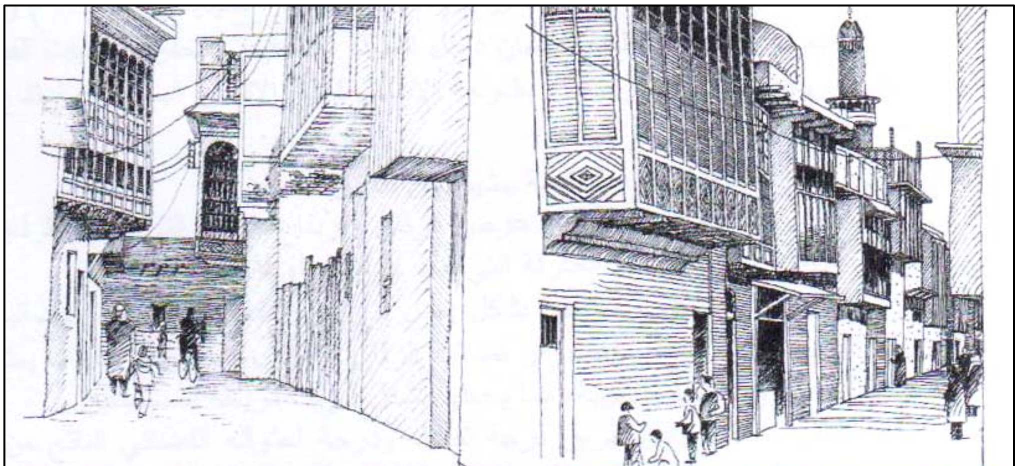

الشكل (4) تجاور الوحدات السكنية واستخدام السوابيط والشناشيل ادى الى تظليل مسارات الحركة ذاتيا لتوفير بيئة مريحة للسابلة في ازقة المدينة التقليدية
المصدر : الزبيدي ، مها ،2006 ،ص52

خاصية المقياس الانساني :

ان هذه العلاقة متمثلة في مستويات التكوين الفضائي العامة والخاصة والتفصيلية ... فعلى المستوى العام يتحدد حجم وابعاد المدينة التقليدية بالدرجة الاولى بامكانية حركة المشاة . وعلى المستوى الخاص ، فاننا نرى ان مفاهيم الدين الاسلامي وتعاليمه ، كان لها أثر كبير في وجود هذه الخاصية في مدننا العربية التقليدية . إذ احترم المصممون المسلمون المقياس الانساني ، وارتبط ارتفاع الابنية بالانسان وكان ذلك انعكاسا اكيدا لثلاث قيم تراثية اسلامية هي التواضع والمساواة والانسانية . (العربى ، 1989 ، ص78-79)

3- البيئة الداخلية

الوحدة والتوجه نحو الداخل :

ان طبيعة العلاقات المركبة للمجتمع الاسلامي ومتطلبات البيئة الطبيعية قد كونت هيكل المدينة العربية التقليدية العمراني والتي امتازت بقوتها وتماسكها الداخلي ، فالتخطيط المتراص للنسيج التقليدي وتداخل مكوناته وتكاملها يعبر عن وحدة التكوين العام (AlBayaty,1983,P.113)

تمتاز المساكن التقليدية بكونها تطل على الداخل فان الكتلة تحتوي قلب المنزل واهم عنصر فيه وهو**الفناء الداخلي** الذي يعتبر من اهم العناصر البيئية والاجتماعية والجمالية الاصيلة المميزة للبيئة السكنية التقليدية ، فهو جاء كحاجة بيئية واجتماعية اساسا ، لكنه بدا يتطور ضمن تلبية تلك الحاجة ، الى ان اصبح تجربة جمالية خاصة بحد ذاته وذلك لغناه بالعناصر(كالاحواض المائية والمزروعات النباتية) التي تمتع وتسر الناظر اضافة الى اشعاره بالراحة النفسية والبيئية والاجتماعية .وفيما يلي سنذكر بعض الخصائص الجمالية الشكلية التي اتسمت بها البيئة السكنية التقليدية نتيجة وجود الفناء الداخلي .

أولاً: الانسيابية الفراغية الداخلية: وهي بعدة أنواع وما يهمنا هي:

الانسيابية الفراغية الجانبية: وهي تعني أن الاتصال بين الفراغ الداخلي والفناء يكون من أحد جوانب الفراغ، وقد وضحت هذه العلاقة في تصميم المسكن العربي التقليدي، حيث الانفتاح بجميع عناصر المسكن على الفناء الداخلي، ومنها المقعد والإيوان لقضاء الأمسيات الجميلة والاستمتاع بالأشجار والورود ونافورات المياه[صوفان، (28 فبراير – 5 مارس 1981م)، 77: 81]، وقد ساعد على تحقيق هذه الانسيابية تخصيص الفناء الداخلي لمسكن واحد؛ مما ساعد على تحقيق مطاب الخصوصية لعناصر المسكن المطلة عليه.

ثانيا : معالجة الهيئة المعمارية الخارجية للمبنى:

يختص هذا المبدأ بمناقشة العلاقة بين الهيئة المعمارية الخارجية للمبنى وبين التكوينات الفضائية له بسبب إطلالة معظم الفضاءات الداخلية الرئيسية على الفناء الداخلي ؛ ونظراً لذلك فإن الهيئة المعمارية الخارجية للمبنى تتسم بسمات خاصة تجعل نمط المباني السكنية التقليدية ذات الأفنية الداخلية يختلف عن نمط المباني الأخرى.

وبشكل عام فإن السمات المميزة لهذه الهيئة المعمارية تتركز في المعالجات المعمارية الاتية:

(1) - كتل واجهاتها الخارجية قليلة:

حيث أن توجيه الفضاءات في مباني الأفنية الداخلية يكون على الفناء الداخلي؛ فإن الأمر يتطلب في بعض الأحيان ألا يكون للمبنى أي فتحات خارجية، وهذا ما ظهر جلياً في النسيج العمراني المتضام الذي ميز عملية التخطيط العمراني للمدن العربية والإسلامية التقليدية، والتي تقع في المناطق الحارة وشديدة الحرارة. ففي بعض الحالات وجدت المباني وليس لها سوى جزء من الواجهة الخارجية يمثل مدخل المبنى، حيث أن الاعتماد يكون على التوجيه إلى الداخل على الفناء الداخلي،(حسن ، nouby@rocketmail.com، 2003).

(2)-الفتحات ذات طبيعة خاصة:

أهم ما يميز الفتحات الخارجية في المساكن التقليدية ذات الأفنية الداخلية - بجانب ندرة هذه الفتحات - ما يأتي:

أولاً: تصغير مسطح الفتحات:

ينطبق هذا المبدأ على الفتحات المطلة على الواجهات الخارجية بشكل خاص، ويتم ذلك بتصغير مسطح الفتحات

أو تجزئة الفتحات الكبيرة إلى فتحات أصغر في المسطح يسهل التعامل معها، وذلك لتقليل كمية الإشعاع الشمسي المكتسب من خلال الفتحات، بجانب تحقيق الخصوصية البصرية.

ثانياً: حماية الفتحات:

هو أسلوب يختص به نمط المباني ذات الأفنية الداخلية التي تقام في المناطق الحارة، ويهدف إلى حماية الفتحات الخارجية عن طريق تغطيتها بالمشربيات (الشناشيل) كما في العمارة الاسلامية التقليدية.

اي ان الشناشيل جاءت لحاجة بيئية واجتماعية حيث انها تمنع الرؤية المعاكسة فهي تؤكد على مبدا الخصوصية ، ولكنها في نفس الوقت اعطت الازقة التقليدية جمالية مميزة فهي تمثل تجربة جمالية ممتعة حسيا وادراكيا وكذلك بيئة امنه للعب الاطفال اضافة الى الجو اللطيف والهادىء.

1-7 تقويم التجربة العراقية

-بعد درسة اهم المميزات الخاصة بالمحلة السكنية ومن النواحي (البيئية – الاجتماعية –الجمالية)تم استخراج عدد من المفردات القيمية والخاصة بكل ناحية من النواحي الثلاث وتم عمل وتوزيع عدد من الاستمارات التقويمية (بالاستناد على تلك المفردات)والتي كانت بنوعين نوع خاص بسكان المجمعات السكنية (مجمع حي السلام ، مجمع (28 نيسان) الصالحية ،ومجمع شارع حيفا – الجزء السادس -) وذلك للتعرف على اراء السكان ومشاكلهم مما يعطي التقويم درجة عالية من الواقعية والنوع الاخر الاستمارات التقويمية الخاصة بالمختصين لاعطاء واستخلاص تقويم يكون على درجة عالية من الموضوعية والتي بنتائج التقويمين نحصل على المشاكل لاقتراح الحلول لها ونقاط الضعف لمحاولة تلافيها في تصاميمنا المستقبلية، وفيما يأتي طرح ومناقشة لاهم النتائج التقويمية .

1-8 مناقشة نتائج الاستمارات التقويمية:

1- التقويم من الناحية البيئية :

تم اعتماد مجموعة من ابرز المشاكل البيئية والمناخية الخاصة ببلدنا واخذ رأي السكان حول مدى معاناتهم من هذه المشاكل للتوصل في النهاية الى تقويمهم لوحدتهم السكنية من الناحية البيئية.

- ممكن ان نستنتج من اجابات السكان المدرجة في الجدول(1-1) المرفق ان ابرز مشكلة بيئية يعاني منها السكان وفي المجمعات السكنية الثلاث هي التوجيه حيث نجد ان اكثر من نصف الاجابات كانت تؤيد وجود هذه المشكلة ، والتي براي الباحثة قد ادت الى مشكلات اخرى وهي دخول كميات كبيرة من الحرارة والاشعة الشمسية غير المرغوب فيها ، مما ادى الى حاجة السكان للاعتماد على وسائل التكييف الميكانيكية .

- اما بالنسبة لنظام التبريد المركزي المعتمد في مجمعي الصالحية وشارع حيفا فهو لا يعمل في اغلب الوحدات السكنية وان كان يعمل فهو لايعمل بالكفاءة المطلوبة وذلك لافتقاره لخدمات الصيانة والادامة الضرورية لمثل هذا النوع من الخدمات للحفاظ على كفاءتها ، مما ادى الى اعتماد السكان على انفسهم لتوفير حلول بديلة لجعل بيئة المسكن مريحة كاستحداث فتحات في الجدران لوضع مكيف الهواء او لوضع مبردة الهواء .

- نجد ان المساحات الخضراء وفي المجمعات السكنية الثلاثة ،كما في الجدول (1-1) ،هي غير كافية او غير ملائمة للجلوس ، ففي مجمع شارع حيفا الفضاءات المتوفرة قليلة جدا وذلك بسبب الكثافة البنائية العالية للمشروع وعلى جانبي الشارع مما ادى الى اعتماد المصمم على فضاءات في الطابق الارضي كمناطق ترفيهية او اعتماد طابق نصفي مسقف تحت الوحدات السكنية ،اما في مجمع الصالحية نجد ان المصمم قد نجح في عمل تدرج فضائي ابتداءا من الساحات العامة في المنطقة المركزية للمشروع وانتهاءا بالفناء الخاص بالمبنى السكني الا انه توجد فضاءات بين البنايات السكنية تبدو كانها مساحات متروكة حيث تفتقر الى المعالجات الضرورية لجعلها اماكن ملائمة للجلوس ، وفي حي السلام فان الفناء الوسطي بين البنايات السكنية والمستغل كموقف

للسيارات قد حددت فيه منطقة للجلوس ولعب الاطفال هو الفضاء الوحيد المحدد والذي يستخدمه السكان امابقية الفضاءات المفتوحة فهي غير محددة بشكل واضح مما ادى الى انتهاءها كمساحات متروكة،لذلك يجب التفكير جديا بتصميم الفضاءات الخارجية حتى لاتبدو كمساحات متروكة باستخدام المعالجات التي استخدمها المعماري العربي المبدع في فناءاته الداخلية كالتشجير والمزروعات التي تلطف الجو وتوفر التظليل والتنويع الضروري في المشهد البصري المعاصر، وايضا استخدام المسطحات المائية وبعض الاثاث المناسب لخلق اجواء تشجع على جلوس السكان وتوفر محيطا امنا للعب الاطفال من خلال مراقبة الاهل وكذلك لزيادة فرص التفاعل الاجتماعي والالتقاء بين السكان .

النتائج النهائية للتقويم البيئي :

وكنتيجة نهائية نجد ان السكان في مجمع حي السلام يقيمون مدى ملائمة الناحية البيئية في مجمعهم السكني لبيئتنا ومناخنا الحار – الجاف كالاتي:

- مدى ملائمة المجمع السكني لمناخ منطقتنا الحارة :

12% جيدة ، 59% متوسطة ،و 29% رديئة .

وهو نتيجة متقاربة مع **نتيجة تقويم المختصين** التي هي : 8% جيدة ، 69% متوسطة ، و 23% رديئة كما نلاحظ في المخطط البياني (1-1) .

- ومن الجدير بالذكر ان (3\1) عدد الوحدات السكنية في حي السلام موجهة باتجاه الشرق - والغرب مما جعل وضعها المناخي حرج نوعا ما وخصوصا في فترة الصيف فستحتاج للاعتماد وبصورة رئيسية على اجهزة التكييف للوصول الى الراحة الحرارية ، و(3\2) من عدد الوحدات السكنية موجهة باتجاه الشمال – والجنوب مما اكسبها ايجابية مناخية عالية مع امكانية التهوية المخترقة مما قلل من اعتمادها على وسائل التكييف.

وكنتيجة نهائية نجد ان السكان في مجمع الصالحية يقيمون مدى ملائمة الناحية البيئية في مجمعهم السكني لبيئتنا ومناخنا الحار – الجاف كالاتي:

- مدى ملائمة المجمع السكني لمناخ منطقتنا الحارة :

8% جيدة ، 77% متوسطة ،و 15% رديئة وهي نتيجة متقاربة مع **نتيجة تقويم المختصين** التي هي : 7% جيدة ، 70% متوسطة ، و 23% رديئة كما نلاحظ في المخطط البياني (1-2) .

- ومن الجدير بالذكر ان (8\3) من عدد الوحدات السكنية في مجمع الصالحية (28نيسان) موجهة باتجاه الجنوب الشرقي – والشمال الغربي ، و(8\5) من عدد الوحدات السكنية موجهة باتجاه الشمال الشرقي – والجنوب الغربي ، وان وحدتين سكنيتين في كل طابق من المباني السكنية قد وجهتا باتجاه جنوب غرب – شمال شرق ، مما سبب سلبية مناخية عالية وصعوبة في تحقيق الراحة الحرارية داخل غرف المعيشة وغرف النوم بشكل خاص.

وكنتيجة نهائية نجد ان السكان في مجمع شارع حيفا السكني يقيمون مدى ملائمة الناحية البيئية في مجمعهم السكني كالاتي:

- مدى ملائمة المجمع السكني لمناخ منطقتنا الحارة :

21% جيدة ، 40% متوسطة ، 21% رديئة،و18% رديئة جدا ، وهي نتيجة مختلفة نوعا ما عن **نتيجة تقويم المختصين** التي هي : 8% جيدة ، 23% متوسطة ، و 54% رديئة، 15% رديئة جدا كما نلاحظ في المخطط البياني (1-3).

- ومن الجدير بالذكر ان (2\1) عدد الوحدات السكنية في مجمع شارع حيفا موجهة باتجاه الشمال الشرقي ، و(2\1) من عدد الوحدات السكنية موجهة باتجاه الجنوب الغربي وهذا يعني افتقار نصف عدد الوحدات السكنية الى معايير التشميس المطلوبة خلال فترة الشتاء ، بينما يتعرض النصف الاخر الى حرارة الشمس العالية صيفا.

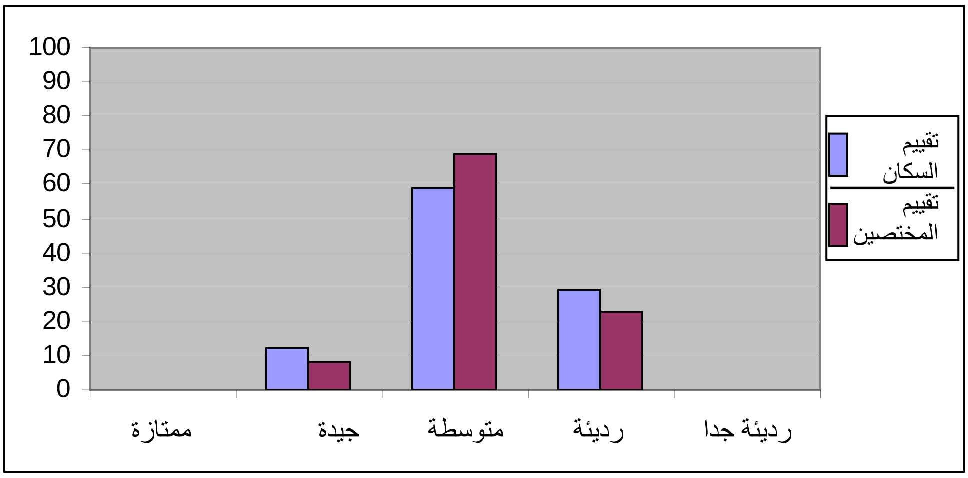

المخطط البياني (1-1) التقويم البيئي لمجمع حي السلام السكني ، المصدر : (الباحثة)

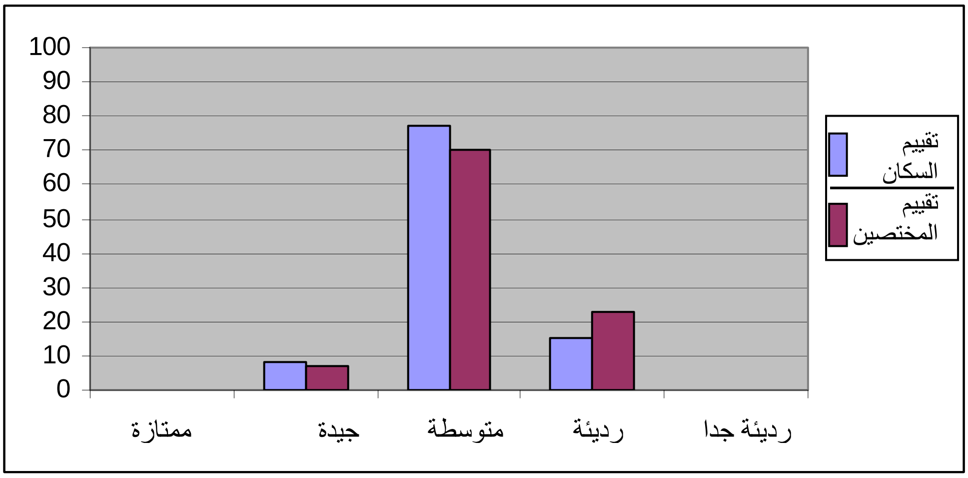

المخطط البياني (2-1) التقويم البيئي لمجمع الصالحية السكني ، المصدر : (الباحثة)

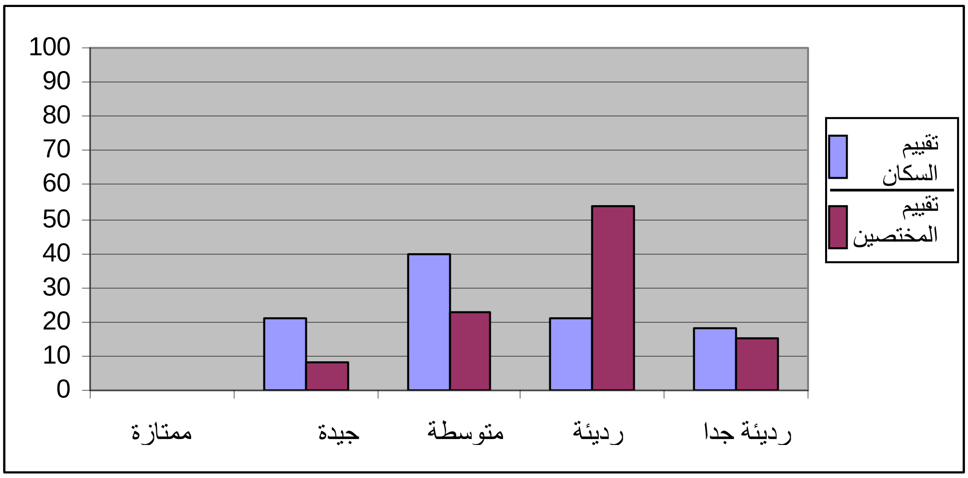

المخطط البياني (3-1) التقويم البيئي لمجمع شارع حيفا السكني ، المصدر : (الباحثة)

3- التقويم من الناحية الاجتماعية : تم الاعتماد على مجموعة من ابرز القيم الاجتماعية التي تهم مجتمعنا وتهم السكان لتشخيص ابرز المشاكل الاجتماعية التي يعانون منها وكما في الجدول (1-2) المرفق.

- حيث نجد ان ابرز مشكلة في الشرفية في مجمع حي السلام كانت بسبب موقع الباب الرئيسي غير المناسب ، وتاتي بعدها مشكلة وجود نوافذ قريبة للوحدات المجاورة ثم وجود ساحات تجمع او شارع ، اما في مجمع الصالحية فقد كانت معاناة السكان من وجود نوافذ قريبة للوحدات المجاورة و وجود ساحات تجمع قريبة وتاتي بعدها موقع الباب الرئيسي ويعود ذلك لكون النظام المتبع في الحركة هو النظام الرواقي مفرد التحميل بتجميع الوحدات بشكل حرف U ، اما في مجمع شارع حيفا فلم يعاني السكان من مشاكل كبيرة في الشرفية .

- لم يجد السكان في مجمع حي السلام مشكلة كبيرة في الخصوصية سوى مع الوحدات السكنية المجاورة ضمن نفس الطابق او في الطابق الاعلى او الاسفل وليس بشكل كبير ، بينما نجد السكان في مجمع الصالحية يعانون من مشكلة كبيرة في الخصوصية مع الوحدات السكنية المجاورة ضمن نفس الطابق او في الطابق الاعلى او الاسفل وتاتي بعدها مشكلة الخصوصية مع الفضاءات المحيطة بالبناية السكنية ثم مع الوحدات السكنية المجاورة ضمن نفس الطابق او في الطابق الاعلى او الاسفل ، اما سكان مجمع شارع حيفا فلم يجدوا ان لديهم مشكلة في الخصوصية .

- كانت اجابات السكان وفي المجمعات السكنية الثلاث متقاربة حول ان اختلاف المستوى الثقافي بين الجيران يؤثر سلبا في سلوك افراد العائلة وخصوصا في مجمع شارع حيفا حيث كانت النسبة 100% كما في الجدول (1-2)، كما ونجد ان اكثر من نصف السكان وفي المجمعات السكنية الثلاث قد فضلوا ان يكون الطريق المؤدي الى بنايتهم السكنية مغلق النهاية وذلك لزيادة الامن والاطمئنان والخصوصية ، اما بالنسبة لتقارب مداخل الوحدات السكنية فابرز معاناة كانت لسكان مجمع الصالحية ياتي بعدها مجمع شارع حيفا ثم مجمع حي السلام .

- وكنتيجة نهائية لتقويم السكان للناحية الاجتماعية لمجمعهم السكني جاء التقويم ضمن النقاط الاتية :

النتائج لمجمع حي السلام السكني :

مدى ملائمة المجمع السكني لقيمنا الاجتماعية الخاصة بمجتمعنا : 18% جيدة ،53% متوسطة ، و29% رديئة، وهي نتيجة متقاربة جدا مع نتيجة **تقويم المختصين** التي هي : 15% جيدة ، 54% متوسطة ، و 31% رديئة كما نلاحظ في المخطط البياني (1-4) .

النتائج لمجمع الصالحية السكني :

مدى ملائمة المجمع السكني لقيمنا الاجتماعية الخاصة بمجتمعنا : 15% جيدة، 62% متوسطة ،8% رديئة ، و15% رديئة جدا، وهي نتيجة متقاربة مع نتيجة **تقويم المختصين** التي هي : 15% جيدة ، 54% متوسطة ، و 23% رديئة ، و8% رديئة جدا كما نلاحظ في المخطط البياني (1-5).

النتائج لمجمع حيفا السكني :

- مدى ملائمة المجمع السكني لقيمنا الاجتماعية الخاصة بمجتمعنا : 22% جيدة، 57% متوسطة ،21% رديئة ، وهي نتيجة متقاربة مع نتيجة تقويم المختصين التي هي : 23% جيدة ، 62% متوسطة ، و 15% رديئة كما نلاحظ في المخطط البياني (1-6).

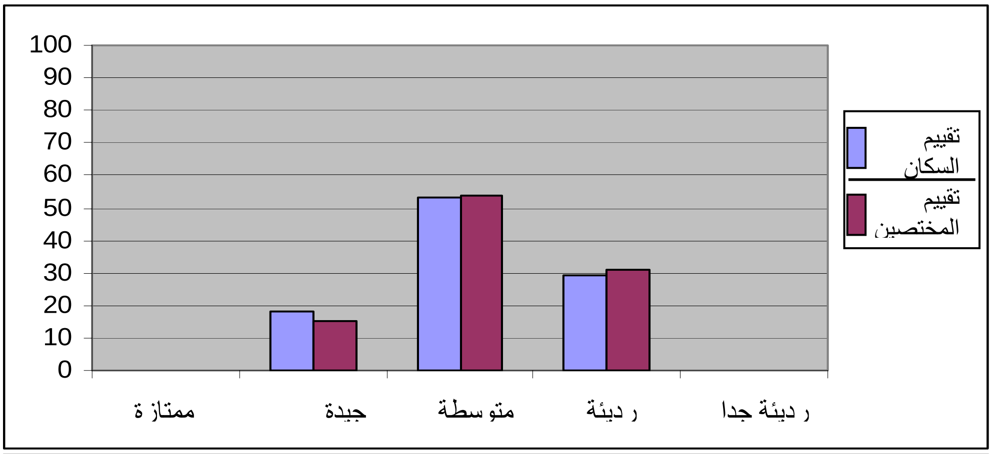

المخطط البياني (4-1) التقويم الاجتماعي لمجمع حي السلام السكني ، المصدر : (الباحثة)

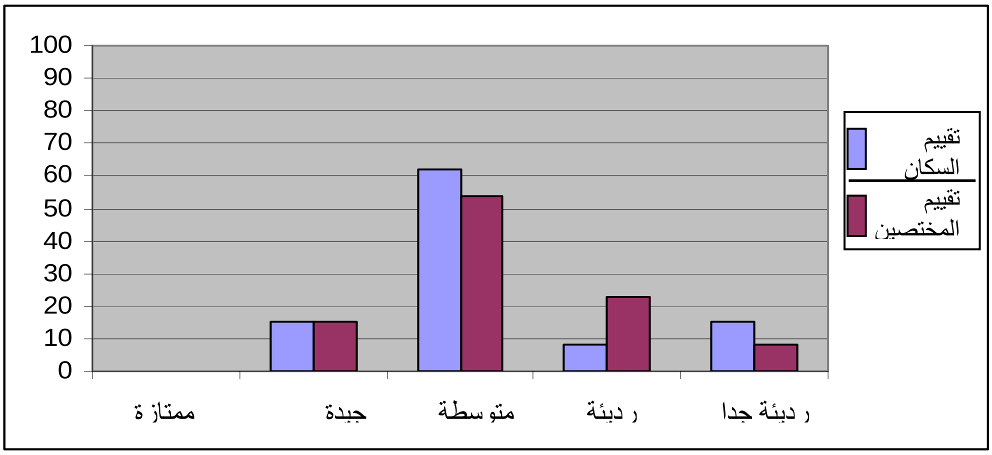

المخطط البياني (5-1) التقويم الاجتماعي لمجمع الصالحية السكني ، المصدر : (الباحثة)

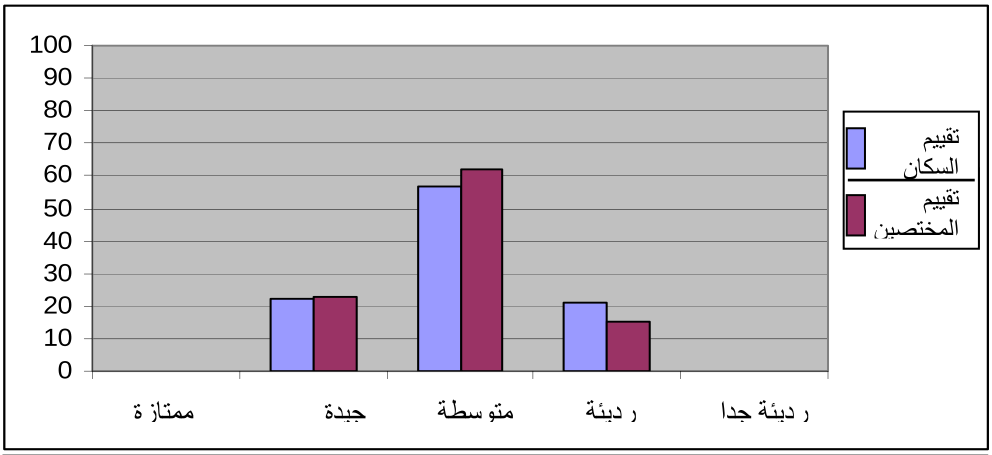

المخطط البياني (9-4) التقويم الاجتماعي لمجمع شارع حيفا السكني ، المصدر : (الباحثة)

2- التقويم من الناحية الجمالية :

- تم اخذ رأي السكان وذلك بسؤالهم حول مجموعة من الخصائص التي تعتبر مهمة في تقويم الناحية الجمالية للمجمع السكني ومدى ملائمة التصميم للقيم الجمالية لمجتمعنا وللذوق العام فجاءت نتيجة التقويم كالاتي : وكما في الجدول (1-3) .

- حيث ان جميع الاجابات للعينة الاستبيانية في مجمع شارع حيفا وافقت على كون الواجهة رصينة ومعبرة عن وظيفتها ، اما في كلا من حي السلام والصالحية فقد كانت نسبة الموافقة جيدة ايضا ، اما بالنسبة للتكامل والوحدة بين المباني والانسجام اللوني بين بنايات المجمع السكني فان اغلب الاجابات كانت بالايجاب مع ملاحظة ان شعور السكان بالوحدة والتكامل بدأ يقل بسبب قيام السكان بالتغييرات الفردية وكلا حسب ذوقه كتغيير الانهاءات ولون الجدران الخارجية مع الاضافات التي تمت على الواجهة كاضافة اقفاص مكيفات الهواء والمبردات وكذلك اضافة الكتائب وتغيير نوع الزجاج ولونه .

وكنتيجة نهائية لتقويم السكان للناحية الجمالية لمجمعهم السكني جاء التقويم ضمن النقاط الاتية :

النتائج لمجمع حي السلام السكني :

- ملائمة التصميم الداخلي للوحدة السكنية : 65% جيدة 29%، متوسطة ، و6% رديئة .

- تصميم الفضاءات الخارجية للمبنى السكني ومقترباته: 29% جيدة، 65%متوسطة ، و6% رديئة .

- جمالية واجهات البنايات السكنية: 24% جيدة، 64% متوسطة ، و12% رديئة .

- الفضاءات الخارجية المحيطة بالبنايات السكنية (بالنسبة لتواجد المسنين ولعب الاطفال و الفضاءات الخدمية الاخرى): 18% جيدة، 64% متوسطة ، و18% رديئة .

- مدى ملائمة المجمع السكني للقيم الجمالية لمجتمعنا : 18% جيدة، 70% متوسطة ، و12% رديئة .

والتي تعتبر نتيجة مختلفة عن **تقويم المختصين** الذي كانت نتيجته 23% جيدة، 31% متوسطة ، و46% رديئة كما نلاحظ في المخطط البياني (1-7).

النتائج لمجمع الصالحية السكني :

- ملائمة التصميم الداخلي للوحدة السكنية : 70% جيدة 15%، متوسطة ، و15% رديئة .

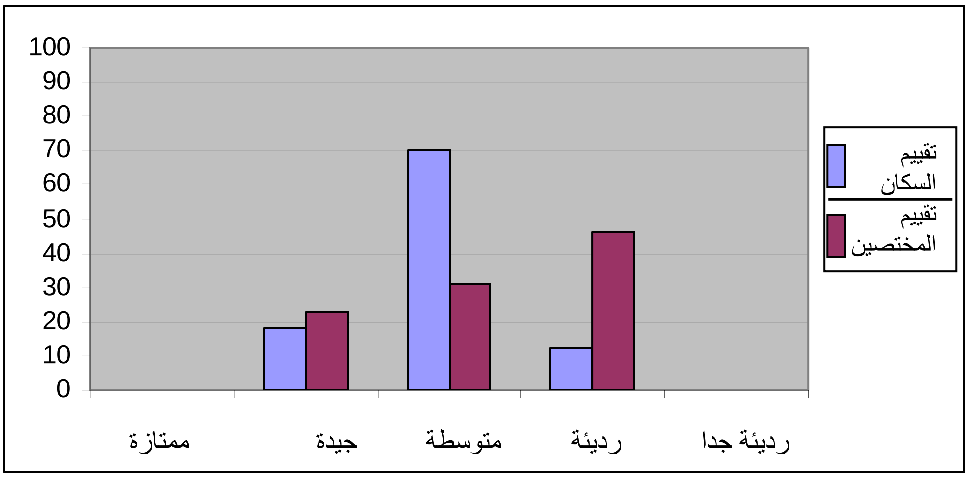

المخطط البياني (1-7) التقويم الجمالي لمجمع حي السلام، المصدر : (الباحثة)

- تصميم الفضاءات الخارجية للمبنى السكني ومقترباته: 38% جيدة، 54%متوسطة ، و8% رديئة .

- جمالية واجهات البنايات السكنية: 8% ممتازة، 38% جيدة ، و54% متوسطة .

- الفضاءات الخارجية المحيطة بالبنايات السكنية (بالنسبة لتواجد المسنين ولعب الاطفال و الفضاءات الخدمية الاخرى): 8% جيدة، 62% متوسطة ، و30% رديئة .

- مدى ملائمة المجمع السكني للقيم الجمالية لمجتمعنا : 30% جيدة، 62% متوسطة ، و8% رديئة .

وهي نتيجة متقاربة مع نتيجة **تقويم المختصين** التي هي : 38% جيدة ، 47% متوسطة ، و 15% رديئة كما نلاحظ في المخطط البياني (1-8).

النتائج لمجمع حيفا السكني :

- ملائمة التصميم الداخلي للوحدة السكنية : 7% ممتازة 43%، جيدة ، و50% متوسطة .

- تصميم الفضاءات الخارجية للمبنى السكني ومقترباته: 57% جيدة، 43%متوسطة.

- جمالية واجهات البنايات السكنية: 57% جيدة ، و43% متوسطة .

- الفضاءات الخارجية المحيطة بالبنايات السكنية (بالنسبة لتواجد المسنين ولعب الاطفال و الفضاءات الخدمية الاخرى): 21% جيدة، 79% متوسطة.

- **مدى ملائمة المجمع السكني للقيم الجمالية لمجتمعنا** :
43% جيدة، 50% متوسطة ، و7% رديئة .

وهي نتيجة متقاربة مع نتيجة **تقويم المختصين** التي هي : 30% جيدة ، 63% متوسطة ، و 7% رديئة كما نلاحظ في المخطط البياني (1-9).

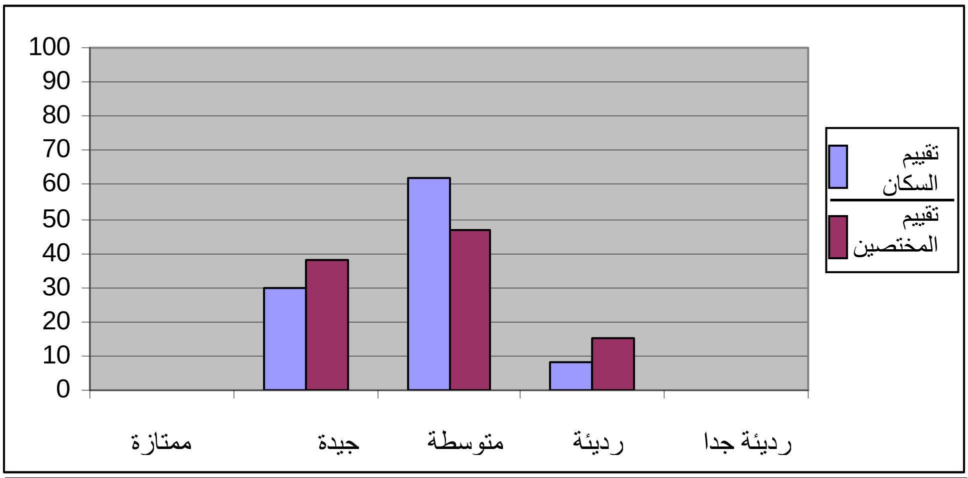

المخطط البياني (1-8) التقويم الجمالي لمجمع الصالحية ، المصدر : (الباحثة)

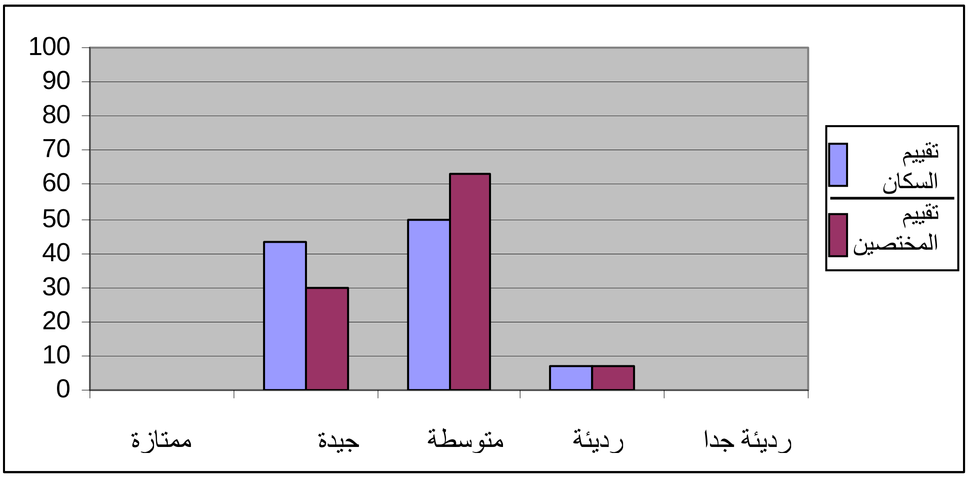

المخطط البياني (1-9) التقويم الجمالي لمجمع شارع حيفا السكني ، المصدر : (الباحثة)

الاستنتاجات

- عملية تصميم المجمع السكني هي عملية معقدة تدخل فيها عدة جوانب (القيم البيئية والجمالية والاجتماعية) و ان فقدان التكامل بينها سيؤدي الى عدة اشكاليات ناتجة عن عدم تحقيق احتياجات السكان الناتج مما سيؤدي الى ان ياخذ الافراد مسالة توفير المسكن الملائم لهم على عاتقهم مما سينتج مشاكل اخرى.

- من خلال استعراض أهم الإشكاليات التى تعـانى منهـا مجمعاتنا السكنية والتى يرى البحث من منطلق الفرضـية البحثية ارتباطها الوثيق بفقدان التكامل بين نواحـي القيم (البيئية – الجمالية – الاجتماعية) في العملية التصميمية، وبعد استعراض الدراسة العملية ونتائجها، يمكن التوصـل إلى الاستنتاجات الاتية:

1- إن عملية تلبية الحاجة السكنية وتـصميم المجمعـات السكنية هي عملية مستمرة وتتطلب التنسيق الفعـال بـين جهود جميع الأطراف بما يحقق أهدافها ويجعـل نتائجهـا تأتي على الوجه المطلوب.

2- إن عدم وجود هذا التنسيق يؤدى إلى حدوث خلل فـى عملية تلبية الحاجة السكنية وبالتالى صعوبة تحقيق أهدافها المختلفة، مما ينعكس بالسلب علـى تـصميم المجمعـات السكنية والمدينة ككل فى شكل إشكاليات معقدة يعانى منها السكان.

5- فى ظل الحاجة السكنية المتفاقمة التي يعاني منها بلادنا في الحقب الأخيرة فإن الأمر يبدو أكثر صعوبة حاليا فـى تحقيق ما يسد هذه الحاجة ويلبي احتياجات السكان في نفس الوقت، إلا أن البحث يرى أن ذلك يمكن تحقيقه من خلال منظومة شاملة لعملية التكامل بين نواحي القيم (البيئيـة – الجمالية – الاجتماعية) التـي تـضمن الحـصول علـى مجمعات سكنية منتمية لبيئتها ومعبرة عن القـيم الجماليـة والاجتماعية للمجتمع وملبية لاحتياجات السكان.

التوصيات :

- وبناء على النتائج الـسابقة فـإن البحـث يقتـرح التوصيات الاتية:

1- توجيه البحث العلمي نحو محاولة إيجاد الـصيغة المناسبة لتحقيق التواصل مع الموروث العمراني وذلك ليس على المستوى الشكلي ولكن الـذهاب الى القيم والمفاهيم التي انتجت هذه العمـارة (اي التواصل على المستوى الفكري) والتي يمكن ان نأخذ منها ما يفيدنا في وقتنا الحاضـر لتحقيـق عمارة عربية معاصرة ذات هوية واحدة .

2- تهيئة المناخ المناسب لتحقيق التكامل المطلوب بين نواحي القيم المختلفة، وذلك بالتوجيـه المناسـب للمصممين والمخططين نحو اسـتثمار المفـاهيم والقيم والحلول التي توفرها لنا بيئتنا التقليدية على النحو الذى يحقق العمارة العربية المعاصرة التي نصبو اليها.

3- تحقيق مشاركة فعالة لكل ناحية من نواحي القـيم في وضع الأطر العامة لعملية تصميم المجمعـات السكنية مع مراعاة الخصوصية الفكرية لعمارتنـا التقليدية، وذلك بما يحقق الاستفادة من الخبـرات السابقة والمحافظة على الأهداف العامة المعاصرة للعملية التصميمية على مختلف مراحلها.

4- للتوصل لتصاميم مجمعات سكنية تشعرنا بالانتماء المكاني يجب مراعاة التكامل بين نـ ـواحي القيم (البيئية – الجمالية – الاجتماعيـة) والخاصـة بالمنطقة التي نصمم فيها .

الجدول (1-1) المشاكل البيئية المصدر :(الباحثة)

المشكلة	مجمع حي السلام السكني		مجمع الصالحية السكني		مجمع شارع حيفا السكني	
	نعم	لا	نعم	لا	نعم	لا
التوجيه غير الصحيح للوحدة السكنية كأن تعاني من اشعة الشمس القوية والمزعجة لوقت طويل (التوجيه الغربي)	%82	%18	%61.5	%38.5	%64	%36
او لاتدخل اشعة الشمس الى فضاءات الوحدة السكنية (التوجيه الشمالي)	%18	%82	%38.5	%61.5	%36	%64
هل تعتقد ان الابواب والشبابيك الموجودة في وحدتك السكنية عازلة جيدة للحرارة والاتربة والبرودة	%29	%71	%31	%69	%21	%79
مساحة النوافذ كبيرة (كميات من الحرارة والاشعة الشمسية غير المرغوب فيها)	%76	%24	%46	%54	%71	%29
الحر الشديد نتيجة وجود وحدتك السكنية في الطابق الاخير	%100	----------	%100	-----------	%100	-----------
ضعف اجهزة التبريد او قلتها	%94	%6	%84.5	%15.5	%93	%7
هل توجد مساحات خضراء كافية ملائمة للجلوس في مقتربات المجمع السكني	%18	%82	%8	%92	-----------	%100
بين الغرف داخل الوحدة السكنية	%70.5	%29.5	%77	%23	%14	%86
بين وحدتين سكنيتين متجاورتين ضمن نفس الطابق او في الطابق الاعلى او الاسفل	%47	%53	%54	%46	%14	%86
بين الوحدة السكنية والممر او الادرج والمصاعد	%71	%29	%31	%69	%7	%93

الجدول (2-1) تقويم النواحي الاجتماعية ، المصدر : (الباحثة)

هل هناك مشكلة في الشرفية على وحدتك السكنية بسبب	**مجمع حي السلام السكني**		**مجمع الصالحية السكني**		**مجمع شارع حيفا السكني**	
	نعم	لا	نعم	لا	نعم	لا
وجود نوافذ قريبة للوحدات المجاورة	%59	%41	%69	%31	%29	%71
وجود ساحات تجمع او شارع	%53	%47	%69	%31	%7	%93
موقع الباب الرئيسي غير مناسب	%65	%35	%31	%69	%29	%71
هل هناك مشكلة في الخصوصية مع الوحدات السكنية المجاورة ضمن نفس الطابق او في الطابق الاعلى او الاسفل	%29	%71	%77	%23	%21	%79
مع البنايات السكنية المجاورة	%24	%76	%38	%62	%7	%93
مع الفضاءات المحيطة بالبناية السكنية	%18	%82	%54	%46	%14	%86
هل هناك خدمات اجتماعية ملائمة وكافية مثل مناطق لتجمع المسنين	%29	%71	%7	%93		%100
ساحات العاب شبابية	%82	%18	%7	%93		%100
مناطق للعب الاطفال	%76	%24	%54	%46		%100
مناطق لتجمع السكان	%47	%53	%7	%93	%7	%93
متنزهات وحدائق عامة	%65	%35	%46	%54		%100
هل تعتقد ان اختلاف المستوى الثقافي بينك وبين الجيران يؤثر سلبا في سلوك	%82	%18	%92	%8	%100	

افراد عائلتك						
هل تفضل ان يكون الطريق المؤدي الى بنايتك السكنية مغلق النهاية	%65	%35	%54	%46	%57	%43
هل تنزعج من تقارب مداخل الوحدات السكنية	%76	%24	%95	%15	%79	%21

الجدول (1-3) تقويم النواحي الجمالية ، المصدر :(الباحثة)

السؤال	مجمع حي السلام السكني		مجمع الصالحية السكني		مجمع شارع حيفا السكني	
	نعم	لا	نعم	لا	نعم	لا
هل تشعر بان واجهة البناية السكنية رصينة ومعبرة عن كونها وحدات سكنية في بيئة عراقية	%76	%24	%76	%24	%100	
هل تشعر بان المباني السكنية ضخمة ومبالغ في مقياسها (الانساني)	%47	%53	%23	%77	%50	%50
هل تشعر بالتكامل والوحدة بين واجهات البنايات السكنية في مجمعك السكني	%59	%41	%62	%38	%86	%14
هل تشعر بالانسجام اللوني بين واجهات البنايات السكنية	%65	%35	%46	%54	%71	%29
هل تشعر بان مساحة الابواب والشبابيك نسبتها ملائمة لواجهة البناية بيئيا واجتماعيا	%41	%59	%62	%38	%71	%29

المصادر:

- الإكيابى ، محمود و نوبى محمد حسن، تكامل القطاعات المختلفة فى عملية التنمية العمرانية للمدينة العربية،2002 .
- الزبيدي ،مها صالح،"**المسكن المتوافق بيئياً...توجه مستقبلي للعمارة المستدامة والحفاظ على البيئة دراسة مقارنة لكفاءة الأداء البيئي للمسكن التقليدي والحديث**"،ندوة الإسكان الثانية(المسكن الميسر)،الهيئة العليا لتطوير مدينة الرياض،الرياض،1425
- السهيري ، عاطف محارب ، **(التكامل في الفعالية البنائية النظرية وتطبيقها على البيت التقليدي البغدادي)** استاذ مساعد / قسم الهندسة المعمارية كلية الهندسة / جامعة بغداد ،ايلول 1999،
- الطالب، طالب حميد، الماضي والمستقبل ونظرتنا للعمارة المعاصرة ،ندوة الخصوصية في العمارة العربية المعاصرة، بغداد 1989،
- العربى ، قدوري ، **التصميم العمراني والمعماري وقيم التراث الاسلامي** ، مجلة المدينة العربية ،منظمة المدن العربية العدد39، الكويت ، سبتمبر ، 1989
- خير الدين، عمرو، (المعالجات البيئية في تخطيط المدن الاسلامية وتصميم مبانيها)، سجل بحوث مؤتمر انتربيلد، القاهرة ، 1997.
- شاهين ، بهجت رشاد ،**بعض خصوصيات السكن العربي المعاصر في المناطق الحارة الجافة** ، المجلة العراقية للهندسة المعمارية ، الاعداد 11-19 ، تشرين الاول، الجامعة التكنلوجية ، بغداد ،2006 .
- صوفان، أسمهان. **"الحي السكنى في المدينة العربية المعاصرة"** ندوة المدينة العربية خصائصها وتراثها الحضاري الإسلامي. (28 فبراير – 5 مارس 1981م). المملكة العربية السعودية: المدينة المنورة
- كمونه ، حيدرعبد الرزاق ،**اهم الخصائص المميزة للموروث المعماري في تخطيط وتصميم المدينة العربية التقليدية**، جريدة القادسية ، بغداد ،10، كانون الاول ،1994
- نوبي محمد حسن ،**(مبادئ التصميم المعماري لنمط المباني ذات الأفنية الداخلية)** ، مدرس التصميم المعماري ونظريات العمارة قسم العمارة - كلية الهندسة - جامعة أسيوط – مصر 2003 بريد إلكتروني: nouby@rocketmail.com.
- AlBayaty, Muthana Jamal ,**Interpreting the Dialogue Between Man and Architectural Form** ,PH.D Dissertation ,University of Pensylvania,1983
- Golany G. S. (1996) **Urban Design Morphology and Thermal Performance Atmospheric Environment**. Vol.30 No.3
Rapoport , Amos **,(Human Aspect of Urban -Form),** per amon press, Y.K., 1977.
Rush, Richard D. **The building systems -integration** handbook,Canada,1986

RELIABILITY ANALYSIS OF THE SEISMIC STABILITY OF EMBANKMENTS REINFORCED WITH STONE COLUMNS

Ahmed S. Jawad
Assistant lecturer, University of Baghdad,
College of Eng., Civil Eng. Dept.

ABSTRACT

Geotechnical engineers have always been concerned with the stabilization of slopes. For this purpose, various methods such as retaining walls, piles, and geosynthetics may be used to increase the safety factor of slopes prone to failure. The application of stone columns may also be another potential alternative for slope stabilization. Such columns have normally been used for cohesive soil improvement. Most slope analysis and design is based on deterministic approach i.e a set of single valued design parameter are adopted and a set of single valued factor of safety (FOS) is determined. Usually the FOS is selected in view of the understanding and knowledge of the material parameters, the problem geometry, the method of analysis and the consequences of failure. This results in different FOS obtained by different designers. This inherent variability characteristic dictates that slope stability problem is a probabilistic problem rather than deterministic problem. Furthermore, the FOS approach cannot quantify the probability of failure or level of risk associated with a particular design situation. The objective of this study is to integrate probabilistic approach as a rational means to incorporate uncertainty in the slope stability analysis. The study was made through a hypothetical problem which includes a sensitivity analysis. The methodology is based on Monte Carlo simulation integrated in commercially available computer program SLOPE/W. The output of the analysis is presented as the probability of failure as a measure of the likelihood of the slope failure. Results of this study have verified that the probability of failure is a better measure of slope stability as compared to the factor of safety because it provides a range of value rather than a single value.

الاعتمادية في تحليل الاستقرارية تحت تاثير الهزات الارضية للسداد الترابية المسلحة بالاعمدة الحجرية

الخلاصة

ان المهندسين الجيوتكتيك غالبا ما يتعاملون مع مسائل تثبيت المنحدرات و تستخدم لهذا الغرض عدة طرق منها الجدران الساندة اوالركائز لزيادة معامل الامان لمنحدرات المائلة الى الفشل. حيث ان استخدام الاعمدة الحجرية قد تعتبر احد الطرق البديلة المحتملة لتثبيت المنحدرات و التي تستخدم لتحسين الترب التي تمتلك خاصية التماسك.

ان معظم طرق التحليل و التصميم مبنية على اساس طرق حسابية تقريبية بمعنى اخر تبني قيمة مفردة للتصميم مبنية على اساس وضع قيمة حسابية واحدة لمعامل الامان.ان قيمة معامل الامان غالبا ما تختار بعد فهم و معرفة متغيرات خواص المادة و الشكل الهندسي للمنحدر و طريقة التحليل وتتابع الفشل و الذي يؤدي الى حصول نتائج مختلفة لمعامل الامان باختلاف المصممين ولذلك فان هذا التباين الموروث في الخواص يملي علينا اعتبار مسالة استقرارية المنحدرات هي مسالة احتمالية اكثر من كونها مسالة حسابية فقط.

ان الهدف من هذا البحث هو ايجاد تقريب احتمالي كمعنى عقلاني يتضمن الشكوك في تحليل السداد الترابية المسلحة بالاعمدة الحجرية حيث ان الدراسة اجريت على مسالة افتراضية تتضمن الحساسية في تباين خواص المواد في التحليل. ان الدراسة مبنية على نموذج Monte Carlo الموجود ضمنيا في البرنامج SLOPE/W. وقد وجد في هذه الدراسة ان احتمالية الفشل احسن مقياس لاستقرارية المنحدر اذا ماقورنت مع معامل الامان بسب انها توفر مجموعة من قيم معامل الامان بدلا من حصول على قيمة واحدة.

Keywords: stone column, slope stability, probability, reliability index, seismic analysis.

INTRODUCTION

Soils are naturally formed materials; consequently their physical properties vary from point to point. This variation occurs even in an apparently homogeneous layer. The variability in the value of soil properties is a major contributor to the uncertainty in the stability of a slope. Laboratory results on natural soils indicate that most soil properties can be considered as random variables conforming to the normal distribution function (Lumb, 1966, Tan et al. 1993).

Deterministic slope stability analyses compute the factor of safety based on a fixed set of conditions and material parameters. If the factor of safety is greater than unity, the slope is considered to be stable. On other hand, if the factor of safety is less than unity, the slope is considered to be unstable or susceptible to failure. Deterministic analyses suffer from limitations such as the variability of the input parameters.

In general, a factor of safety is really an index indicating the relative stability of a slope. It does not imply the actual risk level of the slope due to the variability of input parameters. With probabilistic analysis, two useful indices are available to quantify the stability or the risk level of a slope. These two indices are known as the probability of failure and the reliability index.

METHODS FOR SEISMIC SLOPE STABILITY ANALYSES

Surveys of earth dam performance during earthquakes suggest that embankments constructed of materials that are not vulnerable to severe strength loss as a result of earthquake shaking (most well compacted clayey materials, unsaturated cohesionless materials, and some dense saturated sands, gravels, and silts) generally perform well during earthquakes (Seed et. al., 1978). The embankment, however, may undergo some level of permanent deformation as a result of the earthquake shaking with well-built earth embankments experiencing moderate earthquakes, the magnitude of permanent seismic deformations should be small, but marginally stable earth embankments experiencing major earthquakes may undergo large deformations that may jeopardize the structure's integrity. Simplified procedures have been developed to evaluate the potential for seismic instability and seismically induced permanent deformations (Seed, 1979; Makdisi and Seed, 1978), for the evolution of the seismic stability of natural slopes in clayey materials in most often carried out using various modifications of the following two methods (Duncan and Wright, 2005):

1. Pseudo-static method.
2. Sliding block method.

Pseudo Static Analyses

One of the earliest procedures of analysis for seismic stability is the pseudo static procedure, in which the earthquake loading is represented by a static force, equal to the soil weight multiplied by a seismic coefficient, k. The pseudo static force is used in a conventional limit equilibrium slope stability analysis. The seismic coefficient may be thought of loosely as an acceleration (expressed as a fraction of the acceleration, g, due to gravity) that is produced by the earthquake. However, the pseudo static force is treated as a static force and acts in only one direction, whereas the earthquake accelerations act for only a short time and change direction, tending at certain instances in time to stabilize rather than destabilize the soil.

The term pseudo static is a misnomer, because the approach is actually a static approach that is more correctly termed pseudo dynamic; however. The vertical components of the earthquake accelerations are usually neglected in the pseudo static method, and the seismic coefficient usually represents a horizontal force. Application of a seismic coefficient and pseudo static force in limit quilibrium slope stability analyses is relatively straightforward from the perspective of the mechanics: The pseudo static force is assumed to be a known force and is included in the various equilibrium equations as shown in Figure (1) for an infinite slope with the shear strength expressed in terms of total stresses.

Sliding Block Analyses

Newmark (1965) first suggested a relatively simple deformation analysis based on a rigid sliding block. In this approach the displacement of a mass of soil above a slip surface is modeled as a rigid block of soil sliding on a plane surface as shown in figure (2). When the acceleration of the block exceeds yield acceleration, a_y, the block begins to slip along the plane. Any acceleration that exceeds the yield acceleration causes the block to slip and imparts a velocity to the block relative to the velocity of the underlying mass. The block continues to move after the acceleration falls below the yield acceleration. Movement continues until the velocity of the block relative to the underlying mass goes to zero, as shown in figure (3). The block will slip again if the acceleration again exceeds the yield acceleration. This stick-slip pattern of motion continues until the accelerations fall below the yield acceleration and the relative velocity drops to zero for the last time. To compute displacements, the accelerations in excess of the yield acceleration are integrated once to compute the velocities and a second time to compute the displacements as shown in figure (3).

EMBANKMENTS STABILIZED WITH STONE COLUMNS

A number of factors and parameters such as soil properties, pore water pressure resume, slope geometry, earthquake, and vibration can influence the slope stability. Engineering slope stabilization is generally referred to stop or decrease the possible of instability process of slopes. Preventing the movement of a slope or increasing the safety factor (SF) is possible by using structural or geotechnical methods. Stone columns are method for slope stabilization. Such columns have been used since 1950 normally for cohesive soil improvement. It is a hole with circular section which is filled by gravel, rubble and etc and is an effective method to increase the shear strength on the slip surface of clayey slopes. The most important cases for utilizing stone columns (Barksdale and Bachus, 1983) are:

1. Improving slopes stability of both embankment and natural slopes.
2. Increasing the bearing capacity of shallow foundations constructed on soft soils.
3. Reducing total and differential settlements.
4. Decreasing the liquefaction potential of sandy soils.

RELIABILITY AND PROBABILITY OF FAILURE

The probability of failure can be interpreted in two ways (Mostyn and Li, 1993):

- If a slope is to be constructed many times, what percentage of such slopes would fail.
- The level of confidence that can be placed in a design.

The first interpretation may be relevant in projects where the same slope is constructed many times, while the second interpretation is more relevant in projects where a given design is only constructed once and it either fails or it does not. Nevertheless, the probability of failure is a good index showing the actual level of stability of a slope.

There is no direct relationship between factor of safety and probability of failure. In other words, a slope with a higher factor of safety may not be more stable than a slope with a lower factor of safety (Harr, 1987). For example, a slope with factor of safety of 1.5 and a standard deviation of 0.5 will have a much higher probability of failure than a slope with factor of safety of 1.2 and a standard deviation of 0.1.

The reliability of a slope (R) is an alternative measure of stability that considers explicitly the uncertainties involved in stability analyses. The reliability of a slope is the computed probability that a slope will not fail and is 1.0 minus the probability of failure (Duncan and Wright, 2005):

$$\mathbf{R=1-P_f} \qquad (1)$$

Where:
$\mathbf{P_f}$ is the probability of failure and **R** is the reliability or probability of no failure.
Reliability calculations provide a means of evaluating the combined effects of uncertainties and a means of distinguishing between conditions where uncertainties are particularly high or low.
The reliability index provides a more meaningful measure of stability than the factor of safety. The reliability index (β) is defined in terms of the mean (μ) and the standard deviation (σ) of the trial factors of safety as (Christian et al., 1994):

$$\beta = \frac{\mu - 1}{\sigma} \qquad (2)$$

The reliability index describes the stability of a slope by the number of standard deviations separating the mean factor of safety from its defined failure value of 1.0. It can also be considered as a way of normalizing the factor of safety with respect to its uncertainty.

STATISTICAL ANALYSIS OF SOIL DATA

Probability Density Function

A normal distribution function, often referred to as the Gaussian distribution function, is the most commonly used function to describe the variability of input parameters in probabilistic analyses. The normal distribution is so prevalent because many physical measurements provide frequency distributions that closely approximate a normal curve. A normal distribution function can be represented mathematically as:

$$f(x) = \frac{1}{\sqrt{2\pi\sigma}} e^{-\frac{(\chi-\mu)^2}{2\sigma^2}} \quad -\infty\langle\chi\rangle\infty \qquad (3)$$

Where:
$f(x)$ = relative frequency
σ = standard deviation
μ = mean value

A normal curve is bell shaped, symmetric and with the mean value exactly at middle of the curve. A normal curve is fully defined when the mean value, m and the standard deviation, s are known. A probability density function (PDF) shown in Figure (4) which describes the relative likelihood that the variable will have a certain value within the range of potential values. In this case the random variable is continuously distributed. A PDF can be fitted over the frequency diagram, which is a modified histogram whose ordinate has been scaled, so that the area under the histogram is unity.

Random Number Generation

The random numbers generated from the function are uniformly distributed with values between 0 and 1.0. In order to use the uniformly generated random number in the calculations of the normally distributed input parameters, it is necessary to transform the uniform random number to a normally distributed random number. This "normalization" process is done using the following transformation equation as suggested by SLOPE/W manual (2005):

$$N = \sqrt{(-2\ln R_1)} * (2\pi R_2) \qquad (4)$$

Where:
N = normalized random number
R_1 = uniform random number 1
R_2 = uniform random number 2

The transformation equation requires the generation of two uniform random numbers. The normalized random number can be viewed as the standard normal deviate in a normal curve with a mean value of 0 and standard deviation of 1.

Correlation Coefficient

A correlation coefficient expresses the relative strength of the association between two parameters. Laboratory tests on a wide variety of soils (Lumb, 1970) show that the shear strength parameters c and f are often negatively correlated with correlation coefficient ranges from -0.72 to 0.35. Correlation between strength parameters may affect the probability distribution of a slope. SLOPE/W allows the specification of c and f correlation coefficients for all soil models using c and f parameters. Furthermore, in the case of a bilinear soil model, SLOPE/W

allows the specification of correlation coefficient for f and f2.
Correlation coefficients will always fall between -1 and 1. When the correlation coefficient is positive, c and f are positively correlated implying that larger values of c are more likely to occur with larger values of f. Similarly, when the correlation coefficient is negative, c and f are negatively correlated and reflects the tendency of a larger value of c to occur with a smaller value of f. A zero correlation coefficient implies that c and f are independent parameters.

In SLOPE/W, when estimating a new trial value for f and f2, the normalized random number is adjusted to consider the effect of correlation. The following equation is used in the adjustment:

$$N_A = N_1 k + (1 - | k |) N_2 \tag{5}$$

Where:
k = correlation coefficient between the first and second parameters
N1 = normalized random number for the first parameter
N2 = normalized random number for the second parameter
Na = adjusted normalized random number for the second parameter.

Method of Probabilistic Analysis
Monte Carlo method

The Monte Carlo method is a simple but versatile computational procedure. In general, the implementation of the method involves the following (Yang et al., 1993):

- The selection of a deterministic solution procedure, such as the Spencer's method or the finite element stress method.
- Decisions regarding which input parameters are to be modelled probabilistically and the representation of their variability in terms of a normal distribution model using the mean value and standard deviation.
- The estimation of new input parameters and the determination of new factors of safety many times.
- The determination of some statistics of the computed factor of safety, the probability density and the probability distribution of the problem.

In SLOPE/W, the critical slip surface is first determined based on the mean value of the input parameters using any of the limit equilibrium and finite element stress methods. Probabilistic analysis is then performed on the critical slip surface, taking into consideration the variability of the input parameters. The variability of the input parameters is assumed to be normally distributed with user-specified mean values and standard deviations.
During each Monte Carlo trial, the input parameters are updated based on a normalized random number. The factors of safety are then computed based on these updated input parameters. By assuming that the factors of safety are also normally distributed, SLOPE/W determines the mean and the standard deviations of the factors of safety. The probability distribution function is then obtained from the normal curve.
The number of Monte Carlo trials in an analysis is dependent on the number of variable input parameters and the expected probability of failure. In general, the number of required trials increases as the number of variable input increases or the expected probability of failure becomes smaller. It is not unusual to do thousands of trials in order to achieve an acceptable level of confidence in a Monte Carlo probabilistic slope stability analysis (Mostyn and Li, 1993).

Number of Monte Carlo Trials

Probabilistic slope stability analysis using the Monte Carlo method involves many trial runs. Theoretically, the more trial runs used in an analysis the more accurate the solution will be. How many trials are required in a probabilistic slope stability analysis? Harr, (1987) suggested that the number of required Monte Carlo trials is dependent on the desired level of confidence in the solution as well as the number of variables being considered. Statistically, the following equation can be developed (Harr, 1987):

$$N_{mc} = \left[\frac{(d^2)}{(4(1-\varepsilon)^2)} \right]^m \tag{6}$$

where :
N_{mc} = number of Monte Carlo trials,
ε = the desired level of confidence (0 to 100%) expressed in decimal form,
d = the normal standard deviate corresponding to the level of confidence, and
m = number of variables.

Measure of Random Variables

SLOPE/W assumes that the trial factors of safety are normally distributed. As a result, statistical analysis can be conducted to determine the mean, standard deviation, the probability density function and the probability distribution function of the slope stability problem. The equations used in the statistical analysis are summarized as follows (Lapin, 1983):

Mean factor of safety, μ:

$$\mu = \left(\frac{\sum_{i=0}^{n} F_i}{n} \right) \tag{7}$$

Standard deviation, σ:

$$\sigma = \sqrt{\left(\frac{\sum_{i=0}^{n} (F_i - \mu)^2}{n} \right)} \tag{8}$$

PARAMETRIC STUDY

The parametric study contains the analysis of embankment constructed on soft clays. The material of the embankment body is the same as that of its foundation but strengthened with stone columns. In this section, a one row or two rows (at distance 1.7m from first row) of stone columns are used to reinforce the slope and parametric study has been performed to determine the effect of uncertainties in the geotechnical properties of the slope soil materials and stone column material on the slope stability. The embankment to be analyzed is shown in figure (5). The height of embankment is 10m with 30^0 side slopes and 10m crest width.

The geotechnical properties of the clayey soil and stone column are shown in Tables (1) and (2).

Typically, the strength parameters (C and Φ) and the unit weight could be treated as variables. Table (3) shows a summary of typical reported values of coefficient parameters.

In this section, a study is to be carried out on embankment constructed using different conditions (with and without stone columns). Reliability is studied and different states of standard division are discussed.

Case (1)

Four soil parameters are considered as variables, the strength of the embankment and its foundation, angle of internal friction of the stone column and saturated unit weight of the soil and stone column as shown in Table (4) by making use of the data of Table (3)

The results obtained from analysis of case (1) where the standard deviation with lower limit are shown in Tables (5) and (6) for static and seismic conditions, respectively. In general, the mean factor of safety increases as compared to the factor of safety obtained from state without using stone columns analysis. The probability of failure decreases or the reliability index increases when the stone column of one or two rows is used.

The density function and cumulative distribution function of the factor of safety for this case as obtained by the program Slope/W are shown in Figures (6) to (17) for static and seismic analysis respectively.

Case (2)

In this case the soil is analyzed with a maximum limit of standard division for the strength, angle of internal friction and unit weight of soil as shown in Table (7)

Tables (8) and (9) show the result of analysis where the standard deviation is calculated with upper limit for static and seismic analysis. The effect of increasing the standard deviation on the probability density function and cumulative distribution function of factor of safety are demonstrated in Figures (18) to (29).The reliability index obtained for this case is much less than the reliability index obtained from case (1).

The density function and cumulative distribution function of the factor of safety for this case as obtained by the program Slope/W are shown in Figures (18) to (29) for static and seismic analysis, respectively.

Form static slope stability analysis, it can be noticed from the results based on lower limit and upper limit of standard deviation that the use of one row of stone columns increases the reliability index by about (93) % and (58) %, respectively. An increase in the reliability index to about (94) % and (61) % is obtained when using two rows of stone columns, while when adopting seismic load in slope stability analysis, the increase in reliability index is about (90) % and (83) for one raw of stone column and increase in the reliability index is about (94) % and (91) % for two rows of stone columns. This means that the best improvement in stability is obtained when using one row, then limited benefit is obtained when increasing the number of rows.

CONCLUSIONS

1. A reduction in the probability of failure in the order of about (41-100) % can be obtained when using two rows of stone columns in the embankment with two limits of standard deviation for static slope stability analysis.
2. The effect of seismic load on the probability failure reduction is in the order of about (26-56) % when using two rows of stone columns in the embankment with upper and lower limits of standard deviation.
3. The safety factor values and reliability index of stone column reinforced slopes are influenced by various parameters including geotechnical properties of the stone column material and number of rows.
4. The results obtained from seismic analysis of cases 1 and 2 show that the mean factor of safety increases as compared to the minimum factor of safety obtained from deterministic analysis.
5. The mean safety factor does not change much when standard deviations are varied in the static slope stability analysis However, the probability of failure increase gradually when the standard deviation of the soil parameters increases.
6. There is no direct relationship between the factor of safety and probability of failure, In other words the slope of higher factor safety; it does not mean that the slope is safe because of high probability of failure or low reliability index.

REFERENCES

1. Barksdale R.D., Bachus R.C., 1983. "**Design and Construction of Stone Columns**", Federal Highway Administration Office of Engineering and Highway Operations, Volume I and II, Washington, DC.
2. Christian, J.T., Ladd, C.C. and Baecher, G.B., 1994. "**Reliability Applied to Slope Stability Analysis**" Journal of Geotechnical Engineering, Vol. 120, No. 12. Pp. 2180-2207.
3. Duncan, J., M., Wright, S., G., 2005" **Soil Strength and Slope Stability**" John Wiley & Sons, Inc
4. Duncan, M., and Honorary, 2000. "**Factors of Safety and Reliability in Geotechnical Engineering**" Journal of Geotechnical and Geoenvironmental Engineering, Vol. 126, No. 4, pp. 307-316.
5. Ghazavi M. and Shahmandi A., 2008." **Analytical Static Stability Analysis of Slopes Reinforced by Stone Columns** The 12th International Conference of International Association for Computer Methods and Advances in Geomechanics (IACMAG Goa, India . pp. 2530-2537.
6. Harr, M.E., 1987. "**Reliability-Based Design in Civil Engineering**". McGraw-Hill Book Company.

7. Lapin, L.L., 1983. "**Probability and Statistics for Modern Engineering**." PWS Publishers.
8. Lumb, P., 1966. "**The Variability of Natural Soils**", Canadian Geotechnical Journal, Vol. 3, No. 2, pp. 74-97.
9. Lumb, P., 1970. "**Safety Factors and the Probability Distribution of Soil Strength**" Canadian Geotechnical Journal, Vol. 7, No. 3, pp. 225-242.
10. Makdisi, F. I., and Seed, H. B. 1978.," **Simplified procedure for estimating dam and embankment earthquake-induced deformation**." Geotechnical Journal., ASCE. vol. 104, No.7, pp849–867.
11. Mostyn, G.R. and Li, K.S., 1993. "**Probabilistic Slope Stability Analysis**" - State-of-Play, Proceedings of the Conference on Probabilistic Methods in Geotechnical Engineering, Canberra, Australia. pp. 281-290.
12. Newmark, N. M., 1965," **Effects of earthquakes on dams and embankments**", Geotechnique, Vol. 15, No. 2, pp. 139–160.
13. Seed, H. B. 1979. "**Considerations in the earthquake-resistant design of earth and rockfill dams.**" Geotechnique. vol. 29, No.3, pp.215–263.
14. Seed, H. B., Makdisi, F. I., and DeAlba, P., 1978." **Performance of earth dams during earthquakes**". Geotechnical Journal., ASCE. vol. 104No.7 pp967–994.
15. Slope/W manual. www.geoslope.com
16. Tan, C.P. Donald, I.B. and Melchers, R.E. , 1993." **Probabilistic Slope Stability Analysis**" - State-of-Play, Proceedings of the Conference on Probabilistic Methods in Geotechnical Engineering, Canberra, Australia. pp. 89-110.
17. Yang, D., Fredlund, D.G. and Stolte, W.J., 1993. "A Probabilistic Slope Stability Analysis Using Deterministic Computer Software" Proceedings of the Conference on Probabilistic Methods in Geotechnical Engineering, Canberra, Australia. pp. 267-274.

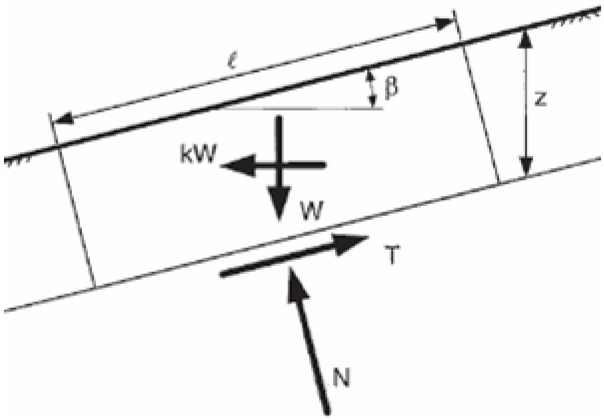

Resolving forces perpendicular to slip plane:

$$N = W\cos\beta - kW\sin\beta$$

Resolving force parallel to slip plane:

$$T = W\sin\beta + kW\cos\beta$$

Weight of sliding block:

$$W = \gamma \ell z \cos\beta$$

Substituting (3) into (1) and (2):

$$N = \gamma \ell z \cos^2\beta - k\gamma \ell z \cos\beta \sin\beta$$

$$T = \gamma \ell z \cos\beta \sin\beta + k\gamma \ell z \cos^2\beta$$

For the stresses on the slip plane:

$$\sigma = \frac{N}{\ell} = \gamma z \cos^2\beta - k\gamma z \cos\beta \sin\beta$$

$$\tau = \gamma z \cos\beta \sin\beta + k\gamma z \cos^2\beta$$

Finally, for the factor of safety (total stresses):

$$F = \frac{s}{\tau} = \frac{c + \sigma\tan\phi}{\tau} = \frac{c + \left(\gamma z \cos^2\beta - k\gamma z \cos\beta \sin\beta\right)\tan\phi}{\gamma z \cos\beta \sin\beta + k\gamma z \cos^2\beta}$$

Figure (1) Derivation of the equation for the factor of safety of an infinite slope with a seismic force (kW)—total stress analyses, after (Duncan and Wright, 2005)

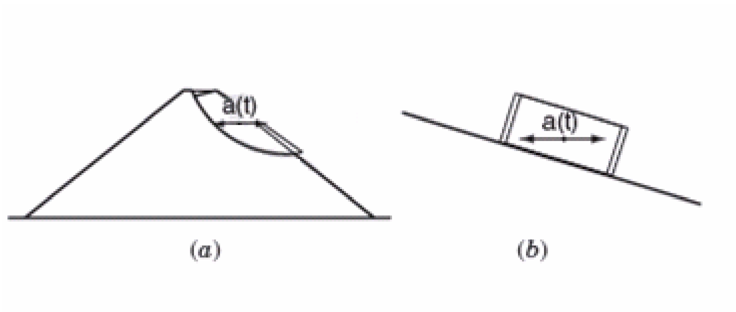

Figure (2) (a) Actual slope; (b) sliding block representation used to compute permanent soil displacements in a slope subjected to earthquake shaking, after (Duncan and Wright, 2005).

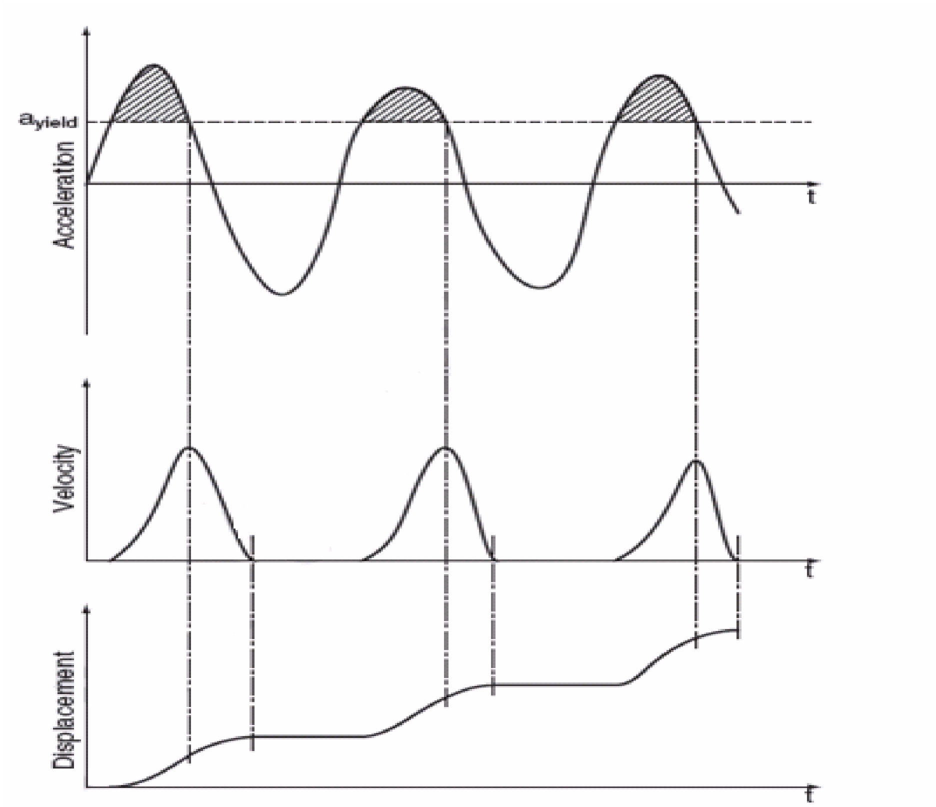

Figure (3) Double integration of acceleration–time history to compute permanent displacements, after (Duncan and Wright, 2005).

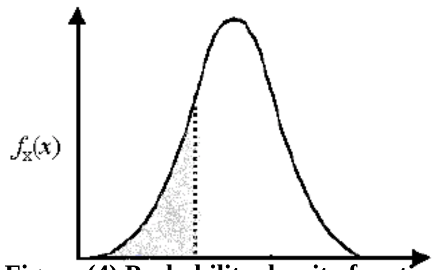

Figure (4) Probability density function

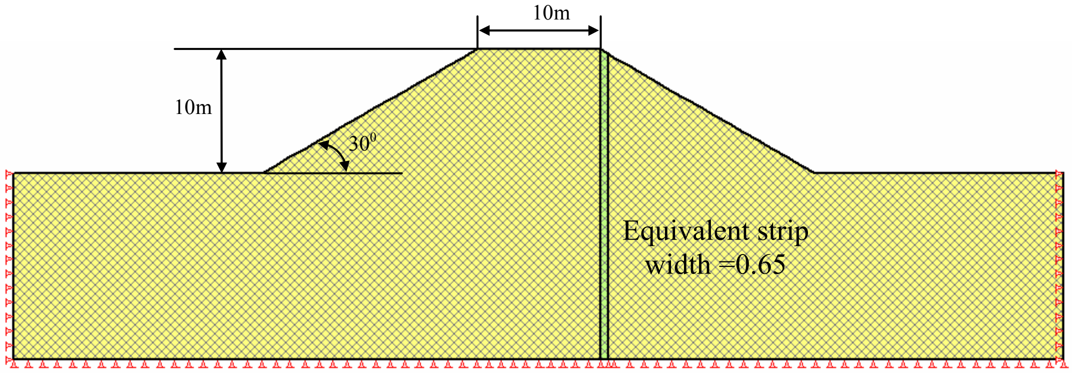

Figure (5) Geometrical specification of slope with stone column (after Ghazavi and Shahmandi, 2008).

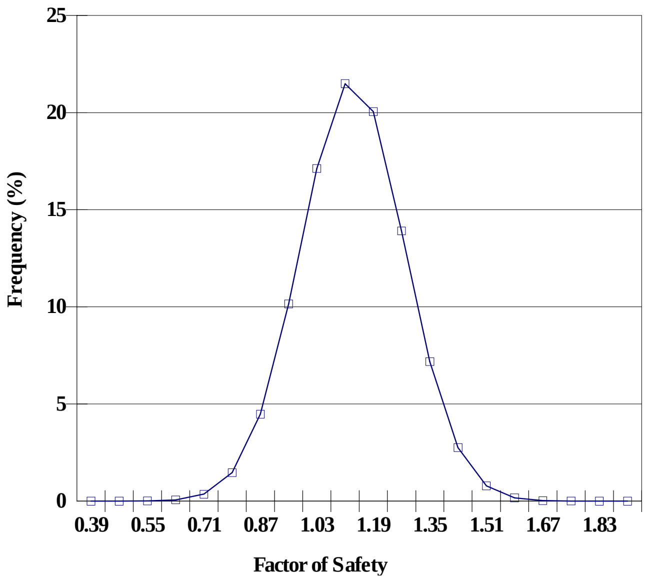

Figure (6) Probability density function without stone columns for static analysis

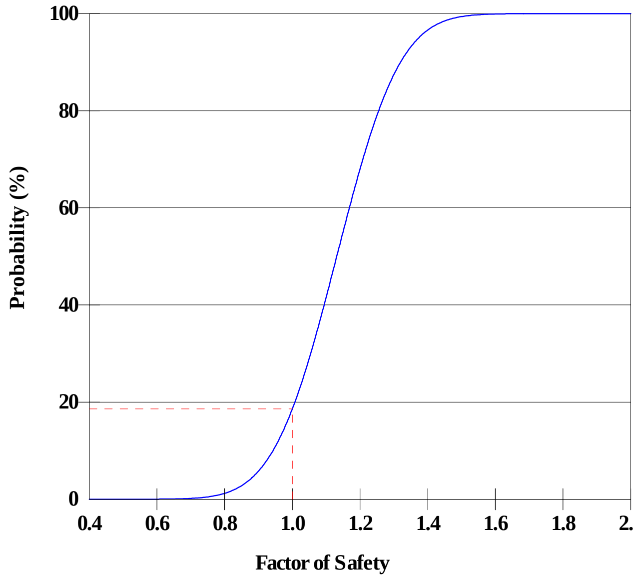

Figure (7) Probability distribution function without stone columns for static analysis

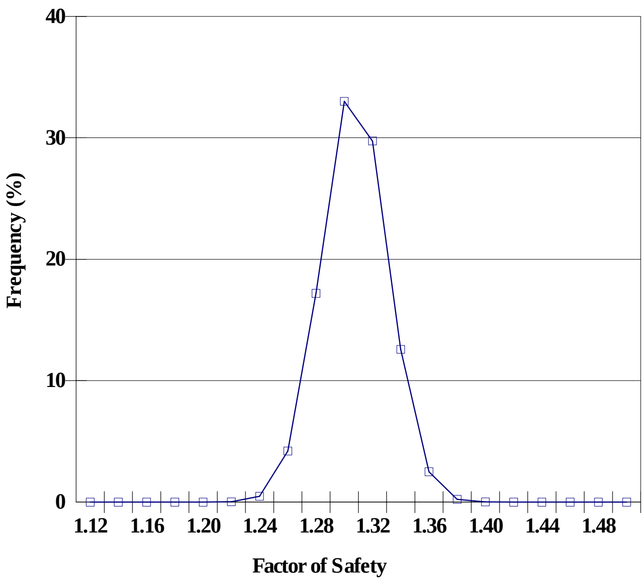

Figure (8) Probability density function with one stone column for static analysis

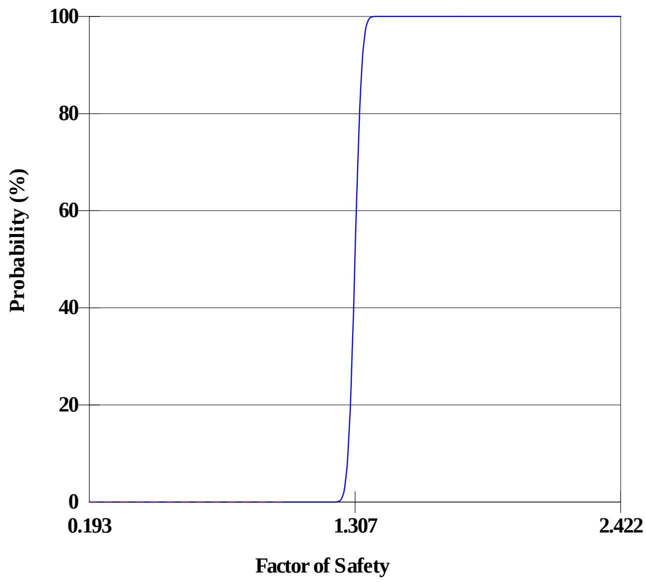

Figure (9) Probability distribution function with one stone column for static analysis

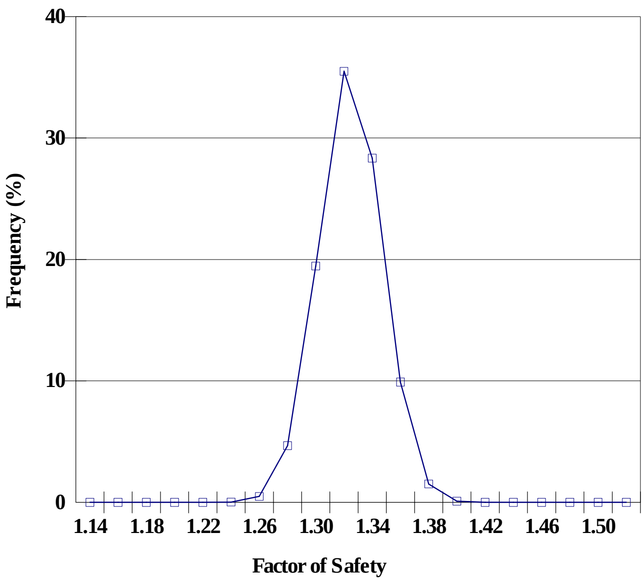

Figure (10) Probability density function with two stone columns for static analysis

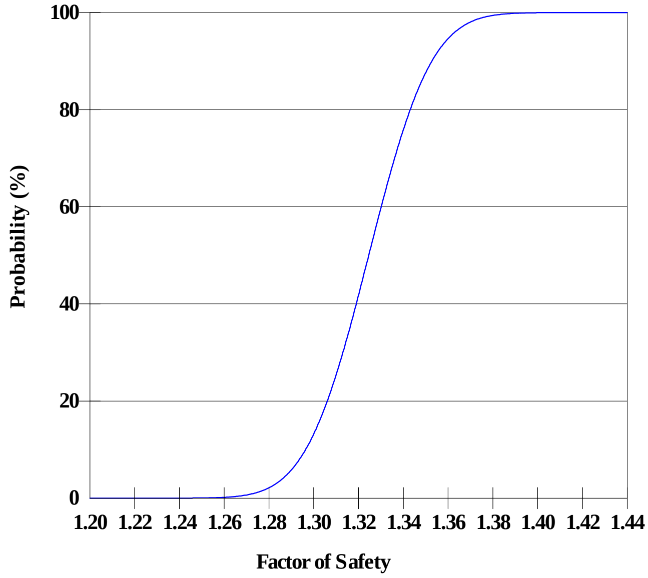

Figure (11) Probability distribution function with two stone columns for static analysis

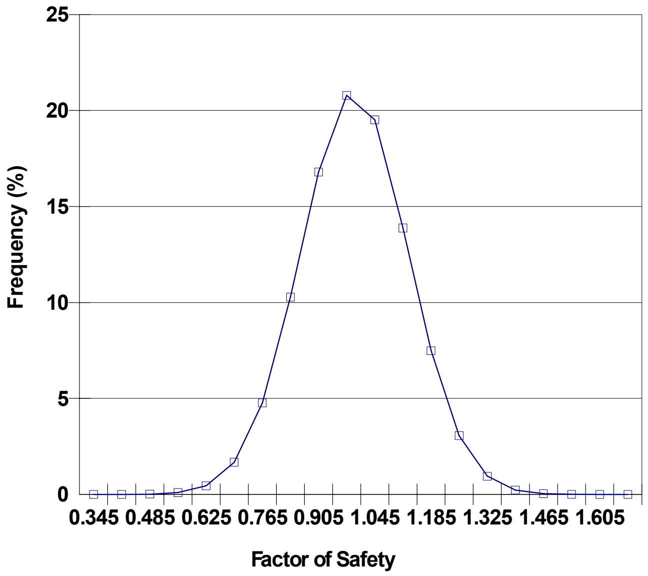

Figure (12) Probability density function without stone columns for seismic analysis

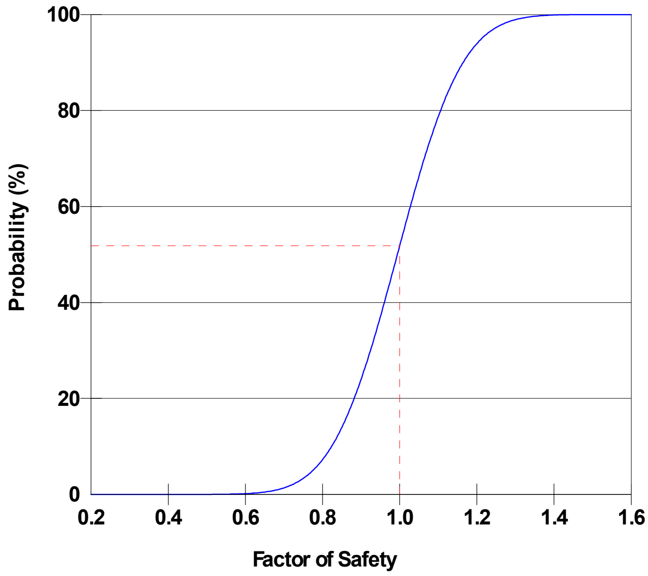

Figure (13) Probability distribution function without stone columns for seismic analysis

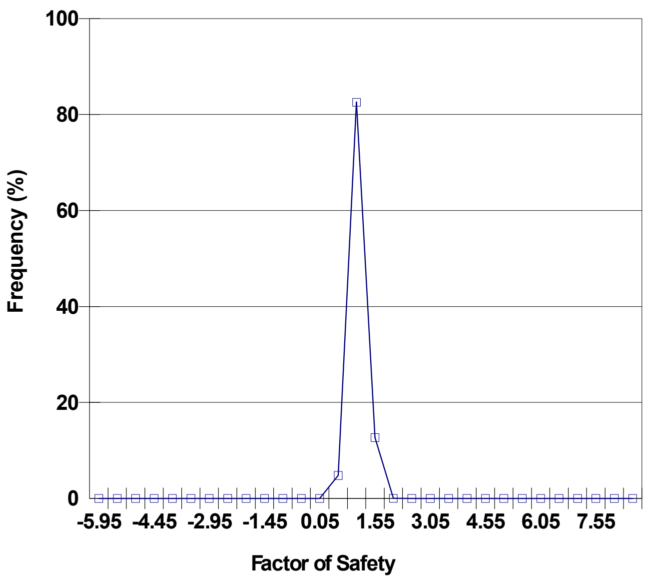

Figure (14) Probability density function with one stone column for seismic analysis

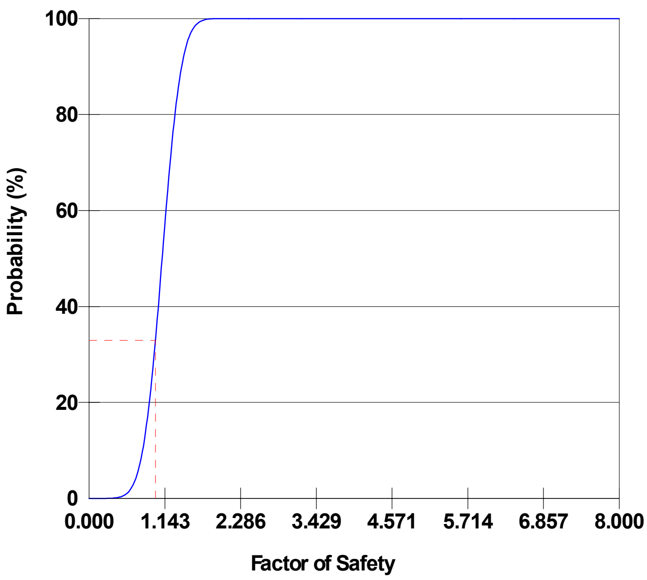

Figure (15) Probability distribution function with one stone column for static analysis

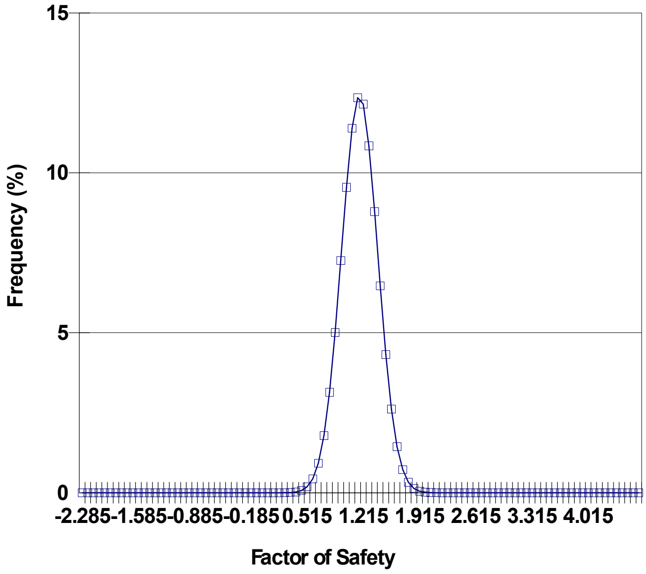

Figure (16) Probability density function with two stone columns for seismic analysis

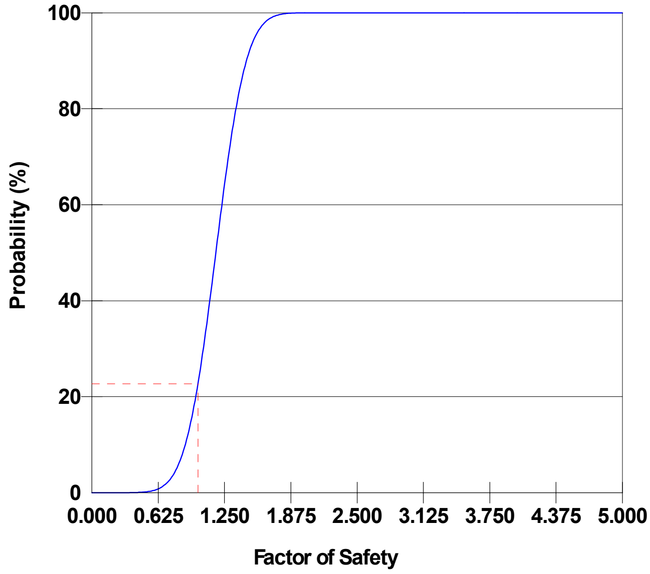

Figure (17) Probability distribution function with two stone columns for seismic analysis

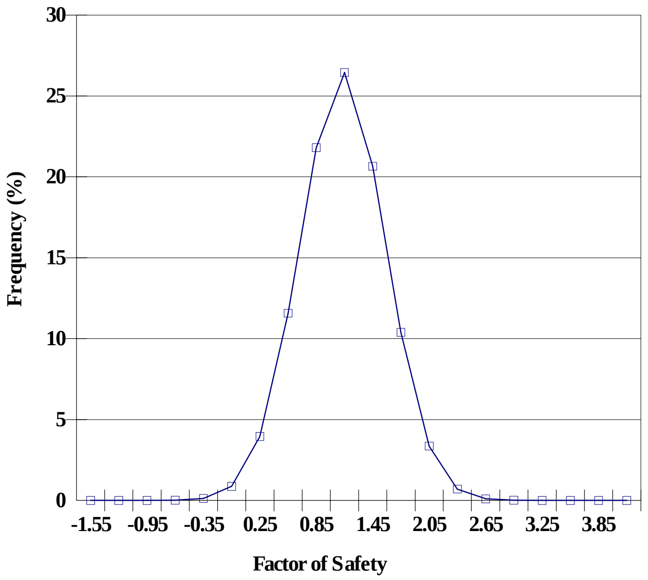

figure (18) Probability density function without stone columns for static analysis

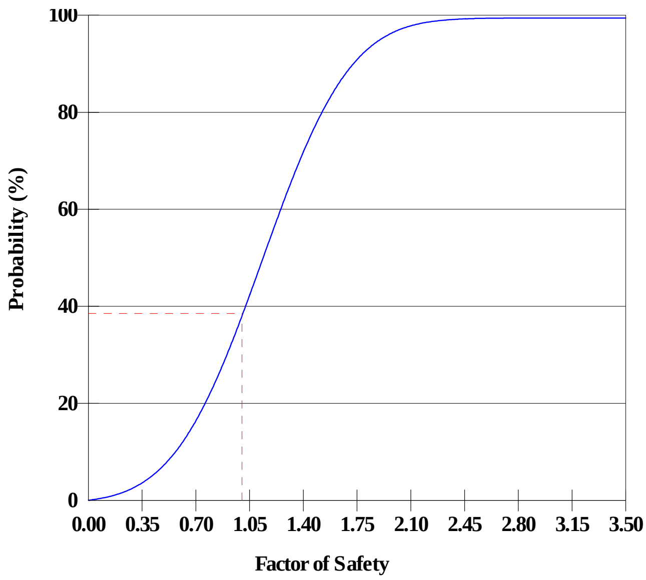

Figure (19) Probability distribution function without stone columns for static analysis

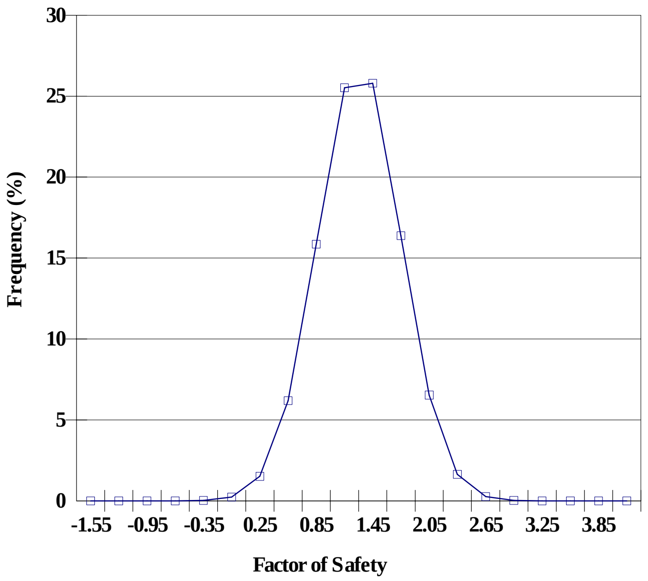

Figure (20) Probability density function with one stone column for static analysis

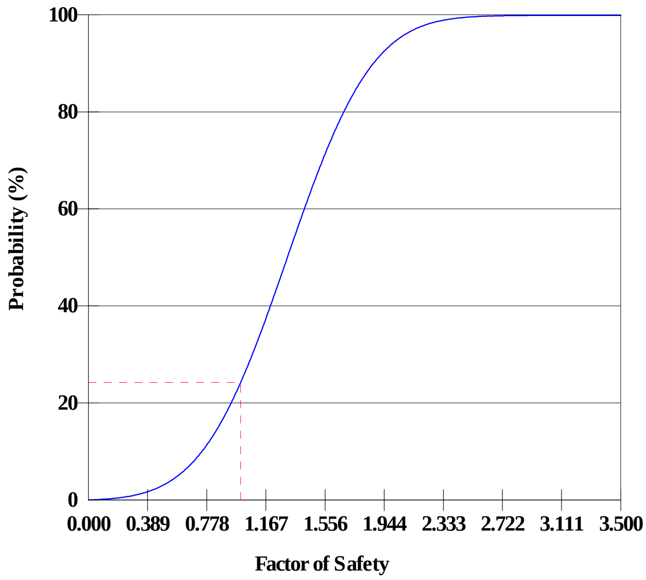

Figure (21) Probability distribution function with one stone column for static analysis

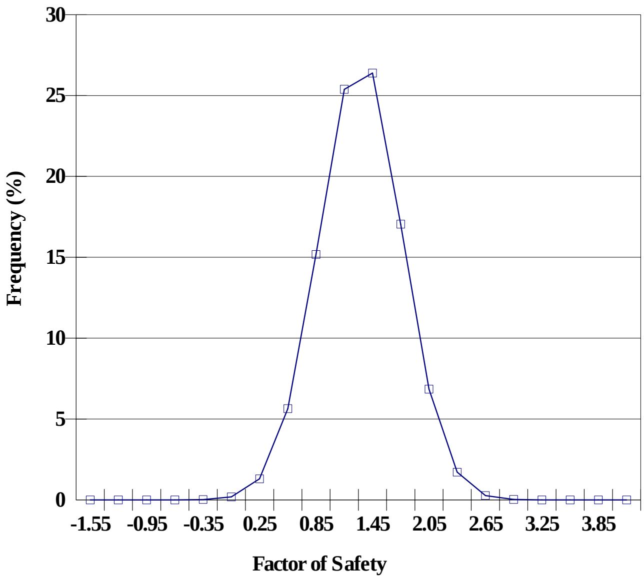

Figure (22) Probability density function with two stone columns for static analysis

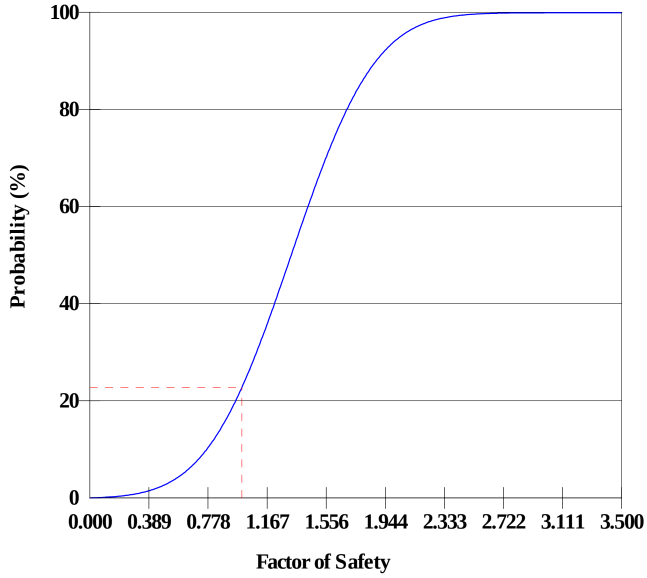

Figure (23) Probability distribution function with two stone columns for static analysis

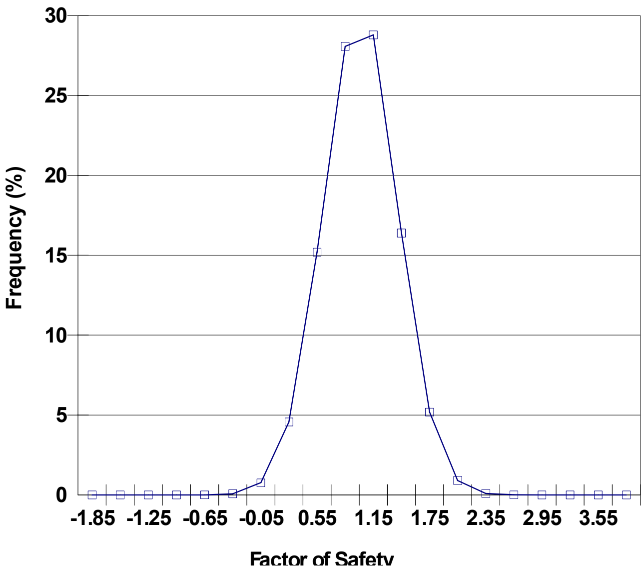

figure (24) Probability density function without stone columns for seismic analysis

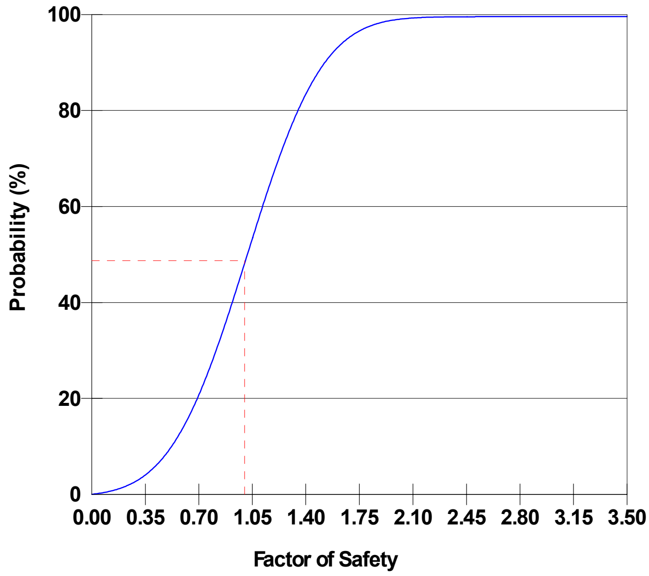

Figure (25) Probability distribution function without stone columns for seismic analysis

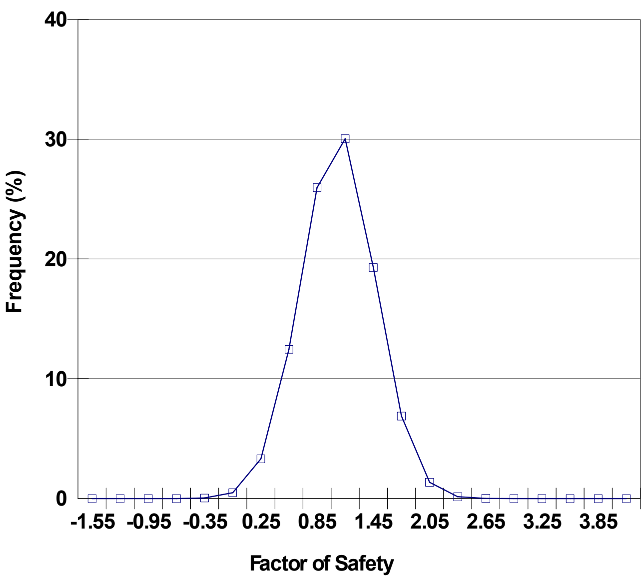

Figure (26) Probability density function with one stone column for seismic analysis

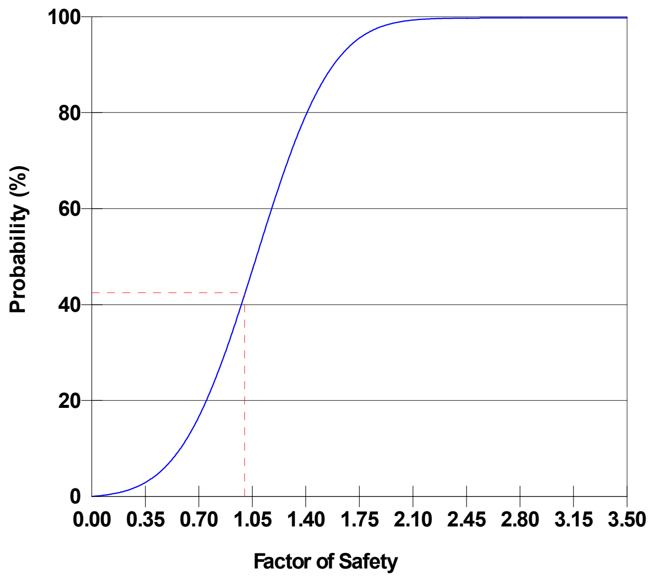

Figure (27) Probability distribution function with one stone column for seismic analysis

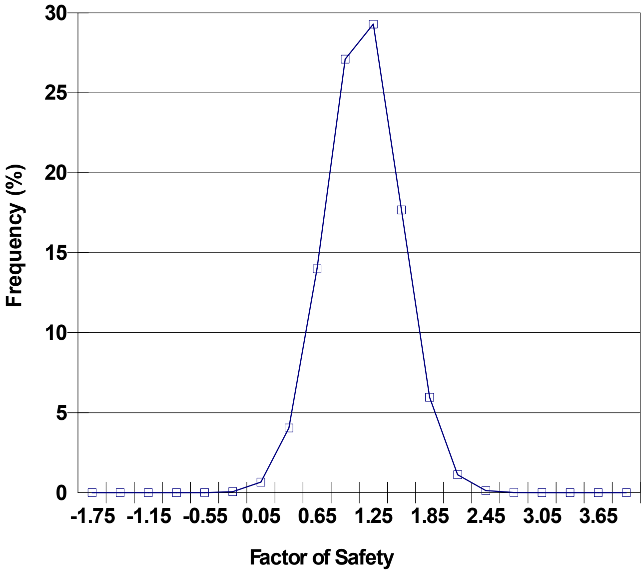

Figure (28) Probability density function with two stone columns for seismic analysis

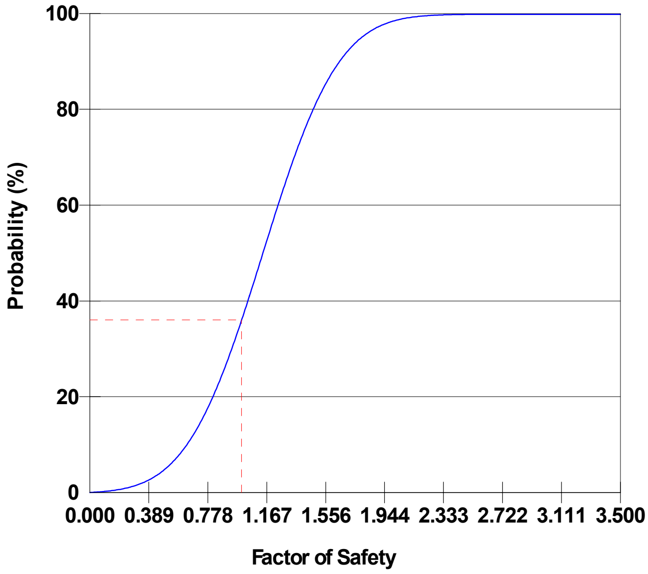

Figure (29) Probability distribution function with two stone columns for seismic analysis

Table 1. Geotechnical properties of clayey soil. (after Ghazavi and Shahmandi, 2008)

Modulus of elasticity [kN/m²]	Poisson's ratio	Undrained cohesion [kN/m²]	Friction angle [degree]	Saturated unit weight [kN/m³]
5000	0.48	25	0	17

Table 2. Geotechnical and geometrical properties of stone column materials (after Ghazavi and Shahmandi, 2008).

Modulus of elasticity [kN/m²]	Poisson's ratio	Undrained cohesion [kN/m²]	Friction angle [degree]	Saturated unit weight [kN/m³]	equivalent strip width [m]
50000	0.3	0	45	22	0.65

TABLE 3. Values of coefficient of Variation for geotechnical properties and in situ tests (after Duncan and Honorary, 2000).

Property or in situ test result	Coefficient of variation (%)	Source
Unit weight (γ)	3-7%	Harr (1984), Kulhawy (1992)
Buoyant unit weight (γ_b)	0-10%	Lacasse and Nadim (1997), Duncan (2000)
Effective stress friction angle (Φ')	2-13%	Harr (1984), Kulhawy (1992)
Undrained shear strength (*Su*)	13-40%	Harr (1984), Kulhawy (1992), Lacasse and Nadim (1997), Duncan (2000)
Un drained strength ratio *($Su/\sigma'v$)*	5-15%	Lacasse and Nadim (1997), Duncan

		(2000)
Compression index (*Cc*)	10-37%	Harr (1984), Kulhawy, (1992), Duncan (2000)
Preconsolidation pressure (*Pp*)	10-35%	Harr (1984), Lacasse and Nadim (1997), Duncan (2000)
Coefficient of permeability saturated clay (k)	68-90%	Harr (1984), Duncan(2000)
Coefficient of permeability of partly saturated clay (k)	130-240%	Harr (1984), Benson et al. (1999)
Coefficient of consolidation (C_v)	33-68%	Duncan (2000)
Standard penetration test blow count (N)	15-45%	Harr (1984), Kulhawy (1992)
Electric cone penetration test (q_c)	5-15%	Kulhawy (1992)
Mechanical cone penetration test (q_c)	15-37%	Harr (1984), Kulhawy (1992)
Dilatometer test tip resistance (q_{DTM})	5-15%	Kulhawy (1992)
Vane shear test undrained strength (*Sv*)	10-20%	Kulhawy (1992)

Note: the coefficient of variation is the ratio of the standard deviation to the mean

Table (4) Soil properties used for cases with different standard deviation

Parameter	Mean	Coefficient of variation (lower limit)/ standard deviation
Cohesion, c (kN/m^3) (soil)	25	13/3.25
Angle of Friction, Φ (stone column)	45	2/0.9
Unit Weight, γ (kN/m^3) (soil)	17	3/0.51
Unit Weight, γ (kN/m^3) (stone column)	22	3/0.66
Horizontal and vertical seismic acceleration	0.05	-----

Table (5) Analysis results of probability for case (1) for static condition.

parameters	values		
	Without stone column	With one raw of stone column	With two row of stone column
FoS(FEM)	1.131	1.307	1.325
Mean F of S	1.131	1.307	1.325
Reliability Index	0.891	13.561	14.433
P (Failure) (%)	18.597490	0.000000	0.000000
Standard Dev.	0.147	0.023	0.022
Min F of S	0.43149	1.2138	1.2217
Max F of S	1.7955	1.4217	1.4333

Table (6) Analysis results of probability for case (1) for seismic condition.

parameters	values		
	Without stone column	With one raw of stone column	With two row of stone column
FoS(Bishop method)	0.993	1.062	1.133
Mean F of S	0.99396	1.1016	1.168
Reliability Index	0.046	0.441	0.748

P (Failure) (%)	51.819581	32.924610	22.684731
Standard Dev.	0.133	0.23	0.225
Min F of S	0.44148	0.57608	0.60839
Max F of S	1.5991	7.3574	4.3708

Table (7) Soil properties used for cases with different standard deviations.

Parameter	Mean	Coefficient of variation (upper limit)/ standard deviation
Cohesion, c (kN/m^3) (soil)	25	40/10
Angle of Friction, φ (stone column)	45	13/5.85
Unit Weight, γ (kN/m^3) (soil)	17	7/1.19
Unit Weight, γ (kN/m^3) (stone column)	22	7/1.54
Horizontal and vertical seismic acceleration	0.05	-----

Table (8) Analysis results of probability for case (2) for static condition

parameters	values		
	Without stone column	With one row of stone column	With two row of stone column
FoS(FEM)	1.131	1.307	1.325
Mean F of S	1.1316	1.307	1.3244
Reliability Index	0.291	0.697	0.746
P (Failure) (%)	38.535780	24.232920	22.752750
Standard Dev.	0.452	0.44	0.435
Min F of S	-1.0388	-0.66468	-0.73564
Max F of S	3.3028	3.3895	3.3771

Table (9) Analysis results of probability for case (2) for seismic condition

parameters	values		
	Without stone column	With one row of stone column	With two row of stone column
FoS(Bishop method)	0.993	1.062	1.133
Mean F of S	1.0128	1.0743	1.14
Reliability Index	0.033	0.19	0.357
P (Failure) (%)	48.689261	42.445001	36.041120
Standard Dev.	0.391	0.391	0.393
Min F of S	0.10973	0.10584	0.10947
Max F of S	3.0975	3.2048	3.2034

PREPARATION OF ACTIVATED CARBONS FROM DATE STONES BY CHEMICAL ACTIVATION METHOD USING $FeCl_3$ and $ZnCl_2$ as ACTIVATING AGENTS

Muthanna J. Ahmed
Chemical Engineering Department-College of Engineering-University of Baghdad-Iraq
E-mail: muthannaj@yahoo.com

ABSTRACT

Date stones were used as precursor for the preparation of activated carbons by chemical activation with ferric chloride and zinc chloride. The effects of operating conditions represented by the activation time, activation temperature, and impregnation ratio on the yield and adsorption capacity towards methylene blue (MB) of prepared activated carbon by ferric chloride activation (FAC) and zinc chloride activation (ZAC) were studied. For FAC, an optimum conditions of 1.25 h activation time, 700 ˚C activation temperature, and 1.5 impregnation ratio gave 185.15 mg/g MB uptake and 47.08 % yield, while for ZAC, 240.77 mg/g MB uptake and 40.46 % yield were obtained at the optimum conditions of 1.25 h activation time, 500 ˚C activation temperature, and 2 impregnation ratio. The equilibrium data for MB adsorption on prepared activated carbons at optimum conditions were well represented by the Langmuir isotherm model, giving maximum MB uptake of 304.51 and 387.54 mg/g for FAC and ZAC, respectively. Also, the results showed that the surface area and iodine number of activated carbon prepared by activation with ferric chloride at optimum conditions were 780.06 m^2/g and 761.40 mg/g, respectively. While 1045.61 m^2/g surface area and 1008.86 mg/g iodine number were obtained for ZAC prepared at optimum conditions.

الخلاصة

يهدف البحث إلى إنتاج الكاربون المنشط من نوى التمر بطريقه التنشيط الكيميائي وباستعمال كلوريد الحديد وكلوريد الزنك كعوامل منشطه. تم دراسة تأثير زمن التنشيط ، درجة حرارة التنشيط ، ونسبة المنشط الكيميائي الى نوى التمر على إنتاجية الكاربون وسعه امتزازه لماده صبغه المثلين الزرقاء. بينت النتائج انه في حاله استخدام كلوريد الحديد كعامل منشط تم الحصول على انتاجيه (47.08 %) وسعه امتزاز (185.15 ملغم/غرام) عند الظروف التشغيليه المثلى والمتمثله بزمن تنشيط (1.25 ساعه) ، درجه حراره تنشيط (700 °م) ، ونسبه عامل منشط الى نوى التمر (1.5). في حين استخدام كلوريد الزنك كعامل منشط اعطى انتاجيه (44.46 %) وسعه امتزاز (240.77 ملغم/غرام) عند الظروف التشغيليه المثلى والمتمثله بزمن تنشيط (1.25 ساعه) ، درجه حراره تنشيط (500 °م) ، ونسبه عامل منشط الى نوى التمر (2). تم تمثيل نتائج امتزاز صبغه المثلين الزرقاء على الكاربون المنشط المحضر بشكل جيد جدا بواسطه معادله لانكماير، حيث تم الحصول على اعلى سعه امتزاز (304.51ملغم/غرام) للكاربون المحضر باستخدام كلوريد الحديد واعلى سعه امتزاز (387.54 ملغم/غرام) للكاربون المحضر باستخدام كلوريد الزنك. ايضا بينت النتائج ان التنشيط بكلوريد الحديد اعطى كاربون منشط ذو مساحه سطحيه (780.06 متر^2 /غرام) ونسبه امتزاز لليود (761.40 ملغرام/غرام). بينما الكاربون المنشط الناتج باستخدام كلوريد الزنك كعامل منشط كان ذو مسحه سطحيه (1045.61 متر^2 /غرام) ونسبه امتزاز لليود (1008.86 ملغرام / غرام).

KEYWORDS: Activated carbon, chemical activation, ferric chloride, zinc chloride, date stones

1. INTRODUCTION

Activated carbon is commonly defined as a carbonaceous material showing a well-developed surface area and porous texture. As a consequence, activated carbon has been widely used as adsorbent, and in catalysis or separation processes (Kalderis et al., 2008; Tamai et al., 2009). The characteristics of activated carbon depend on the physical and chemical properties of the precursor as well as on the activation method (Demiral et al., 2008).

Activated carbon can be produced from any carbonaceous solid precursor which may be either natural or synthetic. The choice of precursor is largely dependent on its availability, cost and purity, but the manufacturing process and intended of application of the product are also important considerations. Due to environmental considerations, agricultural wastes are considered to be a very important precursor because they are cheap, renewable, safe, available at large quantities and easily accusable sources; in addition they have high carbon and low ash content (Kalderis et al., 2008; Mestre et al., 2009).

Date stones as a raw material for the production of activated carbon can be considered as one of the best candidate among the agricultural wastes because it is cheap and quite abundant, especially in Mediterranean countries. They are composed of 42% cellulose, 18% hemi cellulose, 25% sugar and other compounds, 11% lignin and 4% ash. This lignocellulosic composition promotes the preparation of activated carbon from these precursors (Bouchelta et al., 2008).

There are two processes for the preparation of activated carbon: physical activation and chemical activation. Physical activation involves carbonization of a carbonaceous materials followed by activation of the resulting char in the presence of activating agents such as CO_2 or steam. In chemical activation, a raw material is impregnated with an activating reagent such as $ZnCl_2$, H_3PO_4, KOH, etc…, and the impregnated material is heated in an inert atmosphere. There will be a reaction between the precursor and the activating agent used in activation which leads to developments in porosity. Chemical activation is preferred over physical activation owing to the higher yield, simplicity, lower temperature and shorter time needed for activating material, and good development of the porous structure (Guo and Rockstraw, 2007).

The chemical activation process has been widely used by many researchers to prepare low cost activated carbons from different agricultural wastes by various chemical activating agents such as olive stones by H_3PO_4 (Yavuz et al., 2010), pomegranate seeds by $ZnCl_2$ (Ucar et al., 2009), durian shell by KOH (Chandra et al., 2009), Jatropha Curcas fruit shell by NaOH (Tongpoothorn et al., 2011), pissava fibers by H_3PO_4 and $ZnCl_2$ (Avelar et al., 2010), corn grain by KOH (Balathanigaimani et al., 2009), kenaf natural fibers by K_2HPO_4 (Aber et al., 2009), date stones by $ZnCl_2$, H_3PO_4 and KOH (Alhamed , 2009; Haimour and Emeish, 2006; Hameed et al., 2009).

Although the iron chloride salt has similar characteristics to zinc chloride in aqueous solution the ferric cation is smaller than the zinc cation, and this opens up the possibility of producing activated carbon with smaller pores sizes upon their activation. On the other hand, the zinc cation presented in aqueous solution is a well-known pollutant. Moreover, the ferric salt has a low cost in comparison with the zinc salt. The use of ferric chloride is not completely new. Oliveira et al. (2009) and Rufford et al. (2010) used it to prepare activated carbons from coffee husks and waste coffee grounds, respectively. However, there is no information for the preparation of activated carbon using date stones as the precursor with ferric chloride as chemical activating agent.

The main objective of this research is to test the use of ferric chloride as an alternative activating agent to produce activated carbon starting from date stones. The commonly employed activating agent, zinc chloride, is also used, in order to compare the characteristics and adsorption capacity for methylene blue (MB) of resulting activated carbons. The effects of activation time, activation temperature, and impregnation ratio on the yield and MB uptake of prepared activated carbon are also studied.

2. EXPERIMENTAL WORK

2.1 Materials

2.1.1 Precursor: Date stones were used as the precursor in the preparation of activated carbon. The stones as received were first washed with water to get rid of impurities, dried at 110 ˚C for 24 h, crushed using disk mill, and sieved. Fraction with average particle size, d_p, of 2 mm was selected for this study.

2.1.2 Chemicals: The properties of chemicals used are listed in Table 1.

2.2 Experimental procedure

10 g of dried stones was well mixed with 100 ml of $ZnCl_2$ or $FeCl_3$ solution of different impregnation ratios (weight of activating agent/weight of dried stones) (0.5-2.5) for 24 h at room temperature. The impregnated samples were next dried at 110 ˚C until completely dried and stores in a desiccator. For the carbonization of dried impregnated samples a stainless steal reactor (2.5 cm diameter x 10 cm length) was used, as shown in Fig.1. The reactor was sealed at one end and the other end had a removable cover with 2 mm hole at the center to allow for the escape of the pyrolysis gases. The reactor was placed in a furnace and heated at constant rate of 10 ˚C /min and held at different carbonization temperatures (400-800 ˚C) (Olivares-Marin et al., 2006) for different carbonization times (0.5-3.5 h). At the end of activation time the carbonized samples were withdrawn from the furnace and allowed to cool. For the removal of residual $ZnCl_2$ or $FeCl_3$, the samples were soaked with 0.1 M HCl solution such that the liquid to solid ratio is 10 ml/g. The mixtures were left overnight at room temperature, and then filtered and subsequently the samples were repeatedly washed with distilled water until the pH of filtrate reach 6.5-7 (Tan et al., 2007). After that, the samples were dried at 110 ˚C for 24 h, and subsequently were weighed to determine the yield of the product. Finally the samples were stored in tightly closed bottles. The flow diagram for activation process is shown in Fig.2.

2.3 Performance of activation process

The performance of chemical activation process was determined by the product yield, along with its uptake for MB. The yield and MB uptake are determined as follows:

2.3.1 Yield

The yield is defined as the ratio of final weight of the obtained product after washing and drying to the weight of dried precursor initially used. The yield of activated carbon was calculated based on the following equation:

$$\text{Yield}\,(\%) = \frac{W_f}{W_o}\ \text{x}\,100 \qquad (1)$$

Where W_f and W_o are the dry weight of final activated carbon product (g) and the dry weight of date stones (g), respectively.

2.3.2 MB uptake

The MB uptake or adsorption capacity of prepared activated carbon was determined by performing batch adsorption tests in 15 set of 100 ml Erlenmeyer flasks where 50 ml MB aqueous solutions with initial concentration of 250 mg/l was placed in each flask (Alhamed, 2006). The pH of the solution was natural without any pH adjustment. 0.05 g of each of the prepared activated carbon, with average particle size of 0.250 mm, was added to each flask and kept in an isothermal shaker of 120 rpm at room temperature for 24 h to reach equilibrium. Aqueous samples were taken from the solutions and the concentrations were analyzed. All samples were filtered prior to analysis in order to minimize interference of the carbon fines with the analysis. The concentrations of MB in the supernatant solutions were determined using UV-Visible Spectrophotometer (Shimadzu UV-160A) at its maximum wave length of 664 nm. The MB uptake at equilibrium, q_e (mg/g), was calculated by the following equation:

$$q_e = \frac{(C_o - C_e)\,V}{W} \qquad (2)$$

Where C_o and C_e are initial and equilibrium concentrations of the MB (mg/l), respectively, V is the volume of the aqueous MB dye solution (l), and W is the weight of activated carbon used (g).

2.4 Characteristics of prepared activated carbon at optimum conditions

The prepared activated carbons at optimum conditions were characterized by selected physical properties including bulk density and surface area, chemical properties including ash content, pH and conductivity, and adsorption properties including iodine number and maximum MB uptake. The details of characterization methods are illustrated as follows.

2.4.1 Bulk density

Bulk or apparent density is a measure of the weight of material that can be contained in a given volume under specified conditions. The volume used in this determination includes, in addition to the volume of the skeletal solids, the volume of voids among the particles and the volume of the pores within the particles. A 10 ml cylinder was filled to a specified volume with activated carbon that had been dried in an oven at 80 ˚C for 24 h (Ahmedna et al., 1997). The bulk density was then calculated as follows:

$$\text{bulk density} = \frac{W_C}{V_C} \qquad (3)$$

Where W_C is the weight of dried activated carbon (g) and V_C is cylinder volume packed with dried activated carbon (ml).

2.4.3 Ash content

The ash content of an activated carbon is the residue that remains when the carbonaceous portion is burned off. The ash content of activated carbon was determined by standard methods (ASTM Designation D-2866-94, 2000). 0.5 g of activated carbon with average particle size of 0.250 mm was dried at 80 ˚C for 24 h and placed into weighted ceramic crucibles. The samples were heated in an electrical furnace at 650 ˚C for 3 h. Then the crucibles were cooled to ambient temperature and weighed. The percent of ash was calculated as follows:

$$\text{ash}\,(\%) = \frac{W_{S3} - W_{S2}}{W_{S1}} \times 100 \qquad (4)$$

Where W_{S3} is the weight of crucible containing ash (g), W_{S2} is the weight of crucible (g), and W_{S1} is the weight of original activated carbon used (g).

2.4.4 Moisture content

The moisture content of prepared activated carbon was determined using oven drying method (Adekola and Adegoke, 2005). 0.5 g of activated carbon with average particle size of 250 mm was placed into weighed ceramic crucible. The samples were dried at 110 ˚C to constant weight.

Then the samples were cooled to ambient temperature and weighed. The moisture content was calculated by the following equation:

$$\text{mositure}\,(\%) = \frac{W_{m3} - W_{m2}}{W_{m1}} \times 100 \quad (5)$$

Where W_{m3} is the weight of crucible containing original sample (g), W_{m2} is the weight of crucible containing dried sample (g), and W_{m1} is the weight of original sample used (g).

2.4.5 pH measurement

The pH value of prepared activated carbon was determined by immersing 1 g sample in 100 ml deionized water and stirring at 150 rpm for 1 h and the pH of slurry taken (Egwaikhide et al., 2007).

2.4.6 Conductivity measurement

Electrical conductivity was measured by using the method of Ahmedna et al. (1997). A 1 wt% solution of sample in deionized water was stirred at 150 rpm at room temperature for 20 min. Electrical conductivity was measured using an EDT instrument BA 380 conductivity meter with values micro siemens per meter (µs/m).

2.4.7 Maximum MB uptake

The maximum MB adsorption capacity of the activated carbon prepared at optimum conditions were determined by performing adsorption tests in a set of 100 ml Erlenmeyer flasks where 50 ml of MB solutions with initial concentrations of 50-450 mg/l were placed in these flasks. Other operating parameters such as activated carbon dosage, solution temperature and agitation speed were similar as the adsorption studies carried out for determining MB uptake. The concentrations of MB solutions were similarly measured and the amount of adsorption at equilibrium, q_e (mg/g) was calculated using Eq. (2). To determine the maximum MB adsorption capacity of each prepared activated carbon, the experimental adsorption data obtained were fitted to the Langmuir isotherm model, which can be written as follows:

$$q_e = \frac{q_m\, BC_e}{1 + BC_e} \quad (6)$$

Where q_e is the amount of MB adsorbed per unit mass of activated carbon (mg/g), q_m is the maximum amount of MB adsorbed per unit mass of activated carbon (mg/g), C_e is the equilibrium concentration of the MB (mg/l), and B is the Langmuir constant (l/mg). The Langmuir isotherm model was used to fit the experimental data because from the literature and also from the preliminary studies carried out, most of the equilibrium data obtained for adsorption of dyes on activated carbons were found to be the best represented by this model (Hameed et al., 2007).

2.4.8 Iodine number

Iodine number is defined as the milligrams of iodine adsorbed by one gram of activated carbon. Basically, iodine number is a measure of the micropore content of activated carbon (0 to 20 Å) by adsorption of iodine from solution. Iodine number of the prepared carbon was determined as follows: 10 ml of 0.1 N iodine solution in a conical flask is titrate with 0.1 N sodium thiosulfate solution in the presence of 2 drops of 1 wt% starch solution as an indicator, till it becomes colourless. The burette reading is corresponding to V_b. Then weigh very accurately 0.05 g of activated carbon and add it to conical flask containing 15 ml of 0.1 N iodine solution, shake the flask for 4 min and filter it, then titrate 10 ml of filtrate with standard sodium thiosulfate solution using 2 drops of starch solution as indicator, now the burette reading is corresponding to Vs. The iodine number was then calculated by using the following equation (Lubrizol, 2007):

$$IN = \frac{(V_b - Vs) . N . (126.9) . (15/10)}{M} \quad (7)$$

Where IN is iodine number (mg/g), V_b and Vs are volumes of sodium thiosulfate solution required for blank and sample titrations (ml), respectively, N is the normality of sodium thiosulfate solution (mole/l), 126.9 is atomic weight of iodine, and M is the mass of activated carbon used (g).

. 2.4.9. Surface area

The surface areas of the prepared activated carbons were estimated through a calibration curve which has a correlation coefficient of 0.997 between the iodine numbers and BET surface area of some established activated carbons from the literature (Fadhil et al., 2008) as shown in Fig. 3.

3. RESULTS AND DISCUSSION

3.1 Effect of operating conditions

A set of experiments was carried out in order to study the effect of activation time (0.5-3.5 h), activation temperature (400-800 ˚C) and impregnation ratio (R), activator to precursor weight ratio, (0.5-2.5) on the yield and MB uptake of prepared activated carbon using ferric chloride (FAC) and zinc chloride (ZAC).

3.1.1 Effect of activation time

The effect of activation time on yield and MB uptake of prepared activated carbon are shown in Figs. 4 and 5, respectively.

Fig. 4 shows that the yield of FAC and ZAC decreases with increasing activation time. An increase in time from 0.5 to 3.5 h at 600 ˚C and 1.5 impregnation ratio leads to a decrease in yield from 61 to 41 % and 43 to 29 % for FAC and ZAC, respectively. A steep decrease occurs within the first 1.25 h for both FAC and ZAC; this is due to rapid evolution of volatile materials to form stable compounds as explained by Haimour and Emeish (2006).They showed that a steep decrease in yield occurs within the first 1 h for production of activated carbon from date stones using zinc chloride and phosphoric acid. Since zinc chloride removes more volatile materials from the particles compared to ferric chloride, the yield of ZAC was lower than that of FAC as shown in this figure.

Fig. 5 shows that the MB uptake of FAC and ZAC increases with activation time and reaches at maximum of 225.08 mg/g for ZAC and 130.01 mg/g for FAC, at 1.25 h and thereafter it decreases. Activation until 1.25 h probably increases the formation of mesopores that are more effective in adsorption process, but with applying extended activation times, the wall of mesopores perhaps collapses and they turns into macrospores (Budinova et al., 2008). Therefore, the time of 1.25 h was chosen as optimum activation time for both activators. Alhamed (2006) showed that a maximum MB removal of 90 % was obtained at optimum activation time of 1 h for chemical activation of date stones by zinc chloride. Also it can be noted from this figure that MB uptake of ZAC was higher than that of FAC. This may due to higher activity of zinc chloride, as compared with ferric chloride, to produce activated carbon with higher developed pores (Rufford et al., 2010).

3.1.2 Effect of activation temperature

The effect of activation temperature on yield and MB uptake of prepared activated carbon are shown in Figs. 6 and 7, respectively.

It can be seen from Fig.6 that, as the activation temperature increases from 400 to 800 ˚C, the yield decreases from 51 to 37 % and 43 to 27 % for FAC and ZAC, respectively. This is due to the loss of the volatile materials with increasing temperature. Beyond 700 ˚C a lower rate of yield decrease was noticed where a stable structure is formed. This behavior agrees with results obtained from activation of date stones using phosphoric acid (Girgis and El-Hendawy, 2002).

Fig. 7 shows that the MB uptake increases with activation temperature up to 500 ˚C and 700 ˚C for ZAC and FAC, respectively. Therefore, the temperatures of 500 and 700 ˚C were chosen as optimum activation temperatures for ZAC and FAC, respectively. The decrease in adsorption ability of prepared activated carbon with further increase in temperature might be due to the sintering effect at high temperature, followed by shrinkage of the char, and realignment of the carbon structure which resulted in reduced pore areas as well as volume (Mohanty et al., 2006; Lua et al., 2006). These results are in agreements with that of Olivares-Marin et al. (2006) who showed that 500 ˚C was the optimum activation temperature for preparation of activated carbon from cherry stones by chemical activation with zinc chloride.

3.1.3 Effect of impregnation ratio

Figs. 8 and 9 show the effects of impregnation ratio, activator to precursor weight ratio, on yield and MB uptake of prepared activated carbon, respectively.

It was noticed that, as the impregnation ratio increases the yield decreases, as shown in Fig. 8. An increase in impregnation ratio from 0.5 to 2.5 leads to a decrease in yield from 61.03 to 33.97 % and 45.06 to 28.63 % for FAC and ZAC, respectively. This decrease is due to the continuous removal of tar material from the pores. The decreasing rate of yield is lowered beyond an impregnation ratio of 2 where a stable structure is formed, as explained by Sudaryanto et al. (2006) for activated carbon production from cassava peel by chemical activation with potassium hydroxide.

Fig. 9 shows that the MB uptake increases with impregnation ratio up to 2 for ZAC and 1.5 for FAC. For ZAC, an increase in impregnation ratio from 0.5 to 2 leads to an increase in MB uptake from 190.8 to 224.77 mg/g while for FAC, the increase from 0.5 to 1.5 leads to an increase from 63 to 118.15 mg/g. Therefore, the ratios of 2 and 1.5 were chosen as optimum impregnation ratios for ZAC and FAC, respectively. More increase in the concentration of activator perhaps leads to the excessive dehydration and destruction of mesopores and turning them to larger pores which reduces the adsorption efficiency (Kim et al., 2001).

3.2. MB adsorption isotherm on activated carbons prepared at optimum conditions

According to section 3.1, optimum operating conditions were selected as 1.25 h activation time, 500 ˚C activation temperatures, 2 and impregnation ratio for ZAC, and 1.25 h activation time, 700 ˚C activation temperatures, and 1.5 impregnation ratio for FAC.

The experimental equilibrium data for MB adsorption on ZAC and FAC prepared at optimum conditions are compared with that for MB adsorption on two types of commercial activated carbon (CAC1) and (CAC2). These data, calculated from Eq. (2), are fitted with Langmuir isotherm model, Eq. (6), and presented in Fig. 10. This figure shows that the MB adsorption capacity of four samples is in the order CAC1 > ZAC > FAC > CAC2. The calculated constants of Langmuir isotherm equation for the four samples along with the correlations coefficients values R^2 are presented in Table 2. This table shows that the maximum MB uptake of ZAC, FAC, CAC1, and CAC2 are 387.54, 304.51, 395.56 and 155.80 mg/g, respectively. This result for ZAC is higher than that reported by Alhamed (2006), 286 mg/g, for activated carbon produced from date stones by chemical activation with zinc chloride. Fig. 10 shows that the MB uptake of ZAC at a given MB concentration is higher than that of FAC. This is in agreement with Olivera et al. (2009) who found that the maximum MB uptake of activated carbons prepared from coffee husks by activation with ferric chloride and zinc chloride were 260 and 75 mg/g, respectively.

3.3 Characterization of activated carbons prepared at optimum conditions

According to section 2.4, the characteristics of FAC and ZAC prepared at optimum conditions were determined and compared with the characteristics of two types of commercial activated carbons, as summarized in Table 3. The results of this table show that the surface areas of ZAC and FAC are 1045.61 and 780.06 m^2/g, respectively. These results are in agreement with that of Rufford et al. (2010). They showed that the surface area of activated carbon prepared by chemical activation of coffee grounds with zinc chloride and ferric chloride were 977 and 846 m^2/g, respectively. The iodine numbers of ZAC and FAC in this study are higher than reported by Haimour and Emeish (2006), 495 mg/g for activated carbon prepared by chemical activation of date stones using phosphoric acid.

4. CONCLUSSIONS

1. MB uptake of 244.77 mg/g with corresponding yield of 40 % were obtained at optimum conditions of 1.25 h activation time, 500 ˚C activation temperature, and 2 impregnation ratio, for activated carbon prepared by chemical activation with zinc chloride.
2. Optimum conditions of 1.25 h activation time, 700 ˚C activation temperatures, and 1.5 impregnation ratio produced activated carbon with 185.15 mg/g MB uptake and 47.08 % yield for chemical activation of date stones with ferric chloride.
3. The maximum MB uptake of activated carbons prepared by ferric chloride and zinc chloride, as calculated from Langmuir isotherm model, were 304.51 and 387.54 mg/g, respectively.
4. Chemical activation of date stones with zinc chloride, at optimum conditions, produced activated carbon with 1008.86 mg/g iodine number and 1045.61 m^2/g surface area.
5. The iodine number and surface area of activated carbon prepared from date stones by chemical activation with ferric chloride, at optimum conditions, were 761.40 mg/g and 780.06 m^2/g, respectively.

AKNOWLEGMENT

We gratefully acknowledge university of Baghdad for assist and support of this work.

REFERNCES

Aber S., Khataee A. and Sheydaei M., (2009), Optimization of activated carbon fiber preparation from kenaf using K_2HPO_4 as chemical activator for adsorption of phenolic compounds, Bioresource Technology, 100, 6586-6591.

Adekola F.A. and Adegoke H.I., (2005), Adsorption of blue-dye on activated carbons produced from Rice Husk, Coconut Shell and Coconut Coir pitch, Ife Journal of Science, 7(1), 151-157.

Ahmedna M., Marshall W.E., Rao R.M., and Clarke S.J., (1997), Use of filteration and buffers in raw sugar colur measurement, J. Sci. Food Agric., 75(1), 109-116

Alhamed Y.A., (2006), Activated carbon from date stones by $ZnCl_2$ actiivation, JKAU: Eng. Sci., 17 (2), 75-100.

Alhamed Y.A., (2009), Adsorption kinetics and performance of packed bed adsorber for phenol removal using activated carbon from dates stones, J. of Hazardous Material, 170, 763-770.

ASTM standard, (2000), Standard test method for total ash content of activated carbon, Designation D2866-94.

Avelar F.F., Bianchi M.L., Goncalves M., and Damota E.G., (2010), The use of piassava fibers (Attalea funifera) in the preparation of activated carbon, Bioresour. Technol., 101, 4639-4645.

Balathanigaimani M.S., Shim W.G., Park K.H., Lee J.W., and Moon H., (2009), Effect of structural and surface energetic heterogeneity properties of novel corn grain based activated carbon on dye adsorption, Microporoes & Mesoporous Mater., 118, 232-238.

Bouchelta C., Medjran M.S., Bertrand O., and Bellat J., (2008), Preparation and characterization of activated carbon from date stones by physical activation with steam, J. Anal. Appl. Pyrolysis, 28, 70-77.

Brunauer S., Emmett P.H., and Teller E., (1938), Adsorption of gases in multimolecular layers, J. Am. Chem. Soc., 60, 309-319.

Budinova T., Petrov N., Parra J., and Baloutzov V., (2008), Use of an activated carbon from antibiotic waste for the removal of Hg(II) from equous solutions, J. Environm. Manage, 88, 165-172.

Chandra T.C., Mirna M.M., Sunarso J. and Sudaryanto I.S., (2009), Activated carbon from durian shell: preparation and characterization, J. of the Taiwan Institute of chemical Engineers, 40, 457-462.

Demiral H., Demiral I., Tumsek F., and Karabacakoglu B., (2008), Pore strucuture of activayted carbon prepared from hazelnut bagasse by chemical activation, Surface Interface Analysis, 40, 616-619.

Egwaikhide P.A., Akporhonor E.E, and Okieimen, (2007), Utilization of Coconut fibre Carbon in the removal of Soluble Petroluem fraction polutted water, International Journal of physical sciences, 2(2), 047-049.

Fadhil A.B. and Deyab M.M., (2008), Conversion of some fruit stones and shells into activated carbons, The Arabain Journal for Science and Engineering, 33(2A), 175-184.

Girgis B.S. and El-Hendawy A., (2002), Porosity development in activated carbon obtained from date pits under chemical activation with phosphoric acid, Microporoes & Mesoporous Mater., 52, 105-117.

Guo Y. and Rockstraw D.A., (2007), physicochemical properties of carbons prepared from pecan shell by phosphoric acid activation, Bioresour. Technol., 98, 1513-1521.

Haimour N.M. and Emeish S., (2006), Utilization of date stones for production of activated carbon using phosphoric acid, Waste Management, 26, 651-660.

Hameed B.H., Ahmad A.L. and Latiff K.N.A., (2007), Adsorption of basic dye (methylene blue) onto activated carbon prepared from rattan sawdust, Dyes & Pigments, 75, 143-149.

Hameed B.H., Salman S.M. and Ahmad A.L., (2009), Adsorption isotherm and kinetic modeling of 2,4-D-pesticide on activated carbon derived from date stones, J. of Hazardous Material, 163, 121-126.

Kalderis D., Koutoulakis D., Paraskeva P., and Fernaandez-Pereira C., (2008), Adsorption of polluting substances on activated carbons prepared from rice husks and sugar cane bagasse, Chem. Eng. J., 144, 42-50.

Kalderis D., Bethanis S., Paraskeva P., and Diamadopoulos E., (2008), Production of activated carbon from bagasse and ricehusk by a single stage chemical activation method at low retention times, Bioresour. Technol., 99 (15), 6809-6816.

Kim J.W., John M.H., Kim D.S., and Kwon Y.S., (2001), Production of granular activated carbon from waste walnut shell and its adsorption characteristic for Cu^{+2} ion, J Hazard. Mater., 85, 301-315.

Lua A.C., lau F.Y.and Guo J., (2006), Influence of pyrolysis conditions on pore development of oil palm shell activated carbon, J Anal. Appl. Pyrolysis, 27, 96-102.

Lubrizol standard test method, (2006), iodine value, test procedure AATM 1112-01, October 16.

Mestre J., Pires J., Nogueira M.F., and Ania C.O., (2009), Waste derived activated carbons for removal of ibuprofen from solution: role of surface chemistry and pore structure, Bioresour. Technol., 100 (5), 1720-1726.

Mohanty K., Das D., and Biswas M.N., (2006), Preparation and characterization of activated carbons from sterculia alata nutshell by chemical activation with zinc chloride to remove phenol from waste water, Adsorption, 12, 119-132.

Olivares-Marin M., Fernandez-Gonzalez C., Macias-Garcia A., and Gomez-Serrano V., (2006), Preparation of activated carbon from cherry stones by chemical activation with $ZnCl_2$, Applied surface science, 225, 5967-5971.

Oliveira L.C.A., Pereira E., Guimaraes I.R., and Sapag K., (2009), Preparation of activated carbons from coffee husks utilizing $FeCl_3$ and $ZnCl_2$ as activating agents, J. of Hazardous Materails, 165, 87-94.

Rufford T.E., Hulicova-Jurcakova D., Zhu Z., and Lu G.Q., (2010), A comparative study of chemical treatment by $FeCl_3$, $MgCl_2$, and $ZnCl_2$ on microstructure, surface chemistry, and double-layer capacitance of carbons from waste biomass, J. of Material Research, 25 (8), 1451-1459.

Sudaryanto Y., Hartono S.B., Irawaty W., and Ismadji S., (2006), High surface area activated carbon prepared from cassava peel by chemical activation, Bioresour. Technol., 97, 734-739.

Tamai H., Nobuaki U., and Yasuda H., (2009), Preparation of Pd supported mesoporous activated carbons and their catalytic activity, Mater. Chem. Physi. , 114, 10-13.

Tan I.A. W., Hameed B.H. and Ahmad A.L., (2007), Equilibrium and kinetic studies on basic dye adsorption by oil palm fiber activated carbon, Chem. Eng. J., 127, 111-119.

Tongpoothorn W., Sriuttha M., Homchan P. and Ruangviriyachai, (2011), Preparation of activated carbon derived from Jatropha Curcas fruit shell by simple thermo-chemical activation and characterization of their physico-chemical properties, Chem. Eng. Res. & Design, 89, 335-340.

Ucar S., Erdem M., Tay T., Karagoz S., (2009), Preparation and characterization of activated carbon produced from pomegranate seeds by $ZnCl_2$ activation, Applied surface science, 225, 8890-8896.

Yavuz R., Akyildiz H., Karatepe N., Cetinkaya E., (2010), Influence of preparation conditions on porous structures of olive stones activated by H_3PO_4, Fuel Processing Technology, 91, 80-87.

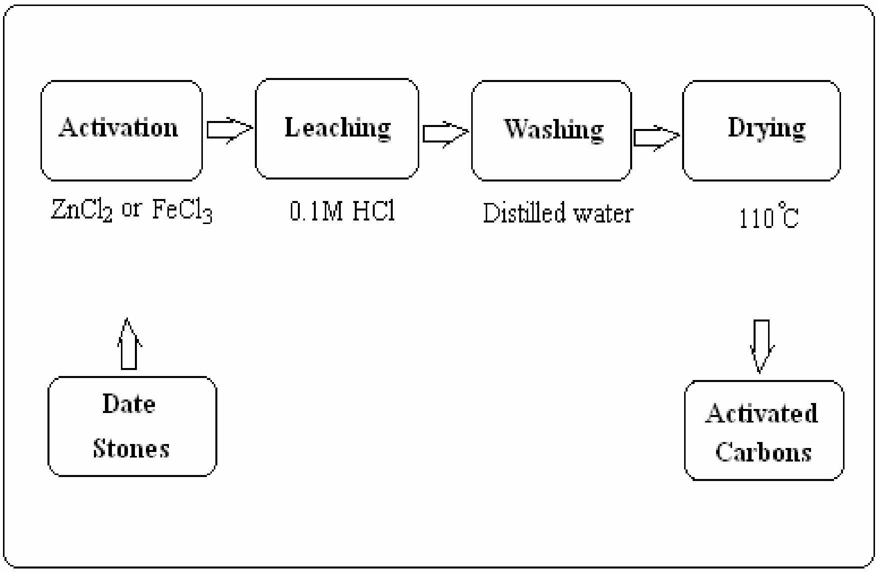

Fig. 1, Flow diagram for activation process

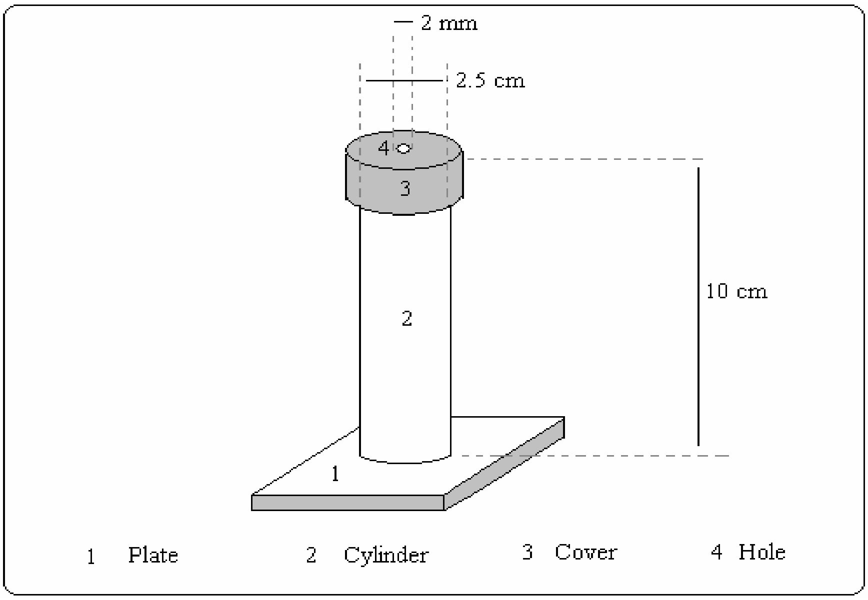

Fig. 2, Dimensions of reactor used for activation process

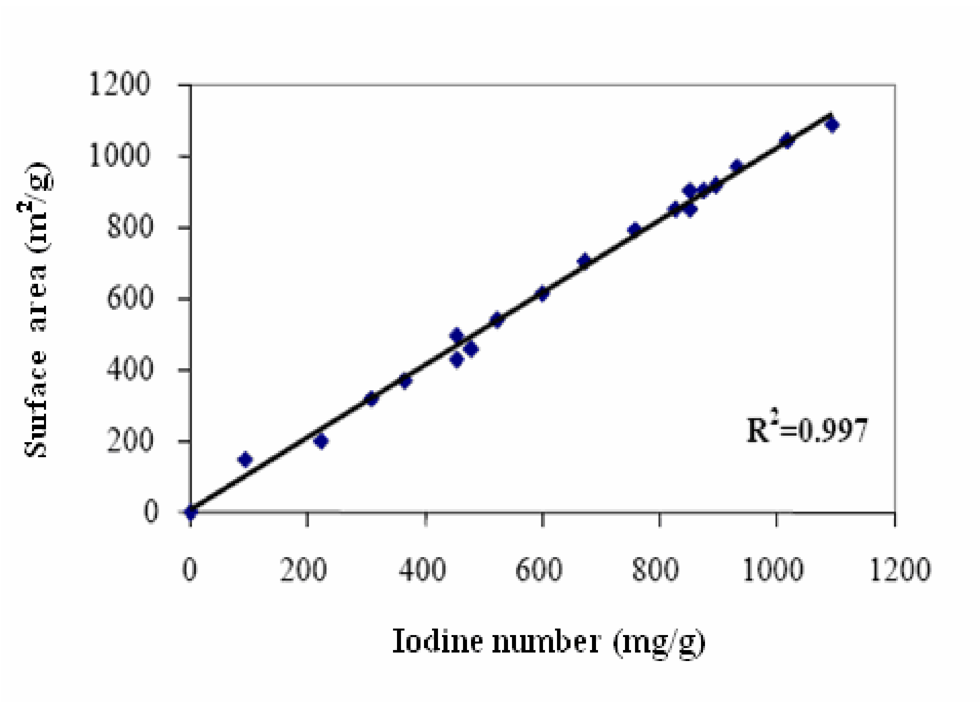

Fig. 3, Estimated surface area calibration curve

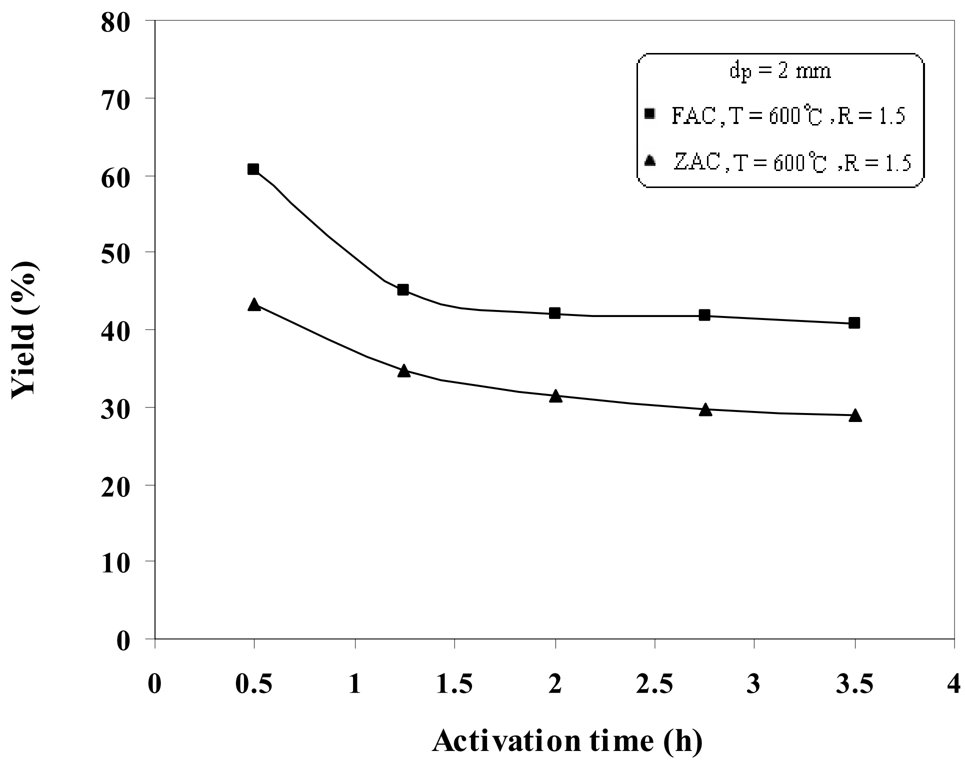

Fig. 4, Effect of activation time on yield of activated carbon

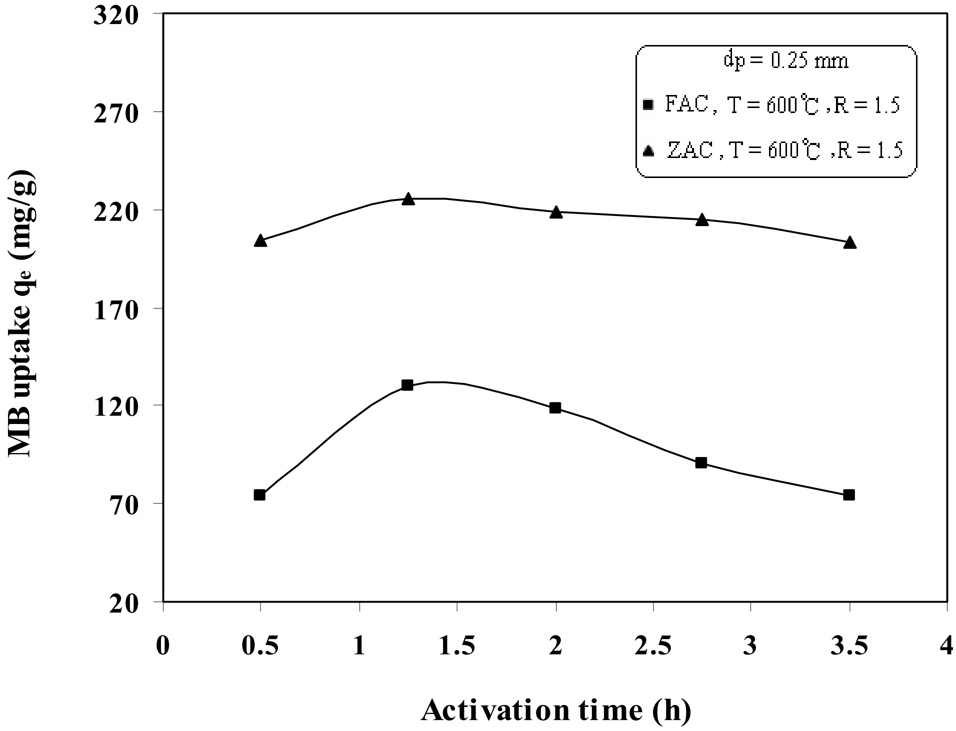

Fig. 5, Effect of activation time on MB uptake of activated carbon

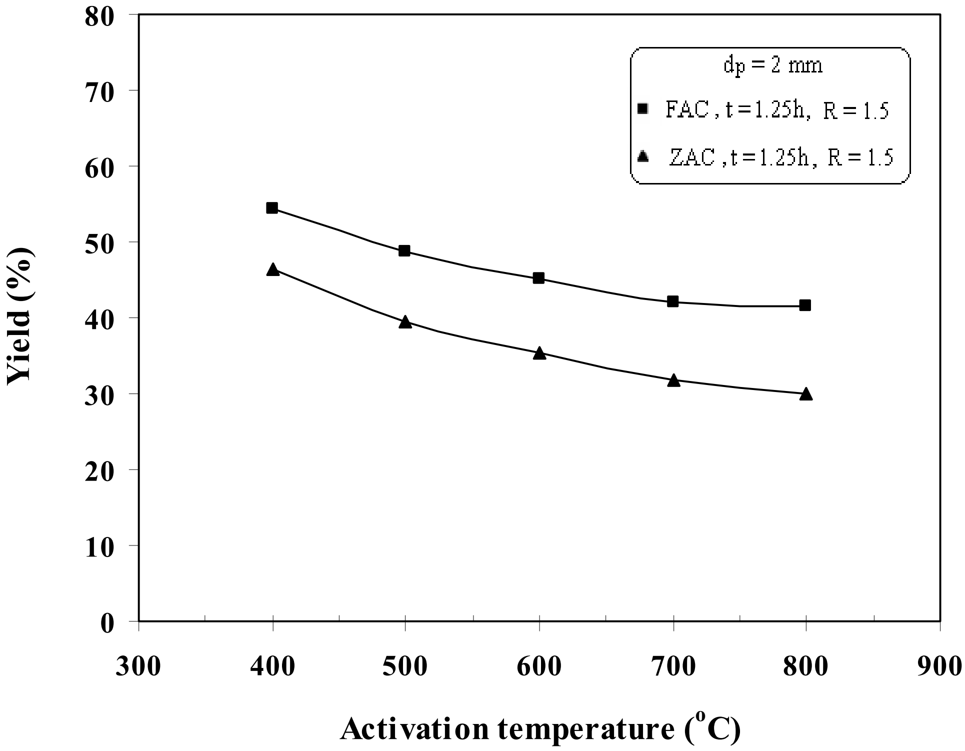

Fig. 6, Effect of activation temperature on yield f activated carbon

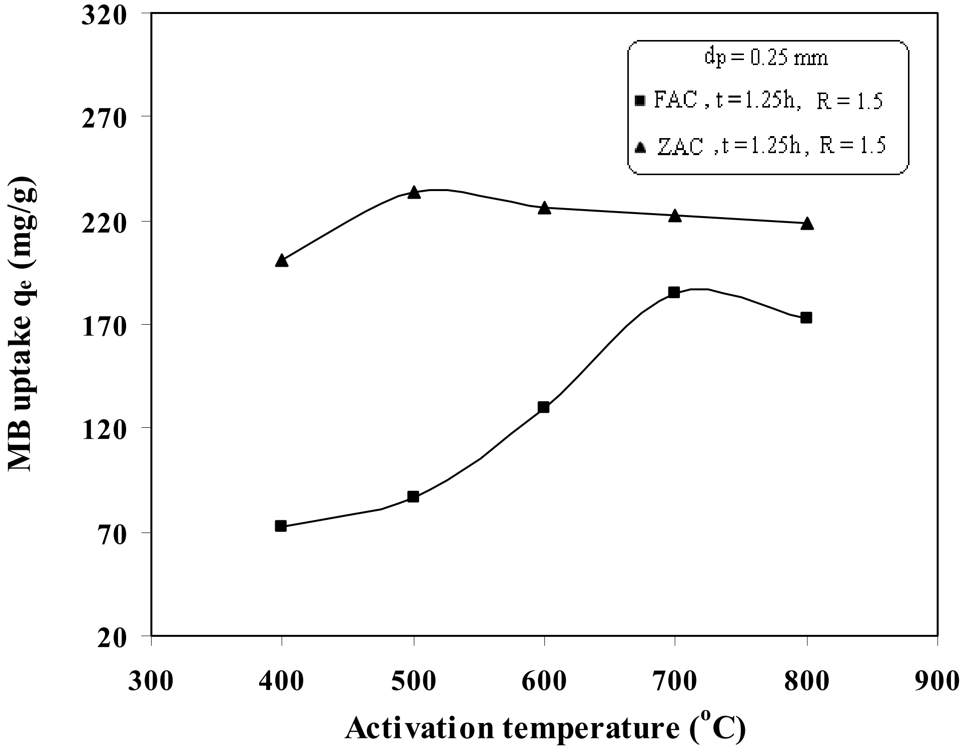

Fig. 7, Effect of activation temperature on MB uptake of activated carbon

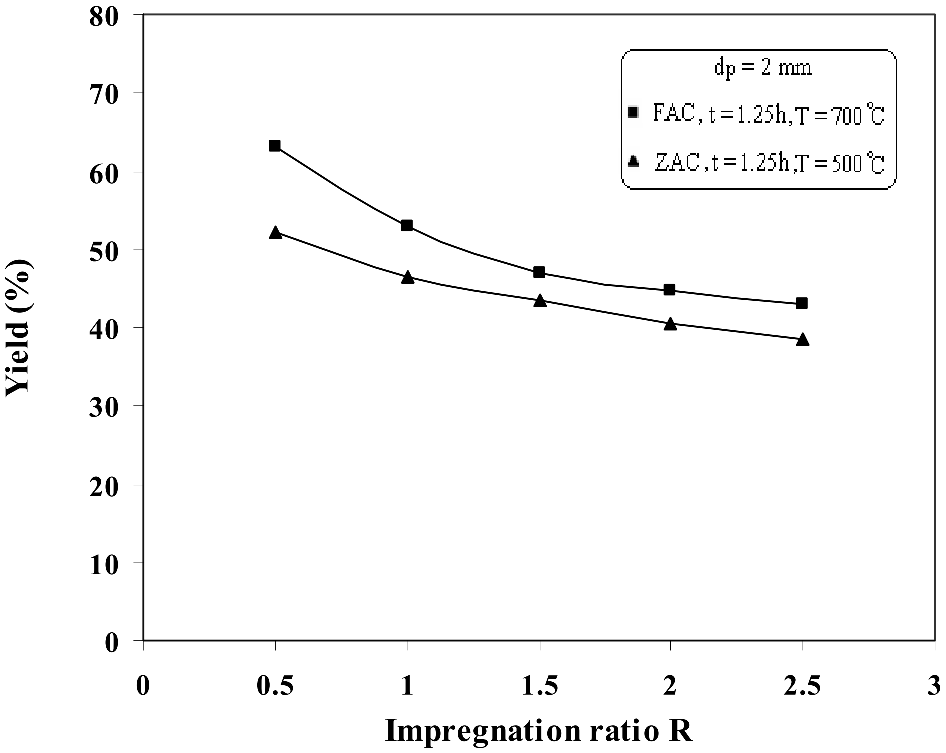

Fig. 8, Effect of impregnation ratio on yield of activated carbon

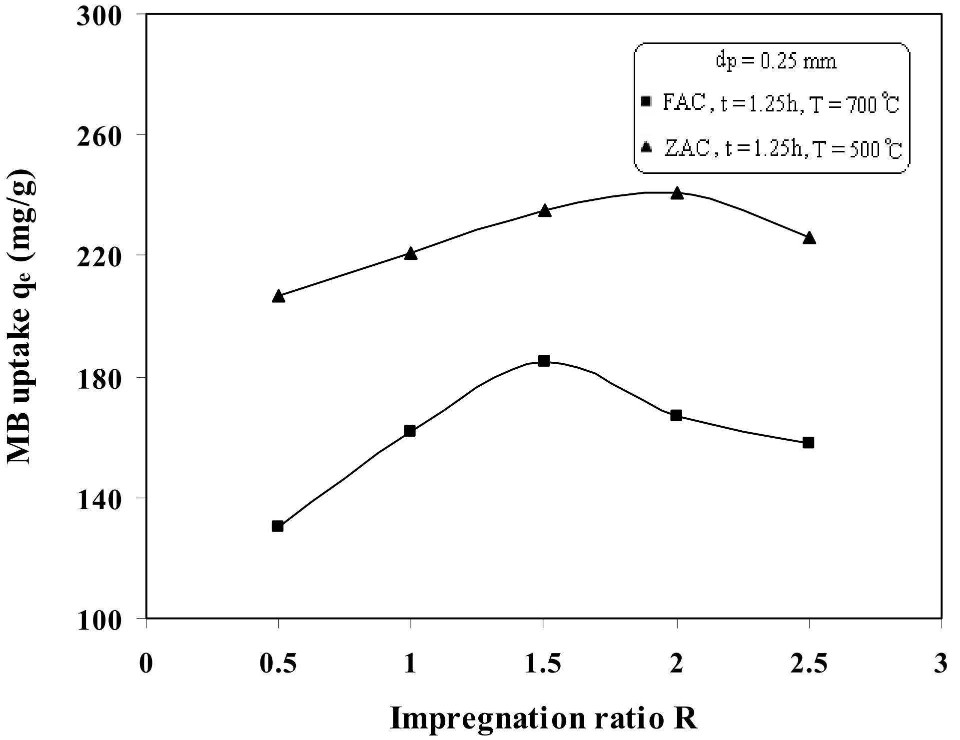

Fig. 9, Effect of impregnation ratio on MB uptake of activated carbon

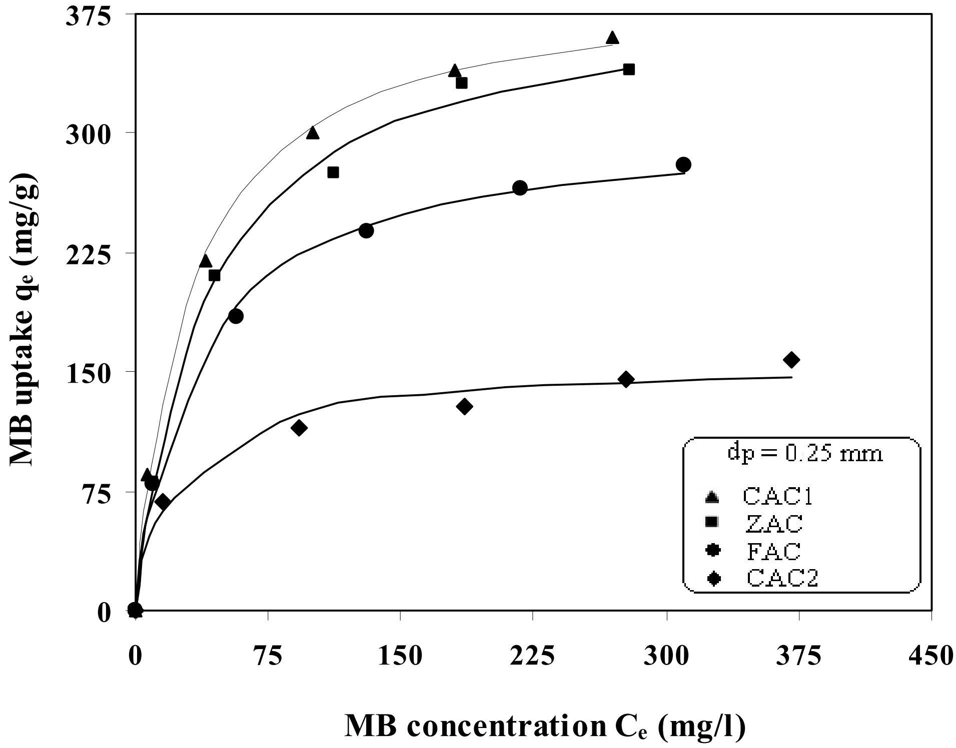

Fig. 10, Equilibrium isotherm of MB adsorption on activated carbons samples correlated with Langmuir equation

Table 1, Properties of chemicals

Compound	Molecular formula	Purity (%)	Source
Zinc Chloride	$ZnCl_2$	98-100	Scharlau Company
Ferric Chloride	$FeCl_3$	99.9	Panreac Company
Methylene Blue	$C_{16}H_{18}N_3SC$	99.9	Fischer Scientific Company
Hydrochloric Acid	HCl	35-38	Poch S.A. Company
Sodium Thiosulfate	$Na_2O_3S_2.5H_2O$	>99	Fluka Chemie AG Company
Iodine	I_2	99.9	Sigma Aldrich Company

Table 2, MB equilibrium isotherm results

MB isotherm results correlated with Langmuir equation			
Sample	q_m (mg/g)	B (l/mg)	R^2
ZAC	387.54	0.0259	0.997
FAC	304.51	0.0298	0.997
CAC1	395.56	0.0333	0.998
CAC2	155.80	0.0413	0.981

Table 3, Characteristics of activated carbons samples

Characteristic	ZAC	FAC	CAC1	CAC2
Yield (%)	40.46	47.08		
bulk density (g/ml)	0.322	0.271	0.454	0.529
surface area (m^2/g)	1045.61	780.06	1080.11	555
ash content (%)	2.04	8.62	4.24	8.80
moisture content (%)	13.86	15.54	11.57	3.51
pH	6.1	6.5	7.3	7
conductivity (µs/m)	330	290	370	330
max. MB uptake (mg/g)	387.54	304.51	395.56	155.80
iodine number (mg/g)	1008.86	761.40	1047.54	552

LDPC CODED MULTIUSER MC-CDMA PERFORMANCE OVERMULTIPATH RAYLEIGH FADING CHANNEL

*Aqiel N. Almaamory
*Assistant Lecturer \ Baghdad University\ College of Engineering\ Electronic and

ABSTRACT

This work presents the simulation of a Low density Parity Check (LDPC) coding scheme with multiuserMulti-Carrier Code Division Multiple Access (MC-CDMA) system over Additive White Gaussian Noise (AWGN) channel and multipath fading channels. The decoding technique used in the simulation was iterative decoding since it gives maximum efficiency with ten iterations. Modulation schemes that used are Phase Shift Keying (BPSK, QPSK and 16 PSK), along with the Orthogonal Frequency Division Multiplexing (OFDM). A 12 pilot carrier were used in the estimator to compensate channel effect. The channel model used is Long Term Evolution (LTE) channel with Technical Specification TS 25.101v2.10 and 5 MHz bandwidth including the channels of indoor to outdoor/ pedestrian channel and Vehicular channel.

.

منظومة(LDPC-MCCDMA)متعدد المستخدمين

الخلاصة

يقدم هذا العمل محاكاة (LDPC) مع (MC-CDMA)متعدد المستخدمين خلال قناة (AWGN) وقناة الخفوت متعدد المسارات . تقنية فتح الشفرات المستخدمة في البحث هي فك الشفرات التكراري لأنه يعطي الكفاءة القصوى مع عشرة تكرارات . نوعيات التضمين المتبعة هي (BPSK,QPSK,16PSK) مع (OFDM) . القناة المستخدمة في النموذج هي قناة الجيل الثالث (LTE) ذات المواصفات التقنية TS 25.101v2.10مع عرض قناة مقداره 5MHz وتشمل القنوات داخل وخارج ألابنيه والقنوات المتحركة .

KEY WORDS

MC-CDMA, OFDM, LDPC, SUM-PRODUCDECODING ALGORITHM, CONVOLUTIONAL CODING.

INTRODUCTION

Recent studies by researchers have combined the principles of CDMA with Orthogonal frequency Division Multiplexing (OFDM) which allows one to use the available spectrum in an efficient way to retain the many advantages of CDMA system if the number of spacing between subcarriers is chosen appropriately, it is unlikely that all the subcarriers will be in deep fade and thus provides frequency diversity [Laith 2007]. This combination of OFDM and CDMA is an alternative for 4G systems, which has the property of variable data rates as well as provides reliable communication systems.
Since 1993, MC-CDMA rapidly has becamea topic of research. Wireless mobile communication systems present several design challenges resulting from the mobility of users throughout the system and the time-varying channel (Multi-path fading). There has been an increasing demand for efficient and reliable digital communication systems. To tackle these problems effectively, an efficient design of forward error coding (FEC) scheme is required for providing high coding gain.
Low-Density Parity-Check (LDPC) codes with iterative decoding algorithm were proposed by Gallager in 1962 [Gallager 1962, MacKay 1997]. These codes have been almost forgotten for about thirty years, in spite of their excellent properties. However, LDPC codes are now recognized as good error correcting codes achieving near Shannon limit performance [Gallager 1963].

MC-CDMA SYSTEM DESCRIPTION

A complete block diagram of an LDPC codedmultiuserMC-CDMA systemis shown in Fig. 1. The data coming from each user is first encoded with the LDPC coding technique. A single data symbol is replicated into *N* parallel copies. Each branch of the parallel stream is multiplied by one chip of a spreading code of length *N*. The resulting chips are then fed to a bank of orthogonal subcarriers. As is commonly done in MC-CDMA, it is assumed that the spreading sequence length *N* equals the number of subcarriers. Each user has its own spreading code C_i.Pilot carriers with double energy are inserted at equal distances within the data.Carrier modulation is efficiently implemented using the inverse fast Fourier transform (IFFT)[Aqiel 2011,Husam 2010,Nathan 1993].
After parallel-to-serial (P/S) conversion, a cyclic prefix (CP) is appended to the resulting signal to minimizethe effects of the channel dispersion. It is assumed that the CP length exceeds the maximum channel delay spreadand therefore, there is no interference among successively transmitted symbols (i.e. there is no interblock interference).
At the receiver side, opposite operation to that done at the transmitter is done. These operations are the OFDM demodulation, dispreading, MPSK demodulation, demapping and the LDPC decoding. For more details about the MC-CDMA system refer to references Husam 2009 and Aqiel 2011 published by the author. Finallydecoding the data stream from every user individually using the iterative decoding algorithms for the LDPC coding scheme.

LDPC CODING

LDPC codes are linear block codes specified by a very sparse (containing mostly 0's and only a small number of 1's) random parity-check matrix, but are not systematic. The parity-check matrix of an LDPC is an $M \times N$ matrix $\mathbf{A}$, where M is the number of parity bits, and N is the transmitted block length ($N = K + M$, with K as the source block length). The matrix $\mathbf{A}$ is specified by a fixed column weight j and a fixed row weight $k = j\, N / M$ (in the MacKay's and Neal's codes k is as uniform as possible [MacKay 1999]), and code rate $R = K / N$. it has been reported that when the block length is relatively large, irregular LDPC codes with nonuniform column weight outperform turbo codes with almost the same block length and code rate [Richardson 2000]. LDPC codes can be decoded using probability propagation algorithm known as the sum-product or belief propagation algorithm [Kschischang 2001], which is represented by a factor graph that contains two types of nodes: the "bit nodes" corresponding to a column of the parity-check matrix, which also corresponds to a bit in codeword and the "check nodes" corresponding to a row of the parity-check matrix, which represents a parity-check equation.

SUM-PRODUCTDECODING ALGORITHM

The decoding problem is to find the most probable vector x such that **A**x mod 2 = 0 , with thelikelihood of x given by $x_n \Pi_n f_n$, where $f_n^0 = 1 - f_n^1$ and $f^1_n = 1/(1 + \exp(-2y_n / \sigma^2))$ for AWGN channel or $f^1_n = (y_n / \sigma^2) \exp[-y^2_n / 2\sigma^2]$ for Rayleigh channel, and y_n , σ^2 represent the received bit and noise variance, respectively. We denote the set of bits, n , that participate in check m as N (m) ≡ {n : A_{mn} = 1} , where A_{mn} represents the element of the mth row and nth column in the parity-check matrix. Similarly, we define the set of checks m in which bit n participates as M(n) ≡ {m : A_{mn} = 1} . We denote a set N (m) with bit n excluded as N (m) \ n. The algorithm has two alternating parts, in which quantities q_{mn} and r_{mn} associated with each non-zero element in the matrix A are iteratively update. The quantity x q_{mn} is meant to be the probability that bit n of x is x , given the information obtained via checks other than check m . The quantity r_{mn} is meant to be the probability of check m being satisfied if bit n of is *x* considered fixed at x and the other bits have a separable distribution given by the probabilities {$q_{mn'}$: n ' □ N (m) \ n } . The aposteriori probabilities for a bit are calculated by gathering all the extrinsic information from the check nodes that connect to it, which can be obtained by the following iterative sum-product procedure [Luis 2006].

Step 1: Initialization The variables q^0_{mn} and q^1_{mn} , which are the probabilities sent from the nth bit node to the $_m th$ check node along a connecting edge of a factor graph, are initialized to the values f^0_n and f^1_n ,respectively.

Step 2: Horizontal Step (bit node to check node) We define $\Delta q_{mn} \equiv q^0{}_{mn} - q^1{}_{mn}$ and compute eq.(1) and eq. (2) for each m, n and x = 0,1 :

$$q^0_{mn} = \prod_{n' \in N(m)\backslash n} q^0_{mn'} \qquad (1)$$

$$r^0{}_{mn} = \{ 1 + (-1)^0 \Delta_{mn}\}/2$$

$$r^0{}_{mn} = \{1 + \Delta_{mn}\}/2 \qquad (2)$$

$$r^1{}_{mn} = \{ 1 - \Delta_{mn} \}/2$$

Where, r_{mn} represents the probability information sent from the m_{th} check node to the nth bit node.

Step 3: Vertical Step (check node to bit node) For each n , m and x = 0,1 we update eq.(3):

$$q^0_{mn} = \alpha_{mn} f^o_n \prod_{m' \in M(n)\backslash m} r^0_{m'n} \qquad (3)$$

Where, α_{mn} is a normalization factor chosen such that $q^0_{mn} + q^1_{mn} = 1$. We can also update the a posteriori probabilities q^0_n and q^1_n, given by eq.(4):

$$q^0_{mn} = \alpha_{mn} f^o_n \prod_{m' \in M(n)\backslash m} r^0_{mn} \qquad (4)$$

Where, α_n is a normalization factor chosen such that $q^o_n + q^1_n = 1$.

Step 4: Check stop criterion soft decision is made on the q^1_n . The resulting decoded vector xˆ is checked against the parity-check matrix A . If Axˆ = 0,the decoder stops and outputs ˆx. Otherwise, it repeats the procedure from the Step 2. The sum-product algorithm sets a maximum number of iterations: if the number of iterations reaches that maximum, the decoder stops and outputs ˆx as the results of the decoding.

SIMULATIONRESULTS

The proposed system is illustrated in Fig. 1. A 20 Mbps was transmitted over the system. Since the channel for the 4th generation is not developed yet, therefore, the LTE channel specifications were used in the simulation process. These channels are Additive White Gaussian Noise AWGN, Vehicular channel. The modulation schemes are the MPSK with M=2,4 and 16. The simulation was done using the MATLAB R2010apackage. A flow chart shown in the Fig.9 show the simulation process.

The system uses LDPC code. The LDPC specifications used are irregular [16384] parity check matrix of rate ½ .The decoding algorithm is Sum-Product Decoding Algorithm,whichis the soft decision type of message passing. This is compared to the convolution code (CC) with the Viterbi decoding algorithm and uncoded system. The performance of the LDPCdecoding depends upon the number of iteration of the decoder. Table 1 summarizes the system specifications for the channel.

Figs.2,3 and 4 shows the variations of BER versus SNR for AWGN channel for uncoded data, convolution coded data and LDPC coded data with MPSK with M= 2,4 and 16 respectively with AWGN channel.

Table 1Simulation parameters for the indoor to outdoor/pedestrian environment

No. of active users	4
Total Number of users	32
Spreading code	Walsh Hadmard
Available bandwidth	5MHz
Sampling Time	170 nS
Spreading factor	64
FFT size	256
Effective symbol Duration	55uS
Guard time duration	¼FFT length
No of paths	8
Doppler velocity	60Km/h
Modulation technique	PSKwith M = 2,4and 16
No. of iterations	10
Convolutional code generator polynomial	[53, 75] octal
CC decoding algorithm	Viterbi

Figs. 5,6 and 7showa comparison for the uncoded data, convolution coded data and LDPC coded data for the Rayleigh fading channel.

The effect of varying the iteration for the decoding algorithm for the LDPC coded data over Rayleigh fading channel is illustrated in Fig. 8 with iterations of 1, 25, 50. 75 and 100. The increase of the number of iterationimprovesthe performance of the system.

Table 2 summarizes the obtained results as a comparison for AWGN channeland Multipath fading channelfor modulation techniques of bpsk, 4psk and 16psk with uncoded, convolution coded (CE) and LDPC coded data.

It can be noticed that there is an improvement in the results of the use of the LDPCcoding technique over others in many dB's of SNR.

Table 2: A comparison for SNR in dB for Uncoded, CE and LDPC for bpsk, 4psk and 16psk for BER of 10^{-4}.

M-psk	SNR/dB for AWGN channel			SNR/dB for indoor to outdoor// pedestrian channel		
	Uncoded	CE	LDPC	Uncoded	CE	LDPC
2psk	5	3.8	2.9	18.2	7	5
4psk	9	4.1	3.2	25	8.7	5.5
16psk	22	12.4	6	--	19.5	15

CONCLUSION:

From the results, it can be noticed that the LDPC gives a better BER for both the AWGNchannel and Rayleigh channel for low SNR and increase for higher values of SNR.

For AWGNchannel with LDPC coded data, the BER is around 10^{-4} for about 1 dB better than convolution coding and 2 dB better than uncoded system for BPSk and 6 dB gain over uncoded for QPSK . The gain increases as the order of modulation increases showing superiority for higher data rates. For low SNR the results contain a little difference from both uncoded data and convolution coded data.

For Rayleigh channel, at a BER of 10^{-4}, the performance of the LDPC coded MC-CDMA system is better than that with convolutional coding one by about 2 and 3 dB for BPSK and 4PSK modulation schemes respectively. It’s better by 4.5dB than convolutional coding for 16PSK. The number of iterations was set to 10 which represents a low computational complexity comparableto covolutional decoder. For better performance and higher computational complexity, the number of iterations can be increased to 100 as shown inFig. 8.

RRFERENCES

Laith Ali Abul-Rahaim. “Design and Simulation of STBC-(OFDM and CDMA) Tranceiver Based on Hybrid Transform,” Ph.D Thesis, University of Technology/Iraq, 2007.

Aqiel N. Almaamory and Husam A. Mohammed, “SCCC-MCCDMA combination performance over multipath Rayleigh fading channel”, Kerbalaa Journal, Vol.8, No.4, 2011.

Husam A. Mohammed, “PCCC MC-CDMA Combination Performance over Multipath Rayleigh Fading Channel” Journal of Engineering/ Baghdad University, V.15, No.3, 2009.

Nathan Yee, Jean-Paul Linnartz and Gerhard Fettweis, "Multi-carrier CDMA in indoor wireless radio networks", 1993.

R. G. Gallager, "Low-Density Parity-Check Codes", *IRE Trans. Inform. Theory*, vol. 8, pp. 21-28, Jan. 1962.

R. G. Gallager,"Low-Density Parity-Check Codes." Cambridge, MA: M.I.T. Press, 1963.

D. J. C. MacKay, R. M. Neal, "Near Shannon Limit Performance of Low Density Parity-Check Codes", *Electronics Letters*, vol. 33, Issue 6, pp. 457-458, 13 March 1997.

D. J. C. MacKay, R. M. Neal, "Good Error-Correcting Codes based on Very Sparse Matrices", *IEEE Trans. Inform. Theory*, vol. 45, pp. 399-431, Mar. 1999.

T. Richardson, A. Shokrollahi, R. Urbanke, "Design of Provably Good Low Density Parity-Check Codes", *IEEE Trans. Inform. Theory*, pp. 199, 25-30 June 2000.

F. R. Kschischang, B. J. Frey, H. A. Loeliger, "Factor Graphs and the Sum-Product algorithm", *IEEE Transactions on Information Theory*, vol. 47, Issue 2, pp. 498-519, Feb. 2001.

Luis Alberto Paredes Hernández and Mariano García Otero” A New LDPC-STB Coded MC-CDMA Systemswith SOVA-Based Decodingand SOFT-NterferenceCancellation”, 14th European Signal Processing Conference (EUSIPCO 2006), Florence, Italy, September 4-8, 2006, copyright by EURASIP

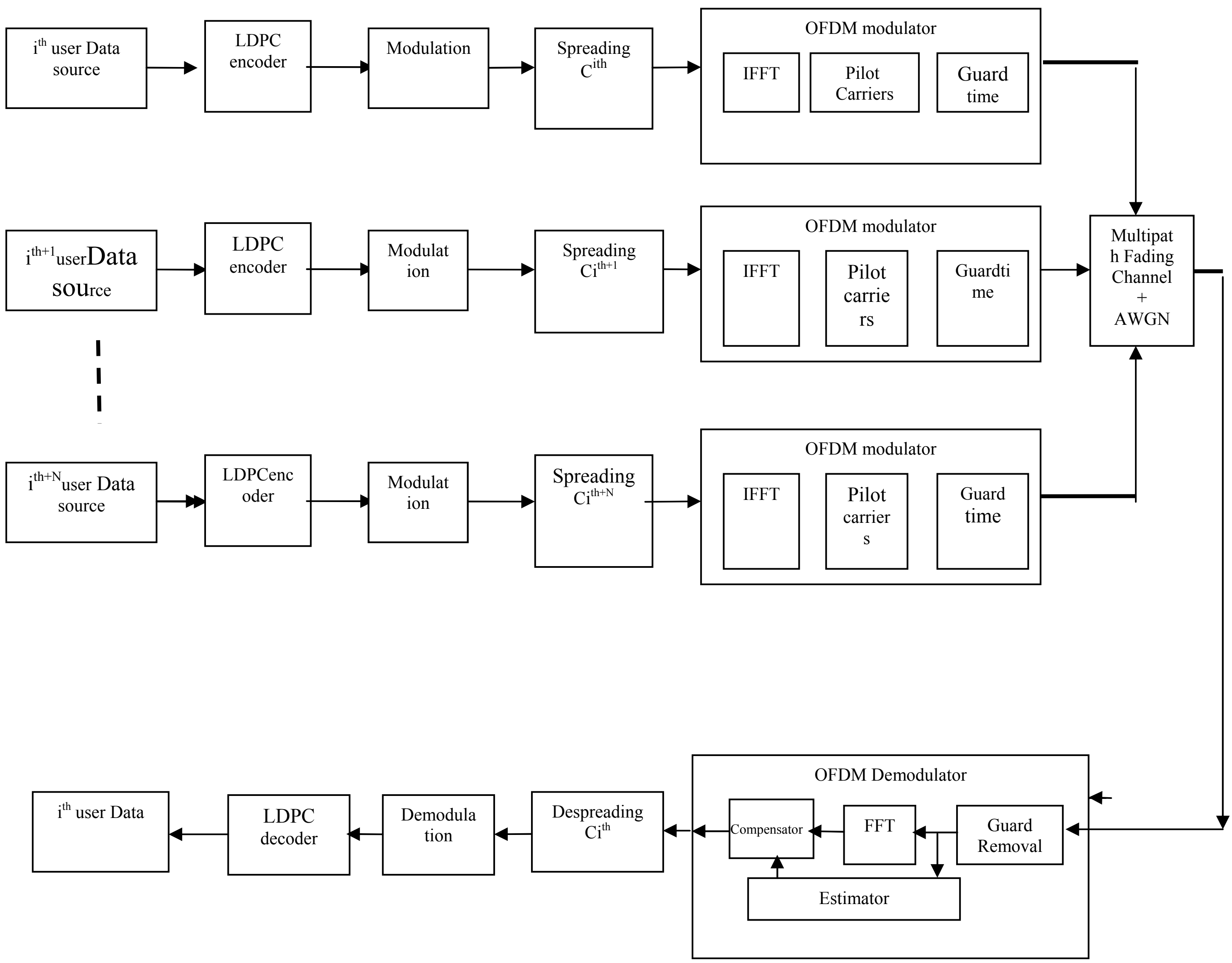

Figure 1 Block Diagram of the LDPC Coded MC-CDMA System.

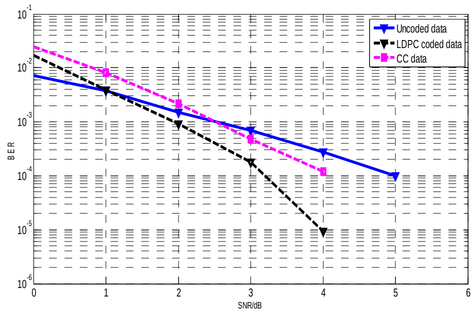

Figure 2 LDPC coded MC-CDMA performance for AWGN channel with BPSK modulation.

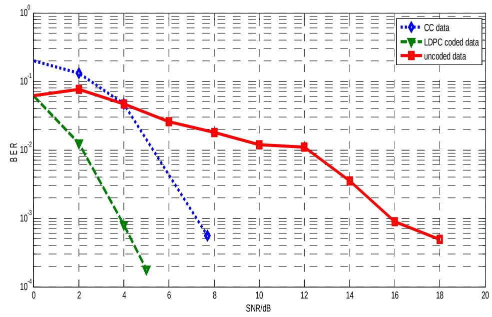

Figure 5 LDPC coded MC-CDMA performance for Rayleigh Fading channel with BPSK modulation.

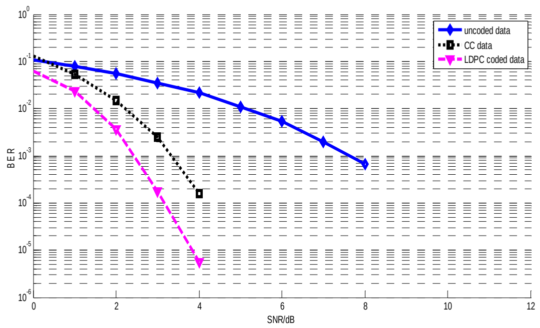

Figure 3 LDPC coded MC-CDMA performance for AWGN channel with QPSK modulation.

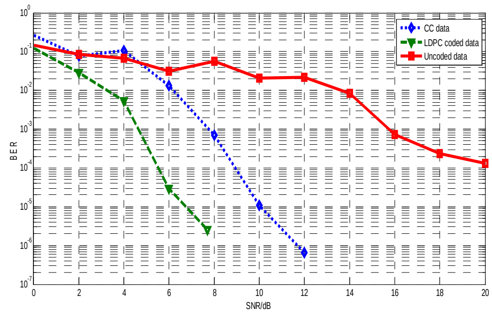

Figure 6 LDPC coded MC-CDMA performance for Rayleigh Fading channel with 4PSK modulation.

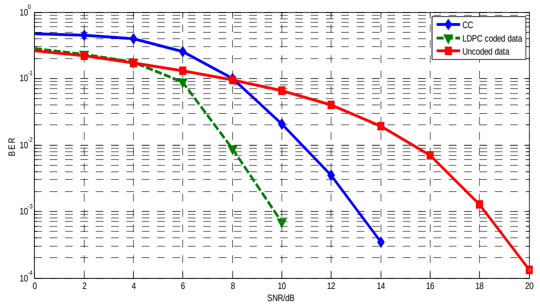

Figure 4 LDPC coded MC-CDMA performance for AWGN channel with 16PSK modulation.

Figure 7 LDPC coded MC-CDMA performance for Rayleigh Fading channel with 16PSK modulation.

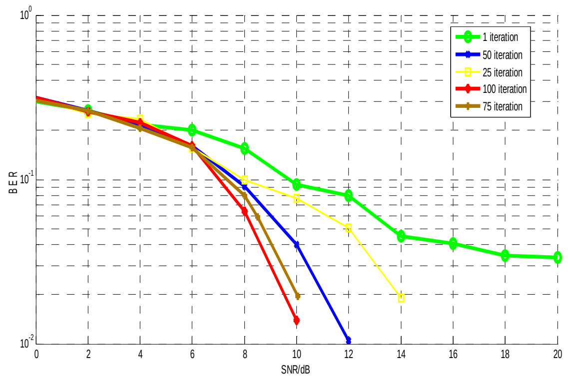

Figure 8 LDPC coded MC-CDMA performance for Rayleigh Fading channel with 16PSK modulation with different number of iterations for decoding process.

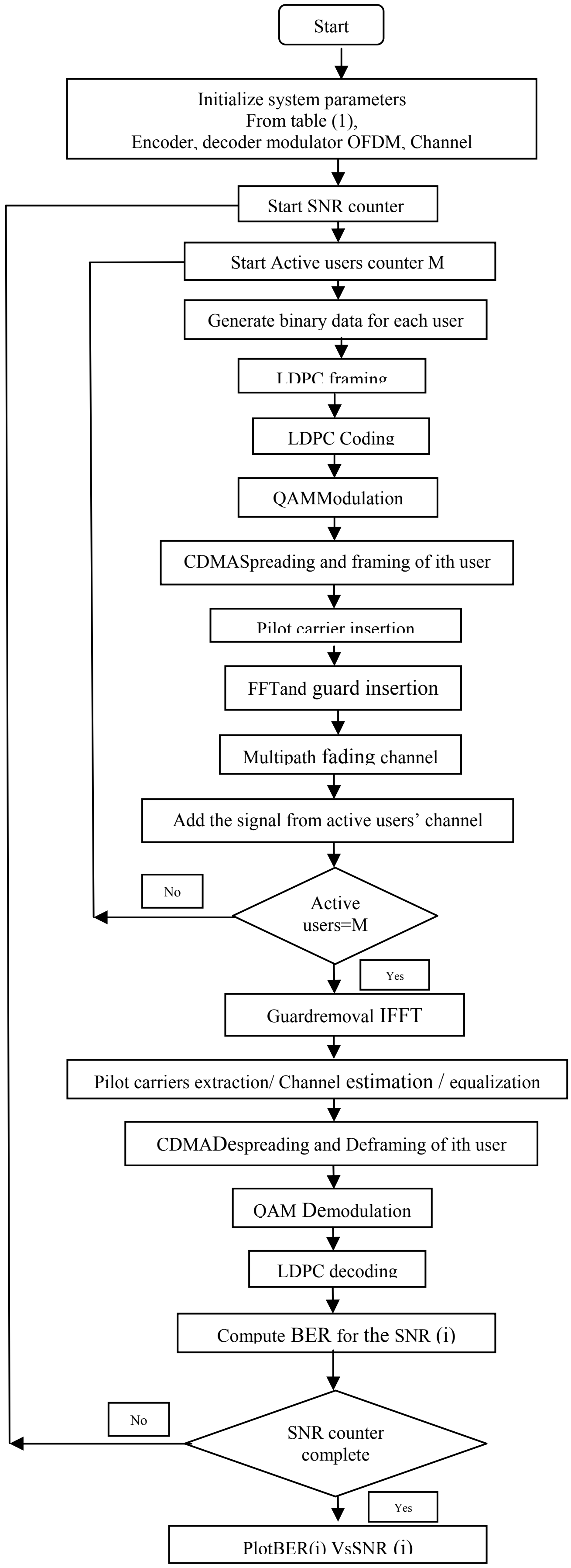

Figure 9Flow chart describe the simulation of the proposed system

DESIGN OF A CONTINUOUS SLIDING MODE CONTROLLER FOR THE ELECTRONIC THROTTLE VALVE SYSTEM

Dr. Shibly Ahmed AL-Samarraie
University of Technology
Control and System Eng. Dept.

ABSTRACT

Lowering the emission, fuel economy and torque management are the essential requirements in the recent development in the automobile industry. The main engine control input that satisfies the above requirements is the throttling angle which adjusts the air mass flow rate to the engine port. Due to the uncertainty and the presence of the nonlinear components in its dynamical model, the sliding mode control theory is utilized in this work for the throttle valve angle control system to design a robust controller for this system in the presence of a nonlinear spring and Coulomb friction. A continuous sliding mode control law which consists of a saturation function, instead of a signum function, and the integral of another saturation function is used in this work. This choice for the control structure will prevent the chattering to occurs but with a certain steady state error. On the other hand, the addition of the integral term will effectively reduce the steady state error according to the choice of its parameters. The simulations result for typical references of the opening throttle angle demonstrate the effectiveness of the proposed controller, especially after the addition of a nonlinear integral term.

Key words: Electronic Throttle Valve, Continuous Sliding Mode Control, Nonlinear Integral Control.

الخلاصة

من المتطلبات الحديثة في صناعة السيارات هي خفض مستوى الإنبعاثات، الإقتصاد في صرف الوقود و إدارة ونقل العزوم. إن المدخل الأساسي للمحرك والذي يحقق المتطلبات أعلاه هوعن طريق زاوية الخنق والتي تتحكم بمعدل جريان الهواء الداخل للمحرك. إن إستخدام نظرية المسيطر المنزلق لتصميم المسيطر وبوجود الإحتكاك ونابض لاخطي في هذا البحث هو بسبب المعرفة الغير دقيقة للتمثيل الرياضي للمنظومة و وجود عناصر لاخطية فيه. إن قانون المسيطر المنزلق المستمر المقترح هنا يحوي على دالة الإشباع بدل دالة الإشارة ودالة إشباع أخرى للجزء التكاملي للمسيطر. إن هيكل المسيطر الذي تم إختياره سوف يمنع ظهور الإرتجاج (chattering) ولكن مع بقاء خطأ دائمي في زاوية الخنق عن الزاوية المطلوبة. إن إضافة الجزء التكاملي الاخطي للمسيطر سيعمل على تقليل الخطأ الدائمي في زاوية الخنق وتبعا لعناصر هذا الجزء التي يتم إختيارها. إن نتائج المحاكات الرياضية ولزاوية خنق معتمدة تبعا للمصادر تؤكد قابلية و فعالية المسيطر المقترح و خصوصا بعد إضافة الجزء التكاملي الاخطي.

INTRODUCTION

The electronic throttling angle control system is the newly common requirement trend in automotive technology. Controlling the throttling angle is the control of the plate opining angle which it controls the air amount that enters to the combustion engine. The air flow rate will directly control the output torque engine and consequently the speed will raised or lowered according to the demand. This reveals the importance of controlling the air fuel ratio.

The air mass rate, traditionally, controlled according to the driver demand where the throttling angle is connecting directly to the accelerator by a wire. In this way, many internal and external conditions are ignored in determining the throttle angle such as fuel efficiency, road, or weather conditions which will negatively affects the engine overall efficiency **(Pan et al., 2008)**. To overcome the above deficiency an electronic control module (ECM) is used to accurately determining the required opining angle. Fig.1 shows the details of the electronic control system . Accordingly, the electronic control unit (ECU) determines the precise amount of fuel delivered to the engine. This amount of fuel is just enough to achieve an ideal air fuel ratio (A/F) (stoichiometry, about 14.7:1). The significance of controlling the air fuel ratio (A/F) is well clarified in Fig. 2 where the emissions lowered to a minimum amount (conversion efficiencies of 98% can be reached). The emission gases are like hydrocarbons (HC), carbon monoxide (CO) and nitrogen oxides (NO_x). For a deviations of ± 0.2 air fuel ratio (A/F) the conversion efficiencies of at least one of the emission components is drastically decreased **(Jun-Mo Kang et al., 1999)** (Fig. 2). This make known's the importance of controlling the air fuel ratio as a consequence of throttle angle control.

For the electronic throttle control system, one can mention two problems. The first is the nonlinearities in system model. This is due to the friction in pedal motion and to the nonlinear behavior of the spring in this system. In fact, it inserts discontinuous elements in the mathematical system model. In addition, the voltage, which it is the input to the electronic throttle valve system, does not actuate the throttle angle directly: and this leads to the mismatch property where the disturbance does not actuate the throttle system through the same input channel. The mismatch property is the second problem. For the application of many control theories, these properties added many difficulties.

Many authors had used the sliding mode control theory in designing a controller for the throttle control system. All of them overcome the first problem (model nonlinearity) by using sliding mode control theory as a robust tool with respect to uncertainty and nonlinearities in system model. In **(Kazushi et al., 2006)**, the inductance in the mathematical model of the DC motor is ignored. Thus, the motor voltage becomes the input to the throttle angle dynamics directly. The performance of the control system in this case depends on the actual inductance value. On the other hand, **(Ozugner et al., 2001)** use the complete throttling system model but with nominization of the throttling system model to a nonlinear canonical form. In the same reference the authors construct the switching manifold as a plane in canonical form of the throttle dynamical system state space and then compute the control action required to force and maintain the state close to switching manifold. The state will slide (the sliding motion) until it reach a region near the origin without reaching the origin. This because they use an approximate form to the signum function in order to represent the friction and the nonlinear spring models by a differentiable functions. A higher order sliding mode control theory was used by **(Reichhartinger et al., 2009)** to design a sliding mode controller to the throttling system. The higher order sliding mode concept eliminate the chattering arising in the classical sliding mode control theory and applied for system which have relative degree greater than one with respect to the switching function as in the case of the throttling system model.

In the present work a continuous sliding mode controller is used containing two saturation functions. The first is used instead of the signum function that is used traditionally in classical sliding mode controller design. The saturation function will remove the chattering that will occur due to the signum function; while the second saturation function is used in the integral term which will help greatly in reducing the steady state error caused by the nonsmooth disturbances affect the throttle valve system model.

In the following sections the mathematical model is presented first in terms of the error function (the deference between the throttle angle and the desired one), after that the proposed continuous sliding mode controller is presented with the corresponding stability prove using the Lyapunov stability criteria. The latter two sections are devoted to the controller parameters calculation and the simulations result which prove the effectiveness of the proposed control law.

MATHEMATICAL MODEL

The electronic throttling valve is shown in Fig. 3. It consists of a DC motor, a motor pinion gear, an intermediate gear, a sector gear, a valve plate, and a nonlinear spring. The mathematical model for the electronic throttle valve consists of the DC. motor mathematical model **(Reichhartinger et al., 2009)**

$$\frac{di}{dt} = -\frac{R}{L}i - \frac{k_m}{L}\omega_m + \frac{1}{L}u \qquad (1)$$

and the mechanical system described by

$$\frac{d\theta}{dt} = \omega$$
$$\frac{d\omega}{dt} = \frac{k_m N}{J}i - \alpha(\theta - \theta_o) - \beta * sign(\theta - \theta_o) - \gamma\omega - \delta * sign(\omega) \qquad (2)$$

where i is the armature current, ω_m is the motor angular velocity, u is the input voltage, k_m is the inductive voltage constant, L and R are the inductance and resistance in the armature circuit, respectively. Also, in eq. (2), θ is the throttle valve angle, ω is the angular velocity of the throttle valve, N is the gear ratio and J is the equivalent moment around the throttle axis, and their values are defined by

$$N = \frac{\omega_m}{\omega} \; \& \; J = N^2 J_m + J_{th} \qquad (3)$$

The model parameters α, β, γ and δ are identified experimentally **(Reichhartinger et al., 2009)** (Table 1) and formally modeled the friction effect, includes both the viscous and Coulomb friction, and the nonlinear spring and which acts on the throttle valve. In addition, the maximum actuator value must not exceed the following constraint **(Reichhartinger et al., 2009)**

$$|u| \leq U_{max} = 10V \qquad (4)$$

Now by ignoring the inductance L and defining the state variables x_1 and x_2 as follows:

$$\left.\begin{aligned} x_1 &= \theta - \theta_r \\ x_2 &= \omega - \omega_r \end{aligned}\right\} \quad (5)$$

the throttle angle dynamical equation is formulated in the present work as:

$$\begin{aligned} \dot{x}_1 &= x_2 \\ \dot{x}_2 &= -a_1(x_1 + \theta_r - \theta_o) - a_2(x_2 + \omega_r) + \\ &bu + d_1(\theta, \omega) - \dot{\omega}_r \end{aligned} \quad (6)$$

Where $a_1 = \alpha, \quad a_2 = \gamma + \frac{k_m^2 N^2}{JR}$,

$b = \frac{k_m N}{JR}$, and

$$d_1(\theta, \omega) = -\beta * sign(\theta - \theta_o) - \delta * sign(\omega)$$

In sliding mode control theory a certain switching function is selected first in terms of the state variable $(s = s(x), x = (x_1, x_2))$. The basic requirement is that when the state at the switching manifold $(s = 0)$, it goes asymptotically to the origin. Thus the following switching function is selected:

$$s(x) = x_2 + \lambda x_1, \ \lambda > 0 \quad (7)$$

It can be simply checked, with the aid of the equation $\dot{x}_1 = x_2$, that when the state is at the switching manifold $(x_2 = -\lambda x_1)$, it is regulated asymptotically to the origin with time constant equal to $(1/\lambda)$. Therefore, the controller u is designed such that it direct the state to the switching manifold and maintain it there for all future time.

Thus, by regarding the switching manifold as the desired output, we derive its dynamical equation as follows:

$$\begin{aligned} \dot{s} = &-a_1(x_1 + \theta_r - \theta_o) - a_2(x_2 + \omega_r) + \\ &bu + d_1(\theta, \omega) - \dot{\omega}_r + \lambda x_2 \end{aligned} \quad (8)$$

Our aim now (the next section), is to design a controller u such that, after a certain time period, the switching function $s(x)$ reaches its zero level (the switching manifold).

CONTINUOUS SLIDING MODE CONTROLLER DESIGN

The sliding mode control approach is recognized as one of the efficient tools to design robust controllers for complex high-order nonlinear dynamic plant operating under uncertainty conditions **(Agrachev et al., 2004)**. The chattering phenomenon generally seems as motion which oscillates about the sliding manifold. There are two possible mechanisms which produce such a motion. The first is in the absence of switching nonidealities such as delays, i.e., when the switching device is ideally switching at an infinite frequency. While the second is by replacing the signum function by a continuous function **(Slotine, 1983)**. The signum function is a discontinuous function used in sliding mode controller formula and its cause the chattering behavior in the dynamical system.

In this work, a continuous sliding mode control law is proposed which consists of a proportional and integral terms for a saturation function but with a different linear intervals. The proposed control law is

$$u = v - k * Sat_{\epsilon_1}(s) - \eta \int_{t_0}^{t} Sat_{\epsilon_2}(s(\tau)) d\tau \quad (9)$$

where $k > 0 \ and \ \eta > 0$, and $Sat_{\epsilon_i}(s)$, $i = 1,2$ is the saturation function defined by;

$$Sat_{\epsilon_i}(s) = \begin{cases} 1 & |s| > \epsilon_i \\ \dfrac{s}{\epsilon_i} & |s| \le \epsilon_i \end{cases}$$

Now, to determine the controller parameters, the following Lyapunov function is candidate

$$V(s) = \frac{1}{2}s^2 \tag{10}$$

Its time rate of change is

$$\dot{V} = s\dot{s} = s * (-a_1(x_1 + \theta_r - \theta_o) - a_2(x_2 + \omega_r) + bu + d_1(\theta, \omega) - \dot{\omega}_r + \lambda x_2)$$

$$= bs * \left\{-\left(\frac{a_1}{b}\right)(x_1 + \theta_r - \theta_o) + \left(\frac{\lambda - a_2}{b}\right)x_2 + u + \left(\frac{1}{b}\right)d_1(\theta, \omega) - \left(\frac{1}{b}\right)(a_2\omega_r + \dot{\omega}_r)\right\} \tag{11}$$

Now, by considering the uncertainty in system parameters, we have

$$-\left(\frac{a_1}{b}\right)(x_1 + \theta_r - \theta_o) + \left(\frac{\lambda - a_2}{b}\right)x_2 - \left(\frac{1}{b}\right)(a_2\omega_r + \dot{\omega}_r) = f_n(x_1, x_2, \omega_r, \dot{\omega}_r) + \Delta(\theta, \omega, \omega_r, \dot{\omega}_r) \tag{12}$$

where

$$f_n(x_1, x_2, \omega_r, \dot{\omega}_r) = -\left(\frac{a_1}{b}\right)_n (x_1 + \theta_r - \theta_o) + \left(\frac{\lambda - a_2}{b}\right)_n x_2 - \left(\frac{1}{b}\right)_n (a_2\omega_r + \dot{\omega}_r) \tag{13}$$

and the sub-script n refers to the nominal system parameters value, while Δ refers to the terms due to the uncertainty in system parameters. Accordingly, Δ is given by;

$$\Delta(\theta, \omega, \omega_r, \dot{\omega}_r) = -\Delta\left(\frac{a_1}{b}\right)(\theta - \theta_o) + \Delta\left(\frac{\lambda - a_2}{b}\right)\omega - \Delta\left(\frac{1}{b}\right)\dot{\omega}_r \tag{14}$$

Consequently, $\dot{V}$ becomes

$$\dot{V} = bs * \left\{f_n(x_1, x_2, \omega_r, \dot{\omega}_r) + \Delta(\theta, \omega, \omega_r, \dot{\omega}_r) + u + \left(\frac{1}{b}\right)d_1(\theta, \omega)\right\}$$

$$= bs * \left\{f_n(x_1, x_2, \omega_r, \dot{\omega}_r) + \Delta(\theta, \omega, \omega_r, \dot{\omega}_r) + v - k * Sat_{\epsilon_1}(s) - \eta\int_{t_o}^{t} Sat_{\epsilon_2}(s(\tau))d\tau + \left(\frac{1}{b}\right)d_1(\theta, \omega)\right\},$$

(15)

The first controller term v, is taken equal to

$$v = -f_n(x_1, x_2, \omega_r, \dot{\omega}_r) \tag{16}$$

and by considering the following

$$Sat_{\epsilon_1}(s) = sgn(s) * Sat_{\epsilon_1}(|s|) \tag{17}$$

eq. (14) becomes

$$\dot{V} = -bs * \left\{k * sgn(s) * Sat_{\epsilon_1}(|s|) - \Delta(\theta, \omega, \omega_r, \dot{\omega}_r) - \left(\frac{1}{b}\right)d_1(\theta, \omega) + \eta * \int_{t_o}^{t} Sat_{\epsilon_2}(s(\tau))d\tau\right\}$$

$$= -b|s| * \left\{k * Sat_{\epsilon_1}(|s|) - sgn(s) * \left(\Delta(\theta, \omega, \omega_r, \dot{\omega}_r) + \left(\frac{1}{b}\right)d_1(\theta, \omega)\right)\right\} - b * \eta * s\int_{t_o}^{t} Sat_{\epsilon_2}(s(\tau))d\tau \tag{18}$$

If k is chosen as

$k > \left|\Delta(\theta,\omega,\omega_r,\dot{\omega}_r) + \left(\frac{1}{b}\right) d_1(\theta,\omega)\right|$, $\forall|s| > \epsilon_1$ (19)

Now for a proper choice of η and ϵ_2, $s * \int_{t_0}^{t} Sat_{\epsilon_2}(s(\tau))d\tau > 0,\ \forall|s| > \epsilon_1$, this leads to

$$\dot{V} \leq 0\ ,\ \forall|s| > \epsilon_1 \tag{20}$$

Also, and according to Khalil **(Khalil, 2002)**, the state will reach and stay in the following interval

$$|x_1| \leq \frac{\epsilon_1}{\lambda} \tag{21}$$

In fact one can omit the addition of the integral term in the control law and select the values of ϵ_1 (for certain λ) according to the required accuracy. Unfortunately, very small value of ϵ_1 will cause a high oscillation around the equilibrium point and may induce the chattering in system dynamical behavior. To increase the accuracy and to prevent the chattering, the integral term is added with an appropriate selection of its gain η and ϵ_2. Namely for

$$\epsilon_2 < \epsilon_1 \tag{22}$$

the steady state error will be bounded by

$$|x_1| \leq \frac{\epsilon_2}{\lambda} \tag{23}$$

The inequality (23) also means that the term $s * \int_{t_0}^{t} Sat_{\epsilon_2}(s(\tau))d\tau > 0,\ \forall|s| > \epsilon_2$, and moreover it is greater than or equal to

$$\frac{|s|}{\eta} * \left\{max\left|\Delta(\theta,\omega,\omega_r,\dot{\omega}_r) + \left(\frac{1}{b}\right) d_1(\theta,\omega)\right| - k * \frac{|s|}{\epsilon_1}\right\}$$

This point can be easily deduced from eq. (18).

COMPUTATIONS OF THE CONTROLLER PARAMETERS

The numerical value of the electronic throttle valve model is presented in Table (1) **(Reichhartinger et al., 2009)**. We need here to calculate four controller design parameters, namely k, ϵ_1, η and ϵ_2. First, the steady state error according to inequality (21) is selected to be less than $0.5\ deg.$, i.e.,

$$\frac{\epsilon_1}{\lambda} = \frac{\pi}{360}$$

Thus for $\lambda = 12,\ \epsilon_1 = 0.1047$.

To begin, we estimate the following bound:

$$h = \max_{t}\left|\Delta(\theta,\omega,\omega_r,\dot{\omega}_r) + \left(\frac{1}{b}\right) d_1(\theta,\omega)\right|$$

The value h is computed according to the reference throttle angle to be considered in the simulations and to the parameters in Table 1, is taken as

$$h = 2.4$$

where the nominal parameters are taken as the mean of the maximal and minimal values. Hence

$$k = 2.5 > h$$

and finally, the integral term parameters are chosen as

$$\eta = 5 \quad and \quad \epsilon_2 = 0.01$$

In the following section the simulations are done based on the electronic throttle model as presented in eq. (1), i.e., the DC. motor mathematical model is included without ignoring the inductance L.

SIMULATIONS RESULT

Through the simulations the system parameters are taken as:

$\alpha = 90,\ \beta = 146,\ \gamma = 47,\ \delta = 62,$
$\theta_o = 0.095,\ km = 0.02,\ R = 1.6,$
$J = 0.0016,\ N = 20\ ,L = 0.0009.$

The first set of simulations is devoted to verify the effectiveness of the proposed controller in eq. (9), namely the controller ability to constrain the error according to the inequalities (21) and (23) without and with the integral term respectively. In these simulations, it is required for the throttle angle to follow a desired opening angle equal to 60^o. The effectiveness is measured here by the steady state error of the switching function $s(t)$. Therefore, we remove the integral term from the control law and plot first the switching function as shown in Fig. 4. As can be seen in this figure the steady state error of $s(t)$ is less than ϵ_1 ($\epsilon_1 = 0.1047$) and consequently the steady state error for the throttle angle is less than $0.5\ deg$ as can be verified in Fig. 5. In addition, the control action is plotted in Fig. 6 which satisfies inequality (4).

Next, we add the integral term to the control law, and plot $s(t)$ with time in Fig. 7. The steady state error is eliminated completely and the throttle angle will follow the desired angle without any steady state error (Fig. 8).

This is the first contribution of adding the nonlinear integral term to the controller formula. The second contribution may be explored when an external torque is added to the model (see **(Pan et al., 2008)** for the realization of adding the external disturbance). The external torque may be taken here as:

$$T_e = 25 * J * \sin\left(100\pi * t\right)$$

The presence of a periodic disturbance causes an oscillation in system response especially when there is no integral term. This feature for the controller when added the integral term is will clarified in Fig. 9 which plots the switching function with and without the integral term. It can also be noted that the integral term eliminate greatly the high frequency oscillation of the switching function and of course with a better accuracy. In fact the steady state error for the switching function will not exceeding 0.01 as selected in previous section and for the throttle angle (Fig. 10) it will be less than $0.05\ deg$. In addition, the plot of the control action with and without the integral term is found in Fig. 11. It can be noted that the actuation voltage is smoother with the integral term and still satisfying the voltage constrain in the inequality (4).

In the second simulations set, the throttle angle is forced to follow a typical opining angle reference. The reference angle consists of a train of different opining throttle angle and with different time durations **(Horn, 2008)**. The throttle angle response and the error between the throttle and the reference angle are plotted in Fig. 12. Also, in Fig. 13, the control action (the voltage) is plotted, where the maximum voltage still satisfying constraint (4).

As a final simulations test, the reference angle will be in a periodic form, as follows:

$$\theta_r = (\pi/180\ ) * (30 + 3 * \sin(\left(\frac{2\pi}{3}\right) * t))$$

In Fig. 14, the ability of the proposed controller is clarified where the throttle angle is forced to follow the reference angle θ_r. In addition the switching function and the control effort are plotted in Fig. 15. It can be seen that the switching function value is constrained by ± 0.03 which exceed ϵ_2. To make the switching function constrained by 0.01 the value of η is taken equal to 75 and $\epsilon_2 = 0.005$. The simulation result in Fig. 16 shows that the switching function is constrained by ± 0.01 after a period of time not to exceed $0.1\ second$ with a maximum control action less than 8 voltage. This situation reveals the flexibility of the proposed controller and its ability to attenuate the disturbances to a small bound without a great increase in the control action value.

CONCLUSIONS

In this paper a continuous sliding mode controller for a throttle valve system was proposed. The saturation function was used in the proportional and the integral terms in the control law to force the state to slide along the switching manifold. A Lyapunov function was used to prove the stability of the continuous sliding mode controller. The addition of a nonlinear integral term helps greatly in preventing the chattering that may occurs due to the requirement of a high precession opening angle; also in reducing the steady state error that occurs due to the presence of the external disturbances, friction and the nonlinear spring model. The simulation results prove first the effectiveness of the proposed controller when constraining the steady state error to lie within $\pm 0.05\ deg$.. Secondly, eliminating the high oscillatory actuation as could be verified clearly from the simulations result. Finally, the last simulation set showed the ability of the proposed controller in controlling the steady stat error by adjusting the integral term parameter η and ϵ_2. This was done without a large increase in the control action and without violating the maximum voltage constraint.

REFERENCES

- Pan Y., Ozguner U., and Da˘gci O. H., (2008),"Variable-Structure Control of Electronic Throttle Valve", *IEEE Transaction on Industrial Electronics,* Vol. 55, No. 11, November, pp. 3899-3907.
- Electronic Throttle Control System-intelligent.http://www.ncttora.com/fsm/2003/4runner/215/ncf/1gr-fe_etcs-i.pdf.
- Jun-Mo Kang and Grizzle J. W., (1999) "Nonlinear Control for Joint Air and Fuel Management in a SI Engine", *Proceedings of the* 1999 *American Control Conference.*
- Kazushi Nakano, Umerujan Sawut, Kohji Higuchi, and Yasusuke Okajima, (2006), "Modeling and Observer-based Sliding-Mode Control of Electronic Throttle Systems", *ECTI Transaction on Electrical ENG., Electronics, and Communication* Vol.4, No.1, pp. 22-28.
- Ozguer U., Hong S., and Pan Y., (2001), “Discrete-time sliding mode control of electronic throttle”, in *Proc. CDC, Orlando, FL*, , pp. 1819–1824.
- Reichhartinger M. and Horn M., (2009), “Application of Higher Order Sliding-Mode Concepts to a Throttle Actuator for Gasoline Engines", *IEEE Transaction on Industrial Electronics*, Vol. 56, No. 9, pp. 3322-3329.
- Agrachev A. A., Morse A. S., Sontag E. D., Sussmann H. J., and Utkin V. I., (2004), *"Nonlinear and Optimal Control Theory"*, Springer, Lectures given at the C.I.M.E. Summer School held in Cetraro, Italy, June 19–29.
- Slotine J.-J. E., (1983), "Tracking control of nonlinear systems using sliding surfaces", Ph.D. Thesis, Massachusetts Institute of Technology, Dept. of Aeronautics and Astronautics.
- Khalil H. K., (2002) *" Nonlinear Systems"*, 3rd Edition, Prentise Hall, USA.

- Horn M. and Reichhartinger M., (2008)" Control of an Electronic Throttle Valve based on Concepts of Sliding-Mode Control", in *Proc. 17th IEEE Int. Conf. Control Appl.*, pp. 251–255.

Table 1: Electronic Throttle Valve Parameters.

Param -eters	Minimal Value	Maximal Value	Units
α	69	95	$1/s^2$
β	143.5	157	rad/s^2
γ	32	54	$1/s$
δ	57	76	rad/s^2
θ_o	0.095	0.095	rad
k_m	0.02	0.02	$V.s/rad$
R	1.3	1.7	Ω
L	0.8×10^{-3}	1×10^{-3}	H
J_m	4×10^{-6}	4×10^{-6}	$kg.m^2$
J_{th}	2×10^{-6}	50×10^{-6}	$kg.m^2$
N	20	20	

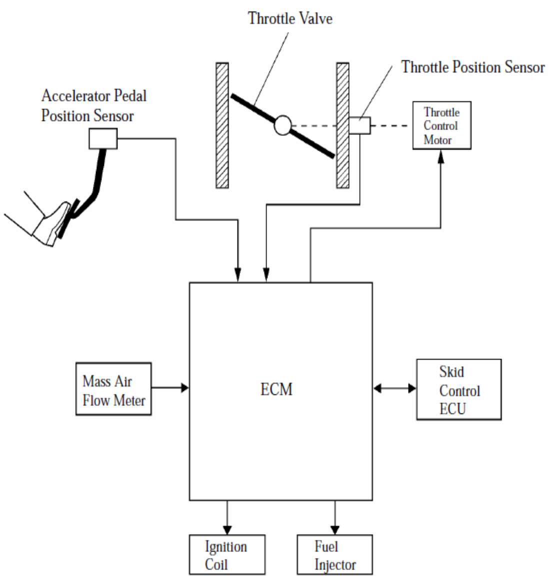

Fig. (1) Electronic control module system diagram**(http://www.ncttora.com/fsm/2003/4runner/215/ncf/1gr-fe_etcs-i.pdf.)**

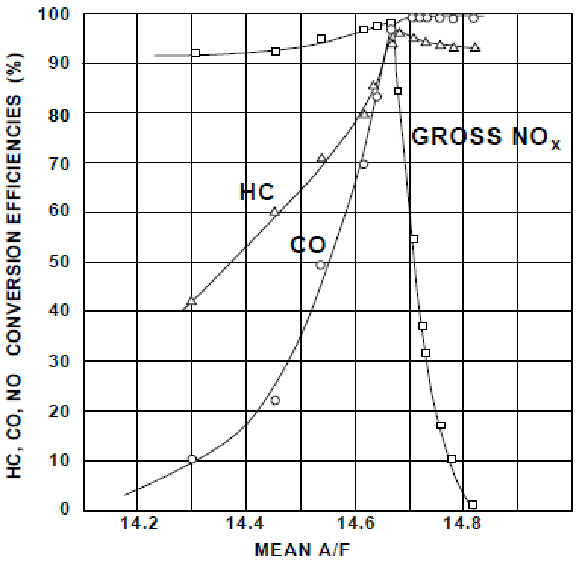

Fig. (2) Steady state conversion efficiency **(Jun-Mo Kang et al., 1999)**.

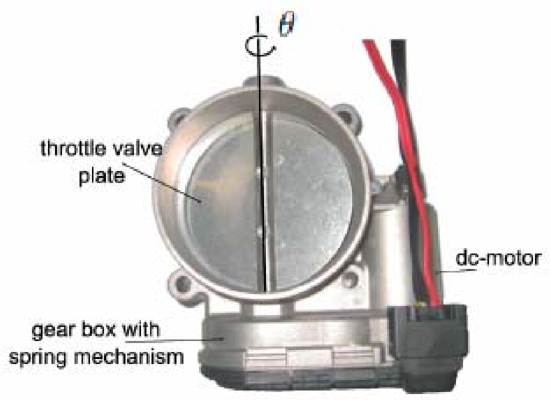

Fig. (3) Electronic Throttle Valve **(Reichhartinger et al., 2009)**

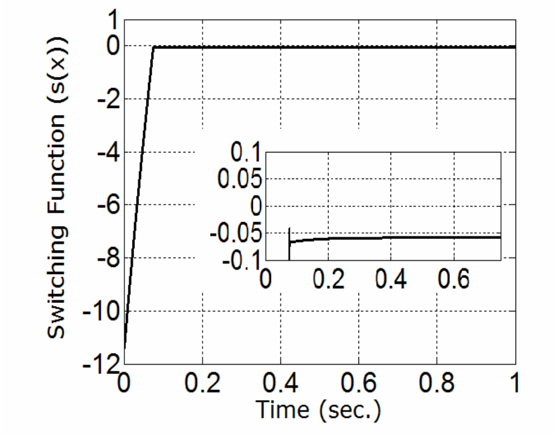

Fig. (4) $s(x)$ vs. time without the integral term.

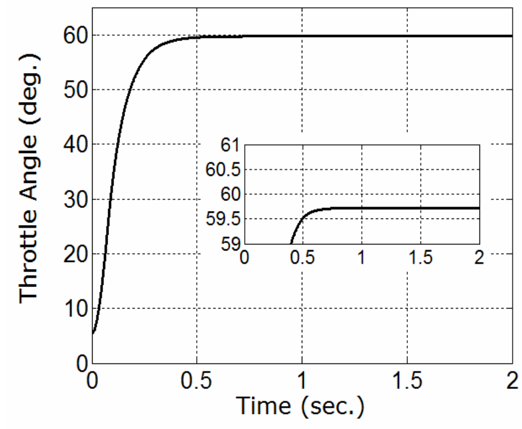

(a)

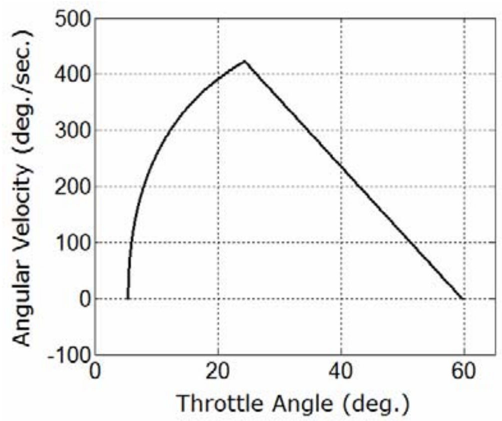

(b)

Fig. (5) Simulation without the integral term a) the throttle angle vs. time b) the phase plot.

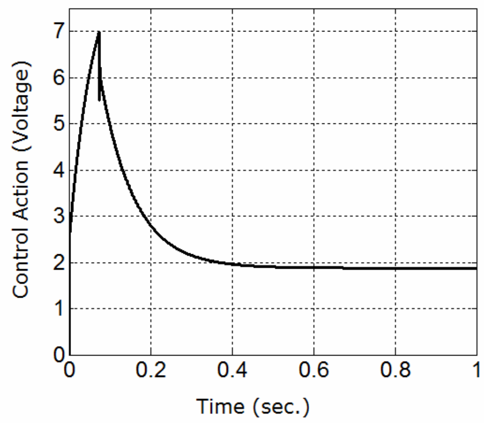

Fig. (6) Control Action vs. time without the integral term.

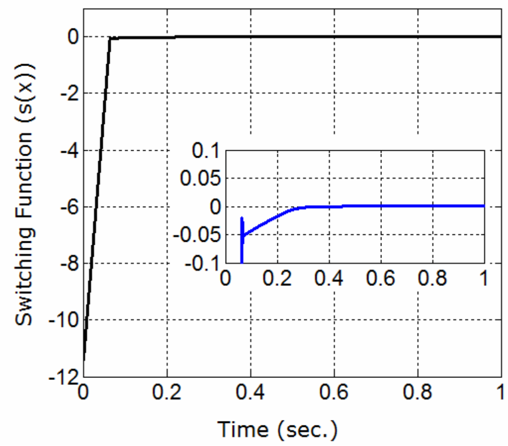

Fig. (7) $s(x)$ vs. time with the integral term.

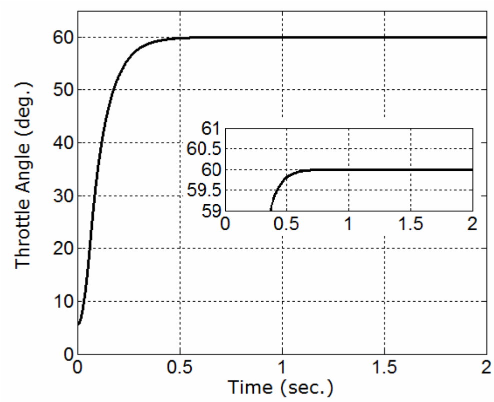

Fig. (8) The throttle angle vs. time with the integral term.

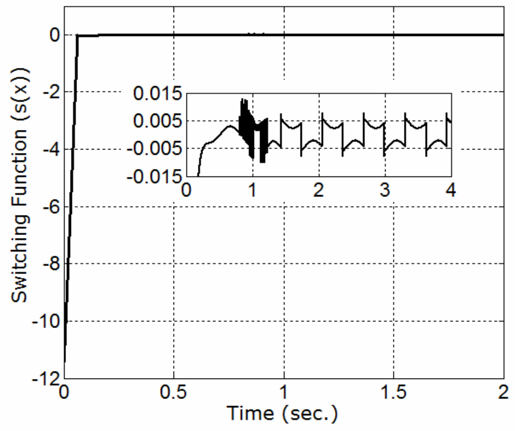

(a)

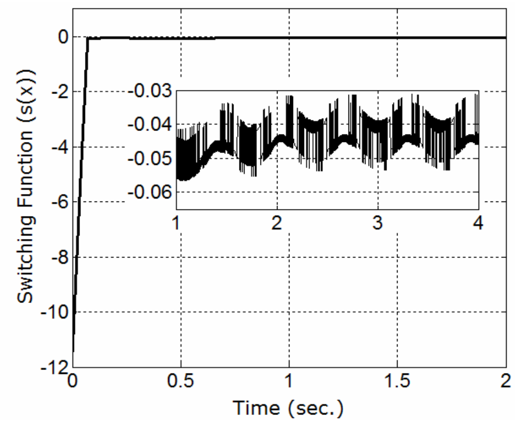

(b)

Fig. (9) $s(x)$ vs. time a) with the integral term b) without the integral term.

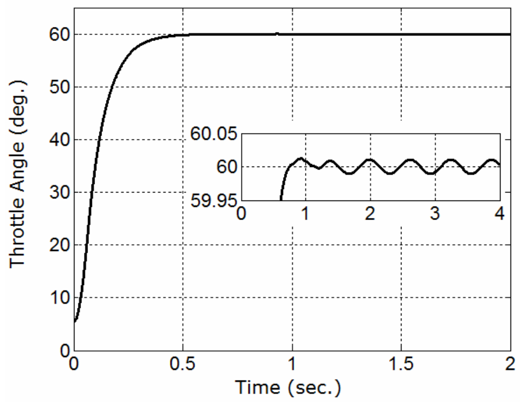

Fig. (10) The throttle angle vs. time with the integral term.

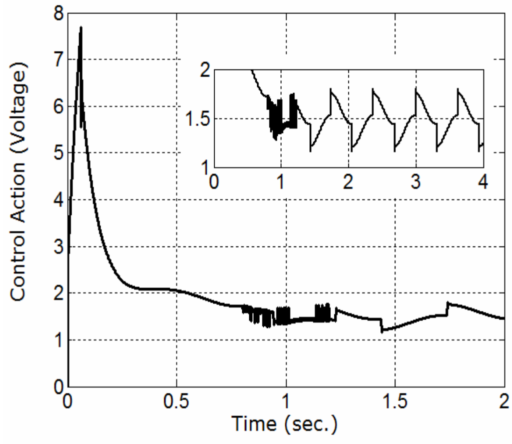

(a)

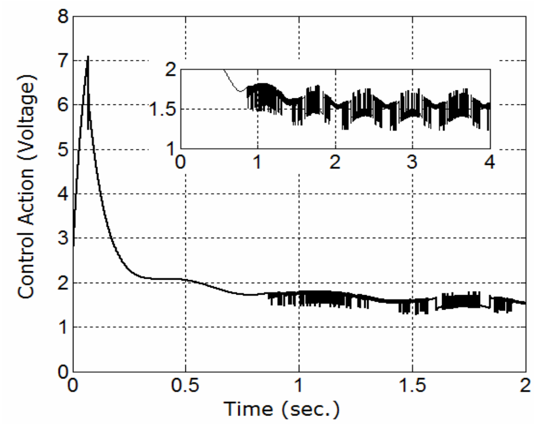

(b)

Fig. (11) Control Action vs. time a) with the integral term b) without the integral term.

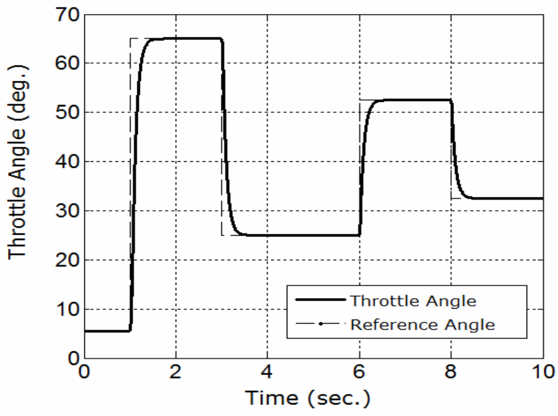

(a)

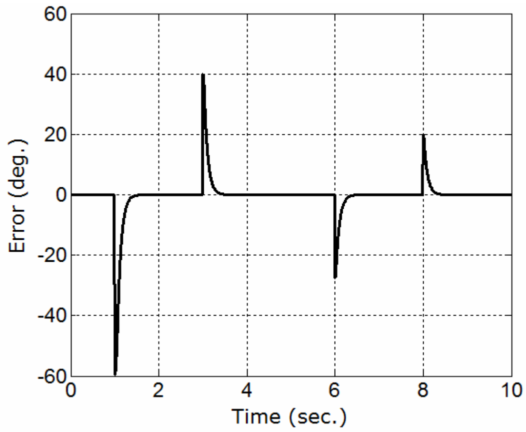

(b)

Fig. (12) a) Throttle angle vs. time b) the error $(\theta - \theta_r)$ vs. time.

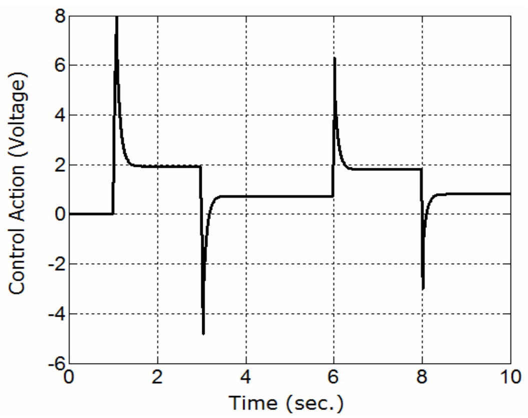

Fig. (13) Control Action vs. time.

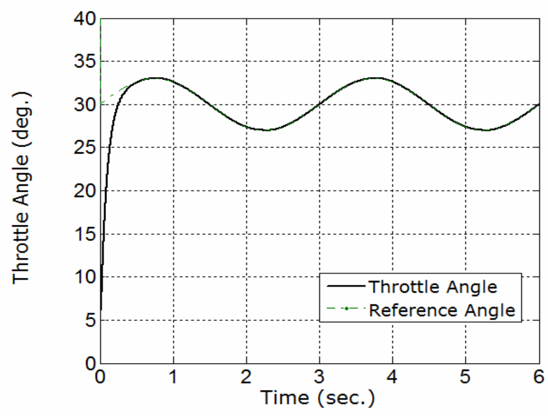

(a)

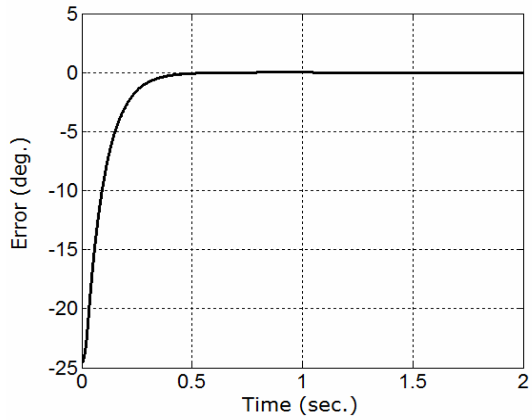

(b)

Fig. (14) a) Throttle angle vs. time b) the error $(\theta - \theta_r)$ vs. time.

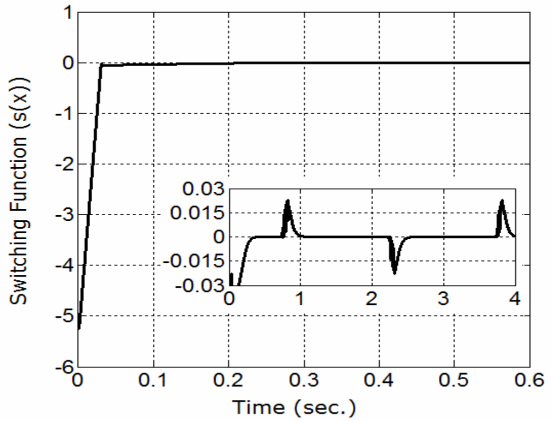

(a)

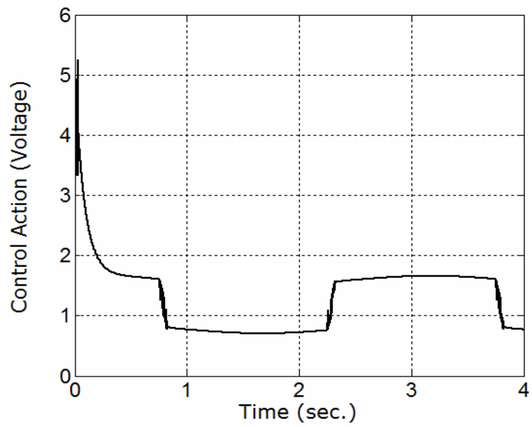

(b)

Fig. (15) a) $s(x)$ vs. time b) control Action vs. time.

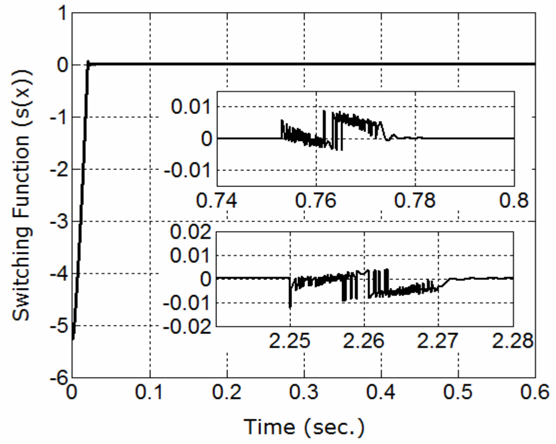

(a)

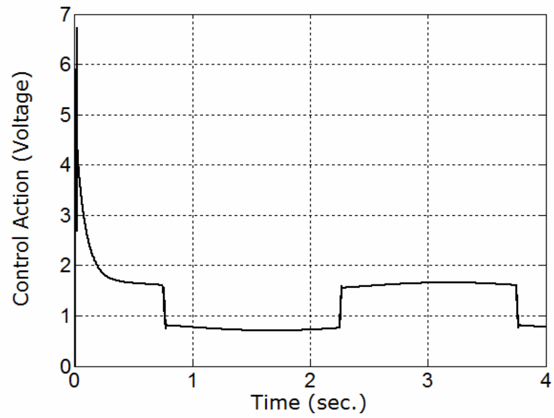

(b)

Fig. (16) Simulation with $\eta = 75$ and $\epsilon_2 = 0.005$ a) $s(x)$ vs. time b) control Action vs. time.

دراسة دور متراكبات النوفولاك في ولوج الجسيمات المشحونة الخفيفة وجعلها عديمة التأثير

رولا عبد الخضر عباس
الجامعة التكنولوجية – قسم العلوم التطبيقية

الخلاصة:-

من المتعارف عليه، أن كل منفعة يمكن أن تعود على الإنسان من جراء استخدام الأشعة المؤينة أو التعرض لها تقام على ضوء الضرر الذي ينتج عنها مما تدفع بالجنس البشري إلى اتخاذ موقف سلبي من جميع التطبيقات النووية وحتى السلمية منها إلا أنه يستطيع بدراسة مكثفة لنتائج التجارب النووية أن يقلل من هذه الإضرار بحيث تتساوى مع الإضرار الناتجة عن أية عملية تكنولوجية أو صناعية أخرى. فهناك العديد من الطرق للسيطرة على التعرض الخارجي للإشعاع وتقليله للحد الأدنى ولا سيما طريقة الأغلفة أو الدروع الواقية لكونها تؤدي فعلاً إلى مستويات عملية أمينة مستوفية شرط احتواءها على الحدود المسموح بها من الملوثات.

تم في هذه الدراسة ولوج جسيمات مشحونة خفيفة (دقائق بيتا) المنبعثة من المصدر المشع (^{90}Sr / ^{90}Y) في حواجز واقية مختلفة مصنعة من مواد متراكبة فينولية مطورة مكونة من مادة النوفولاك المطور بعوامل تحسين النوعية والمدعم بألياف الزجاج القصيرة (Short fiber) مرة وبألياف الاسبست (Asbestos fiber) مرة أخرى. كما أمكن استعمال مواد متراكبة هجينة في كبح هذه الأشعة المؤينة مكونة من مادة النوفولاك المقواة بـ (30% ألياف زجاج + 30% ألياف اسبست) بالإضافة إلى تحضير متراكبات بوليمرية أخرى من مادة الايبوكسي المقواة بألياف الزجاج القصير بغية المقارنة مع متراكبات النوفولاك للتوصل إلى رفع مدى الأمان المرجو من هذه الأغلفة بكبح دقائق بيتا إلى أن تصبح عديمة التأثير. علماً بأن جميع المواد المتراكبة المحضرة دعمت بمواد تقوية بكسر وزني (60%).

عموماً، يعبر عن التناقص في شدة هذه الجسيمات الخفيفة عندما تلج في مادة الهدف المحضرة بقراءة الكاشف الوميضي وفي ضوء النتائج التي حصل عليها أمكن قياس معاملات التوهين بنوعيها الخطية والكتلية مع الأخذ بنظر الاعتبار قياس اكبر سمك من المواد المحضرة يمكن لدقائق بيتا أن تخترقه (x_B) وبتعيين(x_B) قيست R (Range) مدى الدقائق في المتراكبات المحضرة. وأن هذه القياسات هي انسب المقاييس التي يمكن استعمالها في تقدير كفاءة المواد المحضرة لتوهين دقائق بيتا.

ولقد اتضح من النتائج أن مادة الايبوكسي ذات قابلية على كبح الأشعة الجسيمية قيد الدراسة أكبر مما هو عليه في مادة النوفولاك إشارة لانخفاض قيمة (x_B) في مادة الايبوكسي الذي يرافقه انخفاض مدى دقائق بيتا أيضا عما عليه في مادة النوفولاك وتزداد الحالة بصفة عامة بالانخفاض عند تدعيم هذه المواد بالألياف الزجاجية مسببة ارتفاع ملحوظ في معاملات التوهين الخطية والكتلية. ولما كان أهم ما يميز مادة النوفولاك عن الايبوكسي قابليتها العالية على التحمل الحراري، ما يساعد في تحسين خواص الأغلفة الواقية المصنعة منها وخصوصاً متراكباتها المدعمة بالألياف وبدور أهم و أكبر منه في حالة الايبوكسي رغم تفوقها في عملية التوهين.

كما يتضح من نتائج هذه الدراسة أن متراكبات النوفولاك المدعمة بألياف الاسبست تسبب في انخفاض سمك الطبقة التي تلجها دقائق بيتا بدرجة كبيرة، ولذا فأن الأغلفة الواقية المصنعة بآلية التهجين المكونة من مادة النوفولاك التي تضم ألياف الاسبست والزجاج مع بعضها البعض في نفس الوقت تساعد على ظهور خواص فريدة.

وأخيراً أن زيادة تركيز الهيكسامثليين تترأأمين مابين (14%-10%) - في مفهوم الصناعة الكيميائية العضوية – يعني زيادة كثافة الترابط التشابكي، مما يتسبب بارتفاع كفاءة عملية التوهين لهذه المواد.

Study the Role of Novolak Composite in Repress of light Charged Particles and Make it Neutral

ABSTRACT:-

It is well known, that each benefit can be derived for the rights of the use of ionizing radiation or exposure to be held in the light of the damage caused by the human race, which pays to take a negative attitude of all nuclear applications and even peaceful, he can study the results of extensive nuclear testing to minimize the damage to tie with damage resulting from any process of technological or other industry. There are many of the party for control of external exposure to radiation and reduction of the minimum particularly the method of packaging or armor because it actually levels the Secretary to meet the requirement to contain the permissible limits of pollutants .

This has been in the study and enter the light charged particles (beta) emitted by the radioactive source (^{90}Y / ^{90}Sr) in the protective barriers are made of different phenolic composite material consisting of advanced developer novolak factors improve the quality and short glass fiber reinforced (fiber Short) time and fiber asbestos (fiber Asbestos) again. The possible use of hybrid composite materials in curbing such ionizing radiation consisting of reinforced material novolak (30% glass fiber + 30% asbestos fiber) in addition to the preparation of polymeric complexes of other Epoxy reinforced glass fiber in order to short the comparison with complexes novolak to achieve a higher extent safety of these packages, please curb beta minutes to become neutral. Note that all materials prepared overlapped supported the strengthening of materials fracture and weight (60%).

In general, is on the decline in the intensity of light when the particles penetrate the target in the subject to read the prepared reagent detector in the light of the results obtained can be measured both types of linear attenuation coefficients and mass taking into account the measurement of largest thickness of material processed can be for a few particle a house that you walk into it (X_B) and appointment of (X_B) measured R(Rang) particle in the prepared composite. And that these measurements are the most appropriate metrics that can be used to estimate the efficiency of materials prepared for beta particles attenuation. I have discerned from the results that Epoxy with braking radiation on the viability of particulate matter under study than it is in the article novolak reference to the low value (X_B) in epoxy is accompanied by lower beta particles range also asked in the article novolak The situation is generally low when you consolidate these materials, glass fiber, causing a significant increase in linear attenuation coefficients and mass. Since the most important characteristic of the epoxy material novolak usability of high thermal endurance, which helps to improve the characteristics of protective packaging manufacturer, including and especially composite Reinforced and the role of the most important and greater than in the case of epoxy despite its superiority in the process of attenuation .

As evidenced by the results of this study that supported novolak composite Reinforced asbestos fibers causing a decrease in the thickness of the layer braking particles beta significantly and, therefore, the manufacturer of protective packaging machinery, consisting of hybridization novolak article, which includes asbestos, glass fibers with each other at the same time help the emergence of properties unique . And, finally, to increase the focus (HMTA) between (10% - 14%) - the concept of organic chemicals industry - means that the intensity of cross link density, which causes high efficiency of the process of attenuation of these materials.

المقدمة:-

يتعرض كل ما هو موجود على سطح الأرض باستمرار لتأثير الإشعاعات المؤينة، كالأشعة الكونية والمواد المشعة الطبيعة الموجدة في باطن الأرض، أو المصادر الصناعة كالمواد المشعة المستخدمة للإغراض الطبية وما يتساقط من الصناعات النووية، ومن الأمور المسلم بها اليوم، أن جميع أنواع الإشعاعات المؤين كـ (دقائق بيتا Beta، البروتونات Protons، النيوترونات Neutrons، الديترونات Deuterons، أشعة كاما والأشعة السينية $\chi - rays$ and $\gamma -$) تحمل طاقة عالية (High energy)، وعندما تصطدم بالمادة وتتوغل فيها، فإنها تخسر طاقتها تدريجيا، محولة عدد من ذراته إلى ايونات ويحدث هذا في المادة الحية وغير الحية، ولهذا تسمى مثل هذه الإشعاعات بالإشعاعات المؤينة حيث تسبب تغيرات في الخلايا الحية أو البنية البلورية للمواد الصلبة[2][11] [15].

لذا يتوقف التخريب الناتج على طبيعة المادة الماصة للإشعاع وطاقة الإشعاع وشدته، إذ تشير الكثير من الدلائل العلمية المتوفرة بزيادة كمية الإشعاع الممتص من قبل الأجهزة والمعدات العاملة في هكذا حقول، كما هو الحال في العديد من الدوائر الكهربائية المستعملة في تجهيزات القدرة النووية (High- voltage equipment) وكماسكات للمواد المشعة خلال الأجهزة النووية، مما يترتب عليها تأثيرات سلبية على كفاءة الأداء الوظيفي، ولكن ثمة إجراءات محددة يمكن القيام بها للحد من تعرض هذه الأجهزة للتلوث الإشعاعي وذلك باستخدام طلاءات وقائية أو التغليف بمواد بوليمرية مناسبة ذات مقاومة حرارية عالية وتوهين جيد لهذه الأشعة [2] [11] [13].

ونظراً للأهمية المطلقة لمسألة حماية المعدات والأجهزة من الإشعاع المؤين أجريت العديد من دراسات تقييم المخاطر في ضوء نتائج المسوح الميدانية وتحديد مستوى الإشعاع في مناطق العمل أخذاً في الاعتبار تأثير الأشعة المؤينة على الخواص الفيزيائية للمواد بكافة أنواعها المستعملة كأغلفة لهذه المعدات.

ففي تجربة قام بها الباحث (Kadhim) عام (2003) عن عامل التراكم لأشعة الكبح الناتجة عن الامتصاص الكلي لجسيمات بيتا المنبعثة من مصدر (^{90}Sr / ^{90}Y) بمعدل طاقة (2.27 Mev) والكاشف الوميضي ($T\ell$) NaI لمدى طاقي (100-1500)Kev حيث تم قياس عامل التراكم لأشعة الكبح المستمرة (أشعة الكبح المنبعثة من التنكستن كمادة موقفة لجسيمات بيتا) والنافذة لأسماك مختلفة من الرصاص والحديد والألمنيوم فأظهرت النتائج أن عامل التراكم في حالة المصدر الباعث للطاقات المستمرة لأتماثل قيمتها عند المصدر الأحادي أو متعدد الطاقات. أما الدروع المنفردة فقد لاحظ أن قيم عامل التراكم للدروع ذات العدد الذري الواطئ تزداد بزيادة الطاقة وتقل للدروع ذات العدد الذري العالي [18].

هذا وفي عام (2006) صنع الباحث (Bahnam) أربع دروع أسطوانية من مواد متراكبة من مادة الايبوكسي المدعمة بأسود الكاربون مرة وبالكرافيت مرة أخرى وبنسب خلط (40%) و(50%) وزناً من المادة الأساس فقد تم حساب معامل الامتصاص الخطي والكتلي لهذه النماذج المحضرة أولا ومن ثم عامل التراكم للمصدرين الـ (^{60}Co) و (^{137}CS)، فقد استنتج الباحث أن معامل الامتصاص يعتمد على المواد المدعمة وأن عامل التراكم يزداد بزيادة طاقة المصدر المشع المستخدم ويقل مع زيادة نسبة الخلط والكثافة الظاهرية فضلاً عن تقدم في قيم عامل التراكم لنماذج المتراكبات المدعمة بالكاربون على تلك المدعمة بالكرافيت [7].

وفي عام (2007) نجح الباحثان (Abass) و (Fawaz) في صنع دروع واقية محضرة من مادة النوفولاك المدعمة بألياف الزجاج مرة وبألياف الاسبست مرة أخرى بكسر وزني مقداره (60%) تعمل على توهين طاقة أشعة كاما المنبعثة من المصدر (^{60}Co) و (^{137}CS) دون تغير في مكوناتها من راتنج ومواد مقوية فأسهمت هذه الدروع في تحسن كبير في معامل الامتصاص الخطي والكتلي لهذه الأشعة [16].

وكما أوضحت الدراسة التي قام بها الباحث (Abdullah) وجماعته عام (2009) بأهمية حساب قدرة الإيقاف للعناصر الخفيفة مثل (^{6,7}Li، ^{a}Be، ^{10,11}B، ^{17,18}O، ^{19}F وكذلك ^{27}Al) لجسيمات ألفا كدالة للطاقة الحركية من (0.050 إلى 10.0 مليون إلكترون فولت) بخطوات مقدار كل منها (0.050 مليون إلكترون فولت) باستخدام صيغة (زيكلر). لقد تم ترتيب المقاطع العرضية لتفاعلات (ألفا - نيوترون) المتوفر في الأدبيات للعناصر الخفيفة أعلاه كدالة لطاقة جسيمة ألفا قريبة من (0.050 مليون إلى 10مليون إلكترون فولت) بخطوات كل منها (0.050 مليون إلكترون فولت)، باستخدام برنامج (أوتوكاد) و (سبلاين)، واستخدام النتائج الحصيلة النيوترونية (α n/10^{6}) باستخدام برنامج (Quick basic)[8].

أما الدراسة الحالية فهي تهدف إلى الاستفادة من المتراكبات الفينولية المطورة نوع (نوفولاك) والتي استخدم في تحضيرها ألياف الزجاج القصيرة وألياف الاسبست مع إضافة عوامل تحسين النوعية وبكسر وزني قدره (60%) كأغلفة للدوائر الكهربائية المستعملة في تجهيزات القدرة

النووية بغية توفير الحماية لهذه المعدات من خطورة التلوث الإشعاعي بدقائق بيتا الذي أصبح يتضاعف تراكيزه في بعض المواقع بسبب نشاط الإنسان، ولأجل تسهيل تحقيق مثل هذا الهدف توجب متابعة مسار كبح هذه الدقائق بعملية حسابية لمعرفة مدى تبعثر أو تشتت الملوثات الإشعاعية في المتراكبات المحضرة. وأخيرا احتساب معاملات التوهين بنوعيها الخطية والكتلية، عموماً هي معيار لكفاءة الاستخدام لهذه المواد كأغلفة واقية ضمن ذلك المصدر المشع(^{90}Y / ^{90}Sr). وفي نفس الوقت وعلى ضوء مثل هذه الحسابات يحاول هذا البحث التأكيد على أثر التفوق في قابلية التحمل الحراري لمتراكبات النوفولاك المحضرة على متراكبات الايبوكسي في رفع مدى الأمان المرجو عند إقرارها كأغلفة واقية. يضاف إلى ما تقدم تهدف هذه الدراسة للتعرف على دور آلية التهجين ونواتجها في المساهمة الفعالة في تقليل قابلية هذه الأشعة الجسيمية على اختراق المتراكبات الفينولية للتوصل إلى أفضل النتائج.

2- الجانب النظري:-

1-2 أشعاع بيتا) β (.

وهو عبارة عن جسيمات بعضها يحمل شحنة سالبة وبعضها الآخر يحمل شحنة موجبة. وقد تبين عن طريق شحنة أشعاع بيتا وكتلته أن هذا الإشعاع هو أما سيل من الالكترونات وإما سيل من البروتونات وقدرة الاختراق لإشعاع بيتا أكبر بـ (100) مرة من قدرة اختراق إشعاع ألفا [14] [15].

2-2 مدى دقائق بيتا.

يعتبر مدى الجسيمات المشحونة (R) بمثابة سمك الطبقة التي يلجها الجسيم إلى أن يبلغ التوازن الحراري فيختزن في المادة والمعلوم أن هذا المدى يعتمد في الواقع على نوع الجسيم وطاقته وطبيعة المادة الماصة. تمتلك الجسيمات في بداية مسار الكبح سرعة كبيرة، لذا يتبقى لها زمن قليل للتأين. وكلما بطؤت سرعة الجسيم كانت أمكانية تأينه كبيرة وبما أن الفقد من الطاقة في كل تأين واحد هو دائماً نفسه، فأن طاقة الجسم تتناقص دائماً بشدة. وإذا كبحت الجسيمات كلياً فإنها تصبح مرتبطة في المادة. ومن جانب أخر، يكون لدى الجسيمات الخفيفة (الالكترونات) مسار كبح اكبر بكثير من المدى وهكذا فإن مدى الالكترونات الوحيدة الطاقة يتعلق بمسار الكبح [14].

3-2 التأين بوساطة دقائق بيتا.

أن لدقائق بيتا القدرة على تهيج أو تأين الذرات فهي تزيح الإلكترون المداري بفعل قوة التنافر فتخلق زوجاً أيونيا. وتشير المعلومات العلمية أن دقيقة بيتا تفقد جزءاً من طاقتها لتكون الزوج ألايوني وتستمر عملية التأين إلى أن تفقد كل طاقتها الحركية وتصبح ككتلة ساكنة حيث يمكنها أن تتحد بأيون موجب لتكوين ذرة متعادلة أو تبقى إلكترونا طليقاً، عموماً يتولد إشعاع خاص عند كبح هذه الجسيمات المشحونة الخفيفة (الالكترونات) يسمى أشعاع الكبح أو أشعة التوقف (Bremsstrahlung) [15].

4-2 الوسط الموهن (Medium Attenuator).

أن الوسط الموهن المقترح استخدامه كأغلفة واقية عبارة عن مواد متراكبة بوليمرية، فالمواد المتراكبة البوليمرية مصطلح يشير إلى اللدائن المسلحة (plastic Reinforced) والتي فيها يخلط الراتنج (Resin) بالمادة المسلحة (Reinforcing) لتحقيق واحد أو أكثر من الصفات لإكساب المنتج النهائي قوة ومتانة ومواصفات حرارية وكهربائية لا تتوفر في البوليمر الغير المسلح، وبصفة عامة، فإن المكونات الأساسية الداخلة في تكون هذه المتراكبات يمكن تصنيفها بمايلي [2] [17]:-

أ- المادة الأساس (Matrix): وهي المادة التي تقوم بربط مواد التقوية ونقل القوى لها وتدعى أحيانا (بالطور المستمر) التي غالباً ما تكون مطاوعة للحرارة (Thermoplastic) أو غير مطاوعة للحرارة (Thermoset).

ب- مواد التقوية (Reinforcing Materials): وهي تلك المواد التي تعمل على تقوية المادة الأساس فبعضها يأتي من المواد المعدنية الطبيعية أو المواد العضوية أو العضوية التركيبية. عموماً فإن هذه المتراكبات تنحصر بخواص الأطوار الداخلة في تكوينها والكسر الحجمي للأطوار المكونة لها وطبيعة السطح البيني بينهما وهندسية طور التقوية والذي يتمثل بما يلي [12]:-

* شكل طور التدعيم.
* حجم طور التدعيم.
*توزيع طور التدعيم.
*توجهية طور التدعيم.

علاوة على ذلك هناك من الأبحاث ما ينصب على تطور المتراكبات البوليمرية باستعمال مخاليط من مواد التقوية لأنها توفر الفرصة للحصول على خواص ميكانيكية وفيزيائية فريدة قد لا تتوفر في المادة المتراكبة عند استعمال نوع واحد بمفرده من مواد التسليح [3].

مما لا شك فيه أن المواد المتراكبة الهجينة تقوم بجمع نوعين أو أكثر من مواد التقوية المختلفة ضمن المادة الأساس بحيث أن عملية الجمع بين مواد التقوية هذه يعتمد على نوع الاستخدام والخواص المطلوبة وعادة يتم استعمال آلية التهجين بطريقتين هما:

أ - (الهجينات المتحدة العناصر): وفيها تكون المواد المدعمة ممزوجة مع بعضها البعض وتمزج بطريقة عشوائية.
ب- (الهجينات الطبيعية): تتكون من طبقات متبادلة من المواد المدعمة المختلفة [3] [10].

3- الجانب العملي:-

1-3 المواد المستعملة في تصنيع الأغلفة الوقائية.

أ- المادة الأساس (Matrix Material).
تشمل المادة الأساس المستعملة لإنتاج المتراكبات البوليمرية والنوعيات التالية:-

1- مادة الايبوكسي المحتوى على مجاميع الايبوكسايد (Epoxides) نوع كونبكسترا (EP-10) EP-10 (Conbextra) الأردنية المنشأ من قبل شركة (company Fosroc Jordan)، أما المصلد المستعمل فهو (MPDA) (Metapheny lene diamine) حيث يضاف المصلد إلى الراتنج بنسبة (3:1) بمعنى لكل (3) غرامات من مادة الايبوكسي يضاف لها (1) غرام من المادة المصلدة ويحدث التفاعل بينهما عند درجة حرارة الغرفة وهو من تفاعل الإضافة (Addition reaction).

2- راتنج الفينول- فورمالديهايد نوع (نوفولاك) (Novolak)Nov. المتوفر لدى شركة ذات الصواري التي تعمل على استيراد المواد الاساسية الداخلة في تحضير هذا النوع من البوليمرات. أما المصلد المستعمل فهو الهيكسامثلين تترأمين الذي يضاف بنسبة تتراوح مابين (15-8%) [1]. أن النوفولاك هو عبارة عن كتل صخرية يتم طحنها وخلطها مع المادة المصلدة الهيكسامثيلين تترأمين (HMTA) بنسبتين هما (10%) وزناً مرة و(14%) وزناً مرة أخرى.

ب- مواد التدعيم (Reinforcing Materials).
استعملت ثلاث أنواع مواد التقوية وهي:-

1- ألياف زجاجية قصيرة (Short fibers) مقطعة بأطوال معينة تتراوح بين (6-8mm) وذات قطر بحدود (10-14µm) نوع (E).

2- ألياف الاسبست .Asbestos)asb) نوع (Chrysolite) بهيئة ألياف غير مستمرة أشبه بالشعيرات المتقاطعة (Discontinuous fiber whiskers).

3- مضافات تحسن النوعية: أن ابرز المضافات المستخدمة في تحسين صفات المتراكبات الفينولية تتمثل بالمواد الاتية [17]:-
* اوكسيد المغنيسوم (MgO): تعتبر من المواد التي تعمل على زيادة سرعة تفاعلات الترابط التشابكي وبالتالي تقليل زمن التقسية.
* حامض الاوليك (Olic): تعتبر من المواد المزلقة داخل كتلة المتراكبات الفينولية تقوم بدور تحرير السلعة المصنعة من حفر القوالب لتأمين عدم التصاقها.
* بولي خلات الفانييل: تعتبر من مواد التي تجعل المتراكبات الفينولية المطور تمتاز بالمرونة مع الجساءة.
* صبغة الانيلين (Aniline): تعتبر من المواد الملونة العضوية التي تضاف إلى المتراكبات الفينولية لإكساب المنتج النهائي جمالاً ورونقاً.
* سترات الرصاص: تعتبر من المواد المزلقة على شكل مسحوق تقوم بدور تحرير السلعة المصنعة من حفر القالب لتأمين عدم التصاقها.
اشتملت الدراسة الحالية على تحضير متراكبات الايبوكسي وكذا متراكبات النوفولاك المقواة بالألياف القصيرة بمختلف أنواعها بنسبة وزنية تقدر بـ (60%) وذلك بالاعتماد على العلاقة الآتية [16] [17]:-

$$\psi = \frac{W_f}{W_c} \times 100\% \ldots\ldots(1)$$ (الكسر الوزني)

$$W_c = W_m + W_f \ldots\ldots(2)$$

حيث أن (W_c , W_m ,W_f) كتلة الألياف والمادة الأساس والمادة المتراكبة على التوالي.

2-3 طريقة تحضير الأغلفة الوافية
تختلف طريقة القولبة على حسب نوع الراتنج المسلح وعلى ذلك فيمكن تقسيمها إلى نوعين:-

1-2-3 قولبة متراكبات الايبوكسي
تضمنت عملية تحضير متراكبات الايبوكسي الخطوات التالية:[21]

أ - تهيئة القالب (Mold preparation)
لقولبة هذه المواد، استعمل قالب خاص مصنوع من الحديد المغلون، ولضمان عدم التصاق الراتنج على القالب وسهولة استخراج المصبوبات بعد اكتمال عملية الإنضاج والتصلب تم وضع النايلون اللاصق على الجدران الداخلية كمادة عازلة وهكذا أصبح القالب جاهز لعملية الصب.
ب- تقنية تحضير متراكبات الايبوكسي (Preparation technique)

حضرت مادة الايبوكسي ومتراكباتها باستخدام تقنية التشكيل اليدوي (Hand lay – up molding) وكما يلي [21][23]:-

* (تحضير النماذج البوليمرية (الايبوكسي) الغير المدعمة .(Ep
لقد تم وزن الكمية المطلوبة من مادة الايبوكسي لقولبتها، وأضيفت لها كمية من المادة المصلدة بمقدار مناسب بحيث تكون النسبة الوزنية (3:1) بمعنى لكل (3) غرامات من مادة الايبوكسي يضاف لها (1) غرام من المادة المصلدة. إذ توضع المحتويات في وعاء زجاجي وتخلط جيداً للتخلص من فقاعات الهواء، بعدها يصب المزيج في القالب المهيأ مسبقاً تدريجياً ويترك المزيج ليتصلب بدرجة حرارة الغرفة ($22\ ^{o}C$) ولمدة (24 ساعة).

* (تحضير ألواح متراكبات الايبوكسي المدعمة بالياف الزجاج ((Ep.+G.F.)
وتشمل عملية التحضير على وزن كمية من ألياف الزجاج القصيرة المطلوبة بحيث يتحقق الكسر الوزني (60%). تضاف ألياف الزجاج إلى مزيج الايبوكسي والمصلد بالتدريج مع استمرار عملية الخلط الجيدة وذلك منعاً لحدوث التكتلات غير المتجانسة ليصب الخليط في القالب المهيأ مسبقاً مع وضع اللوح المعدني (غطاء القالب) على المحتويات لغرض انتظام السمك.

بعد اكتمال عملية التصلب ولجميع القوالب والتي استغرقت مدة (24) ساعة في درجة حرارة الغرفة ($22\ ^{o}C$) يتم استخراج المصبوبات من القوالب، بعدها تتم عملية الإنضاج اللاحق (Post curing) حيث توضع المصبوبات المحضر بدرجة حرارة ($50\ ^{o}C$) في فرن تجفيف (Oven) ولمدة ثلاث ساعات ما يساعد على إتمام التفاعلات الكيميائية وتقليل الاجهادات الداخلية المتكونة إثناء عملية الصب.

2-2-3 قولبة متراكبات النوفولاك

تضمنت عملية تحضير هذه المواد المراحل الثلاث وهي:-

أ- تهيئة القالب (Mold preparation).
لقولبة هذه المتراكبات استعمل قالب فولاذي ذي جزأين، الجزء الأول عبارة عن الطبعة (cavity)، أما الجزء الثاني فهو الضاغط (plunger) ويترك عادة خلوص بمقدار (0.05-0.13mm) بين جزأي القالب، للسماح للمواد الزائدة (Flash) بالهروب، ومن جانب ثأن غلفت الجدران الداخلية لهذا القالب بمادة مزلقه نوع شمع البرافين قبل تعبئية بالمادة المراد قولبتها وذلك لضمان سهولة استخراج المصبوبات بعد اكتمال عملية الايضاح. حيث تتم عملية القولبة بوضع المتراكبات ضمن الطبعة وتعرضها للضغط والحرارة باستعمال المكابس الحرارية نصف الآلية المصنعة من قبل شركة (Batten/Berge)، كونها تنظم عملية التسخين في كافة أجزاء القالب لتلدين هذه المتراكبات حيث بالتسخين إلى درجة حرارة في حدود ($150\ ^{o}C$) تسيل المادة البوليمرية ثم تتدفق تحت تأثير الضغط إلى كافة أجزاء الطبعة.

ب- تهيئة خليط (Novolak- HMTA):

عادة يتم تحويل كتل النوفولاك إلى مسحوق ذو حجم حبيبي يقدر بـ (75 μm) بدءا بالطحين اليدوي عن طريق استعمال هاون(Mortar) مصنوع من مادة الالومينا وانتهاء بالطحن الكهربائي، بالإضافة إلى سحن مسحوق(HMTA) لتجنب التكتلات غير المتجانسة. يليه خلط (HMTA) مع مسحوق النوفولاك بنسبة وزنية مقدارها (10%) مرة و(14%) مرة أخرى.

جـ - تقنية تحضير متراكبات النوفولاك (Technique Preparation).
1- تحضير النماذج الفينولية الغير المدعمة (.Nov):-
يخلط مزيج (Novolak - HMTA) المحضرة بالخطوة (ب) المذكورة أعلاه مع سترات الرصاص. بعد ذلك يصب الخليط في القالب المهيأ مسبقاً لتكبس تحت ضغط ($24.38kg/cm^2$) ولمدة (15) دقيقة، بعدها تستخرج المصبوبات من القالب.

2- تحضير الواح متراكبات النوفولاك المدعمة
حضرت متراكبات النوفولاك باستخدام تقنية التشرب (Impregnation method):-
* تحضير ألواح متراكبات النوفولاك المدعمة بألياف الزجاج (.Nov.+G.F)[1][17]:-
يذاب خليط (Novolak - HMTA) تبقى وفق الخطوة (ب) في كحول الايثانول باستعمال خلاط ذو سرعة واطئة ليضاف إليه عوامل تحسين النوعية بصورة تدريجية مع استمرار الخلط حيث تغمر ألياف الزجاج حال الانتهاء من عملية الخلط مع الأخذ بنظر الاعتبار تشبع هذه الألياف بالمزيج الراتنجي بشكل جيد لتبدأ بعدها مرحلة التجفيف بواسطة الهواء الساخن ذو درجة حرارة تتراوح في مجال ($70\text{-}80\ ^{o}C$) ولمدة ثلاث ساعات، وبذلك يتم التخلص من كحول الايثانول المستعمل في عملية تحضير المزيج الراتنجي لتكون المادة المحضرة جاهزة للقولبة بتعبئتها بالقالب المهيأ مسبقاً ومن ثم تكبس.
* تحضر ألواح متراكبات النوفولاك المدعمة بألياف الاسبست (.Nov.+asb):-
وتشمل عملية التحضير على وزن كمية من ألياف الاسبست بحيث يتحقق الكسر الوزني (60%) لتضاف إلى المزيج الراتنجي المعد مسبقاً وإتباع الخطوات السابقة الذكر أعلاه للحصول على مادة تضم ألياف الاسبست لتكون جاهزة للقولبة بتعبئتها بالقالب تم كبسها.

* تحضر ألواح متراكبات النوفولاك المدعمة بألياف الزجاج والاسبست (Nov.+asb.F.+G.F.):-
وتشمل عملية التحضير على وزن كمية من ألياف الاسبست والزجاج بحيث يتحقق الكسر الوزني (60%) أي بمعنى (30% G.F.+30% asb.F.) ليضاف هذا المخلوط الليفي إلى المزيج الراتنجي المحضر مسبقاً مع إتباع الخطوات السابقة الذكر أعلاه للحصول على مادة تضم هذا المخلوط الليفي من الاسبست والزجاج لتكون جاهز للقولبة بتعبئتها بالقالب المهيأ ثم كبسها.
هذا ومن الجدير بالذكر أن الضغط المستخدم لكبس جميع المتراكبات الفينولية المحضرة هو ($350\ kg/cm^2$). من جانب ثان، أن الوقت المستغرق لنضج نماذج النوفولاك المقواة بالألياف هو بحدود (30) دقيقة. بعدها تتم عملية الإنضاج اللاحق (Postcuring) حيث توضع المصبوبات الفينولية المقواة والغير المقواة المحضرة بدرجة حرارة ($60\ ^oC$) ولمدة ساعة واحدة. وهذا ومن الجدير بالذكر أن القوالب المجهزة قد قطعت على شكل صفيحه مستطيلة القطع ($3\times3\times0.824\ cm^3$) لأعداد النماذج الخاصة بالاختبار حسب الترتيب الهندسي للمنظومة.

3-3 الترتيب العملي لمنظومة الكشف والقياس

1- تهيئة منظومة العد الالكترونية الموضحة بالشكل (1).
2- الترتيب الهندسي للمنظومة: أن الترتيب الهندسي للمنظومة ليس بالشيئ الهين، لذا حرص في هذه الدراسة على معايرة المنظومة للحصول على أفضل النتائج العملية من خلال الترتيب الجيد لإجزاء المنظومة والتأكد من أنها بشكل فعال للوصول إلى نتائج جيدة قدر الإمكان والشكل (2) يوضح الترتيب الهندسي للمنظومة في المختبر وفيه يتم اتخاذ الحزمة الغير متفاعلة باستخدام زوج من المسددات (collimator) المصنوعة من الرصاص بأبعاد ($5\times10\times15\ cm^3$) يتوسطها ثقب دائري بقطر (10mm). للحصول على الحزمة المنتقاة (Collimated bream). أما بالنسبة للمصدر الباعث لدقائق بيتا فقط استعمل المصدر (^{90}Sr / ^{90}Y) بمعدل طاقة (2.27Mev) وبفعالية تقدر بحوالي ($10\ \mu Ci$) .

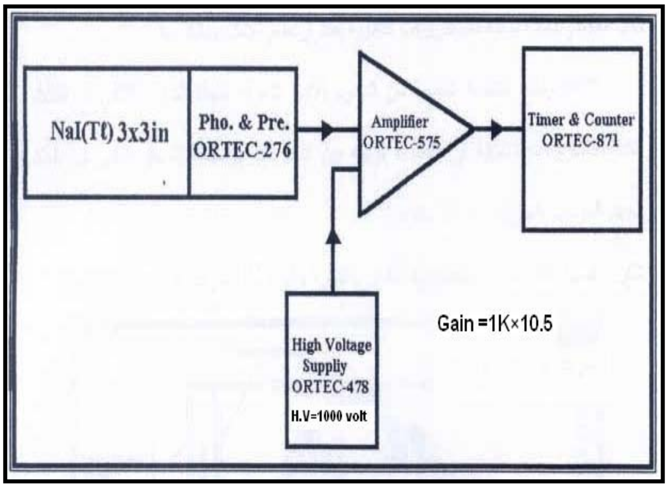

الشكل (1) يوضح منظومة العد المستعملة في قياس معامل الامتصاص.

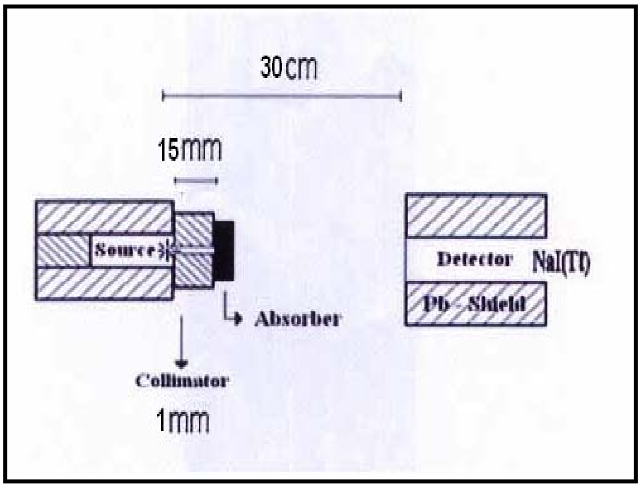

الشكل (2) يوضح الترتيب الهندسي الجيد للمنظومة.

4-3 قياس معامل الامتصاص الخطي والكتلي للمواد المحضرة لدقائق بيتا

تم قياس معامل الامتصاص الخطي عملياً بأتباع الترتيب الهندسي الجيد، اعتمادا على معادلة التوهين الاسية (معادلة لامبر- بيير) [16] [19]:-

$$I = I_o\, e^{-\mu x} \quad .....(3)$$

حيث (I_o) تمثل شدة الأشعة الساقطة و(I) شدة الأشعة بعد قطعها مسافة (x) من المادة الماصة.
(μ): ثابت التناسب ويسمى معامل الامتصاص الخطي والذي يمثل جزء الطاقة النسبي الذي يحذف من الأشعة في كل سنتمتر واحد من مسارها. ويمكن قياس شدة الأشعة بواسطة الكاشف الوميضي لأن قرأته تتناسب طردياً مع شدة الأشعة وبذلك يمكن كتابة المعادلة (3) على الشكل التالي [19]:-

$$N = N_o\, e^{-\mu\, x} \ ......(4)$$

حيث (N_o) تمثل قراءة الكاشف بدون وجود المادة الماصة و(N) تمثل قراءة الكاشف بوجود مادة ماصة سمكها (x) موضوعة بين المصدر والكاشف وبأخذ اللوغاريتم الطبيعي لطرفي المعادلة (4) ينتج:-

$$N = -\mu\, x + \ell n N_o \ .....(5)$$

وهذه تمثل معادلة خط مستقيم ميله يساوي ($-\mu$) ونقطة تقاطعه مع محور (ℓnN) يساوي(ℓnN_o).

ويعرف معامل الامتصاص الكتلي μ_m (Mass absorption coefficient) بما يلي:-

$$\mu_m = \mu / \rho \ \ (cm^2 / gm) \ .....(6)$$

حيث (ρ) هي كثافة المادة الماصة بوحدات (mg/mm^3) وبتعيين النقطة (B) من منحني الامتصاص لجسيمات بيتا وعلى مقياس شبه لوغاريتمي التي عندها تثبت قيمة (ℓnN) تقريباً عند الخلفية الإشعاعية (شكل رقم 3) يمكن معرفة مدى دقائق بيتا (R) في المواد المحضرة وفق منظور تحديد قيمة أكبر سمك للمتراكبات البوليمرية يمكن لدقائق بيتا أن تخترقه (x_B) من تقاطع امتداد الجزء المستقيم للمنحني مع المحور (x) سمك الوسط الماص (المتراكبات المحضرة) [11] [19] وباستعمال المعادلة التالية [14]:-

$$R = \rho\ x_B \ ......(7)$$

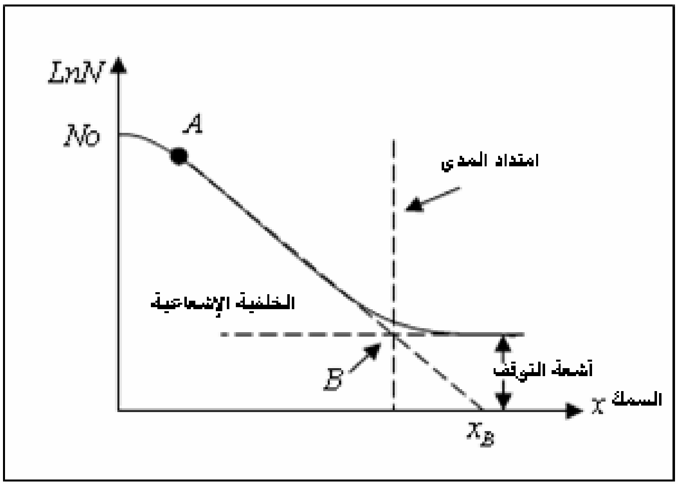

الشكل (3) يوضح العلاقة بين الامتصاصية لجسيمات بيتا على مقياس شبه لوغاريتماني وسمك الوسط الماص [11].

4- النتائج والمناقشة:-

هناك اعتقاد خاطئ قد يبدو حقيقة بناءاً على المعادلة (3) أو (4) وهو أن امتصاص دقائق بيتا من قبل مادة مثل النوفولاك والايبوكسي ومتراكباتهما يتبع بصورة تقريبية العلاقة الآسية (Exponential)، ولكن عملياً وفي حالة استعمال مصدر باعث لدقائق بيتا فقط مثل (^{90}Sr / ^{90}Y) وجد أن الخط البياني بين (ℓnN) وسمك النماذج المحضرة (x) لا يكون خطاً مستقيماً حسب المعادلة (5) وإنما يظهر منحنياً في البداية كما في الإشكال (4- 7) إلى نقطة A ثم يستمر على شكل خط مستقيم تقريباً إلى أن يبلغ سمك النماذج المحضرة حداً معينـاً (نقطة B) وعنده تثبيت قيمة (ℓnN) وهذه القيمة الثابتة تنتج من الأشعة السينية المتولدة نتيجة للتوقف الفجائي لدقائق بيتا داخل النماذج المحضرة وتسمى بأشعة التوقف (Bremsstrahlung)[11]. ألا أن ميل (Slope) الجزء المستقيم للمنحني هو مقدار ثابت يمثل معامل الامتصاص الخطي لأشعة بيتا وكما هو مبين بالجـداول (1-3). علاوة على ذلك تم من هذا الاختبار حساب معامل الامتصاص الكتلي (μ_m) وكما هو مبين بالجداول (4- 6).

1-4 تأثير طبيعة المادة البوليمرية على كفاءة الاستخدام لتوهين دقائق بيتا.

عندما نتكلم عن تحديد كفاءة استخدام المواد لتوهين دقائق بيتا يجب أن نتكلم عن الكفاءة من ثلاث زوايا:

مدى جسيمات بيتا، ومعامل التوهين الخطي والكتلي، ونسبة الاستفادة المئوية من هذه المواد في عملية التوهين. فقد ثبت عملياً أن هذه الجسيمات عند اختراقها الأغلفة المحضرة تفقد جزءاً من طاقتها وتستمر عملية التأين إلي أن تفقد كل طاقتها الحركية فقد أكدت نتائج هذه الدراسة أن دقائق بيتا تفقد كل طاقتها الحركية بعمق كبح في مادة الايبوكسي أقل قليلاً منه في حالة مادة النوفولاك وكما هو مبين بالجداول (7-9) والشكل (8). وعلى ذلك فمعامل الامتصاص الخطي وكذا معامل الامتصاص الكتلي لمادة الايبوكسي يكون أعلى قيمة من معامل الامتصاص الخطي والكتلي لمادة النوفولاك الإشكال (9 و10) ومن الممكن أعزاء التفاوت في قيم معامل الامتصاص الخطي إلى كثافة المادة البوليمرية، حيث تبلغ كثافة مادة الايبوكسي ($1.15 gm/cm^3$) [22] بينما تكون كثافة مادة النوفولاك حوالي ($0.91 gm/cm^3$) [17]، إذ تشير العديد من الأدبيات إلى زيادة معامل الامتصاص الخطي طردياً مع زيادة كثافة الوسط الماص [20]. ومن جانب ثانٍ تبين أن النسبة المئوية للاستفادة من هذه المواد في عملية التوهين تتراوح مابين (31.55%) إلى (43.54%) وكما هو مبين بالشكل (11)، ألا أن احتساب هذه النسبة يجب أن لا يقود العملية إلى التوصل إلى مواصفات نوعية للأغلفة بعيدة عن الواقع العملي بحجة الاهتمام العالي بضرورة الحماية فهناك أيضا العديد من الخصائص التي أقرت حدوداً لمواصفات هذه الأغلفة وعليه يجب أن تكون متوفرة بشكل متزامن مع قابلية التوهين مثل الثبات الحراري.

ففي تجربة عن التحلل الحراري الوزني TGA(Thermogrevimetric analysis) اتضح أن الفقدان في وزن مادة الايبوكسي عند درجة حرارة (500 ^{o}C) يقدر بـ (98.1%) [4] في حين يكون الفقدان في وزن نموذج من النوفولاك ذو نسبة (10%) من (HMTA) حوالي (50.8%) وكذا (38%) من نموذج النوفولاك ذو نسبة (14%) من (HMTA) [17]. وهذه المعلومات العلمية تساعد على فهم سبب تفضل استعمال مادة النوفولاك في صناعة الأغلفة الواقية على الرغم من مساهمتها المنخفضة في توهين الإشعاع الجسيمي مقارنة بمادة الايبوكسي إلا أنها تمتاز بقابليتهما على التحمل الحراري العالي والتي تتفوق بها على مادة الايبوكسي [17].

2-4 تأثير تدعيم مادة النوفولاك وكذا الايبوكسي بألياف الزجاج القصيرة على كفاءة الاستخدام لتوهين دقائق بيتا.

أن استعمال مادة النوفولاك أو الايبوكسي بمفردها لا يكفي لحماية المعدات ما لم تستعمل المواد الحاشية كألياف الزجاج التي تحسن الخواص بشكل عام وتقلل الكلفة. ولقد اتضح من النتائج المتمثلة بالشكل (12) أن تدعيم مادة الايبوكسي وكذا مادة النوفولاك بألياف الزجاج له أثر سلبي على عمق الكبح لدقائق بيتا كمـا هـو مبين فـي الجـداول (7- 9) مما تسبب في ارتفاع قيمة معامل الامتصاص الخطي والكتلي الإشكال (13و 14)، فالمعروف عن المادة الرابطة الراتنجية بانخفاض كثافتها مما يؤدي إلى انخفاض مساهمتها في امتصاص الأشعة الجسيمية (بيتا) مقارنة مع المـادة المتراكبة المدعمة بأليـاف الزجـاج التي تمتاز بكثـافة تقدر بحوالي (2.6 gm/cm^3) [22].

هذا وقد بين أحد الباحثيين في وقت سابق من خلال اختبار (TGA) أن تأثير درجات الحرارة العالية كان واضحاً على مادة النوفولاك الغير المدعمة أكثر مما هو علية في متراكبات النوفولاك نظراً لنقصان سرعة عملية التفكك الحراري بوجود المواد المسلحة الليفية. من جانب ثانٍ، تفوق متراكبات النوفولاك في قابليتها لمقاومة درجات الحرارة العالية على مادة الايبوكسي يؤدي إلى تفوق متراكبات النوفولاك في مقاومتها الحرارية على متراكبات الايبوكسي[17].

وفي ضوء النتائج التي حصل عليها هذا الباحث يمكن تبني حقيقة تفضيل استخدام متراكبات النوفولاك كدروع واقية على متراكبات الايبوكسي على الرغم من كون نسبة الاستفادة من متراكبات الايبوكسي في عملية التوهين تزيد على متراكبات النوفولاك ذات نسبة (10%) من (HMTA) بمقدار (8.7%) بينما تزيد على متراكبات النوفولاك ذات نسبة (14%) من (HMTA) بمقدار (4.91%) (شكل 15).

3-4 تأثير تدعيم مادة النوفولاك بألياف الاسبست على كفاءة الاستخدام لتوهين دقائق بيتا.

من المتعارف عليه، أن ألياف الاسبست تعد المنافس الأقرب إلى ألياف الزجاج إذ تعطي مجالاً أكثر لمنتوجات أقوى واصلب وبكلفة قليلة [6]. فقد لوحظ من هذه الدراسة أن تدعيم النوفولاك بألياف الاسبست نوع (Crysolite) يتسبب عنه انخفاض حاد في سمك الطبقة التي تلجها دقائق بيتا (R) المارة فيها (شكل 16) ولقد أظهرت القياسات ارتفاع قيمة معامل الامتصاص الخطي لمتراكبات النوفولاك المدعمة بألياف الاسبست ذات نسبة (14%) من (HMTA) بمقدار ($0.1093cm^{-1}$) من أجمالي قيمة معامل الامتصاص الخطي لمادة النوفولاك. ونفس الشئ بالنسبة للمتراكبات المدعمة بألياف الاسبست ذات نسبة (10%) من (HMTA) فإن هذا الرقم يصل إلى ($0.11737cm^{-1}$) من أجمالي قيمة معامل الامتصاص الخطي لمادة النوفولاك بينما متراكبات النوفولاك المدعمة بألياف الزجاج تعمل على رفع قيمة معامل الامتصاص الخطي بمقدار ($0.0656cm^{-1}$) من إجمالي قيمة معامل الامتصاص الخطي لمادة النوفولاك ذات نسبة (10%) من (HMTA) في حين تبلغ قيمة معامل الامتصاص الخطي($0.0657cm^{-1}$) من إجمالي قيمة معامل الامتصاص الخطي لمادة النوفولاك ذات نسبـة (14%) مـن (HMTA) (شكل 17) ويعزى سبب هذا الارتفاع بقيمة معامل الامتصاص الخطي إلى تركيب ألياف الاسبست الليفي المغلق (Closed fiber structure) مما يسبب كثافة تراص عالية لهذه الألياف عند استعمالها كمادة حاشية للنوفولاك[5][17]. من جانب ثانٍ، تشير الدراسات السابقة إلى أن المادة المتراكبة المقواة بألياف الاسبست تبدي مقاومة حرارية عالية مقارنة مع بقية متراكبات النوفولاك المحضرة [17].

وهكذا تساعد ألياف الاسبست بتركيبها المتميز في جعل نسبة الاستفادة من متراكبات النوفولاك المحضرة في عملية التوهين منها لا يتجاوز (34.84%) من مجموع الاستفادة الكلية لكافة متراكبات النوفولاك ذات نسبة (14%) من (HMTA) في حين تبلغ نسبة الاستفادة من متراكبات النوفولاك ذات نسبة (10%) من (HMTA) المدعمة بألياف الاسبست حوالي (34.6%) من إجمالي كافة متراكبات النوفولاك المستفادة منها في عملية التوهين (الإشكال18 و19).

كما أظهرت نتائج قياس معامل الامتصاص الكتلي والمتمثلة بالشكل (20) سلوكاً مماثلاً لمعامل الامتصاص الخطي مما يؤكد حالة التناسب بينهما.

4-4 تأثير نسبة (HMTA) في مادة النوفولاك ومتراكباتها على كفاءة الاستخدام لتوهين دقائق بيتا.

من المثبت عملياً بأن زيادة نسبة المادة المصلدة (HMTA) من (10%) إلى (14%) تؤثر بصورة سلبية على مرونة السلاسل البوليمرية المتشابكة لزيادة كثافة الترابط التشابكي (Cross- link density) [9]. وهذا ما أكده احد الباحثين إثناء دراسته لخواص هذه النوع من المتراكبات الميكانيكية والحرارية في وقت سابق [17]، مما يسبب تحسن في كفاءة التوهين بعد انخفاض مدى دقائق بيتا (الشكل 16)، بالإضافة إلى أهمية هذا الانخفاض في تحسين قيم معـاملات التوهين الخطيـة و الكتليـة (الإشكال 17 و20).

5-4 تأثير استعمال آلية التدعيم الهجين على كفاءة الاستخدام لتوهين دقائق بيتا.

تمتاز المواد المتراكبة الهجينة المحضرة بخواص فريدة بما تحويه من مواد تقوية متنوعة خاصة الألياف نتيجة لما تتمتع به الألياف من اختلاف في الخواص الميكانيكية والحرارية بالمقارنة بالمواد المتراكبة المدعمة بنوع واحد من مواد التقوية [16]، ففي تجربة عن مدى جسيمات بيتا في مواد متراكبة مدعمة بألياف الزجاج والاسبست وأخرى دعمت بألياف الزجاج فقط مع تثبيت كل الظروف والعوامل الأخرى، أوضحت النتائج أن مدى دقائق بيتا في المادة المتراكبة الهجينة ذات نسبة (14%) من (HMTA) لم يتجاوز ($63.149mg/mm^3$) و ($65.22mg/mm^3$) للمتراكب الهجيني ذو نسبة (10%) من (HMTA)، أما في حالة المتراكبة المدعمة بألياف الزجاج الخالية من ألياف الاسبست فقد كان مدى جسيمات بيتا في هذه المواد المتراكبة اكبر كبيراً منه في الحالة السابقة (جدول8 و9). كما أدت إلية التهجين إلى ارتفاع معامل الامتصاص الخطي والكتلي لدقائق بيتا في متراكبات النوفولاك (الجداول2- 6) أي أن كفاءة عملية التوهين تزيد (12.96%) في حالة المتراكبات الهجينة ذات (14%) من (HMTA) و(15.02%) في حالة المتراكبات الهجينة ذات نسبة (10%) من (HMTA) (الإشكال18 و19) عما هو عليه في حالة استخدام المتراكبات المدعمة بنوع واحد من الألياف.

5- الاستنتاجات:-

لقد أكدت هذه الدراسة بجلاء أن تدريع دقائق بيتا بمواد لدائنية سواء كانت مادة الايبوكسي أو النوفولاك يؤثر كثيراً على تقليص تراكيز هذه الملوثات الإشعاعية في بعض المواقع. ولقد لوحظ أن استخدام مادة الايبوكسي له تأثير ايجابي في جعل هذه الجسيمات المكبوحة فيها عديمة التأثير بعمق ولوج قليل وبالمقارنة بما يحدث لهذه الجسيمات في مادة النوفولاك... وعلى ذلك فلقد أوضح هذا البحث زيادة جزء الطاقة النسبي الذي يحذف من هذه الأشعة الجسيمية في كل سنتمر واحد من مسارها خلال المواد المحضرة عند تدعيمها بألياف الزجاج، ونظراً لخاصية متراكبات النوفولاك في قدرتها على مقاومة درجات الحرارة العالية التي تعتبر من أهم العوامل الواجب توفرها في تصنيع الدروع الوقائية فقد دعا ذلك إلى تفضيل هذه المتراكبات على متراكبات الايبوكسي في الدراسة الحالية في الوقت الذي تشير فيه – وفق المعلومات المتاحة من النتائج العلمية – بأن نسبة الاستفادة من متراكبات الايبوكسي في عملية التوهين تزيد على متراكبات النوفولاك ذات نسبة (10%) من (HMTA) بمقدار(8.7%) بينما تزيد على متراكبات النوفولاك ذات نسبة (14%) مـن (HMTA) بمقـدار (4.91 %).

ولقد أوضحت النتائج أيضا أن كفاءة التوهين تزداد في حالة تدعيم مادة النوفولاك بألياف الاسبست التي تتصف بالثبات الحراري (Thermal stability). ويضاف إلى ذلك أن كلا النوعين من ألياف الزجاج والاسبست يتضافران لتوحيد الخواص الفيزيائية وبصورة متوازنة في مادة النوفولاك مما يدل على التأثير الايجابي لعملية التهجين في عملية توهين دقائق بيتا.

كما أوضحت النتائج أن زيادة تركيز (HMTA) بنسبة تصل إلى (10%-14%) تؤدي إلى زيادة كثافة الترابط التشابكي وهذا يتسبب عنه انخفاض مدى دقائق بيتا في هذه المتراكبات بمعنى زيادة معاملات التوهين بنوعيها الخطية والكتلية.

هذا مع العلم بأن أبطأ دقائق بيتا في متراكبات النوفولاك يولد أشعة سينية وأن لهذه الأشعة أثار سلبية على المعدات المغلفة بهذه المتراكبات المنتقاة مما يعني ضرورة إحاطة هذه المعدات بطبقة خفيفة من الرصاص قبل تغليفها بالدروع الواقية لامتصاص هذه الأشعة. فكل هذا يجب حسابه عند اختيار أفضل الطرق للوقاية من الأشعة المؤينة الجسيمية كدقائق بيتا.

جدول (1) يستعرض تأثير التدريع بمواد متراكبة من مادة الايبوكسي على معامل الامتصاص الخطي لدقائق بيتا.

معامل الامتصاص الخطي (cm^{-1}).	EP.	EP.+G.F.
	0.106	0.1638

جدول (2) يستعرض تأثير التدريع بمواد متراكبة من مادة نوفولاك ذات نسبة (10% من HMTA) على معامل الامتصاص الخطي لدقائق بيتا.

معامل الامتصاص الخطي (cm^{-1}).	ratio HMTA=10%			
	NOV.	NOV.+ G.F.	NOV+ asb.F.	NOV+Hybrid
	0.0606	0.1262	0.1699	0.1343

جدول (3) يستعرض تأثير التدريع بمواد متراكبة من مادة نوفولاك ذات نسبة (14% من HMTA) على معامل الامتصاص الخطي لدقائق بيتا.

معامل الامتصاص الخطي (cm^{-1}).	ratio HMTA=14%			
	NOV.	NOV.+ G.F.	NOV+ asb.F.	NOV+Hybrid
	0.0768	0.1425	0.19417	0.1496

جدول (4) يستعرض تأثير التدريع بمواد متراكبة من مادة الايبوكسي على معامل الامتصاص الكتلي لدقائق بيتا.

معامل الامتصاص الخطي(cm^2/gm).	EP.	EP.+G.F.
	0.0905	0.1125

جدول (5) يستعرض تأثير التدريع بمواد متراكبة من مادة نوفولاك ذات نسبة (10% من HMTA) على معامل الامتصاص الكتلي لدقائق بيتا.

معامل الامتصاص الكتلي (cm^2/gm).	Ratio of HMTA=10%			
	NOV.	NOV.+ G.F.	NOV+ asb.F.	NOV+Hybrid
	0.0213	0.07025	0.10943	0.0798

جدول (6) يستعرض تأثير التدريع بمواد متراكبة من مادة نوفولاك ذات نسبة (14% من HMTA) على معامل الامتصاص الكتلي لدقائق بيتا.

معامل الامتصاص الكتلي (cm^2/gm).	Ratio of HMTA=14%			
	NOV.	NOV.+ G.F.	NOV+ asb.F.	NOV+Hybrid
	0.02698	0.0743	0.12506	0.08894

جدول (7) يستعرض مدى جسيمات بيتا في مواد متراكبة من مادة الايبوكسي .

R (mg/mm^2)	EP.	EP.+G.F.
	62.6591	49.155

جدول (8) يستعرض مدى جسيمات بيتا في مواد متراكبة من مادة النوفولاك ذات نسبة (10% من HMTA).

R (mg/mm^2)	Ratio of HMTA=10%			
	NOV.	NOV.+ G.F.	NOV+ asb.F.	NOV+Hybrid
	175.882	75.817	63.329	65.22

جدول (9) يستعرض مدى جسيمات بيتا في مواد متراكبة من مادة النوفولاك ذات نسبة (14% من HMTA).

R (mg/mm^2)	Ratio of HMTA=14%			
	NOV.	NOV.+ G.F.	NOV+ asb.F.	NOV+Hybrid
	171.192	70.295	58.718	63.149

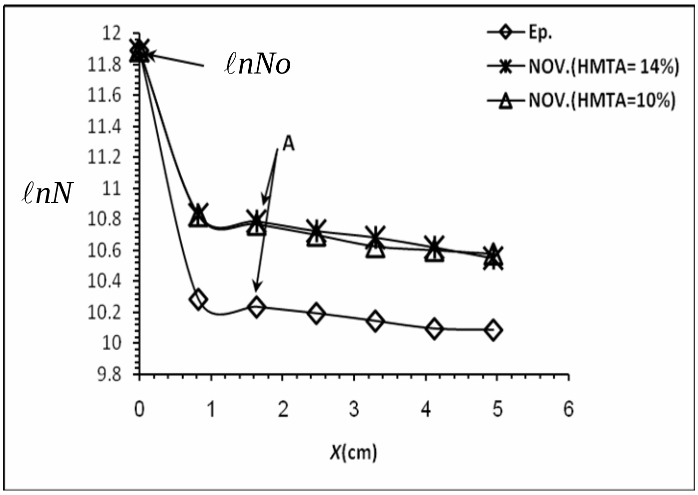

شكل (4) يوضح العلاقة بين (ℓnN) وسمك نماذج ذو طبيعة بوليمرية مختلفة.

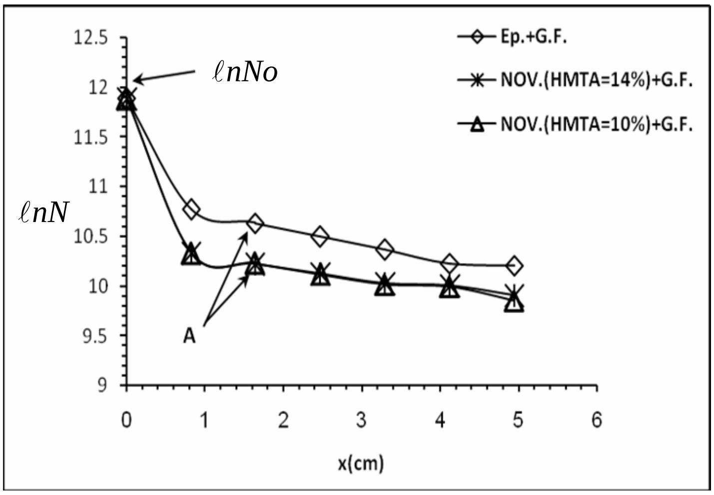

شكل (5) يوضح العلاقة بين (ℓnN) وسمك متراكبات ذات أساس بوليمري مختلف.

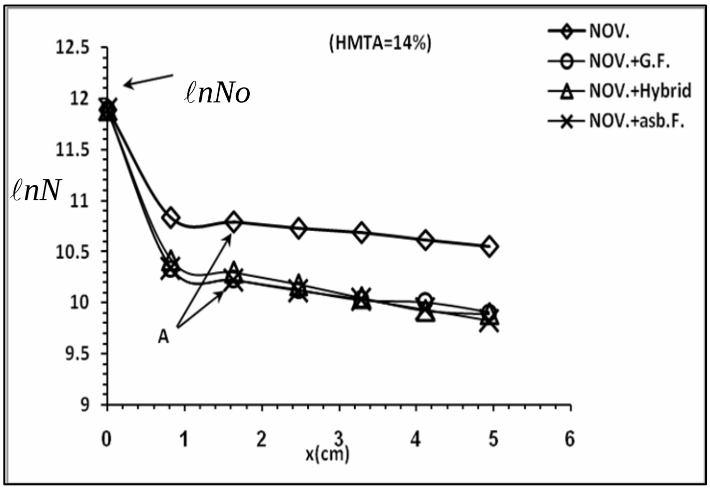

شكل (6) يوضح العلاقة بين (ℓnN) وسمك متراكبات النوفولاك ذات نسبة (14%) وزناً من (HMTA).

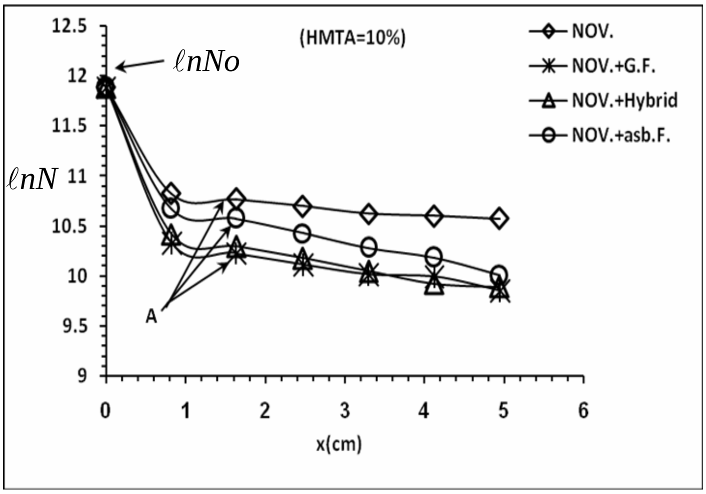

شكل (7) يوضح العلاقة بين (ℓnN) وسمك متراكبات النوفولاك ذات نسبة (10%) وزناً من (HMTA).

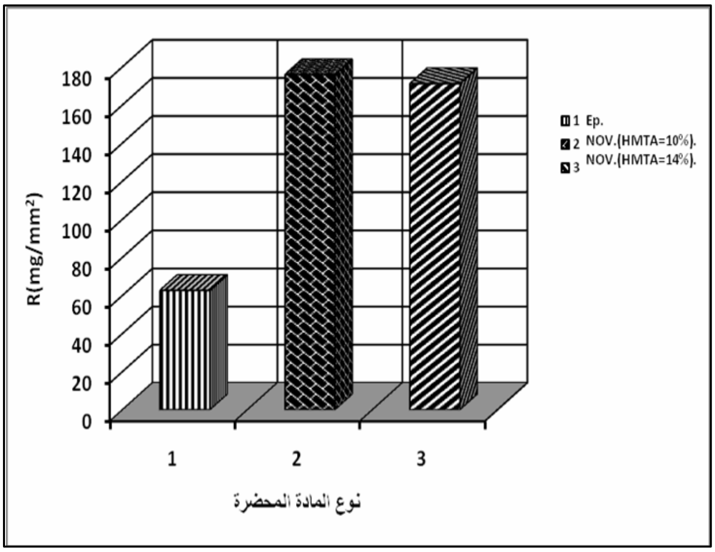

شكل (8) يوضح العلاقة بين مدى جسيمات بيتا ونوع الراتنج الماص لها.

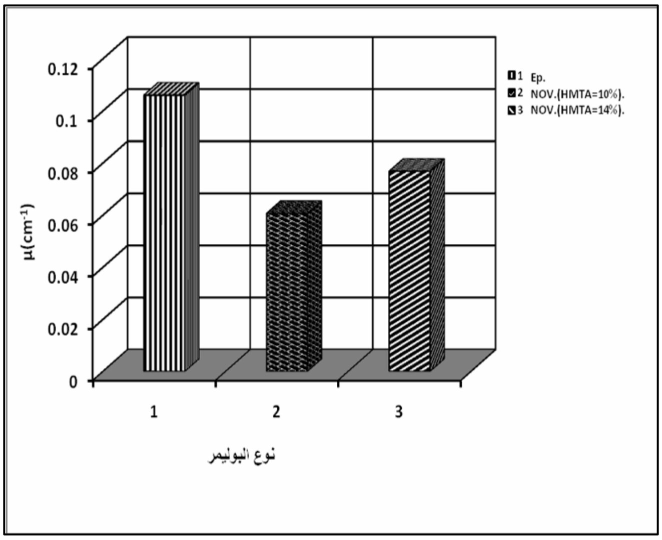

شكل (9) يوضح تأثير نوع الراتنج على جزء الطاقة النسبي الذي يحذف من الأشعة الجسيمة في كل سنتمتر واحد من مسارها.

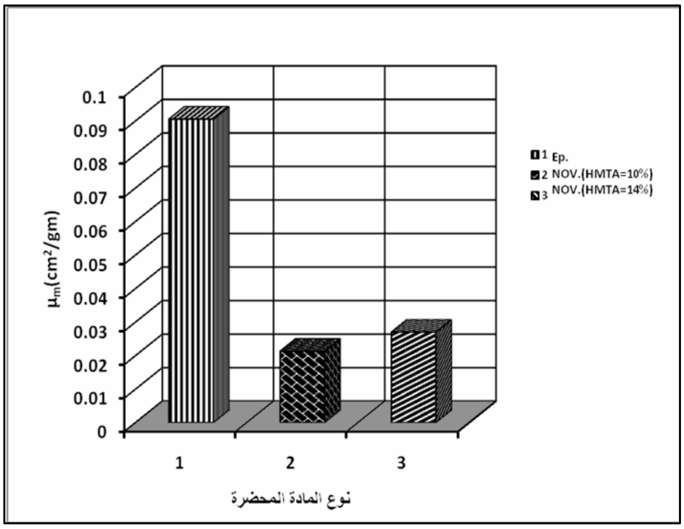

شكل (10) يوضح تأثير نوع الراتنج على معامل امتصاصها الكتلي لأشعة بيتا.

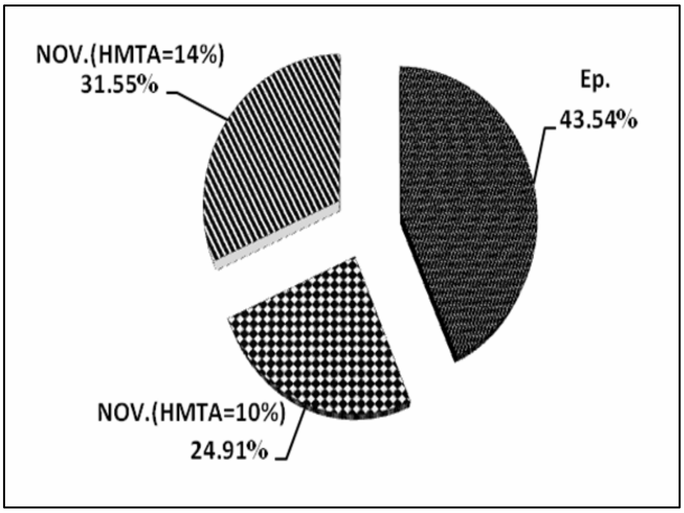

شكل (11) يوضح تأثير أنواع المواد البوليمرية المستعملة في تدريع جسيمات بيتا ونسبة الاستفادة منها في عملية التوهين.

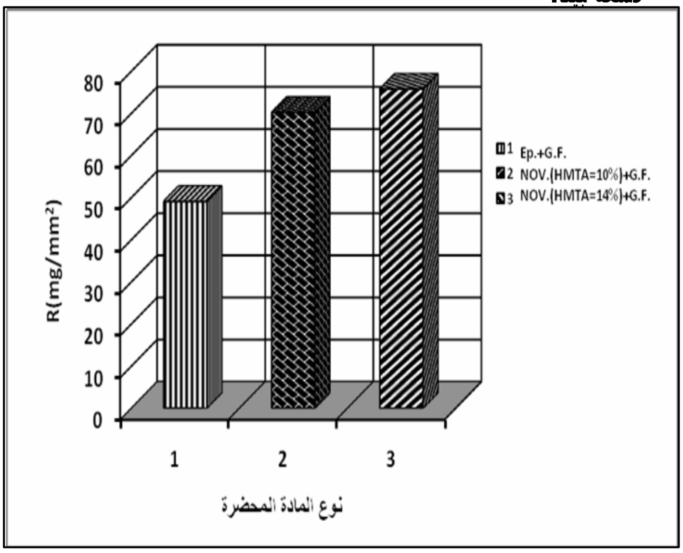

شكل (12) يوضح أثار تدعيم مادة نوفولاك وكذا مادة الايبوكسي بألياف الزجاج القصيرة على مدى جسيمات بيتا فيها.

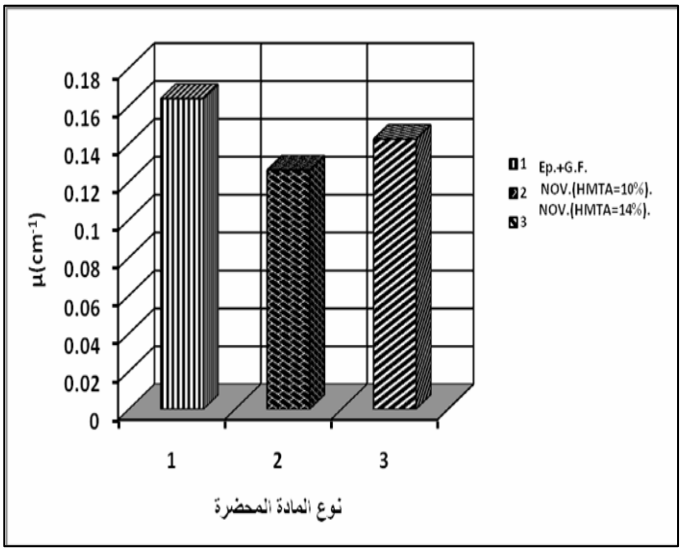

شكل (13) يوضح أثار تدعيم مادة نوفولاك وكذا مادة الايبوكسي بألياف الزجاج القصيرة على معامل امتصاصها الخطي لأشعة بيتا.

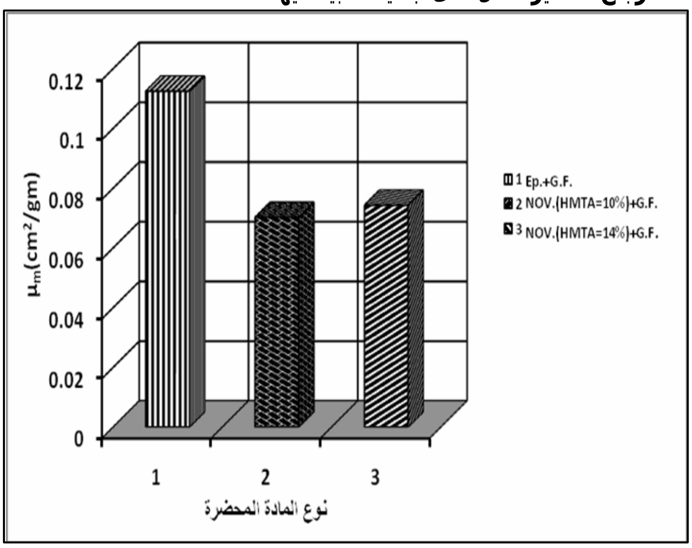

شكل (14) يوضح أثار تدعيم مادة نوفولاك وكذا مادة الايبوكسي بألياف الزجاج القصيرة على معامل امتصاصها الكتلي لأشعة بيتا.

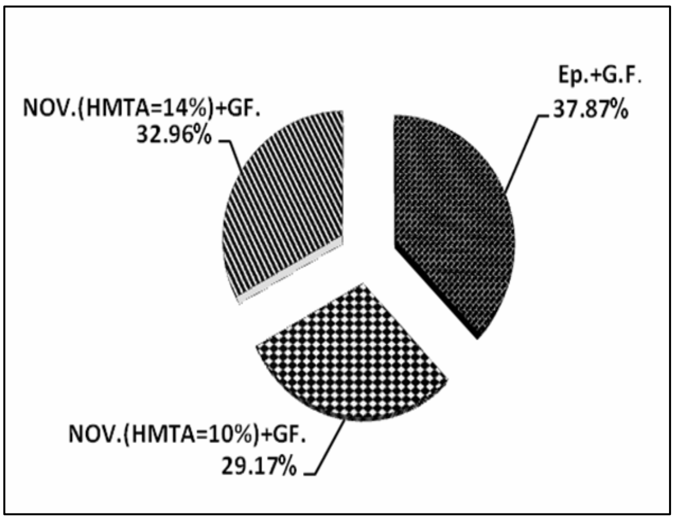

شكل (15) يوضح أنواع المواد المتراكبة المدعمة بألياف الزجاج المستعملة في تدريع جسيمات بيتا ونسبة الاستفادة منها في عملية التوهين.

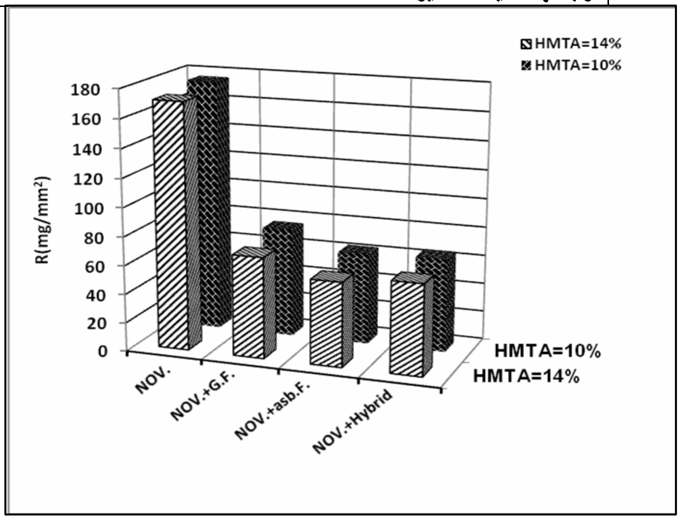

شكل (16) يوضح تأثير نسبة (HMTA) على مدى دقائق بيتا في متراكبات النوفولاك.

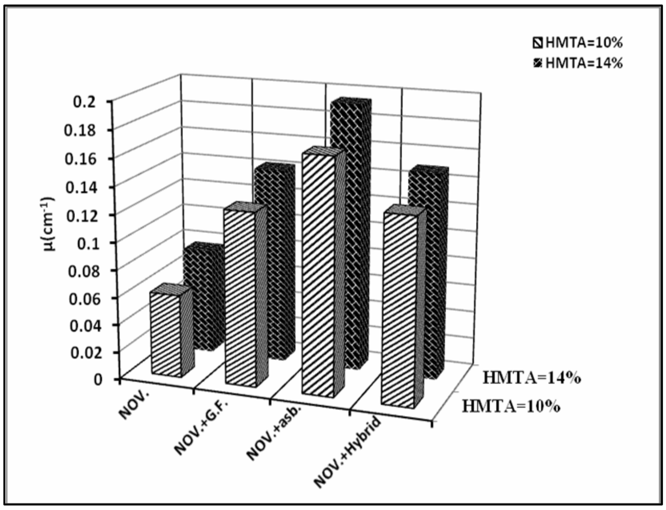

شكل (17) يوضح تأثير نسبة (HMTA) على معامل الامتصاص الخطي لمتراكبات النوفولاك لدقائق بيتا.

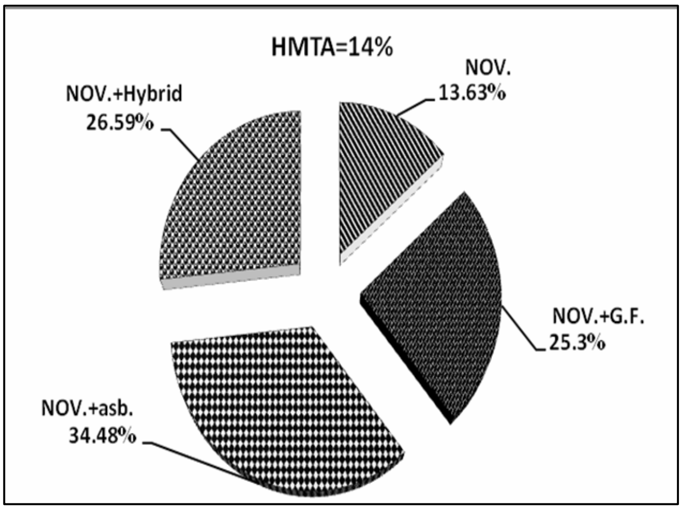

شكل (18) يوضح أنواع متراكبات النوفولاك ذات نسبة (14%) من (HMTA) المستعملة في تدريع دقائق بيتا ونسبة الاستفادة منها في عملية التوهين.

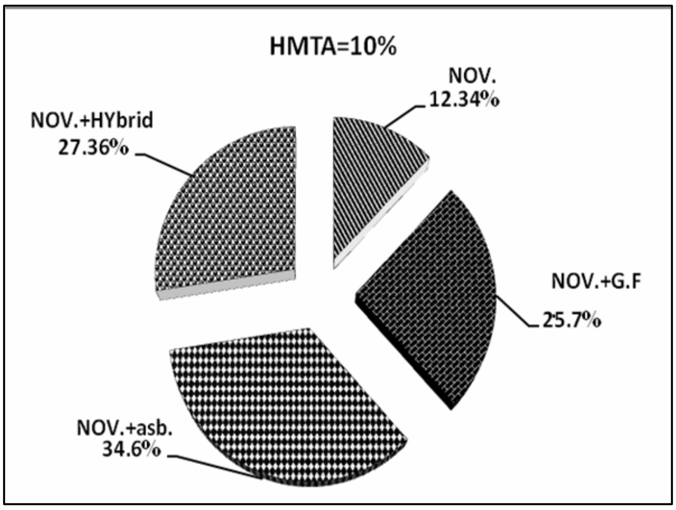

شكل (19) يوضح أنواع متراكبات النوفولاك ذات نسبة (10%) من (HMTA) المستعملة في تدريع دقائق بيتا ونسبة الاستفادة منها في عملية التوهين.

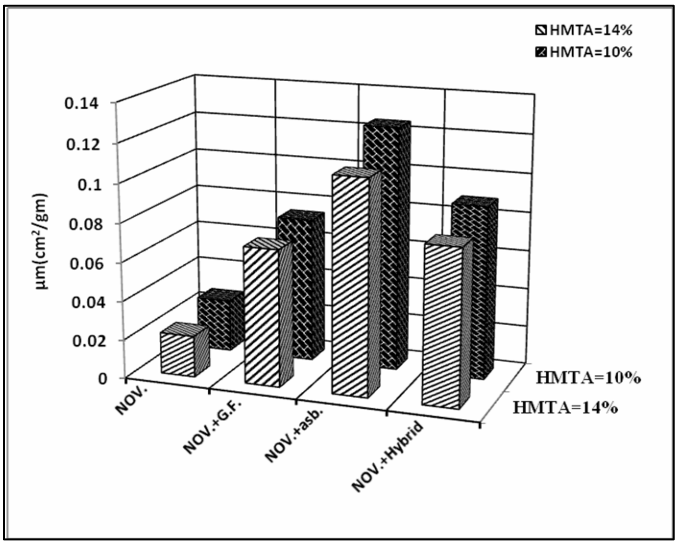

شكل (20) يوضح تأثير نسبة (HMTA) على معامل الامتصاص الكتلي لمتراكبات النوفولاك لدقائق بيتا.

5-المصادر:

1- A. Knop and L.Pilato, "Phenolic Resins Chemistry", Springer verlag, Berlin Meidelbery New York, (1985).

2- A.Knop and W.Scheib , "Chemistry and Application of Phenolic Resin", Springer – verlag, Berlin Heidelberg, New York, (1979)

3- D.Hull, "An Introduction to composite Material", Cambridge University Press, First Published in (1981).

4- G.A. Adams and W.S Hanoush, "Synthesis of some sequential IPN'S of Novolak – epoxy Resins", Iraqi J. Palymer, Vol.3, No.1 (1999), PP.(67-72).

5- L. Kacir and M. Narkis, "Composite", Vol. 10, No.1, Jan. (1979), PP. (31-36).

6- M.O.W.R. Charson,"Polymer Engineering Composites", Applied Science Pub. LTD, London (1977).

7- N.J.Bahnam, "Study Gamma Ray Build up Factor for Black Carbon Graphite ", M. SC. Thesis, Technology University,(2006).

8- R.H.bdullah and L. R. Abdul Rahman, "Zanco Journal of pure and applied science Salahddin - University - Hawler", Vol.21, No.4, (2009), PP.(73-91).

9- .Y. Chiang and S.Y. Yang, "Journal of Applied Polymer Science", Vol.37 (1989), PP. (499-512).

10- Y. Anie, "Composity Material Hantbook ", McGraw- Hill book company, (1980).

11- د. عذاب طاهر الكناني، "التكنولوجيا النووية في صناعة النفط والغاز"، دار للنشر والتوزيع، مصر، (2009).

12- اريج رياض سعيد، "دراسة الخصائص الميكانيكية لمتراكبات بوليمرية مدعمة بمواد طبيعية"، رسالة ماجستير، العلوم التطبيقية، الجامعة التكنولوجية، (2009).

13- د. مثنى عبد الرزاق العمر، "التلوث البيئي" دار وائل للنشر عمان- الاردن، الطبعة الأولى، (2000).

14- د. مطاوع الإسهاب،"الإشعاع النووي والوقاية من الإشعاع والتلوث"، المركز العربي للتعريب والترجمة والتأليف والنشر، دمشق،(1991).

15- د. موسى الجنابي، ود. سعد حمادي القريشي، ود. رياض شريف كامل، " مبادئ العلوم النووية"، دار الشؤون الثقافية العامة ((أفاق عربية)) ، الطبعة الأولى، العراق (1990).

16- رولا عبد الخضر عباس ونبيل فواز، "دراسة معامل الامتصاص الخطي والكتلي لأشعة كاما لمواد متراكبة مدعمة بألياف الزجاج والاسبست"، مجلة علوم المستنصرية، العدد 4، المجلد 18 الصفحة (86-102)، (2007).

17- رولا عبد الخضر عباس، "دراسة الخصائص الحرارية والميكانيكية لمادة النوفولاك ومتراكباتها"، رسالة ماجستير، العلوم التطبيقية، الجامعة التكنولوجية، (2001).

18- عالية أحمد كاظم ،"دراسة عامل التراكم لأشعة الكبح في مواد تدريع مختلفة"، رسالة ماجستير، كلية العلوم- جامعة بغداد، (1978).

19- عباس جاسم حمادي، هرمز موشي يوحنا، طالب هادي قدوري تويج وضياء عبد علي تويج، "تجارب في الفيزياء المتقدمة (النووية- الذرية- الصلبة)"، جامعة بغداد – كلية التربية، (1978).

20- عبد الكريم عبد الله، " قياس وحساب معامل التوهين الخطي والكتلي لأشعة كاما لبعض المواد العازلة (الخشب، واللكنين والسيليلوز"، رسالة ماجستير، كلية العلوم/ الجامعة المستنصرية، (2003).

21- محمد إسماعيل عمر، "تكنولوجيا تصنيع البلاستيك "، دار الكتب العالمية للنشر والتوزيع، القاهرة، (1998).

22- محمد إسماعيل عمر، "تكنولوجيا تصنيع البلاستيك المسلح"، دار الكتب العالمية للنشر والتوزيع، القاهرة، (2001).

23- هدى خالد حميد المجمعي، "دراسة تأثر أشعة كاما في بعض الخواص الميكانيكية لمتراكب الايبوكسي"، رسالة ماجستير، كلية العلوم، جامعة بغداد،(1997).

اختيار مواقع لإنشاء سدود صغيرة في منخفض الكعرة باستخدام تقنيات التحسس النائي والتحليل المكاني

Expert: Dr. Hussain Z. Ali
Ministry of Science and Technology
Dalal J. Ali
M.Sc. in Survey Engineering

الخلاصـة

استخلاص المعالم من السطوح الطبوغرافية هي إنشاء صورة نقطية تمثل ارتفاعات سطح الأرض بالاعتماد على نموذج الارتفاع الرقمي الذي يعتبر الأساس الذي يعتمد عليه تحليل السطوح الطبوغرافية . إن نماذج الارتفاعات الرقمية تستنبط بشكل رئيسي بتطبيق النماذج المجسمة (زوج من الصور) المتوفرة من المسح التصويري وبيانات التحسس النائي أو من الخرائط الطبوغرافية وهنا تم استخدام نموذج ارتفاع رقمي مستخلص من الخرائط الطبوغرافية ، واشتقاق عدد من الخصائص الهامة من نموذج الارتفاع الرقمي مثل الانحدار والتوجيه وظلال الأرض باستخدام برنامج ArcGIS إصدار 9.3 ، والتي تعتبر مدخلات لاستخلاص الخصائص الهيدرولوجية مثل تحديد اتجاه سريان المياه فوق سطح الأرض بعدها تم حساب تراكم السريان و إنتاج خارطة Stream order لتحديد الوديان الموجودة في المنطقة وإنتاج خارطة Basin لتحديد حوض التغذية وبالاعتماد على هذه الطبقات يتم اختيار مواقع للسدود باستخدام برنامج ArcGIS إصدار 9.3 وامتداده Arc Hydro.

الكلمات الرئيسية: نموذج ارتفاع رقمي، حوض التغذية، الانحدار.

ABSTRACT:

Feature extraction from the surface topography is the creation of a bitmap representing the earth's surface elevations based on Digital Elevation Model, which is the base of the analyzing of topographical surfaces. The digital elevation models are mainly derived by stereo pair images (a pair of images) available from the Photogrammetry data and remote sensing, or from topographical maps, and we use a digital elevation model derived from topographical maps, and we derived a number of important properties from digital elevations model such as gradient direction and the Earth's shadow using a ArcGIS ver. 9.3 , which represent the input data to extract the hydrological characteristics such as determining the flow direction , also calculating the flow accumulation , producing the output map Stream to determine the valleys in the region and the production of Basin map to determine the basin of nutrition , the locations of the small dams can be selected using Arc GIS ver. 9.3 and its extension Arc Hydro.

المقدمة

تشكل السدود إحدى التقانات القديمة نسبيا والتي تستخدم أيضا في حصاد مياه الأمطار الناتجة عن مياه السيول التي تجري في الأودية خلال فصل الأمطار ويعرف السد بأنه إنشاء هندسي يقام فوق واد أو منخفض بهدف حجز المياه وان الهدف الرئيسي من السدود هو الحفاظ على المياه من اجل الاستعمال القريب أو البعيد بمعنى الحفاظ عليه من اجل المستقبل [1] , [5].

منطقة الدراسة

تم اختيار منخفض الكعرة كموقع للدراسة ، كما موضح في الشكل (1) ، ويقع المنخفض إلى الشرق من منطقة الحماد تحتوي على سهل واسع يرتفع قليلا باتجاه الغرب وتقطعها شبكة كثيفة من الوديان باتجاه الشرق والشمال الشرقي والتي تكون عبارة عن وديان عميقة وواسعة [7]. وإداريا يقع المنخفض ضمن الحدود التابعة لقضاء الرطبة ضمن محافظة الانبار في غرب العراق ، وتقع منطقة الدراسة بنظام الإحداثيات الفلكي على دائرة العرض (33.25 – 33.45) شمالا وخط الطول (40.00 – 40.50) شرقا . ويمتد منخفض الكعرة باتجاه من الشرق إلى الغرب بمساحة قدرها (2100) كم^2 وبأبعاد تتراوح بين (30×70) كم تقريبا أما الوديان المحيطة به فتشمل أودية الملصي ، النجيلي ، الاغري ، العوجة ، دويخلة ، العجرميات ، ام طيارة ، الرغيلة وام ادية [3].

مشكلة البحث

تتلخص مشكلة البحث بقلة السدود المقامة في منطقة الدراسة وبالتالي هدر كميات كبيرة من المياه [2] ، [4]. إن مشاريع الري والبزل في محافظة الانبار والتي تقع على نهر الفرات وجداوله تعاني من مشكلة قلة المياه نتيجة المخطط التركي السوري في استثمار مياه النهر عن طريق إقامة مشاريع أروائية ضمن أراضيها وبالتالي يؤدي إلى قلة الخزين المائي والذي يؤثر سلبا على جميع النواحي (الزراعية ، الاروائية ، ....الخ) مثل سد أتاتورك على نهر الفرات ، وسد قره قايا على الفرات أيضا ، وبالتالي فان إقامة السدود في هذه المنطقة يساعد في حل هذه المشكلة .

هدف الدراسة

تهدف الدراسة إلى تحقيق ما يلي :

1. إنتاج نموذج ارتفاع رقمي DEM لمنطقة الدراسة باستخدام خارطة طبوغرافية مقروءة ضوئيا بمقياس (25000:1) .
2. دراسة طبوغرافية المنطقة واستخلاص خارطة الانحدار وظلال الأرض والتوجيه باستخدام برنامج ArcGIS والاستفادة من هذه الطبقات في استخلاص المعالم الهيدرولوجية ، بالإضافة إلى دراسة هيدرولوجية المنطقة واستخلاص طبقة الوديان وحوض التغذية بالاعتماد على الامتداد Arc Hydro وذلك لاقتراح مواقع للسدود على الوديان الموجودة في منطقة الدراسة لحجز المياه بدلا من فقدانها بالاعتماد على تقنية حصاد المياه .

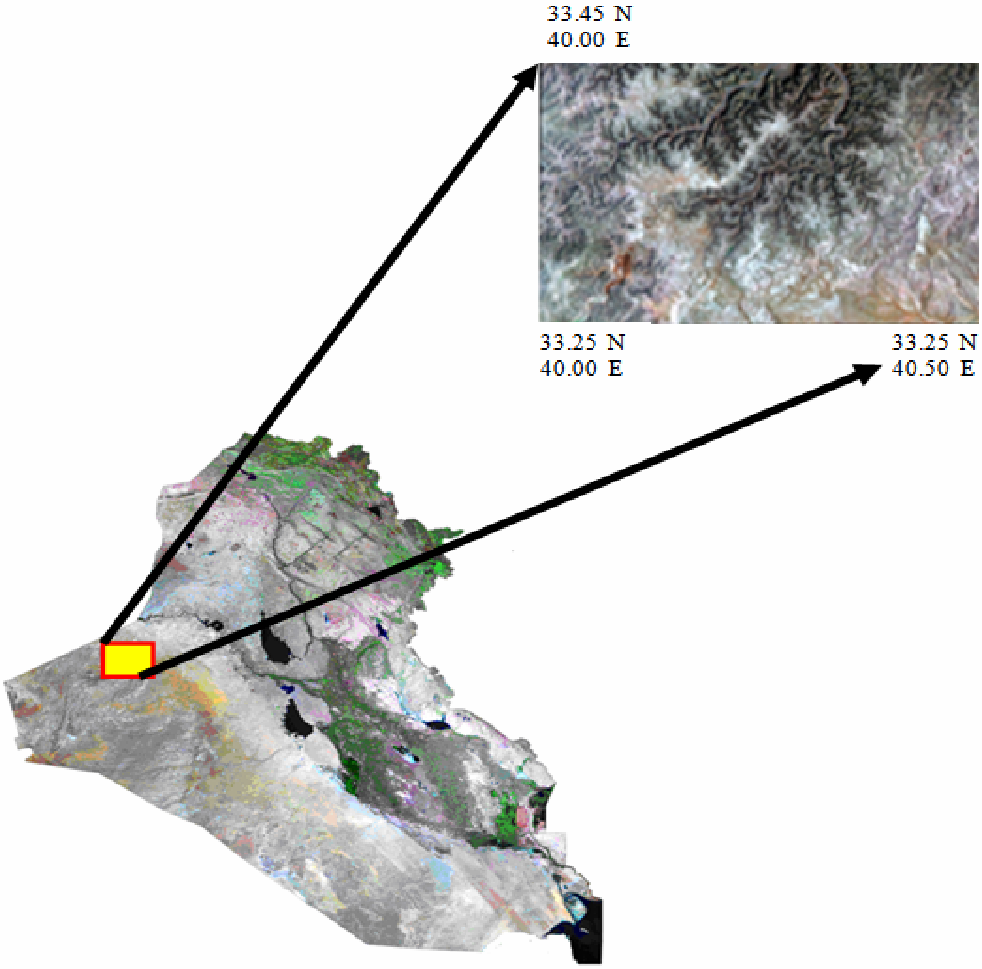

شكل (1) صورة فضائية موزائيك للعراق وموقع منطقة الدراسة.

<u>طريقة العمل</u>

العمل التطبيقي يتكون من عدة مراحل يمكن أن تلخص كالأتي:

1. إنتاج نموذج الارتفاع الرقمي (DEM) من خارطة طبوغرافية مقروءة ضوئيا (بمقياس 1:25000) .
2. تحليل الخصائص الطبوغرافية للمنطقة واستخلاص طبقة الوديان في منطقة الدراسة .
3. تحليل الخصائص الهيدرولوجية للمنطقة واقتراح مواقع للسدود في منطقة الدراسة .

مراحل إنتاج نموذج الارتفاع الرقمي من الخارطة الطبوغرافية

المراحل التالية تشترك في إنتاج نموذج الارتفاع الرقمي (DEM) :-

- **المرحلة الأولى : عملية مسح الخارطة الطبوغرافية وقراءتها ضوئيا .**
- **المرحلة الثانية : إجراء عملية Georeferencing للخارطة المقروءة ضوئيا.** هي عملية إيجاد الإحداثيات الحقيقية لكل النقاط الموجودة على المخططات الورقة . وبذلك بتحويل نظام إحداثيات الخارطة المدخلة من

إحداثيات صورية (سطر ،عمود) إلى إحداثيات نظام (UTM) بصيغة (X , Y) .

ويتم تصحيح الخارطة المدخلة إلى البرنامج بإدخال الإحداثيات الحقيقية للأركان الأربعة للخارطة لكي تربط بنظام أل UTM ، وكالاتي -:

- الخارطة الأولى -:

الخارطة المدخلة الأولى ذات مقياس (25000:1) وبفترة كنتورية مقدارها (5) متر ، جدول (1) وشكل (2) يوضح إحداثيات الأركان لمنطقة الدراسة.

جدول(1) إحداثيات أركان منطقة الدراسة.

Points	Easting(m)	Northing(m)
1	627725	3707700
2	627725	3721150
3	639200	3721150
4	639200	3707700

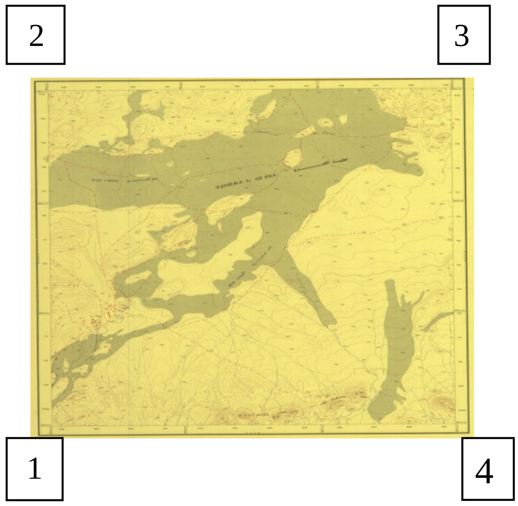

شكل (2) إحداثيات الأركان للخارطة الأولى.

- الخارطة الثانية -:

الخارطة المدخلة الثانية ذات مقياس (25000:1) وبفترة كنتورية مقدارها (5) متر ، جدول (2) وشكل (3) أدناه يوضح إحداثيات الأركان بنظام UT

M للخارطة المدخلة .

جدول (2) إحداثيات الأركان لمنطقة الدراسة.

Points	Easting(m)	Northing(m)
1	616125	3707125
2	616125	3721000
3	627725	3721000
4	627725	3707125

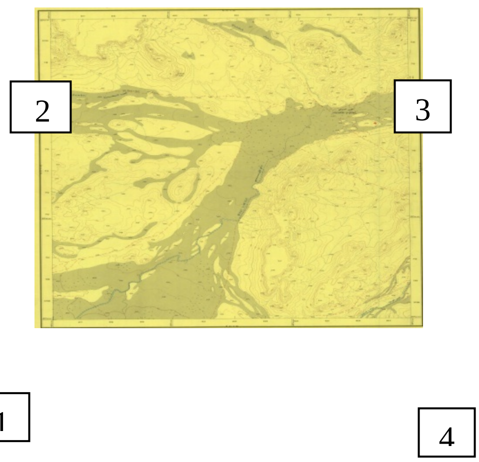

شكل (3):إحداثيات الأركان للخارطة الثانية.

- المرحلة الثالثة: الترقيم على الشاشة – On Screen Digitizing

يتم استدعاء الخرائط المصححة إلى برنامج أل Arc GIS لنقوم برسم أو ترقيم الظواهر المبينة على الصورة أو الخارطة ؛ حيث قمنا بوضع الطبقات التالية :

- الخطوط الكنتورية – خطية .
- نقاط معلومة الارتفاع – نقطية .
- نقاط معلومة الإحداثيات (B.M) – نقطية.

بعدها تم وضع جداول سمات الطبقات المختلفة .

تعتبر هذه الخطوة من أهم خطوات الدراسة التي سيترتب عن مقدار دقتها صحة نتائج الدراسة التي ستبنى عليها التطبيقات الهندسية الأخرى.

- المرحلة الرابعة: إنتاج نموذج ارتفاع رقمي DEM

يتم إنتاج نموذج الارتفاع الرقمي باستخدام طرق الاستكمال وهي خوارزميات رياضية تتطلب عينة من النقاط معلومة الارتفاع في منطقة ما ، ولذلك تم استخدام هذه الطريقة وذلك لتوفر الطبقات المذكورة أعلاه حيث تقوم بإجراء عملية تنبوء حسابي لجميع ارتفاعات المنطقة وتختزن الناتج في صورة نقطية [6]. تفيد نماذج الارتفاع الرقمية في استخلاص العديد من المعلومات المهمة بشكل ألي سواء المعلومات الطبوغرافية مثل حدود الحوض المائي ، شبكة مجاري الأودية ، الخصائص المورفومترية للحوض المائي أو المعلومات الهيدرولوجية التي تعتمد على الخصائص المورفومترية للحوض المائي.

والشكل (4) يوضح نموذج الارتفاع الرقمي مجسم ثلاثي الأبعاد لمنطقة الدراسة.

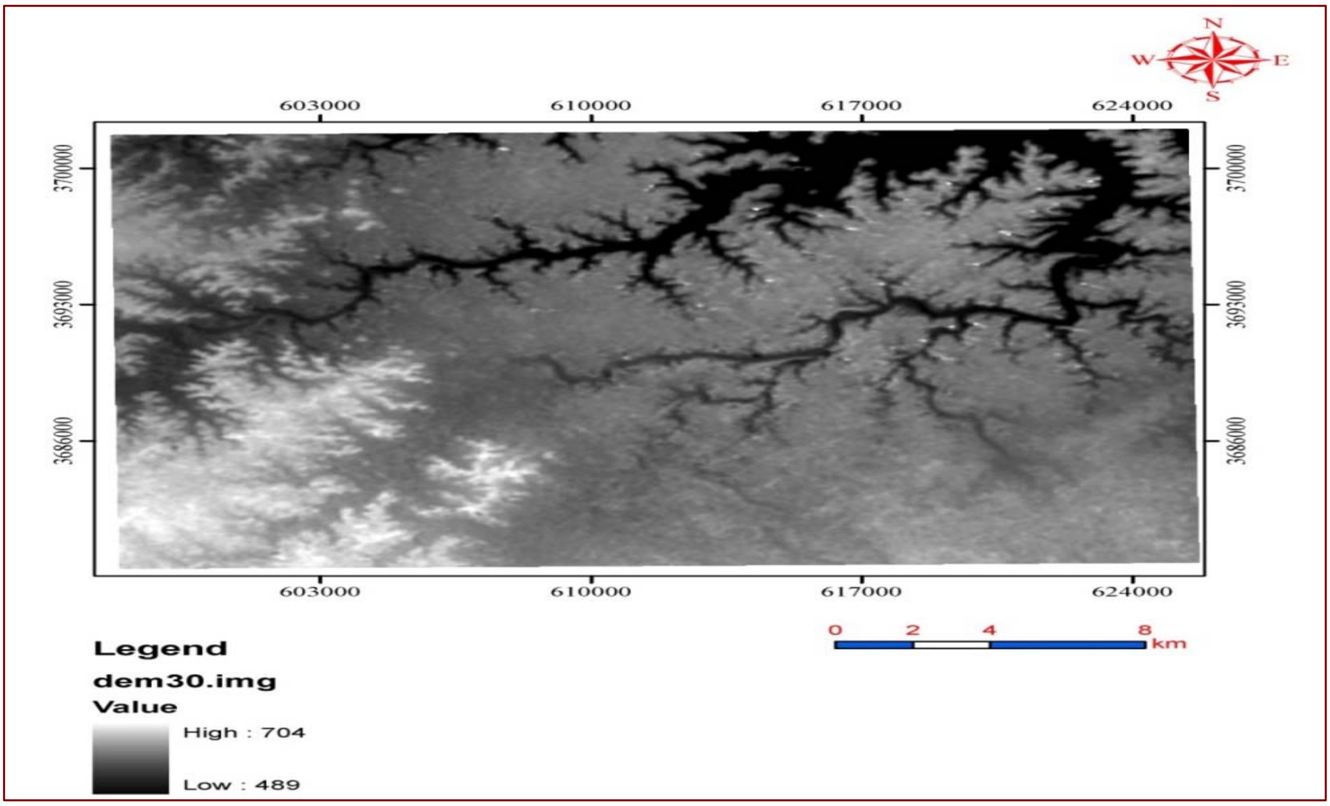

المنتج والشكل (5) يوضح نموذج ارتفاع رقمي

شكل (4) نموذج الارتفاع الرقمي المنتج وبدقة 30متر.

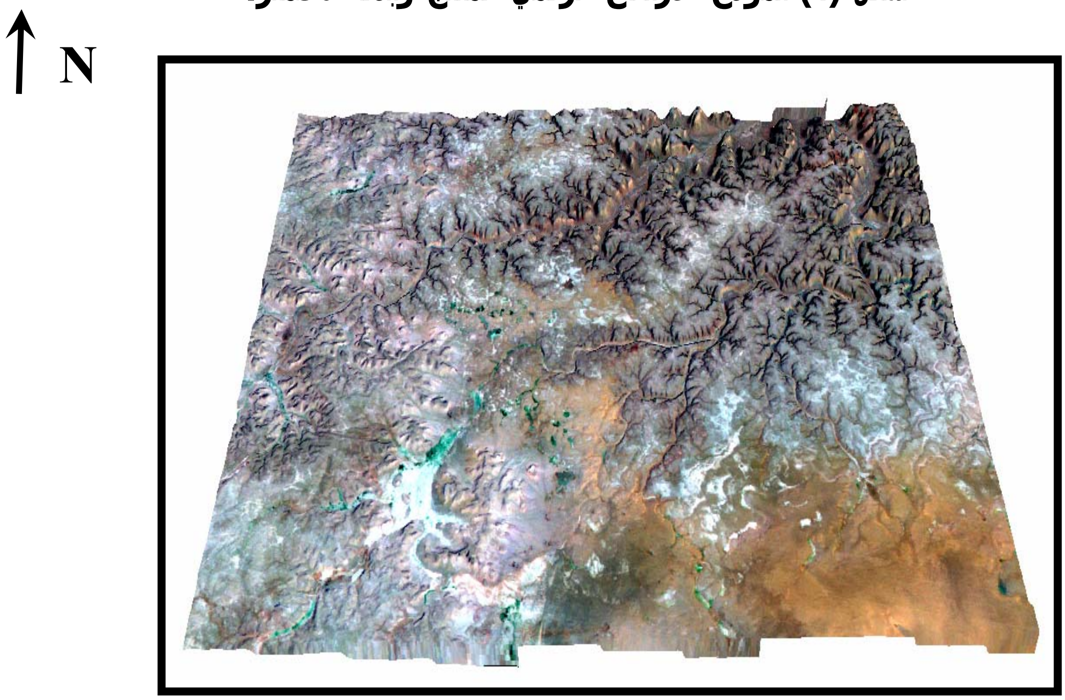

شكل (5) نموذج ارتفاع رقمي مجسم ثلاثي الأبعاد لمنطقة الدراسة.

<u>**الخصائص الطبوغرافية**</u>

إن الدراسة الحالية تأخذ الاتجاه التطبيقي للتقنيات الحديثة ، المتمثل في استخدام نظم المعلومات الجغرافية ، لبناء قاعدة معلومات مكانية ، يمكن من خلالها القيام بعملية التحليل واشتقاق لمختلف الظواهر الطبوغرافية على سطح الأرض ، التي كثيرا ما يحتاج لمعرفتها في الدراسات الجيمورفولوجية والمورفومترية من نموذج الارتفاع الرقمي ، هذه الخصائص هي :

- الانحدار Slope.
- التوجيه Aspect.
- ظلال الأرض Hill Shades.

الانحدار Slope

يقصد بانحدار الأرض ميل الأرض على خط الأفق . ولحساب الانحدار من نموذج الارتفاع الرقمي تقوم الخوارزمية المسؤولة عن حساب الانحدار بقسمة الفارق في الارتفاع بين كل عنصر صورة وما يجاورها على طول الخط الواصل بين مركز عنصر الصورة. والشكل (6) يوضح خارطة الانحدار بالاعتماد على نموذج الارتفاع المنتج . يفيد الانحدار عند تصميم الترع والقنوات وعند اختيار الأماكن المناسبة للتوسع العمراني كما يلعب دورا هاما في تعريف واستخلاص الظواهر الجيومورفولوجية من نماذج الارتفاع الرقمي .

التوجيه Aspect

عندما تكون الأرض منحدرة (غير مسطحة) فإنها تواجه ناحية من الجهات الجغرافية (شمال ، شمال شرق،.... الخ)، المربع الذي يختزن في عناصر ألصورة قيم تمثل الزاوية الذي يواجهها هذا العنصر في نموذج الارتفاع الرقمي مقدرة على المقياس الستيني هي مربع التوجيه. وفي هذا المربع تتراوح قيم العناصر الرقمية بين 0–360 للإشارة إلى الاتجاه الذي تواجهه الأرض، بينما تستخدم القيمة -1 للإشارة إلى

الأرض المسطحة .والشكل (7) يوضح خارطة التوجيه .

Hill Shades ظلال الأرض

ظلال الأرض تمثل الإضاءة الافتراضية لسطح الأرض نتيجة وجود الشمس على ارتفاع 45 وزاوية سمت 315 وتتراوح قيمته من (0 – 255)، الصفر لا تواجه نور الشمس بينما 255تواجه نور الشمس مباشرة.وتمنح ظلال الأرض للبيانات مظهر ثلاثي الأبعاد.وتم إنتاج خارطة ظلال الأرض بالاعتماد على نموذج الارتفاع الرقمي المنتج كما موضح في الشكل (8) .

تحليل بعض الخصائص الهيدرولوجية للمنطقة

تحليل الخصائص الهيدرولوجية لسطح الأرض هو احد أهم تطبيقات تحليل السطوح الأرضية .

الخصائص الهيدرولوجية لسطح الأرض يعنى بها مجموعة الخصائص التي تتحكم في حركة المطر الساقط أو المياه السطحية على الأرض وتجميعه في أحواض تسمى أحواض الصرف والمسيلات المائية .والشكل (9) يوضح خارطة توزيع الوديان في منطقة الدراسة مضاف إليها أحواض التغذية .

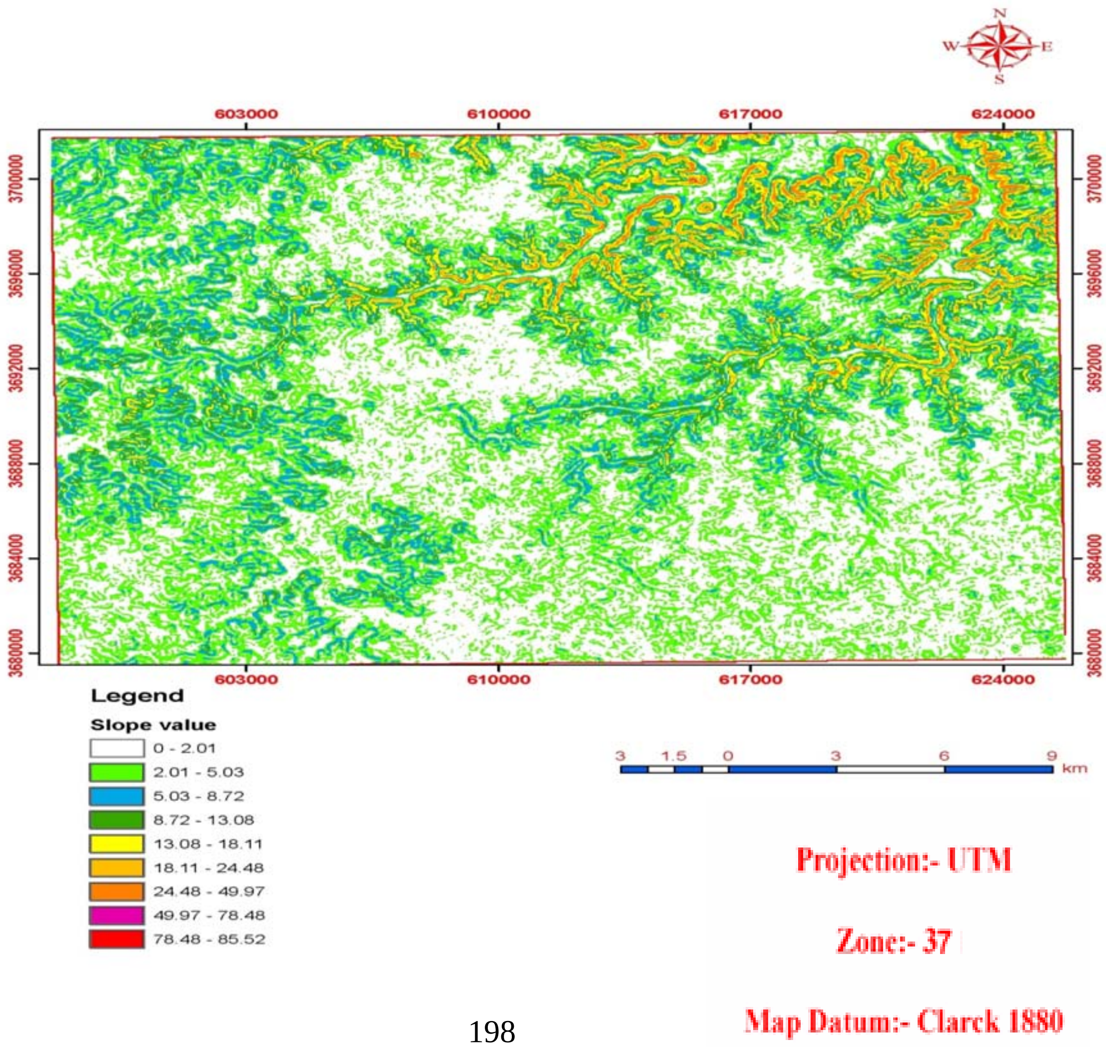

شكل (6): خارطة الانحدار.

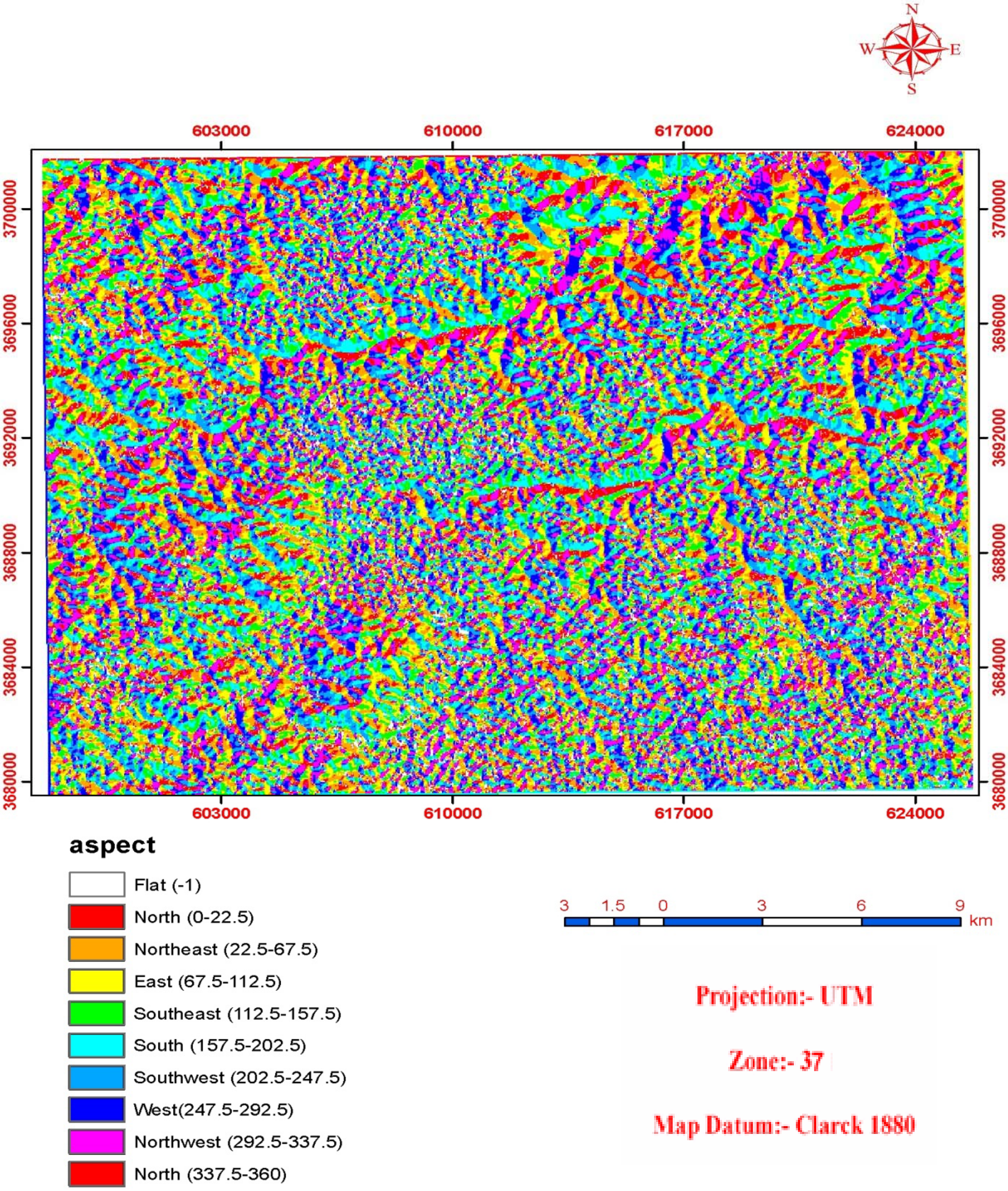

شكل (7): خارطة التوجيه.

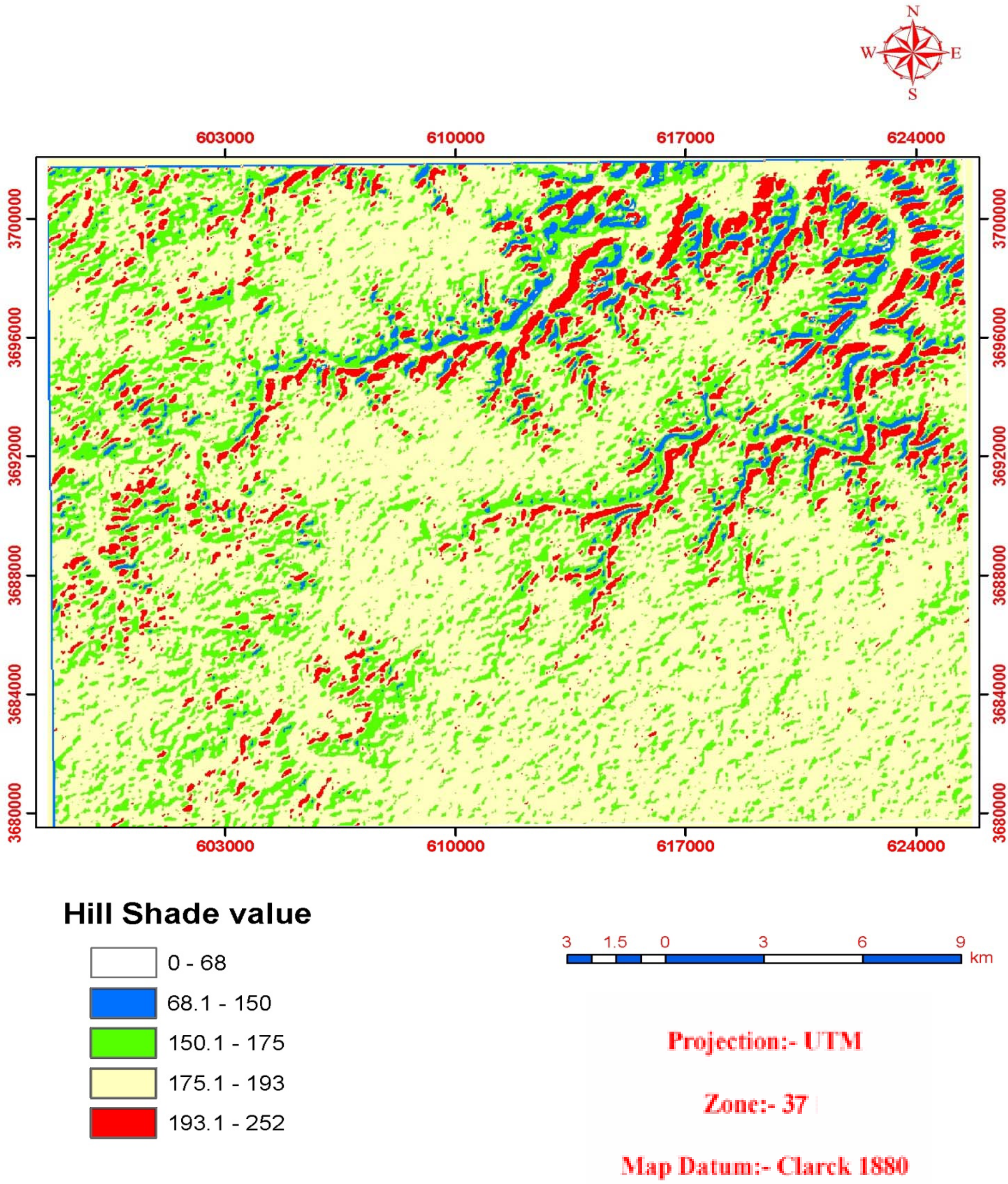

شكل (8): خارطة ظلال الأرض.

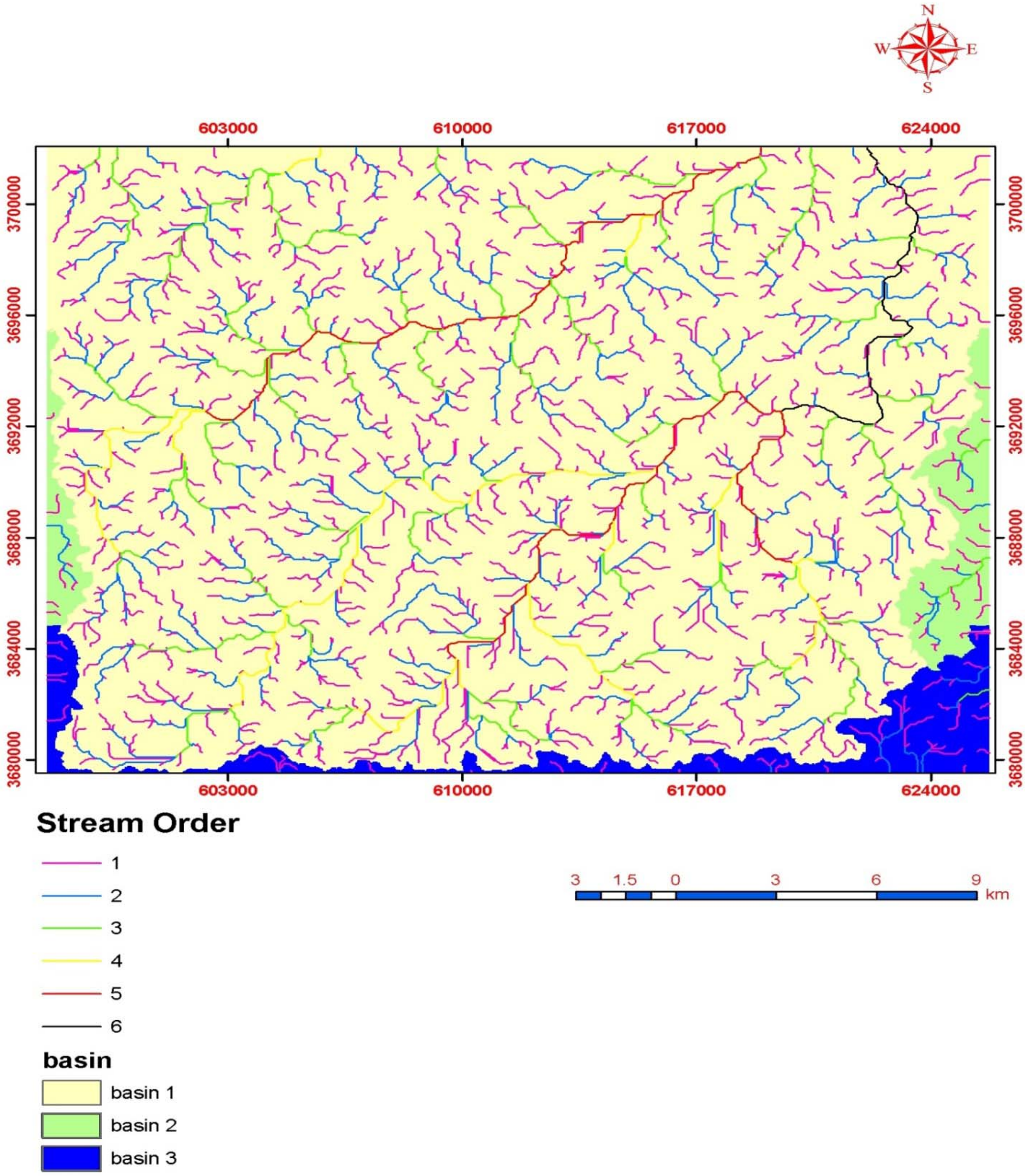

شكل (9): طبقتي توزيع الوديان وأحواض التغذية في منطقة الدراسة.

منهجية تحليل الخصائص الهيدرولوجية :

العنصر الأساسي في تحليل الخصائص الهيدرولوجية هو استخدام نماذج الارتفاعات الرقمية لاستخلاص خصائص السطح الهيدرولوجية .وهو ما يتم عبر سلسلة من الإجراءات التي تنتهي كل منها بإنتاج خريطة تبين احد الخصائص موضوع الدراسة ، وذلك باستخدام الامتداد Arc Hydro.

بداية يتم التعرف على اتجاهات جريان المياه فوق سطح الأرض Flow Direction ويتم ذلك عن طريق استخدام تمثيل رقمي للاتجاهات وهو ما يبينه الشكل (10).

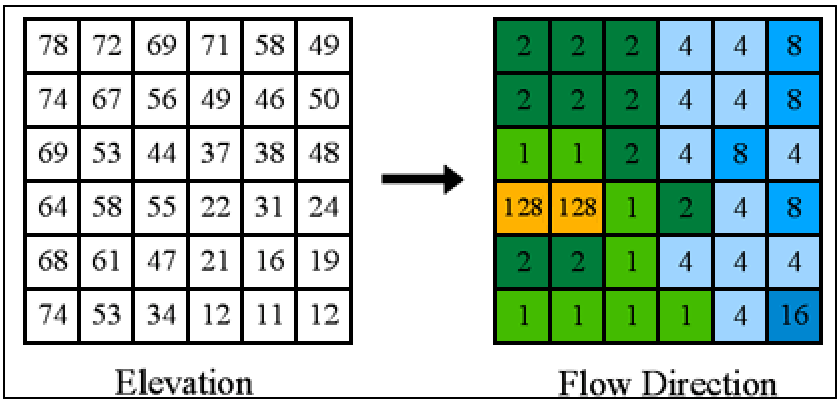

شكل (10):حساب خريطة اتجاه السريان المستنبطة من الخرائط الرقمية.

باستخدام هذا الأمر يحدد اتجاه الانحدار الأشد من اجل كل خلية، كل خلية تجاورها 8 خلايا ويقوم المعالج بتحديد أي الخلايا أكثر انخفاضا بالنسبة للخلية المركزية ويقرر اتجاه الجريان ومفاتيح اتجاه الجريان هي التالية:

1= East, 2=) Southeast, 4= South,

8= Southwest, 16= West, 32= Northwest, 64= North, 128= (Northeast

كما موضح في الشكل (11)

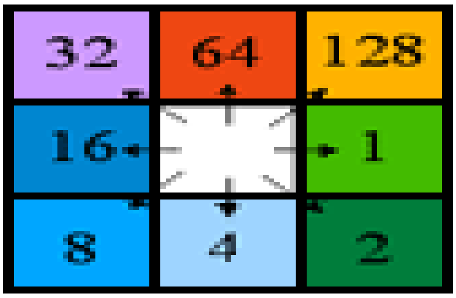

شكل (11) التمثيل الرقمي للاتجاهات (مفاتيح اتجاه الجريان).

فإذا سالت المياه من عنصر ألصورة الذي سقطت عليه (عنصر ألصورة المركزي في الشكل) إلى عنصر ألصورة المجار لها من أعلى ، فان عنصر ألصورة المقابل لعنصر ألصورة المركزي

في الخريطة الجديدة التي تمثل اتجاهات السريان سوف تكون قيمته 64، وبهذه الطريقة يتم التعرف على اتجاه السريان لكل عنصر صورة عن طريق قيمة اتجاه السريان له في الخريطة الخاصة باتجاه السريان .كما في الشكل (12) .

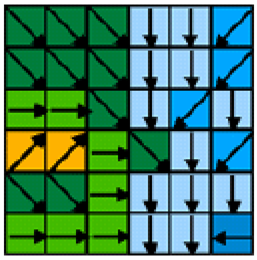

0	0	0	0	0	0
0	1	1	2	2	0
0	3	7	5	4	0
0	0	0	20	0	1
0	0	0	1	24	0
0	2	4	7	35	2

شكل (12): حساب خريطة تراكم السريان المستنبطة من التحليل الرقمي.

بعد حساب اتجاه السريان يتم حساب تراكم الجريان (تجمع الجريان) Flow Accumulation كما في الشكل (13) وهو خريطة تبين التراكم في كل بكسل بناء على ما يحيط به من عناصر ألصورة تصب الماء فيه.وتعتمد هذه الخريطة أساسا على خريطة اتجاهات السريان ، وبالتالي يتم استخلاص الوديان الموجودة في منطقة الدراسة .

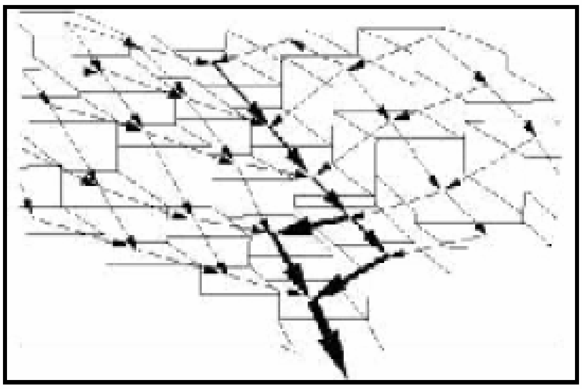

شكل (13): تجمع الجريان Flow Accumulation.

الإجراء التالي يختص بتحديد حوض الصرف (Basin) ، ويتم ذلك عن طريق تحديد سلسلة من البكسلات ينقسم سريان الماء عندها إلى اتجاهين متعارضين احدهما إلى داخل حوض الصرف والثاني إلى خارجه ويفصل بينهما خط تقسيم المياه Watershed.

اختيار مواقع للسدود

من اجل اختيار مواقع للسدود في منطقة الدراسة يتم إتباع التالي:-

- أولا:-

إن التصميم الأمثل للسدود (حصاد المياه) يتم من خلال رصد كميات السيول السنوية التي تسير في الأودية ، تعاني المنطقة الجافة من قلة وندرة أجهزة رصد السيول إضافة إلى المعوقات التي تعيق رصد السيول في المنطقة الجافة وتقلل من دقة البيانات الحقلية ، لذا كان الحل الأمثل هو تقدير تدفقات السيول السنوية من خلال الاعتماد على بيانات الأمطار .

تعتبر معدلات هطل الأمطار من أكثر الموارد الطبيعية أهمية في البيئات الجافة وشبه الجافة. وبالاعتماد على خمس محطات انوائية تحيط بمنطقة الدراسة تم اختيار أعلى كمية أمطار خلال احد أشهر السنة وابتداءا من سنة 2000 وحتى سنة 2008 . والأشكال (14) و (15) و (16) و (17) و (18) تبين العلاقة بين كمية الأمطار والسنين.

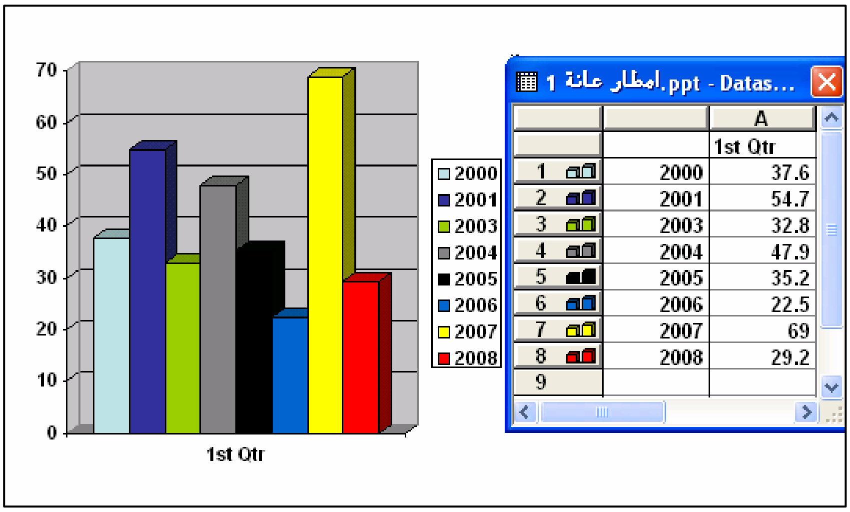

شكل (14): الأمطار المسجلة حسب محطة عانة.

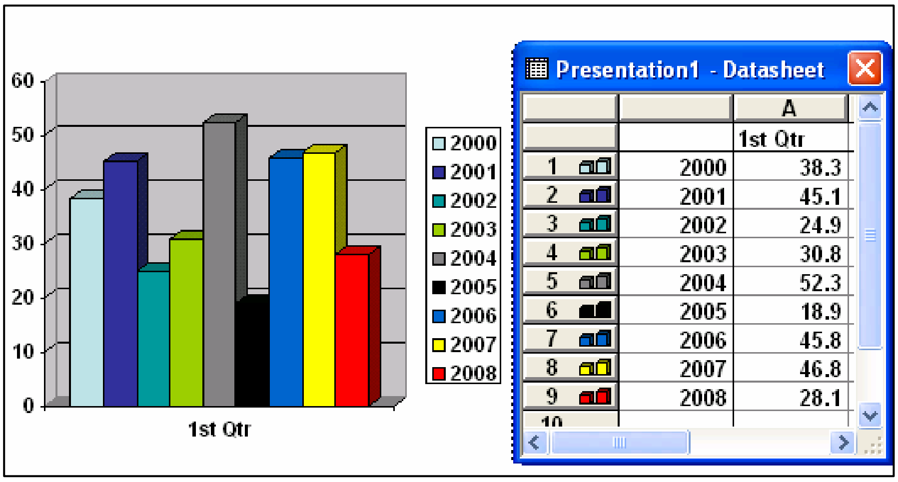

شكل (15): الأمطار المسجلة حسب محطة القائم.

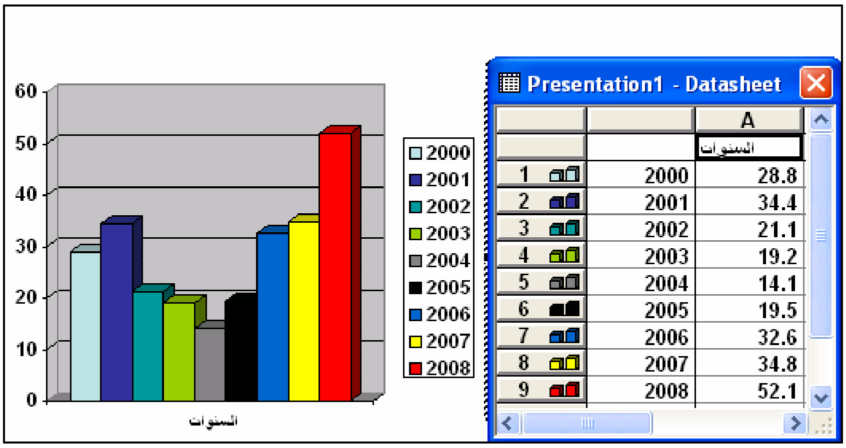

شكل (16): الأمطار المسجلة حسب محطة هيت.

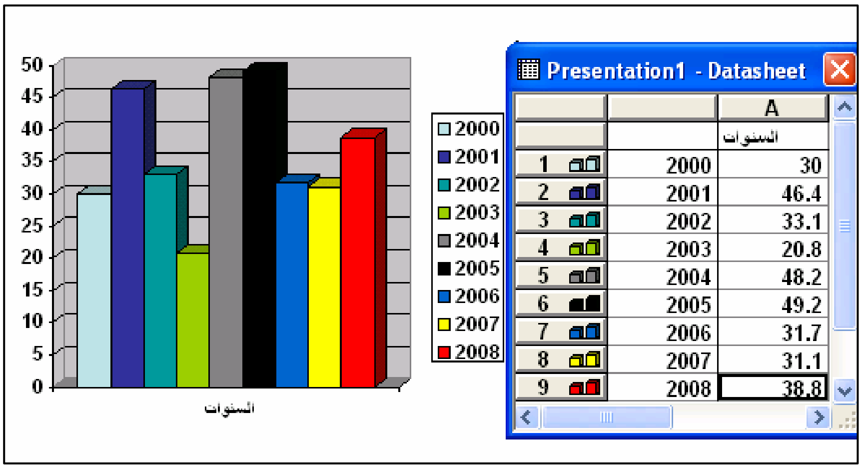

شكل (17): الأمطار المسجلة حسب محطة الرطبة.

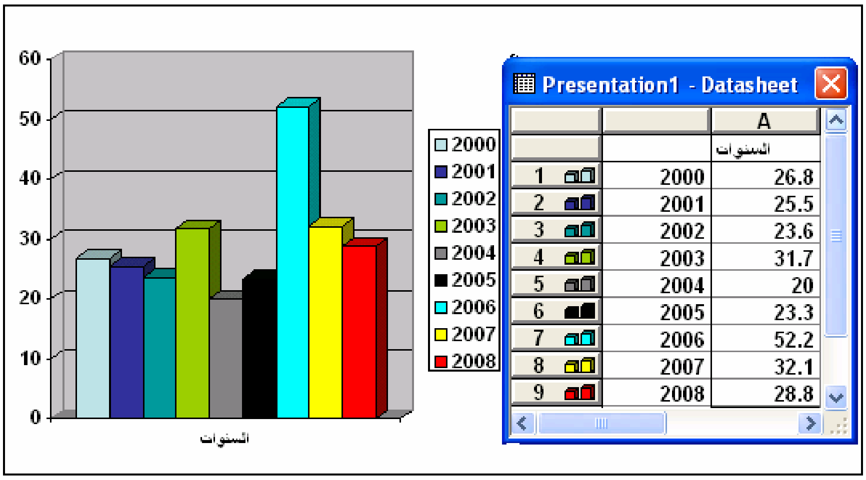

		A
		السنوات
1	2000	26.8
2	2001	25.5
3	2002	23.6
4	2003	31.7
5	2004	20
6	2005	23.3
7	2006	52.2
8	2007	32.1
9	2008	28.8

شكل (18): الأمطار المسجلة حسب محطة الرمادي.

- ثانيا :-

تحتاج هذه المرحلة إلى دمج طبقة الوديان المستخرجة مع خارطة حوض التغذية كما في الشكل (9)

- ثالثا:-

يتم استدعاء خارطة الخطوط الكنتورية ثم يتم تحويل الخطوط الكنتورية إلى نقاط (Points) اقل قيمتان هي (520، 530)وبالاعتماد على هذه القيم تم استنتاج احتمالين لاختيار مواقع السدود وكالاتي:-

1. الاحتمال الأول اختيار مواقع السدود بالاعتماد على اخفض منطقة والبالغ ارتفاعها (520). كما في الشكل (19)
2. الاحتمال الثاني اختيار مواقع السدود بالاعتماد على اخفض ارتفاع والبالغ (530).كما في الشكل (20) .

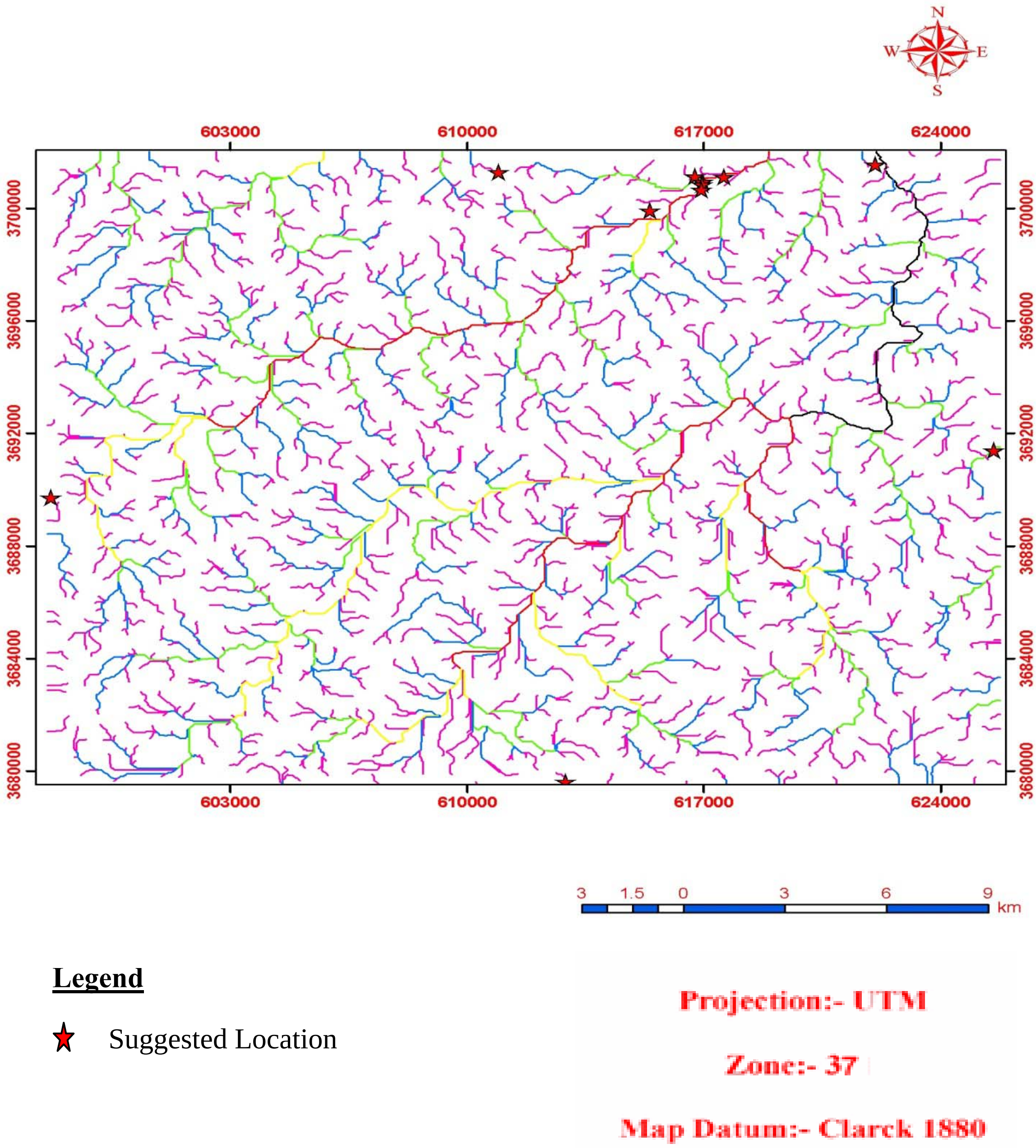

شكل (19): مواقع السدود المحتملة حسب الاحتمال الأول.

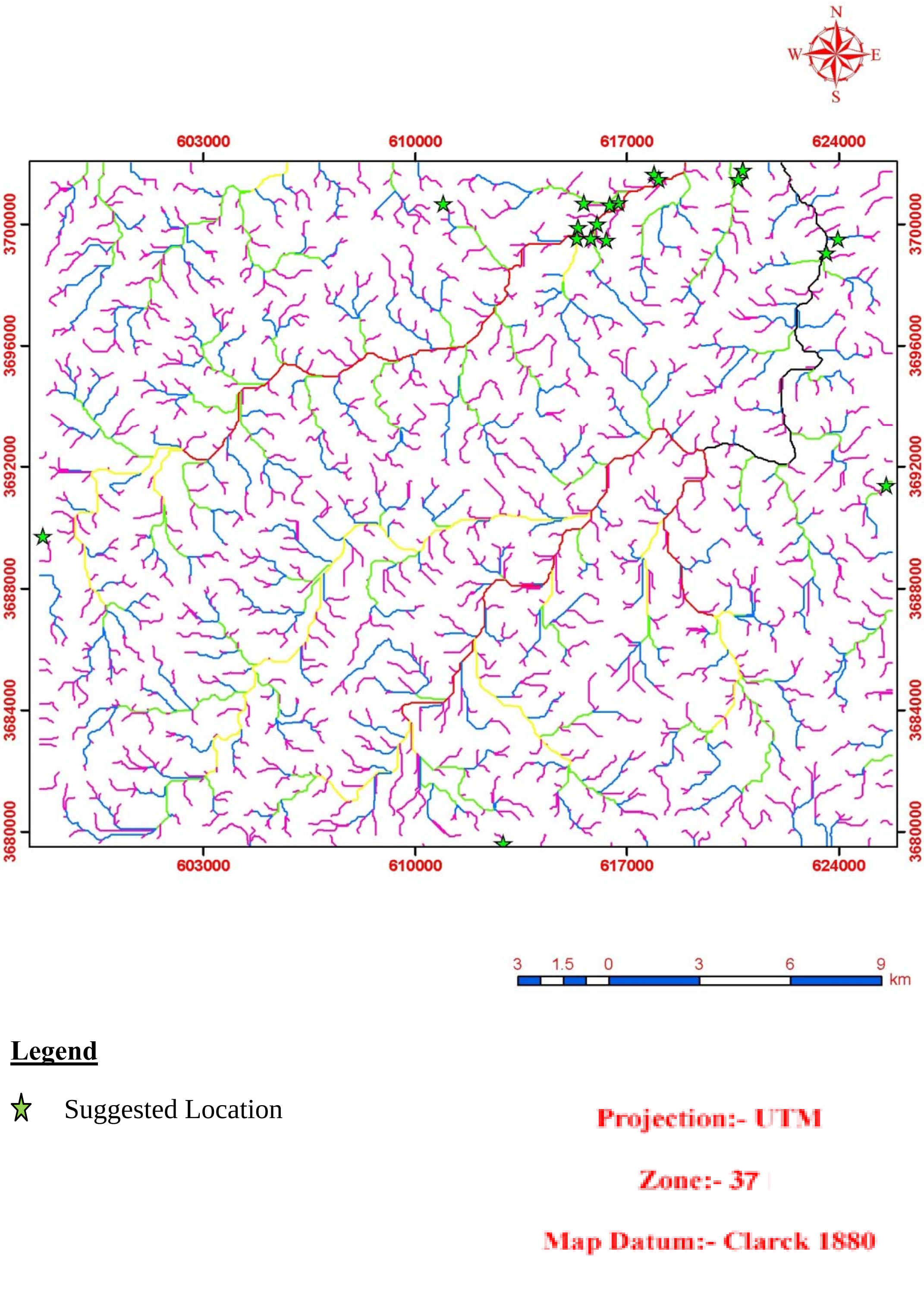

شكل (20): مواقع السدود المحتملة حسب الاحتمال الثاني.

مع الأخذ بعين الاعتبار المحددات التالية :

- أن يقع الموقع المحتمل ضمن حوض التغذية وبخلافه بهمل الموقع.
- أن يقع الموقع المقترح على احد تفرعات الوديان الموجودة في منطقة الدراسة.

بعد تطبيق الاحتمال الأول ظهرت مجموعة من المواقع المقترحة لكن بعد تطبيق الشرطين أعلاه تم حذف مجموعة من المواقع المقترحة لعدم استيفائها للشرطين السابقين. كما موضح في الشكل (21). علما انه تم إنشاء سدين في منطقة الدراسة وسميت بنفس اسم المنطقة.

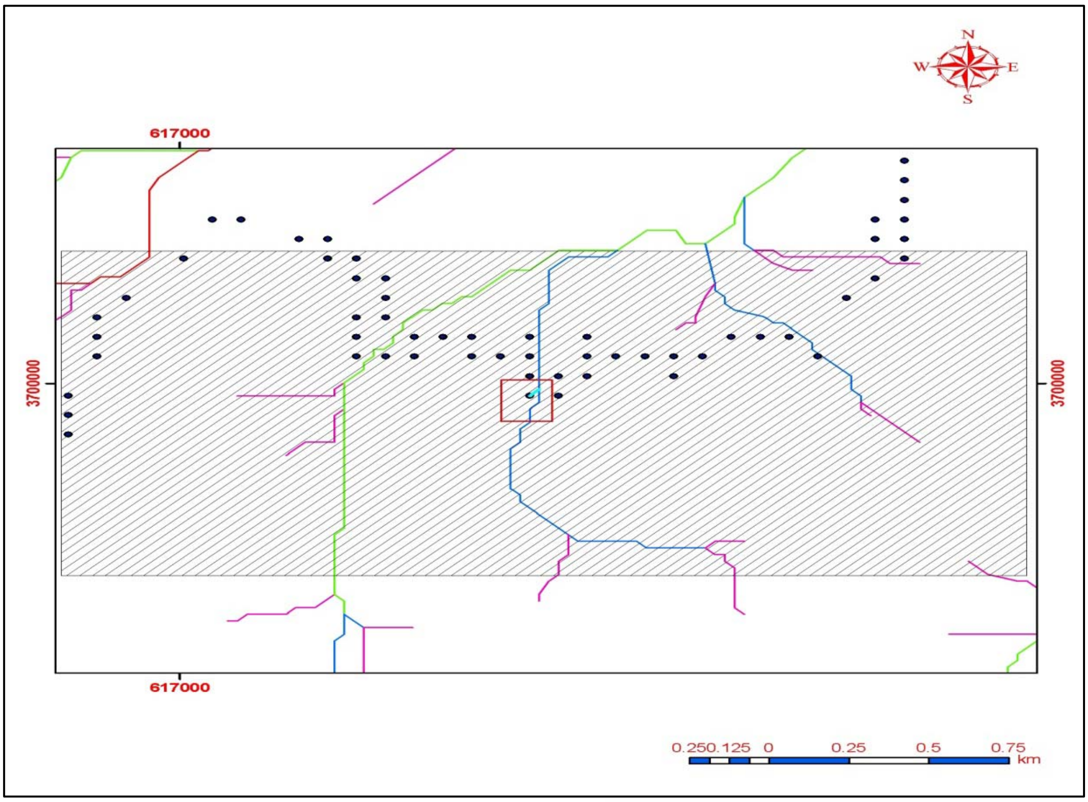

Projection:- UTM

Zone:- 37

Map Datum:- Clarck 1880

شكل (21): يوضح في حالة تطبيق الشرطين.

<u>الاستنتاجات</u>

1. يمكن إنتاج نموذج ارتفاع رقمي من الخرائط الطبوغرافية والمسح الميداني للارتفاعات أو يمكن الحصول عليه من خلال مرئيات الأقمار الصناعية المخصصة لإنتاج نماذج الارتفاعات الرقمية مثل القمر الصناعي (SPOT).
2. نتائج تحليل طبوغرافية السطح تعتبر كمدخلات لإجراء تحليل الخصائص الهيدرولوجية لسطح الأرض أي إن تحليل

الخصائص الهيدرولوجية يعتمد على نتائج تحليل طبوغرافية السطح .

3. لا يمكن حساب عرض الوادي وارتفاع الوادي وأكتاف الوادي والتي كانت عبارة عن شروط أو محددات لاختيار مواقع السدود بنموذج الارتفاع الرقمي المنتج وذلك بسبب دقته التي تصل إلى (30) متر وإنما يمكن حساب عرض الوادي عندما تكون دقة نموذج الارتفاع الرقمي اقل من (1) متر .

4. تم إجراء احتمالين لحساب مواقع لاختيار السدود بتطبيق الشروط التالية:

أ. أن يقع على احد الوديان أو فروعها، وفي حالة عدم وقوعه على أي من الوديان أو حد فروعه يهمل الموقع المقترح.

ب. أن يقع ضمن منطقة حوض التغذية Basin وفي حالة وقوع الموقع المقترح خارج حدود حوض التغذية يهمل.

المصادر

1. الأحمدي ، فهد سالم ،2001، " استخلاص المعالم الهيدرولوجية اللازمة لتصميم السدود بطرق آلية " ، المديرية العامة للمياه بمنطقة المدينة المنورة .
2. الحكيم ، سعيد حسن علي ،1976م ، " دراسة هيدرولوجية حوض نهر الفرات ف العراق " ،رسالة ماجستير ، مقدمة إلى كلية الآداب قسم الجغرافية، جامعة بغداد .
3. الحيالي ، عبد الأمير عباس ، 1995 م ،" نهر الفرات والأمن المائي العربي " ، أطروحة دكتوراه ، مقدمة إلى كلية التربية ، قسم الجغرافية ، الجامعة المستنصرية .
4. الدليمي ، خاف حسين علي ، 1996 م ،" وادي الفرات بين هيت والرمادي "، أطروحة دكتوراه ، مقدمة إلى كلية الآداب ، قسم علوم الأرض ، جامعة بغداد .
5. أل سعود ، مشاعل بنت محمد ، 2005م ،"تطبيقات تقنيات الاستشعار عن بعد والأساليب الجيودسية المتطورة في دراسة مورفو مترية الوديان الجافة "، رسالة ماجستير، مقدمة إلى كلية الآداب ، قسم الجغرافية ، جامعة الملك سعود .
6. العقابي ، احمد قاسم ، 2009م ،" الاستنباط الأمثل لنموذج الارتفاع الرقمي "، رسالة ماجستير ، مقدمة إلى كلية الهندسة ، قسم هندسة المساحة ، جامعة بغداد .
7. الفهداوي ، وليد حنوش حمد ، 2003م ،" التطبيقات الجيومورفولوجية لدراسة الموارد الطبيعية في منخفض الكعرة "، رسالة ماجستير ، مقدمة إلى كلية الآداب ، قسم الجغرافية ، جامعة الانبار .